AGU Reference Shelf 3

Rock Physics & Phase Relations

A Handbook of Physical Constants

Thomas J. Ahrens, Editor

Published under the aegis of the AGU Books Board

Library of Congress Cataloging-in-Publication Data

Rock physics and phase relations : a handbook of physical constants/
Thomas J. Ahrens, editor.
p. cm. — (AGU reference shelf, ISSN 1080-305X ; 3)
Includes bibliographical references and index.
ISBN 0-87590-853-5 (acid-free)
1. Petrology—Handbooks, manuals, etc. I. Ahrens, T. J. (Thomas J.), 1936– . II. Series.
QE433.8.R63 1995
552—dc20 95-3664
CIP

ISBN 0-87590-853-5
ISSN 1080-305X

This book is printed on acid-free paper. ♾

Published by
American Geophysical Union

Printed in the United States of America.

CONTENTS

PREFACE

The purpose of this Handbook is to provide, in highly accessible form, selected critical data for professional and student solid Earth and planetary geophysicists. Coverage of topics and authors were carefully chosen to fulfill these objectives.

These volumes represent the third version of the "Handbook of Physical Constants." Several generations of solid Earth scientists have found these handbooks to be the most frequently used item in their personal library. The first version of this Handbook was edited by F. Birch, J. F. Schairer, and H. Cecil Spicer and published in 1942 by the Geological Society of America (GSA) as Special Paper 36. The second edition, edited by Sydney P. Clark, Jr., was also published by GSA as Memoir 92 in 1966. Since 1966, our scientific knowledge of the Earth and planets has grown enormously, spurred by the discovery and verification of plate tectonics and the systematic exploration of the solar system.

The present revision was initiated, in part, by a 1989 chance remark by Alexandra Navrotsky asking what the Mineral Physics (now Mineral and Rock Physics) Committee of the American Geophysical Union could produce that would be a tangible useful product. At the time I responded, "update the Handbook of Physical Constants." As soon as these words were uttered, I realized that I could edit such a revised Handbook. I thank Raymond Jeanloz for his help with initial suggestions of topics, the AGU's Books Board, especially Ian McGregor, for encouragement and enthusiastic support. Ms. Susan Yamada, my assistant, deserves special thanks for her meticulous stewardship of these volumes. I thank the technical reviewers listed below whose efforts, in all cases, improved the manuscripts.

Thomas J. Ahrens, Editor
California Institute of Technology
Pasadena

Carl Agee
Thomas J. Ahrens
Orson Anderson
Don Anderson
George H. Brimhall
John Brodholt
J. Michael Brown
Bruce Buffett
Robert Butler
Clement Chase
Robert Creaser
Veronique Dehant
Alfred G. Duba
Larry Finger
Michael Gaffey
Carey Gazis
Michael Gurnis
William W. Hay
Thomas Heaton
Thomas Herring
Joel Ita
Andreas K. Kronenberg
Robert A. Langel
John Longhi
Guenter W. Lugmair
Stephen Mackwell
Gerald M. Mavko
Walter D. Mooney
Herbert Palme
Dean Presnall
Richard H. Rapp
Justin Revenaugh
Rich Reynolds
Robert Reynolds
Yanick Ricard
Frank Richter
William I. Rose, Jr.
George Rossman
John Sass
Surendra K. Saxena
Ulrich Schmucker
Ricardo Schwarz
Doug E. Smylie
Carol Stein
Maureen Steiner
Lars Stixrude
Edward Stolper
Stuart Ross Taylor
Jeannot Trampert
Marius Vassiliou
Richard P. Von Herzen
John M. Wahr
Yuk Yung

Classification of Rocks and Their Abundances on the Earth

Myron G. Best

1. INTRODUCTION

Rocks comprising the lithosphere have formed by interactions between matter and various forms of energy--chiefly gravitational and thermal--over the 4.5 Ga history of the Earth. The wide range of rock-forming geologic processes and environmental conditions (intensive parameters) of temperature (T), pressure (P), and concentrations of chemical species related to these complex interactions has created a similarly wide spectrum of rock properties. Significant widely-ranging rock properties are: (1) *Texture*, the size and shape of mineral grains and amount of glass (crystalline and amorphous solids, respectively). (2) *Structure* of grain aggregates, such as bedding. (3) *Composition* of mineral grains comprising the rock, their relative proportions (mode), and the elemental and isotopic composition of the bulk rock.

Bodies of rock formed within a more or less unified geologic system over a particular period of time are rarely strictly homogeneous on any scale of observation. Many rock bodies are anisotropic with regard to texture and structure, which is reflected in anisotropic physical properties such as elastic wave velocity.

Three main categories of rock--magmatic, sedimentary, and metamorphic--are recognized on the basis of geologic processes of origin and indirectly on P-T conditions.
(1) *Magmatic*, or igneous, rocks form by cooling and consequent consolidation of magma at any P, either at depth in the lithosphere or on the surface; these rocks were the first to form on the primitive cooling Earth.
(2) *Sedimentary* rocks form by consolidation of particulate or dissolved material derived by weathering of older rock and deposited by water, ice, organisms, or wind on the surface of the Earth; deposition and processes of consolidation occur at low, near-surface P and T.
(3) *Metamorphic* rocks form by recrystallization in the solid state, usually in the presence of aqueous fluids, changing the texture, structure, and/or composition of the *protolith*--the sedimentary, magmatic, or even metamorphic precursor. Metamorphism is the result of significant changes in the geologic environment from that in which the protolith originated. Temperatures of metamorphism are elevated but submagmatic, pressures range widely, and nonhydrostatic (deviatoric) states of stress are common.

Distinguishing between these three basic kinds of rocks is readily accomplished in most cases, but some instances demand attention to multiple criteria [12, p. 7]. Classification within each of the three basic groups of rocks which follows is based chiefly upon their texture and composition as can be observed mostly in hand sample or outcrop. These are essentially descriptive or nongenetic classifications for the nonspecialist which require little or no detailed laboratory analyses and extensive training in petrology. Texture and composition contain a wealth of genetic information, but the tools to decipher them are beyond the scope of this brief section.

It must be kept in mind that any subdividing by geologists of the broad spectrum of texture and composition in rocks is mostly arbitrary or follows tradition; boundary lines in nomenclature diagrams are *for the convenience of the user and do not denote naturally-occurring divisions.*

M. G. Best, Department of Geology, Brigham Young University, Provo, Utah 84602

Rock Physics and Phase Relations
A Handbook of Physical Constants
AGU Reference Shelf 3

2. CLASSIFICATION OF MAGMATIC ROCKS

Figure 1 presents an overview of the textural-compositional aspects of the most common magmatic rock types and groups that occur in relatively large volume in subduction zone settings, but not exclusively in them. Volcanic and plutonic (intrusive magmatic) environments grade continuously from one to the other, as do many textures, including:

(1) *Glassy*, formed by quick quenching of silicate melt.

(2) *Aphanitic*, microcrystalline, grains are too small to be identifiable without a microscope.

(3) *Phaneritic*, all minerals grains are large enough to be identifiable by naked eye; formed in deep plutons.

(4) *Porphyritic*, larger crystals (phenocrysts) embedded in a finer grained or glassy matrix.

Mineral associations in Figure 1 are useful aids in classifying. Compositional modifiers--*silicic, felsic, intermediate, mafic*, and *ultramafic*--defined chiefly on the basis of mineral proportions but indirectly on concentration of silica can be applied regardless of texture.

The classification of magmatic rocks has recently been systematized by the International Union of Geological Sciences [13] and their guidelines are followed here, with simplifications.

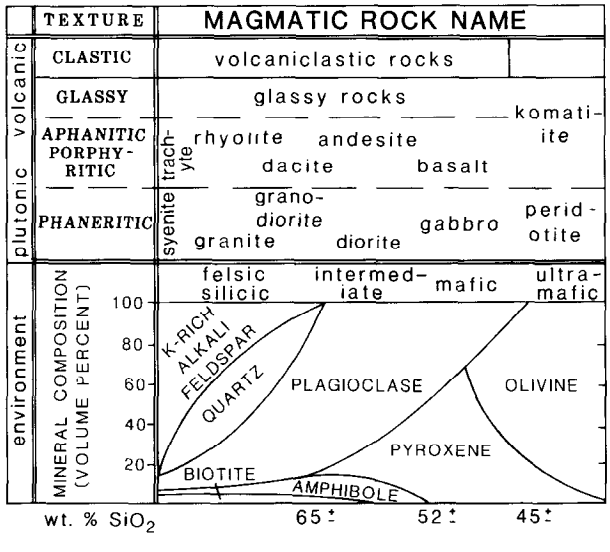

Fig. 1. Classification of common magmatic rock types found commonly, but not exclusively, in subduction zones. Note general mineral associations. Komatiite is a rare but significant rock formed from extruded lava flows almost exclusively in the Archean (>2500 Ma). See Table 4 for mineral compositions.

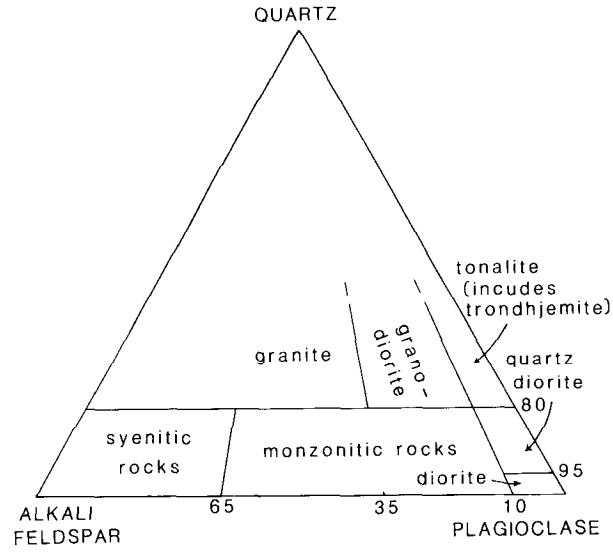

Fig. 2. Classification of phaneritic magmatic rocks containing mostly quartz, potassium-rich alkali feldspar, and plagioclase [simplified from 13]. Note that the rock-type names are independent of mafic (ferromagnesian) minerals (but see Figure 1); hence, the relative proportions of quartz and feldspars must be recalculated from the whole-rock mode. No magmatic rocks contain more than about 40 percent quartz. See Table 4 for mineral compositions.

Names of phaneritic rock types containing mostly quartz and feldspar, but including some biotite and amphibole, are shown in Figure 2. Three special textures in mostly felsic rocks warrant special base names (appended compositional prefixes are optional) as follows:

(1) *Pegmatite*, exceptionally coarse-grained rock; grains generally >1 cm and locally a meter or more.

(2) *Aplite*, fine phaneritic, sugary-textured dike rock.

(3) *Porphyry*, plutonic rock containing phenocrysts in an aphanitic matrix.

Some phaneritic rocks, known as *anorthosite*, are composed of plagioclase, no quartz, and little or no mafic minerals. Phaneritic rocks containing only pyroxene and olivine are classified in Figure 3. These peridotites and pyroxenites occur in some large intrusions of basaltic magma which have experienced crystal fractionation during cooling. But their chief occurrence is in the upper mantle of the Earth, pieces of which commonly possessing metamorphic texture are found as inclusions in alkali basalt and kimberlite (see below) and in *ophiolite*--slices kilometers long of oceanic lithosphere emplaced onto crust overlying subducting plates (Table 1).

In the absence of a whole-rock chemical analysis, glassy

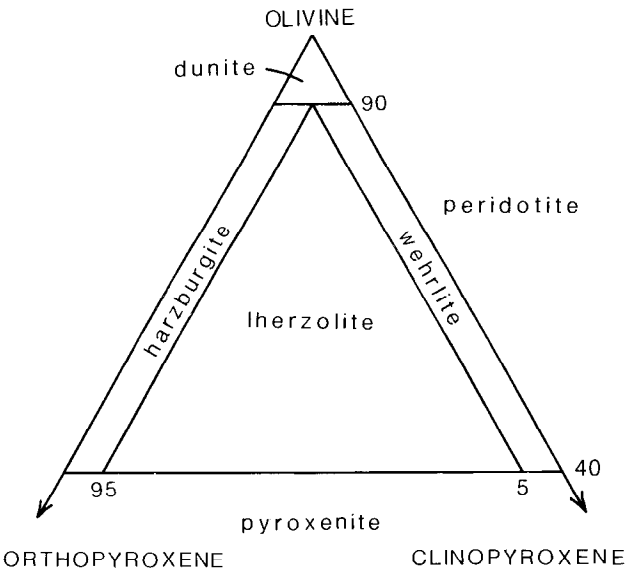

Fig. 3. Classification of phaneritic rocks containing only olivine, clinopyroxene, and orthopyroxene [13]. Rocks containing between 90 and 40 percent olivine are peridotite. Rocks containing <40 percent olivine are pyroxenite. See Table 4 for mineral compositions.

and aphanitic volcanic rocks can only be classified on the basis of their phenocrysts, if present, using Figure 1 as a guide. Preferrably, the amounts of total alkalies and silica in a whole-rock chemical analysis in such rocks can be plotted in Figure 4. Classification based on phenocrysts alone is less accurate because the matrix can contain large amounts of minerals not occurring as phenocrysts; thus an aphanitic rock containing sparse phenocrysts of only plagioclase could be called andesite whereas a whole-rock analysis might reveal it to be rhyolite. The basalt field in Figure 4 can be subdivided on the basis of degree of silica saturation [2]; basalts containing normative nepheline are *alkali basalt* whereas those without are *subalkali* or *tholeiitic basalt*. Color is not a basis for classification of aphanitic and glassy rocks, because they are commonly dark colored regardless of composition; use of "basalt" for all dark aphanitic rock should be avoided.

Wholly-glassy rocks may be called *obsidian* if massive, *pumice* if highly vesicular (frothy), and *perlite* if pervaded by concentric cracks formed during hydration; compositional prefixes from Figure 1 or 4 may be applied, as for example, rhyolite obsidian, basalt pumice, etc. Glassy rocks containing phenocrysts may be labeled *vitrophyre*, e.g., dacite vitrophyre.

In contrast to the volcanic rocks produced by solidification of coherent magma, volcaniclastic rocks [2, 6, 8, and 9] consist of clasts (fragments) produced by volcanic processes. Volcaniclasts are classified by (1) size, as ash (<2mm), lapilli (2-64mm), and block (>64mm; bomb if rounded rather than angular); (2) composition, as vitric (glass), crystal, and lithic (rock); (3) origin, as cognate or juvenile derived from the erupting magma and accidental, xenocrystic, or xenolithic derived by fragmentation of older rock. Consolidated deposits of ash and mixed ash and lapilli are known as *tuff* and *lapilli tuff*, respectively. *Volcanic breccia* refers to consolidated deposits of blocks between which is finer cementing material; many volcanic breccias are formed by movement of wet mud or debris flows on steep slopes of volcanoes, and the Indonesian term *lahar* can be used. *Agglomerate* refers to a consolidated aggregate of bombs. Explosive eruptions produce widespread, well-sorted air-fall tuff and unsorted ash-flow tuff and lapilli ash-flow tuff, or *ignimbrite*, from pyroclastic flows (nuee ardente) [6 and 9]. Compositional names may be applied to any volcaniclastic rock, such as rhyolite lapilli tuff, dacite breccia, etc.

Epiclastic, or sedimentary, processes move volcanic material from the site of deposition and redeposit it elsewhere. Because of the common difficulty [6] in distinguishing primary volcanic, reworked volcanic, and epiclastic deposits, a non-genetic classification based on particle size may be employed [8]. This classification simply uses rock names for familiar sedimentary rocks such as sandstone, conglomerate, etc. based on grain size, but prefixed by "volcanic", such as volcanic sandstone.

Numerous, compositionally unusual, highly alkaline but relatively rare rock types are not indicated on Figures 1-4 but are discussed elsewhere [13 and 17]. One intrusive rock of this kind is *kimberlite* [2] which, although very

TABLE 1. Seismic structure of the oceanic crust [5] and relation of layers below sedimentary layer to ophiolite sequences [2].

Layer	Thickness (km)	Ophiolitic rocks
1	<1	(chert, limestone)
2A	0-1.5	basaltic lava flows
2B	0.6-1.3	sheeted mafic dikes
3A	2-3	gabbroic
3B	2-5	magmaticultramafic
		mantle peridotite

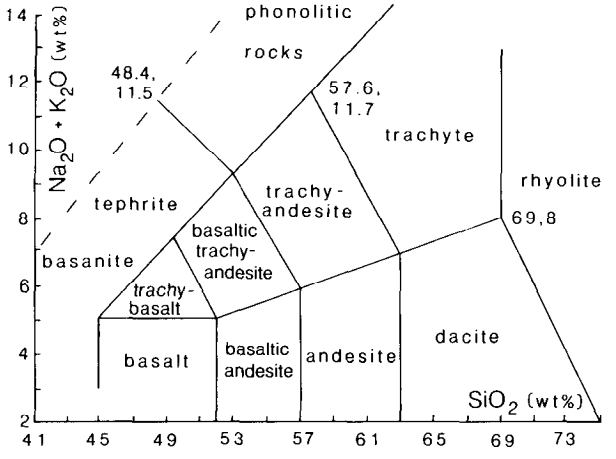

Fig. 4. Chemical classification of glassy and aphanitic volcanic rocks [generalized from 13].

rare, is important because some contain diamond and other upper mantle rock and mineral inclusions.

3. CLASSIFICATION OF SEDIMENTARY ROCKS

Sedimentary rocks originate through a complex sequence of physical, chemical, and biological processes [3 and 4]. Magmatic, sedimentary, and metamorphic source rocks are broken down by weathering to form (1) resistant residual particles, chiefly silicate minerals and lithic fragments, (2) secondary minerals such as clays and iron oxides, and (3) water soluble ions of calcium, sodium, potassium, silica, etc. Weathered material is transported via water, ice, or wind to sites of deposition at mainly lower elevations. There, mineral grains drop to the depositional surface; dissolved matter precipitates either inorganically, where sufficiently concentrated, or by organic processes. Decaying plant and animal residues may also be introduced into the depostional environment. Lithification (consolidation) occurs as deposited material becomes more deeply buried under younger deposits; the increasing P compacts the sediment and aqueous pore solutions interact with the deposited particles to form new, cementing diagenetic (authigenic) minerals.

Sedimentary rocks are thus made of four basic constituents--terrigenous siliclastic particles, chemical and/or biological precipitates, carbonaceous matter, and authigenic material. Most sedimentary rocks are made of one of the first three constituents, which is the basis of the classification of sedimentary rocks [4].

Siliclastic rocks are classified according to their dominant particle size in Table 2. *Diamictite* is a useful nongenetic name for any poorly-sorted rock containing sand or larger size particles in a consolidated, muddy matrix. *Sandstones* contain dominantly sand-size particles that are mostly quartz, feldspar, and polygranular rock (lithic) fragments. Among the dozens of published classification schemes for sandstones [4], most geologists have adopted that of Gilbert [19] shown in Figure 5. *Arenites* are sandstones that contain little or no matrix of particles <0.03mm (fine silt and clay) and sand grains are cemented by carbonate or silica minerals. *Wackes* contain perceptible matrix. Arenites and wackes may be further subdivided on the basis of proportions of quartz, feldspar, and lithic fragments (Figure 5). Not shown in Figure 5 are *arkose,* a loosely defined name for a feldspathic sandstone, and *graywacke,* a controversial name for dark, gray to green, firmly indurated sandstone that is generally a lithic or feldspathic wacke. Siliclastic sedimentary rocks made of silt- and clay-size particles are conventionally referred to as *shale*, but some geologists reserve that term only for laminated (fissile) fine-grained rocks and use *mudrock* for isotropic rocks.

Chemical/biochemical rocks made dominantly of chemical and biochemical precipitates are classified initially by composition. *Limestone* and *dolostone (rock dolomite)* are relatively pure aggregates of calcite and dolomite, respectively. Rare carbonate rocks containing substantial amounts of siliclastic material can be classified according to Mount [14]. Detailed textural classifications of limestones are by Durham [7] and Folk [10]. Rare marine and nonmarine evaporite deposits include *rock salt*, *rock gypsum*, and *rock anhydrite,* which are relatively pure aggregates of the minerals halite, gypsum, and anhydrite, respectively. *Chert* is a rock made of quartz, chalcedony, and/or

TABLE 2. Classification of siliclastic sedimentary rocks composed mostly of terrigenous siliclastic particles [3,4].

Particle (size)	Rock name
boulder, cobble, and pebble (>2mm)	conglomerate; breccia if angular particles
sand (2-1/16mm)	sandstone
silt (1/16-1/256mm) and clay (<1/256mm)	mudrock; shale if fissile

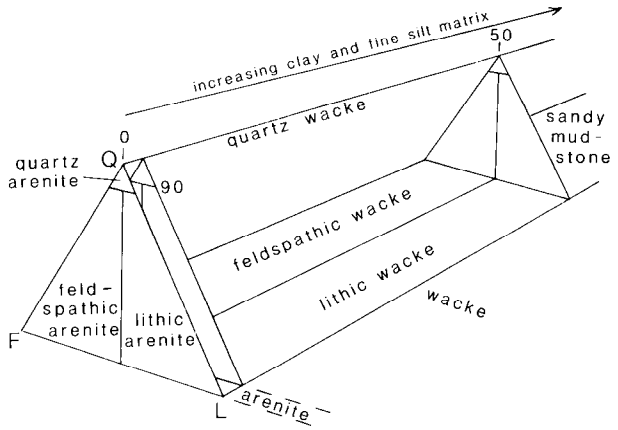

Fig. 5. Classification of sandstones according to proportions of quartz (Q), feldspar (F), and lithic (L) fragments and clay [19].

opal. There is no consensus regarding the classification of iron-rich (>15 weight percent Fe) sedimentary rocks, but the terms *ironstone* and *iron formation* are widely employed; *taconite* is a cherty iron formation. Equally uncertain is the label for phosphate-rich (>15 weight percent P_2O_5) rocks, but *phosphorite* is common.

Carbonaceous rocks are principally coal, which includes, in order of decreasing moisture and increasing carbon and hence thermal energy content, *lignite, bituminous coal*, and *anthracite* (the latter commonly considered to be metamorphic).

4. CLASSIFICATION OF METAMORPHIC ROCKS

Metamorphic rocks can be classified on different bases [2 and 19]: (1) Environment or field occurrence, such as contact, regional; (2) P-T conditions, inherent in the concepts of metamorphic facies, the geographically constrained metamorphic zones, and metamorphic grade based on relative T; (3) chemical composition, such as calcareous, mafic, etc.; (4) protolith, expressed in labels such as metabasalt, metaconglomerate, etc.; (5) texture and structure; (6) composition. Of these six bases, the last two furnish the most direct, and conventional [19], approach for classification of the outcrop and hand sample without resort to specialized and interpretive analyses. Because compositions of metamorphic rocks encompass much of the compositional spectrum of both magmatic and sedimentary rocks, and more, a convenient threefold division based on the manifestation of foliation is employed. *Foliation* is any pervasive planar texture or structure in the rock [2] and, although locally a relict bedding in metasedimentary rocks, it generally reflects the state of stress in the metamorphic system, whether nonhydrostatic (producing anisotropic, foliated texture/structure) or hydrostatic (isotropic). Foliation also reflects metamorphic grade in many rocks because the most strongly foliated rocks contain abundant micas and chlorites that are stable at lower grade (lower T) whereas poorly or non- foliated rocks dominated by feldspars, pyroxenes, garnets, etc. form at higher T.

Because texture/structure is not quantifiable, no "box" or triangular diagrams can be employed; rather, definition of dominant characteristics of a representative sample of each particular rock type [2 and 19] is listed in the following sections. Use of compositional and textural modifiers of the base name is encouraged to make the rock name more specific, e.g., mica-quartz schist, plagioclase-hornblende schist, lineated phyllite, etc. Note that widespread plagioclase in medium- and high-grade metamorphic rocks generally occurs as equidimensional grains, similar to quartz, unlike the tabular grains of magmatic rocks.

4.1. Conspicuously Foliated Rocks

These readily break with a hammer blow along subparallel surfaces usually because of abundant platy mineral grains, such as micas and chlorites.

Slate. Aphanitic, tougher than shale, has a dull luster.

Phyllite. Aphanitic, but because of slightly coarser grain size than slate have a lustrous sheen on foliation surfaces; transitional in character between slate and schist.

Schist. Phaneritic, have weak to well-developed layers of contrasting mineral composition, e.g., layers rich in quartz and feldspar alternating with layers rich in mafic minerals, commonly lineated (linear features observable on foliation surfaces).

4.2. Weakly Foliated Rocks

Subparallel to irregular foliation surfaces and/or compositional layers are evident but not mechanically significant--the rock will tend to break across rather than parallel to foliation.

Gneiss. Phaneritic, generally coarser grained then schist; commonly contain abundant feldspar and quartz alternating with mafic layers or lenses.

Mylonite. Generally aphanitic, but relics of once larger grains may be surrounded by streaky foliation; commonly quartz-rich and hence resembles chert; produced by intense, localized ductile shear deep in crust.

4.3. Nonfoliated to Inconspicuously Foliated Rocks

Characteristically break conchoidally (like glass) because of the more or less isotropic texture; classified chiefly on the basis of composition.

Greenstone. Aphanitic, green because of abundant chlorite and amphibole; relict magmatic minerals may be present in this low-grade rock.

Amphibolite. Phaneritic, dominantly amphibole and plagioclase, but red garnet also common; may be lineated because of alignment of needle-like amphibole grains.

Eclogite. Fine phaneritic aggregate of Na-Al pyroxene and Mg-Fe-Al-Ca garnet; formed at high P.

Serpentinite. Aphanitic aggregate of chiefly serpentine minerals (hydrous magnesian silicates).

Quartzite. Generally fine phaneritic grain size; relict bedding may be conspicuous.

Marble and *dolomarble*. White to gray aggregates of calcite and dolomite, respectively; locally, uneven and streaked layers of silicate minerals and fine graphite mark relict bedding.

Hornfels. Aphanitic to fine phaneritic; relict bedding may be apparent; wall-rock around magmatic intrusions.

TABLE 3. Typical protoliths of common metamorphic rock types.

Rock type	Protolith
slate, phyllite	mudrock, rarely tuff
schist, gneiss	mudrock, sandstones, magmatic rocks
greenstone, amphibolite, eclogite	mafic to intermediate magmatic rocks
serpentinite rocks	ultramafic magmatic
quartzite	quartz arenite, chert
marbles	carbonate rocks
mylonite, hornfels	any rock

TABLE 4. Abundances of rock types and minerals in the continental crust according to Ronov and Yaroshevsky [16]. They assume the lower half of the crust is made of mafic rock.

Rock	Volume (%)
Mudrock/shale	4.2
Chemical/biochemical rocks	2.0
Sandstone	1.7
Granitic	10.4
Dioritic	11.2
Syenitic	0.4
Ultramafic	0.2
Mafic magmatic and metamorphic rocks	42.5
Gneiss	21.4
Schist	5.1
Marble	0.9
Mineral	
Clays and chlorites complex hydrous aluminum silicates containing Mg, Fe, K, Na, Ca	4.6
Calcite $CaCO_3$	1.5
Dolomite $CaMg(CO_3)_2$	0.5
Quartz SiO_2	12
Alkali feldspar $(K,Na)AlSi_3O_8$	12
Plagioclase $(Na,Ca)(Al,Si)_4O_8$	39
Micas $(K,Na,Ca)_2(Al,Mg,Fe,Ti)_{4-6}(Si,Al)_8O_{20}(OH,F)_4$	5
Amphiboles $(Ca,Na,K)_{2-3}(Mg,Fe,Al,Ti)_5(Si,Al)_8O_{22}(OH)_2$	5
Pyroxenes Ortho $(Mg,Fe)SiO_3$ Clino $(Ca,Na)(Mg,Fe,Al,Cr,Ti)(Si,Al)_2O_6$	11
Olivine $(Mg,Fe)_2SiO_4$	3
Fe-Ti oxides	1.5
Others	4.9

Typical protoliths of these metamorphic rock types are listed in Table 3.

Though not conventionally considered as metamorphic, rocks permeated by relatively large volumes of hot aqueous, or hydrothermal, solutions have experienced wholesale conversion of primary minerals into various alteration assemblages; for example, magmatic rocks are converted into clays, micas, quartz, and other alteration products and carbonate minerals in sedimentary rocks into silicates. Such *hydrothermally altered rocks* formed in environments of high fluid/rock ratio are widespread surrounding shallow intrusions emplaced into cooler country rocks where ore deposits have formed [e.g., 11].

5. ABUNDANCES OF ROCK TYPES

The crust of the Earth is inhomogeneous on almost any scale of observation. Estimated abundances of rock types in the deep continental crust are strongly model dependent [18], but despite these and other uncertainties, some generalities can be made (Table 4) [4, 9, and 16]. Presently, sedimentary rocks cover about 80 percent of the total land surface of the globe to a depth of about 2 km on cratons and about 10 km on continental margins and in orogenic belts. Less than 1 km of sedimentary material covers the sea floor over a mafic crust variably altered by sea-floor metamorphism that occurs near spreading ridges [2]. Somewhat more than two-thirds of the volume of sedimentary rock lies in the continents.

REFERENCES

1. Bates, R.L. and J.A. Jackson, *Glossary of Geology, Third Edition*, 788 pp., American Geological Institute, Alexandria, Virginia, 1987.
2. Best, M.G., *Igneous and Metamorphic Petrology*, 630 pp., W.H. Freeman, San Francisco, 1982.
3. Blatt, H., *Sedimentary Petrology, Second Edition*, 514 pp., W.H. Freeman, New York, 1992.
4. Boggs, S., Jr., *Petrology of Sedimentary Rocks*, 707 pp., Macmillan, New York, 1992.
5. Basaltic Volcanism Study Project, *Basaltic Volcanism on the Terrestrial Planets*, 1286 pp., Pergamon Press, New York, 1981.
6. Cas, R.A.F. and J.V. Wright, *Volcanic Successions, Modern and Ancient: A Geological Approach to Processes, Products, and Successions*, 528 pp., Allen and Unwin, London, 1987.
7. Dunham, R.J., Classification of carbonate rocks according to depositional texture, in Classification of Carbonate Rocks, edited by W.E. Ham, pp. 108-121, Am. Assoc. Petroleum Geol. Mem. 1, 1962.
8. Fisher, R.V., Proposed classification of volcanicalstic sediments and rocks, *Geol. Soc. Am. Bull., 72*, 1409-1414, 1961.
9. Fisher, R.V. and H.-U. Schmincke, *Pyroclastic Rocks*, 472 pp., Springer-Verlag, New York, 1984.
10. Folk, R.L., Practical petrographic classification of limestones, *Am. Assoc. Petroleum Geol. Bull., 43*, 1-38, 1959.
11. Guilbert, J.M. and C.F. Park, Jr., *The Geology of Ore Deposits*, 985 pp., W.H. Freeman, New York, 1986.
12. Grout, F.F., *Petrography and Petrology*, 522 pp., McGraw-Hill, New York, 1932.
13. Le Maitre, R.W., *A Classification of Igneous Rocks and Glossary of Terms: Recommendations of the International Union of Geological Sciences, Subcommision on the Systematics of Igneous Rocks*, 193 pp., Blackwell Scientific, Oxford, 1989.
14. Mount, J., Mixed siliclastic and carbonate sediments: A proposed first-order textural compositional classification, Sedimentology, 32, 435-442, 1985.
15. Pettijohn, F.J., *Sedimentary Rocks, 3rd ed.*, 628 pp. Harper and Row, New York, 1975.
16. Ronov, A.B. and A.A. Yaroshevsky, Chemical Composition of the Earth's Crust, in *The Earth's Crust and Upper Mantle*, edited by P.J. Hart, pp. 37-57, American Geophysical Union Monograph 13, 1969
17. Sorensen, H., (Ed.), *The Alkaline Rocks*, 622 pp., John Wiley and Sons, New York, 1974.
18. Taylor, S.R. and S.M. McLennan, *The Continental Crust: Its Composition and Evolution*, 312 pp., Blackwell, Oxford, 1985.
19. Williams, H., F.J. Turner, and C.M. Gilbert, *Petrography: An Introduction to the Study of Rocks in Thin Section, Second Edition*, 626 pp., W.H. Freeman, New York, 1982.

Sediments and Soils: Chemistry and Abundances

Scott M. McLennan

1. INTRODUCTION

The continental crust is widely exposed to the hydrosphere, biosphere and atmosphere. Most primary igneous and metamorphic minerals within the crust, typically forming at elevated pressures and temperatures, are thermodynamically unstable at or near the surface of the earth. Accordingly, a fundamental process of crust-exosphere interaction is the chemical and physical weathering of crustal rocks to form soils and sediment. Calculating the magnitude and efficiency of this process is not a simple matter for a number of reasons, not least being that some 70% of the earth's weathering profiles are formed on sediments and sedimentary rocks and that clastic sediments are themselves largely derived from pre-existing sedimentary rocks.

2. SEDIMENTS

2.1. Mass and Fluxes of Sediment

The overall sedimentary mass is reasonably well known to be about 2.7×10^{24} g, of which between 85-90% is found on continents, including the exposed continents, submerged platforms and passive margins [41]. Precise estimates of the mass of unconsolidated sediment (as opposed to sedimentary rocks) are not readily available and are difficult to make. Sediment consolidation is a complex process with no simple relationship with either age or depth of burial. Estimates of the mass of Cenozoic sediments and sedimentary rocks, by tectonic setting, are given in Table 1. A number of workers have examined changes in the sedimentary mass over time in order to understand sedimentary recycling processes [e.g., 10-12, 32, 33, 40, 41] and the reader is referred there for further discussion.

In contrast, considerable effort has gone into estimating sediment flux from continents into sedimentary basins (notably oceans). Table 2 lists estimates for the particulate flux to the oceans according to transport mechanism. The overall flux is estimated at about 22×10^{15} g yr^{-1} and is dominated by fluvial transport, especially of suspended material. Applicability of such estimates, even for the recent geological past, is uncertain due to strong anthropogenic effects (see below).

Table 3 lists the suspended sediment fluxes to the oceans for the major rivers of the world. An important feature is the large anthropogenic effects on riverine sediment fluxes associated with dam construction and agricultural practice [e.g., 22-24]. Thus, the Colorado River had one of the largest sediment yields prior to dam construction, but now delivers negligible sediment to the lower reaches. Other rivers that have been or shortly will be similarly affected include the Nile, Indus, Mississippi, Zambesi and others. In contrast, accelerated erosion resulting from agricultural activity has increased sediment flux for many rivers; for example, the Huangho River sediment load may be an order of magnitude greater than pre-agricultural rates [25]. In Table 4, suspended flux is compiled according to region. The present global flux of suspended sediment is about 20×10^{15} g yr^{-1}, however if the competing effects of dam building and accelerated erosion are accounted for, the pre-agricultural rate may be as low as $7\text{-}13 \times 10^{15}$ g yr^{-1} [21-24], resulting in an overall sediment flux to the oceans of about $9\text{-}15 \times 10^{15}$ g yr^{-1}, all other rates being equal (see Table 2).

S. M. McLennan, State University of New York, Department of Earth and Space Sciences, Stony Brook, NY 11794-2100

Rock Physics and Phase Relations
A Handbook of Physical Constants
AGU Reference Shelf 3

TABLE 1. Preserved Mass of Cenozoic Sediment, by Tectonic/Sedimentary Setting.

Tectonic Setting	Mass (10^{21}g)
Platforms	53.1
Other Continental Settings	98.7
Passive Margins	140.8
Marginal Basins	121.8
Deep-sea Fans	13.2
Abyssal Plains	91.2
Pelagic	116.6
Cenozoic Total	635.4

Compiled from [11, 12, 32, 33, 41].
Data for Platforms and Other Continental Settings are for Paleocene through Pliocene only.

Complimentary estimates of mass and average sediment accumulation rates are available for the ocean basins. The overall mass of sediment found in the various ocean basins are compiled in Table 5 according to lithology. The estimated acccumulation rates are given in Table 6, and there is reasonably good agreement among various workers. There is a large discrepancy between estimated particulate flux to the ocean ($22x10^{15}$ g yr^{-1}; Table 2) and average accumulation rates of terrigenous and volcanogenic sediments in the ocean basins ($3.9x10^{15}$ g yr^{-1}; Table 6). This is the result of a combination of a large amount of sediment being trapped in estuaries and on

TABLE 2. Total Particulate Flux to Oceans.

Sediment	Flux (10^{15}g yr^{-1})
River suspension	20.0
River bedload and storm	1.50
Marine Erosion	0.25
Glacial	0.20
Aeolian	0.07
Extraterrestial	0.003
World Total	22.0

Data compiled from [10, 23, 24, 31].

TABLE 3. Suspended Sediment Flux to the Oceans From Some Major Rivers of the World.

River	Drainage Area (10^6km^2)	Sediment Discharge (10^{12}g yr^{-1})	Sediment Yield (10^6g km^{-2} yr^{-1})	Rank[a]
Amazon	6.15	1200	195	1
Amur	1.85	52	28	
Colorado	0.64	0.01	0.02	
Colorado (pre-dam)			190	
Columbia	0.67	10	15	
Colum. (pre-dam)			70	
Congo (Zaire)	3.72	43	12	
Copper	0.06	70	1,167	
Danube	0.81	67	83	
Fly	0.076	115	1,513	
Ganges/Brahmap.	1.48	1,060	716	2
Godavari	0.31	170	550	8
Haile	0.05	81	1,620	
Huanghe (Yellow)	0.75	1,050	1,400	3
Hungho (Red)	0.12	130	1,100	
Indus	0.97	59	61	
Indus (pre-dam)			258	
Irrawaddy	0.43	220	620	5
La Plata	2.83	92	33	
Lena	2.49	12	5	
Mackenzie	1.81	42	23	
Magdalena	0.24	220	917	6
Mekong	0.79	160	202	9
Mississippi	3.27	210	64	7
Mississ. (pre-dam)			200	
Narnada	0.089	125	1,404	
Niger	1.21	40	33	
Nile	3.03	(0)	(0)	
Nile (pre-dam)			40	
Ob	2.25	16	6	
Orange	0.89	17	19	
Orange (pre-dam)			100	
Orinoco	0.99	150	152	10
Parana	2.83	79	30	
St. Lawrence	1.03	4	3.9	
Tigris-Euphrates	1.05	?53	?50	
Yangtze	1.81	480	265	4
Yenisei	2.58	13	5	
Yukon	0.84	60	71	
Zambesi	1.20	20	17	
Zambesi (pre-dam)			35	

Data compiled from [13, 22-24] with minor alterations to some drainage areas.
[a]Rank is by Sediment Discharge.

TABLE 4. Suspended Sediment Flux to the Oceans From Major Regions of the World.

Continent	Surface Area (10^6km^2)	Drainage Area (10^6km^2)	Sediment Discharge (10^{12}g yr^{-1})	Drainage Sediment Yield (10^6g km^{-2} yr^{-1})	Continent Sediment Yield (10^6g km^{-2} yr^{-1})
Eurasia (excl. Islands[a])	48.2	32.7	6,800	208	141
S.E. Asian Islands[a]	3.3	3.0	7,600	2,533	2,303
North & Central America	28.2	17.5	1,500	86	53
Africa	30.5	15.3	700	46	23
South America	19.4	17.9	3,300	168	155
Antarctica	4.10	(0)	(0)	(0)	(0)
Australia (excl. Islands[a])	8.2	2.2	65	30	8
Arabia	4.11	(0)	(0)	(0)	(0)
World	146.0	88.6	19,965	225	137

Data compiled from [5, 23, 24].
[a]Japan, New Guinea, New Zealand, Indonesia, Philippines, Taiwan and other S.W. Pacific islands (see [23]).

TABLE 5. Mass of Sediment in the Ocean Basins.

Ocean	Terrigenous (10^{21}g)	Volcanogenic (10^{21}g)	----Biogenic Pelagic---- Carbonate (10^{21}g)	Siliceous (10^{21}g)	Total (10^{21}g)
North Atlantic	69.4	0.7	7.6	1.6	79.3
South Atlantic	34.6	0.0	3.5	0.5	38.6
North Pacific	19.7	3.7	4.6	2.8	30.8
South Pacific	13.8	1.5	9.5	4.1	28.9
Indian	52.4	0.4	18.0	2.5	73.3
Other[a]	(19)	(.5)	(4)	(1)	24.5
World Totals	208.9	6.8	47.2	12.5	275.4
Hay et al. [14][b]	141.7	4.9	107.5	7.9	262.0

Data compiled from [12, 14].
[a]Basins not considered by Howell and Murray [12], including Arctic, Norwegian-Greenland Sea and parts of the Antarctic (see [14]). Lithologic proportions assumed to be equivalent to global averages.
[b]Values calculated on the basis of total pelagic sediment of 140 x 10^{21}g. Terrigenous component includes 24.6 x 10^{21}g of pelagic red clay.

TABLE 6. Accumulation Rate of Sediment in the Ocean Basins.

Ocean	Average Age (10^6yr)	Terrigenous (10^{15}g yr^{-1})	Volcanogenic (10^{15}g yr^{-1})	----Biogenic Pelagic---- Carbonate (10^{15}g yr^{-1})	Siliceous (10^{15}g yr^{-1})	Total (10^{15}g yr^{-1})
North Atlantic	71.1	0.97	0.009	0.11	0.023	1.12
South Atlantic	63.1	0.54	0.0	0.05	0.007	0.61
North Pacific	58.2	0.35	0.066	0.08	0.046	0.53
South Pacific	43.9	0.32	0.033	0.22	0.092	0.66
Indian	55.4	0.95	0.007	0.33	0.046	1.32
Other[a]	(55.3)	(.34)	(.009)	(.07)	(.018)	(.44)
Averages	55.3	3.78	0.124	0.86	0.232	4.98
Hay et al. [14][b]		2.56	0.089	1.94	0.143	4.74
Lisitsyn et al. [17][c]		1.92		1.20	0.191	3.31
Gregor [11][d]		2.30		1.89		4.20

Data compiled from [12, 14].

[a]Basins not considered by Howell and Murray [12], including Arctic, Norwegian-Greenland Sea and parts of the Antarctic (see [14]). Lithologic proportions and age assumed to be equivalent to global averages.

[b]Values calculated on the basis of total pelagic sediment of 140 x 10^{21}g. Terrigenous component includes 24.6 x 10^{21}g of pelagic red clay.

[c]Values of Lisitsyn et al. [17] increased by 10% since all oceans were not included in their survey.

[d]Terrigenous component includes all non-pelagic sediment. Data from [11].

TABLE 7. Average Upper Continental Crust and Various Average Sedimentary Compositions.

Element		Upper Continental Crust[a]	Average Sediment[b]	Average Mud[c]	Average River Particulate[d]	Loess[e]	Average Pelagic Clay[f]
Li	(ppm)	20	21	30	25	30	57
Be	(ppm)	3	2.2	3	–	2	2.6
B	(ppm)	15	75	100	70	–	230
Na	(wt.%)	2.89	1.25	0.89	0.71	1.4	4.0
Mg	(wt.%)	1.33	1.85	1.4	1.2	0.68	2.1
Al	(wt%)	8.04	7.10	10.3	9.4	6.9	8.4
Si	(wt%)	30.8	30.0	29.9	28.9	35.7	25.0
P	(ppm)	700	665	700	1150	--	1500
K	(wt%)	2.80	2.35	3.2	2.0	1.9	2.5
Ca	(wt%)	3.00	6.40	0.93	2.2	0.79	0.93
Sc	(ppm)	11	14	16	18	8	19
Ti	(wt%)	0.30	0.45	0.60	0.56	0.41	0.46
V	(ppm)	60	110	140	170	73	120
Cr	(ppm)	35	74	100	100	44	90
Mn	(ppm)	600	680	850	1050	560	670
Fe	(wt%)	3.50	4.00	5.1	4.8	2.4	6.5
Co	(ppm)	10	16	20	20	11	74
Ni	(ppm)	20	40	60	90	20	230
Cu	(ppm)	25	40	50	100	18	250

TABLE 7. Continued.

Element		Upper Continental Crust[a]	Average Sediment[b]	Average Mud[c]	Average River Particulate[d]	Loess[e]	Average Pelagic Clay[f]
Zn	(ppm)	71	65	85	350	60	200
Ga	(ppm)	17	16	20	25	14	20
Ge	(ppm)	1.6	1.5	2	–	–	2
Rb	(ppm)	112	110	160	100	85	110
Sr	(ppm)	350	385	200	150	192	18
Y	(ppm)	22	21	27	28	25	40
Zr	(ppm)	190	210	210	–	375	150
Nb	(ppm)	25	17	19	–	20	14
Mo	(ppm)	1.5	–	1.0	3	–	27
Cd	(ppb)	98	–	–	1000	–	300
Sn	(ppm)	5.5	5	6	–	5	3.0
Cs	(ppm)	3.7	4.5	6	6	4	6
Ba	(ppm)	550	480	650	600	625	2300
La	(ppm)	30	28.3	38.2	46	35.4	42
Ce	(ppm)	64	58.9	79.6	88	78.6	80
Pr	(ppm)	7.1	6.52	8.83	9.0	8.46	10
Nd	(ppm)	26	24.9	33.9	33	33.9	41
Sm	(ppm)	4.5	4.23	5.55	7.0	6.38	8.0
Eu	(ppm)	0.88	0.86	1.08	1.5	1.18	1.8
Gd	(ppm)	3.8	3.61	4.66	5.4	4.61	8.3
Tb	(ppm)	0.64	0.60	0.774	0.89	0.81	1.3
Dy	(ppm)	3.5	3.61	4.68	5.4	4.82	7.4
Ho	(ppm)	0.80	0.76	0.991	1.1	1.01	1.5
Er	(ppm)	2.3	2.19	2.85	3.1	2.85	4.1
Tm	(ppm)	0.33	0.31	0.405	0.44	0.40	0.57
Yb	(ppm)	2.2	2.14	2.82	3.2	2.71	3.8
Lu	(ppm)	0.32	0.33	0.433	0.52	0.42	0.55
Hf	(ppm)	5.8	5.5	5.0	6	11.4	4.1
Ta	(ppm)	2.2	1.5	2	1.25	–	1
W	(ppm)	2.0	2.1	2.7	–	1.6	1
Pb	(ppm)	20	17	20	150	13	30
Bi	(ppb)	127	–	250	–	–	550
Th	(ppm)	10.7	10.4	14.6	14	11.3	13.4
U	(ppm)	2.8	2.3	3.1	3	2.5	2.6

[a]From Taylor and McLennan [37]. Additional elements available in original reference.
[b]New estimate based on geochemical data from many sources. Weighted average based on relative distribution of sedimentary lithologies during the Cenozoic [31, 32]. Proportions adopted are: Mud : Sand : Carbonate : Evaporite : Siliceous : Volcanogenic = 59 : 16 : 13 : 2 : 1 : 9.
[c]Volatile- and carbonate-free basis; assumed equivalent to average shale with minor ammendments [37].
[d]From Martin and Meybeck [18]. REE estimated assuming smooth chondrite-normalized pattern [see 20]. Concentration of a number of elements is strongly affected by anthropogenic factors (e.g. Cd, Pb).
[e]On a carbonate-free basis. Tm and Lu estimated from chondrite-normalized diagrams. From Taylor et al. [38].
[f]See Taylor and McLennan [37] for details and sources. Includes 1300ppm F and 2.1% Cl. Additional elements available in original reference.

the shallow continental margins [17] and subduction and cannibalistic recycling of continental margin and oceanic sediment [12, 40, 41].

2.2. Chemical Composition of Sediments

The major factors controlling the chemical composition of sedimentary rocks are discussed in Garrels and Mackenzie [10] and Taylor and McLennan [38]. Table 7 lists estimates of the average composition of several sedimentary reservoirs and the upper continental crust. An estimate for the average composition of loess is included because unconsolidated and semi-consolidated loess deposits cover approximately 10% of the earth's surface [31] and there is a growing appreciation that aeolian material is an important component in many soils (see below).

A new estimate for the average composition of sediment was determined by compiling, from numerous sources, average compositions of the various classes of sediment (mud, sand, carbonate, volcanogenic, evaporite, siliceous) and averaging by giving weight according to their relative abundances in the Cenozoic [32, 33]. Average trace element abundances for lithologies such as carbonates, evaporites and siliceous sediments are difficult to estimate; there is a meagre data base and few systematic studies that evaluate the role of minor terrigenous material in controlling the trace element composition of such lithologies. For this estimate, trace element abundances for carbonate, evaporite and siliceous sediments are assumed to be negligible except in certain obvious cases (e.g., Sr in carbonates; B and Ba in siliceous sediment). This assumption likely introduces no more than 5% uncertainty due to the relatively low abundances of these sediments in the geological record. The volcanogenic component was assumed to be equal to average island arc volcanic rock [38]. This estimate of average sediment reflects the long-standing observation that the sedimentary mass does not match upper crustal abundances, but is enriched in ferro-magnesian elements, Ca and B and depleted in Na. These features may be attributable to a combination of preferentially sampling undifferentiated crust at continental margins (e.g., arcs) and perhaps carbonates and recycling sedimentary rocks that have undergone a previous weathering history. Enrichments in B result from adsorption from seawater, with an ultimate hydrothermal origin.

3. SOILS

3.1. Soil Distribution

Soil nomenclature is complex and there are many classification schemes in use around the world, mostly geared to meet agricultural needs. Details of classification, characteristics, timing and global distribution of the various types of soils are available in standard texts [e.g., 4, 26, 35, 37, 42]. In Table 8, the major soil orders, defined by the United States Comprehensive Soil Classification System, are described in terms of general characteristics, environment of formation and areal extent. Although rarely considered, soil distribution is also affected by plate tectonic associations [9]. A useful scheme, the Jackson-Sherman weathering stages, is based on the dominant clay fraction mineralogy [e.g., 35]. Soil develops from (1) *Early Stage* (primary silicates, gypsum, carbonate in clay fraction) under reducing conditions with low water flux; through (2) *Intermediate Stage* (quartz, dioctohedral mica/illite, vermiculite/chlorite, smectites) under conditions of ineffective leaching, moderate alkalinity and oxidation; through (3) *Advanced Stage* (kaolinite, gibbsite, iron and titanium oxides) under conditions of intensive leaching, oxidation and low pH.

The mass of soil at the earth's surface is immense. If we assume an average depth to unweathered rock of 0.5 m and an average density of 1.5 g cm^{-3} (both likely lower limits), at least 10^{20} g (perhaps more realistically $5x10^{20}$ g) of soil is present (the degree to which this material is weathered is, of course, highly variable). This compares with an annual sediment flux of about 10^{16} g yr^{-1} (Table 2 and above discussion), suggesting an expected residence time for soil of $>10^4$ years (not all sediment is derived from soil). The anthropogenic influence on soil distribution is apparent from the estimate that about 0.7% of the earth's topsoil currently is lost annually [8].

3.2. Weathering: Mineralogy and Chemistry

In Table 9, some major weathering reactions are listed along with the corresponding Gibbs free energies [7]. Such data, calculated for unit activities and standard pressure and temperature, reflect the intrinsic instability of most primary igneous/metamorphic minerals in the presence of acidic waters and also provides a general guide to the relative stability of various minerals during the weathering process. In detail, mineral stability during weathering is complex and controlled by many factors, such as pH and other ion activities. Figure 1 illustrates one simple example, showing stability relations among albite and various clay minerals as a function of Na^+/H^+ versus SiO_2. Important areas of recent research have been to document the kinetics of relevant weathering reactions as well as the time scales for development of weathering profiles [e.g., 6, 15, 26, 36] and to quantify the biogeochemistry of the weathering process [e.g., 16, 34].

TABLE 8. Description and Distribution of Major Soil Types.

Soil Order	Description	Environment	Land Area ($10^6 km^2$)	Land Area (%)
MISCELLANEOUS:				
1. Unweathered (Z)	Icefields and mountainous regions devoid of soils	Glaciated; Mountainous.	3.4	2.5
2. Mountain Soil (X)	Complex variety of soils, listed below, with characteristics changing over short distances.	Mountainous	26.2	19.4
VERY LOW DEGREES OF WEATHERING:				
3. Histosol (H)	Organic rich soils formed from accumulation of plant debris that fails to decompose.	Areas of Bogs and Peats.	1.3	1.0
4. Entisol (E)	Soils without pedogenic horizons, forming in regions that are usually wet or usually moist or usually dry.	Mountains, Deserts and Sandy Regions.	11.6	8.6
5. Vertisol (V)	Soils rich in expandable clays; poorly developed due to mixing associated with seasonal cracking.	Areas of seasonal drying.	2.4	1.8
LOW DEGREES OF WEATHERING:				
6. Inseptisol (I)	Soils with pedogenic horizons of minor leaching or alteration. Usually moist regions with plant growth.	Highly variable. Regions of newly formed soils.	12.4	9.1
LOW - MODERATE DEGREES OF WEATHERING:				
7. Aridisol (A)	Soils with pedogenic horizons; may have caliche deposits. Dry regions with little organic matter.	Arid Regions (including Deserts).	24.7	18.3
8. Mollisol (M)	Soils with black, organic rich surface horizons. Typically high in Ca and Mg. Moist or dry.	Grasslands (e.g., Steppes, Prairies).	11.0	8.1
MODERATE DEGREES OF WEATHERING:				
9. Spodosol (S)	Soils with hardpans of Al- and Fe-oxides/ hydroxides in subsurface horizons. Usually moist or usually wet.	Variable. Includes cool wooded areas and areas of podzol.	5.7	4.2
10. Alfisol (A)	Organic-rich soils with strongly leached upper horizons and clay rich lower horizons. Moist.	Mainly temperate forest (young surface, high pH).	17.9	13.3
HIGH DEGREES OF WEATHERING:				
11. Ultisol (U)	Highly weathered, organic-bearing soils with leached upper horizons and clay rich lower horizons. Moist.	Temperate to sub-tropical forest (old surface, low pH).	7.1	5.3
12. Oxisol (O)	Similar to Ultisols but lower clay horizons composed of Al- and Fe-oxides. Lateritic in character.	Intertropical. Highly weathered, old surfaces.	11.3	8.4

Adapted from Buol et al. [4].

TABLE 9. Simplified Weathering Reactions of Some Major Minerals and Associated Free Energies.

Reactant	Reaction	ΔG_r° (kJ mol^{-1})	ΔG_r° (kJ g-atom^{-1})
	OLIVINE		
Fayalite	$Fe_2SiO_4(s) + 1/2O_2(g) = Fe_2O_3(s) + SiO_2(s)$	-220.5	-27.53
Forsterite	$Mg_2SiO_4(s) + 4H^+(aq) = 2Mg^{2+}(aq) + 2H_2O(l) + SiO_2(s)$	-184.1	-16.74
	PYROXENES		
Clinoenstatite	$MgSiO_3(s) + 2H^+(aq) = Mg^{2+}(aq) + H_2O(l) + SiO_2(s)$	-87.4	-12.47
Diopside	$CaMg(SiO_3)_2(s) + 4H^+(aq) = Mg^{2+}(aq) + Ca^{2+}(aq) + H_2O(l) + 2SiO_2(s)$	-133.1	-11.38
	AMPHIBOLES		
Anthophyllite	$Mg_7Si_8O_{22}(OH)_2(s) + 14H^+(aq) = 7Mg^{2+}(aq) + 8H_2O(l) + 8SiO_2(s)$	-574.0	-10.42
Tremolite	$Ca_2Mg_5Si_8O_{22}(OH)_2(s) + 14H^+(aq) = 5Mg^{2+}(aq) + 2Ca^{2+}(aq) + 8H_2O(l) + 8SiO_2(s)$	-515.5	-9.37
	FELDSPARS		
Anorthite	$CaAl_2Si_2O_8(s) + 2H^+(aq) + H_2O(l) = Al_2Si_2O_5(OH)_4(s) + Ca^{2+}(aq)$	-100.0	-5.52
Albite (Low)	$2NaAlSi_3O_8(s) + 2H^+(aq) + H_2O(l) = Al_2Si_2O_5(OH)_4(s) + 4SiO_2(s) + 2Na^+(aq)$	-96.7	-3.14
Microcline	$2KAlSi_3O_8(s) + 2H^+(aq) + H_2O(l) = Al_2Si_2O_5(OH)_4(s) + 4SiO_2(s) + 2K^+(aq)$	-66.5	-2.13
	MICAS		
Muscovite	$2KAl_3Si_3O_{10}(OH)_2(s) + 2H^+(aq) + 3H_2O(l) = 3Al_2Si_2O_5(OH)_4(s) + 2K^+(aq)$	-72.3	-1.34
	METAMORPHIC MINERALS		
Wollastonite	$CaSiO_3(s) + 2H^+(aq) = SiO_2(s) + Ca^{2+}(aq) + H_2O(l)$	-97.5	-13.89
Grossular	$Ca_3Al_2Si_3O_{12}(s) + 6H^+(aq) = Al_2Si_2O_5(OH)_4(s) + SiO_2(s) + 3Ca^{2+}(aq) + H_2O(l)$	-255.2	-9.79
Clinochlore	$Mg_2Al_2Si_3O_{10}(OH)_8(s) + 10H^+(aq) = Al_2Si_2O_5(OH)_4(s) + SiO_2(s) + 5Mg^{2+}(aq) + 7H_2O(l)$	-318.4	-6.90
Spinel	$MgAl_2O_4(s) + 2H^+(aq) + 2H_2O(l) = Al_2O_3{\cdot}3H_2O(s) + Mg^{2+}(aq)$	-95.4	-6.36
Lawsonite	$CaAl_2Si_2O_7(OH)_2{\cdot}H_2O(s) + 2H^+(aq) = Al_2Si_2O_5(OH)_4(s) + Ca^{2+}(aq) + H_2O(l)$	-66.9	-3.18
Kyanite	$2Al_2SiO_5(s) + 5H_2O(l) = Al_2Si_2O_5(OH)_4(s) + Al_2O_3{\cdot}3H_2O(s)$	-70.3	-2.26
	ZEOLITES		
Prehnite	$Ca_2Al_2Si_3O_{10}(OH)_2(s) + 4H^+(aq) = Al_2Si_2O_5(OH)_4(s) + SiO_2(s) + 2Ca^{2+}(aq) + H_2O(l)$	-167.4	-6.69
Zoisite	$2Ca_2Al_3Si_3O_{12}OH(s) + 8H^+(aq) + H_2O(l) = 3Al_2Si_2O_5(OH)_4(s) + 4Ca^{2+}(aq)$	-329.3	-5.98
Laumontite	$CaAl_2Si_4O_{12}{\cdot}4H_2O(s) + 2H^+(aq) = Al_2Si_2O_5(OH)_4(s) + 2SiO_2(s) + Ca^{2+}(aq) + 3H_2O(l)$	-74.1	-2.22
	REDUCED PHASES		
Methane	$CH_4(g) + 2O_2(g) = H_2O(l) + H^+(aq) + HCO_3^-(aq)$	-773.6	-85.94
Pyrite	$2FeS_2(s) + 4H_2O(l) + 71/2O_2(g) = Fe_2O_3(s) + 4SO_4^{2-}(aq) + 8H^+(aq)$	-2,441.4	-73.97

Adapted from Curtis [7].

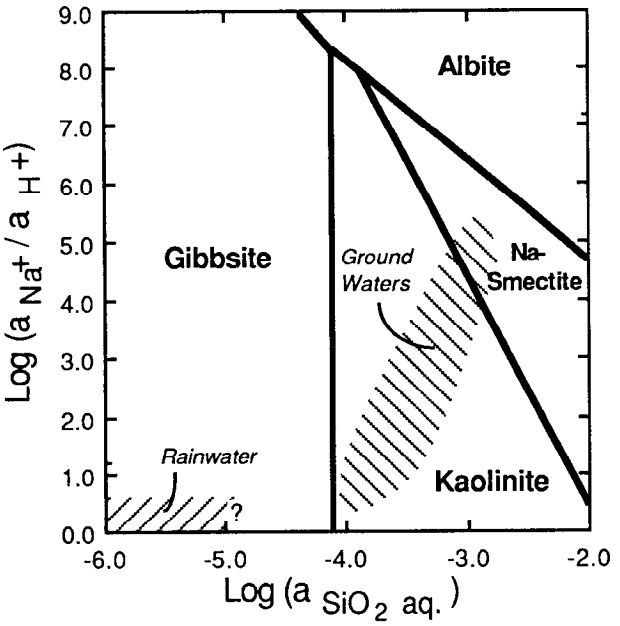

Fig. 1. Plot of a_{Na+} / a_{H+} versus $a_{SiO2(aq)}$ (where a = activity) showing the stability relations among albite and various clay minerals at standard temperature and pressure. Also shown are typical compositions of rainwater and groundwaters taken from a wide varety of igneous terranes. This diagram illustrates both the intrinsic instability of a common igneous/metamorphic mineral in the presence of near surface waters and some of the effects of composition on stability relations. Adapted from [29].

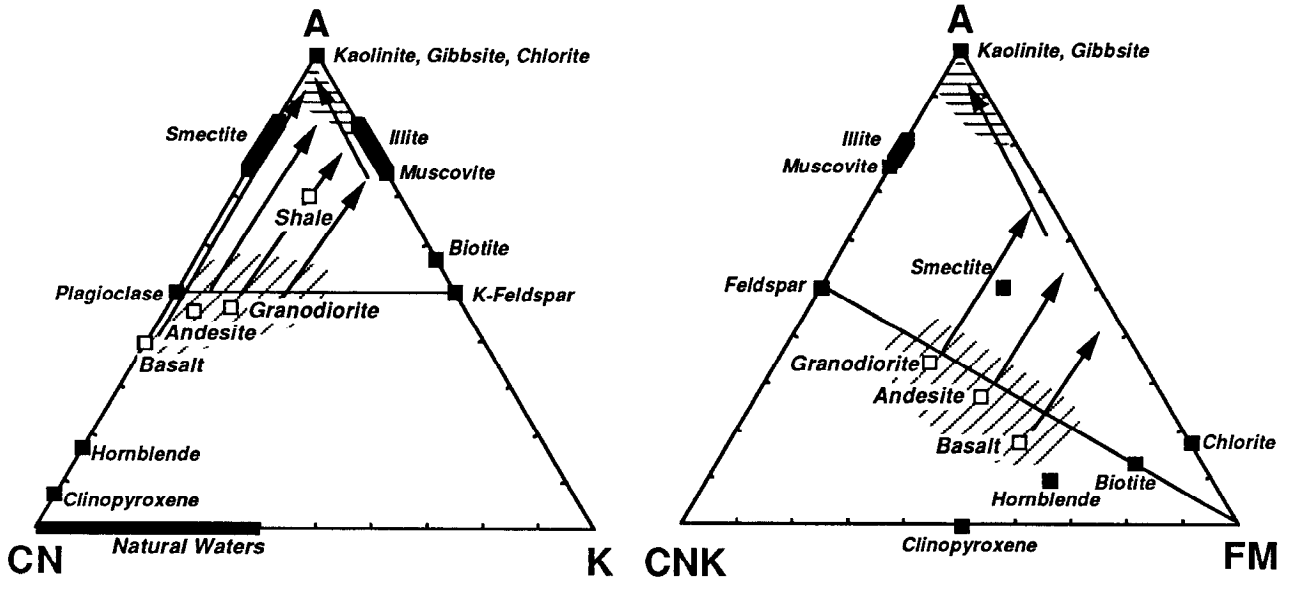

Fig. 2. Ternary plots of A-CN-K and A-CNK-FM [29, 30]. In mole fraction, A=Al_2O_3, C=CaO (in silicate fraction only, corrected for phosphates, carbonates), N=Na_2O, K=K_2O, F=FeO (total iron), M=MgO. Plotted on these diagrams are the positions of major minerals, although note that clay minerals typically have more variable compositions than shown here. Also plotted are some typical rock types and natural waters. The arrows indicate the general trend for increasing degrees of weathering exhibited by the various rock types. In the case of the A-CN-K diagram, the weathering trends shown by geochemical data from weathering profiles match theoretical trends predicted from thermodynamic and kinetic data. In the case of A-CNK-FM, kinetic data are not available and the trends shown are based only on geochemical data from weathering profiles. Diagonal and horizontal hatching indicate, approximately, the regions of Early and Advanced stages of weathering, according to the Jackson-Sherman weathering stages.

TABLE 10. Chemical Composition of Weathered Portions of the Torrongo Granodiorite, Australia.

	Parent Rock	Slightly Weathered	Highly Weathered	Residual Soil Clays
Dominant Mineralogy:	qtz-kfp-plg-biot	qtz-kfp-plg-kao -(±biot)	qtz-kfp -kao-ill -(±plg)	qtz-kao -ill
TiO_2	0.9	0.9	0.8	0.4
FeO	5.5	5.4	5.0	2.3
MgO	2.6	2.6	1.9	0.9
CaO	4.3	3.7	0.34	0.03
K_2O	2.6	2.5	2.3	1.3
Na_2O	3.4	3.3	0.25	0.07
K_2O/Na_2O	0.76	0.76	9.2	18.6
Na_2O/CaO	0.79	0.89	0.73	2.3
K_2O/TiO_2	2.9	2.8	2.9	3.3
Cs	5.0	4.6	4.4	5.7
Rb	121	124	88	141
Ba	1090	890	1074	697
Sr	298	245	52	21
Zr	300	323	261	155
La	25.0	19.4	72.9	17.5
Ce	57.8	41.6	99.3	44.8
Nd	25.4	-	65.3	15.6
Sm	6.02	5.95	14.6	2.92
Eu	1.42	1.24	3.66	0.66
Gd	5.73	6.73	16.4	2.22
Tb	0.85	0.94	3.09	0.26
Ho	1.01	1.0	3.5	0.34
Yb	2.89	3.87	9.99	1.33
Lu	0.48	0.65	1.52	0.19
Cs/Zr(x100)	1.7	1.4	1.7	3.7
Rb/Zr	0.40	0.51	0.34	0.91
Ba/Zr	3.6	2.8	4.1	4.5
Sr/Zr	0.99	0.76	0.20	0.14
La/Zr(x100)	8.3	6.0	27.9	11.3
Yb/Zr(x1,000)	9.6	12.0	38.3	8.6
La/Yb	8.7	5.0	7.3	13.2

Data sources: Nesbitt [27], Nesbitt et al. [28].
Mineral Abbreviations: Quartz - qtz; Plagioclase - plg; K-feldspar - kfp; Biotite - biot; Kaolinite - kao; Illite - ill.

There are numerous data available for major elements in weathering profiles and soils (as well as in soil ground waters). Although not compiled here, sources of data for several characteristic profiles are given in Nesbitt and Young [30]. An approach to quantitatively understanding the bulk chemical changes associated with weathering and soil formation has been developed by Nesbitt and Young [29, 30]. Figure 2 illustrates the general trends expected for weathering of various rock types. Using such diagrams, it is possible to evaluate major element data from weathering profiles in terms of mineralogical changes and degree of weathering.

In contrast, there are few high quality trace element data for soils and weathered material (Maynard [19] cites much available data). Table 10 lists some representative major and trace elements data for a well characterized recent weathering profile on the Torrongo Granodiorite from Australia. This profile appears fairly representative of intermediate to advanced continental weathering (this profile likely represents an ultisol). The distribution of elements has been interpreted on the basis of competing processes of leaching of cations from primary igneous minerals, and their altered clay products, and exchange/adsorption of the same cations onto altered clay minerals deeper in the profile, in sites where the ground water changes pH and other chemical characteristics (affecting ion-exchange capacity) [27, 28]. Thus, for a number of elements, there is a complementary pattern of Cation/Zr between the residual soils and weathered granodiorite, when compared to the unweathered parent.

A difficult issue in all geochemical studies of soils, and the weathering process in general, is evaluating mass transfer of material into or out of the system, where there is clear evidence of volume and density change. A second factor is evidence for a substantial aeolian component in many soil profiles, which can strongly affect the distribution of important trace elements, such as Zr, Hf, Ti and others. This is of some importance since in most cases, estimates of relative movements of elements have been made by assuming one or another element (typically Ti, Zr) is immobile. Brimhall and co-workers [1-3] have recently addressed this problem by first accounting for aeolian contributions and then considering the physical (density, volume, porosity) and structural (strain) development of the soil profile in order to more completely understand mass transfer. Important conclusions are that, in some cases, an aeolian contribution can be substantial and that profiles of element mass loss/gain do not necessarily match profiles of element depletion/enrichment based solely on concentration.

Acknowledgements. I am grateful to Martin Schoonen and the reviewers for comments and to the National Science Foundation (EAR-8957784) for support.

REFERENCES

1. Brimhall, G. H., and W. E. Dietrich, Constitutive mass balance relations between chemical composition, volume, density, porosity, and strain in metasomatic hydrochemical systems: Results on weathering and pedogenesis, *Geochim. Cosmochim. Acta, 51*, 567-587, 1987.
2. Brimhall, G. H., O. A. Chadwick, C. J. Lewis, W. Compston, I. S. Williams, K. J. Danti, W. E. Dietrich, M. E. Power, D. Hendricks, and J. Bratt, Deformational mass transport and invasive processes in soil evolution, *Science, 255*, 695-702, 1991a.
3. Brimhall, G. H., C. J. Lewis, C. Ford, J. Bratt, G. Taylor, and O. Warin, Quantitative geochemical approach to pedogenesis: importance of parent material reduction, volumetric expansion, and eolian influx in lateritization, *Geoderma, 51*, 51-91, 1991b.
4. Buol, S. W., F. D. Hole, and R. J. McCracken, *Soil Genesis and Classification, 2nd Ed.*, 404pp., Iowa State Univ. Press, Ames, 1980.
5. Cogley, J. G., Continental margins and the extent and number of the continents, *Rev. Geophys. Space Phys., 22*, 101-122, 1984.
6. Colman, S. M., and D. P. Dethier (eds.), *Rates of Chemical Weathering of Rocks and Minerals*, 603pp., Academic Press, Orlando, 1986.
7. Curtis, C. D., Stability of minerals in surface weathering reactions: A general thermochemical approach, *Earth Surf. Proc., 1*, 63-70, 1976.
8. Fyfe, W. S., Soil and global change, *Episodes, 12*, 249-254, 1989.
9. Fyfe, W. S., Kronberg, B. I., Leonardos, O. H., and Olorunfemi, N., Global tectonics and agriculture: A geochemical perspective, *Agric. Ecosys. Environ., 9*, 383-399, 1983.
10. Garrels, R. M., and F. T. Mackenzie, *Evolution of Sedimentary Rocks*, 397 pp., Norton, New York, 1971.
11. Gregor, C. B., The mass-age distribution of Phanerozoic sediments, in *The Chronology of the Geological Record*, edited by N. J. Snelling, pp. 284-289, Geological Society of London Memoir 10, Blackwell, Oxford, 1985.
12. Hay, W. W., J. L. Sloan II, and C. N. Wold, Mass/age distribution and composition of sediments on the ocean floor and the global rate of sediment subduction, *J. Geophys. Res., 93*, 14,933-14,940, 1988.
13. Holeman, J. N., Sediment yield of major rivers of the world, *Water Resources Res., 4*, 737-747, 1968.
14. Howell, D. G., and R. W. Murray, A budget for continental growth and denudation, *Science, 233*, 446-449, 1986.
15. Lerman, A., and M. Meybeck (Eds.), *Physical and Chemical Weathering in Geochemical Cycles*, 375pp.,Kluwer, Dordrecht, 1988.
16. Likens, G. E., Bormann, F. H., Pierce, R. S., Eaton, J. S., and Johnson, N. M., *Biogeochemistry of a Forested Ecosystem*, 146pp., Springer-Verlag, New York, 1977.
17. Lisitsyn, A. P., V. N. Lukashin, Ye. G. Gurvich, V. V. Gordeyev, and L. L. Demina, The relation between element influx from rivers and accumulation in ocean sediments, *Geochem. Int., 19*, 102-110, 1982.
18. Martin, J.-M., and M. Meybeck, Elemental mass-balance of material carried by major world rivers, *Marine Chemistry, 7*, 173-206, 1979.
19. Maynard, J. B., Chemistry of modern soils as a guide to interpreting Precambrian paleosols, *J. Geol., 100*, 279-289, 1992.
20. McLennan, S. M., Rare earth elements in sedimentary rocks: Influence of provenance and sedimentary processes, *Rev. Mineral. (Min. Soc. Amer.), 21*, 169-200, 1989.
21. McLennan, S. M., Weathering and global denudation, *J. Geol.* (in press, 1993).
22. Milliman, J. D., Flux and fate of fluvial sediment and water in coastal seas, in *Ocean Margin Processes in Global Change*, edited by R. F. C. Mantoura, J.-M. Martin, and R. Wollast, pp. 69-89, Wiley, 1991.
23. Milliman, J. D., and R. H. Meade, World-wide delivery of river sediment to the oceans, *J. Geol., 91*, 1-21, 1983.
24. Milliman, J. D., and J. P. M. Syvitski, Geomorphic / tectonic control of sediment discharge to the ocean: The importance of small mountainous rivers, *J. Geol.*, 100, 525-544, 1992.
25. Milliman, J. D., Y. S. Qin, M. E. Ren, and Y. Saito, Man's influence on the erosion and transport

of sediment by Asian rivers: The Yellow (Huanghe) example, *J. Geol., 95*, 751-762, 1987.

26. Nahon, D. B., *Introduction to the Petrology of Soils and Chemical Weathering*, 313 pp., John Wiley, New York, 1991.
27. Nesbitt, H. W., Mobility and fractionation of rare earth elements during weathering of a granodiorite, *Nature, 279*, 206-210, 1979.
28. Nesbitt, H. W., G. Markovics, and R. C. Price, Chemical processes affecting alkalis and alkaline earths during continental weathering, *Geochim. Cosmochim. Acta, 44*, 1659-1666, 1980.
29. Nesbitt, H. W., and G. M. Young, Prediction of some weathering trends of plutonic and volcanic rocks based on thermodynamic and kinetic considerations, *Geochim. Cosmochim. Acta, 48*, 1523-1534, 1984.
30. Nesbitt, H. W., and G. M. Young, Formation and diagenesis of weathering profiles, *J. Geol., 97*, 129-147, 1989.
31. Pye, K., *Aeolian Dust and Dust Deposits*, 334 pp., Academic Press, London, 1987.
32. Ronov, A. B., *The Earth's Sedimentary Shell: Quantitative Patterns of its Structure, Compositions, and Evolution*, 80 pp., American Geological Institute Reprint Series V, 1983.
33. Ronov, A. B., V. E. Khain, A. N. Balukhovsky, and K. B. Seslavinsky, Quantitative analysis of Phanerozoic sedimentation, *Sediment. Geol., 25*, 311-325, 1980.
34. Schlesinger, W. H., *Biogeochemistry: An Analysis of Global Change*, 443pp., Academic Press,, San Diego, 1991.
35. Sposito, G., The Chemistry of Soils, Oxford University Press, Oxford, 1989.
36. Steefel, C. I., and P. Van Cappellen, A new kinetic approach to modeling water-rock interaction: The role of nucleation, precursors, and Ostwald ripening, *Geochim. Cosmochim. Acta, 54*, 2657-2677, 1990.
37. Steila, D., *The Geography of Soils*, 222 pp., Prentice Hall, Englewood Cliffs (N. J.), 1976.
38. Taylor, S. R., and S. M. McLennan, The Continental Crust: Its Composition and Evolution, 312pp., Blackwells, 1985.
39. Taylor, S. R., S. M. McLennan, and M. T. McCulloch, Geochemistry of loess, continental crustal composition and crustal model ages, *Geochim. Cosmochim. Acta, 47*, 1897-1905, 1983.
40. Veizer, J., and S. L. Jansen, Basement and sedimentary recycling and continental evolution, *J. Geol., 87*, 341-370, 1979.
41. Veizer, J., and S. L. Jansen, Basement and sedimentary recycling - 2: Time dimension to global tectonics, *J. Geol., 93*, 625-643, 1985.
42. Yatsu, E., *The Nature of Weathering: An Introduction*, 624pp., Sozosha, Tokyo, 1988.

Acoustic Velocity and Attenuation in Porous Rocks

Kenneth W. Winkler and William F. Murphy III

1. INTRODUCTION

The acoustic properties of most crustal rocks are dominated by microcracks, pores, and the fluids contained within them. Dry rocks have much lower elastic moduli than do any of the constituent minerals. They are acoustically much more non-linear (stress-dependent) than other common materials. Fluid-saturated rocks exhibit attenuation and velocity dispersion that is not observed in dry rocks. All of these effects, and others, have been ascribed to the complex nature of the crack/pore structure of rocks, and to the behavior of fluids occupying and flowing within the pore structure.

Our intention here is to provide a concise status report on the present state of knowledge of rock acoustics. Several excellent review volumes have been published [12, 19, 59, 80, 84, 88, 92], and should be consulted for additional information. Our approach will be to present experimental results that illustrate specific aspects of rock acoustics, and show how theoretical models help us understand the observations. Several field applications will also be discussed. Since velocities in rock have been studied more extensively than has attenuation, some sections contain little or no reference to attenuation.

K. W. Winkler and W. F. Murphy III, Schlumberger-Doll Research, Old Quarry Road, Ridgefield, CT 06877-4108

Rock Physics and Phase Relations
A Handbook of Physical Constants
AGU Reference Shelf 3

2. POROSITY

Acoustic well-logs are frequently used to estimate porosity, especially in clean, water-saturated sandstones. This is based on an observation made by Wyllie et al. [103] showing that in clay-free, water-saturated sandstones under high-confining pressure, compressional-wave slowness (1/velocity) has a strong linear correlation with porosity. They proposed the equation-

$$\frac{1}{V_p} = \frac{\phi}{V_f} - \frac{1-\phi}{V_m} \qquad (1)$$

where V_P is the compressional wave velocity in the rock, V_f is the velocity in pore fluid, and V_m is the velocity in the solid matrix. Equation (1) is known as the 'time-average' equation, because the total travel time is the average of the times that a hypothetical linear raypath would spend in the fluid and in the matrix. It is, however, a correlation and not a rigorous theoretical model. Figure 1 shows an example from Gregory [31] where Equation (1) is compared to a suite of sandstone data. Significant amounts of clay in the rock will lower the velocity from the time-average prediction and recent work has attempted to derive correlations to both porosity and clay content (see Section 3).

Attempts to derive the porosity of carbonates from the time-average equation often under-estimate the true porosity. The difference between the derived porosity and true porosity is often called 'secondary porosity'. It is generally believed that secondary porosity is located in rounded, vugular pores whose shape is rather non-compliant and so has a negligible effect on the measured velocity.

The effect of pore shape is very important. A small amount of porosity can have a large effect on velocities if

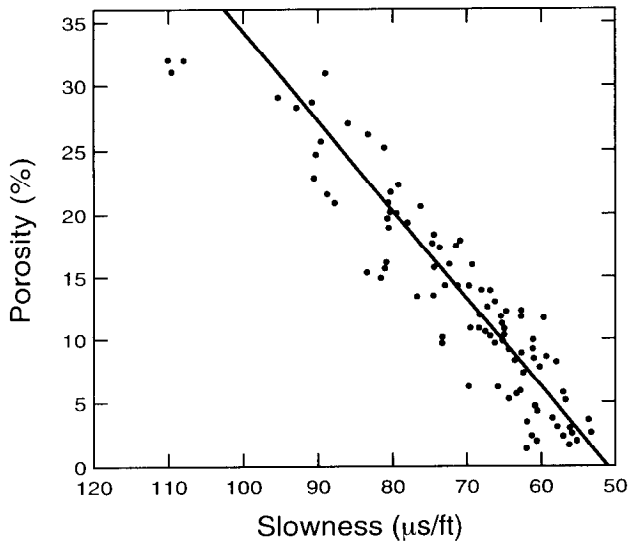

Fig. 1. Compressional wave slowness vs porosity data for water-saturated sandstones from Gregory [28], compared to time-average relation (Equation (1)) for quartz-water system.

the porosity is contained in thin, flat cracks [86]. Such cracks are very compliant to stresses normal to the crack face. If the same amount of porosity is contained in spheroidal pores, it will have a minimal effect on velocity. Various models of velocities in rocks have been based upon distributions of pore aspect ratios [3, 18, 43] or upon generalized crack distribution parameters [60].

3. MINERALOGY

Mineralogy affects rock velocities in two ways. The most obvious is through the bulk and shear moduli of the solid matrix of the rock, which are primary inputs to all velocity models, whether crack-based or mixture models [4, 90]. Indirectly, mineralogy controls the cementation and pore structure of the rock. Other parameters being equal, silica and carbonate cements produce higher velocities than clay cement. Carbonates, being more soluble, often have extremely complex pore structures which are not well described by conventional velocity models.

Pickett [65] found a useful correlation between mineralogy and the ratio of compressional to shear velocities (V_P/V_S) based on the data shown in Figure 2. The values in Table 1 were found to hold over a broad porosity range in consolidated rocks.

In more poorly consolidated rocks, the data tend to diverge from the trends shown in Figure 2, and many empirical attempts have been made to extend the correlations [14]. Several attempts have been made to estimate the effect of clay content on acoustic velocities [15, 32, 42, 82]. These studies have generally found linear correlations relating velocity to both porosity and clay content. However, as with Pickett's results, great care must be taken when extrapolating these correlations beyond the range of sample properties used to derive them. As clay content increases, sandstones grade into shaly sands and shales. A transition occurs from a grain-supported framework with clay in the pore space, to a clay matrix with embedded, isolated grains. Our knowledge of the acoustic properties of shales is somewhat limited, primarily because they are difficult to work with in the lab. Most studies have emphasized the anisotropic nature of shales [39, 67, 85], discussed further in Section 4.2. Velocities in shales are slowest in the direction perpendicular to bedding.

4. STRESS EFFECTS

The complex microstructures of most rocks cause velocities and attenuation to be very sensitive to stress. Increasing confining pressure or decreasing pore pressure cause velocities to increase and attenuation to decrease. Two points of view are useful, depending on the microstructure of a particular rock. Focusing on the pore

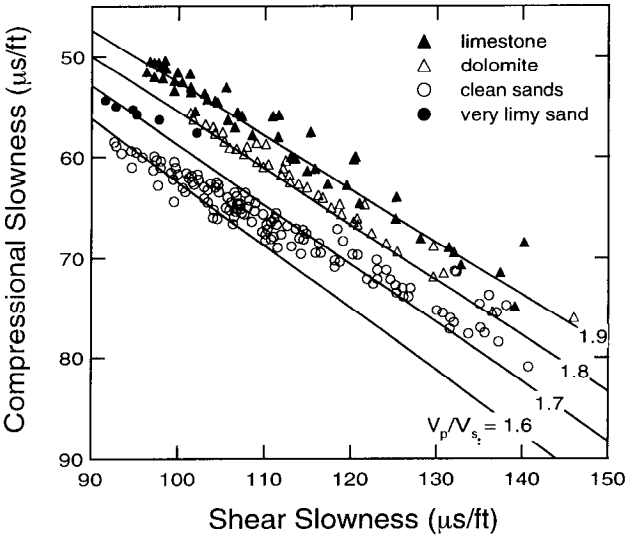

Fig. 2. Compressional wave and shear wave slowness data for several rock types from Pickett [61]. Lines are labeled with Vp/Vs ratios.

TABLE 1. V_P/V_S vs Lithology

lithology	V_P/V_S
limestone	1.9
dolomite	1.8
clean sandstones	1.6-1.7

space, we can imagine that very compliant pores (such as thin cracks) will close under small stresses. Increasing stress will close more and more pores, thereby stiffening the overall frame of the rock. Several theoretical models [18, 47, 60, 86] have utilized this approach. If instead we focus on the grain space, we envision isolated grains pressed together at their contacts. As stress increases, the grain contacts become stiffer, as does the entire frame [8, 9, 24, 41, 54, 55, 83].

4.1 Effective Stress.

When applied to acoustic properties, effective stress is the difference between confining pressure and pore pressure [57]. Imagine a piece of rock totally enclosed by an impermeable jacket. If the rock is immersed in fluid which is pressurized, the fluid pressure will be transmitted through the jacket to the frame of the rock. This pressure is referred to as the external *confining pressure*. Now imagine that we can independently control the pressure of fluid in the connected pore space of the rock. This *pore pressure* acts to oppose the confining pressure. The pore pressure pushes on the inside surface of the jacket; the confining pressure pushes on the outside. Wyllie et al [104] showed very clearly that, to first order, velocities are a function of the effective stress on the rock (confining pressure minus pore pressure). Their data are reproduced in Figure 3. Note that the velocity is independent of confining pressure when the effective stress is held constant (by increasing pore pressure at the same rate as confining pressure). It is generally assumed that attenuation has a similar dependence on effective stress, though we are not aware of such a clear demonstration. Winkler and Nur [100] showed that increasing confining pressure, or decreasing pore pressure, both reduce attenuation in water-saturated rock (see Section 6.4).

4.2 Anisotropy

Anisotropic stresses cause velocities in rock to vary with direction [10, 45, 58, 72]. An example of this effect is shown in Figure 4 from Nur and Simmons [58]. In this experiment, a granite sample was subjected to uniaxial stress, and velocities were measured as a function of azimuth, defined as the angle between the raypath and the uniaxial stress direction. At zero stress, the velocity is virtually independent of azimuth. As stress increases, a strong anisotropy develops. P and SH waves are much more sensitive to stress when propagating parallel to the stress direction than when propagating perpendicular to the stress direction. Nur [56] showed how this data could be modeled by assuming an initially isotropic distribution of cracks in the rock, and allowing cracks to preferentially close depending on how closely their normals are aligned with the uniaxial stress axis. It is likely that stress anisotropy will also create attenuation anisotropy, but no experimental data are available to confirm this.

A more extreme example is shown in Figure 5 for Berea sandstone. These data were taken on a dry cylinder subjected to uniaxial stress. Compressional wave velocities were measured both parallel and perpendicular to the stress axis. Shear wave velocities were measured perpendicular to the stress axis, but with polarizations both parallel and perpendicular to the stress axis. Shear-wave splitting on the order of 20% is observed. Compressional velocities can differ by 50%. As the rock approaches failure at 44 MPa, velocities begin to decrease. This is caused by dilatancy, the opening of

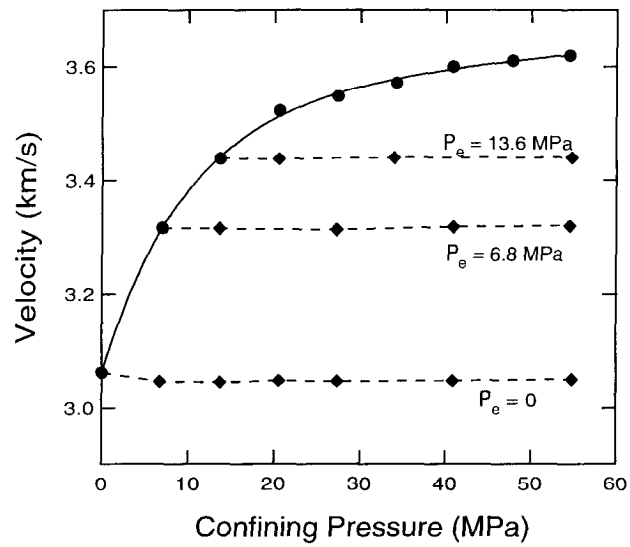

Fig. 3. Compressional wave velocity vs external confining pressure for water-saturated Berea sandstone from Wyllie et al. [99]. Solid curve has zero pore pressure, so effective pressure (Pe) equals confining pressure. On dashed curves, pore pressure increases with confining pressure to maintain a constant value of effective pressure.

microcracks with normals perpendicular to the uniaxial stress direction [11, 45].

Many rocks exhibit velocity anisotropy even under isotropic stress conditions [8, 9, 41]. This is generally caused by preferential alignment of minerals or cracks. Shales in particular are often very anisotropic due to alignment of platy clay minerals [39, 44, 67 68, 85]. Rai and Hanson [68] found shear wave anisotropy of ~39% in a shale. In a field study, White et al. [94] observed ~12% anisotropy in the Pierre shale. Theoretical models of

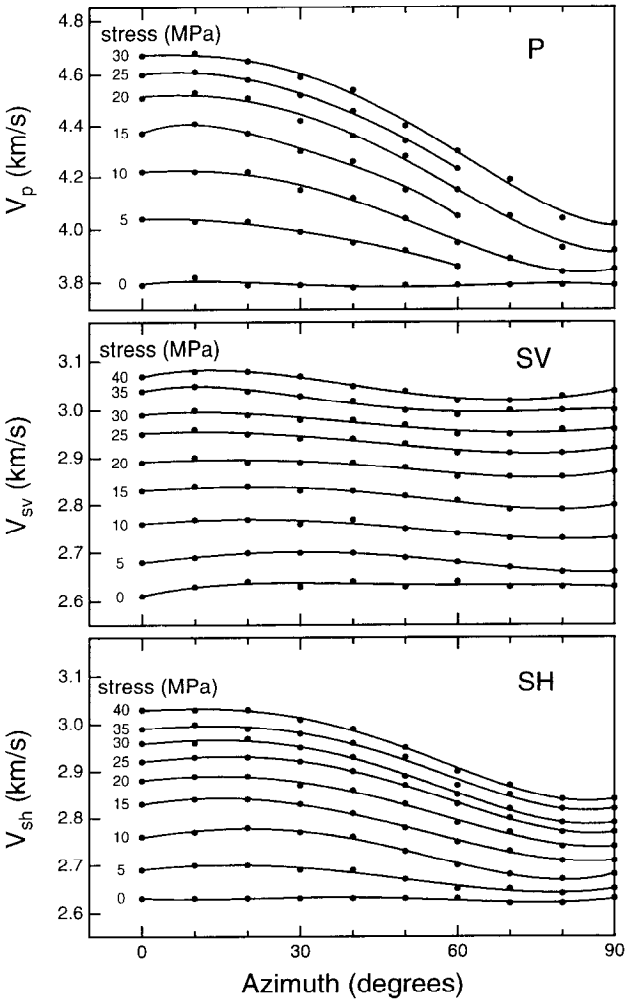

Fig. 4. Velocities vs azimuth in Barre granite under uniaxial stress from Nur and Simmons [55]. Azimuth is the angle between the uniaxial stress direction and the direction of wave propagation. P - compressional waves. SH - shear waves whose polarization direction is always perpendicular to the uniaxial stress direction. SV - shear waves polarized perpendicular to the SH polarization direction.

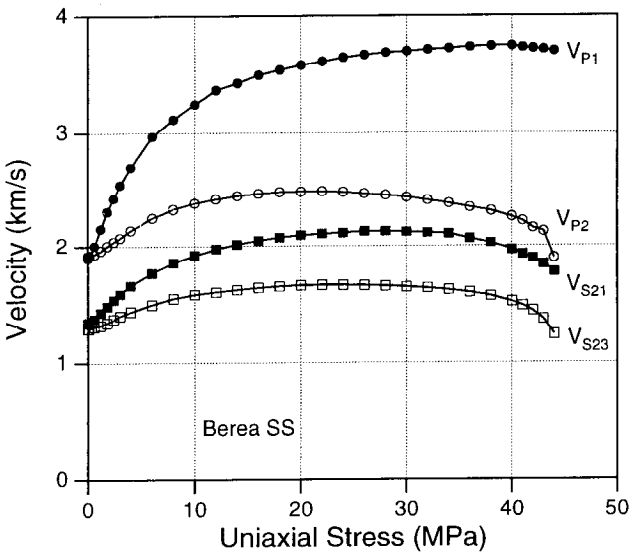

Fig. 5. Compressional and shear wave velocities in dry Berea sandstone as functions of uniaxial stress. V_{P1} - propagates parallel to uniaxial stress direction. V_{P2} - propagates perpendicular to uniaxial stress direction. V_{S21} - propagates perpendicular to uniaxial stress direction and polarized parallel to stress direction. V_{S23} - propagates perpendicular to uniaxial stress direction and polarized perpendicular to stress direction. Very strong stress-induced velocity anisotropy and shear-wave splitting is observed.

velocity anisotropy in rocks are generally based upon aligned microcracks [23, 34, 56]. Thomsen [77] showed that an assumption of weak anisotropy (appropriate for many rocks) results in significant simplification of the governing equations.

4.3 Nonlinear Acoustics

Stress-dependent velocities are part of the more general field of nonlinear acoustics. 'Stress-dependent' refers either to externally applied stress or to the stress-amplitude of the wave itself. Nonlinear acoustics is a well-developed field when applied to liquids or simple solids, such as plastics and metals. In addition to the bulk and shear moduli used in linear elastic theory, higher-order terms called third-order elastic constants are used. Isotropic solids will have three third-order constants; anisotropic solids will have many more. In addition to predicting velocity varying with external stress, nonlinear theory also predicts phenomenon such as harmonic generation and beam-mixing. Only recently have these later effects been demonstrated in rocks using small-amplitude propagating waves [36, 37].

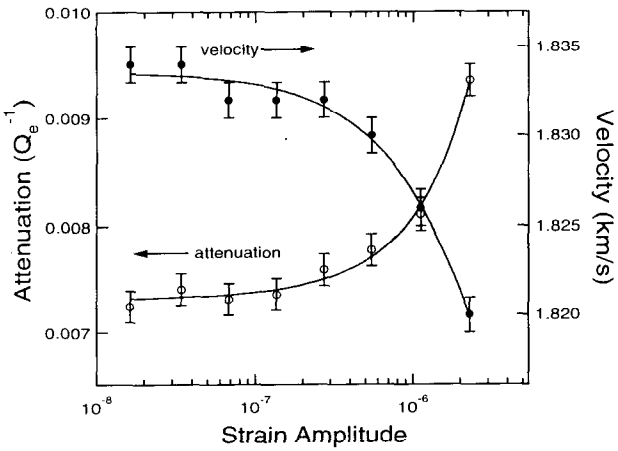

Fig. 6. Extensional wave velocity and attenuation data for dry Massilon sandstone vs strain amplitude from Winkler et al. [97].

Acoustic nonlinearity is readily observed using large-amplitude stress waves. Various studies, usually using resonant bar techniques, have shown that velocity decreases and attenuation increases when maximum strains exceed approximately 10^{-6}. Figure 6 shows data from Winkler et al. [102] that demonstrates both effects. This amplitude dependence of velocities is a dominant cause of the difference between 'static' and 'dynamic' moduli. Static moduli are generally derived from direct measures of stress and strain, with strains exceeding 10^{-6}. Dynamic moduli are measured from propagating acoustic waves with strains generally much less than 10^{-6}. At low effective stresses, it is often observed that dynamic moduli are larger than static moduli [74]. The words 'static' and 'dynamic' imply a frequency dependence which does not exist in dry rocks (see Section 6.1). Cook and Hodgson [22] showed that static moduli vary with the size of the stress cycle used to measure them, with smaller stress cycles yielding larger moduli.

5. FLUID EFFECTS IN LOW-FREQUENCY LIMIT

As will be discussed below, fluid-solid interactions in rock can produce significant frequency dependence in both velocity and attenuation. For water-saturated rocks, the frequency dependence appears to be minimal below about 1000 Hz, but for oil-saturated rocks the frequency dependence may persist to much lower frequencies, scaling with the product of frequency times viscosity. In the low-frequency limit, fluid and solid motions are in phase.

In this limit, equations derived by Gassmann [28] allow us to compute elastic moduli of fluid saturated rock knowing the properties of both the dry frame and the fluid. Gassmann's equations are also the low-frequency limit of Biot theory [5], a more comprehensive theory discussed below. Gassmann's equations require the bulk modulus of the matrix material (K_S), the bulk modulus of the pore fluid (K_f), the bulk modulus of the dry frame (K_b), the shear modulus of the dry frame (N_b) and the porosity (ϕ). K and N are the bulk and shear moduli of the saturated rock.

$$K = K_b + \frac{\left(K_s - K_b\right)^2}{K_s\left(1 - \phi - \frac{K_b}{K_s} + \phi\frac{K_s}{K_f}\right)} \tag{2}$$

$$N = N_b \tag{3}$$

Note that the shear modulus of the rock is the same dry or saturated, so the only effect pore fluids have on shear velocity is through increasing the density. The bulk modulus of the rock is increased by the addition of pore fluid, which essentially stiffens the pores with respect to compression. The bulk modulus of hydrocarbon pore

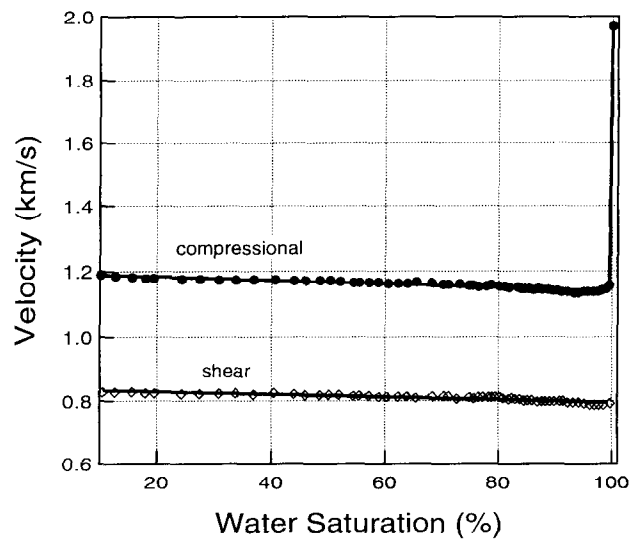

Fig. 7. Compressional wave and shear wave velocities in Massilon sandstone as a function of water saturation from Murphy [48]. Data were taken below 700 Hz. Biot-Gassmann predictions fit data very well. Data corresponds to attenuation data in Figure 12.

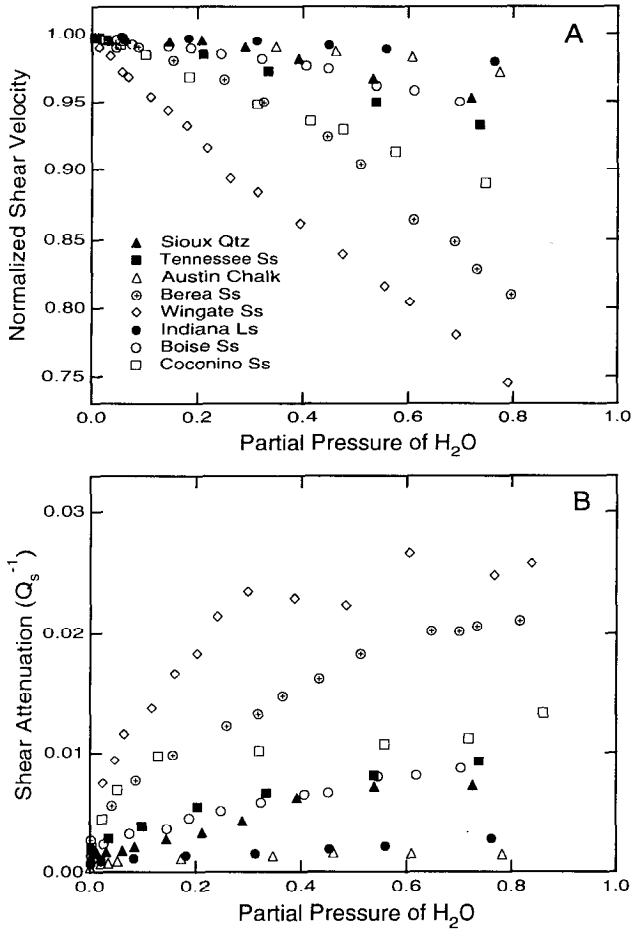

Fig. 8. Shear wave velocity (normalized) and attenuation data as functions of partial pressure of water vapor for several rocks from Clark et al. [18]. Water vapor decreases velocity and increases attenuation in nominally 'dry' rocks.

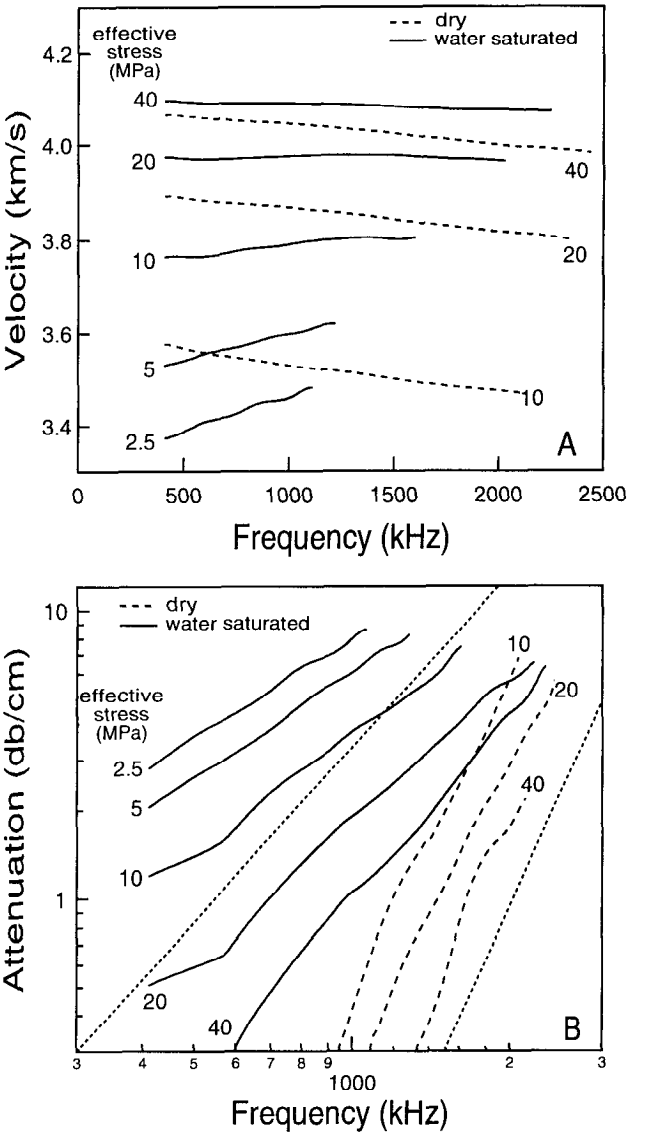

Fig. 9. Phase velocity (A) and attenuation (B) vs frequency in Berea sandstone from Winkler [91]. Dashed lines - dry rock. Solid lines - water saturated rock. Effective stress is indicated on the plots. On B, dotted reference lines having slopes of 2 and 4 are also plotted. Scattering theory predicts slopes of four on a log-log plot of attenuation (db/cm) vs frequency, and predicts velocity decreasing with increasing frequency.

fluids can vary significantly with pressure, temperature, and composition [20, 89]. When the pore fluid is a mixture of liquid and gas, then an effective fluid bulk modulus can be input to equation (2). Figure 7 shows data taken by Murphy [51] at ~1 kHz, along with velocities calculated using Gassmann's equation. As saturation increases, V_P and V_S decrease up to very high saturations due to increasing density. As gas is eliminated at the highest saturations, there is a rapid increase in the fluid bulk modulus which causes both K and V_P to increase. Figure 7 shows that the V_P/V_S ratio can be used as a gas indicator, but it is insensitive to the amount of gas in the rock. The gas effect on V_P sometimes produces 'bright spots' on reflection seismograms, and has been used as a direct hydrocarbon indicator (discussed more fully in Section 7).

One problem with applying Gassmann's equations is that the dry frame moduli, K_b and N_b, are not easily determined, even in the laboratory. This is because both moduli are very sensitive to chemical interactions between the pore fluid and the frame. Rocks dried with heat and high vacuum have relatively high velocities and

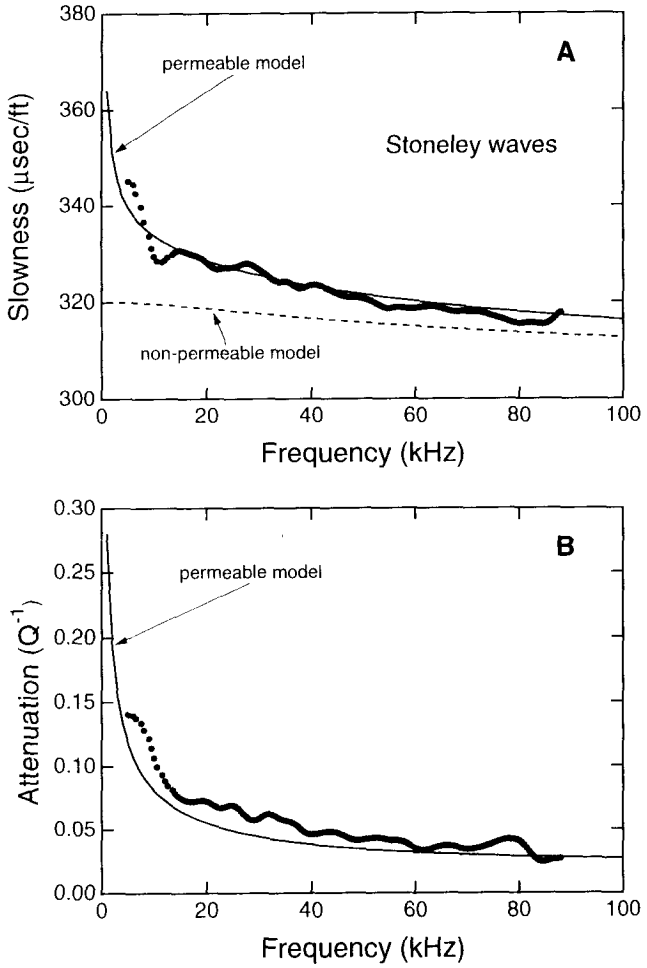

Fig. 10. Stoneley wave slowness and attenuation vs frequency in Berea sandstone measured in the laboratory by Winkler et al. [94]. Solid lines are model predictions (not fits) which include rock permeability. Dashed line indicates predicted slowness for non-permeable rock. Negligible attenuation is predicted in non-permeable rock. Permeability enhances both slowness and attenuation at low frequencies.

virtually no attenuation [78]. As monolayers of liquid are deposited on the internal surface of rock, velocity decreases and attenuation increases. Representative data from Clark et al. [21] are shown in Figure 8, where attenuation and normalized velocity are plotted as functions of water partial pressure. These data have been modeled [54, 83] as fluid monolayers lowering the surface energy of the grains and thereby reducing the cohesion and stiffness of the grain contacts. From a practical point of view, it is necessary to use K_b and N_b for the *wetted-frame* in Gassmann's equations so that the chemical effects are incorporated into the frame moduli. This is often done simply by avoiding extreme efforts to dry the rock in the lab, assuming that 'room-dry' rocks have a water-wet frame. However, care must be taken if precise theoretical predictions are planned.

A recent application of Gassmann's equation by Murphy et al. [53] inverts Equation (2) to solve for the fluid bulk modulus, K_f, in terms of V_P and V_S measured in saturated rocks. To do this, they must assume a ratio of K_b/N_b in dry sandstone, which they take to be 0.9. They show that in high-porosity sandstones, the calculated value of K_f has sufficient resolution to distinguish between gas, oil and water. A field example is discussed in Section 7.

6. ATTENUATION/DISPERSION MECHANISMS

Several mechanisms have been identified that contribute to attenuation and velocity dispersion of acoustic waves (dispersion being the frequency dependence). Each mechanism can dominate under certain experimental conditions of frequency, saturation and strain amplitude. It appears that under typical conditions in the earth's crust, in homogeneous rocks, attenuation and dispersion are dominated by viscous fluid/solid interactions. In heterogeneous rocks, scattering can cause significant dispersion and loss (not absorption) of energy, but we will only discuss this mechanism as it pertains to grain/pore scale heterogeneities. Attenuation and dispersion are physically related, one implying the other. Bourbié et al. [12] provide an extensive discussion of this relationship. For most mechanisms, attenuation varies with frequency. Frequencies having high attenuation also have the greatest dispersion. Attenuation is generally presented as either Q or α, defined by [80]

$$\frac{1}{Q} = \frac{M_i}{M_r} = \frac{\alpha v}{\pi f} \tag{4}$$

where M_i and M_r refer to the real and imaginary parts of an elastic modulus, v is the velocity of a wave controlled by modulus M, and f is frequency.

6.1 Friction

For many years, frictional sliding between grains was considered a dominant mechanism of attenuation in rocks. In addition to its intuitive simplicity, friction predicts attenuation independent of frequency (constant Q) and no velocity dispersion. This was consistent with some early experimental data on dry rocks [64], and with data on

saturated rocks over limited frequency bands [38]. It was also consistent with the cusped nature of stress-strain loops measured in low-frequency experiments, implying a non-linear mechanism [30, 49]. More recent work, however, has shown that attenuation can have significant frequency dependence, with corresponding velocity dispersion. The frictional mechanism is now associated with amplitude dependent velocity and attenuation (Figure 6) that is only important at large strain amplitudes [46, 70, 102]. At atmospheric pressures, strains > 10^{-6} are generally required to observe amplitude dependence. At larger effective stresses, even larger strains are needed [102]. The frictional mechanism probably is most important in the near field of seismic sources such as explosions and earthquakes.

6.2 Scattering

Acoustic scattering occurs whenever velocity or density heterogeneities occur on the same length scale as the acoustic wavelength. Although the scattered energy is not absorbed by the rock as heat, it does result in energy loss to the primary acoustic pulse. Scattering also reduces the velocity of the primary pulse, causing velocity to decrease as frequency increases. Most scattering models are designed for systems of weak scatterers, and so have not been successful in quantitatively predicting scattering in rocks. Sayers [71] presented a model predicting attenuation (α) increasing with the fourth power of frequency and velocity decreasing with the second power of frequency.

Winkler [96] presented experimental results showing scattering effects in sandstones at ultrasonic frequencies, where the scatterers are the grains and pores of the rock. Figure 9 shows velocity and attenuation data for Berea sandstone as functions of both frequency and effective stress. The attenuation data are plotted on a log-log scale for easy estimation of the slope. In dry rock, attenuation is well-fit by a fourth-power frequency dependence, and velocity decreases with increasing frequency, both in agreement with theory. In water-saturated rock, these effects are not so clearly observed because of the addition of fluid-flow effects (discussed below). However, at high effective stresses, fluid-flow effects are minimized and the data approach the trends expected for a scattering mechanism.

6.3 Macroscopic Flow (Biot)

Biot [5, 6] developed a theory of wave propagation in fluid saturated porous media that focuses on macroscopic fluid-flow. Various applications of Biot theory to porous media have been discussed by Johnson [35]. Biot theory

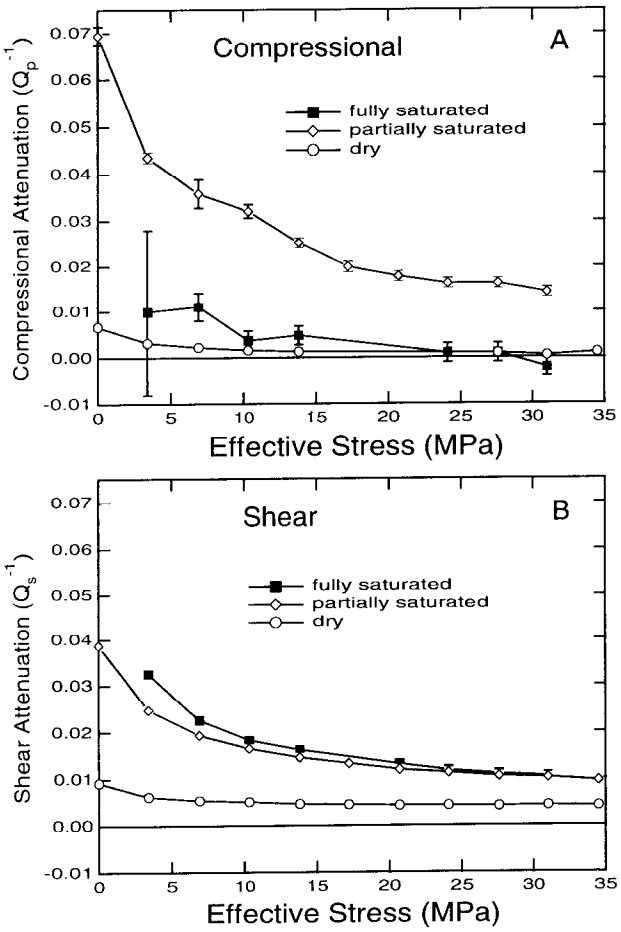

Fig. 11. Compressional and shear wave attenuation vs effective stress in Massilon sandstone from Winkler and Nur [95]. Data taken at frequencies near 1 kHz. Data are shown for dry, partially water-saturated (~95%) and fully water-saturated rock. Data are from resonant bar experiment, so compressional data was calculated from torsional and extensional data, resulting in larger error bars.

shows that acoustic waves create relative motion between the fluid and the solid frame due to inertial effects. As the matrix is accelerated, the fluid lags behind, resulting in viscous dissipation of acoustic energy. At low frequencies, the viscous skin depth is much larger than the pore size and fluid and solid are virtually locked together, moving in phase. Velocity is minimum and there is little attenuation. At high frequencies, the viscous skin depth is very small and the fluid and solid are essentially decoupled. Velocity is a maximum, and attenuation is low. For water-saturated rocks, the critical frequency in the

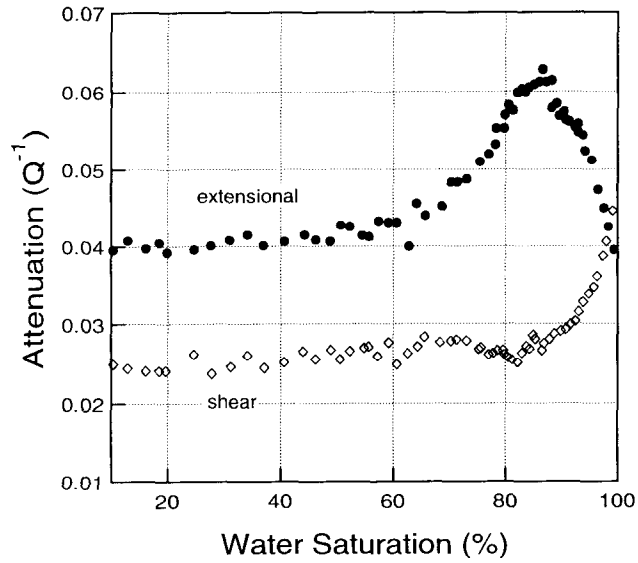

Fig. 12. Extensional wave and shear wave attenuation in Massilon sandstone as a function of water saturation from Murphy [48]. Data were taken below 700 Hz. Data corresponds to attenuation data in Figure 7. Extensional (and compressional) attenuation is maximum in partially saturated rock. Shear attenuation is maximum in fully saturated rock.

Biot theory, where attenuation and dispersion are maximum, is often on the order of 100 kHz. Increasing viscosity pushes the critical frequency even higher. Therefore seismic waves and sonic logging are almost always in the low-frequency range of Biot theory. The low-frequency limit of Biot theory gives Gassmann's equations, discussed above.

For typical sandstones, Biot theory predicts a maximum of one to two percent velocity dispersion between its low- and high-frequency limits [97]. Predicted attenuation is also rather small, with minimum Q's on the order of 100. As will be seen, many rocks show much more dispersion and attenuation than this. An interesting prediction of Biot theory is the existence of a second compressional wave dominated by the properties of the pore fluid (often called the Biot slow wave). At low frequencies this wave is diffusive and at high frequencies it is propagatory. The propagating wave is very difficult to observe in rocks, though it has been seen in synthetic materials [66].

The diffusive mode of the slow wave is of practical importance for permeability estimation using borehole Stoneley waves. The Stoneley wave is a guided mode propagating primarily in the borehole fluid and applying pressure against the borehole wall. This pressure generates a diffusive wave in the pore fluid in the rock. Modeling has shown that this energy conversion from Stoneley wave to diffusive wave causes both attenuation and increased slowness of the Stoneley wave [16, 17, 69, 91]. These models were experimentally confirmed by Winkler et al. [99]. Their data for both slowness and attenuation vs frequency in Berea sandstone are shown in Figure 10, along with model predictions. In practice, it is possible to invert Stoneley slowness and/or attenuation measurements to estimate the permeability of rock formations [33].

6.4 Local-Flow

The Biot theory (discussed above) is concerned with macroscopic fluid-flow controlled by the permeability of the rock. Another fluid-flow absorption/dispersion mechanism, often called 'local-flow', is based upon microscopic fluid motion which is not coherent over macroscopic length scales. The pore space of a rock is generally very heterogeneous, some regions being very compliant while others are very stiff. This can result in fluid being squeezed out of grain contacts into nearby pores, or squeezed between adjacent cracks having different orientations with respect to a passing stress wave. This model has been addressed theoretically by many authors [7, 48, 55, 61, 63, 83]. While most of these models can be fit to experimental data, none of them yet have the predictive power of the Biot theory. This is

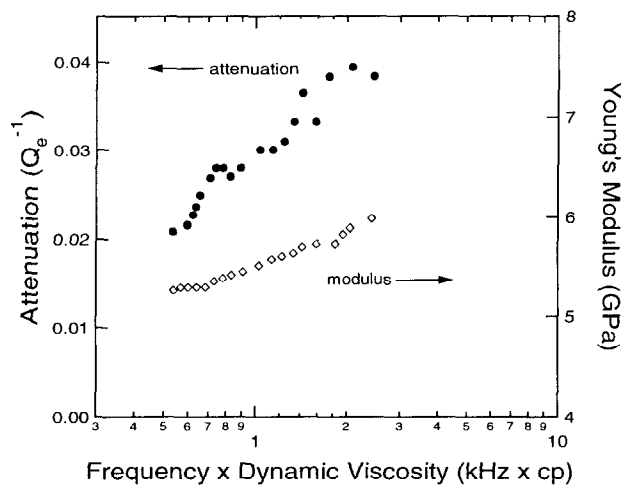

Fig. 13. Extensional attenuation and modulus vs product of frequency and viscosity, from Jones and Nur [37]. For one centipoise water-saturated rock, the horizontal axis becomes a kHz scale. Rock is Berea sandstone with 10 MPa confining pressure and 4.5 MPa pore pressure.

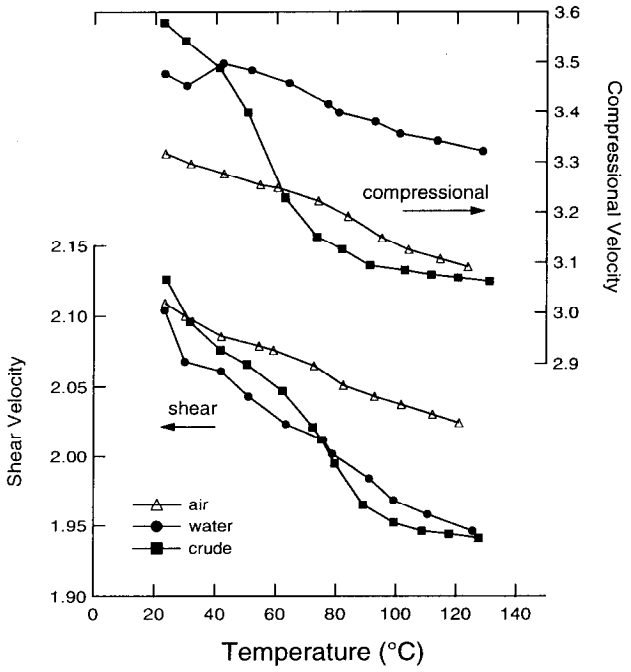

Fig. 14. Compressional and shear velocities in Boise sandstone as functions of temperature, from Wang and Nur [82]. Rock is saturated with air (dry), water, or crude oil. Effective stress is 15 MPa.

because they are all highly dependent on details of the microstructure that cannot yet be adequately quantified.

Nevertheless, many experimental results have been interpreted in terms of the local-flow mechanism [25, 41, 50, 51, 52, 75, 79, 87, 96, 97, 98, 100, 101]. These experiments have addressed effects of saturation, stress, temperature, viscosity and frequency. Winkler and Nur [100] showed (Figure 11) that shear wave attenuation increases monotonically with saturation, while compressional wave attenuation is greater in partially saturated rock than in fully saturated rock. More detailed data taken by Murphy [50] are shown in Figure 12. These effects, along with the overall magnitude of attenuation, are consistent with theoretical predictions. At low pressures, the attenuation is approximately an order of magnitude greater than that predicted by Biot theory.

The local flow mechanism predicts that absorption and dispersion will scale with the product of frequency and viscosity ($\omega\eta$). By varying viscosity as well as frequency, experimentalists have been able to effectively broaden the frequency range available to any particular experimental technique. Many experimental results now exist showing attenuation varying with $\omega\eta$, with associated velocity dispersion [25, 40, 50, 75, 79, 101]. Some of these observations may have been affected by fluid-flow to the boundaries of the sample, and therefore are not truly representative of a local-flow mechanism [26, 93]. However, some measurements are not affected by boundary flow. Figure 13 is an example from Jones and Nur [40] in which cylindrical samples were resonated in torsion. The samples were jacketed and under confining pressure. While the complete absorption peak has not been mapped, the frequency dependence is clear.

When pore fluid viscosity varies strongly with temperature, velocities can be significantly affected. At low temperature the viscosity is high and fluid cannot flow easily, so the measurement is on the high-frequency, high-velocity, unrelaxed side of the local-flow mechanism. As temperature increases, viscosity decreases, fluid flows more easily and velocity decreases as we move to the relaxed side of the absorption/dispersion mechanism. This effect is especially strong when the rock is saturated with viscous hydrocarbons. Figure 14 has data from Wang and Nur [87] showing velocities changing with temperature for air-, water- and oil-saturated sandstone.

The concept of relaxed vs unrelaxed velocities was explored in some detail by Murphy [52] and Winkler [97, 98]. Murphy showed that acoustic measurements made near 1 kHz could be well described using Gassmann's equations, but ultrasonic data were better described using a model with unrelaxed pore fluid [61]. Winkler used ultrasonic velocity measurements on dry rock as input to Gassmann's equations to calculate the low-frequency velocity limit for saturated rock. He then noted that ultrasonic velocity measurements on saturated rock always exceeded this low-frequency limit in a manner consistent with dispersion caused by the local-flow mechanism. This showed that ultrasonic lab measurements were being affected by mechanisms operating at lower frequencies, and so were not entirely representative of velocities at seismic or sonic frequencies.

7. FIELD APPLICATIONS

Via the techiques of surface seismics, vertical seismic profiling, well-to-well seismics, and sonic well-logging, acoustics is the most widely used phenomenon for exploring and characterizing the earth's crust. The acoustic properties of interest are intrinsic velocities and attenuation, and impedance contrasts at structural interfaces.

Velocities are often used for lithology identification using correlations such as Pickett's crossplot (Figure 2).

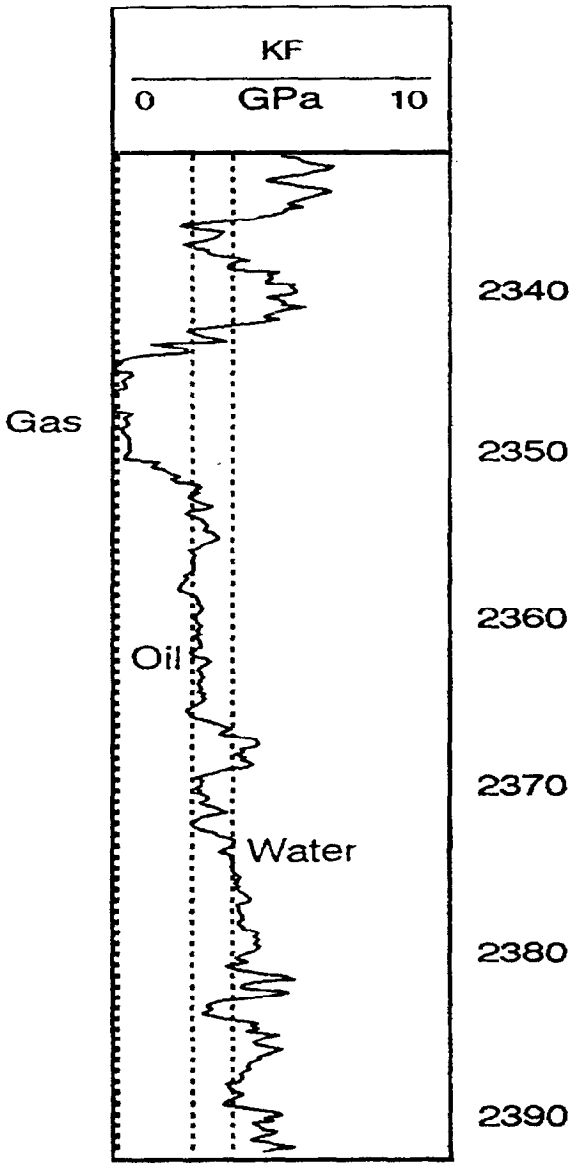

Fig. 15. Well-log from the Gulf of Mexico showing the bulk modulus of the pore fluid calculated by Murphy et al. [41]. Dotted lines are reference values for gas, oil, and water.

Additional information can be found by correlating velocities with other rock properties, such as density derived from nuclear well logs. When velocities are measured as continuous functions of depth in wellbores, the data can be integrated to yield the total acoustic travel-time to any depth, thereby providing depth calibration for surface reflection seismograms. The V_P/V_S ratio is often used as a qualitative indicator of the presence of gas, since gas will reduce the compressional velocity, but not the shear velocity (Figure 7). Under suitable conditions of high porosity and small clay content, it is possible to calculate the pore fluid bulk modulus, thus distinguishing between gas, oil and water. Figure 15 from Murphy et al. [53] shows the results of such a calculation for an oil well in the Gulf of Mexico. The solid curve indicates the calculated bulk modulus of the pore fluid. The dashed reference lines labeled 'gas', 'oil' and 'water' represent the bulk moduli of those pore fluids. The presence of gas is indicated from 2343 to 2350 meters, oil from 2350 to 2365 meters and from 2368 to 2373 meters, and water elsewhere.

Attenuation data are not routinely used to determine rock properties because it is very difficult to get accurate measurements of attenuation, either from seismics or well-logs. It has long been known that the presence of gas will reduce compressional wave amplitudes, resulting in cycle-skipping on sonic logs. This is consistent with laboratory attenuation data (Figures 11 and 12). Attenuation is potentially more sensitive than velocity to the amount of gas in a rock.

Both velocity and attenuation have been used to estimate formation permeability from borehole Stoneley waves. High permeability decreases velocity and increases attenuation, consistent with theoretical models

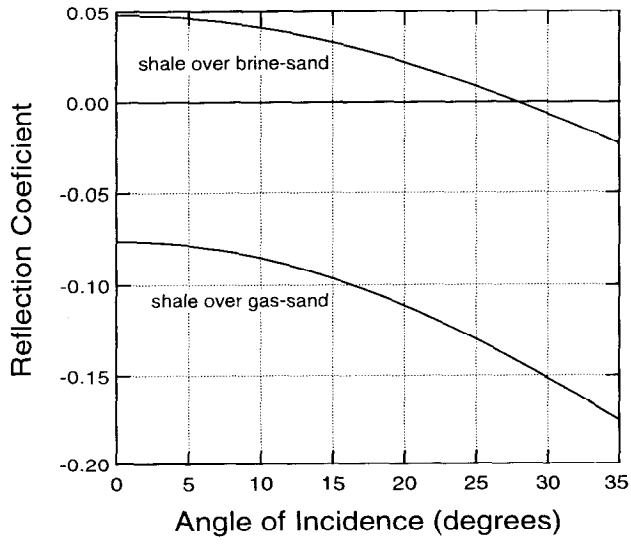

Fig. 16. Reflection coefficient vs angle of incidence for compressional waves at a shale/brine-sand interface, and a shale/gas-sand interface. Curves were calculated using Equation (5) and the rock properties in Table 2. These curves are the basis of AVO interpretation.

TABLE 2. AVO Velocity Model

lithology	V_P (m/s)	V_S (m/s)	ρ (g/cc)
shale	2377	941	2.27
brine sand	2664	1253	2.23
gas sand	2249	1301	2.06

and lab experiments (Figure 10). This technique is still gaining acceptance in the field, but has been successfully used under a wide variety of conditions [13, 17, 33, 62].

Use of rock acoustics for 'direct detection of hydrocarbon' has received considerable interest in recent years. In its simplest form, it has been observed that the low compressional velocity of gas reservoirs often produces a high impedance contrast with the overlying rock layer. This creates a high reflection coefficient between the layers and produces a so-called 'bright spot' (large amplitudes) on reflection seismograms. Bright spots can also be generated by oil reservoirs containing large volumes of dissolved gas which lowers the bulk modulus of the pore fluid [2, 20]. In practice, many compressional wave bright spots are found to be caused by lithology contrasts rather than by pore fluid contrasts. One way to distinguish the two is to look for corresponding shear wave bright spots, which will be caused by lithology contrasts but not by hydrocarbons.

In the absence of shear seismic data, an alternative technique for identifying hydrocarbon-related bright spots is known as amplitude variation with offset, or AVO. This technique makes use of the fact that the reflection coefficient of a seismic wave varies with the angle of incidence at the reflector. At normal incidence, the reflection coefficient is a function of compressional wave velocities and densities, only. At non-normal incidence, the reflection coefficient is also a function of the contrast in shear wave velocities. The full equations for reflection coefficient vs incidence angle are very complicated [105], but with suitable approximations [1, 73, 95], the following equation has simplified AVO interpretation-

$$R_{PP}(\theta) \approx R_P + (R_P - 2R_S)\sin^2\theta \quad . \tag{5}$$

R_{PP} is the reflection coefficient at angle θ, R_P and R_S are the compressional and shear reflection coefficients at normal incidence. Figure 16 shows the results of applying Equation (5) to a shale overlying a brine-saturated sandstone, and overlying a gas-saturated sandstone. The input rock parameters are given in Table 2, taken from Swan [76].

For the shale over gas-sand, the reflection coefficient is slightly negative at normal incidence and becomes more negative with increasing angle. For the shale over brine-sand, the reflection coefficient is positive at normal incidence and becomes negative with increasing angle. In principle, by modeling the variation of reflection coefficient with angle of incidence, it is possible to determine both R_P and R_S. In practice, the technique is complicated by many effects such as attenuation, anisotropy, beam spreading, etc. Nevertheless, for several years AVO has been a subject of great interest in the seismic exploration community. A recent review volume by Castagna and Backus [14] is recommended.

REFERENCES

1. Aki, K. and P.G. Richards, *Quantitative seismology: Theory and methods,* W.H. Freeman and Co., 1980.
2. Batzle, M. and Z. Wang, Seismic properties of pore fluids, *Geophysics, 57,* 1396, 1992.
3. Berryman, J.G., Long-wavelength propagation in composite elastic media II. Ellipsoidal inclusions, *J.A.S.A., 68,* 1820, 1980.
4. Berryman, J.G., Mixture theories for rock properties, this volume.
5. Biot, M.A., Theory of propagation of elastic waves in a fluid saturated porous solid. I. Low-frequency range, *J. Acoust. Soc. Am., 28,* 168, 1956a.
6. Biot, M.A., Theory of propagation of elastic waves in a fluid saturated porous solid. II. High-frequency range, *J. Acoust. Soc. Am., 28,* 179, 1956b.
7. Biot, M.A., Mechanics of deformation and acoustic propagation in porous media, *J. Appl. Phys., 33,* 1482, 1962.
8. Birch, F., The velocity of compressional waves in rocks to 10 kilobars, Part 1, J. *Geophys. Res.,*

65, 1083, 1960.

9. Birch, F., The velocity of compressional waves in rocks to 10 kilobars, Part 2, *J. Geophys. Res., 66,* 2199, 1961.
10. Bonner, B.P., Shear wave birefringence in dilating granite, *Geophys. Res. Lett., 1,* 217, 1974.
11. Brace, W.F., B.W. Paulding, and C. Scholz, Dilatancy in the fracture of crystalline rocks, *J. Geophys. Res., 71,* 3939, 1966.
12. Bourbié, T., O. Coussy, and B. Zinszner, *Acoustics of Porous Media,* Institut Français du Pétrole Publications, Gulf Publishing Co., 1987.
13. Burns, D.R., Predicting relative and absolute variations of in-situ permeability from full-waveform acoustic logs, *The Log Analyst, 32,* 246, 1991.
14. Castagna, J.P. and M.M. Backus, *Offset-dependent reflectivity - Theory and practice of AVO analysis,* Investigations in Geophysics Series, S.E.G., 1993.
15. Castagna, J.P., M.L. Batzle, and R.L. Eastwood, Relationships between compressional-wave and shear-wave velocities in clastic silicate rocks, *Geophysics, 50,* 571, 1984.
16. Chang, S.K., H. L. Liu, and D.L. Johnson, Low-frequency tube waves in permeable rocks, *Geophysics 53,* 519, 1988.
17. Cheng, C.H., Z. Jinzhong, and D.R. Burns, Effects of in-situ permeability on the propagation of Stoneley (tube) waves in a borehole, *Geophysics, 52,* 1279, 1987.
18. Cheng, C.H. and M.N. Toksöz, Inversion of seismic velocities for the pore aspect ratio spectrum of a rock, *J. Geophys. Res., 84,* 7533, 1979.
19. Christensen, N.I., Seismic Velocities, in CRC Handbook of Physical Properties of Rocks, Vol. II, edited by Robert S. Carmichael, CRC Press, 1982.
20. Clark, V.A., The effect of oil under in-situ conditions on the seismic properties of rocks, *Geophysics, 57,* 894, 1992.
21. Clark, V.A., B.R. Tittmann, and T.W. Spencer, Effect of volatiles on attenuation (Q^{-1}) and velocity in sedimentary rocks, *J. Geophys. Res., 85,* 5190, 1980.
22. Cook, N.G.W. and K. Hodgson, Some detailed stress-strain curves for rock, *J. Geophys. Res., 70,* 2883, 1965.
23. Crampin, S., Effective anisotropic elastic constants for wave propagation through cracked solids, *Geophys. J. Roy. Ast. Soc., 76,* 133, 1984.
24. Digby, P.J., The effective elastic moduli of porous granular rocks, *J. Appl. Mech. ASME 28,* 803, 1982.
25. Dunn, K.J., Acoustic attenuation in fluid-saturated porous cylinders at low frequencies, *J. Acoust. Soc. Am., 79,* 1709, 1986.
26. Dunn, K.J., Sample boundary effect in acoustic attenuation of fluid-saturated porous cylinders, *J. Acoust. Soc. Am.,* 81, 1259, 1987.
27. Gardner, G.H.F., M.R.J. Wyllie, and D.M. Droschak, Effects of pressure and fluid saturation on the attenuation of elastic waves in sands, J. Pet. Tech., 189, 1964.
28. Gassmann, F., Uber die elastizitat poroser medien, *Vier. der Natur. Gesellschaft, 96,* 1, 1951.
29. Gordon, R.B. and L.A. Davis, Velocity and attenuation of seismic waves in imperfectly elastic rock, *J. Geophys. Res., 73,* 3917, 1968.
30. Gordon, R.B. and D. Rader, Imperfect elasticity of rock: Its influence on the velocity of stress waves, in *Structure and Physical Properties of the Earth's Crust,* Geophys. Monograph Series, v.14, edited by G. Heacock, 235, 1971.
31. Gregory, A.R., Aspects of rock physics from laboratory and log data that are important to seismic interpretation, *Am. Assoc. Petr. Geol. Mem., 26,* 15, 1977.
32. Han, D.-h., A. Nur, and D. Morgan, Effects of porosity and clay content on wave velocities in sandstones, *Geophysics, 51,* 2093, 1986.
33. Hornby, B.E. W.F. Murphy, H.L. Liu, and K. Hsu, Reservoir sonics: A North Sea case study, *Geophysics, 57,* 146, 1992.
34. Hudson, J.A., Wave speeds and attenuation of elastic waves in material containing cracks, Geophys. J. Roy. Ast. Soc., 64, 133, 1981.
35. Johnson, D.L., Recent developments in the acoustic properties of porous media, in *Frontiers in Physical Acoustics,* Course XCIII, North-Holland, Amsterdam, 1986.
36. Johnson, P.A., A. Migliori, and T.J. Shankland, Continuous wave phase detection for probing nonlinear elastic wave interactions in rocks, *J. Geophys. Res., 89,* 598, 1991.
37. Johnson, P.A., T.J. Shankland, R.J. O'Connell and J.N. Albright, Nonlinear generation of elastic waves in crystalline rock, *J. Geophys. Res., 92,* 3597, 1987.
38. Johnston, D.H. and M.N. Toksöz, Ultrasonic P and S wave attenuation in dry and saturated rocks under pressure, *J. Geophys. Res., 85,* 925, 1980.
39. Jones, L.E.A. and H. Wang, Ultrasonic velocities in Cretaceous shales from the Williston basin, Geophysics, 46, 288, 1981.
40. Jones, T. and A. Nur, Velocity and attenuation in sandstone at elevated temperatures and pressures, Geophys. Res. Lett., 10, 140, 1983.
41. King, M.S., Wave velocities in rocks as a function of changes in overburden pressure and pore fluid saturants, *Geophysics, 31,* 50, 1966.
42. Kowallis, B., L.E.A. Jones, and H. F. Wang, Velocity-porosity-clay

content: Systematics of poorly consolidated sandstones, *J. Geophys. Res., 89,* 10355, 1984.

43. Kuster, G.T. and M.N. Toksöz, Velocity and attenuation of seismic waves in two-phase media: Part 1. Theoretical formulations, *Geophysics, 39,* 587, 1974.
44. Lo, Tien-when, K.B. Coyner, and M.N. Toksoz, Experimental determination of elastic anisotropy of Berea sandstone, Chicopee shale, and Chelmsford granite, *Geophysics, 51,* 164.
45. Lockner, D.A., J.B. Walsh, and J.D. Byerlee, Changes in seismic velocity and attenuation during deformation of granite, *J. Geophys. Res., 82,* 5374, 1977.
46. Mavko, G.M., Frictional attenuation: An inherent amplitude dependence, *J. Geophys. Res., 80,* 1444, 1979.
47. Mavko, G.M. and A. Nur, The effect of nonelliptical cracks on the compressibility of rocks, *J. Geoph. Res., 83,* 4769, 1978.
48. Mavko, G.M. and A. Nur, Wave attenuation in partially saturated rocks, *Geophysics, 44*, 161, 1979.
49. McKavanagh, B. and F.D. Stacey, Mechanical hysteresis in rocks at low strain amplitudes and seismic frequencies, *Phys. Earth Planet. Int., 8,* 246, 1974.
50. Murphy, W.F., Effects of partial water saturation on attenuation in Massilon sandstone and Vycor porous glass, *J. Acoust. Soc. Am., 71,* 1458, 1982.
51. Murphy, W.F., Acoustic measures of partial gas saturation in tight sandstones, *J. Geophys. Res., 89,* 11,549, 1984.
52. Murphy, W.F., Sonic and ultrasonic velocities: Theory versus experiment, *Geophys. Res. Lett., 12,* 85, 1985.
53. Murphy, W., A. Reischer, and K. Hsu, Modulus decomposition of compressional and shear velocities in sand bodies, *Geophysics, 58,* 227, 1993.
54. Murphy, W.F., K.W. Winkler, and R.L. Kleinberg, Frame modulus reduction in sedimentary rocks: The effect of adsorption on grain contacts, *Geophys. Res. Lett., 1,* 805, 1984.
55. Murphy, W.F., K.W. Winkler, and R.L. Kleinberg, Acoustic relaxation in sedimentary rocks: Dependence on grain contacts and fluid saturation, *Geophysics, 51,* 757, 1986.
56. Nur, A., Effects of stress on velocity anisotropy in rocks with cracks, *J. Geophys. Res., 76,* 2022, 1971.
57. Nur, A. and J.D. Byerlee, An exact effective stress law for elastic deformation of rock with fluids, *J. Geophys. Res., 76,* 6414, 1971.
58. Nur, A. and G. Simmons, Stress-induced velocity anisotropy in rock: An experimental study, *J. Geophys. Res., 74,* 6667, 1969.
59. Nur, A. and Z. Wang, *Seismic and Acoustic Velocities in Reservoir Rocks: Vol. 1, Experimental Studies,* S.E.G., Geophysics Reprint Series No. 10, 1989.
60. O'Connell, R.J. and B. Budiansky, Seismic velocities in dry and saturated cracked solids, *J. Geophys. Res., 79*, 5412, 1974.
61. O'Connell, R.J. and B. Budiansky, Viscoelastic properties of fluid-saturated cracked solids, *J. Geophys. Res., 82*, 5719, 1977.
62. Paillet, F.L., Qualitative and quantitative interpretation of fracture permeability using acoustic full-waveform logs, *The Log Analyst, 32,* 256, 1991.
63. Palmer, I.D. and M.L. Traviolia, Attenuation by squirt flow in under-saturated gas sands, *Geophysics, 45,* 1780, 1981.
64. Peselnick, L. and W.F. Outerbridge, Internal friction in shear and sher modulus of Solenhofen limestone over a frequency range of 10^7 cycles per second, *J. Geoph. Res., 66,* 581, 1961.
65. Pickett, G.R., Acoustic character logs and their applications in formation evaluation, *J. Petr. Tech., 15,* 650, 1963.
66. Plona, T.J., Observations of a second bulk compressional wave in a porous medium at ultrasonic frequencies, *Appl. Phys. Lett., 36,* 259, 1980.
67. Podio, A.L., A.R. Gregory, and M. E. Gray, Dynamic properties of dry and water-saturated Green River shale under stress, *Soc. Petr. Eng. J., 8,* 389, 1968.
68. Rai, C.S. and K.E. Hanson, Shear-wave velocity anisotropy in sedimentary rocks: A laboratory study, *Geophysics, 53,* 800, 1988.
69. Rosenbaum, J.H., Synthetic microseismograms: logging in porous formations, *Geophysics, 39*, 14, 1974.
70. Savage, J. C., Comments on paper by R.B. Gordon and L.A. Davis, 'Velocity and attenuation of seismic waves in imperfectly elastic rock', *J. Geophys. Res., 74,* 726, 1969.
71. Sayers, C.M., Ultrasonic velocity dispersion in porous materials, *J. Phys. D., 14,* 413, 1981.
72. Sayers, C.M., J.G. van Munster and M.S. King, Stress-induced ultrasonic anisotropy in Berea sandstone, *Int. J. Rock Mech., 27,* 429.
73. Shuey, R.T., A simplification of the Zoeppritz equations, *Geophysics, 50,* 609, 1985.
74. Simmons, G. and W.F. Brace, Comparison of static and dynamic measurements of compressibility of rocks, *J. Geophys. Res., 70,* 5649, 1965.
75. Spencer, J.W., Stress relaxations at low frequencies in fluid-saturated rocks: Attenuation and modulus dispersion, *J. Geophys. Res., 86,* 1803, 1981.

76. Swan, H.W., Properties of direct AVO hydrocarbon indicators, in *Offset-dependent reflectivity - Theory and practice of AVO analysis*, Investigations in Geophysics Series, ed. J.P. Castagna and M.M. Backus, S.E.G., 1993.
77. Thomsen, L., Weak elastic anisotropy, *Geophysics, 51*, 1954, 1986.
78. Tittmann, B.R., J.M. Curnow, and R.M. Housley, Internal friction quality factor Q>3100 achieved in lunar rock 70215,85, *Proc. Lunar Sci. Conf. 6th*, 3217, 1975.
79. Tittmann, B.R., H. Noadler, V.A. Clark, L.A. Ahlberg, and T.W. Spencer, Frequency dependence of seismic attenuation in saturated rocks, *Geophys. Res. Lett., 8*, 36, 1981.
80. Toksöz, M.N. and D.H. Johnston, *Seismic Wave Attenuation*, S.E.G., Geophysics Reprint Series No. 2, 1981.
81. Toksöz, M.N., D.H. Johnston, and A. Timur, Attenuation of seismic waves in dry and saturated rocks: I. Laboratory measurements, *Geophysics, 44*, 681, 1979.
82. Tosaya, C. and A. Nur, Effects of diagenesis and clays on compressional velocities in rocks, *Geophys. Res. Lett., 9*, , 1982.
83. Tutuncu, A.N. and M.M. Sharma, The influence of fluids on grain contact stiffness and frame moduli in sedimentary rocks, *Geophysics, 57*, 1571, 1992.
84. Vassiliou, M., C.A. Salvado, and B.R. Tittmann Seismic Attenuation, in CRC Handbook of Physical Properties of Rocks, Vol. III, edited by Robert S. Carmichael, CRC Press, 1982.
85. Vernik, L. and A. Nur, Ultrasonic velocity and anisotropy of hydrocarbon source rocks, *Geophysics, 57*, 727, 1992.
86. Walsh, J.B., The effect of cracks on the compressibility of rock, *J. Geophys. Res., 70*, 381, 1965.
87. Wang, Z. and A. Nur, Wave velocities in hydrocarbon-saturated rocks: Experimental results, *Geophysics, 55*, 723, 1990.
88. Wang, Z. and A. Nur, *Seismic and Acoustic Velocities in Reservoir Rocks: Vol. 2, Theoretical and Model Studies*, S.E.G., Geophysics Reprint Series No. 10, 1992.
89. Wang, Z., A. Nur, and M. Batzle, Acoustic velocities in petroleum oils, *J. Petr. Tech., 42*, 192, 1990.
90. Watt, J.P., G.F. Davies, and R.J. O'Connell, Elastic properties of composite materials, *Rev. Geophys. Space Phys., 14*, 541, 1976.
91. White, J.E., *Seismic Waves: Radiation, Transmission and Attenuation*, McGraw-Hill, N.Y., 302 pp., 1965.
92. White, J.E., *Underground Sound: Application of seismic waves*, Elsevier, Amsterdam, 253 pp., 1983.
93. White, J.E., Biot-Gardner theory of extensional waves in porous rods, *Geophysics, 51*, 742, 1986.
94. White, J.E., L. Martineau-Nicoletis, and C. Monash, Measured anisotropy in Pierre shale, *Geophysical Prospecting, 31*, 709, 1983.
95. Wiggins, R., G.S. Kenny, and C.D. McClure, A method for determining and displaying the shear-velocity reflectivities of a geologic formation, European Patent Application 0113944, 1983.
96. Winkler, K.W., Frequency dependent ultrasonic properties of high-porosity sandstones, *J. Geophys. Res., 88*, 9493, 1983.
97. Winkler, K.W., Dispersion analysis of velocity and attenuation in Berea sandstone, *J. Geophys. Res., 90*, 183, 1985.
98. Winkler, K.W., Estimates of velocity dispersion between seismic and ultrasonic frequencies, *Geophysics, 51*, 6793, 1986.
99. Winkler, K.W., H. Liu, and D. L. Johnson, Permeability and borehole Stoneley waves: Comparison between experiment and theory, *Geophysics, 54*, 66, 1989.
100. Winkler, K. and A. Nur, Pore fluids and seismic attenuation in rocks, *Geophys. Res. Lett., 6*, 1, 1979.
101. Winkler, K.W. and A. Nur, Seismic attenuation: Effects of pore fluids and frictional sliding, *Geophysics, 47*, 1, 1982.
102. Winkler, K., A. Nur, and M. Gladwin, Friction and seismic attenuation in rocks, *Nature, 277*, 528, 1979.
103. Wyllie, M.R.J., A.R. Gregory, and L.W. Gardner, Elastic wave velocities in heterogeneous and porous media, *Geophysics, 21*, 41, 1956.
104. Wyllie, M.R.J., A.R. Gregory, and G.H.F. Gardner, An experimental investigation of factors affecting elastic wave velocities in porous media, Geophysics, 23, 459, 1958.
105. Zoeppritz, K., On the reflection and propagation of seismic waves, Erdbebenwellen VIIIB, Gottinger Nachrichtcn, I, 66, 1919.

Shock Wave Data for Rocks

Thomas J. Ahrens and Mary L. Johnson

1. INTRODUCTION

Shock wave equation of state data for rocks is the primary physical starting point for calculation of the effect of meteorite impact and explosions on the surfaces or in the crusts of the earth, moon, and other terrestrial planets [2,3,12,25,32,37,38,39,40,43], and primitive bodies such as comets and asteroids [9,54].

2. EQUATIONS OF STATE

Rocks are, by definition, composed of one or more minerals, and hence largely their equation of state behavior (Table 1) reflects the behavior of their constitutive minerals. The Hugoniot of rocks demonstrate the same regimes as sketched in Figures 1 and 2.

Dynamic yielding behavior for porous rock, like ceramics which have been more extensively studied, reflect both the Hugoniot elastic limit of the porous mineral aggregate, as well as the porous rock. [15,46].

Mixture theories are quite successful in synthesizing the Hugoniots of rocks from knowledge of the equations of state of constituent minerals.

For silicate rocks, Telegin et al. [47] have demonstrated good agreement between the observed Hugoniot and the calculated Hugoniot based upon an oxide mixture model. According to this model,

$$C_o = a_{oo} + a\ a_o\rho_o + \sum_i a_i Z_i \quad (1a)$$

$$S = b_{oo} + b_o\rho_o + \sum_i b_i Z_i \quad (1b)$$

where ρ_o is the initial density, Z_i is the mass fraction of component oxide i, and a_{oo}, a_o, the a_i's, b_{oo}, b_o, and the b_i 's, are constants. This approach works well in the high pressure regime (4, of Fig. 2). More successful over the pressure range of the entire Hugoniot is the mineral mixture model [8].

$$V(P) = \sum_i V_i(P)\ M_i \quad (2)$$

where V_i is the volume of constituent mineral, i, at pressure P and M_i is the mass fraction of mineral, i. Using the Rankine-Hugoniot equations, U_s and U_p are computed from the resulting P-V relation. Additional examples of construction of a theoretical Hugoniot from constituent minerals are given in [6] and [4].

T. J. Ahrens and M. L. Johnson, Seismological Laboratory, 252-21, California Institute of Technology, Pasadena, CA 91125

Present Address: M. L. Johnson, Gemological Institute of America, 1639 Stewart Street, Santa Monica, CA 90404

Rock Physics and Phase Relations
A Handbook of Physical Constants
AGU Reference Shelf 3

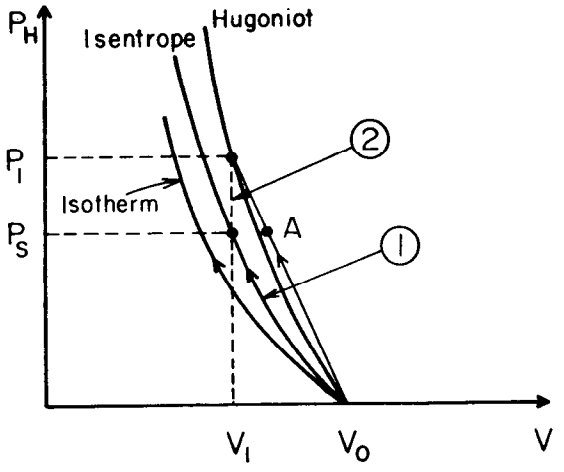

FIG. 1. Pressure-volume compression curves. For isentrope and isotherm, the thermodynamic path coincides with the locus of states, whereas for shock, the thermodynamic path is a straight line to point P_1, V_1, on the Hugoniot curve, which is the locus of shock states.

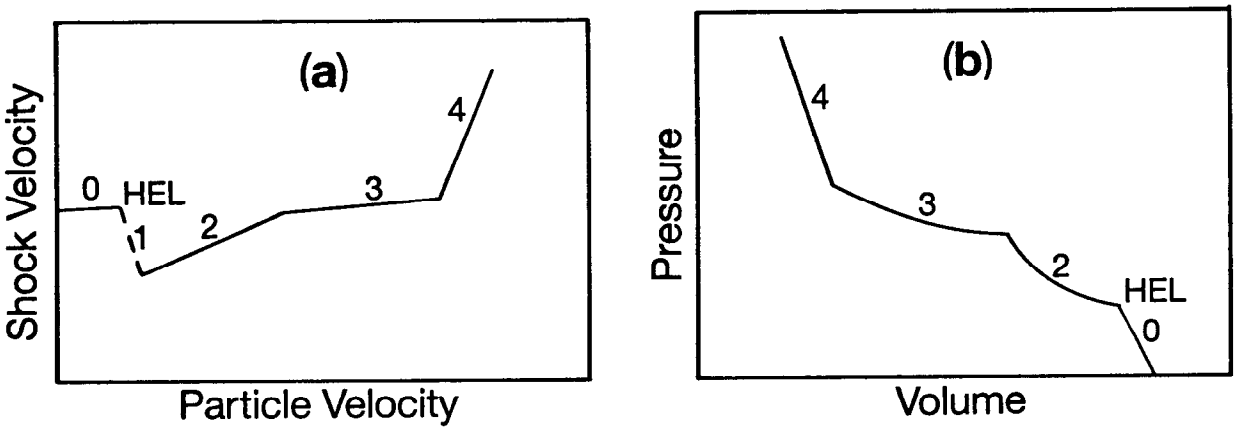

FIG. 2. Sketch of shock velocity-particle relation (a) and corresponding pressure-volume Hugoniot curves (b) for a mineral which undergoes dynamic yielding and a phase change.

0: compression up to the Hugoniot Elastic Limit (HEL)
1: transition via dynamic yielding to a quasi-hydrostatic state
2: low pressure state
3: mixed region
4: high pressure state

TABLE 1. Equations of State of Rocks

Rock Name	Locality, Comments	Sample Density (Mg/m^3)	C_0 (km/sec)	error ΔC_0 (km/sec)	S	error ΔS	lower U_p (km/sec)	upper U_p (km/sec)	Phase*	No. of Data	References
Albitite	Sylmar, PA	2.610	5.42	0.09	0.09	0.10	0	1.287	2	3	
			4.83	0.05	0.51	0.03	1.287	2.017	3	4	
			2.73	0.17	1.49	0.05	2.017	3.903	4	8	[11,33,35,53]
Andesite	Amchitka Is., Alaska	2.59	3.60	0.08	0.98	0.05	0.45	2.49	2	9	
			1.7	1.0	1.8	0.3	2.49	3.16	4	4	[10]
Anorthosite	Lunar 60025	2.229	2.02	0.10	1.57	0.03	2.036	5.196	2	11	[28,29]
Anorthosite	a	2.774	5.73	0.07	0.07	0.08	0	1.99	1	15	
			3.2	0.5	1.46	0.13	1.99	4.99	2	19	
			4.45	0.15	1.23	0.01	4.99	28.65	4	7	[3,5,11,13,14, 33,35,53]
Basalt	low density[b]	2.793	5.80	0.15	-1.2	0.3	0.291	0.79	1	4	
			4.2	0.2	0.71	0.12	0.79	2.1	2	6	
			2.4	0.2	1.60	0.06	2.1	5.94	4	14	[5 ,30,52]
Basalt	high density[c]	3.200	4.96	0.14	0.88	0.10	0.385	1.963	2	8	
			4.09	0.15	1.35	0.04	1.913	5.99	4	12	[1,6,48]
Molten basalt	synthetic $An_{36}Di_{64}$[d]	2.615	3.67	-	0.19	-	0.44	0.65	1	2	
			2.93	0.15	1.46	0.13	0.65	1.72	2	4	
			0.8	0.4	2.6	0.2	1.72	2.06	4	3	[42]
Molten basalt	Komatiite[e]	2.745	3.13	0.02	1.47	0.02	0.47	2.1	2	12	[36]
Volcanic Breccia	Amchitka Is., Alaska	1.82	-0.5	-	3.2	-	1.1	1.22	1	2	
			3.3	-	0.0	-	1.22	1.44	3	2	
			-1.1	-	3.1	-	1.44	1.65	2	2	
			1.9	0.2	1.2	0.9	1.65	3.25	4	3	[10]
Bronzitite	Bushveld, Transvaal	3.296	6.28	0.08	0.56	0.05	0.485	2.147	2	7	
			4.3	0.2	1.45	0.08	2.147	3.08	3	4	[11,33,35,53]
Bronzitite	Stillwater, Montana	3.277	5.99	-	1.56	-	0	0.483	1	2	
			6.47	0.06	0.60	0.04	0.483	2.131	2	25	
			5.16	0.07	1.17	0.03	2.043	3.481	3	21	[11,33,35,53]

TABLE 1. Equations of State of Rocks (continued)

Rock Name	Locality, Comments	Sample Density (Mg/m^3)	C_0 (km/sec)	error ΔC_0 (km/sec)	S	error ΔS	lower U_p (km/sec)	upper U_p (km/sec)	Phase*	No. of Data	References
Bronzitite	Pyroxenite (unspecified)	3.29	6.26	0.19	0.96	0.14	0.6	1.74	1	3	
			8.35	-	-0.21	-	1.74	2.26	2	2	
			5.1	0.2	1.30	0.07	2.26	5.8	3	4	[48]
Chalk	Dover, England	1.365	1.0	0.7	1.5	0.7	1.414	1.959	2	4	[50]
Chalk	(unspecified)	1.705	1.15	0.12	1.60	0.04	1.65	4.34	2	5	[31]
Chalk	(unspecified)	2.02	1.74	0.06	1.61	0.02	1.51	4.18	2	5	[31]
Chalk	moist	2.2	2.68	0.06	1.49	0.02	0.89	3.61	2	5	[31]
Clay	f	1.457	1.86	0.17	0.97	0.07	1.04	3.54	2	9	[23]
Clay	not given; 4% water	2.15	2.52	-	0.71	-	0.005	0.96	1	2	
			1.86	0.09	1.36	0.04	0.96	3.32	2	3	[7]
Clay	not given; 4-20% water[g]	2.11	1.8	0.2	3.1	0.7	0.127	0.42	1	4	
			2.69	0.11	1.30	0.05	0.42	3.28	2	12	
			1.9	0.2	1.55	0.06	3.26	4.37	4	3	[7,24]
Diabase	h	3.00	4.89	0.11	1.20	0.15	0	0.915	2	6	
			5.68	0.06	0.25	0.05	0.843	1.758	3	14	
			3.61	0.07	1.41	0.02	1.713	3.727	4	21	[11,33,35,53]
Olivine Diabase	not given	3.13	6.8	-	0.1	-	0.61	1.45	3	2	
			4.9	0.3	1.22	0.07	1.45	5.92	4	4	[35,48]
Dolomite	i	2.828	6.2	0.5	0.4	0.5	0.495	1.15	1	5	
			5.30	0.10	1.16	0.03	1.12	5.32	2	19	[31,45,52]
Dunite	low density[j]	3.262	6.38	0.09	0.81	0.06	0	2.4	2	55	
			4.82	0.16	1.33	0.05	2.399	5.95	4	29	[11,21,27,33, 34,35,48,53]
Dunite	high density[k]	3.791	5.5	0.2	1.8	0.4	0	0.701	2	3	
			6.35	0.11	0.49	0.07	0.701	2.429	3	18	
			4.0	0.2	1.47	0.08	2.429	3.407	4	13	[11,33,34,35, 53]

TABLE 1. Equations of State of Rocks (continued)

Rock Name	Locality, Comments	Sample Density (Mg/m^3)	C_0 (km/sec)	error ΔC_0 (km/sec)	S	error ΔS	lower U_p (km/sec)	upper U_p (km/sec)	Phase*	No. of Data	References
Eclogite	l	3.480	5.55	0.14	2.0	0.3	0	0.73	1	7	
		-	6.34	0.06	0.92	0.03	0.714	3.305	4	45	[33,34,35,53]
Feldspar Peridotite	not given	3.22	5.78	-	0.93	-	1.4	2.73	2	2	
			4.59	0.06	1.373	0.014	2.73	5.84	4	3	[48]
Gabbro	m	2.941	6.4	0.7	0.2	1.4	0.286	0.608	1	5	
			8.1	0.2	-2.6	0.3	0.515	0.878	2	9	
			5.8	0.2	-0.64	0.19	0.864	1.677	3	13	
			3.3	0.3	1.41	0.10	1.629	3.059	4	17	[27,33,35]
Enstatite Gabbro	not given	3.15	4.98	0.14	1.28	0.04	1.44	5.88	2	4	[48]
Gneiss	n	2.79	5.30	-	0.20	-	0.704	1.788	1	2	
			2.68	0.19	1.54	0.04	1.788	6.047	2	10	[45]
Granite	o	2.657	5.6	0.2	-0.2	0.3	0	1.00	1	21	
			4.88	0.13	0.41	0.09	0.945	2.044	2	27	
			2.06	0.17	1.66	0.05	2.034	6.01	4	58	[10,23,33,34, 35,52,53]
Granodiorite	p	2.664	5.879	0.015	0.383	0.017	0.2	3.191	1	14	
			2.2	0.4	1.64	0.08	3.191	5.999	2	10	[45,52]
Jadeite	Burma	3.335	6.41	0.06	1.30	0.08	0	1.005	1	3	
			6.57	0.10	1.09	0.07	0.986	1.94	2	8	
			7.44	0.12	0.64	0.04	1.94	3.434	3	8	[33,34,35,53]
Limestone	Salisbury Plane, England	1.742	0.00	0.18	2.61	0.15	0.56	1.67	2	10	
			2.24	0.15	1.18	0.06	1.51	3.8	4	11	[52]
Limestone	q	2.286	1.8	0.2	2.11	0.18	0.789	1.62	2	7	
			2.6	0.2	1.43	0.07	1.62	5.05	4	7	[5,30]

TABLE 1. Equations of State of Rocks (continued)

Rock Name	Locality, Comments	Sample Density (Mg/m^3)	C_o (km/sec)	error ΔC_o (km/sec)	S	error ΔS	lower U_p (km/sec)	upper U_p (km/sec)	Phase*	No. of Data	References
Limestone	r	2.597	6.7	0.8	-16	7	0.036	0.163	1	4	
			3.70	0.13	-1.0	0.5	0.163	0.387	3	3	
			2.67	0.17	2.26	0.16	0.387	1.487	2	18	
			3.4	0.2	1.54	0.07	1.487	5.791	4	21	[5 ,10,23,45,50, 52]
Marble	s	2.697	5.2	0.4	-2.8	1.6	0.086	0.43	1	8	
			3.71	0.10	1.48	0.08	0.43	2.56	2	16	[5,22 ,26,52]
Marble	t	2.841	5.4	0.3	1.14	0.18	0.913	3.08	2	10	[23]
Olivinite	not given	3.376	6.38	0.09	1.01	0.09	0.59	1.33	1	4	
			7.1	0.6	0.4	0.3	1.27	2.2	3	6	
			5.21	0.11	1.27	0.02	2.04	9.07	4	11	[48]
Pumice	u	0.55	0.31	-	1.06	-	2.32	2.96	2	2	
			-0.54	0.05	1.347	0.011	2.96	6.19	4	3	[30]
Quartzite	not given	2.65	4.72	0.09	1.24	0.17	0.25	0.79	1	4	
			5.621	0.006	0.062	0.004	0.79	2.05	2	4	
			2.3	0.3	1.59	0.07	2.05	6.18	3	4	
			4.32	0.06	1.258	0.006	6.18	12.37	4	5	[49]
Quartzite	v	2.648	6.13	0.02	0.05	0.02	0.135	2.7	2	45	[5,52]
Quartzite	w	2.646	5.43	0.10	1.0	0.3	0.174	0.54	1	9	[5,52]
Sand	x	1.61	1.70	0.08	0.46	0.08	0.5	0.86	1	12	
			1.0	0.4	1.7	0.3	0.82	1.72	2	14	
			2.1	0.2	1.10	0.09	1.71	3.88	4	16	[19 ,23,52]
Wet Sand	4% water[y]	1.72	1.61	0.14	1.26	0.06	1.14	3.49	2	5	
			-0.15	-	1.76	-	3.49	3.74	4	2	[52]
Wet Sand	10% water[y]	1.84	1.79	-	1.45	-	1.11	1.98	2	2	
			3.05	-	0.82	-	1.98	2.79	3	2	
			0.8	0.3	1.62	0.10	2.79	3.44	4	3	[52]

TABLE 1. Equations of State of Rocks (continued)

Rock Name	Locality, Comments	Sample Density (Mg/m^3)	C_0 (km/sec)	error ΔC_0 (km/sec)	S	error ΔS	lower U_p (km/sec)	upper U_p (km/sec)	Phase*	No. of Data	References
Wet Sand	19% water[y]	1.96	2.75	0.14	1.11	0.07	1.01	2.71	2	6	
			1.2	0.4	1.68	0.12	2.67	3.52	4	6	[52]
Wet Sand	z	1.985	3.39	0.08	1.14	0.05	0.98	1.94	2	4	[23]
Sandstone	aa	1.993	3.11	0.16	-1.7	0.5	0.058	0.508	1	20	
			1.58	0.09	1.49	0.07	0.472	2.041	2	23	
			2.9	0.6	0.8	0.3	1.70	2.18	3	7	
			0.57	0.14	1.63	0.03	2.57	6.43	4	11	[5,44]
Serpentine	bb	2.621	5.30	0.15	0.90	0.11	0.431	2.025	2	10	
			6.5	0.4	0.20	0.18	1.719	2.561	3	10	
			3.8	0.5	1.34	0.12	2.658	5.427	4	16	[11,33,51,53]
Shale	cc	2.545	1.6	0.3	5.3	0.5	0.104	0.72	1	29	
			3.85	0.17	1.38	0.16	0.656	1.39	3	33	
			4.56	0.11	0.79	0.05	1.388	2.832	2	63	
			2.3	0.3	1.61	0.09	2.821	3.877	4	38	[7,18,24,33,41]
Oil Shale	dd	2.239	3.66	0.07	1.18	0.03	0.663	2.812	2	51	
			7.1	0.5	-0.04	0.16	2.802	3.108	3	6	
			3.3	0.4	1.28	0.12	3.091	4.343	4	30	[10,16,17,33]
Soil (peat)	not given	0.32	0.00	-	1.66	-	0.5	1.5	2	-	[20]
Tuff	low density[ee]	1.298	1.18	0.10	1.25	0.04	0.95	3.653	2	38	
			5.4	0.6	0.04	0.18	3.344	4.061	3	6	
			0.9	1.3	1.3	0.3	4.057	5.52	4	15	[10,23,33]
Tuff	medium density[ff]	1.610	1.29	0.12	1.43	0.04	1.026	5.19	2	27	[10,23,33]
Tuff	high density[gg]	1.851	2.45	0.19	1.13	0.10	0.78	2.82	2	74	
			1.7	0.3	1.48	0.06	2.79	6.50	4	57	[10,23,33,45]

*Phases: 1) Elastic shock; 2) Low pressure phase; 3) Mixed region; 4) High pressure phase.

TABLE 1. Equations of State of Rocks (continued)

[a]Tahawus, NY; San Gabriel Anorthosite, CA; Apollo 15,418; "gabbroic anorthosite", locality unspecified; Agua Dulce Canyon, CA
[b]Vacaville basalt, Mt. Vaca Quad. CA; locality unspecified; Nevada Test Site, NV
[c]Terrestrial dolerite - locality not given; lunar basalt 70215
[d]Starting temperature 1673 K
[e]Synthetic: matching komatiite from Munro Township, Ontario; starting temperature 1773 K
[f]Lakebed Area 5, Nevada Test Site, NV
[g]not given; 4-20%-water; also site U2, Nevada Test Site, Nye Co. NV
[h]Centreville, VA; Frederick, MD
[i]Hole U10B, Nevada Test Site, NV; Banded Mtn., Nevada Test Site, NV; Ferris Wheel Dolomite, Nevada Test Site, NV; not given
[j]Jackson County, NC; Twin Sisters Peaks, WA; not given
[k]Mooihoek Mine, Transvaal
[l]Healdsburg, CA; Sunnmore, Norway
[m]Bytownite gabbro, Duluth, MN; San Marcos, Escondido, CA
[n]Rock Cove, Nevada Test Site, Nevada
[o]near Lithonia, GA; near Shoal Nuclear Detonation, Fallon NV; near area 15, Nevada Test Site, Nevada
[p]Hardhat; Climax Stock Granodiorite, Nevada Test Site, NV
[q]Kaibab Limestone, AZ; Spergen Limestone, Bedford, IL
[r]Solenhofen, Bavaria; Banded Mountain limestone, Nevada Test Site, NV
[s]Yule Marble, Gunnison City, CO; Vermont Marble, West Rutland, VT; not given
[t]Area 15, Nevada Test Site, NV
[u]U. S. Pumice Mine, Mono Craters, Lee Vining, CA
[v]Novaculite, Arkansas
[w]Eureka quartzite, Confusion Mountain, nr. Ely, NV
[x]synthetic SiO_2; Ottawa banding sand, Ottawa IL, at -10°C; oven furnace sand (silica sand); not given
[y]Ottawa banding sand, Ottawa IL at -10°C
[z]Oven furnace sand (silica sand), locality not given
[aa]Coconino sandstone, Flagstaff, AZ; Massillon sandstone, Glenmont, OH; St. Peters sandstone, Klondike, MO
[bb]Ver-myen, Italy; antigorite, Thurman NY; chrysotile, Quebec
[cc]Gas shale, Devonian, Lincoln Co., WY; clay shale, locality not given; shales, Site U2, Nevada Test Site, Nye Co., NV
[dd]Green River, Rifle CO; Laramie oil shale; Mahogany ledge oil shale
[ee]Areas 3, 12, 16, buff Rainier Mesa Tuff, white Rainier Mesa Tuff, and unspecified, Nevada Test Site, NV
[ff]Areas 3, 12, 16, pink Rainier Mesa Tuff, and unspecified, Nevada Test Site, NV
[gg]Rainier Mesa Tuff, Areas 3, 12, 16, Pahute Mesa Tuff, and unspecified, Nevada Test Site, NV

Acknowledgments. Research supported by NSF, NASA, and DoD. Contribution #5333, Division of Geological and Planetary Sciences, California Institute of Technology.

REFERENCES

1 Ahrens, T. J., I. Jackson, and R. Jeanloz, Shock compression and adiabatic release of a titaniferous mare basalt, *Proc. 8th Lunar Sci. Conf.*, 3437-3455, 1977.

2 Ahrens, T. J., and J. D. O'Keefe, Shock melting and vaporization of lunar rocks and minerals, *The Moon*, *1*, 214-249, 1972.

3 Ahrens, T. J., and J. D. O'Keefe, Equation of state and impact-induced shock-wave attenuation on the moon, in *Impact and Explosion Cratering*, edited by D. J. Roddy, R. O. Pepin and R. B. Merrill, pp. 639-656, Pergamon Press, New York, 1977.

4 Ahrens, T. J., J. D. O'Keefe, and R. V. Gibbbons, Shock compression of a recrystallized anorthositic rock from Apollo 15, *Proc. of the Fourth Lunar Science Conf., Suppl. 4, Geochim. et Cosmochim. Acta*, *3*, 2575-2590, 1973.

5 Ahrens, T. J., and J. V. G. Gregson, Shock compression of crustal rocks: data for quartz, calcite, and plagioclase rocks, *J. Geophys. Res.*, *69*, 4839-4874, 1964.

6 Ahrens, T. J., and J. P. Watt, Dynamic properties of mare basalts: Relation of equations of state to petrology, in *Lunar and Planetary Sci. Conf.*, vol. XI, pp. 2059-2074, Pergamon Press, Houston, TX, 1980.

7 Al'tshuler, L. V., and M. N. Pavlovskii, Response of clay and clay shale to heavy dynamic loading, *J. Appl. Mech. Tech. Phys.*, *1*, 161-165, 1971.

8 Al'tshuler, L. V., and I. I. Sharipdzhanov, Additive equations of state of silicates at high pressures, *Izv. Earth Phys., Engl. Transl.*, *3*, 167-177, 1971.

9 Asphaug, E., and H. J. Melosh, The Stickney impact of Phobos: A dynamical model, *Icarus*, *101*, 144-164, 1993.

10 Bass, R. C., Additional Hugoniot data for geologic materials, Sandia Corporation, Research Report, SC-RR-66-548, 29 pp., 1966.

11 Birch, F., Compressibility: Elastic Constants, in *Handbook of Physical Constants, revised edition*, edited by S. P. Clark Jr., pp. 153-159, The Geological Society of America, New York, 1966.

12 Bjork, R. L., Analysis of the formation of Meteor Crater, Arizona: A preliminary report, *J. Geophys. Res.*, *66*, 3379-3387, 1961.

13 Boslough, M. B., and T. J. Ahrens, Shock wave properties of anorthosite and gabbro, *J. Geophys. Res.*, *90*, 7814-7820, 1985.

14 Boslough, M. B., S. M. Rigden, and T. J. Ahrens, Hugoniot equation of state of anorthite glass and lunar anorthosite, *Geophys. J. R. astr. Soc.*, *84*, 455-473, 1986.

15 Brar, N. S., Z. Rosenberg, and S. J. Bless, Applying Stenberg's model to the Hugoniot elastic limit of porous boron carbide specimens, *J. Appl. Phys.*, *69*, 7890-7891, 1991.

16 Carter, W. J., Hugoniots of Green River Oil Shale, Los Alamos Scientific Laboratory, Explosively Produced Fracture of Oil Shale - Annual Report, March 1976-March 1977, LA-6817-PR, 1977.

17 Carter, W. J., Hugoniots of Green River oil shale, in *Proceedings of the 6th International Conference on High Pressure Physics and Technology*, (to be published), Boulder, Colorado, 1977.

18 Carter, W. J., and B. W. Olinger, in *Proceedings, ERDA Enhanced Oil, Gas Recovery and Improved Drilling Methods*, vol. 2, Petroleum Publishing Co., Tulsa, 1977.

19 Dianov, M. D., N. A. Zlatin, S. M. Mochalov, G. S. Pugashev, and L. K. Rosomakho, Shock compressibility of dry and water-saturated sand, *Sov. Tech. Phys. Lett.*, *2*, 207-208, 1977.

20 Dianov, M. D., N. A. Zlatin, G. S. Pugashev, and L. K. Rosomakho, Shock compressibility of finely dispersed media, *Sov. Tech. Phys. Lett.*, *5*, 285, 1979.

21 Dick, R. D., T. A. Weaver, and B. Olinger, Shock compression of the Webster dunite, *EOS*, *54*, 475, 1973.

22 Dremin, A. N., and G. A. Adadurov, Shock adiabatic for marble, *Sov. Phys. Doklady*, *4*, 970-973, 1959.

23 Flanagan, T. J., The Hugoniot equation of state of materials for the Ferris Wheel program, Sandia Corporation, Miscellaneous Report, SC-M-66-451, 22 pp., 1966.

24 Gaffney, E. S., Dynamic material properties of geologic materials from the U2 site, Defense Nuclear Agency, DNA 3417F, 22 pp., 1973.

25 Gault, D. E., and E. D. Heitowit, The partition of energy for hypervelocity impact craters formed in rock, in *Proceedings of the 6th Hypervelocity Impact Symposium*, pp. 420-456, Cleveland, Ohio, 1963.

26 Gregson, V. G., C. F. Peterson, and J. C. Jamieson, Stanford Res. Inst., AFCRL 63-662, 1963.

27 Hughes, D. S., and R. G. McQueen, Density of basic rocks at very high pressures, *Trans. Am. Geophys. Union*, *39*, 959-965, 1958.

28 Jeanloz, R., and T. J. Ahrens, The equation of state of a lunar anorthosite: 60025, in *Lunar and Planet. Sci. Conf. 9th*, pp. 2789-2803, Pergamon Press, Houston, TX, 1978.

29 Jeanloz, R., and T. J. Ahrens, Anorthite, thermal equation of state to high pressures, *Geophys. J. R. astr. Soc.*, *62*, 529-549, 1980.

30 Jones, A. H., W. M. Isbell, F. H. Shipman, R. D. Perkins, S. J. Green, and C. J. Maiden, Material properties measurements for selected materials, NASA Ames, Interim Report, NAS2-3427, MSL-68-9, 55 pp., 1968.

31 Kalashnikov, N. G., M. N. Pavlovskiy, G. V. Simakov, and R. F. Trunin, Dynamic compressibilty

of calcite-group minerals, *Isv. Earth Phys., Engl. Transl.*, 2, 23-29, 1973.

32 Kieffer, S. W., and C. H. Simonds, The role of volatiles and lithology in the impact cratering process, *Rev. Geophys. Space Phys.*, *18*, 143-181, 1980.

33 Marsh, S. P. (Ed.), *LASL Shock Hugoniot Data*, pp. 1-658, University of California Press, Berkeley, 1980.

34 McQueen, R. G., The equation of state of mixtures, alloys, and compounds, in *Seismic Coupling-Proceedings of a meeting sponsored by the Advanced Research Projects Agency, January 15-16, 1968*, edited by G. Simmons, Stanford Research Institute, Menlo Park, CA, 1968.

35 McQueen, R. G., S. P. Marsh, and J. N. Fritz, Hugoniot equation of state of twelve rocks, *J. Geophys. Res.*, *72*, 4999-5036, 1967.

36 Miller, G. H., E. M. Stolper, and T. J. Ahrens, The equation of state of a molten komatiite I: Shock wave compression to 36 GPa, *J. Geophys. Res.*, *96*, 11831-48, 1991.

37 O'Keefe, J. D., and T. J. Ahrens, Impact-induced energy partitioning, melting, and vaporization on terrestrial planets, *Proc. Lunar Sci. Conf., 8th, Vol. 3, Geochim. Cosmochim. Acta, Suppl. 8*, 3357-3374, 1977.

38 O'Keefe, J. D., and T. J. Ahrens, Meteorite impact ejecta: Dependence on mass and energy lost on planetary escape velocity, *Science*, *198*, 1249-1251, 1977.

39 O'Keefe, J. D., and T. J. Ahrens, Cometary and meteorite swarm impact on planetary surfaces, *J. Geophys. Res.*, *87*, 6668-6680, 1982.

40 O'Keefe, J. D., and T. J. Ahrens, Impact-induced melting on planetary surfaces, in *Proc. 1992 Sudbury Conference on Large Body Impacts and Planetary Evolution*, edited by B. Dressler and R. V. Sharpton, pp. in press, Geol. Soc. Am. Spec. Pap., Boulder, CO, 1993.

41 Olinger, B. W., Dynamic properties of Devonian shales in Evaluation of Methods for Stimulation and Characterization of Eastern Gas Shales, April-June 1977, compiled by W. J. Carter and N. E. Vandenborgh, Los Alamos Scientific Laboratory, LA-7094-PR, 1978.

42 Rigden, S. M., T. J. Ahrens, and E. M. Stolper, Shock compression of molten silicates: Results for a model basaltic composition, *J. Geophys. Res.*, *93*, 367-382, 1988.

43 Roddy, D. J., S. H. Schuster, M. Rosenblatt, L. B. Grant, P. J. Hassig, and K. N. Kreyenhagen, Computer simulations of large asteroid impacts into oceanic and continental sites---Preliminary results on atmospheric, cratering and ejecta dynamics, *Int. J. Impact Eng.*, *5*, 525-541, 1987.

44 Shipman, F. H., V. G. Gregson, and A. H. Jones, A shock wave study of Coconino sandstone, *NASA Report, MSL-7-14*, 46, 1970.

45 Shipman, F. H., W. M. Isbell, and A. H. Jones, High pressure Hugoniot measurements for several Nevada test site rocks, DASA Report 2214, MSL-68-15, 114 pp., 1969.

46 Steinberg, D. J., Equations of state for the ceramics BeO and B_4C, Lawrence Livermore Laboratory, UCID-16946, 1-10 pp., 1975.

47 Telegin, G. S., V. G. Antoshev, V. A. Bugayeva, G. V. Simakov, and R. F. Trunin, Calculated determination of Hugoniot curves of rocks and minerals, *Izv. Earth Phys.*, *16*, 319-324, 1980.

48 Trunin, R. F., V. I. Gon'shakova, G. V. Simakov, and N. E. Galdin, A study of rocks under the high pressures and temperatures created by shock compression, *Izv. Earth Phys.*, *9*, 579-586, 1965.

49 Trunin, R. F., G. V. Simakov, M. A. Podurets, B. N. Moiseyev, and L. V. Popov, Dynamic compressibility of quartz and quartzite at high pressure, *Izv. Earth Phys.*, *1*, 8-12, 1971.

50 Tyburczy, J. A., and T. J. Ahrens, Dynamic compression and volatile release of carbonates, *J. Geophys. Res.*, *91*, 4730-4744, 1986.

51 Tyburczy, J. A., T. S. Duffy, T. J. Ahrens, and M. A. Lange, Shock wave equation of state of serpentine to 150 GPa: Implications of the occurrence of water in the Earth's lower mantle, *J. Geophys. Res.*, *96*, 18011-18027, 1991.

52 van Thiel, M., (editor), Compendium of Shock Wave Data, University of California, Lawrence Livermore Laboratory, UCRL-50801, Vol. 1, Rev. 1, 755 pp., 1977.

53 van Thiel, M., A. S. Kusubov, and A. C. Mitchell, Compendium of Shock Wave Data, Lawrence Radiation Laboratory (Livermore), UCRL-50108, 1967.

54 Watts, A. W., R. Greeley, and H. J. Melosh, The formation of terrains antipodal to major impacts, *Icarus*, *93*, 159-168, 1991.

Pressure-Volume-Temperature Properties of H_2O-CO_2 Fluids

Teresa S. Bowers

1. INTRODUCTION

Pressure-volume-temperature properties of water and carbon dioxide have been accurately measured for decades, and equations of state (EOS) describing the relationship between these properties have been suggested for nearly as long. Most of the information found in the chapter by Kennedy and Holser in the 1969 Handbook of Physical and Chemical Constants is as correct today as it was then. However, considerable new information has recently become available concerning such things as the properties of water in the near-critical region, the effect of carbon dioxide on the dielectric constant of water, and very high pressure volumes of water and carbon dioxide achieved through shock compression.

Data prescribing the pressure-volume-temperature properties of water, carbon dioxide and water-carbon dioxide mixtures are tabulated herein. Related properties, including enthalpy, entropy, heat capacity, sound speed, and the dielectric constant, that can be derived through EOS are tabulated as well. A description of each property is given, and the relevance of each property to the understanding of geophysical or geochemical problems is briefly described. The relationship of each property to other properties, and sources of data or tabulated values are also given. Where data sources provide data for overlapping conditions, the sources are used preferentially in the order that they are listed. Experimental data are given in bold type in all tables. Smoothed or interpolated values are given in regular type, while information calculated from an EOS is given in italics. The use of data from multiple sources produces some discontinuities in the tabulated information.

The second section provides information on EOS. A variety of EOS exist for water, carbon dioxide, and water-carbon dioxide mixtures, and are used to calculate values of properties in the absence of measurements, and to derive derivative or integral properties.

2. WATER

2.1 Volume

Volume, or density, is usually measured. All other properties can be related by derivatives or integrals to volume. Detailed measurements of the volume of water at elevated pressures and temperatures have been made by (8) and (25). Water volumes are tabulated here in Table 1a-d from 0° to 2000°C and 1 bar to 250 Kbar based on data and tabulations of (15), (10) and (33). The work of (15) is based on a variety of measurements, including those of (25). Table 2 gives water densities at higher pressures and temperatures obtained from shock experiments by (24) and (28). Additional shock experiment data can be found in (1) and (3).

2.2 Thermodynamic Functions

The thermodynamic properties presented here for water are taken from Haar et al. (15). Haar et al. use an equation of state for water that represents its properties by a molar Helmholtz energy function, A, which is written in terms of temperature (T) and density (ρ). Other thermodynamic properties can be derived from the appropriate derivatives of the Helmholtz function. Those presented here include entropy (S), enthalpy (H), and heat capacity at constant pressure (C_p). Expressions relating these properties to the Helmholz function and to each other are given in Table 3.

T. S. Bowers, Gradient Corporation, 44 Brattle Street, Cambridge, MA 02138

Rock Physics and Phase Relations
A Handbook of Physical Constants
AGU Reference Shelf 3

TABLE 1a. Water Volume, cm^3/mole

Pbars/T°C	0	20	40	60	80	100	120	140	160
1	*18.0191*	*18.0479*	*18.1574*	*18.3239*	*18.5385*	*30557.*	*32304.*	*34030.*	*35740.*
10	*18.0108*	*18.0405*	*18.1502*	*18.3165*	*18.5307*	*18.7898*	*19.0937*	*19.4447*	*19.8473*
25	*17.9971*	*18.0281*	*18.1381*	*18.3043*	*18.5179*	*18.7761*	*19.0786*	*19.4276*	*19.8277*
50	*17.9744*	*18.0077*	*18.1183*	*18.2843*	*18.4968*	*18.7534*	*19.0535*	*19.3994*	*19.7956*
100	*17.9297*	*17.9674*	*18.0791*	*18.2443*	*18.4551*	*18.7085*	*19.0044*	*19.3445*	*19.7326*
150	*17.8857*	*17.9275*	*18.0405*	*18.2052*	*18.4142*	*18.6648*	*18.9563*	*19.2906*	*19.672*
200	*17.8425*	*17.8883*	*18.0023*	*18.1666*	*18.3738*	*18.6215*	*18.9092*	*19.2383*	*19.612*
250	*17.7998*	*17.8497*	*17.9648*	*18.1286*	*18.3343*	*18.5794*	*18.8631*	*19.1870*	*19.555*
300	*17.7580*	*17.8115*	*17.9279*	*18.0911*	*18.2952*	*18.5377*	*18.8179*	*19.1370*	*19.497*
350	*17.7168*	*17.7740*	*17.8915*	*18.0544*	*18.2571*	*18.4968*	*18.7736*	*19.0880*	*19.443*
400	*17.6762*	*17.7371*	*17.8555*	*18.0180*	*18.2192*	*18.4569*	*18.7302*	*19.0400*	*19.389*
500	*17.5969*	*17.6645*	*17.7850*	*17.9470*	*18.1455*	*18.3785*	*18.6455*	*18.9469*	*19.284*
600	*17.5200*	*17.5941*	*17.7166*	*17.8778*	*18.0738*	*18.3028*	*18.5639*	*18.8575*	*19.185*
700	*17.4454*	*17.5252*	*17.6497*	*17.8106*	*18.0043*	*18.2293*	*18.4848*	*18.7714*	*19.090*
800	*17.3732*	*17.4584*	*17.5847*	*17.7450*	*17.9367*	*18.1580*	*18.4084*	*18.6882*	*18.998*
900	*17.3031*	*17.3934*	*17.5213*	*17.6813*	*17.8708*	*18.0888*	*18.3343*	*18.6078*	*18.910*
1000	*17.2352*	*17.3298*	*17.4593*	*17.6189*	*17.8067*	*18.0214*	*18.2625*	*18.5302*	*18.825*
1200	*17.106*	*17.207*	*17.340*	*17.499*	*17.683*	*17.892*	*18.124*	*18.382*	*18.663*
1400	*16.984*	*17.092*	*17.225*	*17.384*	*17.566*	*17.769*	*17.994*	*18.241*	*18.511*
1600	*16.870*	*16.982*	*17.117*	*17.274*	*17.452*	*17.652*	*17.870*	*18.110*	*18.369*
1800	*16.764*	*16.877*	*17.013*	*17.169*	*17.346*	*17.540*	*17.753*	*17.984*	*18.234*
2000	*16.665*	*16.776*	*16.913*	*17.068*	*17.241*	*17.432*	*17.639*	*17.865*	*18.106*
2200	*16.569*	*16.683*	*16.818*	*16.973*	*17.142*	*17.330*	*17.531*	*17.749*	*17.984*
2400	*16.481*	*16.591*	*16.728*	*16.879*	*17.049*	*17.231*	*17.429*	*17.641*	*17.868*
2600	*16.398*	*16.504*	*16.640*	*16.791*	*16.957*	*17.137*	*17.330*	*17.537*	*17.757*
2800	*16.319*	*16.422*	*16.555*	*16.704*	*16.868*	*17.045*	*17.234*	*17.436*	*17.650*
3000	*16.243*	*16.342*	*16.474*	*16.622*	*16.784*	*16.957*	*17.142*	*17.339*	*17.548*
3200	*16.171*	*16.267*	*16.396*	*16.542*	*16.701*	*16.872*	*17.054*	*17.245*	*17.448*
3400	*16.103*	*16.193*	*16.321*	*16.467*	*16.622*	*16.789*	*16.967*	*17.157*	*17.355*
3600	*16.036*	*16.121*	*16.249*	*16.391*	*16.546*	*16.710*	*16.885*	*17.068*	*17.263*
3800	*15.973*	*16.052*	*16.178*	*16.321*	*16.472*	*16.634*	*16.805*	*16.985*	*17.175*
4000	*15.912*	*15.984*	*16.110*	*16.250*	*16.400*	*16.559*	*16.728*	*16.904*	*17.090*
4500	*15.766*	*15.832*	*15.946*	*16.085*	*16.231*	*16.384*	*16.544*	*16.712*	*16.888*
5000	*15.631*	*15.669*	*15.793*	*15.932*	*16.074*	*16.220*	*16.373*	*16.533*	*16.701*
5500		*15.519*	*15.645*	*15.787*	*15.926*	*16.067*	*16.214*	*16.368*	*16.526*
6000		*15.375*	*15.505*	*15.652*	*15.789*	*15.924*	*16.065*	*16.213*	*16.364*
6500		*15.234*	*15.369*	*15.524*	*15.660*	*15.791*	*15.924*	*16.065*	*16.211*
7000			*15.240*	*15.402*	*15.539*	*15.665*	*15.793*	*15.928*	*16.067*
7500			*15.115*	*15.287*	*15.423*	*15.546*	*15.669*	*15.798*	*15.932*
8000			*14.998*	*15.177*	*15.314*	*15.434*	*15.551*	*15.674*	*15.804*
8500			*14.890*	*15.072*	*15.211*	*15.326*	*15.440*	*15.557*	*15.681*
9000				*14.973*	*15.114*	*15.225*	*15.333*	*15.447*	*15.564*
9500				*14.879*	*15.020*	*15.130*	*15.233*	*15.341*	*15.454*
10000				*14.793*	*14.932*	*15.038*	*15.137*	*15.240*	*15.348*
12000					*14.620*	*14.712*	*14.791*	*14.876*	*14.966*
14000						*14.436*	*14.499*	*14.566*	*14.640*
16000							*14.247*	*14.297*	*14.357*
18000								*14.060*	*14.107*
20000									*13.883*

Values calculated by (15).

TABLE 1b. Water Volume, cm^3/mole

Pbars/T°C	180	200	220	240	260	280	300	320	340
1	*37443.*	*39136.*	*40822.*	*42507.*	*44188.*	*45865.*	*47541.*	*49214.*	*50886.*
10	*3502.9*	*3709.5*	*3906.9*	*4097.7*	*4284.0*	*4466.7*	*4646.9*	*4824.9*	*5001.2*
25	*20.2867*	*20.8166*	*21.4349*	*1520.0*	*1612.3*	*1698.7*	*1781.4*	*1861.2*	*1939.1*
50	*20.2491*	*20.7712*	*21.3789*	*22.0982*	*22.9727*	*760.82*	*816.20*	*866.41*	*913.21*
100	*20.1758*	*20.6834*	*21.2711*	*21.9611*	*22.7899*	*23.8202*	*25.1766*	*346.77*	*386.70*
150	*20.104*	*20.599*	*21.169*	*21.832*	*22.621*	*23.587*	*24.821*	*26.529*	*29.379*
200	*20.036*	*20.518*	*21.070*	*21.711*	*22.464*	*23.374*	*24.511*	*26.019*	*28.258*
250	*19.969*	*20.439*	*20.976*	*21.594*	*22.316*	*23.179*	*24.237*	*25.597*	*27.485*
300	*19.904*	*20.363*	*20.886*	*21.484*	*22.179*	*22.999*	*23.992*	*25.237*	*26.889*
350	*19.841*	*20.291*	*20.799*	*21.380*	*22.048*	*22.832*	*23.769*	*24.920*	*26.401*
400	*19.780*	*20.219*	*20.717*	*21.279*	*21.925*	*22.675*	*23.563*	*24.639*	*25.986*
500	*19.663*	*20.084*	*20.558*	*21.090*	*21.695*	*22.390*	*23.197*	*24.152*	*25.305*
600	*19.551*	*19.956*	*20.409*	*20.915*	*21.486*	*22.134*	*22.877*	*23.740*	*24.759*
700	*19.443*	*19.836*	*20.270*	*20.753*	*21.293*	*21.902*	*22.592*	*23.383*	*24.300*
800	*19.342*	*19.720*	*20.136*	*20.599*	*21.115*	*21.689*	*22.334*	*23.068*	*23.904*
900	*19.243*	*19.609*	*20.012*	*20.455*	*20.947*	*21.493*	*22.100*	*22.783*	*23.556*
1000	*19.149*	*19.504*	*19.893*	*20.320*	*20.790*	*21.309*	*21.886*	*22.527*	*23.244*
1200	*18.971*	*19.306*	*19.672*	*20.068*	*20.502*	*20.978*	*21.500*	*22.073*	*22.707*
1400	*18.805*	*19.122*	*19.466*	*19.839*	*20.245*	*20.684*	*21.162*	*21.682*	*22.253*
1600	*18.650*	*18.953*	*19.279*	*19.630*	*20.009*	*20.419*	*20.861*	*21.340*	*21.859*
1800	*18.504*	*18.792*	*19.102*	*19.436*	*19.794*	*20.178*	*20.590*	*21.034*	*21.511*
2000	*18.366*	*18.643*	*18.938*	*19.256*	*19.594*	*19.956*	*20.342*	*20.756*	*21.201*
2200	*18.234*	*18.501*	*18.783*	*19.086*	*19.409*	*19.751*	*20.115*	*20.504*	*20.918*
2400	*18.110*	*18.366*	*18.638*	*18.928*	*19.234*	*19.560*	*19.906*	*20.272*	*20.661*
2600	*17.991*	*18.238*	*18.501*	*18.778*	*19.072*	*19.382*	*19.710*	*20.057*	*20.425*
2800	*17.877*	*18.115*	*18.369*	*18.636*	*18.917*	*19.214*	*19.528*	*19.857*	*20.205*
3000	*17.767*	*18.000*	*18.243*	*18.501*	*18.771*	*19.056*	*19.355*	*19.670*	*20.001*
3200	*17.663*	*17.888*	*18.124*	*18.373*	*18.632*	*18.906*	*19.192*	*19.493*	*19.810*
3400	*17.562*	*17.782*	*18.011*	*18.250*	*18.501*	*18.764*	*19.039*	*19.328*	*19.630*
3600	*17.467*	*17.679*	*17.901*	*18.133*	*18.375*	*18.629*	*18.893*	*19.171*	*19.461*
3800	*17.373*	*17.580*	*17.794*	*18.020*	*18.256*	*18.501*	*18.755*	*19.021*	*19.301*
4000	*17.283*	*17.485*	*17.694*	*17.913*	*18.140*	*18.376*	*18.623*	*18.881*	*19.147*
4500	*17.070*	*17.259*	*17.456*	*17.661*	*17.872*	*18.090*	*18.317*	*18.553*	*18.798*
5000	*16.874*	*17.054*	*17.238*	*17.429*	*17.627*	*17.830*	*18.041*	*18.259*	*18.484*
5500	*16.692*	*16.861*	*17.036*	*17.216*	*17.402*	*17.593*	*17.789*	*17.993*	*18.202*
6000	*16.521*	*16.683*	*16.849*	*17.020*	*17.194*	*17.373*	*17.558*	*17.748*	*17.942*
6500	*16.362*	*16.515*	*16.674*	*16.836*	*17.000*	*17.171*	*17.344*	*17.522*	*17.704*
7000	*16.211*	*16.359*	*16.510*	*16.663*	*16.820*	*16.980*	*17.144*	*17.313*	*17.485*
7500	*16.068*	*16.211*	*16.355*	*16.501*	*16.650*	*16.804*	*16.958*	*17.117*	*17.279*
8000	*15.935*	*16.070*	*16.207*	*16.348*	*16.490*	*16.636*	*16.784*	*16.935*	*17.088*
8500	*15.807*	*15.937*	*16.068*	*16.204*	*16.339*	*16.477*	*16.620*	*16.762*	*16.908*
9000	*15.687*	*15.811*	*15.937*	*16.067*	*16.196*	*16.330*	*16.463*	*16.600*	*16.739*
9500	*15.569*	*15.690*	*15.811*	*15.935*	*16.061*	*16.187*	*16.315*	*16.447*	*16.578*
10000	*15.460*	*15.575*	*15.692*	*15.811*	*15.932*	*16.052*	*16.175*	*16.301*	*16.427*
12000	*15.061*	*15.160*	*15.261*	*15.364*	*15.467*	*15.571*	*15.676*	*15.782*	*15.888*
14000	*14.721*	*14.806*	*14.894*	*14.982*	*15.072*	*15.162*	*15.252*	*15.344*	*15.434*
16000	*14.425*	*14.497*	*14.573*	*14.651*	*14.728*	*14.807*	*14.887*	*14.966*	*15.045*
18000	*14.162*	*14.224*	*14.288*	*14.357*	*14.425*	*14.494*	*14.564*	*14.633*	*14.703*

TABLE 1b. (continued)

Pbars/T°C	180	200	220	240	260	280	300	320	340
20000	*13.928*	*13.979*	*14.034*	*14.094*	*14.153*	*14.215*	*14.276*	*14.337*	*14.398*
25000		*13.46*	*13.49*	*13.55*	*13.58*	*13.62*	*13.67*	*13.71*	*13.76*
30000					*13.12*	*13.15*	*13.19*	*13.22*	*13.26*
40000		*12.46*					*12.70*		
50000							*12.20*		
60000							*11.84*		
70000							*11.54*		
80000									
90000									
100000							*10.36*		
150000							*9.26*		
200000							*8.61*		
250000							*8.18*		

Values calculated by (15), (10) and (33).

TABLE 1c. Water Volume, cm^3/mole

Pbars/T°C	360	380	400	420	440	460	480	500	600
1	*52558.*	*54228.*	*55898.*	*57567.*	*59235.*	*60903.*	*62570.*	*64236.*	*72567.*
10	*5176.4*	*5350.4*	*5523.3*	*5695.8*	*5867.5*	*6038.6*	*6209.2*	*6379.5*	*7226.0*
25	*2015.1*	*2089.9*	*2163.5*	*2236.5*	*2308.6*	*2380.1*	*2451.3*	*2521.7*	*2869.9*
50	*957.6*	*1000.2*	*1041.5*	*1081.7*	*1121.0*	*1159.7*	*1197.7*	*1235.2*	*1417.7*
100	*419.77*	*449.01*	*475.77*	*500.79*	*524.52*	*547.29*	*569.27*	*590.64*	*691.11*
150	*226.48*	*257.18*	*281.99*	*303.61*	*323.17*	*341.33*	*358.43*	*374.73*	*448.67*
200	*32.876*	*148.74*	*179.19*	*201.60*	*220.34*	*236.89*	*252.01*	*266.08*	*327.33*
250	*30.564*	*40.033*	*108.11*	*136.56*	*156.60*	*173.04*	*187.40*	*200.39*	*254.49*
300	*29.310*	*33.740*	*50.32*	*88.62*	*112.20*	*129.52*	*143.80*	*156.31*	*205.94*
350	*28.436*	*31.600*	*37.936*	*55.352*	*79.50*	*97.92*	*112.44*	*124.74*	*171.35*
400	*27.761*	*30.290*	*34.403*	*42.509*	*52.729*	*74.77*	*89.14*	*101.23*	*145.52*
500	*26.745*	*28.609*	*31.169*	*34.937*	*40.799*	*49.436*	*59.81*	*70.12*	*109.86*
600	*25.984*	*27.496*	*29.417*	*31.944*	*35.374*	*40.064*	*46.146*	*53.232*	*86.95*
700	*25.376*	*26.662*	*28.226*	*30.164*	*32.614*	*35.737*	*39.668*	*44.400*	*71.56*
800	*24.869*	*25.995*	*27.327*	*28.919*	*30.847*	*33.191*	*36.036*	*39.423*	*60.98*
900	*24.435*	*25.442*	*26.610*	*27.972*	*29.571*	*31.460*	*33.686*	*36.284*	*53.54*
1000	*24.053*	*24.968*	*26.013*	*27.210*	*28.586*	*30.175*	*32.007*	*34.108*	*48.180*
1200	*23.408*	*24.188*	*25.058*	*26.030*	*27.118*	*28.337*	*29.703*	*31.227*	*41.219*
1400	*22.877*	*23.560*	*24.311*	*25.136*	*26.046*	*27.044*	*28.143*	*29.344*	*36.987*
1600	*22.423*	*23.033*	*23.698*	*24.419*	*25.204*	*26.057*	*26.981*	*27.979*	*34.151*
1800	*22.026*	*22.581*	*23.178*	*23.823*	*24.516*	*25.262*	*26.064*	*26.921*	*32.103*
2000	*21.675*	*22.185*	*22.729*	*23.311*	*23.934*	*24.601*	*25.311*	*26.066*	*30.537*
2200	*21.360*	*21.832*	*22.333*	*22.866*	*23.433*	*24.035*	*24.675*	*25.350*	*29.290*
2400	*21.075*	*21.513*	*21.978*	*22.471*	*22.992*	*23.543*	*24.125*	*24.738*	*28.267*
2600	*20.814*	*21.225*	*21.659*	*22.116*	*22.599*	*23.109*	*23.642*	*24.204*	*27.402*
2800	*20.572*	*20.960*	*21.367*	*21.796*	*22.246*	*22.718*	*23.214*	*23.732*	*26.660*
3000	*20.349*	*20.715*	*21.099*	*21.502*	*21.924*	*22.367*	*22.828*	*23.311*	*26.013*
3200	*20.140*	*20.488*	*20.852*	*21.232*	*21.630*	*22.044*	*22.479*	*22.929*	*25.440*
3400	*19.946*	*20.277*	*20.621*	*20.981*	*21.358*	*21.751*	*22.158*	*2.581*	*24.927*
3600	*19.762*	*20.077*	*20.407*	*20.749*	*21.106*	*21.477*	*21.862*	*22.262*	*24.464*
3800	*19.589*	*19.891*	*20.205*	*20.531*	*20.872*	*21.225*	*21.589*	*21.967*	*24.044*
4000	*19.425*	*19.715*	*20.016*	*20.327*	*20.652*	*20.987*	*21.335*	*21.695*	*23.659*
4500	*19.050*	*19.313*	*19.585*	*19.87*	*20.16*	*20.47*	*20.77*	*21.08*	*22.83*
5000	*18.717*	*18.958*	*19.205*	*19.46*	*19.73*	*20.00*	*20.29*	*20.57*	*22.12*

TABLE 1c. (continued)

Pbars/T°C	360	380	400	420	440	460	480	500	600
5500	*18.416*	*18.638*	*18.866*	*19.10*	*19.35*	*19.58*	*19.85*	*20.11*	*21.51*
6000	*18.142*	*18.349*	*18.560*	*18.77*	*19.01*	*19.22*	*19.46*	*19.71*	*20.99*
6500	*17.892*	*18.084*	*18.281*	*18.48*	*18.68*	*18.90*	*19.11*	*19.35*	*20.52*
7000	*17.661*	*17.841*	*18.025*	*18.21*	*18.41*	*18.61*	*18.81*	*19.01*	*20.11*
7500	*17.445*	*17.614*	*17.787*	*17.966*	*18.146*	*18.329*	*18.519*	*18.710*	*19.73*
8000	*17.245*	*17.405*	*17.567*	*17.735*	*17.904*	*18.077*	*18.254*	*18.434*	*19.39*
8500	*17.056*	*17.207*	*17.362*	*17.519*	*17.679*	*17.843*	*18.009*	*18.178*	*19.06*
9000	*16.879*	*17.023*	*17.169*	*17.319*	*17.470*	*17.623*	*17.780*	*17.940*	*18.77*
9500	*16.713*	*16.849*	*16.987*	*17.130*	*17.272*	*17.418*	*17.567*	*17.719*	*18.502*
10000	*16.555*	*16.685*	*16.816*	*16.951*	*17.086*	*17.225*	*17.366*	*17.510*	*18.259*
12000	*15.996*	*16.105*	*16.214*	*16.326*	*16.440*	*16.553*	*16.668*	*16.786*	*17.394*
14000	*15.528*	*15.620*	*15.714*	*15.807*	*15.903*	*16.000*	*16.097*	*16.195*	*16.703*
16000	*15.124*	*15.206*	*15.285*	*15.366*	*15.449*	*15.532*	*15.614*	*15.697*	*16.128*
18000	*14.773*	*14.842*	*14.912*	*14.984*	*15.054*	*15.124*	*15.196*	*15.269*	*15.638*
20000	*14.460*	*14.521*	*14.582*	*14.645*	*14.706*	*14.768*	*14.831*	*14.894*	*15.213*
25000	*13.80*	*13.85*	*13.89*	*13.94*	*13.98*	*14.03*	*14.07*	*14.12*	*14.36*
30000	*13.28*	*13.31*	*13.35*	*13.39*	*13.42*	*13.46*	*13.49*	*13.51*	*13.69*
40000			*12.96*					*13.23*	*13.51*
50000			*12.41*					*12.62*	*12.84*
60000			*12.01*					*12.18*	*12.36*
70000			*11.68*					*11.83*	*11.98*
80000			*11.35*					*11.49*	*11.63*
90000			*10.92*					*11.07*	*11.22*
100000			*10.35*					*10.53*	*10.71*
150000			*9.42*					*9.57*	
200000			*8.70*					*8.81*	
250000			*8.27*					*8.34*	

Values calculated by (15), (10) and (33).

TABLE 1d. Water Volume, cm³/mole

Pbars/T°C	700	800	900	1000	1200	1400	1600	1800	2000
1	*80892.*	*89213.*	*97540.*	*105860.*	*122490.*	*139120.*	*155750.*	*172380.*	*189020.*
10	*8067.7*	*8906.4*	*9743.*	*10579.*	*12247.*	*13916.*	*15580.*	*17245.*	*18910.*
25	*3212.8*	*3552.8*	*3890.7*	*4227.5*	*4898.6*	*5567.8*	*6235.9*	*6903.2*	*7570.0*
50	*1594.4*	*1768.3*	*1940.0*	*2110.6*	*2449.1*	*2785.6*	*3121.1*	*3455.6*	*3790.0*
100	*785.32*	*876.12*	*964.8*	*1052.1*	*1224.4*	*1394.6*	*1563.8*	*1732.2*	*1900.0*
150	*515.6*	*578.9*	*639.9*	*699.6*	*816.5*	*931.2*	*1044.7*	*1157.7*	*1270.1*
200	*380.73*	*430.28*	*477.57*	*523.42*	*612.5*	*699.6*	*785.3*	*870.5*	*955.2*
250	*299.86*	*341.19*	*380.21*	*417.76*	*490.2*	*560.7*	*629.8*	*698.3*	*766.4*
300	*246.01*	*281.86*	*315.35*	*347.37*	*408.8*	*468.1*	*526.1*	*583.5*	*640.5*
350	*207.60*	*239.52*	*269.07*	*297.10*	*350.6*	*401.9*	*452.0*	*501.4*	*550.4*
400	*178.90*	*207.83*	*234.39*	*259.45*	*306.8*	*352.2*	*396.5*	*440.0*	*483.0*
500	*138.96*	*163.64*	*185.96*	*206.81*	*245.9*	*282.9*	*318.7*	*353.8*	*388.6*
600	*112.76*	*134.42*	*153.82*	*171.80*	*205.2*	*236.6*	*267.0*	*296.5*	*325.5*
700	*94.49*	*113.81*	*131.01*	*146.88*	*176.2*	*203.6*	*229.9*	*255.5*	*280.7*
800	*81.25*	*98.60*	*114.08*	*128.31*	*154.51*	*178.86*	*202.14*	*224.75*	*246.93*
900	*71.36*	*87.02*	*101.05*	*113.97*	*137.66*	*159.64*	*180.56*	*200.82*	*220.68*
1000	*63.81*	*77.97*	*90.78*	*102.58*	*124.24*	*144.25*	*163.30*	*181.69*	*199.67*
1200	*53.27*	*64.97*	*75.76*	*85.79*	*104.24*	*121.27*	*137.41*	*152.97*	*168.14*
1400	*46.50*	*56.21*	*65.42*	*74.08*	*90.10*	*104.93*	*118.96*	*132.49*	*145.62*
1600	*41.85*	*50.03*	*57.98*	*65.54*	*79.65*	*92.76*	*105.18*	*117.12*	*128.74*
1800	*38.52*	*45.47*	*52.41*	*59.07*	*71.65*	*83.36*	*94.49*	*105.21*	*115.61*

TABLE 1d. (continued)

Pbars/T°C	700	800	900	1000	1200	1400	1600	1800	2000
2000	*36.01*	*42.03*	*48.12*	*54.05*	*65.34*	*75.92*	*85.99*	*95.70*	*105.12*
2200	*34.05*	*39.33*	*44.72*	*50.05*	*60.26*	*69.88*	*79.07*	*87.94*	*96.57*
2400	*32.48*	*37.15*	*41.98*	*46.79*	*56.08*	*64.91*	*73.34*	*81.50*	*89.43*
2600	*31.19*	*35.37*	*39.73*	*44.09*	*52.61*	*60.73*	*68.53*	*76.06*	*83.41*
2800	*30.09*	*33.87*	*37.83*	*41.83*	*49.67*	*57.18*	*64.43*	*71.43*	*78.26*
3000	*29.15*	*32.61*	*36.23*	*39.91*	*47.15*	*54.14*	*60.89*	*67.43*	*73.83*
3200	*28.34*	*31.51*	*34.84*	*38.23*	*44.97*	*51.49*	*57.81*	*63.94*	*69.94*
3400	*27.62*	*30.56*	*33.64*	*36.79*	*43.06*	*49.18*	*55.11*	*60.88*	*66.52*
3600	*26.97*	*29.71*	*32.57*	*35.51*	*41.38*	*47.13*	*52.71*	*58.16*	*63.49*
3800	*26.39*	*28.95*	*31.64*	*34.37*	*39.91*	*45.31*	*50.59*	*55.74*	*60.79*
4000	*25.87*	*28.27*	*30.79*	*33.37*	*38.57*	*43.69*	*48.68*	*53.56*	*58.35*
4500	*24.75*	*26.83*	*29.02*	*31.26*	*35.78*	*40.27*	*44.68*	*49.00*	*53.26*
5000	*23.84*	*25.67*	*27.60*	*29.56*	*33.58*	*37.56*	*41.49*	*45.36*	*49.18*
5500	*23.06*	*24.70*	*26.43*	*28.20*	*31.78*	*35.37*	*38.90*	*42.41*	*45.85*
6000	*22.39*	*23.89*	*25.44*	*27.04*	*30.28*	*33.53*	*36.75*	*39.94*	*43.09*
6500	*21.80*	*23.17*	*24.59*	*26.05*	*29.01*	*31.98*	*34.93*	*37.85*	*40.75*
7000	*21.29*	*22.54*	*23.85*	*25.19*	*27.91*	*30.65*	*33.37*	*36.07*	*38.73*
7500	*20.83*	*21.98*	*23.19*	*24.43*	*26.95*	*29.47*	*32.00*	*34.50*	*37.00*
8000	*20.41*	*21.49*	*22.61*	*23.76*	*26.09*	*28.45*	*30.81*	*33.15*	*35.47*
8500	*20.02*	*21.02*	*22.09*	*23.15*	*25.33*	*27.55*	*29.74*	*31.92*	*34.12*
9000	*19.67*	*20.63*	*21.60*	*22.61*	*24.66*	*26.72*	*28.79*	*30.84*	*32.90*
9500	*19.35*	*20.25*	*21.17*	*22.11*	*24.03*	*25.98*	*27.92*	*29.87*	*31.82*
10000	*19.06*	*19.89*	*20.75*	*21.66*	*23.47*	*25.31*	*27.15*	*28.99*	*30.83*
12000	*18.041*	*18.72*	*19.42*	*20.14*	*21.62*	*23.11*	*24.63*	*26.14*	*27.67*
14000	*17.240*	*17.800*	*18.382*	*18.982*	*20.21*	*21.48*	*22.75*	*24.03*	*25.33*
16000	*16.580*	*17.052*	*17.544*	*18.050*	*19.10*	*20.18*	*21.28*	*22.39*	*23.51*
18000	*16.025*	*16.427*	*16.847*	*17.281*	*18.18*	*19.11*	*20.09*	*21.06*	*22.05*
20000	*15.546*	*15.894*	*16.254*	*16.629*	*17.412*	*18.234*	*19.084*	*19.953*	*20.837*
25000	*14.59*	*14.83*	*15.08*	*15.35*	*15.91*	*16.52*	*17.15*	*17.82*	*18.52*
30000	*13.85*	*14.03*	*14.21*	*14.39*	*14.81*	*15.26*	*15.76*	*16.27*	*16.83*
40000	*13.79*	*14.07*		*15.11*					
50000	*13.06*	*13.28*		*14.40*					
60000	*12.54*	*12.72*		*13.76*					
70000	*12.14*	*12.29*		*13.21*					
80000	*11.78*	*11.92*		*12.71*					
90000	*11.38*	*11.53*		*12.27*					
100000	*10.89*	*11.06*		*11.85*					
150000				*10.32*					
200000				*9.35*					
250000				*8.71*					

Values calculated by (15), (10) and (33).

TABLE 2. Shock-Compressed Water Data

Pressure (Kb)	Density (g/cm^3)	Temperature (K)
292.	*2.05*	**2067.**
316.	*2.08*	**2067.**
383.	*2.16*	**2533.**
489. ± 9.	**2.26 ± 0.01**	**3280.**
585. ± 11.	**2.34 ± 0.01**	**3830.**
619. ± 12.	**2.36 ± 0.01**	**4090.**
710. ± 30.	**2.41 ± 0.02**	**4480.**
800. ± 18.	**2.47 ± 0.01**	**5270.**

Values from (24) and (28).

TABLE 3. Thermodynamic Functions

Entropy (S)	$S=-\frac{\partial A}{\partial T}$
Enthalpy (H)	$H=U+\frac{P}{\rho}$
	$P=\rho^2\frac{\partial A}{\partial \rho}$
	$U=A+TS$
Heat Capacity (C_p)	$C_p=C_v+\frac{T}{\rho^2}\frac{(\partial P/\partial T)^2}{\partial P/\partial \rho}$
	$C_v=-T^2\frac{\partial^2 A}{\partial T^2}$
	$\frac{\partial P}{\partial T}=\rho^2\frac{\partial^2 A}{\partial \rho \partial T}$
Gibbs Free Energy (G)	$G=A+\frac{P}{\rho}$

Gibbs Free Energy (G), which is not tabulated here or in Haar et al., can be derived from the relationship for G given in Table 3, or from rearrangement of those equations, by $G = H - TS$. G can then be calculated from values for H and S given in Tables 4 and 5.

Enthalpies, entropies, and heat capacities are tabulated from 0° to 2000°C and 1 bar to 30 Kbar in Tables 4a-c, 5a-c, and 6a-c, respectively. Properties of water along the coexistence curve for liquid and vapor are compiled in Table 7. This table includes the pressure and temperature of coexistence, and the volumes, enthalpies and entropies of the coexisting phases. Values given in Tables 4 through 7 are taken from (15). Additional thermodynamic properties as well as additional pressure-temperature intervals for the properties can be found in (15).

An alternate form of the thermodynamic properties called the apparent properties are given by (16) and (19), among others. The conversion from the values of enthalpy and entropy listed here to values of apparent molal enthalpies and entropies requires the addition of triple point values of H and S, respectively. This conversion is described in detail, and triple point values necessary to make the conversions are given on page 568 of (19).

2.3 Sound Speed

The speed of sound in water can be derived from an EOS. Mathematical relationships are presented in (15), (19) and (23). Sound speeds are given in Table 8a-c from 0° to 2000°C and 1 bar to 30 Kbar. Values are obtained from (15). (23) describes the effects that two phase fluid mixtures of water and another component can have on sound speed, and presents equations and graphs showing sound speeds in mixtures of water, steam and air.

2.4 Dielectric Constant

The dielectric constant (ϵ) of a fluid is a complex function of pressure and temperature that provides a measure of the fluid's electrostatic permittivity. It is useful in assessing electrostatic interactions in a fluid. The dielectric constant controls the extent of ion association that takes place in a solution, and hence, affects mineral solubilities. Isopleths of the dielectric constant are often used to predict the values of association constants for aqueous species outside the pressure and temperature range for which they have been measured. Values of the dielectric constant are compiled in Table 9a-c from 0° to 1000°C and 1 bar to 10 Kbar, and are taken from (15) and (2).

TABLE 4a. Water Enthalpy, kJ/kg

Pbars/T°C	0	20	40	60	80	100	120	140	160
1	*0.06*	*83.93*	*167.59*	*251.22*	*334.97*	*2675.9*	*2716.3*	*2756.2*	*2795.8*
25	*2.51*	*86.18*	*169.71*	*253.24*	*336.88*	*420.87*	*505.40*	*590.63*	*676.75*
50	*5.05*	*88.52*	*171.92*	*255.34*	*338.87*	*422.75*	*507.16*	*592.26*	*678.22*
100	*10.10*	*93.20*	*176.33*	*259.53*	*342.85*	*426.52*	*510.70*	*595.53*	*681.19*
150	*15.11*	*97.85*	*180.74*	*263.72*	*346.84*	*430.29*	*514.24*	*598.83*	*684.2*
200	*20.08*	*102.48*	*185.13*	*267.90*	*350.82*	*434.07*	*517.81*	*602.15*	*687.2*
250	*25.02*	*107.09*	*189.50*	*272.08*	*354.80*	*437.85*	*521.38*	*605.49*	*690.3*
300	*29.92*	*111.68*	*193.87*	*276.25*	*358.79*	*441.64*	*524.96*	*608.85*	*693.4*
350	*34.79*	*116.25*	*198.23*	*280.41*	*362.77*	*445.44*	*528.56*	*612.22*	*696.5*
400	*39.63*	*120.80*	*202.57*	*284.57*	*366.75*	*449.24*	*532.16*	*615.61*	*699.7*
500	*49.20*	*129.85*	*211.23*	*292.88*	*374.71*	*456.84*	*539.40*	*622.44*	*706.0*
600	*58.65*	*138.83*	*219.84*	*301.16*	*382.66*	*464.46*	*546.66*	*629.32*	*712.5*
700	*67.99*	*147.75*	*228.41*	*309.41*	*390.60*	*472.09*	*553.96*	*636.25*	*719.0*
800	*77.22*	*156.60*	*236.94*	*317.64*	*398.54*	*479.72*	*561.27*	*643.23*	*725.6*
900	*86.35*	*165.38*	*245.43*	*325.85*	*406.46*	*487.36*	*568.61*	*650.24*	*732.3*
1000	*95.40*	*174.11*	*253.88*	*334.03*	*414.38*	*495.00*	*575.96*	*657.28*	*739.0*
1200	*113.2*	*191.4*	*270.7*	*350.3*	*430.2*	*510.3*	*590.7*	*671.5*	*752.5*
1400	*130.8*	*208.5*	*287.3*	*366.5*	*445.9*	*525.6*	*605.5*	*685.7*	*766.2*
1600	*148.2*	*225.4*	*303.8*	*382.6*	*461.6*	*540.8*	*620.3*	*700.1*	*780.1*
1800	*165.3*	*242.2*	*320.2*	*398.7*	*477.3*	*556.1*	*635.2*	*714.5*	*794.0*
2000	*182.4*	*258.8*	*336.5*	*414.6*	*492.9*	*571.3*	*650.0*	*729.0*	*808.1*
3000	*267.0*	*340.6*	*416.6*	*493.4*	*570.2*	*647.2*	*724.4*	*801.8*	*879.2*
4000	*352.1*	*421.0*	*495.0*	*570.7*	*646.5*	*722.4*	*798.5*	*874.8*	*951.1*
5000	*439.4*	*500.6*	*571.7*	*646.8*	*722.1*	*797.2*	*872.4*	*947.8*	*1023.3*
6000		*579.4*	*646.1*	*721.5*	*796.9*	*871.5*	*946.0*	*1020.7*	*1095.5*
7000			*717.4*	*794.4*	*871.0*	*945.5*	*1019.4*	*1093.4*	*1167.7*
8000			*785.5*	*865.2*	*944.2*	*1019.2*	*1092.6*	*1166.1*	*1239.8*
9000				*934.0*	*1016.6*	*1092.7*	*1165.8*	*1238.6*	*1311.8*
10000				*1001.4*	*1088.2*	*1165.9*	*1238.9*	*1311.1*	*1383.7*
20000									*2104.*

Values calculated by (15).

TABLE 4b. Water Enthalpy, kJ/kg

Pbars/T°C	180	200	220	240	260	280	300	350	400
1	*2835.3*	*2874.8*	*2914.4*	*2954.0*	*2993.8*	*3033.8*	*3073.9*	*3175.3*	*3278.0*
25	*764.01*	*852.76*	*943.56*	*2850.8*	*2906.4*	*2958.4*	*3008.0*	*3125.8*	*3239.2*
50	*765.28*	*853.79*	*944.25*	*1037.40*	*1134.33*	*2855.9*	*2923.5*	*3067.7*	*3195.5*
100	*767.88*	*855.91*	*945.75*	*1038.03*	*1133.69*	*1234.23*	*1342.38*	*2922.2*	*3096.1*
150	*770.5*	*858.1*	*947.4*	*1038.9*	*1133.4*	*1232.2*	*1337.4*	*2691.3*	*2974.7*
200	*773.2*	*860.4*	*949.1*	*1039.9*	*1133.4*	*1230.7*	*1333.4*	*1645.4*	*2816.9*
250	*776.0*	*862.7*	*951.0*	*1041.1*	*1133.7*	*1229.7*	*1330.4*	*1623.1*	*2578.1*
300	*778.8*	*865.2*	*952.9*	*1042.4*	*1134.2*	*1229.0*	*1328.0*	*1608.1*	*2150.7*
350	*781.6*	*867.6*	*954.9*	*1043.8*	*1134.9*	*1228.7*	*1326.1*	*1596.8*	*1988.3*
400	*784.5*	*870.1*	*957.0*	*1045.4*	*1135.7*	*1228.6*	*1324.8*	*1588.1*	*1930.8*
500	*790.3*	*875.3*	*961.4*	*1048.9*	*1137.9*	*1229.2*	*1323.1*	*1575.3*	*1874.1*
600	*796.2*	*880.7*	*966.1*	*1052.7*	*1140.7*	*1230.5*	*1322.6*	*1566.7*	*1843.0*
700	*802.3*	*886.2*	*971.0*	*1056.8*	*1143.8*	*1232.5*	*1323.0*	*1560.8*	*1822.8*
800	*808.5*	*891.9*	*976.1*	*1061.1*	*1147.3*	*1234.9*	*1324.2*	*1556.9*	*1808.7*
900	*814.7*	*897.7*	*981.3*	*1065.7*	*1151.2*	*1237.8*	*1325.9*	*1554.4*	*1798.4*
1000	*821.1*	*903.6*	*986.7*	*1070.6*	*1155.3*	*1241.1*	*1328.2*	*1553.1*	*1790.9*
1200	*833.9*	*915.7*	*997.9*	*1080.7*	*1164.2*	*1248.6*	*1334.0*		*1781.5*

TABLE 4b. (continued)

Pbars/T°C	180	200	220	240	260	280	300	350	400
1400	*847.0*	*928.1*	*1009.5*	*1091.4*	*1173.9*	*1257.1*	*1341.1*		*1777.2*
1600	*860.3*	*940.8*	*1021.5*	*1102.6*	*1184.2*	*1266.3*	*1349.2*		*1776.3*
1800	*873.8*	*953.6*	*1033.8*	*1114.2*	*1195.0*	*1276.2*	*1358.0*		*1777.8*
2000	*887.3*	*966.7*	*1046.3*	*1126.1*	*1206.2*	*1286.7*	*1367.6*		*1781.2*
3000	*956.7*	*1034.2*	*1111.6*	*1189.1*	*1266.6*	*1344.3*	*1422.1*		*1815.2*
4000	*1027.4*	*1103.6*	*1179.7*	*1255.6*	*1331.5*	*1407.4*	*1483.3*		*1864.5*
5000	*1098.7*	*1174.0*	*1249.1*	*1324.1*	*1398.9*	*1473.5*	*1548.2*		*1921.4*
6000	*1170.3*	*1245.0*	*1319.4*	*1393.6*	*1467.6*	*1541.4*	*1615.1*		*1982.8*
7000	*1242.0*	*1316.2*	*1390.1*	*1463.8*	*1537.2*	*1610.4*	*1683.4*		*2047.0*
8000	*1313.7*	*1387.4*	*1461.0*	*1534.3*	*1607.2*	*1680.0*	*1752.5*		*2113.0*
9000	*1385.2*	*1458.7*	*1531.9*	*1604.9*	*1677.6*	*1750.0*	*1822.1*		*2180.2*
10000	*1456.8*	*1529.9*	*1602.9*	*1675.7*	*1748.1*	*1820.3*	*1892.1*		*2248.4*
20000	*2169.*	*2238.*	*2308.*	*2379.*	*2450.*	*2521.*	*2592.*		*2943.*
30000					*3140.*	*3210.*	*3280.*		*3630.*

Values calculated by (15).

TABLE 4c. Water Enthalpy, kJ/kg

Pbars/T°C	500	600	700	800	900	1000	1200	1500	2000
1	*3488.2*	*3705.0*	*3928.8*	*4159.7*	*4397.5*	*4642.0*	*5150.0*	*5953.3*	*7376.7*
25	*3462.2*	*3686.3*	*3914.7*	*4148.6*	*4388.7*	*4634.9*	*5145.2*	*5950.6*	*7375.8*
50	*3433.9*	*3666.2*	*3899.7*	*4137.0*	*4379.4*	*4627.4*	*5140.2*	*5947.7*	*7374.8*
100	*3374.0*	*3624.7*	*3869.0*	*4113.5*	*4360.9*	*4612.5*	*5130.3*	*5942.2*	*7373.1*
150	*3309.3*	*3581.5*	*3837.6*	*4089.6*	*4342.2*	*4597.7*	*5121.*	*5937.*	*7371.*
200	*3239.4*	*3536.7*	*3805.5*	*4065.4*	*4323.5*	*4582.8*	*5111.*		*7370.*
250	*3164.2*	*3490.4*	*3773.0*	*4041.1*	*4304.7*	*4568.0*	*5101.*		*7369.*
300	*3083.5*	*3443.1*	*3740.1*	*4016.7*	*4285.9*	*4553.3*	*5092.*		*7367.*
350	*2997.3*	*3394.7*	*3706.9*	*3992.2*	*4267.2*	*4538.5*	*5082.*		*7366.*
400	*2906.7*	*3345.8*	*3673.8*	*3967.8*	*4248.5*	*4523.9*	*5073.*		*7365.*
500	*2724.2*	*3247.7*	*3607.8*	*3919.5*	*4211.5*	*4495.0*	*5055.*		*7363.*
600	*2571.9*	*3152.3*	*3543.5*	*3872.3*	*4175.4*	*4466.7*	*5037.*		*7361.*
700	*2466.9*	*3063.8*	*3481.9*	*3826.7*	*4140.3*	*4439.1*	*5019.*		*7359.*
800	*2397.7*	*2985.4*	*3424.2*	*3783.3*	*4106.6*	*4412.5*	*5002.*		*7357.*
900	*2350.3*	*2918.7*	*3371.1*	*3742.4*	*4074.6*	*4386.9*	*4985.*		*7355.*
1000	*2316.2*	*2863.4*	*3323.1*	*3704.3*	*4044.3*	*4362.6*	*4970.*		*7354.*
1200	*2271.4*	*2781.1*	*3242.*	*3637.*	*3989.*	*4318.*	*4940.*		*7351.*
1400	*2244.1*	*2726.2*	*3179.*	*3581.*	*3942.*	*4279.*	*4913.*		*7348.*
1600	*2227.0*	*2688.8*	*3132.*	*3535.*	*3902.*	*4244.*	*4889.*		*7346.*
1800	*2216.3*	*2663.0*	*3096.*	*3498.*	*3868.*	*4215.*	*4868.*		*7344.*
2000	*2210.0*	*2645.0*	*3069.*	*3469.*	*3841.*	*4191.*	*4850.*		*7343.*
3000	*2215.0*	*2616.5*	*3012.*	*3396.*	*3764.*	*4119.*	*4796.*		*7346.*
4000	*2249.1*	*2634.2*	*3015.*	*3388.*	*3750.*	*4103.*	*4784.*		*7364.*
5000	*2296.*	*2671.*	*3043.*	*3409.*	*3767.*	*4117.*	*4797.*		*7394.*
6000	*2351.*	*2719.*	*3084.*	*3445.*	*3799.*	*4147.*	*4826.*		*7431.*
7000	*2410.*	*2773.*	*3134.*	*3490.*	*3842.*	*4188.*	*4866.*		*7476.*
8000	*2472.*	*2831.*	*3188.*	*3541.*	*3891.*	*4235.*	*4912.*		*7524.*
9000	*2537.*	*2892.*	*3246.*	*3597.*	*3944.*	*4287.*	*4962.*		*7576.*
10000	*2602.*	*2955.*	*3306.*	*3655.*	*4001.*	*4343.*	*5016.*		*7630.*
20000	*3288.*	*3628.*	*3966.*	*4302.*	*4636.*	*4968.*	*5627.*		*8218.*
30000	*3974.*	*4312.*	*4646.*	*4976.*	*5303.*	*5628.*	*6271.*		*8804.*

Values calculated by (15).

TABLE 5a. Water Entropy, kJ/kg-K

Pbars/T°C	0	20	40	60	80	100	120	140	160
1	*-.00015*	*0.29619*	*0.57225*	*0.83115*	*1.07526*	*7.3609*	*7.4665*	*7.5655*	*7.6591*
25	*0.00003*	*0.29568*	*0.57132*	*0.82987*	*1.07369*	*1.30502*	*1.52568*	*1.73714*	*1.94068*
50	*0.00020*	*0.29514*	*0.57034*	*0.82855*	*1.07205*	*1.30308*	*1.52343*	*1.73456*	*1.93773*
100	*0.00045*	*0.29405*	*0.56839*	*0.82592*	*1.06881*	*1.29924*	*1.51899*	*1.72947*	*1.93192*
150	*0.00060*	*0.29292*	*0.56644*	*0.82331*	*1.06560*	*1.29546*	*1.51462*	*1.72447*	*1.9262*
200	*0.00066*	*0.29176*	*0.56449*	*0.82072*	*1.06243*	*1.29172*	*1.51032*	*1.71957*	*1.9207*
250	*0.00063*	*0.29057*	*0.56253*	*0.81814*	*1.05928*	*1.28803*	*1.50607*	*1.71474*	*1.9152*
300	*0.00051*	*0.28935*	*0.56057*	*0.81557*	*1.05617*	*1.28439*	*1.50189*	*1.70999*	*1.9098*
350	*0.00031*	*0.28810*	*0.55861*	*0.81302*	*1.05308*	*1.28078*	*1.49777*	*1.70532*	*1.9046*
400	*0.00003*	*0.28682*	*0.55665*	*0.81048*	*1.05002*	*1.27722*	*1.49370*	*1.70073*	*1.8994*
500	*-.00076*	*0.28419*	*0.55270*	*0.80544*	*1.04398*	*1.27021*	*1.48571*	*1.69173*	*1.8893*
600	*-.00184*	*0.28144*	*0.54874*	*0.80045*	*1.03803*	*1.26334*	*1.47793*	*1.68300*	*1.8796*
700	*-.00318*	*0.27860*	*0.54477*	*0.79550*	*1.03217*	*1.25661*	*1.47032*	*1.67450*	*1.8701*
800	*-.00476*	*0.27566*	*0.54078*	*0.79059*	*1.02640*	*1.25000*	*1.46289*	*1.66621*	*1.8609*
900	*-.00655*	*0.27264*	*0.53678*	*0.78571*	*1.02070*	*1.24351*	*1.45561*	*1.65813*	*1.8520*
1000	*-.00854*	*0.26954*	*0.53276*	*0.78087*	*1.01508*	*1.23713*	*1.44848*	*1.65023*	*1.8433*
1200	*-0.0130*	*0.2631*	*0.5247*	*0.7713*	*1.0040*	*1.2247*	*1.4346*	*1.6350*	*1.8266*
1400	*-0.0180*	*0.2565*	*0.5166*	*0.7618*	*0.9932*	*1.2126*	*1.4213*	*1.6203*	*1.8106*
1600	*-0.0233*	*0.2497*	*0.5084*	*0.7524*	*0.9827*	*1.2008*	*1.4083*	*1.6062*	*1.7953*
1800	*-0.0287*	*0.2427*	*0.5003*	*0.7432*	*0.9723*	*1.1894*	*1.3958*	*1.5926*	*1.7806*
2000	*-0.0342*	*0.2357*	*0.4922*	*0.7340*	*0.9621*	*1.1782*	*1.3837*	*1.5795*	*1.7665*
3000	*-0.0587*	*0.2014*	*0.4522*	*0.6897*	*0.9138*	*1.1258*	*1.3274*	*1.5193*	*1.7024*
4000	*-0.0736*	*0.1699*	*0.4139*	*0.6482*	*0.8692*	*1.0783*	*1.2770*	*1.4662*	*1.6465*
5000	*-0.0744*	*0.1417*	*0.3761*	*0.6086*	*0.8280*	*1.0349*	*1.2312*	*1.4183*	*1.5967*
6000		*0.1166*	*0.3364*	*0.5697*	*0.7896*	*0.9950*	*1.1895*	*1.3748*	*1.5517*
7000			*0.2916*	*0.5298*	*0.7532*	*0.9584*	*1.1513*	*1.3350*	*1.5106*
8000			*0.2412*	*0.4876*	*0.7181*	*0.9247*	*1.1164*	*1.2985*	*1.4728*
9000				*0.4430*	*0.6839*	*0.8936*	*1.0845*	*1.2651*	*1.4381*
10000				*0.3974*	*0.6507*	*0.8648*	*1.0554*	*1.2345*	*1.4061*
20000									*1.205*

Values calculated by (15).

TABLE 5b. Water Entropy, kJ/kg-K

Pbars/T°C	180	200	220	240	260	280	300	350	400
1	*7.7482*	*7.8335*	*7.9153*	*7.9942*	*8.0702*	*8.1438*	*8.2152*	*8.3846*	*8.5432*
25	*2.13760*	*2.32926*	*2.51719*	*6.3522*	*6.4586*	*6.5543*	*6.6424*	*6.8395*	*7.0146*
50	*2.13421*	*2.32533*	*2.51258*	*2.69770*	*2.88298*	*6.0867*	*6.2067*	*6.4482*	*6.6456*
100	*2.12756*	*2.31766*	*2.50361*	*2.68702*	*2.86988*	*3.05497*	*3.24697*	*5.9425*	*6.2114*
150	*2.1211*	*2.3102*	*2.4950*	*2.6768*	*2.8575*	*3.0394*	*3.2261*	*5.4404*	*5.8799*
200	*2.1147*	*2.3030*	*2.4866*	*2.6670*	*2.8458*	*3.0250*	*3.2073*	*3.7277*	*5.5521*
250	*2.1085*	*2.2959*	*2.4785*	*2.6576*	*2.8347*	*3.0114*	*3.1902*	*3.6790*	*5.1388*
300	*2.1025*	*2.2890*	*2.4707*	*2.6485*	*2.8240*	*2.9986*	*3.1744*	*3.6421*	*4.4723*
350	*2.0966*	*2.2823*	*2.4630*	*2.6398*	*2.8138*	*2.9865*	*3.1596*	*3.6118*	*4.2136*
400	*2.0907*	*2.2758*	*2.4556*	*2.6313*	*2.8040*	*2.9750*	*3.1457*	*3.5857*	*4.1134*
500	*2.0795*	*2.2631*	*2.4413*	*2.6151*	*2.7854*	*2.9534*	*3.1202*	*3.5417*	*4.0022*
600	*2.0686*	*2.2510*	*2.4278*	*2.5998*	*2.7680*	*2.9334*	*3.0970*	*3.5051*	*3.9312*
700	*2.0581*	*2.2394*	*2.4148*	*2.5853*	*2.7517*	*2.9149*	*3.0757*	*3.4733*	*3.8774*
800	*2.0479*	*2.2281*	*2.4023*	*2.5714*	*2.7362*	*2.8975*	*3.0560*	*3.4451*	*3.8335*
900	*2.0381*	*2.2173*	*2.3904*	*2.5582*	*2.7215*	*2.8811*	*3.0375*	*3.4196*	*3.7960*
1000	*2.0286*	*2.2068*	*2.3789*	*2.5455*	*2.7075*	*2.8655*	*3.0202*	*3.3962*	*3.7632*
1200	*2.0103*	*2.1868*	*2.3570*	*2.5216*	*2.6812*	*2.8366*	*2.9883*		*3.7072*

TABLE 5b. (continued)

Pbars/T°C	180	200	220	240	260	280	300	350	400
1400	*1.9929*	*2.1680*	*2.3365*	*2.4993*	*2.6570*	*2.8101*	*2.9593*		*3.6601*
1600	*1.9763*	*2.1501*	*2.3172*	*2.4784*	*2.6344*	*2.7856*	*2.9327*		*3.6191*
1800	*1.9605*	*2.1331*	*2.2989*	*2.4587*	*2.6132*	*2.7628*	*2.9081*		*3.5828*
2000	*1.9453*	*2.1168*	*2.2815*	*2.4401*	*2.5932*	*2.7414*	*2.8851*		*3.5500*
3000	*1.8772*	*2.0445*	*2.0249*	*2.3589*	*2.5071*	*2.6501*	*2.7883*		*3.4203*
4000	*1.8187*	*1.9832*	*2.1407*	*2.2917*	*2.4368*	*2.5766*	*2.7114*		*3.3243*
5000	*1.7670*	*1.9296*	*2.0851*	*2.2340*	*2.3770*	*2.5145*	*2.6470*		*3.2473*
6000	*1.7205*	*1.8817*	*2.0358*	*2.1833*	*2.3247*	*2.4607*	*2.5915*		*3.1828*
7000	*1.6782*	*1.8384*	*1.9914*	*2.1379*	*2.2782*	*2.4130*	*2.5426*		*3.1274*
8000	*1.6395*	*1.7988*	*1.9511*	*2.0967*	*2.2363*	*2.3702*	*2.4990*		*3.0787*
9000	*1.6039*	*1.7625*	*1.9141*	*2.0592*	*2.1981*	*2.3314*	*2.4595*		*3.0355*
10000	*1.5710*	*1.7289*	*1.8800*	*2.0246*	*2.1632*	*2.2960*	*2.4236*		*2.9966*
20000	*1.354*	*1.502*	*1.647*	*1.788*	*1.924*	*2.055*	*2.181*		*2.746*
30000					*1.802*	*1.930*	*2.055*		*2.619*

Values calculated by (15).

TABLE 5c. Water Entropy, kJ/kg-K

Pbars/T°C	500	600	700	800	900	1000	1200	1500	2000
1	*8.8342*	*9.0979*	*9.3405*	*9.5662*	*9.7781*	*9.9781*	*10.3485*	*10.8444*	*11.5506*
25	*7.3235*	*7.5960*	*7.8436*	*8.0724*	*8.2862*	*8.4876*	*8.8597*	*9.3569*	*10.0640*
50	*6.9760*	*7.2586*	*7.5117*	*7.7438*	*7.9598*	*8.1626*	*8.5365*	*9.0350*	*9.7431*
100	*6.5971*	*6.9022*	*7.1671*	*7.4062*	*7.6266*	*7.8324*	*8.2100*	*8.7112*	*9.4212*
150	*6.3452*	*6.6767*	*6.9544*	*7.2009*	*7.4260*	*7.6350*	*8.016*	*8.520*	*9.232*
200	*6.1417*	*6.5039*	*6.7955*	*7.0498*	*7.2797*	*7.4919*	*7.877*		*9.098*
250	*5.9616*	*6.3593*	*6.6659*	*6.9282*	*7.1631*	*7.3785*	*7.767*		*8.993*
300	*5.7936*	*6.2324*	*6.5547*	*6.8254*	*7.0653*	*7.2840*	*7.677*		*8.907*
350	*5.6320*	*6.1174*	*6.4563*	*6.7355*	*6.9805*	*7.2025*	*7.599*		*8.834*
400	*5.4745*	*6.0111*	*6.3673*	*6.6551*	*6.9052*	*7.1305*	*7.531*		*8.770*
500	*5.1780*	*5.8184*	*6.2097*	*6.5148*	*6.7751*	*7.0070*	*7.415*		*8.664*
600	*4.9373*	*5.6471*	*6.0723*	*6.3942*	*6.6644*	*6.9027*	*7.319*		*8.576*
700	*4.7669*	*5.4957*	*5.9502*	*6.2878*	*6.5674*	*6.8118*	*7.235*		*8.502*
800	*4.6474*	*5.3640*	*5.8410*	*6.1926*	*6.4809*	*6.7311*	*7.161*		*8.437*
900	*4.5590*	*5.2514*	*5.7431*	*6.1067*	*6.4028*	*6.6584*	*7.095*		*8.379*
1000	*4.4897*	*5.1558*	*5.6552*	*6.0286*	*6.3317*	*6.5921*	*7.035*		*8.327*
1200	*4.3849*	*5.0052*	*5.506*	*5.892*	*6.207*	*6.475*	*6.929*		*8.236*
1400	*4.3063*	*4.8927*	*5.385*	*5.778*	*6.100*	*6.375*	*6.838*		*8.159*
1600	*4.2430*	*4.8048*	*5.285*	*5.680*	*6.007*	*6.288*	*6.758*		*8.091*
1800	*4.1898*	*4.7331*	*5.203*	*5.596*	*5.927*	*6.210*	*6.687*		*8.031*
2000	*4.1437*	*4.6728*	*5.133*	*5.524*	*5.855*	*6.142*	*6.623*		*7.976*
3000	*3.9740*	*4.4624*	*4.891*	*5.267*	*5.595*	*5.886*	*6.380*		*7.765*
4000	*3.8570*	*4.3254*	*4.738*	*5.103*	*5.426*	*5.715*	*6.212*		*7.613*
5000	*3.767*	*4.223*	*4.626*	*4.983*	*5.302*	*5.589*	*6.085*		*7.495*
6000	*3.693*	*4.140*	*4.537*	*4.889*	*5.205*	*5.490*	*5.985*		*7.400*
7000	*3.630*	*4.072*	*4.463*	*4.812*	*5.125*	*5.408*	*5.903*		*7.320*
8000	*3.576*	*4.013*	*4.400*	*4.746*	*5.057*	*5.339*	*5.832*		*7.251*
9000	*3.529*	*3.961*	*4.345*	*4.688*	*4.998*	*5.279*	*5.771*		*7.190*
10000	*3.487*	*3.916*	*4.297*	*4.638*	*4.946*	*5.226*	*5.717*		*7.136*
20000	*3.223*	*3.637*	*4.004*	*4.333*	*4.630*	*4.902*	*5.382*		*6.788*
30000	*3.095*	*3.506*	*3.868*	*4.191*	*4.482*	*4.748*	*5.217*		*6.591*

Values calculated by (15).

TABLE 6a. Water Heat Capacity at Constant Pressure, kJ/kg-K

Pbars/T°C	0	20	40	60	80	100	120	140	160
1	*4.228*	*4.183*	*4.182*	*4.183*	*4.194*	*2.042*	*2.005*	*1.986*	*1.977*
25	*4.215*	*4.175*	*4.176*	*4.177*	*4.189*	*4.211*	*4.243*	*4.282*	*4.332*
50	*4.202*	*4.168*	*4.170*	*4.172*	*4.183*	*4.206*	*4.237*	*4.275*	*4.323*
100	*4.177*	*4.153*	*4.159*	*4.161*	*4.173*	*4.195*	*4.224*	*4.261*	*4.306*
150	*4.153*	*4.139*	*4.148*	*4.151*	*4.163*	*4.184*	*4.212*	*4.247*	*4.290*
200	*4.130*	*4.125*	*4.137*	*4.141*	*4.153*	*4.174*	*4.201*	*4.234*	*4.275*
250	*4.109*	*4.112*	*4.126*	*4.131*	*4.143*	*4.163*	*4.190*	*4.222*	*4.260*
300	*4.089*	*4.100*	*4.116*	*4.122*	*4.133*	*4.154*	*4.179*	*4.210*	*4.246*
350	*4.070*	*4.087*	*4.106*	*4.113*	*4.124*	*4.144*	*4.169*	*4.198*	*4.233*
400	*4.053*	*4.076*	*4.097*	*4.104*	*4.115*	*4.135*	*4.159*	*4.187*	*4.220*
500	*4.021*	*4.054*	*4.078*	*4.086*	*4.098*	*4.117*	*4.140*	*4.165*	*4.195*
600	*3.992*	*4.034*	*4.061*	*4.070*	*4.082*	*4.100*	*4.121*	*4.145*	*4.172*
700	*3.967*	*4.015*	*4.045*	*4.054*	*4.066*	*4.083*	*4.104*	*4.126*	*4.151*
800	*3.945*	*3.998*	*4.030*	*4.040*	*4.051*	*4.068*	*4.087*	*4.108*	*4.131*
900	*3.926*	*3.983*	*4.015*	*4.026*	*4.037*	*4.053*	*4.072*	*4.091*	*4.112*
1000	*3.909*	*3.968*	*4.002*	*4.012*	*4.023*	*4.039*	*4.057*	*4.075*	*4.094*
1200	*3.880*	*3.942*	*3.977*	*3.988*	*3.998*	*4.013*	*4.030*	*4.045*	*4.061*
1400	*3.856*	*3.919*	*3.955*	*3.965*	*3.975*	*3.989*	*4.004*	*4.019*	*4.032*
1600	*3.833*	*3.899*	*3.936*	*3.945*	*3.954*	*3.967*	*3.981*	*3.994*	*4.005*
1800	*3.810*	*3.880*	*3.918*	*3.926*	*3.935*	*3.947*	*3.961*	*3.972*	*3.981*
2000	*3.786*	*3.861*	*3.901*	*3.909*	*3.917*	*3.929*	*3.941*	*3.951*	*3.959*
3000	*3.61*	*3.76*	*3.83*	*3.84*	*3.85*	*3.85*	*3.86*	*3.87*	*3.87*
4000	*3.32*	*3.60*	*3.77*	*3.79*	*3.79*	*3.80*	*3.81*	*3.82*	*3.82*
5000	*2.89*	*3.32*	*3.71*	*3.77*	*3.76*	*3.76*	*3.77*	*3.77*	*3.77*
6000		*2.85*	*3.68*	*3.80*	*3.74*	*3.72*	*3.73*	*3.74*	*3.74*
7000			*3.67*	*3.89*	*3.77*	*3.70*	*3.70*	*3.71*	*3.72*
8000			*3.64*	*4.06*	*3.83*	*3.69*	*3.66*	*3.68*	*3.69*
9000				*4.29*	*3.95*	*3.70*	*3.64*	*3.65*	*3.67*
10000				*4.53*	*4.09*	*3.72*	*3.61*	*3.62*	*3.64*
20000									*3.22*

Values calculated by (15).

TABLE 6b. Water Heat Capacity at Constant Pressure, kJ/kg-K

Pbars/T°C	180	200	220	240	260	280	300	350	400
1	*1.974*	*1.975*	*1.980*	*1.986*	*1.994*	*2.003*	*2.013*	*2.040*	*2.070*
25	*4.397*	*4.484*	*4.602*	*2.903*	*2.678*	*2.532*	*2.433*	*2.299*	*2.245*
50	*4.386*	*4.469*	*4.583*	*4.740*	*4.967*	*3.614*	*3.181*	*2.672*	*2.468*
100	*4.365*	*4.442*	*4.547*	*4.689*	*4.889*	*5.186*	*5.675*	*4.027*	*3.100*
150	*4.345*	*4.417*	*4.513*	*4.643*	*4.821*	*5.076*	*5.470*	*8.838*	*4.177*
200	*4.327*	*4.394*	*4.482*	*4.601*	*4.761*	*4.983*	*5.311*	*8.138*	*6.371*
250	*4.309*	*4.372*	*4.454*	*4.562*	*4.707*	*4.904*	*5.182*	*6.994*	*13.270*
300	*4.292*	*4.350*	*4.427*	*4.527*	*4.659*	*4.834*	*5.075*	*6.401*	*25.080*
350	*4.276*	*4.331*	*4.402*	*4.494*	*4.615*	*4.773*	*4.984*	*6.022*	*11.671*
400	*4.260*	*4.312*	*4.378*	*4.464*	*4.575*	*4.718*	*4.906*	*5.752*	*8.717*
500	*4.231*	*4.277*	*4.335*	*4.409*	*4.504*	*4.623*	*4.775*	*5.384*	*6.789*
600	*4.204*	*4.245*	*4.296*	*4.361*	*4.443*	*4.544*	*4.670*	*5.138*	*6.011*
700	*4.180*	*4.216*	*4.261*	*4.318*	*4.390*	*4.477*	*4.584*	*4.959*	*5.571*
800	*4.157*	*4.189*	*4.229*	*4.280*	*4.342*	*4.419*	*4.510*	*4.820*	*5.280*
900	*4.135*	*4.164*	*4.200*	*4.245*	*4.300*	*4.367*	*4.447*	*4.708*	*5.071*
1000	*4.115*	*4.141*	*4.173*	*4.213*	*4.262*	*4.321*	*4.391*	*4.615*	*4.911*
1200	*4.078*	*4.099*	*4.124*	*4.156*	*4.196*	*4.243*	*4.298*	*4.469*	*4.678*

TABLE 6b. (continued)

Pbars/T°C	180	200	220	240	260	280	300	350	400
1400	*4.046*	*4.062*	*4.082*	*4.108*	*4.140*	*4.178*	*4.223*	*4.357*	*4.515*
1600	*4.016*	*4.03*	*4.05*	*4.07*	*4.09*	*4.12*	*4.16*	*4.27*	*4.39*
1800	*3.990*	*4.00*	*4.01*	*4.03*	*4.05*	*4.08*	*4.11*	*4.20*	*4.30*
2000	*3.966*	*3.97*	*3.98*	*4.00*	*4.01*	*4.03*	*4.06*	*4.13*	*4.22*
3000	*3.87*	*3.87*	*3.87*	*3.88*	*3.88*	*3.89*	*3.90*	*3.93*	*3.97*
4000	*3.81*	*3.81*	*3.80*	*3.80*	*3.79*	*3.79*	*3.80*	*3.81*	*3.83*
5000	*3.77*	*3.76*	*3.75*	*3.74*	*3.74*	*3.73*	*3.73*	*3.73*	*3.74*
6000	*3.74*	*3.73*	*3.72*	*3.70*	*3.69*	*3.69*	*3.68*	*3.68*	*3.68*
7000	*3.71*	*3.70*	*3.69*	*3.68*	*3.67*	*3.65*	*3.65*	*3.63*	*3.63*
8000	*3.69*	*3.68*	*3.67*	*3.66*	*3.64*	*3.63*	*3.62*	*3.60*	*3.60*
9000	*3.67*	*3.67*	*3.66*	*3.64*	*3.63*	*3.61*	*3.60*	*3.58*	*3.57*
10000	*3.66*	*3.66*	*3.64*	*3.63*	*3.61*	*3.60*	*3.59*	*3.56*	*3.55*
20000	*3.37*	*3.47*	*3.53*	*3.56*	*3.56*	*3.56*	*3.55*	*3.51*	*3.47*
30000					*3.46*	*3.50*	*3.52*	*3.51*	*3.48*

Values calulated by (15).

TABLE 6c. Water Heat Capacity at Constant Pressure, kJ/kg-K

Pbars/T°C	500	600	700	800	900	1000	1200	1500	2000
1	*2.135*	*2.203*	*2.273*	*2.343*	*2.412*	*2.478*	*2.599*	*2.750*	*2.931*
25	*2.228*	*2.259*	*2.310*	*2.370*	*2.431*	*2.493*	*2.608*	*2.755*	*2.934*
50	*2.335*	*2.322*	*2.351*	*2.398*	*2.452*	*2.508*	*2.618*	*2.761*	*2.937*
100	*2.584*	*2.458*	*2.437*	*2.456*	*2.494*	*2.540*	*2.64*	*2.77*	*2.94*
150	*2.891*	*2.610*	*2.529*	*2.518*	*2.538*	*2.573*	*2.66*	*2.78*	*2.95*
200	*3.269*	*2.778*	*2.627*	*2.583*	*2.583*	*2.606*	*2.68*	*2.79*	*2.95*
250	*3.737*	*2.961*	*2.729*	*2.649*	*2.630*	*2.640*	*2.70*	*2.80*	*2.96*
300	*4.312*	*3.160*	*2.836*	*2.716*	*2.677*	*2.674*	*2.72*	*2.81*	*2.96*
350	*5.006*	*3.373*	*2.945*	*2.785*	*2.724*	*2.709*	*2.74*	*2.83*	*2.97*
400	*5.799*	*3.597*	*3.057*	*2.854*	*2.771*	*2.743*	*2.76*	*2.84*	*2.97*
500	*7.239*	*4.062*	*3.283*	*2.992*	*2.866*	*2.812*	*2.80*	*2.86*	*2.98*
600	*7.534*	*4.500*	*3.503*	*3.126*	*2.957*	*2.879*	*2.84*	*2.88*	*2.99*
700	*6.992*	*4.846*	*3.705*	*3.253*	*3.045*	*2.943*	*2.88*	*2.90*	*3.00*
800	*6.383*	*5.058*	*3.880*	*3.369*	*3.126*	*3.004*	*2.91*	*2.92*	*3.01*
900	*5.908*	*5.138*	*4.022*	*3.472*	*3.201*	*3.061*	*2.95*	*2.94*	*3.02*
1000	*5.557*	*5.123*	*4.129*	*3.561*	*3.269*	*3.113*	*2.98*	*2.96*	*3.03*
1200	*5.092*	*4.955*	*4.246*	*3.698*	*3.382*	*3.204*	*3.04*	*3.00*	*3.05*
1400	*4.801*	*4.754*	*4.270*	*3.785*	*3.468*	*3.277*	*3.10*	*3.03*	*3.06*
1600	*4.60*	*4.58*	*4.24*	*3.83*	*3.53*	*3.34*	*3.14*	*3.06*	*3.08*
1800	*4.46*	*4.44*	*4.19*	*3.85*	*3.57*	*3.38*	*3.18*	*3.08*	*3.09*
2000	*4.34*	*4.33*	*4.13*	*3.85*	*3.60*	*3.41*	*3.21*	*3.11*	*3.11*
3000	*4.02*	*4.00*	*3.90*	*3.76*	*3.61*	*3.48*	*3.30*	*3.18*	*3.16*
4000	*3.86*	*3.84*	*3.77*	*3.68*	*3.58*	*3.48*	*3.34*	*3.23*	*3.19*
5000	*3.75*	*3.74*	*3.69*	*3.62*	*3.54*	*3.47*	*3.35*	*3.25*	*3.21*
6000	*3.68*	*3.67*	*3.63*	*3.58*	*3.51*	*3.45*	*3.35*	*3.26*	*3.22*
7000	*3.63*	*3.62*	*3.59*	*3.54*	*3.49*	*3.44*	*3.35*	*3.27*	*3.23*
8000	*3.59*	*3.58*	*3.55*	*3.52*	*3.47*	*3.42*	*3.34*	*3.27*	*3.23*
9000	*3.56*	*3.55*	*3.53*	*3.49*	*3.45*	*3.41*	*3.34*	*3.27*	*3.24*
10000	*3.53*	*3.52*	*3.50*	*3.47*	*3.44*	*3.40*	*3.34*	*3.27*	*3.24*
20000	*3.42*	*3.39*	*3.37*	*3.35*	*3.33*	*3.31*	*3.28*	*3.24*	*3.22*
30000	*3.41*	*3.35*	*3.32*	*3.29*	*3.26*	*3.23*	*3.20*	*3.17*	*3.16*

Values calculated by (15).

TABLE 7. Water Properties at Saturation

T,°C	P,bars	V_{liq}	V_{gas}	H_{liq}	H_{gas}	S_{liq}	S_{gas}
0.01	*0.0061173*	*18.0200*	*3711116.*	*0.00*	*2500.5*	*0.00000*	*9.1541*
10	*0.012281*	*18.0216*	*1915461.*	*41.99*	*2518.9*	*0.15097*	*8.8986*
20	*0.023388*	*18.0488*	*1040928.*	*83.84*	*2537.2*	*0.29621*	*8.6651*
30	*0.042455*	*18.0955*	*592654.*	*125.67*	*2555.3*	*0.43653*	*8.4513*
40	*0.073814*	*18.1581*	*351816.*	*167.50*	*2573.4*	*0.57228*	*8.2550*
50	*0.12344*	*18.2349*	*216859.*	*209.33*	*2591.2*	*0.70374*	*8.0745*
60	*0.19932*	*18.3244*	*138255.*	*251.15*	*2608.8*	*0.83119*	*7.9080*
70	*0.31176*	*18.4260*	*90884.*	*293.01*	*2626.1*	*0.95494*	*7.7540*
80	*0.47373*	*18.5388*	*61413.*	*334.93*	*2643.1*	*1.07530*	*7.6112*
90	*0.70117*	*18.6630*	*42548.*	*376.93*	*2659.6*	*1.19253*	*7.4784*
100	*1.0132*	*18.7981*	*30152.*	*419.06*	*2675.7*	*1.30689*	*7.3545*
120	*1.9848*	*19.1018*	*16074.*	*503.78*	*2706.2*	*1.52776*	*7.1297*
140	*3.6119*	*19.4519*	*9170.0*	*589.24*	*2733.8*	*1.73936*	*6.9302*
160	*6.1766*	*19.8524*	*5532.5*	*675.65*	*2758.0*	*1.94293*	*6.7503*
180	*10.019*	*20.3098*	*3495.6*	*763.25*	*2777.8*	*2.13966*	*6.5853*
200	*15.537*	*20.8339*	*2293.8*	*852.38*	*2792.5*	*2.33076*	*6.4312*
220	*23.178*	*21.4390*	*1552.3*	*943.51*	*2801.3*	*2.51753*	*6.2847*
240	*33.447*	*22.1456*	*1076.3*	*1037.24*	*2803.0*	*2.70135*	*6.1423*
260	*46.895*	*22.9846*	*760.17*	*1134.38*	*2796.2*	*2.88382*	*6.0009*
280	*64.132*	*24.0049*	*543.43*	*1236.08*	*2779.2*	*3.06691*	*5.8565*
300	*85.838*	*25.2889*	*390.35*	*1344.05*	*2748.7*	*3.25336*	*5.7042*
320	*112.79*	*26.9957*	*278.82*	*1461.25*	*2699.7*	*3.44760*	*5.5356*
340	*145.94*	*29.4976*	*194.36*	*1593.8*	*2621.3*	*3.6587*	*5.3345*
360	*186.55*	*34.1151*	*125.43*	*1761.0*	*2482.0*	*3.9153*	*5.0542*
365	*198.09*	*36.2482*	*108.60*	*1816.7*	*2424.6*	*3.9994*	*4.9520*
370	*210.30*	*39.7577*	*89.954*	*1889.7*	*2340.2*	*4.1094*	*4.8098*
373.5	*219.30*	*46.7948*	*69.560*	*1991.6*	*2207.3*	*4.2640*	*4.5977*
373.976	*220.55*	*55.958*		*2086*		*4.409*	

Values calculated by (15).

TABLE 8a. Water Sound Speed, m/sec

Pbars/T°C	0	20	40	60	80	100	120	140	160
1	*1401.0*	*1483.2*	*1528.4*	*1549.5*	*1552.8*	*472.8*	*486.1*	*498.7*	*510.8*
25	*1405.2*	*1487.5*	*1532.9*	*1554.3*	*1558.*	*1547.3*	*1524.3*	*1490.5*	*1447.0*
50	*1409.6*	*1491.9*	*1537.5*	*1559.2*	*1563.3*	*1553.0*	*1530.6*	*1497.4*	*1454.6*
100	*1418.1*	*1500.6*	*1546.6*	*1568.9*	*1573.7*	*1564.3*	*1542.8*	*1510.8*	*1469.4*
150	*1426.5*	*1509.2*	*1555.6*	*1578.5*	*1584.0*	*1575.4*	*1554.8*	*1523.9*	*1483.8*
200	*1434.9*	*1517.6*	*1564.4*	*1587.9*	*1594.0*	*1586.2*	*1566.5*	*1536.6*	*1497.7*
250	*1443.1*	*1526.0*	*1573.1*	*1597.1*	*1603.9*	*1596.8*	*1577.9*	*1549.0*	*1511.3*
300	*1451.3*	*1534.2*	*1581.7*	*1606.2*	*1613.5*	*1607.1*	*1589.1*	*1561.1*	*1524.5*
350	*1459.6*	*1542.4*	*1590.2*	*1615.1*	*1623.1*	*1617.3*	*1600.1*	*1573.0*	*1537.4*
400	*1467.9*	*1550.6*	*1598.6*	*1623.9*	*1632.4*	*1627.3*	*1610.8*	*1584.6*	*1550.0*
500	*1484.6*	*1566.8*	*1615.1*	*1641.2*	*1650.7*	*1646.8*	*1631.7*	*1607.0*	*1574.2*
600	*1501.9*	*1583.0*	*1631.4*	*1658.1*	*1668.5*	*1665.7*	*1651.8*	*1628.6*	*1597.4*
700	*1519.6*	*1599.2*	*1647.5*	*1674.6*	*1685.9*	*1684.0*	*1671.3*	*1649.4*	*1619.7*
800	*1538.1*	*1615.5*	*1663.4*	*1690.9*	*1702.8*	*1701.9*	*1690.2*	*1669.5*	*1641.1*
900	*1557.3*	*1632.0*	*1679.2*	*1706.9*	*1719.4*	*1719.2*	*1708.5*	*1688.9*	*1661.8*
1000	*1577.1*	*1648.6*	*1695.0*	*1722.7*	*1735.6*	*1736.2*	*1726.3*	*1707.7*	*1681.8*
1200	*1619.0*	*1682.6*	*1726.5*	*1753.8*	*1767.3*	*1769.0*	*1760.7*	*1743.8*	*1719.9*
1400	*1663.1*	*1717.3*	*1757.9*	*1784.4*	*1798.1*	*1800.6*	*1793.4*	*1778.0*	*1755.8*
1600	*1708.9*	*1752.7*	*1789.4*	*1814.6*	*1828.1*	*1831.1*	*1824.9*	*1810.7*	*1789.9*

TABLE 8a. (continued)

Pbars/T°C	0	20	40	60	80	100	120	140	160
1800	*1755.5*	*1788.4*	*1821.0*	*1844.4*	*1857.5*	*1860.8*	*1855.2*	*1842.0*	*1822.3*
2000	*1802.0*	*1824.3*	*1852.5*	*1874.0*	*1886.3*	*1889.6*	*1884.5*	*1872.1*	*1853.4*
3000	*2012.*	*1990.*	*2005.*	*2018.*	*2025.*	*2025.*	*2020.*	*2009.*	*1993.*
4000	*2161.*	*2108.*	*2135.*	*2152.*	*2154.*	*2149.*	*2141.*	*2129.*	*2113.*
5000	*2273.*	*2163.*	*2234.*	*2272.*	*2275.*	*2265.*	*2252.*	*2237.*	*2221.*
6000		*2181.*	*2316.*	*2382.*	*2388.*	*2374.*	*2356.*	*2337.*	*2318.*
7000			*2423.*	*2493.*	*2497.*	*2476.*	*2453.*	*2430.*	*2408.*
8000			*2606.*	*2619.*	*2603.*	*2574.*	*2544.*	*2517.*	*2492.*
9000				*2766.*	*2711.*	*2667.*	*2630.*	*2598.*	*2571.*
10000				*2928.*	*2821.*	*2758.*	*2711.*	*2675.*	*2644.*
20000									*3227.*
30000									

Values calculated by (15).

TABLE 8b. Water Sound Speed, m/sec

Pbars/T°C	180	200	220	240	260	280	300	350	400
1	*522.4*	*533.7*	*544.7*	*555.3*	*565.7*	*575.8*	*585.7*	*609.5*	*632.2*
25	*1394.4*	*1333.0*	*1262.4*	*521.7*	*537.6*	*551.9*	*565.1*	*594.8*	*621.3*
50	*1402.9*	*1342.6*	*1273.5*	*1194.6*	*1104.1*	*519.0*	*538.4*	*577.3*	*608.9*
100	*1419.4*	*1361.3*	*1294.9*	*1219.7*	*1134.3*	*1036.1*	*919.7*	*533.2*	*581.0*
150	*1435.4*	*1379.2*	*1315.3*	*1243.3*	*1162.4*	*1070.6*	*964.6*	*464.1*	*547.5*
200	*1450.8*	*1396.4*	*1334.8*	*1265.7*	*1188.6*	*1102.3*	*1004.4*	*662.0*	*505.8*
250	*1465.8*	*1413.0*	*1353.4*	*1287.0*	*1213.3*	*1131.6*	*1040.2*	*744.7*	*448.6*
300	*1480.3*	*1429.1*	*1371.4*	*1307.3*	*1236.6*	*1158.9*	*1073.0*	*808.3*	*419.0*
350	*1494.4*	*1444.6*	*1388.7*	*1326.7*	*1258.8*	*1184.4*	*1103.2*	*861.1*	*536.1*
400	*1508.1*	*1459.7*	*1405.4*	*1345.4*	*1279.8*	*1208.6*	*1131.3*	*906.8*	*627.3*
500	*1534.4*	*1488.5*	*1437.1*	*1380.6*	*1319.2*	*1253.2*	*1182.4*	*983.8*	*756.3*
600	*1559.5*	*1515.8*	*1466.9*	*1413.4*	*1355.6*	*1293.7*	*1228.1*	*1048.0*	*850.7*
700	*1583.5*	*1541.7*	*1495.0*	*1441.1*	*1389.3*	*1331.0*	*1269.6*	*1103.6*	*926.6*
800	*1606.5*	*1566.4*	*1521.7*	*1473.0*	*1420.9*	*1365.6*	*1307.6*	*1152.9*	*990.8*
900	*1628.5*	*1590.0*	*1547.1*	*1500.5*	*1450.6*	*1397.9*	*1342.9*	*1197.4*	*1046.8*
1000	*1649.8*	*1612.7*	*1571.4*	*1526.5*	*1478.7*	*1428.3*	*1375.8*	*1238.0*	*1096.7*
1200	*1690.1*	*1655.5*	*1617.0*	*1575.2*	*1530.8*	*1484.2*	*1435.9*	*1310.2*	*1183.1*
1400	*1727.9*	*1695.4*	*1659.2*	*1619.9*	*1578.3*	*1534.8*	*1489.7*	*1373.4*	*1256.6*
1600	*1763.6*	*1733.*	*1699.*	*1662.*	*1622.*	*1581.*	*1539.*	*1430.*	*1321.*
1800	*1797.4*	*1768.*	*1736.*	*1700.*	*1663.*	*1624.*	*1584.*	*1481.*	*1379.*
2000	*1829.7*	*1802.*	*1771.*	*1737.*	*1701.*	*1664.*	*1626.*	*1528.*	*1431.*
3000	*1973.*	*1949.*	*1923.*	*1894.*	*1864.*	*1832.*	*1800.*	*1718.*	*1638.*
4000	*2094.*	*2072.*	*2048.*	*2022.*	*1995.*	*1967.*	*1938.*	*1865.*	*1793.*
5000	*2201.*	*2180.*	*2157.*	*2132.*	*2106.*	*2080.*	*2053.*	*1985.*	*1918.*
6000	*2298.*	*2276.*	*2253.*	*2229.*	*2204.*	*2179.*	*2153.*	*2087.*	*2023.*
7000	*2386.*	*2364.*	*2341.*	*2316.*	*2292.*	*2267.*	*2241.*	*2178.*	*2116.*
8000	*2468.*	*2445.*	*2420.*	*2396.*	*2371.*	*2346.*	*2321.*	*2259.*	*2198.*
9000	*2545.*	*2520.*	*2495.*	*2470.*	*2445.*	*2420.*	*2395.*	*2333.*	*2273.*
10000	*2616.*	*2590.*	*2564.*	*2538.*	*2513.*	*2488.*	*2462.*	*2401.*	*2342.*
20000	*3177.*	*3135.*	*3099.*	*3065.*	*3034.*	*3004.*	*2976.*	*2910.*	*2850.*
30000					*3423.*	*3389.*	*3357.*	*3285.*	*3221.*

Values calculated by (15).

TABLE 8c. Water Sound Speed, m/sec

Pbars/T°C	500	600	700	800	900	1000	1200	1500	2000
1	674.6	713.9	750.7	785.3	818.3	849.8	909.3	991.7	1115.9
25	668.3	710.2	748.6	784.3	817.9	850.0	910.1	993.1	1117.7
50	661.6	706.4	746.5	783.3	817.7	850.3	911.1	994.6	1119.5
100	647.7	698.9	742.6	781.7	817.6	851.2	913.	998.	1123.
150	633.3	691.7	739.1	780.4	817.8	852.5	916.	1001.	1127.
200	618.9	684.8	736.0	779.5	818.3	853.9	918.	1005.	1131.
250	604.5	678.4	733.2	778.8	819.0	855.5	921.	1008.	1135.
300	590.9	672.7	730.8	778.4	819.9	857.2	924.	1012.	1139.
350	579.0	667.8	729.0	778.3	820.9	859.0	927.	1015.	1143.
400	570.4	664.1	727.7	778.5	822.1	861.0	930.	1019.	1146.
500	572.2	661.2	727.3	780.1	825.2	865.2	935.	1026.	1154.
600	608.0	666.1	730.3	783.6	829.4	870.1	941.	1033.	1162.
700	667.0	680.2	737.5	789.3	834.9	875.8	948.	1039.	1169.
800	732.6	702.9	748.9	797.4	841.8	882.4	954.	1047.	1176.
900	796.3	732.6	764.2	807.9	850.4	890.0	961.	1054.	1184.
1000	855.6	767.3	783.1	820.8	860.5	898.8	969.	1061.	1191.
1200	960.2	843.8	829.0	852.3	885.1	919.4	986.	1076.	1205.
1400	1049.1	921.2	882.1	890.0	914.4	943.8	1005.	1092.	1220.
1600	1126.	995.	938.	932.	947.	971.	1026.	1109.	1235.
1800	1194.	1062.	995.	976.	982.	1001.	1049.	1127.	1250.
2000	1255.	1125.	1050.	1021.	1019.	1032.	1073.	1146.	1265.
3000	1491.	1373.	1288.	1234.	1205.	1194.	1202.	1247.	1344.
4000	1660.	1552.	1469.	1409.	1370.	1346.	1331.	1352.	1426.
5000	1795.	1692.	1611.	1551.	1508.	1478.	1449.	1452.	1507.
6000	1906.	1808.	1729.	1669.	1624.	1591.	1554.	1544.	1584.
7000	2002.	1906.	1829.	1769.	1723.	1689.	1648.	1629.	1657.
8000	2087.	1993.	1916.	1856.	1809.	1774.	1730.	1706.	1725.
9000	2163.	2070.	1994.	1933.	1886.	1850.	1804.	1776.	1788.
10000	2233.	2140.	2064.	2003.	1955.	1918.	1870.	1839.	1847.
20000	2740.	2643.	2560.	2490.	2430.	2381.	2310.	2254.	2242.
30000	3107.	3006.	2916.	2836.	2765.	2704.	2605.	2511.	2459.

Values calculated by (15).

TABLE 9a. Water Dielectric Constant

Pbars/T°C	0	25	50	75	100	125	150	175
1	87.90	78.38	69.88	62.28	55.51	1.01	1.00	1.00
10	87.94	78.41	69.91	62.32	55.55	49.50	44.08	39.20
50	88.10	78.56	70.05	62.46	55.69	49.65	44.24	39.36
100	88.29	78.85	70.27	62.60	55.78	49.71	44.31	39.47
200	88.75	79.24	70.63	62.94	56.11	50.06	44.67	39.85
300	89.20	79.62	70.98	63.28	56.44	50.39	45.01	40.21
400	89.64	79.99	71.32	63.60	56.76	50.71	45.33	40.55
500	90.07	80.36	71.65	63.92	57.07	51.02	45.65	40.88
600	90.48	80.72	71.98	64.23	57.38	51.32	45.96	41.19
700	90.88	81.07	72.30	64.53	57.67	51.61	46.25	41.50
800	91.27	81.41	72.61	64.83	57.96	51.90	46.54	41.79
900	91.65	81.74	72.92	65.12	58.24	52.18	46.82	42.08
1000	92.02	82.07	73.22	65.41	58.52	52.45	47.10	42.36
1200	92.73	82.70	73.81	65.96	59.06	52.98	47.62	42.89
1400	93.39	83.30	74.37	66.49	59.57	53.49	48.13	43.40
1600	94.01	83.88	74.91	67.01	60.07	53.97	48.61	43.88

TABLE 9a. (continued)

Pbars/T°C	0	25	50	75	100	125	150	175
1800	*94.59*	*84.43*	*75.43*	*67.50*	*60.55*	*54.44*	*49.07*	*44.34*
2000	*95.14*	*84.96*	*75.93*	*67.98*	*61.01*	*54.89*	*49.52*	*44.79*
2500	*96.37*	*86.19*	*77.11*	*69.11*	*62.10*	*55.95*	*50.56*	*45.82*
3000	*97.44*	*87.30*	*78.19*	*70.16*	*63.11*	*56.94*	*51.53*	*46.78*
3500	*98.40*	*88.31*	*79.18*	*71.13*	*64.05*	*57.86*	*52.42*	*47.66*
4000	*99.25*	*89.26*	*80.11*	*72.03*	*64.93*	*58.71*	*53.26*	*48.48*
4500	*100.04*	*90.14*	*80.98*	*72.87*	*65.76*	*59.52*	*54.05*	*49.26*
5000	*100.77*	*90.99*	*81.79*	*73.66*	*66.53*	*60.28*	*54.80*	*49.98*
6000		*92.60*	*83.30*	*75.11*	*67.96*	*61.68*	*56.17*	*51.33*
7000			*84.69*	*76.41*	*69.24*	*62.95*	*57.42*	*52.55*
8000			*85.95*	*77.58*	*70.40*	*64.10*	*58.55*	*53.66*
9000				*78.65*	*71.45*	*65.16*	*59.60*	*54.69*
10000				*79.62*	*72.41*	*66.13*	*60.57*	*55.64*

Values calculated by (15) and (2).

TABLE 9b. Water Dielectric Constant

Pbars/T°C	200	225	250	275	300	325	350	375
1	*1.00*	*1.00*	*1.00*	*1.00*	*1.00*	*1.00*	*1.00*	*1.00*
10	*1.04*	*1.03*	*1.03*	*1.03*	*1.03*	*1.02*	*1.02*	*1.02*
50	*34.93*	*30.86*	*27.05*	*1.19*	*1.16*	*1.14*	*1.13*	*1.12*
100	*35.11*	*31.12*	*27.42*	*23.90*	*20.40*	*1.28*	*1.23*	*1.20*
200	*35.51*	*31.57*	*27.94*	*24.54*	*21.25*	*17.91*	*14.09*	*2.00*
300	*35.90*	*31.99*	*28.42*	*25.10*	*21.95*	*18.86*	*15.69*	*12.03*
400	*36.26*	*32.39*	*28.86*	*25.60*	*22.55*	*19.63*	*16.75*	*13.78*
500	*36.61*	*32.76*	*29.27*	*26.07*	*23.09*	*20.27*	*17.57*	*14.90*
600	*36.94*	*33.12*	*29.66*	*26.49*	*23.57*	*20.84*	*18.25*	*15.75*
700	*37.26*	*33.46*	*30.02*	*26.89*	*24.02*	*21.35*	*18.84*	*16.46*
800	*37.57*	*33.78*	*30.37*	*27.27*	*24.43*	*21.81*	*19.37*	*17.07*
900	*37.86*	*34.09*	*30.70*	*27.62*	*24.82*	*22.23*	*19.84*	*17.61*
1000	*38.15*	*34.39*	*31.01*	*27.96*	*25.18*	*22.63*	*20.28*	*18.10*
1200	*38.70*	*34.96*	*31.61*	*28.58*	*25.85*	*23.35*	*21.06*	*18.94*
1400	*39.21*	*35.49*	*32.16*	*29.16*	*26.45*	*23.99*	*21.74*	*19.68*
1600	*39.70*	*35.99*	*32.67*	*29.69*	*27.01*	*24.57*	*22.36*	*20.33*
1800	*40.17*	*36.46*	*33.16*	*30.19*	*27.53*	*25.11*	*22.92*	*20.92*
2000	*40.61*	*36.91*	*33.61*	*30.66*	*28.01*	*25.61*	*23.44*	*21.45*
2500	*41.65*	*37.95*	*34.67*	*31.73*	*29.10*	*26.73*	*24.58*	*22.63*
3000	*42.59*	*38.90*	*35.62*	*32.69*	*30.07*	*27.71*	*25.57*	*23.63*
3500	*43.47*	*39.76*	*36.48*	*33.55*	*30.93*	*28.58*	*26.45*	*24.51*
4000	*44.28*	*40.57*	*37.28*	*34.35*	*31.72*	*29.37*	*27.23*	*25.30*
4500	*45.04*	*41.32*	*38.02*	*35.08*	*32.45*	*30.09*	*27.95*	*26.01*
5000	*45.75*	*42.02*	*38.71*	*35.76*	*33.13*	*30.76*	*28.61*	*26.67*
6000	*47.07*	*43.31*	*39.98*	*37.01*	*34.36*	*31.96*	*29.80*	*27.83*
7000	*48.26*	*44.47*	*41.12*	*38.13*	*35.45*	*33.03*	*30.84*	*28.85*
8000	*49.35*	*45.54*	*42.16*	*39.14*	*36.43*	*33.99*	*31.78*	*29.75*
9000	*50.36*	*46.52*	*43.11*	*40.07*	*37.33*	*34.86*	*32.62*	*30.56*
10000	*51.29*	*47.43*	*43.99*	*40.92*	*38.16*	*35.66*	*33.39*	*31.30*

Values calculated by (15) and (2).

TABLE 9c. Water Dielectric Constant

Pbars/T°C	400	450	500	600	700	800	900	1000
1	*1.00*	*1.00*	*1.00*	*1.00*	*1.00*	*1.00*	*1.00*	*1.00*
10	*1.02*	*1.02*	*1.01*	*1.01*	*1.01*	*1.01*	*1.01*	*1.01*
50	*1.11*	*1.09*	*1.08*	*1.06*	*1.05*	*1.04*	*1.03*	*1.03*
100	*1.17*	*1.14*	*1.11*	*1.08*	*1.10*	*1.08*	*1.07*	*1.06*
200	*1.64*	*1.42*	*1.32*	*1.22*	*1.23*	*1.18*	*1.15*	*1.13*
300	*5.95*	*2.07*	*1.68*	*1.41*	*1.38*	*1.29*	*1.24*	*1.20*
400	*10.47*	*3.85*	*2.34*	*1.69*	*1.56*	*1.43*	*1.34*	*1.28*
500	*12.18*	*6.58*	*3.44*	*2.07*	*1.78*	*1.57*	*1.45*	*1.36*
600	*13.31*	*8.54*	*4.89*	*2.57*	*2.04*	*1.74*	*1.57*	*1.46*
700	*14.18*	*9.89*	*6.31*	*3.17*	*2.32*	*1.92*	*1.70*	*1.56*
800	*14.90*	*10.90*	*7.50*	*3.83*	*2.64*	*2.12*	*1.84*	*1.66*
900	*15.52*	*11.72*	*8.48*	*4.52*				
1000	*16.06*	*12.40*	*9.29*	*5.21*	*3.34*	*2.56*	*2.15*	*1.89*
1200	*17.00*	*13.53*	*10.60*	*6.46*				
1400	*17.79*	*14.44*	*11.63*	*7.53*				
1500					*5.09*	*3.76*	*3.00*	*2.53*
1600	*18.47*	*15.21*	*12.48*	*8.42*				
1800	*19.09*	*15.88*	*13.20*	*9.19*				
2000	*19.65*	*16.48*	*13.83*	*9.85*	*6.57*	*4.89*	*3.85*	*3.18*
2500	*20.85*	*17.74*	*15.14*	*11.18*	*7.75*	*5.89*	*4.65*	*3.81*
3000	*21.87*	*18.78*	*16.19*	*12.20*	*8.73*	*6.75*	*5.37*	*4.41*
3500	*22.75*	*19.67*	*17.07*	*13.03*	*9.55*	*7.49*	*6.02*	*4.96*
4000	*23.54*	*20.44*	*17.83*	*13.71*	*10.27*	*8.15*	*6.60*	*5.47*
4500	*24.24*	*21.13*	*18.49*	*14.29*	*10.90*	*8.73*	*7.13*	*5.94*
5000	*24.89*	*21.75*	*19.08*	*14.79*	*11.48*	*9.26*	*7.61*	*6.37*
6000	*26.03*	*22.84*	*20.09*	*15.59*				
7000	*27.02*	*23.76*	*20.93*	*16.21*				
8000	*27.89*	*24.56*	*21.64*	*16.69*				
9000	*28.66*	*25.26*	*22.25*	*17.05*				
10000	*29.36*	*25.87*	*22.77*	*17.32*				

Values calculated by (15) and (2).

3. CARBON DIOXIDE

3.1 Volume

Volumes of carbon dioxide are compiled from 0° to 1000°C and 25 bars to 40 Kbar. Values given in Table 10a-b to a maximum pressure of 10 Kbar are taken from experimental studies by (21), (20), (39) and (35). Values from 20 to 40 Kbar are derived from the EOS given by (29). Table 11 gives shock-compressed data at higher pressures and temperatures, calculated by (31). Additional shock experiment data can be found in (32).

3.2 Dielectric Constant

Dielectric constants of carbon dioxide have not been measured. They are of interest because they must be known in order to predict the effect that adding carbon dioxide to water will have on the dielectric constant of the fluid. Therefore, dielectric constants of carbon dioxide are presented here, where they are calculated after the method given in (40) by:

$$\frac{(2\epsilon+1)(\epsilon-1)}{9\epsilon} = \frac{4\pi N^{\circ}\rho\alpha}{3M}$$

where ϵ is the dielectric constant, N° is Avogadro's number, ρ is the density, M is the molecular weight, and α is the molecular polarizability of carbon dioxide. A value of 2.63×10^{-24} cm^3 is used for the molecular polarizability. Dielectric constants are calculated from 0° to 1000°C and 50 bars to 10 Kbars, at the same pressure-temperature points for which volume or density information for carbon dioxide is available. These calculated values are given in Table 12a-b.

TABLE 10a. Carbon Dioxide Volume, cm^3/mole

Pbars/T°C	0	20	40	60	80	100	150	200	250	300
25	732.3	835.1	924.6	1007.	1084.	1164.	1354.	1528.	1712.	1889.
50	46.5	309.3	387.8	447.3	498.4	543.3	653.0	751.0	849.6	940.4
75	46.1	54.3	190.9	255.0	299.6	337.2	417.6	490.1	558.5	622.5
100	45.4	51.5	69.0	153.5	198.7	234.5	301.2	360.7	413.2	462.8
150	44.1	48.8	56.1	72.9	102.4	132.2	188.3	231.6	270.2	306.9
200	43.28	47.15	52.30	60.79	74.16	91.40	134.7	169.9	200.8	228.9
250	42.52	45.84	50.18	55.79	64.04	74.85	106.0	134.5	160.4	184.3
300	41.80	44.76	48.49	53.08	58.95	66.38	89.36	112.6	134.4	154.4
350	41.25	43.88	47.13	50.97	55.72	61.47	79.31	98.00	116.6	134.2
400	40.78	43.15	46.04	49.42	53.39	58.13	72.40	87.92	103.9	119.2
450	40.38	42.52	45.12	48.16	51.68	55.63	67.70	80.86	94.20	108.1
500	39.92	41.99	44.38	47.12	50.22	53.70	63.89	75.45	86.91	99.03
600	39.20	41.06	43.13	45.44	48.01	50.85	58.92	67.87	77.09	86.50
700	38.59	40.27	42.12	44.13	46.34	48.70	55.51	62.89	70.49	78.23
800	38.04	39.61	41.29	43.11	45.05	47.14	52.97	59.29	65.82	72.43
900	37.62	39.04	40.57	42.21	43.97	45.84	51.01	56.50	62.29	68.16
1000	37.17	38.50	39.93	41.45	43.07	44.77	49.38	54.26	59.39	64.67
1200	36.37	37.56	38.83	40.16	41.56	43.02	46.89	50.97	55.21	59.55
1400	35.77	36.83	37.96	39.14	40.38	41.66	45.00	48.51	52.14	55.78
1500						41.08	44.14	47.37	50.72	54.16
2000						38.70	41.18	43.73	46.33	48.93
2500						37.16	39.07	41.24	43.42	45.56
3000						35.92		39.34	41.23	43.11
3500						35.02		38.06	39.48	41.20
4000						34.20		36.90		39.57
5000						33.04		35.11		37.17
6000						31.97		33.64		35.29
7000						31.02		32.38		33.73
8000						*30.21*		*31.48*		*32.74*
9000						*29.57*		*30.62*		*31.67*
10000						*29.01*		*29.87*		*30.72*
20000						*25.84*		*26.72*		*27.51*
30000						*24.70*		*25.35*		*25.95*
40000						*24.07*		*24.60*		*25.08*

Values from (21), (20), (39), (35) and (29).

TABLE 10b. Carbon Dioxide Volume, cm^3/mole

Pbars/T°C	350	400	450	500	600	700	800	900	1000
25	2066.	2234.	2405.	2574.	2915.	3260.	3607.	3930.	4273.
50	1031.	1120.	1206.	1294.	1462.	1636.	1804.	1974.	2147.
75	684.5	744.7	804.6	864.7	980.2	1095.	1209.	1322.	1434.
100	513.5	558.5	606.2	650.1	737.2	824.2	909.3	995.7	1081.
150	340.6	373.6	405.3	436.2	496.2	554.3	613.0	669.9	728.7
200	255.1	281.2	305.4	328.7	374.9	420.0	464.3	507.0	552.2
250	205.9	226.6	246.4	265.4	303.5	339.6	375.2	410.2	446.4
300	173.3	190.7	207.9	224.3	255.6	286.2	316.4	346.0	374.9
350	150.3	166.1	181.0	195.3	222.4	249.1	274.6	299.8	326.0
400	134.0	147.7	160.7	173.5	197.6	220.9	243.7	265.6	288.2
450	121.0	133.7	145.8	157.1	179.1	199.6	219.1	239.1	259.3
500	110.9	122.2	132.9	143.5	163.4	181.9	200.3	217.9	235.6
600	96.03	105.5	114.6	123.5	140.2	156.1	171.4	186.1	200.6

TABLE 10b. (continued)

Pbars/T°C	350	400	450	500	600	700	800	900	1000
700	86.01	93.96	101.8	109.5	123.9	137.5	150.9	163.7	175.8
800	79.11	85.79	92.50	99.17	111.9	123.9	135.5	146.8	157.4
900	74.03	79.82	85.51	91.23	102.6	113.5	123.6	133.5	142.9
1000	69.96	75.12	80.21	85.21	95.26	105.0	114.1	123.0	131.5
1200	63.93	68.23	72.37	76.45	84.51	92.27	99.96	107.3	114.3
1400	59.47	63.15	66.77	70.26	77.01	83.64	90.04	96.24	102.2
1500	57.60								
2000	51.47	53.90	56.14	*59.19*	*64.26*	*69.33*	*74.41*	*79.48*	*84.55*
2500	47.65	49.60	51.39						
3000	44.97	46.76	48.45	*50.03*	*53.51*	*56.99*	*60.47*	*63.96*	*67.44*
3500	42.86	44.43	45.87						
4000	41.11	42.25		*45.10*	*47.82*	*50.53*	*53.25*	*55.97*	*58.69*
5000		39.24		*41.71*	*43.92*	*46.13*	*48.34*	*50.54*	*52.75*
6000		36.96		*39.13*	*40.95*	*42.78*	*44.61*	*46.43*	*48.26*
7000		35.09		*37.03*	*38.56*	*40.08*	*41.60*	*43.12*	*44.64*
8000		*34.01*		*35.28*	*36.54*	*37.81*	*39.08*	*40.34*	*41.61*
9000		*32.72*		*33.76*	*34.81*	*35.86*	*36.91*	*37.95*	*39.00*
10000		*31.58*		*32.43*	*33.29*	*34.15*	*35.00*	*35.86*	*36.71*
20000		*28.24*		*28.93*	*29.58*	*30.20*	*30.80*	*31.38*	*31.94*
30000		*26.50*		*27.02*	*27.52*	*27.99*	*28.45*	*28.89*	*29.32*
40000		*25.54*		*25.97*	*26.37*	*26.77*	*27.14*	*27.51*	*27.86*

Values from (21), (20), (39), (35) and (29).

TABLE 11. Shock-Compressed Carbon Dioxide Data

Pressure (Kb)	Volume (cm^3/m)	Temperature (K)
275.2 ± 2.4	**17.36 ± 0.18**	*3800*
340.	**17.**	*4500*
421.9 ± 3.2	**15.96 ± 0.16**	*5500*
545.3 ± 5.3	**14.17 ± 0.23**	*6600*
708.2 ± 7.4	**13.16 ± 0.25**	*8100*

Values from (31).

TABLE 12a. Carbon Dioxide Dielectric Constant

Pbars/T°C	0	20	40	60	80	100	150	200	250	300
50	*1.480*	*1.066*	*1.052*	*1.045*	*1.041*	*1.037*	*1.031*	*1.027*	*1.024*	*1.021*
100	*1.492*	*1.430*	*1.314*	*1.135*	*1.103*	*1.087*	*1.067*	*1.056*	*1.049*	*1.044*
150	*1.508*	*1.455*	*1.392*	*1.296*	*1.206*	*1.158*	*1.109*	*1.088*	*1.076*	*1.066*
200	*1.519*	*1.473*	*1.422*	*1.359*	*1.291*	*1.233*	*1.155*	*1.122*	*1.102*	*1.089*
300	*1.539*	*1.500*	*1.459*	*1.416*	*1.371*	*1.327*	*1.238*	*1.187*	*1.155*	*1.134*
400	*1.554*	*1.521*	*1.485*	*1.449*	*1.413*	*1.377*	*1.298*	*1.242*	*1.203*	*1.176*
500	*1.567*	*1.537*	*1.505*	*1.473*	*1.442*	*1.411*	*1.340*	*1.285*	*1.245*	*1.213*
600	*1.578*	*1.550*	*1.521*	*1.492*	*1.464*	*1.435*	*1.371*	*1.319*	*1.279*	*1.247*
700	*1.589*	*1.562*	*1.535*	*1.508*	*1.482*	*1.457*	*1.396*	*1.346*	*1.307*	*1.274*
800	*1.598*	*1.572*	*1.547*	*1.521*	*1.497*	*1.473*	*1.417*	*1.369*	*1.330*	*1.297*
900	*1.605*	*1.581*	*1.557*	*1.533*	*1.510*	*1.488*	*1.434*	*1.389*	*1.349*	*1.317*
1000	*1.613*	*1.590*	*1.567*	*1.544*	*1.522*	*1.500*	*1.449*	*1.406*	*1.368*	*1.336*

TABLE 12a. (continued)

Pbars/T°C	0	20	40	60	80	100	150	200	250	300
1200	*1.628*	*1.606*	*1.584*	*1.563*	*1.542*	*1.523*	*1.475*	*1.434*	*1.398*	*1.367*
1400	*1.640*	*1.620*	*1.599*	*1.579*	*1.560*	*1.541*	*1.497*	*1.458*	*1.423*	*1.394*
1500						*1.549*	*1.508*	*1.471*	*1.436*	*1.407*
2000						*1.583*	*1.548*	*1.510*	*1.482*	*1.453*
3000						*1.633*		*1.573*	*1.547*	*1.522*
4000						*1.672*		*1.618*		*1.571*
5000						*1.702*		*1.653*		*1.611*
6000						*1.728*		*1.684*		*1.645*
7000						*1.751*		*1.711*		*1.677*
8000						*1.771*		*1.737*		*1.705*
9000						*1.789*		*1.759*		*1.732*
10000						*1.806*		*1.781*		*1.757*

Values calculated after method of (40).

TABLE 12b. Carbon Dioxide Dielectric Constant

Pbars/T°C	350	400	450	500	600	700	800	900	1000
50	*1.019*	*1.018*	*1.017*	*1.015*	*1.014*	*1.012*	*1.011*	*1.010*	*1.010*
100	*1.039*	*1.036*	*1.033*	*1.031*	*1.027*	*1.025*	*1.022*	*1.020*	*1.019*
150	*1.059*	*1.054*	*1.050*	*1.046*	*1.041*	*1.036*	*1.033*	*1.030*	*1.028*
200	*1.080*	*1.072*	*1.066*	*1.062*	*1.054*	*1.048*	*1.043*	*1.040*	*1.036*
300	*1.119*	*1.108*	*1.099*	*1.091*	*1.080*	*1.071*	*1.064*	*1.059*	*1.054*
400	*1.155*	*1.140*	*1.129*	*1.119*	*1.104*	*1.093*	*1.084*	*1.077*	*1.071*
500	*1.190*	*1.171*	*1.157*	*1.145*	*1.126*	*1.114*	*1.103*	*1.094*	*1.087*
600	*1.221*	*1.200*	*1.183*	*1.169*	*1.148*	*1.133*	*1.121*	*1.110*	*1.102*
700	*1.248*	*1.226*	*1.207*	*1.192*	*1.169*	*1.151*	*1.137*	*1.126*	*1.117*
800	*1.271*	*1.249*	*1.229*	*1.213*	*1.188*	*1.169*	*1.154*	*1.141*	*1.132*
900	*1.291*	*1.268*	*1.249*	*1.233*	*1.206*	*1.185*	*1.169*	*1.156*	*1.145*
1000	*1.309*	*1.286*	*1.267*	*1.250*	*1.222*	*1.201*	*1.184*	*1.170*	*1.159*
1200	*1.340*	*1.317*	*1.298*	*1.281*	*1.252*	*1.230*	*1.211*	*1.196*	*1.184*
1400	*1.368*	*1.345*	*1.325*	*1.308*	*1.279*	*1.255*	*1.236*	*1.220*	*1.206*
1500	*1.381*								
2000	*1.430*	*1.407*	*1.391*	*1.370*	*1.338*	*1.312*	*1.289*	*1.270*	*1.252*
3000	*1.498*	*1.479*	*1.459*	*1.443*	*1.412*	*1.385*	*1.361*	*1.340*	*1.321*
4000	*1.549*	*1.531*		*1.496*	*1.465*	*1.438*	*1.414*	*1.392*	*1.373*
5000		*1.574*		*1.540*	*1.511*	*1.484*	*1.460*	*1.438*	*1.419*
6000		*1.611*		*1.580*	*1.552*	*1.526*	*1.502*	*1.481*	*1.461*
7000		*1.644*		*1.616*	*1.589*	*1.564*	*1.542*	*1.521*	*1.502*
8000		*1.677*		*1.649*	*1.625*	*1.601*	*1.580*	*1.561*	*1.542*
9000		*1.705*		*1.682*	*1.659*	*1.638*	*1.618*	*1.599*	*1.581*
10000		*1.734*		*1.712*	*1.693*	*1.673*	*1.655*	*1.638*	*1.622*

Values calculated after method of (40).

4. WATER - CARBON DIOXIDE MIXTURES

4.1 Volume

Volumes of mixtures of water and carbon dioxide are presented in Table 13a-d from 300° to 800°C and 50 bars to 6 Kbars, for mole fractions of carbon dioxide of 0.2, 0.4, 0.6 and 0.8. Data are taken from (36), (13), (14), (12) and (41).

4.2 Solvus

The solvus in the water-carbon dioxide system has been determined by (37), (38) and (36). The more recent work of (36) most closely matches that of (38), although some departures are noted. Although (36) does not include tab-

TABLE 13a. Volume of Water-Carbon Dioxide Mixtures, cm^3/mole, X_{CO2}= 0.2

Pbars/T°C	400	450	500	550	600	650	700	750	800
50			1254.	1342.	1417.	1506.	1600.	1674.	1730.
100		562.0	611.5	657.0	700.7	745.2	792.2	834.5	868.2
150	316.0	358.5	396.4	428.8	461.2	491.6	523.4	554.5	579.6
200	214.0	252.5	289.0	314.9	341.0	365.1	389.2	414.3	434.6
250	151.0	193.5	227.0	246.7	268.7	289.3	308.9	330.2	347.2
300	115.0	151.0	178.0	201.4	220.6	238.8	255.5	274.1	288.8
350		125.4	149.0	169.1	186.4	202.8	217.5	234.0	247.1
400	75.0	103.0	126.9	145.1	160.9	175.9	189.1	204.1	215.8
450		90.4	108.0	126.5	141.4	155.1	167.2	180.9	191.5
500	57.0	79.0	91.0	111.8	126.1	138.4	149.7	162.5	172.1
600	53.0	60.0	76.0		96.2	107.	118.	127.	
700		53.2	62.2	71.7	82.0	91.8	101.	108.	
800		48.2	56.5	63.5	72.5	80.3	87.7	94.8	
900			52.4	58.1	64.8	71.5	78.4	84.8	
1000				54.3	59.9	65.2	71.2	77.0	
1200					52.8	56.2	61.0	64.7	
1400						50.4	55.1	57.5	
1600							50.4	52.8	
1800									
2000	29.31		33.00		37.37		42.33		
3000	26.46		28.93		31.57		34.34		
4000	24.92		26.81		28.71		30.58		
5000	23.88		25.41		26.88		28.25		
6000	23.08		24.37		25.54		26.59		

Values from (36), (13), (14), (12), (41).

TABLE 13b. Volume of Water-Carbon Dioxide Mixtures, cm^3/mole, X_{CO2}= 0.4

Pbars/T°C	300	400	450	500	550	600	650	700	750	800
50				1256.	1348.	1415.	1510.	1604.	1669.	1728.
100			578.5	621.5	667.6	706.8	751.8	799.4	837.3	874.2
150		336.0	375.0	409.3	441.0	470.0	499.5	531.3	559.8	587.6
200		238.0	271.5	303.0	327.9	351.3	373.7	397.5	420.9	443.3
250		180.0	213.0	243.5	260.3	279.9	298.4	317.4	337.5	356.1
300		148.0	171.0	195.0	215.4	232.4	248.4	264.2	281.9	297.6
350			147.7	167.0	183.5	198.6	212.8	226.3	242.3	255.8
400		107.0	127.0	144.8	159.8	173.5	186.2	198.0	212.6	224.4
450			113.2	127.5	141.5	154.3	165.6	176.1	189.6	200.1
500	56.96	83.0	100.0	112.0	127.0	139.3	149.2	158.7	171.3	180.7
600	50.44	72.0	80.0	93.0		106.	115.	124.	133.	
700	46.17	58.0	67.3	75.5	83.7	91.4	100.	106.	114.	
800	43.44	53.0	61.3	67.8	74.1	81.3	88.6	94.8	101.	
900	41.18	49.4	56.8	62.7	67.8	73.8	80.3	85.5	91.4	
1000	39.74		53.2	58.8	63.3	68.5	74.4	78.7	83.7	
1200				52.9	57.0	61.1	64.6	68.8	72.3	
1400					52.8	55.5	58.7	61.8	65.0	
1600					49.6	51.3	54.2	56.6	59.0	
1800							50.7	53.0	54.8	
2000		36.19		40.27		44.85		49.84	51.0	
3000		31.92		34.68		37.56		40.52		
4000		29.84		31.98		34.11		36.21		
5000		28.45		30.20		31.88		33.48		
6000		27.30		28.76		30.13		31.38		

Values from (36), (13), (14), (12) and (41).

TABLE 13c. Volume of Water-Carbon Dioxide Mixtures, cm^3/mole, X_{CO2}= 0.6

Pbars/T°C	300	400	450	500	550	600	650	700	750	800
50	937.75			1256.	1352.	1420.	1517.	1606.	1671.	1736.
100	463.66		592.5	627.8	675.0	714.5	759.4	805.1	842.5	882.7
150	280.18	352.0	388.0	418.0	449.7	478.6	507.4	538.3	566.0	595.7
200	193.32	257.0	286.0	314.0	337.3	360.4	381.8	405.1	427.5	450.9
250	161.28	201.0	227.0	252.0	270.2	289.4	306.7	325.4	344.3	363.3
300	129.58	173.0	187.0	207.0	225.7	242.2	256.9	272.4	288.9	304.6
350	108.01		162.4	180.0	194.1	208.6	221.5	234.7	249.3	262.6
400	93.81	127.0	142.5	157.7	170.6	183.7	195.1	206.6	219.7	231.3
450	84.36		127.6	141.0	152.6	164.6	174.8	184.8	196.8	207.1
500	76.52	104.0	115.5	127.0	138.3	149.8	158.6	167.4	178.6	188.0
600	66.14	87.0	95.0	107.0		119.	127.	134.	142.	
700	59.58	71.2	79.0	88.2	96.6	105.	111.	117.	122.	
800	54.96	64.5	71.7	78.7	86.4	93.5	98.8	104.	110.	
900	51.33	60.4	66.5	72.1	78.3	84.7	89.5	94.4	99.2	
1000	48.83	57.1	62.5	67.5	72.5	78.4	82.9	87.4	91.9	
1200		52.7	56.6	61.1	64.4	69.0	72.9	76.9	79.4	
1400		48.8	52.4	56.0	59.6	62.7	65.8	68.8	71.7	
1600			48.8	53.0	55.6	58.1	60.9	63.7	65.4	
1800				50.4	52.5	54.4	56.7	59.3	61.0	
2000		42.69		47.12	50.0	51.98	53.7	57.20		
3000		37.01		40.04		43.23		46.56		
4000		34.31		36.67		39.10		41.61		
5000		32.49		34.41		36.38		38.38		
6000		30.90		32.50		34.13		35.78		

Values from (36), (13), (14), (12) and (41).

TABLE 13d. Volume of Water-Carbon Dioxide Mixtures, cm^3/mole, X_{CO2}= 0.8

Pbars/T°C	300	400	450	500	550	600	650	700	750	800
50	943.58			1265.	1361.	1434.	1530.	1606.	1683.	1750.
100	460.58		600.0	635.8	683.2	724.8	768.7	809.4	851.0	891.2
150	305.05	365.0	397.5	425.9	457.6	487.8	515.7	544.3	573.4	602.4
200	224.46	270.0	297.0	323.5	345.2	369.1	389.6	412.1	434.4	456.6
250	178.79	217.0	237.0	259.5	278.0	297.8	314.3	332.9	350.9	368.6
300	147.64	182.0	199.0	216.0	233.6	250.4	264.5	280.2	295.3	309.7
350	127.93		173.6	189.0	202.1	216.7	229.1	242.7	255.6	267.8
400	111.71	140.0	153.0	166.7	178.8	191.7	202.9	214.8	225.8	236.7
450	101.05		137.8	151.0	160.8	172.6	182.6	193.1	202.8	212.9
500	92.22	113.0	125.0	135.0	146.7	157.8	166.5	175.9	184.4	194.5
600	79.72	100.0	107.0	115.0	122.	129.	136.	143.	150.	
700	71.80	84.7	91.9	99.2	107.	114.	121.	126.	131.	
800	65.87	77.0	82.7	90.0	96.7	103.	108.	113.	118.	
900	60.95	70.9	76.8	82.8	88.2	93.6	98.9	103.	108.	
1000	58.08	66.6	71.5	77.1	82.1	87.1	92.1	95.5	99.5	
1200		60.2	64.6	69.1	73.0	76.8	80.6	84.3	87.9	
1400		56.0	59.7	63.4	66.5	69.5	72.9	76.3	79.6	
1600		52.8	56.0	59.5	62.0	64.4	67.2	70.3	72.8	
1800		50.1	53.1	56.1	58.6	60.5	63.1	65.6	68.1	
2000		48.58	49.9	53.33	55.8	58.37	59.5	63.70		
3000		41.73		44.97		48.40		51.99		
4000		38.34		40.86		43.53		46.32		
5000		36.01		38.06		40.24		42.52		
6000		34.02		35.73		37.55		39.46		

Values from (36), (13), (14), (12) and (41).

ulations of the solvus composition, Table 14 reproduces values taken visually from their graphs.

4.3 Dielectric Constant

The addition of CO_2 to H_2O affects the electrostatic properties of the solution and subsequently influences ion association and mineral solubilities. It is useful to know the effect of CO_2 on the dielectric constant of H_2O because this information can be used to estimate how ion association constants change in H_2O-CO_2 mixtures by assuming, as for pure H_2O, that ion association constants do not vary along isopleths of the dielectric constant.

Dielectric constants of water-carbon dioxide mixtures have not been measured, but they can be calculated from the dielectric constants of pure water and carbon dioxide following the approach of (27) as outlined by (40):

$$\epsilon_{mix}=(\epsilon_{CO_2}{}^{1/3}+V_f(\epsilon_{H_2O}{}^{1/3}-\epsilon_{CO_2}{}^{1/3}))^3$$

where V_f is the volume fraction of water in the solution. Calculated dielectric constants for water-carbon dioxide mixtures are presented in Table 15a-d from 400° to 1000°C and 50 bars to 10 Kbars, for mole fractions of carbon dioxide of 0.2, 0.4, 0.6 and 0.8.

5. EQUATIONS OF STATE

5.1 Water

Equations of state for water that are commonly used include those by (16), (10) and (15). The equation by (16) covers a pressure-temperature range to 10 Kbar and from 25° to 900°C. This work is extended by (10) to pressures of 100 Kbar. The EOS proposed by (15) is valid to 2000°C and 30 Kbar. Recently, new EOS for water based on the work of (26) have been proposed by (34), (17) and (19). These EOS give thermodynamic functions for water with smooth transitions between the critical point and far from the critical region. The EOS presented by (17) is tested to 10 Kbar and 1000°C, although the author states that it may be extrapolated to 250 Kbar and 2000°C. The work by (19) concentrates on the critical region, with equations describing fluid properties from 200 to 450 bars and 350° to 475°C. The EOS given by (34) covers the entire fluid region where data exist and can be used to 1000°C and 250 Kbar. This equation fits the high pressure data better than the equations of (15) and (17). EOS for water to higher temperatures and pressures have also been developed from the method of molecular dynamics. (7) presents a molecular dynamics study tested over the pressure-temperature range from 0.5 to 40 Kbars and 25° to 2100°C. Use of this equation by the authors to predict water volumes at 300 Kbars results in predictions which deviate by less than 10% from the volume results of shock-wave experiments. An additional molecular dynamics study by (4) yields an EOS for water from 5 to 1000 Kbar and approximately 500° to 3700°C.

5.2 Carbon Dioxide

Equations of state for carbon dioxide in common use

TABLE 14. The H_2O-CO_2 Solvus, Mole Fraction CO_2

TEMP, °C	500 bars		1000 bars		1500 bars	
	$X(CO_2)$liq	$X(CO_2)$vap	$X(CO_2)$liq	$X(CO_2)$vap	$X(CO_2)$liq	$X(CO_2)$vap
230		.87		.86		.82
240		.84		.80	.08	.77
250		.78		.74	.12	.72
260		.71	.08	.68	.16	.66
270		.65	.12	.62	.23	.56
280		.59	.17	.49	-	-
290		.54	-	-		
300	.08	.47				
310	.18	.34				
TEMP, °C	2000 bars		2500 bars		3000 bars	
	$X(CO_2)$liq	$X(CO_2)$vap	$X(CO_2)$liq	$X(CO_2)$vap	$X(CO_2)$liq	$X(CO_2)$vap
230		.80		.81		.86
240	.07	.76	.13	.77	.13	.80
250	.15	.71	.15	.73	.13	.73
260	.20	.66	.18	.67	.14	.68
270	-	-	.26	.51	.17	.55

Values from (36).

TABLE 15a. Dielectric Constant of Water-Carbon Dioxide Mixtures, X_{CO2}= 0.2

Pbars/T°C	400	500	600	700	800	900	1000
50	*1.090*	*1.066*	*1.050*	*1.042*	*1.034*	*1.026*	*1.026*
100	*1.139*	*1.093*	*1.069*	*1.084*	*1.068*	*1.060*	*1.052*
200	*1.464*	*1.256*	*1.182*	*1.189*	*1.150*	*1.126*	*1.110*
300	*2.948*	*1.508*	*1.327*	*1.306*	*1.238*	*1.199*	*1.168*
400	*4.064*	*1.910*	*1.526*	*1.440*	*1.346*	*1.279*	*1.232*
500	*4.772*	*2.476*	*1.776*	*1.596*	*1.451*	*1.363*	*1.296*
600	*5.377*	*3.119*	*2.083*	*1.772*	*1.574*	*1.454*	*1.373*
700	*5.902*	*3.706*	*2.425*	*1.954*	*1.699*	*1.549*	*1.449*
800	*6.354*	*4.200*	*2.777*	*2.154*	*1.835*	*1.649*	*1.524*
900	*6.744*	*4.624*	*3.129*				
1000	*7.091*	*4.984*	*3.469*	*2.565*	*2.121*	*1.864*	*1.690*
1200	*7.690*	*5.593*	*4.069*				
1400	*8.209*	*6.096*	*4.580*				
2000	*9.390*	*7.226*	*5.683*	*4.252*	*3.446*	*2.898*	*2.516*
3000	*10.757*	*8.502*	*6.873*	*5.351*	*4.429*	*3.742*	*3.233*
4000	*11.739*	*9.397*	*7.659*	*6.137*	*5.155*	*4.399*	*3.820*
5000	*12.539*	*10.101*	*8.255*	*6.776*	*5.744*	*4.945*	*4.319*
6000	*13.222*	*10.694*	*8.726*				
7000	*13.822*	*11.206*	*9.113*				
8000	*14.367*	*11.651*	*9.441*				
9000	*14.855*	*12.062*	*9.710*				
10000	*15.314*	*12.421*	*9.944*				

Values calculated after method of (40).

TABLE 15b. Dielectric Constant of Water-Carbon Dioxide Mixtures, X_{CO2}= 0.4

Pbars/T°C	400	500	600	700	800	900	1000
50	*1.071*	*1.053*	*1.041*	*1.034*	*1.028*	*1.022*	*1.022*
100	*1.110*	*1.076*	*1.058*	*1.069*	*1.056*	*1.049*	*1.043*
200	*1.330*	*1.199*	*1.146*	*1.151*	*1.121*	*1.104*	*1.091*
300	*1.978*	*1.371*	*1.253*	*1.239*	*1.190*	*1.161*	*1.137*
400	*2.409*	*1.615*	*1.391*	*1.335*	*1.270*	*1.222*	*1.188*
500	*2.738*	*1.917*	*1.552*	*1.444*	*1.347*	*1.286*	*1.237*
600	*3.037*	*2.229*	*1.739*	*1.560*	*1.433*	*1.351*	*1.295*
700	*3.306*	*2.505*	*1.936*	*1.677*	*1.519*	*1.420*	*1.351*
800	*3.542*	*2.740*	*2.129*	*1.800*	*1.610*	*1.490*	*1.406*
900	*3.746*	*2.946*	*2.316*				
1000	*3.931*	*3.123*	*2.492*	*2.043*	*1.793*	*1.636*	*1.524*
1200	*4.252*	*3.429*	*2.799*				
1400	*4.536*	*3.688*	*3.059*				
2000	*5.181*	*4.281*	*3.620*	*2.958*	*2.558*	*2.266*	*2.049*
3000	*5.931*	*4.964*	*4.248*	*3.544*	*3.098*	*2.747*	*2.474*
4000	*6.465*	*5.445*	*4.670*	*3.964*	*3.491*	*3.111*	*2.808*
5000	*6.902*	*5.831*	*5.000*	*4.312*	*3.815*	*3.417*	*3.094*
6000	*7.278*	*6.164*	*5.272*				
7000	*7.611*	*6.456*	*5.503*				
8000	*7.920*	*6.715*	*5.708*				
9000	*8.197*	*6.961*	*5.883*				
10000	*8.464*	*7.181*	*6.046*				

Values calculated after method of (40).

TABLE 15c. Dielectric Constant of Water-Carbon Dioxide Mixtures, X_{CO2}= 0.6

Pbars/T°C	400	500	600	700	800	900	1000
50	*1.053*	*1.040*	*1.032*	*1.027*	*1.022*	*1.018*	*1.018*
100	*1.083*	*1.060*	*1.047*	*1.054*	*1.044*	*1.039*	*1.035*
200	*1.225*	*1.148*	*1.113*	*1.114*	*1.094*	*1.082*	*1.072*
300	*1.525*	*1.260*	*1.189*	*1.178*	*1.145*	*1.125*	*1.108*
400	*1.720*	*1.402*	*1.279*	*1.244*	*1.202*	*1.170*	*1.146*
500	*1.885*	*1.561*	*1.378*	*1.316*	*1.255*	*1.215*	*1.183*
600	*2.037*	*1.716*	*1.487*	*1.389*	*1.313*	*1.261*	*1.224*
700	*2.175*	*1.851*	*1.597*	*1.461*	*1.369*	*1.308*	*1.264*
800	*2.296*	*1.968*	*1.701*	*1.534*	*1.427*	*1.355*	*1.303*
900	*2.401*	*2.072*	*1.800*				
1000	*2.497*	*2.162*	*1.891*	*1.674*	*1.541*	*1.450*	*1.383*
1200	*2.664*	*2.320*	*2.050*				
1400	*2.812*	*2.454*	*2.185*				
2000	*3.149*	*2.764*	*2.474*	*2.171*	*1.976*	*1.826*	*1.707*
3000	*3.539*	*3.124*	*2.808*	*2.487*	*2.273*	*2.099*	*1.957*
4000	*3.816*	*3.377*	*3.034*	*2.712*	*2.488*	*2.301*	*2.148*
5000	*4.044*	*3.583*	*3.216*	*2.902*	*2.668*	*2.474*	*2.312*
6000	*4.240*	*3.763*	*3.370*				
7000	*4.414*	*3.923*	*3.503*				
8000	*4.579*	*4.065*	*3.625*				
9000	*4.726*	*4.204*	*3.733*				
10000	*4.869*	*4.329*	*3.837*				

Values calculated after method of (40).

TABLE 15d. Dielectric Constant of Water-Carbon Dioxide Mixtures, X_{CO2}= 0.8

Pbars/T°C	400	500	600	700	800	900	1000
50	*1.035*	*1.027*	*1.023*	*1.019*	*1.017*	*1.014*	*1.014*
100	*1.059*	*1.045*	*1.037*	*1.039*	*1.033*	*1.030*	*1.027*
200	*1.141*	*1.103*	*1.083*	*1.080*	*1.068*	*1.060*	*1.054*
300	*1.270*	*1.168*	*1.131*	*1.122*	*1.103*	*1.091*	*1.081*
400	*1.359*	*1.242*	*1.184*	*1.164*	*1.140*	*1.122*	*1.108*
500	*1.438*	*1.319*	*1.239*	*1.207*	*1.175*	*1.152*	*1.133*
600	*1.512*	*1.390*	*1.296*	*1.249*	*1.210*	*1.181*	*1.160*
700	*1.580*	*1.454*	*1.352*	*1.289*	*1.243*	*1.211*	*1.187*
800	*1.639*	*1.509*	*1.404*	*1.330*	*1.278*	*1.240*	*1.212*
900	*1.689*	*1.560*	*1.452*				
1000	*1.736*	*1.603*	*1.496*	*1.405*	*1.342*	*1.297*	*1.262*
1200	*1.817*	*1.681*	*1.573*				
1400	*1.889*	*1.747*	*1.640*				
2000	*2.051*	*1.900*	*1.783*	*1.661*	*1.576*	*1.507*	*1.450*
3000	*2.238*	*2.078*	*1.952*	*1.824*	*1.733*	*1.655*	*1.590*
4000	*2.371*	*2.204*	*2.069*	*1.940*	*1.846*	*1.764*	*1.695*
5000	*2.480*	*2.307*	*2.165*	*2.040*	*1.942*	*1.858*	*1.787*
6000	*2.574*	*2.398*	*2.248*				
7000	*2.658*	*2.480*	*2.322*				
8000	*2.738*	*2.554*	*2.391*				
9000	*2.809*	*2.626*	*2.454*				
10000	*2.880*	*2.692*	*2.516*				

Values calculated after method of (40).

include those by (6) and (35). (6) gives an equation for the thermodynamic properties of carbon dioxide from -50° to 1000°C and from 1 bar to 10 Kbars. Their equation is a version of the Redlich Kwong EOS for CO_2 (9), which was fit by (9) to experimental density data for carbon dioxide from 0° to 800°C and pressures up to 1400 bars. Several other modified Redlich Kwong EOS exist for CO_2. (35) presents an equation for carbon dioxide volumes from 2 to 10 Kbars and 100° to 1000°C. More recently, (29) have presented an EOS for carbon dioxide obtained by fitting parameters not only to PVT data, but also to phase equilibrium data. They report that this equation is reliable in the range of 1 bar to 42 Kbars, and approximately 200° to 1500°C. Molecular dynamic studies yield an EOS by (5) over a pressure-temperature range from 5 to 1000 Kbar and approximately 200° to 3700°C.

5.3 Water - Carbon Dioxide Mixtures

A recent summary of EOS for H_2O-CO_2 mixtures (30) provides information for a large number of EOS, however the EOS currently in most common use for H_2O-CO_2 mixtures include that by (18) as modified by (11), and that by (22). The former (18, 11) EOS is modified after the work of (9), and can be used to 700°C and several Kbars. (22) apply their EOS from 400° to 800°C and from 500 bars to 30 Kbar.

Acknowledgments: I would like to thank Mike Sterner, Bob Bodnar, and John Tanger for their helpful advice, Kim Reynolds for help with the tables, and John Brodholt for his aid in supplying calculations for some of the shock experiment information. I also thank John Brodholt and Mike Sterner for their constructive reviews of the manuscript.

REFERENCES

1. Ahrens, T. J., and J. D. O'Keefe, Shock vaporization and the accretion of the icy satellites of Jupiter and Saturn, in *Ices in the Solar System,* edited by J. Klinger et al., pp. 631-654, D. Reidel, 1985.
2. Archer, D. G., and P. Wang, The dielectric constant of water and Debye-Huckel limiting law slopes, *J. Phys. Chem. Ref. Data, 19,* 371-411, 1990.
3. Bakanova, A. A., V. N. Zubarev, Yu. N. Sutulov, and R. F. Trunin, Thermodynamic properties of water at high pressures and temperatures, *Sov. Phys. JETP 41,* 544-548, 1976.
4. Belonoshko, A., and S. K. Saxena, A molecular dynamics study of the pressure-volume-temperature properties of super-critical fluids: I. H_2O, *Geochim. Cosmochim. Acta, 55,* 381-387, 1991.
5. Belonoshko, A., and S. K. Saxena, A molecular dynamics study of the pressure-volume-temperature properties of supercritical fluids: II. CO_2, CH_4, CO, O_2, and H_2, *Geochim. Cosmochim. Acta, 55,* 3191-3208, 1991.
6. Bottinga, Y., and P. Richet, High pressure and temperature equation of state and calculation of the thermodynamic properties of gaseous carbon dioxide, *Amer. J. Sci., 281,* 615-660, 1981.
7. Brodholt, J., and B. Wood, Molecular dynamics of water at high temperatures and pressures, *Geochim. Cosmochim. Acta, 54,* 2611-2616, 1990.
8. Burnham, C. W., J. R. Holloway, and N. F. Davis, The specific volume of water in the range 1000 to 8900 bars, 20° to 900°C, *Amer. J. Sci. 256-A,* 70-95, 1969.
9. de Santis, R., G. J. F. Breedveld, and J. M. Prausnitz, Thermodynamic properties of aqueous gas mixtures at advanced pressures, *Ind. Eng. Chem., Process Des. Develop., 13,* 374-377, 1974.
10. Delany, J. M., and H. C. Helgeson, Calculation of the thermodynamic consequences of dehydration in subducting oceanic crust to 100 Kb and > 800°C, *Am. Jour. Sci., 278,* 638-686, 1978.
11. Flowers, G. C., Correction of Holloway's (1977) adaptation of the modified Redlich-Kwong equation of state for calculation of the fugacities of molecular species in supercritical fluids of geologic interest, *Contrib. Mineral. Petrol., 69,* 315-318, 1979.
12. Franck, E. U., and K. Tödheide, ThermischeEigenschaftenüberkritische Mischungen von Kohlendioxyd und Wasser bis zu 750°C und 2000 Atm, *Z. Phys. Chem. N. F., 22,* 232-245, 1959.
13. Gehrig, M., Phasengleichgewichte und pVT-Daten ternarer Mischungen aus Wasser, Kohlendioxid und Natriumchlorid bis 3 kbar und 550°C, Ph.D. thesis, 109 pp., Universität Karlsruhe, 1980.
14. Greenwood, H. J., The compressibility of gaseous mixtures of carbon dioxide and water between 0 and 500 bars pressure and 450° and 800° centigrade, *Am. Jour. Sci., 267-A,* 191-208, 1969.
15. Haar, L., J. S. Gallagher, and G. S. Kell, *NBS/NRC Steam Tables. Thermodynamic and transport properties and computer programs for vapor and liquid states of water in SI units,* Hemisphere Pub. Co., Washington, 1984.
16. Helgeson, H. C., and D. H. Kirkham, Theoretical prediction of the thermodynamic behavior of aqueous electrolytes at high pressures and temperatures: I. Summary of the thermodynamic/electrostatic properties of the solvent, *Am. Jour. Sci., 274,* 1089-1198, 1974.
17. Hill, P. G., Unified fundamental equation for the thermodynamic properties of H_2O, *J. Phys. Chem. Ref. Data, 19,* 1233-1273, 1990.
18. Holloway, J. R., Fugacity and activity of molecular species in supercritical fluids, in *Thermodynamics in Geology,* edited by D. G. Fraser, pp. 161-181, D. Reidel, Dordrecht, Holland, 1977.
19. Johnson, J. W., and D. Norton, Critical phenomena in hydrothermal systems: state, thermodynamic, electro-

static, and transport properties of H_2O in the critical region, *Am. Jour. Sci., 291,* 541-648, 1991.

20. Jůza, J., V. Kmoníček, and O. Šifner, Measurements of the specific volume of carbon dioxide in the range of 700 to 4000b and 50 to 475°C, *Physica, 31,* 1735-1744, 1965.
21. Kennedy, G. C., Pressure-volume-temperature relations in CO_2 at elevated temperatures and pressures, *Am. Jour. Sci., 252,* 225-241, 1954.
22. Kerrick, D. M., and G. K. Jacobs, A modified Redlich-Kwong equation for H_2O, CO_2, and H_2O-CO_2 mixtures at elevated pressures and temperatures, *Am. J. Sci., 281,* 735-767, 1981.
23. Kieffer, S. W., Sound Speed in Liquid-Gas Mixtures: Water-air and water-steam, *J. Geophys. Res., 82,* 2895-2904, 1977.
24. Kormer, S. B., Optical study of the characteristics of shock-compressed condensed dielectrics, *Soviet Physics Uspekhi, 11,* 229-254, 1968.
25. Köster, H., and E. U. Franck, Das spezifische Volumen des Wassers bei hohen Drucken bis 600°C und 10 kbar, *Ber. Buns. Physik. Chem. 73,* 716-722, 1969.
26. Levelt-Sengers, J. M., H. R. Kamgar-Parsi, F. W. Balfour, and J. V. Sengers, Thermodynamic properties of steam in the critical region, *J. Phys. Chem. Ref. Data, 12,* 1-28, 1983.
27. Looyenga, H., Dielectric constants of heterogeneous mixtures, *Physica, 31,* 401-406, 1965.
28. Lyzenga, G. A., T. J. Ahrens, W. J. Nellis, and A. C. Mitchell, The temperature of shock-compressed water, *J. Chem. Phys., 76,* 6282-6286, 1982.
29. Mäder, R. K., and R. G. Berman, An equation of state for carbon dioxide to high pressure and temperature, *Am. Min., 76,* 1547-1559, 1991.
30. Mäder, R. K., H_2O-CO_2 mixtures: a review of P-V-T-X data and an assessment from a phase-equilibrium point of view, *Can. Min., 29,* 767-790, 1991.
31. Nellis, W. J., A. C. Mitchell, F. H. Ree, M. Ross, N. C. Holmes, R. J. Trainor, and D. J. Erskine, Equation of state of shock-compressed liquids: Carbon dioxide and air, *J. Chem. Phys., 95,* 5268-5272, 1991.
32. Nellis, W. J., F. H. Ree, M. van Thiel, and A. C. Mitchell, Shock compression of liquid carbon monoxide and methane to 90 GPa (900 kbar), *J. Chem. Phys., 75,* 3055-3063, 1981.
33. Rice, M. H., and J. M. Walsh, Equation of state of water to 250 kilobars, *J. Chem. Phys., 26,* 825-830, 1957.
34. Saul, A., and W. Wagner, A fundamental equation for water covering the range from the melting line to 1273 K at pressures up to 25000 MPa, *J. Phys. Chem. Ref. Data, 18,* 1537-1564, 1989.
35. Shmonov, V. M., and K. I. Shmulovich, Molal volumes and equation of state of CO_2 at temperatures from 100 to 1000°C and pressures from 2000 to 10,000 bars, *Dokl. Akad. Nauk SSSR., 217,* 206-209, 1974.
36. Sterner, S. M., and R. J. Bodnar, Synthetic fluid inclusions. X: Experimental determination of P-V-T-X properties in the CO_2-H_2O system to 6 kb and 700°C, *Am. Jour. Sci., 291,* 1-54, 1991.
37. Takenouchi, S., and G. C. Kennedy, The binary system H_2O-CO_2 at high temperatures and pressures, *Am. Jour. Sci., 262,* 1055-1074, 1964.
38. Tödheide, K., and E. U. Franck, Das Zweiphasengebiet und die kritische Kurve im System Kohlendioxide-Wasser bis zu Drucken von 3500 bar, *Z. Phys. Chem. N. F., 37,* 387-401, 1963.
39. Tsiklis, D. S., L. R. Linshits, and S. S. Tsimmerman, Measurement and calculation of the molar volume and thermodynamic properties of carbon dioxide at high pressures and temperatures, *Proc. 1st Intern. Conf. Calorimetry and Thermodynamics,* Warsaw, 649-656, 1969.
40. Walther, J. V., Determining the thermodynamic properties of solutes in crustal fluids, *Am. Jour. Sci., 291,* 453-472, 1991.
41. Zakirov, I. V., The P-V-T relations in the H_2O-CO_2 system at 300 and 400°C up to 1000 bar, *Geochem. Int., 21,* 13-20, 1984.

Experimental Trace Element Partitioning

John H. Jones

1. INTRODUCTION

This summary emphasizes experimental partitioning, and mainly experimental data have been tabulated here, with few data inferred from natural systems (e.g., phenocryst/matrix partitioning) as such data may be difficult to interpret [e.g., 101]. Further, whenever data on natural basaltic compositions are available, these will be given preference over experiments in synthetic systems. The data tabulated here will also tend to be more representative of basaltic (as opposed to granitic) systems. It should also be remembered that partition coefficients (D) and ratios of partition coefficients (K_D) are complex functions of temperature, pressure, oxygen fugacity, and bulk chemical composition — not numbers to be looked up on a stone tablet. However, this compilation may serve as a guide to the most important intensive variables. For detailed modeling, it is recommended that methods such as those devised by Nielsen [109] and Colson et al. [23] be employed. The reader is also referred to the excellent earlier compilation by Irving [54]. Also, Ryerson and Hess [121] give a good summary of liquid/liquid partitioning in silicate systems.

In addition, this compilation is generally lacking those partition coefficients based on beta track mapping [e.g., 104]. At the time of most of those studies, it was not realized that each individual beta produces several "tracks" [63]. Therefore, the number of events assumed by optical track counters is seriously overestimated, and the counting statistics error bars are subsequently underestimated. Probably because of this confusion concerning counting statistics, there has been some serious questioning of the beta track results during the last decade [4, 30]. Because of these uncertainties, I have chosen not to present beta track partition coefficients.

1.1. Terminology

The terminology used here will be that of [9]. Simple partition coefficients are either by weight

$$D_M^{xl/liq} = C_M^{xl}/C_M^{liq} \quad (1)$$

where D is the partition coefficient of element *M* and C is the weight concentration of M in the crystal (xl) or coexisting liquid (liq), or by cation fraction

$$D_{M*}^{xl/liq} = X_M^{xl}/X_M^{liq} \quad (2)$$

where X is the cation fraction of species *M*. In addition, some partitioning data are presented as K_D, the exchange coefficient, where

$$K_{D_{M/N}}^{xl/liq} = D_{M*}^{xl/liq}/D_{N*}^{xl/liq} = D_M^{xl/liq}/D_N^{xl/liq}. \quad (3)$$

K_D's are sometimes preferable to D's because they are less sensitive to temperature and composition. Because of canceling terms, K_D can be calculated in terms of either D or molar D.

In the subsequent sections, D's are often parameterized in terms of other D's. Usually in these cases, the D of the trace element is regressed *versus* the D of a major element.

J. H. Jones, NASA/Johnson Space Center, SN4, Houston, TX 77058

Rock Physics and Phase Relations
A Handbook of Physical Constants
AGU Reference Shelf 3

The slopes of these D *vs.* D correlations may be thought of as K_D's, as given by equation (3). Again, because many of the pressure, temperature, and compositional terms that are important to variation of D's are canceled in the formulation of a K_D, D *vs.* D regressions are often quite useful in predicting D's of trace elements when the exact pressures and temperatures of magmatic events are poorly constrained. Further, if one D is based on a major element, bulk chemical analyses, sometimes augmented by microprobe analyses, may be sufficient to approximately predict the D's of minor and trace elements.

1.2. Abbreviations

For convenience, a number of abbreviations will be used in this review. These are given here alphabetically:

an — anorthite
apa — apatite
aug — augite
Ca-pv — calcium perovskite
carb — carbonate liquid
diop — diopsidic pyroxene
gar — garnet
ilm — ilmenite
liq — silicate liquid
lm — liquid metal/sulfide
maj — majorite
mel — melilite
Mg-pv — magnesian perovskite
ol — olivine
opx — orthopyroxene, low-Ca pyroxene
per — periclase
pig — pigeonite
plag — plagioclase
pyx — pyroxene
rut — rutile
sm — solid metal
sp — spinel
zir — zircon

1.3. Henry's Law

An important issue that has haunted the practitioners of experimental trace element partitioning is that of Henry's law. Henry's law is said to be obeyed if the partition coefficient does not depend upon the concentration of the tracer. There has been some question as to whether "trace" elements doped at the wt.% level, for the purposes of electron microprobe analysis, are truly in the Henry's law region [49, 103]. The main challenge to percent-level doping came from beta track studies, which have subsequently been disputed, as noted above. It is the opinion of this reviewer that, in the majority of cases, percent-level doping falls within the Henry's law region. Jones and Burnett [64] compared the results of three different experimental studies of $D_{Sm}^{diop/liq}$. When experiments of similar bulk composition were compared, $D_{Sm}^{diop/liq}$ was found to be identical within error (wt.% level [45]; 200 to 5000 ppm [116]; 50 ppm [64]). This issue has also been discussed in detail by [139], who arrived at the same conclusion using rather different arguments. With the advent of ion probe analysis, however, many of these issues may be settled by doping at truly trace concentrations [e.g., 4].

2. COMPATIBLE AND MODERATELY COMPATIBLE ELEMENTS — Mg, Fe, Mn, Ni, Co ± (Sc, Cr, V, Ge, Ga)

2.1. Olivine and Subcalcic Pyroxene

Linear relations have been established between $D_{MgO*}^{ol/liq}$ and the molar D's of other elements [8, 60], as shown by equation (4) for FeO.

$$D_{FeO*}^{xl/liq} = A\, D_{MgO*}^{xl/liq} + B \qquad (4)$$

This relationship appears to hold over a wide range of temperatures and pressures. Figure 1 shows $D_{FeO*}^{ol/liq}$ *vs.* $D_{MgO*}^{ol/liq}$ for experiments up to 40 kbar.

Because the great majority of the octahedral sites in olivine and subcalcic pyroxene are occupied by Fe and Mg, this type of linear relationship between $D_{FeO*}^{ol/liq}$ and $D_{MgO*}^{ol/liq}$ allows $D_{MgO*}^{ol/liq}$ to be calculated directly from the bulk composition of a basalt [8, 60, 131]. Specifically, for olivine and subcalcic pyroxene:

$$D_{MgO*}^{xl/liq} = (F - B\, X_{FeO}^{liq})/(A\, X_{FeO}^{liq} + X_{MgO}^{liq}) \qquad (5)$$

where F is the cation fraction of octahedral sites available (i.e., for olivine F = 0.667, and for orthopyroxene F = 0.5); X_i is the cation fraction of *i* in the silicate liquid; and values for A and B for FeO may be looked up in Tables 1 and 2. This calculated value of $D_{MgO*}^{ol/liq}$ can then be substituted into similar linear $D_{i*}^{ol/liq}$ *vs.* $D_{MgO*}^{ol/liq}$ equations for minor and trace elements to predict partition coefficients for these elements, using the regression coefficients from Tables 1 and 2. Figure 2 shows that forsterite contents of experimental olivines, predicted in this way, appear reliable to pressures of 140 kbar.

Equation (5) for calculating D_{MgO*} nearly always gives very good agreement with experimentally determined D_{MgO*}. Consequently, it appears that any discrepancy between predicted and measured D values is because the other

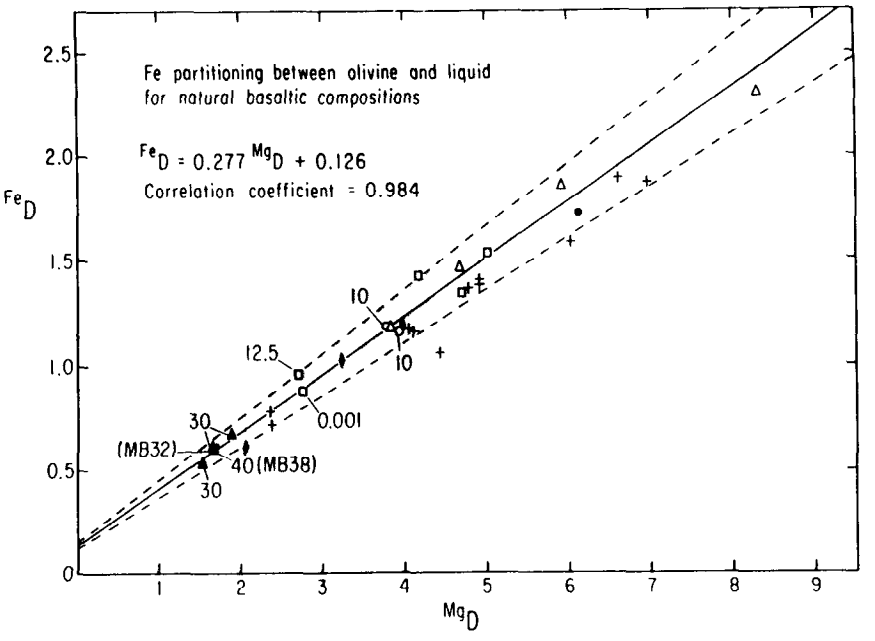

Figure 1. Experimental $D^{xl/liq}_{FeO^*}$ *vs.* $D^{xl/liq}_{MgO^*}$. The figure is from [60] and shows that $D^{xl/liq}_{FeO^*}$ may be parameterized as a linear function of $D^{xl/liq}_{MgO^*}$. Different symbols refer to different experimental studies and are identified in [60]. Numbers beside some symbols refer to the pressure of the experiment in kbar; unnumbered symbols are 1-bar experiments. The same types of regressions can also be made for orthopyroxene.

elements (i.e., Fe, Ni, Mn, etc.) do not behave in the simple way predicted by equation (4). Tables 1 and 2 are taken from [8]; see [8] for references to individual data sets. In addition, Table 3 gives $D^{ol/liq}_{MgO^*}$ and $D^{opx/liq}_{MgO^*}$ for a variety of basalt compositions. It is important to remember, however, that the values tabulated in Table 3 do not imply that these liquids are actually in equilibrium with olivine and orthopyroxene, only that these are the predicted D's *if* such equilibrium pertains.

Occasionally, the magma composition of interest is so far removed from those used in the regressions that the systematics described above no longer apply. One well-documented case is that of lunar high-Ti basalts, which have lower values of $K^{ol/liq}_{D_{FeO/MgO}}$ than low-Ti basalts. Jones [61] has shown that, even in this case, the model may be modified to predict the correct $K^{ol/liq}_{D_{FeO/MgO}}$. For high-Ti basalts, Ti and Fe act as though they form $FeTi_2O_5$ complexes in the silicate liquid, leaving only a fraction of

TABLE 1. Regression Parameters for Molar Olivine/Liquid Partition Coefficients

$D_{i^*} = A\ D_{MgO^*} + B$

Element	A	B	Number of Experiments	Correlation Coefficient r	σ D_{i^*}
FeO#	0.298	0.027	898	0.93	0.13
Mn	0.259	-0.049	204	0.91	0.23
Ni	3.346	-3.665	148	0.92	2.0
Co	0.786	-0.385	68	0.96	0.23
Sc	0.063	-0.034	11	0.88	0.02
Mg	1.00	0.00	898	-	0.168

#Corrected for Fe_2O_3 in the liquid, see [8].

the total FeO available for partitioning into olivine and lowering the $K_{DFeO/MgO}^{ol/liq}$. $K_{DFeO/MgO}^{ol/liq}$ in high-Ti systems may be modeled as,

$$K_{DFeO/MgO}^{ol/liq}* = K_{DFeO/MgO}^{ol/liq}(\text{Ti-free})[(X_{FeO} - X_{Ti}/2)/X_{FeO}] \quad (6)$$

where $K_{DFeO/MgO}^{ol/liq}$(Ti-free) is the K_D that would be calculated by assuming that Ti had no effect on K_D, using equations (4) and (5), and the X's are cation fractions in the silicate liquid. The model may be further refined by regressing the measured K_D *versus* the model K_D*. For lunar basalts this results in

$$K_{DFeO/MgO}^{ol/liq} = 0.866\ K_{DFeO/MgO}^{ol/liq}* + 0.079. \quad (7)$$

It should be emphasized that, although this type of formulation appears to work well for FeO, the effect of Ti on other elements such as Ni is unknown.

Other moderately compatible elements of interest are Cr and V. However, these elements exist in multiple valence states and generalizations are difficult. Even so, at low oxygen fugacity (~IW) $D_{Cr}^{ol/liq}$ = ~1 and $D_{Cr}^{pig/liq}$ = ~2 [e.g., 127]. Similarly, $D_V^{ol/liq}$ = ~1 and $D_V^{pig/liq}$ = ~3 [118]. At terrestrial fo_2's $D_V^{ol/liq}$ is probably about 0.3 [32] and $D_{Cr}^{ol/liq}$ = ~0.8 and $D_{Cr}^{pig/liq}$ = ~2-3 [84]. This similarity in $D_{Cr}^{ol/liq}$ between low and high fo_2 environments may be somewhat misleading, see [124]. It should also be remembered that these elements are highly compatible in spinel and the various Fe-Ti oxide minerals. For a detailed analysis of Cr partitioning among orthopyroxene, spinel, and liquid, see [3].

Capobianco and Watson [19] and Malvin and Drake [87] have shown that $D_{Ge}^{ol/liq}$ is about unity.

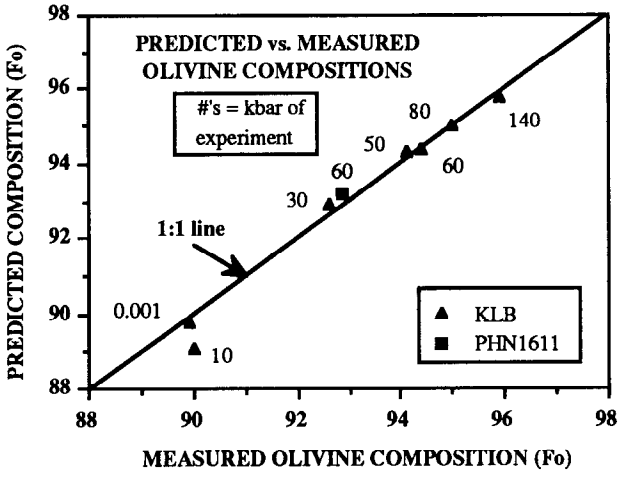

Figure 2. Predicted *vs.* measured major element compositions of high-pressure experimental olivines. Data are from [132] and [130]. Predictions are based on the regression of Jones [60]. Numbers beside symbols indicate the pressure of the experiment in kbar. The regression of Figure 1 was used to predict the Fo content of high pressure experimental olivines. The regression, which was determined using experiments ≤ 40 kbar, appears to have robust predictive powers for pressures up to 140 kbar.

2.2. Garnet, Augite and Plagioclase

Transition elements such as Ni and Co are not compatible in plagioclase, but Ga and Ge are weakly incompatible, $D_{Ga}^{an/liq}$ and $D_{Ge}^{an/liq}$ are 0.86 and 0.51, respectively [87]. No information such as that in Tables 1 and 2 is available for garnet, augite or plagioclase. However, on the basis of the compilation of [54], it is believed that garnet can concentrate Co, Ni, Sc and Cr, at least in a hydrous dacitic system (950°C, 30 kbar). For augite, there is also no detailed study of transition element partitioning. The experimental study of [82] for diopside/liquid partitioning is probably still the best comprehensive data set available for transition element partitioning into calcic pyroxene. The 1-bar study of Gallahan and Nielsen [41] on natural basaltic compositions indicates that $D_{Sc}^{aug/liq}$ varies from ~2-5; $D_{Cr}^{aug/liq}$ = ~4-5 at fo_2 = QFM [84].

2.3. Ultra-High Pressure Phases

Recent advances in high pressure technology have allowed

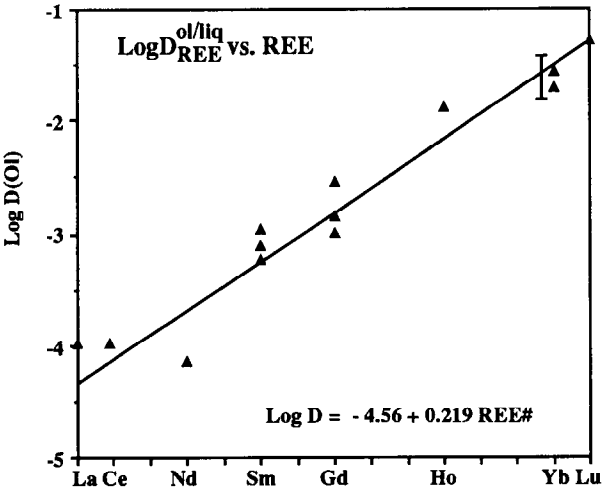

Figure 3. $LogD_{REE}^{ol/liq}$ *vs.* element. Data are mainly from [93]. A range D values (bar) from [23] are also shown. The data are consistent with the regression LogD = -4.56 + 0.29 REE#. Symbols for La and Ce are upper limits and are not included in the regression.

TABLE 2. Regression Parameters for Molar Subcalcic Pyroxene Partition Coefficients
$D_{i*} = A\ D_{MgO*} + B$

Element	A	B	Number of Experiments	Correlation Coefficient r	σ D_{i*}
FeO#	0.129	0.264	146	0.91	0.26
Mn	0.352	-0.025	108	0.91	0.24
Ni	1.206	-0.263	10	0.87	0.239
Co	0.467	0.14	7	0.98	0.02
Sc	0.522	-0.66	8	0.95	0.16
Mg	1.00	0.00	167	–	0.154

#Corrected for Fe_2O_3 in the liquid, see [8].

TABLE 3. Typical D_{MgO*} Values for Planetary Basalts

D_{MgO*}	Komatiite#	Alkali Olivine Basalt	MORB#	Andesite	Lunar Mare Basalt	Eucrite	Shergottite#
Olivine	1.8	4.2	4.8	8.4	2.6	4.6	3.8
Orthopyroxene	1.3	3.2	3.3	6.6	2.0	3.8	2.9

#Fe_2O_3 taken to be 10% of FeO total.

TABLE 4. K_D(xl/liq) of Phases from Ultra-High Pressure Experiments

Phase	(T,P) Conditions*	$K_{D_{Fe/Mg}}$	$K_{D_{Mn/Mg}}$	$K_{D_{Ni/Mg}}$	$K_{D_{Co/Mg}}$	Reference
Olivine	(1900, 16)	0.38	0.27	0.61	–	[112]
	(1800, 7.5)	0.34	0.29	1.0	0.56	[89]
	(2080, 10)	0.33	–	0.67	0.53	[89]
β-spinel	(2200, 20)	0.39	0.35	–	–	[56]
	(2260, 16.5)	1.25	0.83	1.7	1.7	[89]
Majorite Garnet**	(2200, 20)	0.31	0.54	–	–	[56]
	(1900, 16)	0.48	0.73-1.17	0.21	–	[112]
	(2260, 16.5)	0.33	–	0.22	0.33	[90]
	(2225, 16)	0.38	–	0.25	0.38	[90]
	(2000, 20)	0.34	1.27	–	0.59	[149]
	(2100, 25)	0.41	–	–	–	[111]
	(2050, 26)	0.41	–	–	–	[1]
Mg-Perovskite	(2400, 25)	0.5	1.0	–	–	[91]
	(~2400, 25)	0.31	–	–	–	[56]
Magnesiowüstite	(<2400, 25)	1.5	0.9	–	–	[91]
	(2225, 16)	0.75	–	1.7	1.3	[90]
	(2050, 26)	3.6	2.4	5.2	–	[1]

*T in °C and pressure in GPa.
**Because of the large scatter in the $K_{D_{Fe/Mg}}$ data, no majorite data from [73] are reported.

TABLE 5. Partitioning of Cr, Sc, Ge and Ga at Ultra-High Pressures

Phase	(T,P)*	D_{Cr}	D_{Sc}	D_{Ge}	D_{Ga}	Reference
β-spinel	(2260, 16.5)	0.8	0.2	1.2	0.6	[90]
Majorite	(2260, 16.5)	1.5	1.5	–	0.8	[90]
	(2100, 16)	–	1.7	–	–	[73]
	(1950, 16)	2.33	1.64	–	–	[112]
	(2250, 16)	1.4	1.5	–	0.7	[90]
	(2000, 20)	1.0	–	–	–	[149]
Magnesiowüstite	(2225, 16)	2.2	0.1	–	0.63	[90]
	(2050, 26)	1.3	–	–	–	[1]

*In °C and GPa.

exploration of (P,T) space that has previously been inaccessible. Partitioning studies involving β-spinel, majorite garnet, (Mg,Fe)-perovskite, Ca-perovskite, and magnesiowüstite have begun. However, comparison between different experiments from different laboratories is difficult because of differences in experimental conditions. Here I will confine myself to tabulating K_D's for compatible and moderately compatible elements (Table 4), which may not be strong functions of temperature and pressure. As can be seen, there is substantial agreement for some elements and substantial disagreement for others. Clearly, more work is needed. In the future, compilations of D *vs.* D relationships, such as equation (2), may be recognized for phases such as majorite garnet. At the present time, however, the complexity of Al partitioning with pressure precludes such a simple functional form [51].

Data for other moderately compatible elements are summarized in Table 5. In addition, Yurimoto and Ohtani [149] report a $D_V^{maj/liq}$ of 1.1-2.5.

3. RARE EARTH ELEMENTS (REE) AND Sr (Eu^{2+}) IN MAJOR ROCK-FORMING MINERALS

3.1. Olivine/Liquid

The difficulty of measuring the small partition coefficients of REE in olivine has limited the number of good studies. The data used here are from [23, 93, 110]. The data are presented in Figure 3 which shows the variation of logD *vs.* atomic number. The individual data points are from [93] and the averages of [110]. The vertical line shows the variation in $D_{Yb}^{ol/liq}$ observed by [23]. Clearly, variations of a factor of two are easily possible. The best fit line is a regression of logD *vs.* REE#, where La = 1 and Lu = 15. The La and Ce data are upper limits and are not included in the regression. Although not shown, it is probable that this REE pattern will have a substantial negative Eu ano-maly at low fo_2 [96]. Although not shown, the study of [5], using ion probe analysis, confirms the pattern of [93] and extends it to the light rare earths (LREE). The low Sr partition coefficient of Beattie [5], 5 x 10^{-5} to 1.1 x10^{-4}, also confirms the presence of a Eu anomaly at low fo_2.

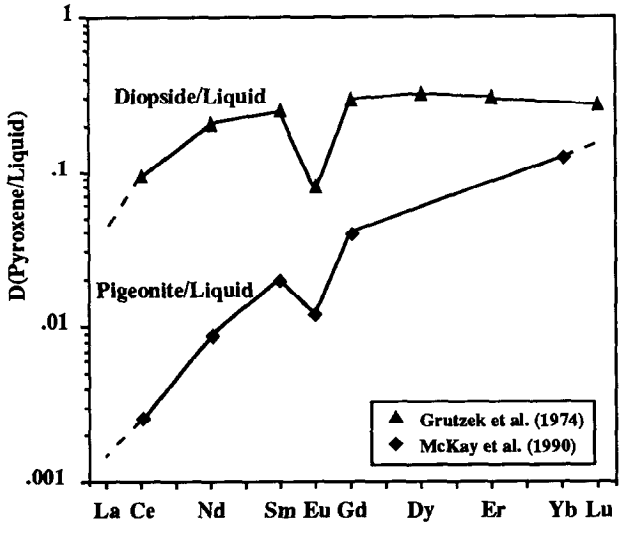

Figure 4. $D^{pyx/liq}$ *vs.* element. Typical high-Ca and low-Ca pyroxene D patterns are shown. Diopside pattern is from [45] and the pigeonite pattern is from [96]. Both experiments were performed at one bar. These patterns are appropriate for reducing conditions where most Eu exists as Eu^{2+}. At high fo_2 where Eu^{2+} is destabilized, the patterns should be smooth.

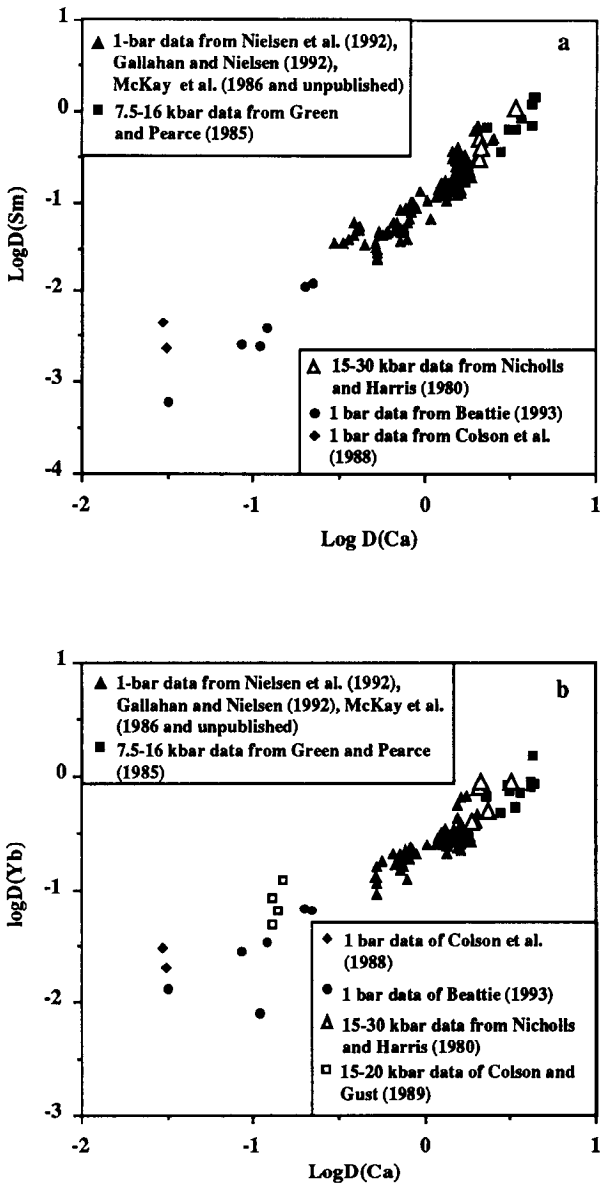

Figure 5. (a). $LogD_{Sm}^{pyx/liq}$ *vs.* $LogD_{Ca}^{pyx/liq}$. $D_{Sm}^{pyx/liq}$ correlates well with $D_{Ca}^{pyx/liq}$ over a wide range of pyroxene compositions, although there is significant scatter. Data from [96] are for a shergottite composition, and the data from [110] are for natural terrestrial compositions. High pressure pyroxenes appear to fall on the one-bar trend. Pyroxenes with low D_{Ca} are subcalcic and those with high D_{Ca} are augitic. Regressions of LogD *vs.* $LogD_{Ca}^{pyx/liq}$ may allow an estimation of D_{REE} when the composition of the pyroxene is known but the D_{REE} is not. (b). $LogD_{Yb}^{pyx/liq}$ *vs.* $LogD_{Ca}^{pyx/liq}$. D_{Yb} appears to behave similarly to D_{Sm}.

3.2. Pyroxene/Liquid

Figure 4 shows typical low-Ca pyroxene and high-Ca pyroxene D_{REE} patterns. Although the exact value of D depends on temperature, pressure and bulk composition, there is a good correlation of $logD_{REE}$ *vs.* $logD_{Ca}$. Presented below are 1-bar pyroxene partitioning data from [5, 23, 41, 98, 110] and unpublished data from McKay. These 1-bar data are augmented by high-pressure data from [22, 42, 108]. Figure 5a,b shows $logD_{Sm}$ and $logD_{Yb}$ *vs.* $logD_{Ca}$, illustrating the results of these experimental studies. Most of the studies presented here were performed on natural terrestrial basaltic compositions near QFM. The studies of [98] were performed on a shergottite composition, near QFM, at temperatures of 1140-1170°C. Most of the pyroxenes in this data set are pigeonites or augites, but some are orthopyroxenes. The CaO content of pyroxenes is clearly important in determining D_{REE}.

Regression parameters for pyroxene $logD_{REE}$ *vs.* $logD_{Ca}$ trends are tabulated in Table 6 below. Because there are more experiments for Sm and Yb than for other elements, the functional form, determined for Sm and Yb, has been used to parameterize the other REE. In order to use this table, it is necessary to have a prior estimate of the $D_{Ca}^{pyx/liq}$ values pertinent to the study. The scatter about the regression line is primarily real and quite significant. Even so, the scatter is rather less than the overall range of D values.

Note the regular decrease in $\partial logD_{REE}/\partial logD_{Ca}$ with increasing atomic number. This decrease is very regular within the scatter of the data and may be parameterized by REE#. The regression parameters of Table 6 have been plotted vs. atomic number in Figure 6. The slopes change linearly with REE# and the intercepts are a smooth function of REE#. This gives added confidence, for those elements for which there is minimal data, that the regression parameters are reasonable. Thus, it is possible to obtain partition coefficients for elements that have not been studied experimentally, e.g., promethium. To estimate a $logD_{Pm}$ from a $logD_{Ca}$, simply calculate the slope of the regression by using REE# = 5 in the equation of Figure 6 and estimate an intercept by interpolating between the intercepts of Sm and Nd. Table 7 gives hypothetical values of $logD_{Ca}$ for pyroxenes from a variety of planetary basalts. Once again, these estimated partition coefficients are not meant to imply that these basalts always have these pyroxenes on their liquidi. The best technique is to use the Ca contents of actual crystal-liquid pairs.

The negative Eu anomaly implied by the data of Table 6 is small (~10-20%) but is only defined for the fo_2 region near QFM. As fo_2 decreases to near IW, the negative europium anomaly will also increase. At lunar oxygen fugacities the

TABLE 6. Pyroxene/Liquid REE Partition Coefficients near QFM

$LogD_{REE} = A\ LogD_{Ca} + B$

REE	A	B	r^2	σ $logD_{REE}$	N	Reference
La	1.608	-1.704	0.799	0.254	96	[5, 41, 98, 108]
Ce	1.474	-1.695	0.927	0.203	31	[5, 98]
Nd	1.284	-1.226	0.890	0.072	131	[98]
Sm	1.388	-0.974	0.900	0.151	205	[5, 23, 41, 42, 98, 108, 110]
Eu	0.810	-0.936	0.311	0.052	8	[98]
Gd	1.122	-0.732	0.864	0.168	62	[23, 41, 98, 110]
Ho	1.106	-0.570	0.894	0.194	49	[5, 41, 42, 108, 110]
Yb	0.784	-0.649	0.860	0.116	164	[5, 22, 23, 42, 98, 108, 110]
Lu	0.946	-0.740	0.806	0.075	17	[41, 98]

D_{Eu} for pigeonite is about ~75% that of Gd [96]. At these same conditions, D_{Sr}, an analog for $D_{Eu^{2+}}$, is nearly an order of magnitude lower than D_{Gd} [96]. In the work by [45] on diopside-liquid partitioning, D_{Sr} was 0.078 compared to the expected $D_{Eu^{3+}}$ of ~0.29.

3.3. Ultra-High Pressure Phases — Garnet, Majorite, β-Spinel, and Perovskite

3.3.1. Garnet and Majorite. There are surprisingly few data on garnet-liquid partitioning. The most recent major study on a natural system [108] included no REE lighter than Sm. Consequently, Sm-Nd fractionations by garnet must either be inferred or taken from studies on synthetic systems. Figure 7 shows a typical garnet-synthetic liquid D_{REE} pattern from [126]. There are no low pressure (<30 kbar) data for D_{Sr}. Kato et al. [73] report that at very high pressures (>150 kbar) D_{Sr} is <0.1.

Figure 8 shows that the potential exists for systematizations of garnet partition coefficients much like those of pyroxene. The regression lines of $logD_{REE}$ *vs.* $logD_{Ca}$ in Figure 8 are for the garnet-liquid data of [108] (triangles). The other symbols are for garnet-liquid and majorite-liquid partition coefficients from other investigations [73, 112] and Colson (unpublished). Although there is scatter [e.g., open squares show the individual D_{Sm} values of [73] that were averaged (solid square)], all but one of the ultra-high pressure D's are adequately fit by the regressions to the data of [108], which were all obtained at pressures of ≤ 36 kbar. More work is needed to evaluate this suggestion.

Beattie [7] reports $D_{Sr}^{gar/liq}$ of 0.5-1.25 x 10^{-3} at pressures of 30-36 kbar and temperatures of 1300-1565°C (graphite capsules).

3.3.2. β-Spinel. No REE or Sr partitioning data are available for β-spinel.

3.3.3 Perovskite and Periclase. McFarlane et al. [89] report measurements of a $D_{Sm}^{Mg\text{-}pv/liq}$ of 0.2, a $D_{Sm}^{Ca\text{-}pv/liq}$ of 0.7, and a $D_{Sm}^{per/liq}$ of 0.03; and Kato et al. [74] report a D_{Yb} for Mg-perovskite of 0.6, with a large associated error. The McFarlane et al. data must also be considered approximate because the Ca-perovskite and periclase were not in direct contact with the silicate liquid. Ito and Takahashi [56] report a $D_{La}^{Ca\text{-}pv/liq}$ of 5. Again, this

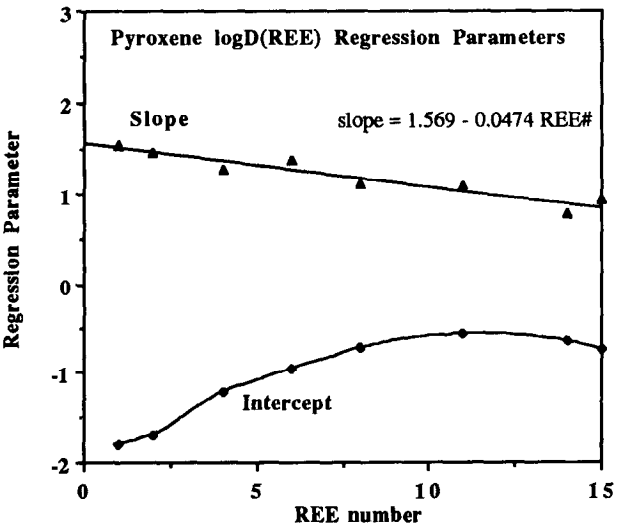

Figure 6. Regression parameters for pyroxene $LogD_{REE}$ *vs.* $LogD_{Ca}$ regressions, plotted *vs.* REE#. The slopes of the regressions decrease linearly with REE# and the intercepts are smooth with REE#. The partitioning behaviors of rare earths that have not been studied experimentally may be inferred by interpolating the regression parameters of the figure.

TABLE 7. Hypothetical LogD_{Ca} for Planetary Basalts

Typical Pyroxenes	Komatiite	Alkali Olivine Basalt	MORB	Andesite	Lunar Mare Basalt	Eucrite	Shergottite
Orthopyroxene (0.75 wt.% CaO)	-1.0	-1.1	-1.2	-1.2	-0.92	-1.1	-1.1
Pigeonite (3 wt.% CaO)	-0.41	-0.51	-0.57	-0.55	-0.32	-0.54	-0.52
Augite (18 wt.% CaO)	0.37	0.26	0.21	0.22	0.46	0.24	0.25

value should be treated with caution, as the source of the La was probably the $LaCrO_3$ heater. There are no Sr data for Mg-perovskite. Kato et al. [73] report a D_{Sr} of 2.4 for Ca-perovskite.

3.4. Plagioclase/Liquid Partitioning

The status of plagioclase/liquid partitioning is somewhat uncertain. After the pioneering work by [31], little has been published. The best data for lunar compositions are from McKay [94, 95, 145, and unpublished], which do not seem to be strongly temperature dependent. Figure 9 compares the unpublished plagioclase D_{REE} pattern of McKay (1 bar, 1240°C) for a lunar highlands composition with that of [31] for a synthetic composition similar to a basaltic andesite (1 bar, 1300°C). While the Drake and Weill [31] D_{LREE} are about a factor of three higher than those of McKay, the slope of the pattern is about the same. This suggests that the main cause of the differences in D_{LREE} between these studies is bulk composition. However, at the heavy REE (HREE) end of the pattern, the Drake and Weill [31] values are about an order of magnitude higher than those of McKay. It is likely that the HREE partition coefficients of [31] have been influenced by secondary fluorescence or other analytical problems [e.g., 93]. Table 8 gives McKay's preferred partition coefficients at 1240°C.

3.5. Alkali Feldspar/Liquid Partitioning

There are no experimental REE partitioning data for alkali feldspars. Long [83] gives a value for D_{Sr} of 2.7, at 8 kbar and 720-780°C.

3.6. Amphibole/Liquid Partitioning

Figure 10 summarizes the D_{REE} data of [108]. Other studies have tended to be in synthetic systems [54] or have utilized the phenocryst-matrix technique. The Nicholls and Harris [108] data appear to be in qualitative agreement with other techniques. Plots of D_{REE} vs. D_{Ca} are not terribly helpful in deciphering amphibole-liquid partitioning systematics because of the paucity of data.

4. ACTINIDES AND Pb

4.1. Clinopyroxene/liquid and Phosphate/Liquid Partitioning

Traditionally, most of the actinide partitioning data have been from synthetic systems, collected by D. S. Burnett and coworkers. Consequently, direct application to basaltic liquids has not always been possible. A summary is given in Table 9. In general, partition coefficients are very low for U and Th (except for phosphate/liquid partitioning) and

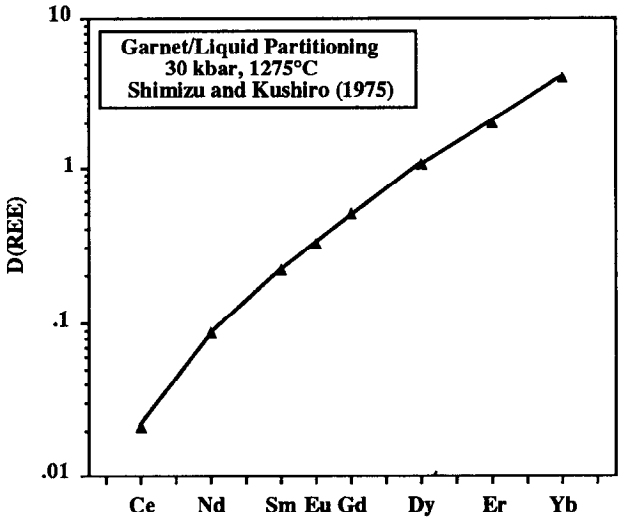

Figure 7. $D_{REE}^{gar/liq}$ *vs.* element. A typical garnet D_{REE} pattern for a synthetic, FeO-free composition. D changes by nearly three orders of magnitude from La to Lu.

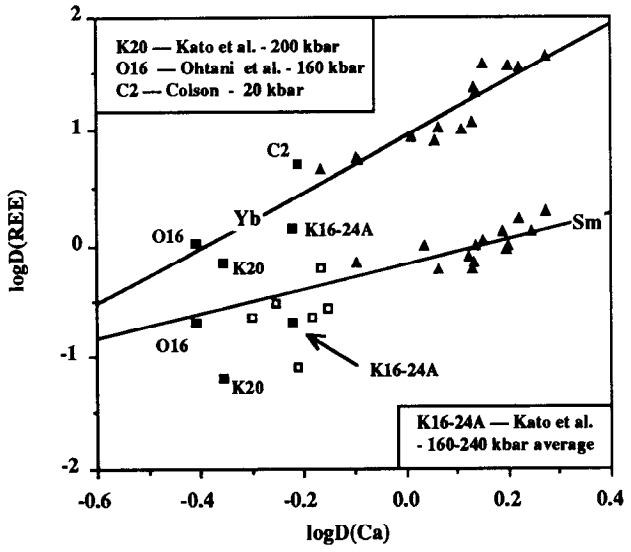

Figure 8. $LogD^{gar/liq}_{Sm, Yb}$ *vs.* $LogD^{gar/liq}_{Ca}$. Triangles are from [108] and the lines are regressions to the data from [108]. Other high pressure and ultra-high pressure experiments are labeled (solid symbols, see text). Open squares are the data of [73] that were averaged to get the value (solid square – K16-24A) reported by [73]. Although there is much scatter, there is a suggestion that the parameterizations of D_{REE} that were useful for pyroxenes may also be useful for garnet and majorite.

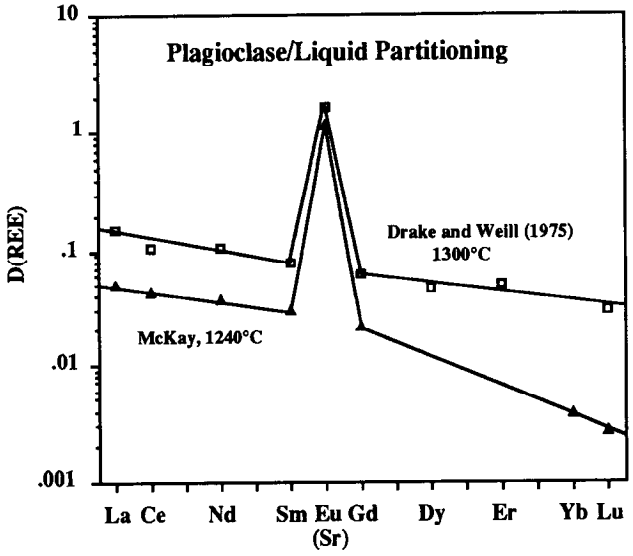

Figure 9. $D^{plag/liq}_{REE}$ *vs.* element. Open squares are from [31] and the solid triangles are from McKay (unpublished). The Eu value from McKay is for an oxygen fugacity appropriate for lunar systems and the "Eu" value from [31] is for Sr. The McKay data are probably the best indicator of the general plagioclase/liquid D pattern. Differences in the LREE between the two studies are probably due to differences in bulk composition.

Pu behaves much like a light REE, such as Nd. Actinides appear to reside in Ca sites in the major rock-forming silicates and phosphates. In accessory phases they may substitute for Ti, Nb, or Zr.

Experiments generally confirm the merrilite/apatite fractionations of actinides and lanthanides observed in equilibrated chondrites. Merrilite concentrates Pu, Th and the REE, whereas apatite concentrates U. Consequently, Th/U and Pu/U ratios of merrilite are high and Th/U and Pu/U ratios of apatite are low [e.g., 62].

Adding P_2O_5 to the silicate liquid causes actinide partition coefficients to decrease, sometimes dramatically [11]. Jones and Burnett [64] showed that P_2O_5 decreased $D^{diop/liq}_{Pu}$ by about a factor of two, $D^{diop/liq}_{Sm}$ by about 50%, and $D^{diop/liq}_{Al}$ is not affected at all. Consequently, Jones and Burnett [64] concluded that Pu and, to a lesser extent, Sm were complexed by phosphate ligands in the silicate liquid.

In the same series of experiments as those for U (Table 9), Watson et al. [144] measured diopside/melt partition coefficients for Pb. Their D's, which averaged about 0.01, may have been affected by the oxygen fugacity (air) and could be somewhat low if there was any Pb^{4+} present. Watson et al. [143] also give approximate apatite/liquid partition coefficients for Pb of 0.1-0.4. However, again, oxygen fugacity was not controlled.

The data from non-synthetic systems have been very limited. However, LaTourette and Burnett [78] have recently published augite/liquid partition coefficients for U and Th (Table 10). These are comparable to or higher than those for diopside/liquid in synthetic systems. In addition, Beattie [6] has reported U, Th and Pb partition coefficients in synthetic systems (some of which approach natural compositions) using the ion probe. Beattie's partition coefficients tend to be much lower than those of [78], but Beattie's clinopyroxenes also tend to have much lower alumina contents as well. A regression of logD(Th) *vs.* logD(Al) for the one-bar experiments of [78] and [6] yields a very acceptable regression ($r^2 = 0.88$),

$$\log D_{Th} = 1.84 \log D_{Al} - 0.81. \quad (8)$$

Thus, it appears that partition coefficients of the actinides are quite sensitive to the availability of charge balancing

TABLE 8. Plagioclase/Liquid Partition Coefficients*

La	Ce	Nd	Sm	Eu	Gd	Yb	Lu
0.051	0.044	0.038	0.031	1.15	0.021	0.0038	0.0027

*G.A. McKay, personal communication.

cations such as Al. The 10 kbar data of [6] also fall along this one-bar regression.

4.2. Olivine/Liquid and Orthopyroxene Liquid

Beattie [6] reports that D for U, Th and Pb entering olivine and opx is much smaller than that for clinopyroxene. For olivine, typical D values were found to be 5 x 10^{-6}, 3 x 10^{-6}, and 3 x 10^{-4} for U, Th and Pb, respectively. For opx, D_U and D_{Th} are reported to be 3 x 10^{-5} and 7 x 10^{-5}, respectively.

4.3. Feldspar/Liquid Partitioning

Leeman [80] has measured sanidine/liquid and plagioclase/liquid partition coefficients for Pb, using the phenocryst-matrix technique. Plagioclase/liquid partition coefficients increase from 0.1 to 0.7 as melt composition changes from basaltic to rhyolitic. Sanidine/liquid partition coefficients for Pb are near unity.

4.4. Zircon/Liquid Partitioning

In a phenocryst-matrix study, LaTourette and Burnett [77] report that, in a natural granitic system, $D_U^{zir/liq} < 24$.

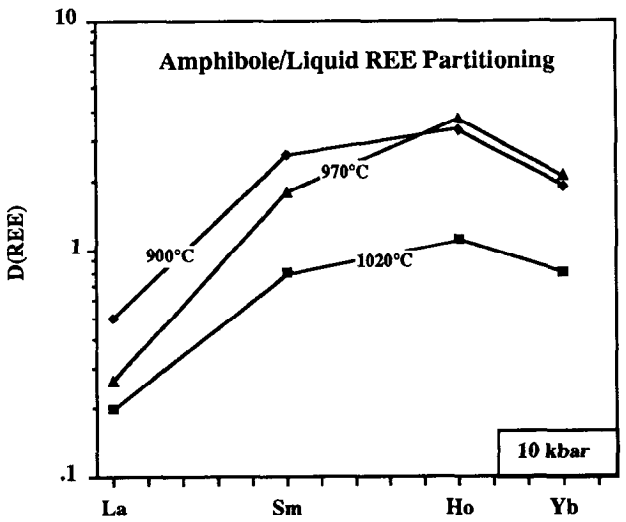

Figure 10. D_{REE} *vs.* element for amphibole/liquid. Data are from [108].

4.5. Garnet/Liquid Partitioning

For garnet, Beattie [7] reports D_U and D_{Th} of 0.9 - 2 x 10^{-2} and 1.5 - 3.3 x 10^{-3}, respectively. Unlike pyroxene and olivine, garnet seems to prefer U over Th.

4.6. Ultra-High Pressure Partitioning

Kato et al. [73] report $D^{Ca\text{-}pv/liq}$ for U and Th of 20 and 25, respectively. They also report $D^{gar/liq} < 0.1$ for U and Th.

4.7. Liquid/Liquid Partitioning

In addition to the studies cited above, there has been limited work on the partitioning of actinides between immiscible liquids. Dickinson and Jones [28] reported a lunar basaltic liquid/granitic liquid partition coefficient for Th of 7 (1060°C, 1 bar, iron capsule). Jones et al. [71] reported carbonate liquid/silicate liquid partition coefficients for Pb, Ra, Pa, Th and U of 0.61, 0.15, 0.28 and 0.35, respectively (1250°C, 10 kbar, graphite capsule).

5. HIGHLY INCOMPATIBLE AND/OR HIGH FIELD STRENGTH ELEMENTS — Rb, Cs, Ba, Zr, Hf, Nb, Ta (as well as Ca in Olivine and Fe in Plagioclase)

5.1. Olivine-Orthopyroxene/Liquid

Almost no quantitative information is known about these elements in olivine and low-Ca pyroxene, although the clinopyroxenes of [40] reported below approach the compositional range of orthopyroxene. Beattie [5] reports $D_{Ba}^{ol/liq}$ of 1-5 x 10^{-5} and $D_{Ba}^{opx/liq}$ of 4-10 x 10^{-3}, but even these low values may be upper limits to the true D.

Jurewicz and Watson [72] report that $K_{DCaO/MgO}^{ol/liq}$ can be parameterized as

$$K_{DCaO/MgO}^{ol/liq} = 0.01\ [(-0.08\pm0.015)\ Fo + (9.5\pm0.2)] \qquad (9)$$

where Fo is the forsterite content of the olivine.

5.2. Clinopyroxene/Liquid

5.2.1. High field strength elements. Forsythe et al. [40] report that D's for incompatible high field strength elements may be parameterized using D_{Ti}. The range of natural compositions and temperatures investigated by [40] was extensive, such that D_{Zr} varied from 0.014 to 1.11. For comparison, Watson and Ryerson [142] found that at 9-10 kbar and 950-1000°C $D_{Zr}^{aug/liq}$ was 0.27. Also, McCallum and Charette [88] found $D_{Zr}^{aug/liq}$ to be 0.05-0.22 and $D_{Nb}^{aug/liq}$ to be 0.01-0.03 at (1100-1130°C, 1 bar, ~IW). In the synthetic Di-An-Ab system, Dunn and McCallum [35] found $D_{Zr}^{diop/liq}$ to be 0.05-0.45 (depending on temperature and melt composition) and $D_{Nb}^{diop/liq}$ to be ≤0.02.

TABLE 9. Summary of Actinide Partitioning Data in Di-An-Ab and Di-An*

Phase	Temperature	Pressure	fo_2	D_{Th}	D_U	D_{Pu}
Diopside#						
P_2O_5 = 0	1275-1225	1 bar	≤Co-CoO	–	–	0.17
	1275**	1 bar	0.2 (air)	–	~0.00035	–
	1310-1275	1 bar	Ni-NiO	0.011	0.0034	–
	1310-1275	1 bar	QFM	0.012	0.0055	–
	1310-1275	1 bar	IW+1	0.010	0.0089	–
	1390-1375	20 kbar	10^{-9}	0.029	0.018	–
P_2O_5 = 1.5	1285-1235	1 bar	10^{-9}	–	–	0.11
P_2O_5 = 6.9	1390-1375	20 kbar	10^{-9}	0.0019	0.0019	0.053
P_2O_5 = 10.5	1390-1375	20 kbar	10^{-9}	0.0032	0.0028	0.064
Merrilite	1310-1230	1 bar	0.2 (air)	1.27	0.0024	<0.6
	1310-1230	1 bar	10^{-9}	1.30	0.48	3.7
	1390-1375	20 kbar	10^{-9}	1.15	0.58	3.5
Apatite	1390-1375	20 kbar	10^{-9}	1.22	1.69	–

*Unless otherwise noted, data are from [12, 13, 64, 78]. An fo_2 of 10^{-9} refers to either Co-CoO at 1 bar or graphite at 20 kbar.
**From [144].
#*Initial* P_2O_5 contents of the silicate liquid.

The pyroxenes in the experiments of [40] ranged from low-Ca pigeonite, near the opx-pig boundary, to augite. All are grown from natural basaltic compositions. Oxygen fugacity was either QFM or QFM+2; pressure was either 5 or 10 kbar. For these experiments,

$$D_{Zr} = 0.55\ D_{Ti}, \quad (10)$$

$$D_{Hf} = 1.5\ D_{Ti}, \quad (11)$$

$$D_{Nb} = 0.038\ D_{Ti}, \quad (12)$$

$$D_{Ta} = 0.15\ D_{Ti} - 0.004. \quad (13)$$

Clearly, in order for these relations to be useful, enough must be known about the system of interest that an estimate of D_{Ti} may be made. However, this is a standard element for microprobe analysis of natural pyroxenes and in many cases the data may exist already. If not, they should be obtained. Johnson [57] measured D_{Ti} = 0.36 and D_{Zr} = 0.15 for two MORB compositions at 1245-1250°C and 8-10 kbar. This result is probably within error of the trend of [40]. Johnson and Kinzler [58] report ranges of D's measured from experiments at 8-15 kbar and 1240-1355°C on MORB and other basalts: Ti — 0.41-0.56; Zr — 0.12-0.27; Hf — 0.24-0.44; and Nb — 0.06. Watson et al. [144] measured a D_{Hf} of ~0.36 for diopside/liquid in the Di-An-Ab system at 1275°C in air.

McKay et al. [97] found $D_{Hf}^{pig/liq}$ to be 0.048 for a lunar mare basalt at 1140-1120°C and ~IW. Calculating $D_{Hf}^{pig/liq}$ using the formula of [40] yields a value of 0.23. Several reasons for this discrepancy may exist: (i) at low oxygen fugacity, some of the Ti may exist as Ti^{3+}, with a concomitant change in D; (ii) the Forsythe et al. [40] relationship may not hold for lunar pigeonites; or (iii) the high Ti concentration of the lunar basalt (~8 wt.%) may have significantly affected the melt structure. Of these, the change in Ti valence seems most likely.

Dunn [34] reported a series of 1-bar experiments to investigate changes in D with Mg# and temperature. The FeO-free endmember was made to mimic the composition of [144]. All experiments, except those run in air, were performed at QFM. Results are reported in Table 11, but the CaO contents of the pyroxenes were not given. The reasons for the change in $D_{Lu,Hf}$ values with change in fo_2 (at Mg# = 1.0) are unclear. The reasons for the constancy of D_{Sr} and D_Y are also unclear.

5.2.2. Highly incompatible alkali and alkaline earth elements. Most of the work on these elements has been done in synthetic systems. Even so, some relative incompatibilities may be inferred from these experiments.

TABLE 10. Summary of Actinide Clinopyroxene/Liquid Partitioning in Basaltic Systems

Temperature	Pressure	fo_2	D_{Th}	D_U	D_{Pb}	Composition	Reference
1190-1160°C	1 bar					Takashima Alkali Basalt	[78]
		Ni-NiO	0.027	0.010	–		
		QFM	0.036	0.011	–		
		IW+1	0.016	0.004	–		
1200-1180°C	1 bar					Juan de Fuca Tholeiite	[78]
		Ni-NiO	0.013	0.0038	–		
		QFM	0.012	0.0047	–		
		IW+1	0.008	0.015	–		
1200°C	14 kbar					Kilauea Tholeiite	[133]
		QFM(?)	0.021	0.014	–		
1200-1300°C	1 bar					Various Synthetic Mixes	[6]
		QFM+0.8	0.005	0.002	–		
		IW+0.5	0.0005	0.0005	–		
		IW+0.5	0.0014	0.0014	–		
		IW+0.5	0.0005	0.0005	–		
		IW+0.5	0.0004	0.0004	–		
		Air	0.004	0.0003	–		
		Air	0.003	0.0001	–		
		Air	0.003	0.00011	–		
		Air	0.0008	0.00006	–		
1240°C	10-12 kbar	QFM				Various Synthetic Mixes	[6]
			0.0019	0.0013	0.0075		
			0.005	0.004	0.01		
			0.001	0.001	0.005		
			0.0012	0.0009	0.005		

TABLE 11. Change in $D^{cpx/liq}$ with Mg# and Temperature*

Element	D					
Sc	2.6	–	–	–	–	–
V	<0.15	0.89	–	–	3.6	–
Sr	0.12	–	0.09	0.09	–	0.09
Y	0.27	–	0.16	0.16	–	0.17
Zr	0.33	–	–	–	–	–
Nb	<0.008	–	–	–	–	–
Lu	0.29	0.23	–	–	0.43	–
Hf	0.48	0.18	–	–	0.64	–
Ta	0.03	–	–	–	0.06	–
Mg#	1.0 (Air)	1.0	0.8	0.6	0.5	0.4
T(°C)	1270	1270	1235	1205	1180	1157

*From [34].

Shimizu [125] performed 15-30 kbar experiments at 1100-1200°C and measured diopside/liquid partition coefficients for Rb, Cs and Ba in the Di-An-Ab system. D_{Rb} was found to be 0.001-0.004, D_{Cs} was 0.0003-0.004, and D_{Ba} was 0.0008-0.002. Working in the same system in air at one bar and 1275°C, Watson et al. [144] measured a D_{Cs} of 0.004. Brenan and Watson [14] performed augite/carbonate liquid partitioning at 1150°C and 15 kbar and found D_{Ba} = 0.00047 and D_{Cs} = 0.00023. (For comparison to silicate systems, Walker and Jones [135] found that $D_{Ba}^{carb/liq}$ at 1100°C and 10 kbar was 2.1, and the systematics of their experiments predict that $D_{Cs}^{carb/liq}$ will be about 3.)

5.3. Plagioclase/Liquid

No experimental measurements have been made of Hf, Ta, or Cs in plagioclase. McCallum and Charette [88] give an upper limit for $D_{Zr,Nb}$ of <0.01.

Drake and Weill [31] presented measurements of D_{Ba} in natural and synthetic systems at one bar pressure. D_{Ba} ranged from 0.14 to 0.6. Regression of lnD *vs.* 1/T, either using all the data or using only natural liquids, gives similar results. The regression of [31] is

$$\ln D_{Ba} = 11800/T - 8.85 \quad (14)$$

where T is in Kelvin. At a given temperature, the D_{Ba} values of [94, 95] are somewhat lower than those of [31] (D_{Ba} = 0.15-0.16, 1200-1240°C), possibly because of the low alkali contents of their lunar liquids (however, see Section 3.4 on REE partitioning into plagioclase). It has been shown that D_{Ba} increases as the concentration of K in the feldspar increases [83].

Experimental results for Rb are less numerous than those for Ba. McKay and Weill [94, 95] give one-bar D_{Rb} values of 0.017 and 0.08 at 1200 and 1240°C, respectively, for lunar basalt compositions. This increase of D with temperature is counter-intuitive and is probably because the 1240°C experiment contained larger amounts of alkalis.

Longhi et al. [85] presented plagioclase/liquid D_{Mg} and D_{Fe} data for lunar basalts. Their experiments were performed using iron capsules (sealed in evacuated silica tubes) at temperatures of ~1200°C. These authors found that D_{Fe} was 0.02 and that D_{Mg} was ~0.05.

Phinney [114] found that D_{Fe} of plagioclase remained rather constant (~0.03) in one-bar experiments at 1180°C as fo_2 varied from IW-1 to QFM. Above QFM the partition coefficient increased, presumably because of the increasing amount of Fe^{3+} in the silicate liquid.

5.4. Garnet/Liquid

Almost no experiments have been performed for garnet/liquid partitioning of highly incompatible elements. Irving and Frey [55] report a D_{Hf} of 0.53 for a natural dacite composition (+15% H_2O) at 950°C and 30 kbar. Beattie [7] reports D_{Ba} for garnet at 30-36 kbar and 1300-1565°C of 1-6 x 10^{-5}, but even these low values may represent upper limits to the true D.

5.5. Ultra-High Pressure Partitioning

Kato et al. [73] report that $D^{maj/liq}$ for K, Sr, Ba, Cs, Rb, La, Th, U and Nb are all less than 0.1. However, Hf and Zr were found to have $D^{maj/liq}$ of 0.2-0.8 and 0.15-0.6, respectively [73]. Kato et al. [74] also found that Zr and Hf partition strongly into Mg-perovskite, where measured $D^{Mg\text{-}pv/liq}$ ranged from 1.7-21 and 1.1-3.3, respectively. For comparison, Yurimoto and Ohtani [149] found D_{Zr} and D_{Hf} for majorite-liquid to both be 0.4; and Ohtani et al. [112] found majorite-liquid D_{Zr} and D_{Hf} to be 0.46 and 0.69, respectively.

6. SIDEROPHILE ELEMENTS

6.1. Solid Fe-Ni Metal/Liquid Metal, Troilite/Liquid Metal, and Schreibersite/Liquid Metal Partitioning

With some notable exceptions such as P, many siderophile elements in the Fe-Ni system show only small preferences for the solid or liquid. Consequently, D values are typically near unity, within a factor of two. As non-metals such as S and P are added to the system, most siderophile elements' D's increase. In some cases, though, the opposite is true. For example, as S is added to the Fe-Ni system, $D_{Cr}^{sm/lm}$ drops rapidly, because Cr is chalcophile. In general, S has the strongest effect on partitioning, the effect of P is weaker and the effect of C is weakest. This, however, is only a generality and may not hold for a specific element. The basic strategy for estimating parti-tion coefficients in complex metallic systems (i.e., Fe-Ni-S-P-C) is to sum the effects of nonmetals, extrapolating from simpler systems containing only one nonmetal.

Below, most data in this subsection are given as regression parameters for partition coefficients in the ternary Fe-Ni-S, Fe-Ni-P, and Fe-Ni-C systems following [67]. The D's are *molar* D values. This is somewhat inconven-ient, but the systematics do not work for *weight* D's. As a simple rule of thumb, at low S concentrations molar and weight D's are nearly the same; at high S concentrations in the Fe-Ni-S system the molar D is lower by about 30%.

6.1.1. Parameterization. It has been found, empirically, that solid metal/liquid metal (i.e., sm/lm) D's are best parameterized using composition of the metallic liquid, as opposed to using temperature or some other parameter-

TABLE 12. $\ln D_{M*}^{sm/lm}$ in the Fe-Ni-S System#

$\ln D_{M*}^{sm/lm}$	Slope β	Intercept $\ln D_{oM*}^{sm/lm}$ $X_N = 0$	σ lnD	Correlation Coefficient (r)	Number of Data Points
P	-1.433	-2.433	0.156	0.984	33
Cr	0.533	-0.684	0.016	1.000	3
Co	-0.671	-0.028	0.034	0.998	4
Ni	-0.339	-0.101	0.056	0.983	50
Ga	-1.497	-0.406	0.165	0.994	4
Ge	-1.753	-0.547	0.132	0.993	21
Ir	-2.600	0.498	0.145	0.995	12
Au	-1.137	-1.398	0.143	0.991	11

#Modified from [67].

TABLE 13. $\ln D_{M*}^{sm/lm}$ in the Fe-Ni-P System#

$\ln D_{M*}^{sm/lm}$	Slope β	Intercept $\ln D_{oM*}^{sm/lm}$ $X_N = 0$	σ lnD	Correlation Coefficient (r)	Number of Data Points
Ga	-1.167	-0.433	0.032	0.998	3
Ge	-0.888	-0.523	0.063	0.991	8
Ir	-1.018	0.430	0.135	0.970	6
Au	-0.750	-1.117	0.153	0.948	6
Ni	0	-0.101	–	–	15
P	~0	-2.433	–	–	19

#Modified from [67].

TABLE 14. $\ln D_{M*}^{sm/lm}$ in the Fe-Ni-C System#

$\ln D_{M*}^{sm/lm}$	Slope β	Intercept $\ln D_{oM*}^{sm/lm}$ $X_N = 0$	σ lnD	Correlation Coefficient (r)	Number of Data Points
Ge	-1.129	-0.572	0.081	0.978	9
Ir	-1.631	0.382	0.195	0.969	6
Au	-1.905	-1.248	0.104	0.992	6
Ni	-0.441	-0.140	0.041	0.953	9

#Data from [66, 148].

ization. In detail, $\ln D_{M*}^{sm/lm}$ is regressed vs. $\ln(1-\alpha n X_N)$, where X_N is the mole fraction of nonmetal and α is a constant for a particular ternary system. Jones and Malvin [67] demonstrated that this particular type of formulation will sum the effects of nonmetals from simpler systems such as Fe-Ni-S and Fe-Ni-P to predict partitioning in the Fe-Ni-S-P system. However, there were few data from the Fe-Ni-C system available at that time and still no partitioning data yet exists on the Fe-Ni-S-C or Fe-Ni-P-C systems to further test the model of [67].

Thus, for the binary system Fe-Ni, $D_{M*}^{sm/lm}$ is either measured directly, estimated from Fe-M binary phase diagrams, or taken as the y-intercept of regressions of $\ln D_{M*}^{sm/lm}$ vs. $\ln(1-\alpha n X_N)$, and will be designated as $D_{oM*}^{sm/lm}$.

For ternary systems, such as Fe-Ni-S, Fe-Ni-P, and Fe-Ni-C,

$$\ln D_{M*}^{sm/lm} = \ln D_{oM*}^{sm/lm} + \beta_N \ln(1- \alpha_N n X_N) \quad (15)$$

where β_N is a regression constant for each tracer element;

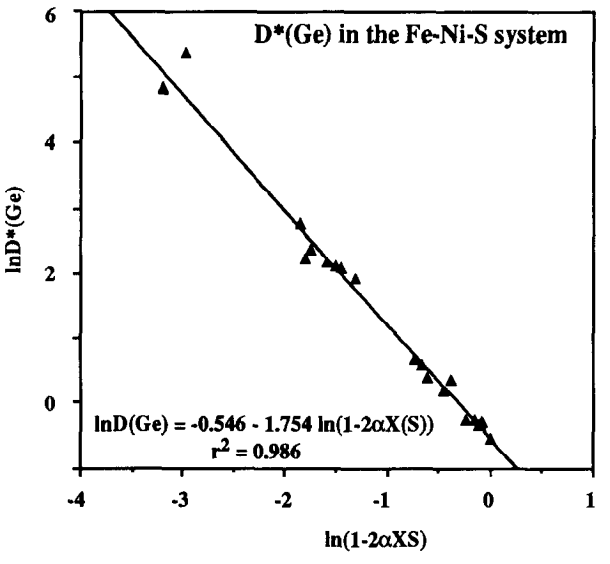

Figure 11. $\ln D_{Ge^*}^{sm/lm}$ *vs.* $\ln(1 - 2\alpha X_S)$. The type of parameterization given in the figure serves to linearize solid metal/liquid metal partition coefficients in the Fe-Ni-S, Fe-Ni-P and Fe-Ni-C systems. In the case shown, D changes by a factor of 250 as S is added to the nonmetal-free system.

α_N is taken to be 1.09, 1.36, and 1 in the S-, P- and C-bearing systems, respectively; and n is a stoichiometry coefficient, being either 2, 4 or 4 in the S-, P- and C-bearing systems, respectively. Data for these systems are tabulated in Tables 12, 13, 14. Figure 11 shows the parameterization of $\ln D_{Ge^*}^{sm/lm}$ in the Fe-Ni-S system. The parameter $\ln(1 - \alpha_S n X_S)$ serves to linearize the $\ln D_{M^*}^{sm/lm}$ data over a range of ~200 in D (0.58-~150).

For quaternary systems such as Fe-Ni-S-P (and perhaps others),

$$\ln D_{M^*}^{sm/lm} = \ln D_{oM^*}^{sm/lm} + [(2X_S\beta_S + 4X_P\beta_P)/(2X_S + 4X_P)] [\ln(1 - 2\alpha_S X_S - 4\alpha_P X_P)]. \quad (16)$$

In principle, this type of summation could be extended to quinternary systems and beyond, but experimental tests of the veracity of this method have only been performed for a very limited number of tracers in the quaternary Fe-Ni-S-P system.

6.1.2. Effect of pressure. All the experiments summarized above were performed at one bar. There is very limited data on how these partition coefficients may change with pressure. However, Jones and Walker [68] found that, using the parameterization of [67], most of their partition

TABLE 15. Partition Coefficients (wt.%) Near the Fe-S Eutectic Temperature

	Ni	Mo	Rh	Pd	Ag	Au	Tl	Pb	Ru
				D (Solid metal/liquid metal)					
Fleet & Stone [38]	1.4	–	60	1.4	–	–	–	–	–
	±0.15	–	±30	±0.3	–	–	–	–	–
Jones et al. [70]	~2	2.7	–	1.3	~0.01	6.4	0.00002	<0.00005	–
	–	±0.2	–	±0.1	–	±0.4	±0.00001	–	–
				*D (Troilite/liquid metal)**					
Fleet and Stone [38]	0.23	–	0.2	~0.02	–	–	–	–	1.1
	±0.05	–	±0.1	–	–	–	–	–	±0.6
Jones et al. [70]	~0.1	2.0	–	0.007	~0.01	–	0.0003	~0.005	–
	–	±0.2	–	±0.005	–	–	±0.0001	–	–
				*D (Schreibersite/liquid metal)***					
Jones et al. [70]	1.5-3	10.6	–	1.01	≤0.02	0.11	0.00001	0.024	–
	–	±0.4	–	±0.02	–	±0.05	±0.000005	±0.013	–

*"Troilite" may in some cases be pyrrhotite $Fe_{1-x}S$.

**Schreibersite is $(Fe,Ni)_3P$.

TABLE 16. Variation of D (Solid Metal/Silicate Liquid) With fo_2 Along Isotherms

Element	Reference	Isotherm	D equation	Valence
	Metal/Silicate Partition Coefficients That Are Compatible With Accepted Ionic Valences			
P	[107]	1190	$\log D(P) = -1.21 \log fo_2 - 15.95$	5+
P	[107]	1300	$\log D(P) = -1.53 \log fo_2 - 17.73$	
P	[123]	1300	$\log D(P) = -1.16 \log fo_2 - 13.00$	
P	[123]	1600	$\log D(P) = -0.90 \log fo_2 - 7.02$	
W	[123]	1600	$\log D(W) = -1.07 \log fo_2 - 8.68$	4+
W	[115]	1300	$\log D(W) = -1.07 \log fo_2 - 12.23$	
W	[115]	1600	$\log D(W) = -0.91 \log fo_2 - 7.02$	
Ga	[123]	1300	$\log D(Ga) = -0.77 \log fo_2 - 8.22$	3+
Ga	[123]	1600	$\log D(Ga) = -0.68 \log fo_2 - 5.45$	
Ga	[33]	1190	$\log D(Ga) = -0.92 \log fo_2 - 11.9$	
Ga	[33]	1300	$\log D(Ga) = -0.77 \log fo_2 - 8.8$	
Mo	[115]	1300	$\log D(Mo) = -1.01 \log fo_2 - 9.31$	4+
Mo	[115]	1600	$\log D(Mo) = -0.98 \log fo_2 - 5.66$	
Mo	[123]	1300	$\log D(Mo) = -0.89 \log fo_2 - 8.03$	
Co	[52]	1260	$\log D(Co) = -0.67 \log fo_2 - 6.18$	2+
Ni	[52]	1260	$\log D(Ni) = -0.54 \log fo_2 - 3.16$	2+
	Metal/Silicate Partition Coefficients That Are Not Compatible With Accepted Ionic Valences			
Ga	[115]	1300	$\log D(Ga) = -0.35 \log fo_2 - 2.6$	1.5+
Ga	[115]	1600	$\log D(Ga) = -0.35 \log fo_2 - 1.8$	1.5+
Ge	[123]	1300	$\log D(Ge) = -0.52 \log fo_2 - 3.27$	2+
Ge	[123]	1600	$\log D(Ge) = -0.50 \log fo_2 - 1.57$	2+
Co	[123]	1300	$\log D(Co) = -0.22 \log fo_2 - 0.51$	1+
Co	[123]	1600	$\log D(Co) = -0.33 \log fo_2 - 0.95$	1+
Ni	[123]	1300	$\log D(Ni) = -0.21 \log fo_2 + 0.83$	1+
Ni	[123]	1600	$\log D(Ni) = -0.32 \log fo_2 - 0.09$	1+
W	[123]	1300	$\log D(W) = -1.65 \log fo_2 - 18.51$	6+

coefficients (Au, Ni, P) remained unchanged up to 80 kbar. $D_{Ge^*}^{sm/lm}$ did, however, increase by a factor of two at 80 kbar. The Jones and Walker [68] $D_{Ni^*}^{sm/lm}$ data were also consistent with those of [134], who performed Ni partitioning experiments at 60 and 150 kbar. On the basis of limited data, it appears that pressure has only a weak effect on solid metal/liquid metal partitioning. However, the highly siderophile elements may show modest (~2x) increases at pressures near 100 kbar.

6.1.3. Experiments near the Fe-S eutectic temperature. Fleet and Stone [38] and Jones et al. [70] have performed reconnaissance experiments at temperatures of 900-1000°C. Attainment of equilibrium at these temperatures is sometimes difficult and variation in D's of a factor of two are observed (Table 15). Even so, these experiments probably give the correct sense of partitioning. The partition coefficients are given below *by weight* (Table 15).

TABLE 17. High Pressure Partition Coefficients, Metal/Silicate and Metal/Oxide, for V, Cr and Mn*

Fe metal/	T (°C)	P (GPa)	D_V	D_{Cr}	D_{Mn}
olivine	1700	10	0.25 ± 0.08	0.5 ± 0.25	0.08 ± 0.03
clinopyroxene	1500	3	0.14 ± 0.04	0.5 ± 0.15	0.02
garnet	1500	3	0.1 ± 0.06	0.5 ± 0.12	0.03 ± 0.01
majorite	1700	17	0.15 ± 0.07	0.22 ± 0.07	0.07 ± 0.03
β-spinel	1700	17	0.18 ± 0.07	0.33 ± 0.16	0.1 ± 0.05
perovskite	1800	24.5	0.18	0.3	0.1
Magnesiowüstite	1700-2000	15-22	0.1 ± 0.05	0.2 ± 0.08	0.08 ± 0.02

*From [120].

TABLE 18. Partition Coefficients of Some Siderophile Elements at Low Oxygen Fugacity*

Element	*Liquid Sil./Liquid Met.*	*Solid Met./Liquid Met.*	*Solid Sil./Liquid Sil.***
W	1	36	0.01
Re	5×10^{-4}	83	<1
Ir	5×10^{-5}	83	>10
Mo	8×10^{-4}	2.5	0.01
Ni	2×10^{-4}	1.3	10
Co	7×10^{-3}	2.3	3
Au	1×10^{-4}	1.3	<1
P	0.24	1.7	0.02
Ga	0.8	6	0.4
Ag	0.01	0.01	0.4
Pb	0.15	~0.0005	0.04

*Appropriate for T = 1250-1270°C, $\log fo_2$ = -12.75 (QFI-1), C_S^{lm} = ~25 wt.% [65].
**Inferred from natural systems and experiments.

TABLE 19. Silicate Liquid/Sulfide Liquid Partition Coefficients for Some Siderophile Elements at High fo_2

Element	T (°C)	P	fo_2	D	Reference	Wt.% S
Pt	1300	1 bar	<MW	0.01-0.0001	[39]	42-49
Pd	1300	1 bar	<MW	0.001-0.00001	[39]	42-49
Ir	1300	1 bar	<MW	0.001-0.00001	[39]	42-49
Pt	1200	1 bar	$10^{-9.2}$ (MW)	0.0001	[128]	37-38
Pd	1200	1 bar	MW	0.00001	[128]	37-38
Ir	1200	1 bar	MW	0.00001	[128]	37-38
Au	1200	1 bar	MW	0.001	[128]	37-38

MW = magnetite-wüstite buffer.

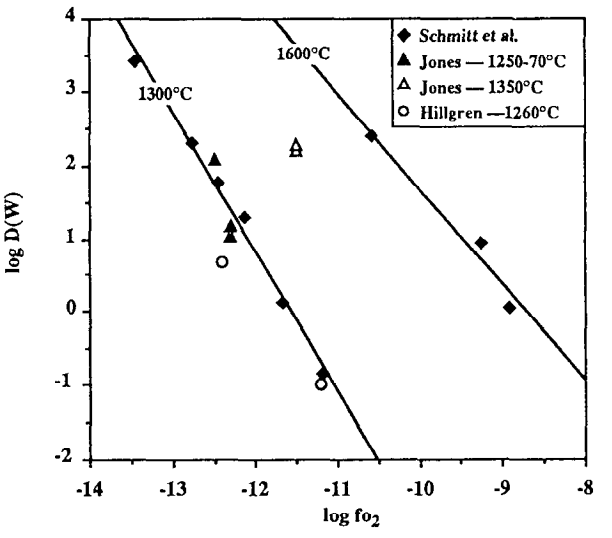

Figure 12. $LogD_W^{sm/lm}$ *vs.* $Logfo_2$. Data at 1300 and 1600°C are from [123] in a nonmetal-free system (diamonds). Lower-temperature data obtained from S-bearing systems from Jones (unpublished; solid triangles) and from [52], solid circles, agree reasonably well with the data from [123], whereas they should not. Apparently the introduction of S has served to increase $D_W^{sm/lm}$. Open triangles are from Jones (unpublished) at 1350°C.

6.1.4. Ultra-high pressure partitioning. Ringwood et al. [119] have presented partition coefficients for Cr, V and Mn between iron metal and Fe-O liquid at high pressure. At 1700°C and 160 kbar, the solid metal/liquid metal partition coefficients for V, Cr and Mn are 0.14, 0.20, and 0.25, respectively.

6.2. Solid Metal/Silicate Liquid Partitioning.

6.2.1. Low pressure partitioning. Presently this sub-discipline is in a state of some confusion. Different laboratories and workers have obtained different results, depending on the composition of the system, the presence of nonmetals such as S, and the analytical technique employed. In addition, controversial claims have been made for the presence of zero-valent Ni and Co in silicate liquids [21, 36] and for other non-traditional valences of the tracer element in the silicate liquid [115, 123]. Others, such as [2], typically obtain the traditionally accepted valences and do not see evidence of zero-valent Ni and Co in the silicate phase. The compilation of 1-bar data below (Table 16) separates the experiments which yield traditional valences from those which do not.

6.2.2. Ultra-high pressure partitioning. Although there was no silicate liquid present, Ringwood et al. [120] have presented partition coefficients for V, Cr and Mn between solid Fe metal and other solid silicate or oxide phases. A summary of these results is given in Table 17. Many of these data have large error bars and should be considered preliminary. Even so, differences in D probably reflect real differences in siderophility. For example, Mn typically always has the smallest value of D.

6.3. Liquid Metal/Liquid Silicate

In an ideal world the parameterizations of solid metal/silicate liquid and those of solid metal/liquid metal would be sufficient to yield liquid metal/liquid silicate partition coefficients. However, as might be expected given the uncertainties described earlier in the section, there appear to be significant differences between systems that contain nonmetals and those that do not. Therefore it is often not possible to calculate an accurate liquid metal/silicate liquid partition coefficient using a solid metal/silicate liquid D obtained from a nonmetal-free experiment and a solid metal/liquid metal D from a nonmetal-bearing experiment.

Figure 12 shows several data sets for $D_W^{sm/liq}$ to illustrate this problem. The Hillgren [52] and Jones (unpublished) experiments contained S, whereas the Schmitt et al. [123] experiments did not. The 1250-1270°C D_W data of [52] and those of Jones scatter about the Schmitt et al. 1300°C line, even though the experiments were performed at significantly lower temperatures. The 1350°C data of Jones (unpublished); shows the amount of change in D that might be expected over a 50-100°C temperature interval. The addition of S appears to have caused the W partition coefficients to increase significantly.

Because of the difficulty of these experiments, an issue that has not really been addressed is that of Henry's law. Fleet et al. [39] have presented data which suggest that, for highly siderophile elements such as Ir and Pt, Henry's law is not obeyed when there is as much as a few hundred ppm of these elements in the metallic liquid. In other words, it may be that many metal/silicate partitioning experiments that utilize %-level doping were not performed within the Henry's law region.

TABLE 20. Liquid Metal/Liquid Silicate Partitioning of V, Cr and Mn*

$LogD^{lm/ls} = A\ Logfo_2 + B$

LogD	A	B	r^2
V	-0.76	-10.3	0.95
Cr	-0.42	-5.31	0.76
Mn	-0.58	-8.73	0.91

*From [32].

TABLE 21. Henry's Law Constants for Noble Gas Solubilities in Silicate Liquids at 1350°C*

Composition	He	Ne	Ar	Kr	Xe
Andesite	–	–	15.4±1.0	11.4±0.8	8.3±1.1
Leucite-Basanite	70±9	42±7	12.2±0.8	9.3±0.6	3.5±0.5
Tholeiite	64±8	35±6	8.7±0.6	6.3±0.4	2.7±0.4
Alkali-olivine basalt	57±7	26±5	6.4±0.4	4.4±0.3	1.5±0.2
Ugandite	48±6	21±4	4.5±0.3	3.0±0.2	1.0±0.1

*Data from [86]; Values in units of 10^{-5} cm^3/g/atm at STP.

Another possible problem is that of the NiS content of the system. Fleet et al. [39] observed that the liquid metal/liquid silicate partition coefficients of Ir and Pd depended more on Ni content of the metallic liquid than on fo_2. *A priori*, given the extent of solid and liquid solution in the Fe-Ni-S system, this result seems unlikely. An alternative explanation is that the concentration of NiS in these experiments is the best indicator of the true oxygen fugacity. With the exception of those that contained graphite, the experiments of [39] were self-buffered. Consequently, reactions involving Ni may ultimately control the fo_2 of the system. Note that, if this interpretation is correct, $D^{lm/liq}$ *decreases* with decreasing oxygen fugacity. If so, this would suggest that noble metals do not enter the silicate liquid as oxide species. This observation may also explain the problem with W discussed above. More work is necessary to resolve this issue.

6.3.1. Siderophile element partitioning. Two examples are presented below: (i) an internally consistent set of partition coefficients for a particular temperature at a low fo_2 (Table 18) from [65]; and (ii) liquid metal/silicate liquid partition coefficients obtained from experiments at high fo_2 (Table 19) from [39, 128].

Fleet and MacRae [37] have also presented data for olivine/sulfide liquid equilibria for Fe and Ni. Also, Klöck and Palme [75] and Peach et al. [113] have presented siderophile-chalcophile partitioning data from naturally-occurring immiscible, sulfide-silicate liquids.

TABLE 22. Henry's Law Constant for Noble Gas Solubility *vs.* Atomic Radius (Å)

Basalt Composition	Slope (-a)*
Leucite-Basanite	0.869
Tholeiite	0.958
Alkali-Olivine Basalt	1.055
Ugandite	1.141

*From [86]. In units of cm^3 STP/(g atm)/Å.

6.3.2. V-Cr-Mn partitioning. Drake et al. [32] have presented V, Cr and Mn partition coefficients between S-bearing liquid metal and silicate liquid. Regressions of their (1 bar, 1260°C) data give the oxygen fugacity dependencies of the partitioning behaviors of these elements. Three Cr experiments at low oxygen fugacity (two of which were reversals) are omitted from the regression. Results are given in Table 20. The valences implied by these regressions are approximately 3+, 2+ and 2+ for V, Cr and Mn, respectively.

7. NOBLE GASES

7.1. Vapor-Silicate Liquid Partitioning.

The solubilities of noble gases in silicate melts are complex functions of several variables: pressure, melt composition, temperature. Good discussions are given by [17, 86, 147]. In general, noble gas solubilities remain constant or (counterintuitively) increase with increasing temperature, increasing pressure, and increasing molar volume of the silicate liquid. Noble gases with small atomic radius are more soluble than their larger counterparts (He is more soluble than Xe). These observations are consistent with the notion that noble gases squeeze into "holes" in the silicate liquid. The higher the temperature or molar volume, the bigger the available hole. The smaller the gas atom, the easier the fit. Below are regressions for some of these dependencies.

Most noble gas experiments at one bar indicate that Henry's law is obeyed in vapor-liquid equilibrium:

$$X_i = k_i P_i \qquad (17)$$

where X is the solubility of gas *i* in cm^3/g at STP, k is the Henry's law constant and P is the partial pressure of *i*. A summary of Henry's law constants is given in Table 21.

Thus, if there was a partial pressure of 10^{-8} atmospheres of Ar above a 1350°C andesitic melt, we would predict that the melt would contain 15.4 x 10^{-13} cm^3 STP Ar per gram of

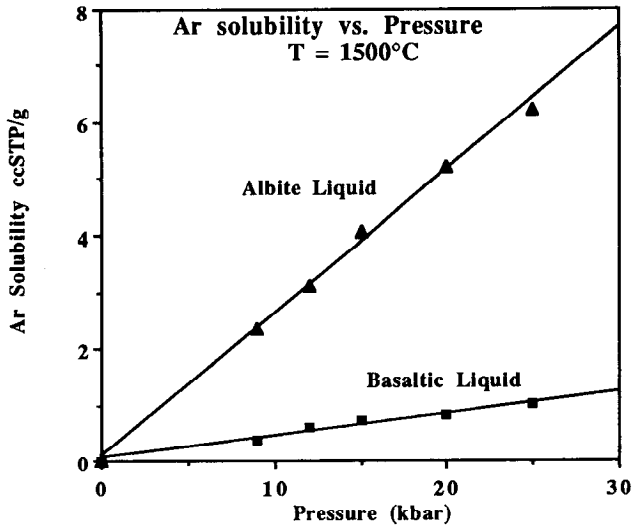

Figure 13. Ar solubility in silicate liquid *vs.* pressure. Triangles represent the solubility of Ar in a melt of albite composition and the squares illustrate solubility in a tholeiite. The linear fits to the data indicate that Henry's law is obeyed. Data are from [147].

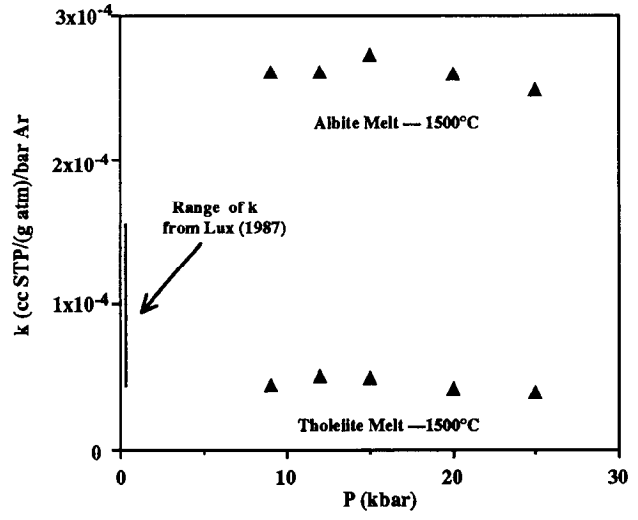

Figure 14. Henry's law constant for Ar solubility in silicate liquid *vs.* pressure. Data from Figure 11 are compared to those of [86]. This figure reemphasizes the constancy of the Henry's law constant with pressure and illustrates that the results from [147] are broadly consistent with those of [86].

melt. Changing the temperature slightly should have little effect on this calculation.

For different atomic radii, k_i changes as

$$\ln k_i = a\, r^2(i) + b. \quad (18)$$

For the melts studied by Lux [86], *b* is constant at -5.8±0.2, whereas *a* is a function of melt composition (Table 22).

Studies to date indicate that pressure plays a strong role in noble gas solubilities, but in a predictable manner. Figure 13 shows that Ar solubility increases with increasing pressure. However, it appears that noble gases obey Henry's law and that the Henry's law constant does not greatly change in the region 1 bar - 25 kbar. Figure 14 shows Henry's law constants for Ar in selected high pressure experiments of White et al. [147] and for the 1-bar experiments of Lux [86]. The similarity between k_{Ar} of the basalts of [86] and [147], as well as the constancy of the k's of [147], implies a very weak pressure dependence on k.

7.2. Mineral-Melt Partitioning

Crystal-liquid partitioning of noble gases is a field that is still in its infancy. There has been speculation that large partition coefficients (>~0.1) for noble gases were actually due to incomplete separation of crystal and glass prior to gas extraction and mass spectrometric analysis. To avoid this difficulty, M. J. Drake and coworkers [e.g., 17] have attempted to simultaneously equilibrate separate aliquots of

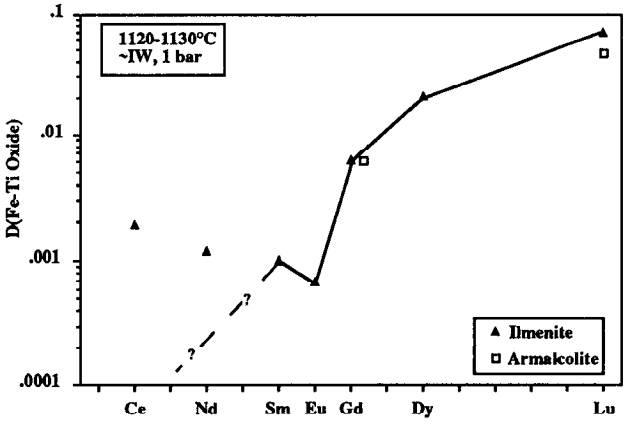

Figure 15. D_{REE} for Fe-Ti oxides. Data are from [93] and [106]. Ilmenite and armalcolite D patterns appear similar. The apparent enrichment in $D_{LREE}^{Ilm/liq}$ may be an artifact of incomplete separation of glass from crystal. The negative Eu anomaly is appropriate for reducing conditions only.

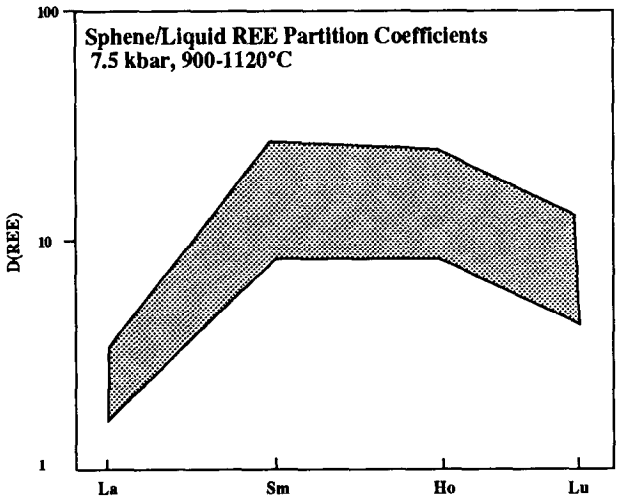

Figure 16. D_{REE} for sphene/liquid. Data are from [43]. The D pattern is rather similar to that for amphibole (see Figure 10), but the absolute D values are somewhat higher. The similarity of temperatures and pressures between the sphene experiments of [43] and the amphibole experiments of [108] suggests that this difference is real.

crystals and liquid under a flowing noble gas. The difficulty is that the crystals have defect structures that are determined by their past history and, consequently, plagioclases (for example) of different provenance yield different partition coefficients. It may be that the solubility of noble gases in minerals is not determined by chemical reactions, but by some physical process. Because of these uncertain-ties no data will be tabulated here. However, data can be found in [15, 16, 17, 53].

8. ACCESSORY PHASES

8.1. Ilmenite-Armalcolite/Liquid

Figure 15 shows ilmenite and armalcolite REE partition coefficients from [97] and [106]. It is possible that the partition coefficients for the LREE are influenced by incomplete separation of crystal and glass. McKay et al. [97] also measured Zr and Hf partition coefficients, which were 0.33 and 0.42 for ilmenite and 0.9 and 1.5 for armalcolite, respectively. These values for Zr are in basic agreement with those of [88]. McCallum and Charette [88] also measured D_{Nb} = 0.81 for ilmenite and D_{Nb} = 1.4 for armalcolite in a high-Ti mare basalt at 1100-1130°C and ~IW (1 bar). Green and Pearson [44] report D_{Nb} = 2.3 and D_{Ta} = 2.7 for a hydrous, ilmenite-saturated basaltic andesite at 950°C and 7.5 kbar near the magnetite-wüstite (MW) buffer. Ringwood and Essene [118] measured Cr and V partition coefficients for ilmenite and armalcolite in a 1-bar experiment on a mare basalt composition at 1200°C near IW. The D_V for ilmenite and armalcolite was 18 and 12, respectively. The D_{Cr} for ilmenite and armalcolite was 7 and 6, respectively. LaTourette and Burnett [77] report that D_U for ilmenite/natural granitic liquid is <0.13.

8.2. Rutile/Liquid

Ryerson and Watson [122] have given an expression for rutile saturation in silicate liquids, expressed as $D_{TiO_2}^{rut/liq}$.

$$\ln D_{TiO2}^{rut/liq} = \ln (100/TiO_2(\text{wt.\%. liq})) = -3.16 + (9373/T) + 0.026\,P - 0.152\,FM \quad (19)$$

where T is temperature in Kelvin, P is pressure in kbar and FM is a melt composition parameter

$$FM = [Na + K + 2(Ca + Fe + Mg)]/(Al * Si) \quad (20)$$

and all element symbols represent cation fraction in the silicate liquid. If $100/TiO_2$(liq) exceeds the calculated D, then rutile should be unstable.

Green and Pearson [44] give rutile partition coefficients for Nb and Ta. Experimental conditions were 1000°C and 4-16 kbar near MW. Liquid compositions were hydrous andesite and trachyte. D_{Nb} = 26-30 and D_{Ta} = 44-45. The sense of partitioning is similar to that observed by [146] in synthetic systems.

8.3. Sphene/Liquid

Green and Pearson [43] have measured D_{REE} and D_{Sr} for sphene/liquid over a wide range of temperatures, pressures,

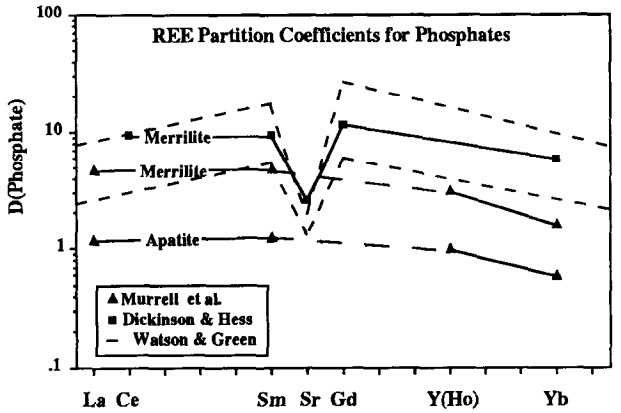

Figure 17. D_{REE} for apatite and merrilite (whitlockite). Data are from [102, 26, 140]. While the patterns of both phosphate minerals are similar, merrilite concentrates REE over apatite [102]. Both minerals will have negative Eu anomalies at low oxygen fugacity.

TABLE 23. Zircon/Liquid Partition Coefficients

$D_{REE}^{zir/liq}$	La	Sm	Ho	Lu
Watson [138]	1.4-2.1	26-40	>340	72-126
Dickinson et al. [27]	0.1-0.3	0.5-1.0	3.0-7.0	–

TABLE 24. Magnetite/Liquid Partition Coefficients*

Ni	Co	Mn	Cr	Sc	V
20-80	6-17	1.7-1.8	100-600	0.8-3.3	~0-70

*From [81].

bulk compositions, and oxygen fugacities. The range of D_{REE} observed at 7.5 kbar is shown in Figure 16. Strontium in these same experiments gave D values ranging from <0.1 to 0.47. Green and Pearson [44] also measured Nb and Ta partition coefficients for sphene. Silicate melts were hydrous basaltic andesite, andesite, and trachyte at 950-1000°C and 4-16 kbar at MW. Partition coefficients for Nb ranged from 3.5 to 7.6 and those for Ta ranged from 10.6 to 19.6.

8.4. Apatite-Merrilite (Whitlockite)/Liquid

Harrison and Watson [48] found that the saturation surface of apatite for silicate liquids was relatively insensitive to variables other than temperature and silica activity. The experimental data are well fitted by

$$\ln D_P^{apa/liq} = \ln (\text{wt.\% } P_2O_5(\text{apatite})/\text{wt.\% } P_2O_5(\text{liquid}) = [(8400 + ((SiO_2 - 0.5)\, 2.64 \times 10^4))/T] - [3.1 + (12.4\,(SiO_2 - 0.5))] \quad (21)$$

where T is in Kelvin and SiO_2 is wt. fraction silica in the silicate liquid. This relationship also predicts the D_P of the merrilite experiments of [59], further corroborating the model of [48] and suggesting that at *some* combination of silica and phosphorus activities *some* phosphate phase will crystallize. If water or halogens are present, the phase will be apatite; if they are absent the phosphate will be merrilite.

The best comparison of REE partitioning between merrilite/liquid and apatite/liquid is probably that of [102], even though the experiments were performed in a synthetic system (1200-1300°C, 1 bar, Di-An-Ab). The data are shown in Figure 17 along with the whitlockite data of [26] for a lunar basalt (1108°C, 1 bar) and the apatite data of [140], which span a wide range of conditions and compositions (950-1120°C, 7.5-20 kbar, basaltic-granitic). Merrilite accommodates lanthanides (and Pu^{3+}) over actinides, whereas apatite accommodates actinides over lanthanides (and Pu^{3+}). Strontium, which should behave similarly to Eu^{2+} is clearly excluded compared to the trivalent REE.

REE partitioning into whitlockite is particularly complex. For example, using wt.%-level doping, Henry's law is typically not obeyed because of complex interactions between the necessity for coupled substitution and the crystallography of merrilite [50, 99]. See section 4.1 for a summary of actinide partitioning into merrilite and apatite.

8.5. Zircon/Liquid

Watson and Harrison [141] have defined the zircon saturation surface in hydrous granitic melts using the relationship

$$\ln D_{Zr} = \ln(\text{wt.\% Zr in zircon/wt.\% Zr in the silicate liquid}) = \{-3.8 - [0.85\,(M-1)]\} + 12900/T \quad (22)$$

where T is temperature in Kelvin and M is defined as the cation fraction ratio

$$M = (Na + K + 2\,Ca)/(Al * Si). \quad (23)$$

This relationship appears to hold from 750 to 1500°C and 2-6 kbar. However, Watson and Harrison caution that the saturation equation is not a universal solution and does not describe the zircon saturation behavior observed by [76, 137] in other systems. Additional zircon solubility measurements on a lunar basalt and granite compositions have been given by [27].

REE partitioning into zircon has been investigated by [27, 138]. Experimental conditions were: 800°C and 2 kbar [138]; and 1135°C and 1 bar [27]. Watson's [138] composition of the silicate was that of a synthetic granite with 5 wt.% ZrO_2. Except in the case of La, Watson's partition coefficients are calculated by mass balance, because concentrations of the other REE in the silicate glass were too low to be measured. The results are given below. Dickinson et al. [27] carried out their experiments using high- and low-silica lunar compositions and measured partition coefficients directly. These results are summarized in Table 23. LaTourette and Burnett [77] report that, in a natural granitic system, $D_U^{zir/liq} < 24$.

TABLE 25. Hibonite/Liquid Partitioning of REE and Sr*

La	Sm	Sr	Gd	Yb
7	2.7	0.55	1.5	0.1

*From [29].

TABLE 26. Perovskite/Liquid Partitioning of REE, Sr and Sc

D	La	Sm	Eu	Tb	Yb	Lu	Sr	Sc
Ringwood [117]	15	17	–	–	1.2	–	1.0	–
Nagasawa et al. [105]	2.6	2.7	2.3	1.6	0.49	0.41	0.73	0.16

8.6. Magnetite/Liquid

Lindstrom [81] has measured a suite of transition element partition coefficients for magnetite/alkalic basalt at 1 bar, at log fo_2's of -4.2 to -12.9, and at 1110-1170°C. Ranges of D's are given in Table 24. D_V, in particular, is a strong function of fo_2 [54]. The values for Ni are similar to but larger than those of Leeman [79] for a Kilauea tholeiite [D_{Ni} = 19 (1250°C); D_{Ni} = 12 (1300°C)], although Leeman's experiments were performed at higher tempera-tures. LaTourette and Burnett [77] report that D_U for magnetite/natural granitic liquid is < 0.13.

8.7. Spinel/Liquid

Comprehensive studies of spinel partitioning have been given by Delano and coworkers [25, 47] and by Barnes [3]. These authors have investigated the spinel partitioning behavior of multi-valent species such as Cr and V as a function of temperature and fo_2 at one bar in basaltic systems. Hanson and Delano [47] and Delano [25] have shown that $D_{Cr}^{sp/liq}$ and (to a lesser extent) $D_V^{sp/liq}$ are strong functions of fo_2.

Nagasawa et al. [105], working in a synthetic system at one bar, find that D_{REE} are uniformly low 0.006-0.02 and that D_{Sc} is 0.05.

TABLE 27. Partitioning Between Augite and Carbonate/Silicate Liquid

Element	D(aug/carb)*	D(carb/liq)+	D(aug/liq)#
Nb	0.0059	0.52	0.0031
Mo	0.0090	5.8	0.052
Ba	0.00057	1.8	0.0010
Ce	0.030	1.0	0.030
Pb	0.0055	0.61	0.0034
Ra	–	1.8	–
Th	0.0093	0.28	0.0025
Pa	–	0.15	–
U	0.0048	0.35	0.0017

*55 kbar and 1200°C [136].
+10 kbar and 1250°C [71].
#Calculated using columns 1 and 2.

Capobianco and Drake [18] have presented data for Pd, Ru and Rh partitioning between spinel and liquid in a synthetic system (1450 and 1300°C, 1 bar). Palladium was not detectable in the spinels (D_{Pd} < 0.02) of [18], whereas $D_{Ru}^{sp/liq}$ = 22-25, regardless of temperature. Rhodium is apparently even more compatible in spinel than Ru (D_{Rh} ~100). Zoning in the spinels of the Rh-doped experiments indicates that Rh enters as $MgRh_2O_4$. In an Fe-bearing system at 1250°C, $D^{sp/liq}$ for Pd, Ru and Rh increases to 8000, 300 and 0.8, respectively [20].

8.8. Melilite/Liquid

Several studies of melilite partitioning have been carried out in systems appropriate for investigation of Allende Ca-, Al-rich inclusions. Melilite partitioning is particularly interesting because, unlike other minerals, its REE partition coefficients decrease with decreasing temperature [10]. This is a case where the composition of the solid phase (i.e., charge balance) is the dominant control on partitioning. Beckett et al. [10] give regressions for melilite partition coefficients that rely only on the composition of the melilite. In their one-bar experiments, synthetic liquids at high temperature (1420-1450°C) were slowly cooled so that melilite would fractionally crystallize until quenched at 1330-1170°C. The melilite zoning profiles were then analyzed and partition coefficients reconstructed. Their regressions are given below.

$$D_{Be}\ (\pm 0.2) = 2.24\ X_{Ak} \quad (24)$$

$$D_{Sc}\ (\pm 0.002) = 0.027\ X_{Ge} \quad (25)$$

$$D_{Ba}\ (\pm 0.007) = 0.04 \quad (26)$$

$$D_{La}\ (\pm 0.034) = 0.094\ (X_{Ge}/X_{Ak}) \quad (27)$$

$$D_{Ce}\ (\pm 0.024) = 0.072\ (X_{Ge}/X_{Ak}) \quad (28)$$

$$D_{Tm}\ (\pm 0.015) = 0.047\ (X_{Ge}/X_{Ak}) \quad (29)$$

where X_{Ak} and X_{Ge} are respectively the mole fractions of the åkermanite and gehlenite components in the melilite.

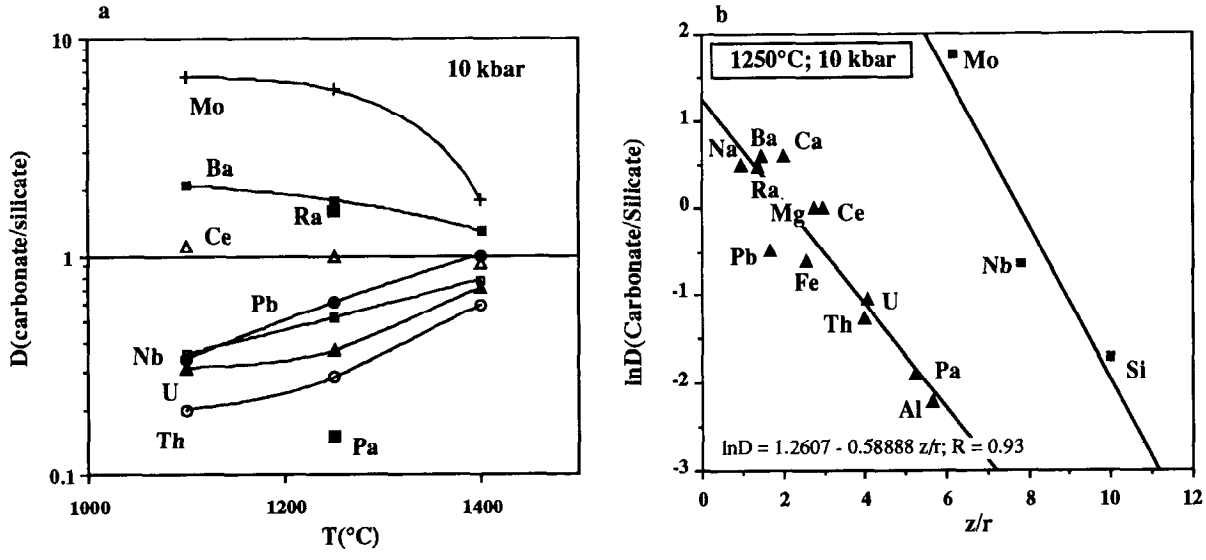

Figure 18. (a) $D^{carb/liq}$ *vs.* T. D's for a suite of elements are given as a function of T [71]. The experiments were all carried out at 10 kbar in graphite capsules. As the silicate and carbonate liquids converge in composition, all D's approach unity. (b) $\ln D^{carb/liq}$ *vs.* z/r. Partitioning in the 10 kbar, 1250°C experiment of (a) is shown as a function of ionic field strength (z/r, where z is ionic charge and r is ionic radius). For $z/r < 6$ partitioned elements form a regular array. It appears that for $z/r > 6$ there may be a second array containing elements that form anionic complexes. A regression line and a correlation coefficient are given for the D's having $z/r < 6$.

This variation in D with composition probably explains the differences in D_{REE} measured by [105, 117] (see [54]). Nagasawa et al. [105] also measured $D_{Sc}^{mel/liq}$ of 0.05-0.08 (1500°C, 1 bar), values that are several times larger than the maximum value predicted by [10]. The cause of this discrepancy is possibly that Nagasawa et al. [105] failed to achieve complete separation of crystal and glass. However, the D_{La} predicted by the equation of [10] is also about 4 times lower than that measured by [117]. The data of [105, 117] indicate that, at low fo_2, $D_{Eu^{2+}}$ and D_{Sr} are 0.75-1.2 (i.e., near unity).

8.9. Hibonite/Liquid

Drake and Boynton [29] have presented REE partitioning data for hibonite/liquid (1470°C, 1 bar) in a synthetic system. As can be seen in Table 25, at low fo_2 there will be a significant negative Eu anomaly.

8.10. Perovskite($CaTiO_3$)/Liquid

Perovskite/liquid partitioning has been investigated by [105, 117]. Ringwood [117] crystallized perovskite over the interval 1500-1350°C at one bar in a synthetic system. The Nagasawa et al. [105] experiments were performed at 1420°C at one bar, also in a synthetic system. A summary of results is given in Table 26. The large difference between the D_{LREE} of these two investigations is most probably due to differences in temperature.

9. PARTITIONING IN SYSTEMS CONTAINING CARBONATE LIQUIDS

There have been suggestions that carbonate-rich magmas may play a role in basalt petrogenesis [e.g., 100] and certainly carbonate liquids are observed in some alkali volcanic provinces, such as east Africa [e.g., 24]. But as yet, there are very few studies of trace element partitioning in carbonate-bearing systems.

9.1. Carbonate Liquid/Silicate Liquid (Carb/Liq) Partitioning

As a first approximation, it might be hoped that, if mineral/liq partition coefficients are known, mineral/carb partitioning may be calculated by multiplying through by carb/liq D's. Enough is not known to accurately test this notion, except that carb/liq D's are seldom more than a factor of a few from unity (e.g., [14]).

Carbonate liquid/silicate liquid partition coefficients have been presented by [46, 71]. Jones and coworkers [71] found

TABLE 28. Partitioning Among Augite, Olivine, and Carbonate Liquid*

D	Ba	Cs	Sr	Ce	Gd	Yb
Augite/carb	0.00047	0.00023	0.043	0.16	0.50	0.30
Olivine/carb	–	–	0.00020	–	–	0.10

*From [14].

that, as temperature increased, all partition coefficients approached (but did not reach) unity, as the liquids followed the two-liquid solvus and became more and more similar in composition (Table 27 and Figure 18). In addition, they found that there was a linear relationship between lnD and z/r (where *z* refers to ionic charge and *r* refers to ionic radius [121]) at least for values of $z/r < 6$ (Figure 18). With the exception of a few elements (e.g., Fe, Al and Hf), the data of [46] are in general agreement with those of [71]. However, the systematics of the data set of [71] are somewhat simpler, in that no tracer was observed to switch its preference for a particular liquid, as was seen in the experiments of [46]. It should be pointed out, though, that the pressure regimes of [71] and [46] and did not overlap and so there remains the possibility of systematic differences between the two studies.

Jones and Walker [69] have extended the study of [71] to P_2O_5- and F-bearing systems. However, addition of $Ca_3(PO_4)_2$ and CaF_2 components had little effect on partitioning. Both P and F were strongly partitioned into the carbonate liquid, and the addition of these components appears to promote miscibility.

In addition, Jones and Walker [69] investigated the Soret effect for their standard suite of tracers in a mixture of Na, Mg and Ca carbonates. No Soret effect was observed, indicating that carbonate/silicate partitioning should be only weakly dependent upon the composition of the carbonate liquid.

9.2 Mineral/Carb Partitioning

Walker et al. [136] have presented $D^{aug/carb}$ for a suite of trace elements. These, combined with $D^{carb/liq}$ may be used to estimate $D^{aug/liq}$. These estimates are typically in general agreement with measured values of $D^{aug/liq}$. All experiments were at high pressure (>10 kbar) in graphite capsules.

Brenan and Watson [14] have measured aug/carb and ol/carb partition coefficients for a suite of elements. Their results at 1150°C and 15 kbar are summarized in Table 28.

The $D_{Ce}^{aug/liq}$ found by [14] is quite a bit higher than that of [136]. This may reflect differences in (P, T) conditions or bulk composition.

Sweeney et al. [129] have measured amphibole/carb and garnet/carb partition coefficients at 18-33 kbar and 960-1000°C. Their representative partition coefficients are given in Table 29.

Acknowledgments. In preparing this chapter I have had the assistance of many colleagues, too numerous to mention individually, who kindly sent me reprints and preprints. Thank you, everyone. In addition, Gordon McKay, Paul Beattie, Roger Nielsen, Russ Colson, and Kevin Johnson allowed me access to access to their unpublished data, which were critical to the well-being of the chapter. Tom Ahrens, Paul Beattie, John Longhi, and Steve Jurewicz provided constructive reviews of earlier drafts. Yvette Damien and Don Bogard provided the camera-ready text. Despite all this help, there are may still be errors and omissions; these, of course, are my own. This work was supported by NASA grant 152-12-24.

TABLE 29. Partitioning Among Amphibole, Garnet, and Carbonate Liquid*

D	Ti	Nb	Zr	Ta	Ce	Y	Lu	Sr	Ba	Na	K	Rb
amphibole/carb	3.9	0.21	0.76	0.54	<0.07	0.26	–	0.10	0.12	0.57	1.8	0.38
garnet/carb	1.55	0.018	2.8	<0.12	<0.024	2.6	>17	0.01	<0.03	0.014	<0.15	<0.03

*From [129].

REFERENCES

1. Agee, C. B., A new look at differentiation of the Earth from melting experiments on the Allende meteorite, *Nature, 346,* 834-837, 1990.
2. Amelin, A. A., and C. J. Capobianco, The partitioning of Co and Ni in a simple metal/silicate system as a function of oxygen fugacity and temperature (abstract), in *Lunar and Planet. Sci. XXIII,* pp. 29-30, Lunar and Planetary Institute, Houston, 1992.
3. Barnes, S. J., The distribution of chromium among orthopyroxene, spinel and silicate liquid at atmos-pheric pressure, *Geochim. Cos-mochim. Acta, 50,* 1889-1909, 1986.
4. Beattie, P., The occurrence of apparent non-Henry's law behavior in experimental partitioning studies, *Geochim. Cosmochim. Acta, 57,* 47-55, 1993*a*.
5. Beattie, P., Trace element partitioning between silicate melts and olivines and orthopyroxenes, *Geochim. Cosmochim. Acta,* submitted, 1993*b*.
6. Beattie, P., The effect of partial melting of spinel peridotite on uranium series disequilibria: constraints from partitioning studies, *Earth Planet. Sci. Lett.,* submitted, 1993*c*.
7. Beattie, P., ^{226}Ra-^{230}Th-^{238}U dis-equilibrium and melting processes beneath ridge axes, *Nature,* sub-mitted, 1993*d*.
8. Beattie, P., C. Ford and D. Russell, Partition coefficients for olivine-melt and orthopyroxene-melt systems, *Cont. Mineral. Petrol., 109,* 212-224, 1991.
9. Beattie, P., M. Drake, J. Jones, W. Leeman, J. Longhi, G. McKay, R. Nielsen, H. Palme, D. Shaw, E. Takahashi, and E. Watson, Terminology for trace element partitioning, *Geochim. Cosmochim. Acta,* in press, 1993.
10. Beckett, J. R., A. J. Spivack, I. D. Hutcheon, G. J. Wasserburg, and E. M. Stolper, Crystal chemical effects on the partitioning of trace elements between mineral and melt: an experimental study of melilite with applications to refractory inclusions from carbonaceous chondrites, *Geochim. Cosmochim. Acta, 54,* 1755-1774, 1990.
11. Benjamin, T. M., W. R. Heuser, and D. S. Burnett, Laboratory studies of actinide partitioning relevant to ^{244}Pu chronometry, *Proc. Lunar Planet. Sci. Conf., 9th,* 1393-1406, 1978.
12. Benjamin, T. M., W. R. Heuser, D. S. Burnett, and M. G. Seitz, Actinide crystal-liquid partitioning for clinopyroxene and $Ca_3(PO_4)_2$, *Geochim. Cosmochim. Acta, 44,* 1251-1264, 1980.
13. Benjamin, T. M., J. H. Jones, W. R. Heuser, and D. S. Burnett, Laboratory actinide partitioning: whitlockite/liquid and the influence of actinide concentration levels, *Geochim. Cosmochim. Acta, 47,* 1695-1705, 1983.
14. Brenan, J. M., and E. B. Watson, Partitioning of trace elements between carbonate melt and clinopyroxene and olivine at mantle P-T conditions, *Geochim. Cosmochim. Acta, 55,* 2203-2214, 1992.
15. Broadhurst, C. L., M. J. Drake, B. E. Hagee, and T. J. Bernatowicz, Solubilities and partitioning of noble gases in mineral-melt systems -I. Synthesis and reversal experiments for Ar in anorthite and coexisting melt (abstract), in *Lunar and Planet. Sci. XIX,* pp. 136-137, Lunar and Planetary Institute, Houston, 1988*a*.
16. Broadhurst, C. L., M. J. Drake, B. E. Hagee, and T. J. Bernatowicz, Solubilities and partitioning of noble gases in mineral-melt systems -II. Synthesis experiments for Ne, Ar, Kr, and Xe in anorthite, diopside, forsterite, and coexisting melts (abstract), in *Lunar and Planet. Sci. XIX,* pp. 138-139, Lunar and Planetary Institute, Houston, 1988*b*.
17. Broadhurst, C. L., M. J. Drake, B. E. Hagee, and T. J. Bernatowicz, Solubility and partitioning of Ar in anorthite, diopside, forsterite, spinel and synthetic liquids, *Geochim. Cosmochim. Acta, 54,* 299-309, 1990.
18. Capobianco, C. J., and M. J. Drake, Partitioning of ruthenium, rhodium, and palladium between spinel and silicate melt and implications for platinum group element fractionation trends, *Geochim. Cosmochim. Acta, 54,* 869-874, 1990.
19. Capobianco, C. J., and E. B. Watson, Olivine/silicate melt partitioning of germanium: an example of a nearly constant partition coefficient, *Geochim. Cosmochim. Acta, 46,* 235-240, 1982.
20. Capobianco, C. J., R. L. Hervig, and M. J. Drake, Effect of iron on Ru, Rh and Pd crystal/melt partitioning (abstract), *Eos Trans. AGU, 71,* 1611, 1990.
21. Colson, R. O., Solubility of neutral nickel in silicate melts and implications for the Earth's siderophile element budget, *Nature, 357,* 65-68, 1992.
22. Colson, R. O., and D. Gust, Effects of pressure on partitioning of trace elements between low-Ca pyroxene and melt, *Am. Min., 74,* 31-36, 1989.
23. Colson, R. O., G. A. McKay, and L. A. Taylor, Temperature and composition dependencies of trace element partitioning: olivine/melt and low-Ca pyroxene/melt, *Geochim. Cosmochim. Acta, 52,* 539-553, 1988.
24. Dawson, J. B., Sodium carbonatite extrusions from Oldoinyo Lengai, Tanzania: implications for carbonatite complex genesis,

in *Carbonatites, Genesis and Evolution* (K. Bell, ed.), pp. 255-277, Unwin Hyman, Boston, 1989.

25. Delano, J. W., Experimental constraints on the oxidation state of the lunar mantle (abstract), in *Lunar and Planet. Sci. XXI*, pp. 278-279, Lunar and Planetary Institute, Houston, 1990.
26. Dickinson, J. E., and P. C. Hess, Role of whitlockite and apatite in lunar felsite (abstract), in *Lunar and Planet. Sci. XIV*, pp. 158-159, Lunar and Planetary Institute, Houston, 1983.
27. Dickinson, J. E., P. C. Hess, and M. J. Rutherford, Zircon saturation and REE partition coefficients in lunar basalts and granites (abstract), in *Lunar and Planet. Sci. XII*, pp. 229-231, Lunar and Planertary Institute, Houston, 1981.
28. Dickinson, T., and J. H. Jones, Ba and Th partitioning between immiscible silicate melts: further evaluation of role of silicate liquid immiscibility in the petrogenesis of lunar granites (abstract), *Meteoritics, 24*, 262, 1989.
29. Drake, M. J., and W. V. Boynton, Partitioning of rare earth elements between hibonite and melt and implications for nebular condensation of the rare earth elements, *Meteoritics, 23*, 75-80, 1988.
30. Drake, M. J., and J. R. Holloway, Partitioning of Ni between olivine and silicate melt: the "Henry's Law problem" re-examined, *Geochim. Cosmochim. Acta, 45*, 431-437, 1981.
31. Drake, M. J., and D. F. Weill, Partition of Sr, Ba, Ca, Y, Eu^{2+}, Eu^{3+}, and other REE between plagioclase feldspar and magmatic liquid: an experimental study, *Geochim. Cosmochim. Acta, 39*, 689-712, 1975.
32. Drake, M. J., H. E. Newsom, and C. J. Capobianco, V, Cr, and Mn in the Earth, Moon, EPB, and SPB and the origin of the Moon: Experimental studies, *Geochim. Cosmochim. Acta, 53*, 2101-2111, 1989.
33. Drake, M. J., H. E. Newsom, S. J. B. Reed, and M. C. Enright, Experimental determination of the partitioning of gallium between solid iron metal and synthetic basaltic melt: electron and ion microprobe study, *Geochim. Cosmochim. Acta, 48*, 1609-1615, 1984.
34. Dunn, T., Partitioning of Group III, IV, and Vb transition metals, Sr and Lu between clinopyroxene and melts: Mg# effects (abstract), *Eos Trans. AGU, 69*, 1512, 1988.
35. Dunn, T., and I. S. McCallum, The partitioning of Zr and Nb between diopside and melts in the system diopside-anorthite-albite, *Geo-chim. Cosmochim. Acta, 46*, 623-629, 1982.
36. Ehlers, K., T. L. Grove, T. W. Sisson, S. I. Recca, and D. A. Zervas, The effect of oxygen fugacity on the partitioning of nickel and cobalt between olivine, silicate melt and metal, *Geochim. Cosmochim. Acta, 56*, 3733-3743, 1992.
37. Fleet, M. E., and N. D. MacRae, Partition of Ni between olivine and sulfide: equilibria with sulfide-oxide liquids, *Cont. Mineral. Petrol., 100*, 462-469, 1988.
38. Fleet, M. E., and W. E. Stone, Partitioning of platinum-group elements in the Fe-Ni-S system and their fractionation in nature, *Geochim. Cosmochim. Acta, 55*, 245-253, 1991.
39. Fleet, M. E., W. E. Stone, and J. H. Crockett, Partitioning of palladium, iridium, and platinum between sulfide liquid and basalt melt: effects of melt composition, concentration and oxygen fugacity, *Geochim. Cosmochim. Acta, 55*, 2545-2554, 1991.
40. Forsythe, L. M., R. L. Nielsen, and M. R. Fisk, New experimentally determined clinopyroxene-melt high strength element partition coefficients (abstract), in *AGU 1991 Fall Meeting Program and Abstracts*, supplement to *Eos Trans. AGU*, p. 548, 1991.
41. Gallahan, W. E., and R. L. Nielsen, The partitioning of Sc, Y and the rare earth elements between high-Ca pyroxene and natural mafic to intermediate lavas at 1 atmosphere, *Geochim. Cosmochim. Acta, 56*, 2387-2404, 1992.
42. Green, T. H., and N. J. Pearson, Rare earth element partitioning between clinopyroxene and silicate liquid at moderate to high pressure, *Cont. Mineral. Petrol., 91*, 24-36, 1985.
43. Green, T. H., and N. J. Pearson, Rare earth element partitioning between sphene and coexisting silicate liquid at high pressure and temperature, *Chem. Geol., 55*, 105-119, 1986.
44. Green, T. H., and N. J. Pearson, An experimental study of Nb and Ta partitioning between Ti-rich minerals and silicate liquids at high pressure and temperature, *Geochim. Cosmochim. Acta, 51*, 55-62, 1987.
45. Grutzeck, M. S., Kridelbaugh, and D. Weill, The distribution of Sr and REE between diopside and silicate liquid, *Geophys. Res. Lett., 1*, 273-275, 1974.
46. Hamilton, D. L., P. Bedson, and J. Esson, The behaviour of trace elements in the evolution of carbonatites, in *Carbonatites, Genesis and Evolution* (K. Bell, ed.), pp. 405-427, Unwin Hyman, Boston, 1989.
47. Hanson, B. Z., and J. W. Delano, Experimental data bearing on the oxidation state of chromium and vanadium in mafic volcanics (abstract), in *Lunar and Planet. Sci. XXI*, pp. 481-482, Lunar and Planetary Institute, Houston, 1992.
48. Harrison, T. M., and E. B. Watson, The behavior of apatite during crustal anatexis: equi-

librium and kinetic considerations, *Geochim. Cosmochim. Acta, 48,* 1467-1477, 1984.

49. Harrison, W. J., An experimental study of the partitioning of samarium between garnet and liquid at high pressures (abstract), in papers presented to the International Conference of Trace Element Geochemistry, Sedona, Arizona, pp. 412-42, 1977.
50. Haskin, L. A., B. L. Jolliff and R. O. Colson, Effects of REE^{3+} saturation on the substitution in whitlockite of 2 REE^{3+} + vacancy in Ca(IIA) for 3 Ca^{2+} (abstract), in *Lunar and Planet. Sci. XXIII,* pp. 501-502, Lunar and Planetary Institute, Houston, 1992.
51. Herzberg, C., and T. Gasparik, Garnet and pyroxenes in the mantle: a test of the majorite fractionation hypothesis, *J. Geophys. Res., 96,* 16263-16274, 1991.
52. Hillgren, V. J., Partitioning behavior of Ni, Co, Mo, and W between basaltic liquid and Ni-rich metal: implications for the origin of the Moon and lunar core formation, *Geophys. Res. Lett., 18,* 2077-2080, 1991.
53. Hiyagon, H., and M. Ozima, Partition of noble gases between olivine and basalt melt, *Geochim. Cosmochim. Acta, 50,* 2045-2057, 1986.
54. Irving, A. J., A review of experimental studies of crystal/liquid trace element partitioning, *Geochim. Cosmochim. Acta, 42,* 743-770, 1978.
55. Irving, A. J., and F. A. Frey, Effect of composition on the partitioning of rare earth elements, Hf, Sc, and Co between garnet and liquid: experimental and natural evidence (abstract), *Eos Trans. AGU, 57,* 339, 1976.
56. Ito, E., and E. Takahashi, Melting of peridotite at uppermost lower-mantle conditions, *Nature, 328,* 514-517, 1987.
57. Johnson, K. T. M., Trace element geochemistry of oceanic peridotites and silicate melt inclusions: implications for mantle melting and ocean ridge magma genesis, Ph.D. Thesis, M.I.T.-Woods Hole Oceanographic Institution, pp. 260, 1990.
58. Johnson, K. T. M., and R. J. Kinzler, Partitioning of REE, Ti, Zr, Hf, and Nb between clinopyroxene and basaltic liquid: an ion microprobe study (abstract), *Eos Trans. AGU, 70,* 1388, 1989.
59. Jones, J. H., Studies of the geochemical similarity of plutonium and samarium and their implications for the abundance of ^{244}Pu in the early solar system, Ph.D. thesis, California Institute of Technology, pp. 197, 1981.
60. Jones, J. H., Temperature- and pressure-independent correlations of olivine/liquid partition coefficients and their application to trace element partitioning, *Cont. Mineral. Petrol., 88,* 126-132, 1984.
61. Jones, J. H., Partitioning of Mg and Fe between olivine and liquids of lunar compositions: the roles of composition, pressure and Ti speciation (abstract), in *Lunar and Planet. Sci. XIX,* pp. 561-562, Lunar and Planetary Institute, Houston, 1988.
62. Jones, J. H., and D. S. Burnett, The distribution of U and Pu in the St. Severin chondrite, *Geochim. Cosmochim. Acta, 43,* 1895-1905, 1979.
63. Jones, J. H., and D. S. Burnett, Quantitative radiography using Ag x-rays, *Nuclear Inst. and Methods, 180,* 625-633, 1981.
64. Jones, J. H., and D. S. Burnett, Experimental geochemistry of Pu and Sm and the thermodynamics of trace element partitioning, *Geochim. Cosmochim. Acta, 51,* 769-782, 1987.
65. Jones, J. H., and M. J. Drake, Geochemical constraints on core formation in the Earth, *Nature, 322,* 221-228, 1986.
66. Jones, J. H., and C. A. Goodrich, Siderophile trace element partitioning in the Fe-Ni-C system: preliminary results with application to ureilite petrogenesis (abstract), *Meteoritics, 24,* 281-282, 1989.
67. Jones, J. H., and D. J. Malvin, A nonmetal interaction model for the segregation of trace metals during solidification of Fe-Ni-S, Fe-Ni-P, and Fe-Ni-S-P alloys, *Metall. Trans., 21B,* 697-706, 1990.
68. Jones, J. H., and D. Walker, Partitioning of siderophile elements in the Fe-Ni-S system: 1 bar to 80 kbar, *Earth Planet. Sci. Lett., 105,* 127-133, 1991.
69. Jones, J. H., and D. Walker, Parti-tioning of Nb, Mo, Ba, Ce, Pb, Th, and U between immiscible carbonate and silicate liquids: evaluating the effects of P_2O_5, F, and carbonate composition (ab-stract), in *Lunar and Planet. Sci. XXIV,* Lunar and Planetary Institute, Houston, in press, 1993.
70. Jones, J. H., S. R. Hart, and T. M. Benjamin, Experimental partitioning studies near the Fe-FeS eutectic, with an emphasis on elements important to iron meteorite chronologies (Pb, Ag, Pd and Tl), *Geochim. Cosmochim. Acta, 57,* 453-460, 1993.
71. Jones, J. H., D. Walker, D. A. Pickett, and M. T. Murrell, An experimental study of partitioning between carbonate and silicate liquids (abstract), in *Lunar and Planet. Sci. XXIII,* pp. 627-628, Lunar and Planetary Institute, Houston, 1992.
72. Jurewicz, A. J. G., and E. B. Watson, Cations in olivine, part 1: Calcium partitioning and calcium-magnesium distribution between olivines and coexisting melts, with petrologic applications, *Cont. Mineral. Petrol., 99,* 176-185, 1988.
73. Kato, T., A. E. Ringwood, and T. Irifune, Experimental determination of element partitioning between silicate perovskites, garnets and liquids: constraints

on early differentiation of the mantle, *Earth Planet. Sci. Lett., 89,* 123-145, 1988*a*.

74. Kato, T., A. E. Ringwood, and T. Irifune, Constraints on element partition coefficients between $MgSiO_3$ perovskite and liquid determined by direct measurements, *Earth Planet. Sci. Lett., 90,* 65-68, 1988*b*.
75. Klöck, W., and H. Palme, Partitioning of siderophile and chalco-phile elements between sulfide, olivine, and glass in a naturally reduced basalt from Disko Island, Greenland, *Proc. Lunar Planet. Sci. Conf., 18th,* 471-483, 1988.
76. Larsen, L., Measurement of solubility of zircon ($ZrSiO_4$) in synthetic granitic melts (abstract), *Eos Trans. AGU, 54,* 479, 1973.
77. LaTourette, T. Z., and D. S. Burnett, Fe-Ti oxide and zircon partition coefficients for uranium in silica-rich liquid from partially melted granitic blocks erupted at Mt. Mazama (Crater Lake), Oregon (abstract), *Eos Trans. AGU, 70,* 1403, 1989.
78. LaTourette, T. Z., and D. S. Burnett, Experimental determination of U and Th partitioning between clinopyroxene and natural and synthetic basaltic liquid, *Earth Planet. Sci. Lett., 110,* 227-244, 1992.
79. Leeman, W. P., Experimental determination of partitioning of divalent cations between olivine and basaltic liquid, Ph.D. thesis, University of Oregon, Part II, pp. 231-303, 1974.
80. Leeman, W. P., Partitioning of Pb between volcanic glass and co-existing sanidine and plagioclase feldspars, *Geochim. Cosmochim. Acta, 43,* 171-175, 1979.
81. Lindstrom, D. J., Experimental study of the partitioning of the transition metals between diopside and coexisting liquid, Ph.D. thesis, University of Oregon, pp. 188, 1976.
82. Lindstrom, D. J., and D. F. Weill, Partitioning of transition metals between diopside and coexisting silicate liquids. I. nickel, cobalt, and manganese, *Geochim. Cosmochim. Acta, 42,* 817-831, 1978.
83. Long, P. E., Experimental determination of partition coefficients for Rb, Sr, and Ba between alkali feldspar and silicate liquid, *Geochim. Cosmochim. Acta, 42,* 833-846-1978.
84. Longhi, J., and V. Pan, The parent magmas of the SNC meteorites, *Proc. Lunar Planet. Sci. Conf., 19th,* 451-464, 1989.
85. Longhi, J., D. Walker, and J. F. Hays, Fe and Mg in plagioclase, *Proc. Lunar Sci. Conf., 7th,* 1281-1300, 1976.
86. Lux, G., The behavior of noble gases in silicate liquids: solution, diffusion, bubbles and surface effects, with applications to natural samples, *Geochim. Cosmochim. Acta, 51,* 1549-1560, 1987.
87. Malvin, D. J., and M. J. Drake, Experimental determination of crystal/melt partitioning of Ga and Ge in the system forsterite-anorthite-diopside, *Geochim. Cosmochim. Acta, 51,* 2117-2128, 1987.
88. McCallum, I. S., and M. Charette, Zr and Nb partition coefficients: implications for the genesis of mare basalts, KREEP, and sea floor basalts, *Geochim. Cosmochim. Acta, 42,* 859-870, 1978.
89. McFarlane, E. A., M. J. Drake, and C. Herzberg, Olivine, beta spinel and majorite/melt partitioning and the early thermal history of the earth (abstract), in *Lunar and Planetary Sci. XXI,* pp. 759-760, Lunar and Planetary Institute, Houston, 1990.
90. McFarlane, E. A., M. J. Drake, and C. Herzberg, Magnesio-wüstite/ melt and majorite/melt partitioning and the early thermal history of the earth (abstract), in *Lunar and Planet. Sci. XXII,* pp. 875-876, Lunar and Planetary Institute, Houston, 1991.
91. McFarlane, E. A., M. J. Drake, D. C. Rubie, and T. Gasparik, Mantle mineral/silicate melt partition coefficients (abstract), in *Lunar and Planet. Sci. XXIII,* pp. 883-884, Lunar and Planetary Institute, Houston, 1992.
92. McKay, G. A., Partitioning of REE between olivine, plagioclase, and synthetic basaltic melts: implications for the origin of lunar anorthosites (abstract), in *Lunar and Planet. Sci. XIII,* pp. 493-494, Lunar and Planetary Institute, Houston, 1982.
93. McKay, G. A., Crystal/liquid partitioning of REE in basaltic systems: Extreme fractionation of REE in olivine, *Geochim. Cosmochim. Acta, 50,* 69-79, 1986.
94. McKay, G. A., and D. F. Weill, Petrogenesis of KREEP, *Proc. Lunar Sci. Conf., 7th,* 2427-2447, 1976.
95. McKay, G. A., and D. F. Weill, KREEP petrogenesis revisited, *Proc. Lunar Sci. Conf., 8th,* 2339-2355, 1977.
96. McKay, G. A., J. Wagstaff, and L. Le, REE distribution coefficients for pigeonite: constraints on the origin of the mare basalt europium anomaly (abstract), in *Lunar and Planet. Sci. XXI,* pp. 773-774, Lunar and Planetary Institute, Houston, 1990.
97. McKay, G. A., J. Wagstaff, and S.-R. Yang, Zirconium, hafnium and rare earth element partition coefficients for ilmenite and other minerals in high-Ti lunar mare basalts: an experimental study, *Proc. Lunar Planet. Sci. Conf., 16th,* in supplement to *J. Geophys. Res., 91,* D229-D237, 1986*a*.
98. McKay, G. A., J. Wagstaff, and S.-R. Yang, Clinopyroxene REE distribution coefficients for shergottites: the REE content of the Shergotty melt, *Geochim. Cosmochim. Acta, 50,* 927-937, 1986*b*.

99. McKay, G. A., J. Wagstaff, L. Le, and D. J. Lindstrom, Whitlockite/melt partitioning and Henry's law: Shergotty late-stage minerals (abstract), in *Lunar and Planet. Sci. XVIII*, pp., 625-626, Lunar and Planetary Institute, Houston, 1987.
100. McKenzie, D., Some remarks on the movement of small melt fractions in the mantle, *Earth Planet. Sci. Lett., 95*, 53-72, 1989.
101. Michael, P. J., Partition coefficients for rare earth elements in mafic minerals of high silica rhyolites: the importance of accessory mineral inclusions, *Geochim. Cosmochim. Acta, 52*, 275-282, 1988.
102. Murrell, M. T., M. Brandriss, D. S. Woolum, and D. S. Burnett, Pu-REE-Y partitioning between apatite and whitlockite (abstract), in *Lunar and Planet. Sci. XV*, pp. 579-580, Lunar and Planetary Institute, Houston, 1984.
103. Mysen, B. O., Limits of solution of trace elements in minerals according to Henry's law: review of experimental data, *Geochim. Cosmochim. Acta, 42*, 871-885, 1978.
104. Mysen, B. O., and M. G. Seitz, Trace element partitioning determined by beta-track mapping – an experimental study using carbon and samarium as examples, *J. Geophys. Res., 80*, 2627-2635, 1975.
105. Nagasawa, H., H. D. Schreiber, and R. V. Morris, Experimental mineral/liquid partition coefficients of the rare earth elements (REE), Sc and Sr for perovskite, spinel and melilite, *Earth Planet. Sci. Lett., 46*, 431-437, 1980.
106. Nakamura, Y., H. Fujimaki, M. Tatsumoto, G. A. McKay, and J. Wagstaff, Hf, Zr, and REE partition coefficients between ilmenite and liquid: implications for lunar petrogenesis, *Proc. Lunar Planet. Sci. Conf., 16th*, in supplement to *J. Geophys. Res., 91*, D239-D250, 1986.
107. Newsom, H. E., and M. J. Drake, Experimental investigations of the partitioning of phosphorus between metal and silicate phases: implications for the Earth, Moon and eucrite parent body, *Geochim. Cosmochim. Acta, 47*, 93-100, 1983.
108. Nicholls, I. A., and K. L. Harris, Experimental rare earth element partition coefficients for garnet, clinopyroxene, and amphibole co-existing with andesitic and basaltic liquids, *Geochim. Cosmochim. Acta, 44*, 287-308, 1980.
109. Nielsen, R. H., A method for the elimination of the compositional dependence of trace element distribution coefficients, *Geochim. Cosmochim. Acta, 49*, 1775-1779, 1985.
110. Nielsen, R. H., W. E. Gallahan, and F. Newberger, Experimentally determined mineral-melt partition coefficients for Sc, Y and REE for olivine, orthopyroxene, pigeonite, magnetite and ilmenite, *Cont. Mineral. Petrol., 110*, 488-499, 1992.
111. Ohtani, E., and H. Sawamoto, Melting experiment on a model chondritic mantle composition at 25 GPa, *Geophys. Res. Lett., 14*, 733-736, 1987.
112. Ohtani, E., I. Kawabe, J. Moriyama, and Y. Nagata, Partitioning of elements between majorite garnet and melt and implications for petrogenesis of komatiite, *Cont. Mineral. Petrol., 103*, 263-269, 1989.
113. Peach, C. L., E. A. Mathez, and R. R. Keays, Sulfide melt-silicate melt distribution coefficients for noble metals and other chalcophile elements as deduced from MORB: implications for partial melting, *Geochim. Cosmochim. Acta, 54*, 3379-3399, 1990.
114. Phinney, W. C., Partition coefficients for iron between plagioclase and basalt as a function of oxygen fugacity: implications for Archean and lunar anorthosites, *Geochim. Cosmochim. Acta*, 56, 1885-1895, 1992.
115. Rammensee, W., Verteilungsgleichgewichte von Spurenelementen swischen Metallen und Silikaten, Ph.D. Thesis, Universität Mainz, Germany, 1978.
116. Ray, G. L., N. Shimizu, and S. R. Hart, An ion microprobe study of the partitioning of trace elements between clinopyroxene and liquid in the system diopside-albite-anorthite, *Geochim. Cosmochim. Acta, 47*, 2131-2140, 1983.
117. Ringwood, A. E., Some aspects of the minor element chemistry of lunar mare basalts, *The Moon, 12*, 127-157, 1975.
118. Ringwood, A. E., and E. Essene, Petrogenesis of Apollo 11 basalts, internal constitution and origin of the Moon, *Proc. Apollo 11 Lunar Sci. Conf.*, pp. 769-799, Pergamon, New York, 1970.
119. Ringwood, A. E., T. Kato, W. Hibberson, and N. Ware, High-pressure geochemistry of Cr, V, and Mn and implications for the origin of the Moon, *Nature, 347*, 174-176, 1990.
120. Ringwood, A. E., T. Kato, W. Hibberson, and N. Ware, Partitioning of Cr, V, and Mn between mantles and cores of differentiated planetesimals: implications for giant impact hypothesis of lunar origin, *Icarus, 89*, 122-128, 1991.
121. Ryerson, F. J., and P. C. Hess, Implications of liquid-liquid distribution coefficients to mineral-liquid partitioning, *Geochim. Cosmochim. Acta, 42*, 921-932, 1978.
122. Ryerson, F. J., and E. B. Watson, Rutile saturation in magmas: implications for Ti-Nb-Ta depletion in island-arc basalts, *Earth Planet. Sci. Lett., 86*, 225-239, 1987.
123. Schmitt, W., H. Palme, and H. Wänke, Experimental determination of metal/silicate partition coefficients for P, Co, Ni, Cu, Ga, Ge, Mo, and W and some implications for the early evolution of the Earth, *Geochim. Cosmochim.*

Acta, 53, 173-185, 1989.

124. Schreiber, H. D., and L. A. Haskin, Chromium in basalts: experimental determination of redox states and partitioning among synthetic silicate phases, *Proc. Lunar Sci. Conf., 7th,* pp. 1221-1259, Pergamon, New York, 1976.
125. Shimizu, N., An experimental study of the partitioning of K, Rb, Cs, Sr and Ba between clinopyroxene and liquid at high pressures, *Geochim. Cosmochim. Acta, 38,* 1789-1798, 1974.
126. Shimizu, N., and I. Kushiro, The partitioning of rare earth elements between garnet and liquid at high pressures: preliminary ex-periments, *Geophys, Res. Lett., 2,* 413-416, 1975.
127. Stolper, E. M., Experimental petrology of the eucritic meteorites, *Geochim. Cosmochim. Acta, 41,* 587-611, 1977.
128. Stone, W. E., J. H. Crockett, and M. E. Fleet, Partitioning of palladium, iridium, platinum, and gold between sulfide liquid and basalt melt at 1200°C, *Geochim. Cosmochim. Acta, 54,* 2341-2344, 1990.
129. Sweeney, R. J., D. H. Green, and S. H. Sie, Trace and minor element partitioning between garnet and amphibole and carbonatitic melt, *Earth Planet. Sci. Lett., 113,* 1-14, 1992.
130. Takahashi, E., Melting of a dry peridotite KLB-1 up to 14 GPa: implications on the origin of peridotitic upper mantle, *J. Geophys. Res., 91,* 9367-9382, 1986.
131. Takahashi, E., and T. N. Irvine, Stoichiometric control of crystal-liquid single component partition coefficients, *Geochim. Cosmochim. Acta, 45,* 1181-1185, 1981.
132. Takahashi, E., and C. M. Scarfe, Melting of peridotite to 14 GPa and the genesis of komatiite, *Nature, 315,* 566-568, 1985.
133. Tatsumoto, M., Isotopic composition of lead in oceanic basalt and its implication to mantle evolu-tion, *Earth Planet. Sci. Lett., 38,* 63-87, 1978.
134. Urakawa, S., M. Kato, and M. Kumazawa, Experimental study on the phase relations in the system Fe-Ni-O-S up to 15 GPa, in *High Pressure Research in Mineral Physics* (M. H. Manghanani and Y. Syono, eds.), pp 95-111, Terra Scientific Publishing Co. and the American Geophysical Union, Washington, D.C., 1987.
135. Walker, D., and J. H. Jones, Experimental Partitioning of Nb, Mo, Ba, Ce, Pb, Th and U Between Carbonate and Silicate Liquids (abstract), in *AGU 1991 Fall Meeting Program and Abstracts,* supplement to *Eos Trans. AGU,* p. 574, 1991.
136. Walker, D., P. Beattie, and J. H. Jones, Partitioning of U-Th-Pb and other incompatibles between augite and carbonate liquid at 1200°C and 55 kbar (abstract), *AGU 1992 Fall Meeting Program and Abstracts,* supplement to *Eos Trans. AGU,* p. 616, 1992.
137. Watson, E. B., Zircon saturation in felsic liquids: experimental results and applications to trace element geochemistry, *Cont. Mineral. Petrol., 70,* 407-419, 1979.
138. Watson, E. B., Some experimentally determined zircon/liquid partition coefficients for the rare earth elements, *Geochim. Cosmochim. Acta, 44,* 895-897, 1980.
139. Watson, E. B., Henry's law behavior in simple systems and in magmas: criteria for discerning concentration-dependent partition coefficients in nature, *Geochim. Cosmochim. Acta, 49,* 917-923, 1985.
140. Watson, E. B., and T. H. Green, Apatite/liquid partition coefficients for the rare earth elements and strontium, *Earth Planet. Sci. Lett., 56,* 405-421, 1981.
141. Watson, E. B., and T. M. Harrison, Zircon saturation revisited: temperature and composition effects in a variety of crustal magma types, *Earth Planet. Sci. Lett., 64,* 295-304, 1983.
142. Watson, E. B., and F. J. Ryerson, Partitioning of zirconium between clinopyroxene and magmatic liquids of intermediate composition, *Geochim. Cosmochim. Acta, 50,* 2523-2526, 1986.
143. Watson, E. B., T. M. Harrison, and F. J. Ryerson, Diffusion of Sm, Sr, and Pb in fluor-apatite, *Geochim. Cosmochim. Acta, 49,* 1813-1823, 1985.
144. Watson, E. B., D. Ben Othman, J.-M. Luck, and A. W. Hofmann, Partitioning of U, Pb, Cs, Yb, Hf, Re and Os between chromian diopsidic pyroxene and haplobasaltic liquid, *Chem. Geol., 62,* 191-208, 1987.
145. Weill, D. F., and G. A. McKay, The partitioning of Mg, Fe, Sr, Ce, Sm, Eu, and Yb in lunar igneous systems and a possible origin for KREEP by equilibrium partial melting, *Proc. Lunar Sci. Conf., 6th,* 1143-1158, 1975.
146. Wendlandt, R. F., Partitioning of niobium and tantulum [sic] between rutile and silicate melt (abstract), *Eos Trans. AGU, 71,* 1658, 1990.
147. White, B. S., M. Brearley, and A. Montana, Solubility of argon in silicate liquids at high pressures, *Am. Min., 74,* 513-529, 1989.
148. Willis, J., and J. I. Goldstein, The effects of C, P, and S on trace element partitioning during solidification in Fe-Ni alloys, *Proc. Lunar Planet. Sci. Conf., 13th,* in supplement to *J. Geophys. Res., 87,* A435-A445, 1982.
149. Yurimoto, H., and E. Ohtani, Element partitioning between majorite and liquid: a secondary ion mass spectrometric study, *Geophys. Res. Lett., 19,* 17-20, 1992.

Thermal Conductivity of Rocks and Minerals

Christoph Clauser and Ernst Huenges

1. INTRODUCTION

The interior heat of the earth is transmitted to its surface mainly by three mechanisms: radiation, advection, and conduction. In the earth's lithosphere conduction of heat generally dominates amoung these mechanisms. However, there are two exceptions:

(1) If the hydraulic permeability of crustal material is sufficiently high, convection driven advection of heat can be an equally or even much more efficient transfer mechanism, provided sufficiently strong driving forces are supplied by forced or free convection systems. This is often the case in sedimentary basins. However, fluid driven heat advection can be important also in crystalline rocks and on a crustal scale (Etheridge et al., 1983, Torgersen, 1990, Clauser, 1992).

(2) At ambient temperatures above 600 °C radiation of heat begins to contribute sizeably to the overall heat transfer in most polycrystalline materials, but it is really efficient only above 1200 °C. However, with single crystals and glasses (e.g. obsidian) radiation becomes important from temperatures as low as 200-400 °C. For the usual range of crustal temperatures and temperature gradients a linearization of the radiation law yields a "radiative thermal conductivity" which can be formally added to the coefficient of lattice or phonon thermal conductivity in Fourier's law of heat conduction. Thermal conductivities determined at very high temperatures in the laboratory always include this radiative component. Radiative thermal conductivity will therefore not be treated separately here; a review of heat radiation in the earth is given by Clauser (1988).

C. Clauser, Niedersächsisches Landesamt für Bodenforschung, Geowissenschaftliche Gemeinschaftsaufgaben (NLfB-GGA), Postfach 510153 D-30631 Hannover, Germany

Present Address: C. Clauser, NLfB-GGA (Geological Survey), Stillweg 2, D-30655 Hannover, Germany

E. Huenges, Niedersächsisches Landesamt für Bodenforschung, Kontinentales Tiefbohrprogramm (NLfB-KTB), Postfach 510153 D-30631 Hannover, Germany

Rock Physics and Phase Relations
A Handbook of Physical Constants
AGU Reference Shelf 3

2. BACKGROUND

2.1 Fourier's law

Fourier's law of heat conduction defines heat flow density q_i, the vector of specific energy flow rate, as the product of the thermal conductivity tensor λ_{ij} and the temperature gradient vector $\partial T/\partial x_j$:

$$q_i = \lambda_{ij} \cdot \frac{\partial T}{\partial x_j} \qquad (1)$$

Temperature measurements are usually performed along vertical profiles in boreholes. Therefore only the vertical component of the temperature gradient is generally known from measurements. Thermal conductivity for many rocks is, to a good approximation, isotropic, particularly for volcanic and plutonic rocks. In these cases heat flow will be predominantly vertical, and it is sufficient to consider only the vertical component of (1). In contrast to this, thermal conductivity of many sedimentary and metamorphic rocks is strongly anisotropic, and lateral heat flow will be significant. Hence information on anisotropy is often needed,

requiring laboratory measurements in different directions. Anisotropy exists on several scales : (1) On the microscopic scale many minerals are anisotropic (Table 3). (2) On the laboratory scale, the thermal conductivity of many rocks is also anisotropic. However, even if rocks are composed of anisotropic minerals, random orientation of the crystals within the rock may make the rock's thermal conductivity appear isotropic macroscopically. (3) Still on a larger scale, if rocks are exposed to folding, orogeny or other tectonic processes, the thermal conductivity of the resulting rock formation may be either isotropic as or anisotropic.

2.2 Measurement techniques

Thermal conductivity can be measured in the laboratory on rock samples, i.e. cores or cuttings, or in-situ in boreholes or with marine heat flow probes. There are numerous steady state and transient techniques available for measuring thermal conductivity, the most prominent being the "divided bar" and the "needle probe" method. As these methods are discussed in detail in several textbook and review articles (Beck, 1965, 1988, Davis, 1988, Desai et al., 1974, Kappelmeyer & Hänel, 1974, Roy et al., 1981, Somerton, 1992, Tye, 1969), we will neither address them here again nor comment on the many details involved in performing the actual measurements.

As is the case with most other petrophysical properties, in-situ thermal conductivity may deviate significantly from laboratory values, even if the effect of temperature, pressure and pore-fluid is accounted for. The reason for this problem is a certain scale dependence in which different aspects are involved: in-situ measurements, as a rule, represent an average over a much larger rock volume than laboratory measurements performed on small samples. On the other hand, small-scale variations may thus be lost. Which thermal conductivity is the "correct" one will depend on the specific question. This problem is quite similar to one encountered in hydrology: the difficulty of defining a "representative elementary volume" for which sensible averages for transport parameters like permeability and dispersion lengths can be defined.

2.3 Indirect methods

When no data are available or no direct measurements can be performed, thermal conductivity can be inferred from a number of indirect data: mineralogical composition and saturating fluids, well-log correlations, and correlations with other physical parameters. While some of these methods are based on well defined physical models, others are purely empirical.

Estimation from mineral content and saturating fluids. Thermal conductivity of rocks may be estimated from their mineral content, as minerals, due to their well defined composition, exhibit a much smaller variance in thermal conductivity than rocks. Similarly, as a porous rock's bulk thermal conductivity varies with different saturants, it may be of interest to know the thermal conductivity of a rock when it is saturated with other fluids than those used in the laboratory measurement. Numerous models have been proposed for this, but all have their disadvantages: some overestimate while others underestimate systematically the true bulk thermal conductivity. Most of them are valid only for a specific range of volume ratios (or porosities), and yield completely unreasonable results outside this range. Parallel and series model are easy to understand, but have the disadvantage of being rather special cases, applicable mostly to bedded sediments. They lead to the well known arithmetic and harmonic means, respectively, and define upper and lower limits for all other models. Thus they constrain the maximum variance of possible predictions. Quite successful in describing the data in many cases, but unfortunately without a clearly defined physical model, the geometric mean falls in between these two extremes. If λ_i is the thermal conductivity and n_i the volume fraction of the i-th phase relative to the total volume, with $1=\sum n_i$, these three means are defined by:

$$\lambda_{ari} = \sum n_i \cdot \lambda_i \qquad \text{(a)}$$

$$\lambda_{har} = 1 \Big/ \sum \frac{n_i}{\lambda_i} \qquad \text{(b)} \qquad (2)$$

$$\lambda_{geo} = \prod \lambda_i^{n_i} \qquad \text{(c)}$$

In this context it must suffice to present only these three most well known models, as this subject can be addressed only briefly here. Beck (1988) reviews the topic in considerable detail, and, in particular, presents and discusses several other well known mixing-models. Somerton (1992) discusses unconsolidated sands, effects of multi-fluid saturation, and illustrates the topic with many examples from hydrocarbon reservoirs. Horai (1991) tests the results of predictions from several different mixing-models on a remarkable data set in which porosity virtually varies from 0-100 %. As can be expected, most of the models tested were valid only for certain porosity ranges. Only two more recent two-phase models, assuming that

pores can be treated as spheroidal inclusions in a homogeneous and isotropic material, are capable of explaining the complete data set (Horai, 1991). However, additional information on the spheroids' aspect ratio or orientation, respectively, is required by these two models.

Given the typical conductivity ratios we observe in nature, i.e. < 10, most of the conductivity models work to within 10-15 % accuracy. For larger ratios some break down more than others, and the geometric mean is one of them. The reason why it is still quite popular with many, even in extreme cases, is that it has often been found that errors introduced in the inverse problem (i.e. in predicting the matrix conductivity from measurements on samples saturated with one fluid) are automatically compensated for when using this incorrect matrix value in the subsequent forward calculation (i.e. in predicting the bulk conductivity of the matrix saturated with another fluid).

Well-log correlations. There are three different ways in which well-logs can be used to infer estimates for in-situ thermal conductivity:

(1) One approach is to establish empirical relationships between thermal conductivity and parameters derived from well logs, such as porosity, bulk density, sonic (p-wave) velocity, and seismic travel times. In principle, this approach is not limited to well logs, if petrophysical parameters are known from laboratory measurements, for instance. A useful summary of these different approaches is presented by Blackwell (1989), who also illustrates their application to a specific case.

(2) The second approach is, in principle, an extension of the mixing-model approach to the borehole scale: the volume fractions of the different mineral (or fluid) phases are either taken directly from induced gamma ray spectroscopy logs (Williams & Anderson, 1990) or determined from a joint analysis of other logs such as gamma ray, sonic traveltime, gamma density, and neutron porosity (Demongodin et al., 1991). Then an appropriate mixing model is applied. Both approaches apply the geometric mean as mixing model and test their method on detailed data from two case-study boreholes. A limitation of both methods is that mineralogy-based conductivity models cannot account for the effect of anisotropy observed in many sedimentary and metamorphic rocks.

(3) In a third approach, Willams & Anderson (1990) derive a phonon conduction model for thermal conductivity, which utilizes temperature, acoustic velocity, and bulk density measurements from well-logs. The method is claimed to be accurate to within ± 15 %, both in isotropic and anisotropic formations. Its application, however, is limited to unfractured rocks, since the effects of fracturing on compressional and shear velocities lead to inaccurate results. There are indications, however, that shear-wave birefringence may pose a limit to the application of this method in foliated rocks as well (Pribnow et al., 1993).

2.4 Sources of data

For a large number of rocks thermal conductivity data are available and classified according to rock name and origin in several extensive compilations (Birch, 1942, Clark, 1966, Desai et al., 1974, Kappelmeyer & Hänel, 1974, Roy et al., 1981, Čermák & Rybach, 1982, Robertson, 1988). However, it is important to realize that compilations for rocks are inevitably comprised of data that are heterogeneous in many respects, such as mineral composition, porosity, saturation, and experimental conditions. This is responsible for the great variability of thermal conductivity for each particular rock. Therefore, the merit of a summary purely according to rock type is limited if users are interested primarily in general questions of heat transfer in the earth rather than in data from a specific location.

2.5 Outline of this compilation

In this review we therefore take a complementary approach to those previous compilations. We do not attempt to present a complete table of all available thermal conductivity data published to date. Instead, we build on the data compiled previously (Birch & Clark, 1940a,b, Clark, 1966, Desai et al., 1974, Kappelmeyer & Hänel, 1974, Roy et al., 1981, Čermák & Rybach, 1982, Robertson, 1988) and arrange them into four basic groups: sedimentary, metamorphic, volcanic, and plutonic rocks.

Data on thermal conductivity of minerals is not quite as abundant as for rocks. Both measurements on single crystals and on mineral powder are reported in the literature. In this review we present a summary of both types of data from original contributions and from previous compilations by Birch & Clark (1940a,b), Sass (1965), Clark (1966), Horai & Simmons (1969), Horai (1971), Dreyer (1974), Robertson (1988), and Diment & Pratt (1988).

3. THERMAL CONDUCTIVITY OF ROCKS

Inspection of any of the compilations quoted above reveals that thermal conductivity may vary by as much as a factor of two to three for any given rock type. This is due

to the natural variation of a rock's mineral content as well as to several physical and diagenetic factors. All rocks are therefore arranged into the four basic groups characterizing the special conditions prevailing at their formation, deposition, or metamorphism: sediments, volcanics, plutonics, and metamorphics. In each group we study statistical quantities (such as histograms, median, mean, and standard deviation) and investigate the variation of thermal conductivity with those factors that have the most pronounced effect on this group of rocks. These are petrological aspects or petrophysical influences such as porosity (in sediments and volcanic rocks), the dominant mineral phase (in metamorphic and plutonic rocks), and anisotropy (in sediments and metamorphic rocks). More recent data was included, mainly (but not only) from the German continental deep drilling project KTB, when the existing data base seemed insufficient for our statistical approach. Where additional specific data is available, the effect of temperature, pressure, saturation, and saturant is demonstrated.

3.1 Thermal conductivity of sedimentary, volcanic, plutonic, and metamorphic rocks

Before any details are discussed we first provide an overview on the distribution of thermal conductivity in general as well as on the variation of thermal conductivity with ambient temperature for the four basic rock-types.

Influence of porosity and the dominant mineral phase. Figure 1 shows histograms for thermal conductivity according to rock type. For sedimentary rocks (Figure 1a) the controlling factors on thermal conductivity are porosity and origin of a particular sediment. It appears as if chemical sediments, mainly formed by precipitation of dissolved minerals or by compaction of organic material, and low porosity (< about 30 %) physical sediments, formed by the compaction and cementation of clastic material, have nearly identical frequency distributions, means, and medians. In contrast, high porosity (> about 80 %), mainly marine physical sediments display a distribution which is biased towards low conductivities, with mean and median about half the size of the former two. This, of course, is due to the low-conductivity fill of the void space, which can be either air or water.

For volcanic rocks (Figure 1b), spanning nearly the total possible range of porosity from 0-1, porosity is again the controlling factor on thermal conductivity: mean and median of the high- and low-porosity histograms differ by nearly a factor of two, and the high porosity distribution is clearly skewed towards low conductivities.

Plutonic and metamorphic rocks display a much smaller porosity. Here the dominant mineral phase controls different conductivity distributions. For plutonic rocks the feldspar content determines the nature of the histogram (Figure 1c): while rocks with a low feldspar content (i.e. less than about 60 %) seem to define a nearly symmetrical histogram, a high content in feldspar biases the distribution towards low conductivities. Interestingly enough, means and medians for both distributions are nearly identical within the given standard deviation.

Metamorphic rocks may be classified according to their quartz content. Figure 1d displays the resulting bimodal distribution. While the low conductivity part is made up of rocks with low quartz-content, the high-conductivity portion consists of quartzite only.

Influence of ambient temperature. Thermal conductivity is a function of temperature. Lattice (or phonon) thermal conductivity varies inversely with temperature. As thermal expansions increases with temperature, but differently for all minerals, "thermal cracking" by differential expansion may create contact resistances between mineral grains, thus contributing to the observed decrease of conductivity with temperature. This effect is probably not as severe in water-saturated rocks as it is in dry rocks, the condition in which most laboratory experiments are conducted. Conductivity-temperature determinations of crystalline water-saturated rocks are now under way in some laboratories. The "radiative thermal conductivity", in contrast, follows a T^3-law (see e.g. Clauser 1988). Thus measurements on thermal conductivity as function of increasing temperature generally show initially a decrease with temperature, until around 1000-1200 °C the radiative component balances and sometimes even inverts this decreasing trend.

Figure 2a shows this effect for sediments. Up to 300 °C there is a reduction by nearly a factor of two, both for clastic and carbonaceous sediments. Above 300 °C the decrease in thermal conductivity comes nearly to an end, with carbonates decreasing still a little more than clastic sediments. However, as there are very few data for this temperature range, this last observation is not very sound statistically.

Volcanic rocks (Figure 2b) display quite a different behaviour, depending on their opacity, i.e. on how well they transmit thermal energy by radiation. Due to this additional "radiative thermal conductivity", volcanic glasses and rocks with a small iron content experience an increase in thermal conductivity for temperatures above 800-1000 °C (see e.g. Clauser, 1988). In contrast, conduction dominated rocks show a much more pronounced decrease in thermal

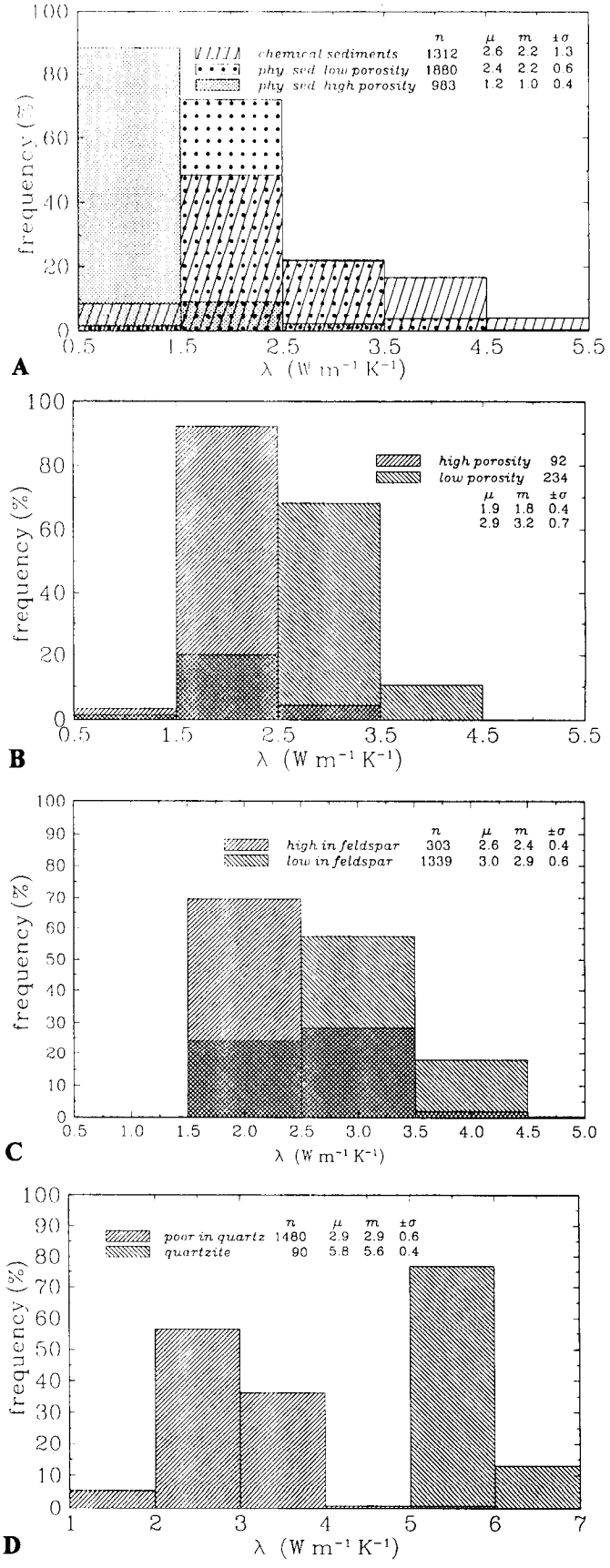

Fig. 1. Histograms of thermal conductivity for sedimentary, volcanic, plutonic, and metamorphic rocks. All data, taken from [14], were measured at room temperature and atmospheric pressure. n is the number of data, m the median, μ the mean, and σ the standard deviation for all three data sets. Please note that superposition of different domains results in new hatchure styles in some diagrams.

(a). Thermal conductivity of sedimentary rocks, subdivided according to chemical or physical sedimentation processes. Histogram for chemical sediments includes data for limestone, coal, dolomite, hematite, chert, anhydrite, gypsum, rock salt, and sylvinite. For physical sediments the influence of porosity is considered additionally: low porosity sediments include data from shale (including dolomitic, pyritic, and carbonaceous shale), marl, clayey marl, marlstone, conglomerate, tuff-conglomerate, tuffite, breccia, quartz breccia, and sandstone (including limy and quartz sandstone), while high-porosity sediments are ocean- and lake-bottom sediments.

(b). Thermal conductivity of volcanic rocks, subdivided according to porosity. The high porosity histogram represents data fom lava, tuff, tuff breccia, and mid-ocean ridge basalt (MORB). Low porosity data are from rhyolite, liparite, trachodolerite, andesite, and basalt (excluding MORB).

(c). Thermal conductivity of plutonic rocks, subdivided according to feldspar content. Histogram for high feldspar content (i.e. more than about 60 %) is made up of data from syenite (including alkali and nepheline syenite), granosyenite, syenite porphyry, and anorthosite. Data for variable, but generally lower feldspar content (i.e. less than about 60 %) are from granite (including alkali granite, plagiogranite, granodiorite, tonalite, quartz monzonite), quartz- and quartz-feldspar-porphyry, diorite (including monzonite), gabbro (including quartz and olivine gabbro), porphyrite dykes (lamporphyre, diabase, quartz dolerite), and ultramafic rocks (pyroxenite, peridotite, lherzolite, hypersthenite, bronzitite, dunite, olivinite, hornblendite, cumberlandite).

(d). Thermal conductivity of metamorphic rocks, subdivided according to quartz content. Histogram for high quartz content is made up of data fom quartzite. Data for low quartz content are from quartz-mica schist, gneisses, marble, serpentinite, talc, serpentinized peridotite, hornfels, eclogite, albitite, leptite, schist, slate, phyllite, amphibolite, mylonite and greenstone.

conductivity. An inversion of this decrease cannot be seen with statistical confidence. However, above around 900 °C this trend seems to come to a halt, with thermal conductivity on a level of about 50 % of the room-temperature value. Again, there are quite few data points above 500 °C.

There does not seem to be a very significant radiative contribution in plutonic rocks (Figure 2c). However the decrease of thermal conductivity with temperature is quite different, depending on the feldspar content: while there is hardly any significant decrease (~ 10 %) in conductivity up to 300 °C for rocks that are rich in feldspar, rocks that are poor in feldspar decrease by more than 40 % over this range. Above this temperature the decrease is more gentle, spreading an additional 20 % over the next 700 K. Interestingly, there is a large amount of data available for this high-temperature range. The different behaviour of rocks with a high feldspar content is due to the increase in thermal conductivity with temperature of some plagioclase feldspars (Birch & Clark, 1940a) which compensates the decrease in thermal conductivity with temperature observed for most other minerals and rocks (other notable exceptions are fused silica as well as volcanic and silica glasses; see also discussion of empirical relationships below).

For metamorphic rocks, the decrease of thermal conductivity with temperature depends on the content in a dominant mineral phase, similar to plutonic rocks. Quartzites decrease rapidly, by nearly a factor of three up to a temperature of about 500 °C. Above this, there is only a very mild further decrease. For rocks that are poor in quartz the decrease in conductivity is not quite as dramatic, amounting to about one third of the room-temperature value up to 200 °C. Then it remains roughly constant up to 500 °C. Above this, up to 750 °C, it decreases again to about one third of the room-temperature value. There are again many data available for this high-temperature range, at least for mafic rocks.

Often data on thermal conductivity is available for room-temperature conditions only, even though it is required at elevated temperatures. For this purpose we will discuss some empirical relationships that have been proposed for extrapolation on the basis of data measured at elevated temperatures. It is emphasized, however, that there is no real substitute for individual measurements.

It has been long recognized that for moderate temperatures λ varies inversely with temperature (Birch & Clark, 1940b). For this temperature range several approaches have been suggested as how to infer thermal conductivity at elevated temperatures. Based on the analysis of available tabulated data of thermal conductivity as function of temperature Zoth & Hänel (1988) suggest a relationship of the form

$$\lambda(T) = A + \frac{B}{350 + T}\ , \tag{3a}$$

where λ is given in W m^{-1} K^{-1}, T in °C, and the empirical constants A and B are determined from a least-squares fit to measured data for different rock types (Table 1). Linear relationships between temperature and the inverse of λ, the thermal resistivity, discriminate between temperature-dependent contributions and other factors, which are independent of temperature (such as micro-cracks, grain boundaries, pore volume, as well as mineralogical composition, shape and orientation of crystals and their fragments):

$$\frac{1}{\lambda(T)} = D + E \cdot T, \tag{3b}$$

where λ is again in W m^{-1} K^{-1} and T is in K. By measuring λ and plotting the thermal resistivity versus temperature D and E may be determined as intercept and slope of a linear regression. Buntebarth (1991) determined D and E from measurements on 113 samples of metamorphic rocks from the KTB borehole (mostly gneisses and metabasites) in the temperature range 50-200 °C. The arithmetic means of 66 individual values for D and E determined for gneiss are $\bar{D} = 0.16 \pm 0.03$ m K W^{-1} and $\bar{E} = 0.37 \pm 0.14 \cdot 10^{-3}$ m W^{-1}. The corresponding means of D- and E-values determined on 36 metabasite samples are $\bar{D} = 0.33 \pm 0.03$ m K W^{-1} and $\bar{E} = 0.22 \pm 0.14 \cdot 10^{-3}$ m W^{-1}. Sass et al. (1992) likewise distinguish between the effects of composition and temperature on thermal conductivity. They propose a quite general empirical relation for $\lambda(T)$, the thermal conductivity in W m^{-1} K^{-1} at temperature T in °C as a function of $\lambda(25)$, the measured room-temperature thermal conductivity:

$$\lambda(T) = \frac{\lambda(0)}{1.007 + T \cdot \left(0.0036 - \frac{0.0072}{\lambda(0)}\right)}$$

where (3c)

$$\lambda(0) = \lambda(25) \cdot \left[1.007 + 25 \cdot \left(0.0037 - \frac{0.0074}{\lambda(25)}\right)\right].$$

Equation (3c) is derived from the classical experimental data set of Birch and Clark (1940a,b), who measured thermal conductivity as function of temperature in the range 0-200 °C and higher on 38 samples from a large suite of materials including volcanic, metamorphic, plutonic and sedimentary rocks. Their results for granites clearly show

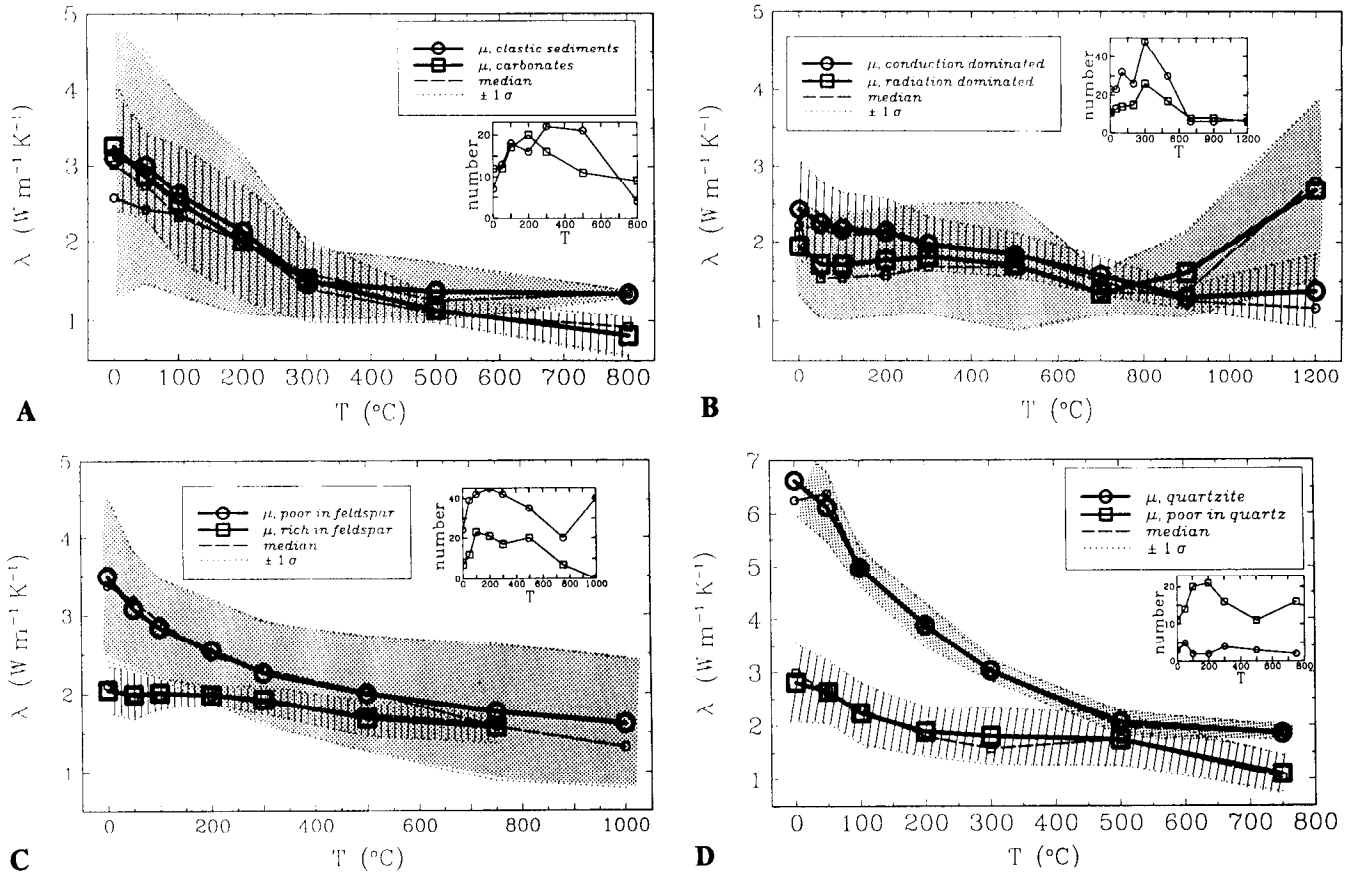

Fig. 2. Variation of thermal conductivity with temperature for various rocks. Two groups of data are considered in each plot, and for various temperature ranges (half-way up and down to the next reference temperature) median, mean, and standard deviation are computed. Full line, big symbols, and shading correspond to means and standard deviations, broken line and small symbols to medians. The inset illustrates the number of data available in different temperature ranges. Measurements were performed either with a divided bar or a line-source apparatus in dry condition and at atmospheric pressure. Please note that superposition of different domains results in new hatchure styles in some diagrams.

(a). Sedimentary rocks. Two curves are shown for carbonates (limestone and dolomite) and clastic sediments, i.e. (quartz) sandstone and shale. Data taken from [23] and [14].

(b). Volcanic rocks. Two curves are shown for rocks with weak (basalt, rhyolite (also altered or porphyritic), dacite, tuff) and strong radiative component (basalt glass, obsidian, diabase dolerite). Data taken from [23] and [14].

(c). Plutonic rocks. Two curves are shown for rocks which are rich in feldspar (syenite, anorthosite, hypersthenite) and poor in feldspar (granite, alkali granite, diorite, quartz diorite, monzonite, tonalite, gabbro, hornblende gabbro, peridotite, lherzolite, bronzitite, dunite, olivinite, granodiorite). Data taken from [23], [14], and [46].

(d). Metamorphic rocks. Two curves are shown for quartzites and for rocks which are poor in quartz (marble, serpentinite, eclogite, albitite, slate, amphibolite). Data taken from [23], [14], and [46].

the coupled effect of composition and temperature, as the normalized thermal resistivity $\lambda(0)/\lambda(T)$ is a linear function of temperature whose slope increases with $\lambda(0)$, the conductivity at 0 °C. Sass et al. (1992) report a successful test of equation (3c) on an independent data set over a temperature range of 0-250 °C for rocks ranging in composition from felsic gneiss to amphibolite: in spite of some slight systematic differences, the deviations between measured values and predictions made on the basis of equation (3c) were well within the range attributable to experimental

TABLE 1. Constants A and B from equation (3a) for different rock types.[a]

rock type	T (°C)	A	B
(1) rock salt	-20- 40	-2.11	2960
(2) limestones	0- 500	0.13	1073
(3) metamorphic rocks	0-1200	0.75	705
(4) acid rocks	0-1400	0.64	807
(5) basic rocks	50-1100	1.18	474
(6) ultra-basic rocks	20-1400	0.73	1293
(7) rock types (2)-(5)	0- 800	0.70	770

[a]after [57]

error. This suggests that equation (3c) yields useful estimates of the temperature dependence of thermal conductivity for crystalline rocks, independent of mineralogy.

3.2 Influence of various factors for selected rock types

Apart from temperature, thermal conductivity also varies with pressure, degree of saturation, pore fluid, dominant mineral phase, and anisotropy.

Pressure. The effect of overburden pressure is twofold, different for two distinct pressure ranges. First, fractures and microcracks developed during stress release, when the sample was brought to the surface, begin to close again with increasing pressure. This reduces thermal contact resistance as well as porosity, which is usually filled with a low conductivity fluid. When an overburden pressure of about 15 MPa is reached, this process comes to an end. A further pressure increase to 40 MPa does not affect thermal conductivity significantly (Figure 3a). If pressure is still further increased the second effect becomes apparent, the reduction of the rock's intrinsic porosity, i.e. that which is not artificially created by stress release. Figure 3b illustrates this effect for granite and for metamorphic rocks. While both curves indicate about a 10 % increase over the total range of pressures from 0-500 MPa, the increase is stronger over the first 50 MPa due to the first effect discussed previously.

Porosity and saturating fluid. If porosity is important (i.e. >> 1 %) the saturating fluid's thermal conductivity may significantly affect the bulk thermal conductivity of the saturated rock. Results are shown for three low conductivity saturants, water, oil, and air with room-temperature conductivities of about 0.6, 0.12-0.17, and 0.025 W m^{-1} K^{-1}, respectively (Grigull & Sandner, 1990). For plutonic rocks, figure 4a demonstrates this effect for air and water on a remarkable data set of Hawaiian marine basalt, that nearly spans the total possible range of porosity from 0-1. For sedimentary rocks Figure 4b illustrates this for quartz sandstones saturated with air, oil, and water. In both cases the resulting bulk conductivity behaves according to the saturant's thermal conductivity. Additionally, contact resistances during measurements on dry rock samples will also reduce thermal conductivity.

Partial saturation. The effect of partial saturation varies depending whether the rock is porous or fractured. Porosity in porous rocks consists of "bottlenecks" formed at the contact between individual grains and the bulk pore space. Dry bottlenecks act as thermal contact resistances between grains, while the bulk pore volume contributes according to its size to the effective thermal conductivity. Figures 5a-5c illustrate how both types of pore space influence thermal conductivity under partially saturated conditions. Figure 5a shows how thermal conductivity varies in sandstones of low- to medium-porosity with the degree of oil saturation. Initially, there is a rapid increase in conductivity with saturation: starting from completely unsaturated conditions, where conductivity reaches only about 80 % of the saturated value, 90 % is reached at a saturation level of about 10 %. The remaining 10 % deficit in conductivity is spread rather evenly over the remaining 90 % of saturation. Fig. 5b illustrates these two effects for water-saturation in a medium-porosity sandstone. The behavior is quite similar to the preceeding case: starting from a completely unsaturated conductivity of only about 60 % of the saturated value, 80 % is reached again at a saturation level of only about 10 %. The remaining 20 % deficit in conductivity is made up for during the remaining 90 % of saturation. Physically this observation indicates that the filling of intergranular bottlenecks, which accounts for only about 10 % or 20 % of the total porosity, respectively, significantly reduces contact resistance between individual grains. Replacing low conductivity air by the higher conductivity fluid in the major part of the pore volume accounts for the second effect.

If only fractures contribute to the total porosity, such as in crystalline rock, the pore space consists of bottlenecks only, and we observe the first effect alone. This is illustrated in Figure 5c for a granite of 1 % porosity. Starting from completely unsaturated conditions, with only about 80 % of the saturated conductivity, there is a more or less linear increase until 100 % is reached for complete saturation. In contrast, porous rocks with a considerable

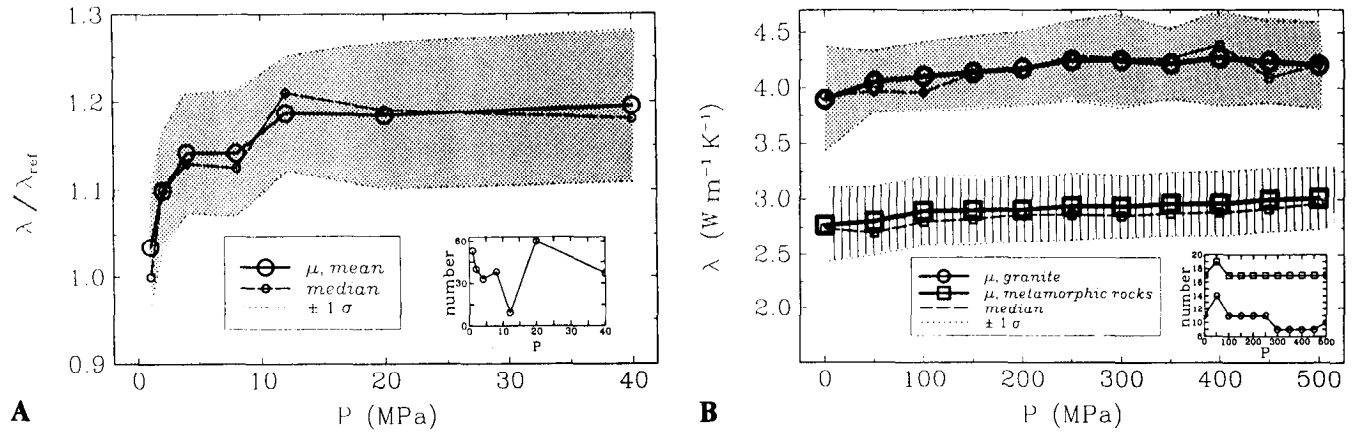

Fig. 3. Variation of thermal conductivity with uniaxial pressure for various rocks. For several temperature ranges (half-way up and down to the next reference temperature) median, mean, and standard deviation are computed. Full line, big symbols, and shading correspond to means and standard deviations, broken line and small symbols to medians. The inset illustrates the number of data available in different temperature ranges.

(a). Anhydrite, sandstone, dolomite, limestone, porphyry, diabasic basalt, basaltic lava, and granite. In order to make results for such a diverse group of rocks comparable, thermal conductivity values are normalized relative to the thermal conductivity measured at the lowest reported pressure level for each specimen (0-4 Mpa). All data, taken from [23], [14], and [46], were measured either with a divided bar or a line-source apparatus in dry condition.

(b). Two groups of crustal rocks. Two curves are shown, the upper curve for granite and the lower curve for predominantly metamorphic rocks (amphibolite, serpentinite as well as gabbro). All data (taken from [46] and Seipold: written personal communication 1993) were measured in dry condition with a line-source apparatus.

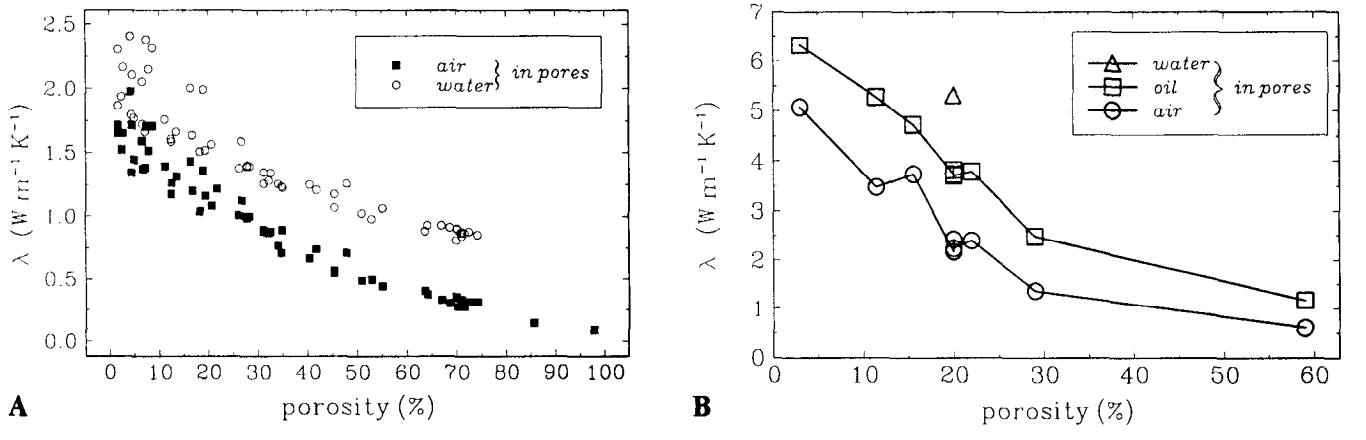

Fig. 4. Variation of thermal conductivity with porosity.

(a). Hawaiian basalt. All data, taken from [40], were measured with a divided-bar apparatus at 35 °C and under 3 MPa of uniaxial pressure, both in dry and in fully saturated condition.

(b). Quartz sandstone. All data ([36], taken from [23]) were measured with a line-source apparatus at room temperature and atmospheric pressure in air-, oil-, and water-saturated condition.

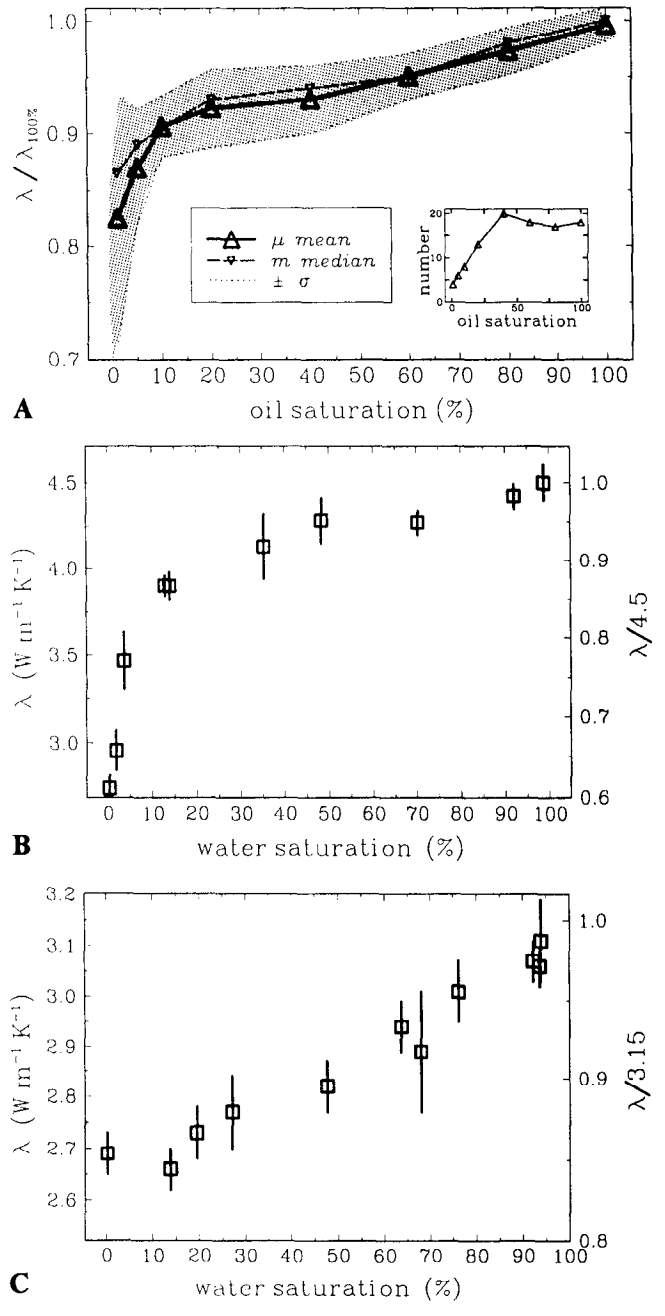

Fig. 5. Variation of thermal conductivity with partial saturation.

(a.) Sandstone (3-30 % porosity). Thermal conductivity values are normalized relative to the thermal conductivity measured at 100 % saturation. The inset illustrates the number of data available at different levels of saturation. For each saturation range (half-way up and down to the next reference point) median, mean, and standard deviation are computed. Full line, big symbols, and shading correspond to means and standard deviations, broken line and small symbols to medians. All data ([36], taken from [23]) were measured with a line-source apparatus at room temperature and atmospheric pressure, both dry and partially saturated with Soltrol "C", an oil from Phillips Petroleum Co. (Bartlesville, Ok.).

(b). Sandstone (18 % porosity). All data, taken from [39], were measured with a half-space line-source apparatus at room temperature and atmospheric pressure, both dry and partially saturated with water. The degree of saturation was determined by weighing. Squares are means and vertical lines are standard deviations determined from multiple measurements.

(c). Granite (1 % porosity). All data, taken from [39], were measured with a half-space line-source apparatus at room temperature and atmospheric pressure, both dry and partially saturated with water. The degree of saturation was determined by weighing. Squares are means and vertical lines are standard deviations determined from multiple measurements.

amount of bulk pore volume, display this linear conductivity increase within the first 10 % of saturation.

Dominant mineral phase and anisotropy. The variation of thermal conductivity with the dominant mineral phase was previously discussed in the context of plutonic and metamorphic rocks in general (Figures 1c and 1d). Figure 6a demonstrates this dependence for two particular metamorphic rock types, a low-conductivity amphibolite, and a high conductivity gneiss. Apart from the obvious shift between the two histograms which is due to the different mineral content, Figure 6a illustrates the effects of anisotropy: measurements on both rock types were performed parallel and perpendicular to the apparent direction of foliation. While for amphibolite the means, medians and histograms are nearly identical for either direction, this is not the case for gneiss. Here the means and medians differ by about 20 %, and the histograms are skewed towards lower values for measurements

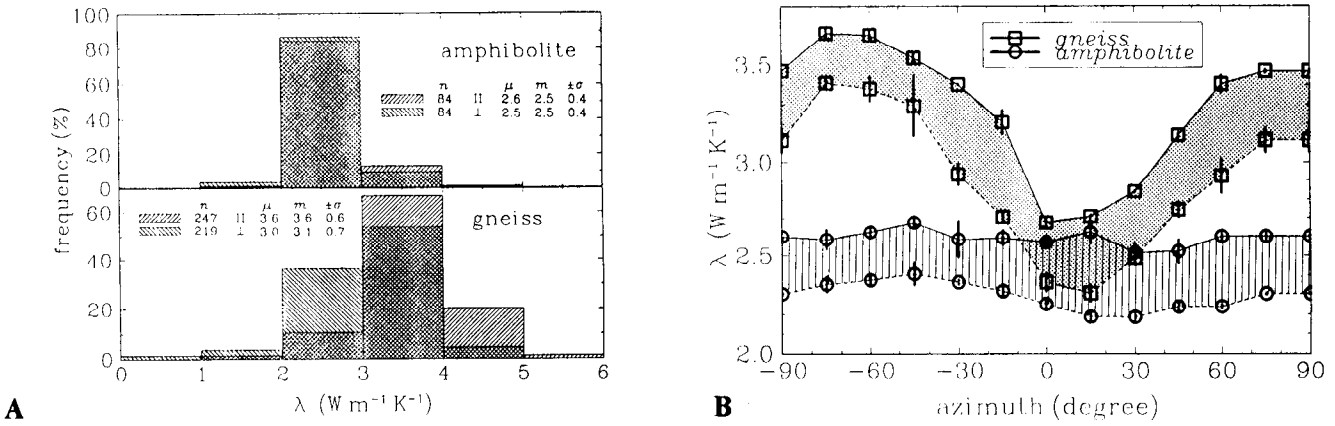

Fig. 6. Thermal conductivity of two metamorphic rocks from the KTB-VB pilot hole, an amphibolite, consisting mostly of low-conductivity, basic minerals and a felsic gneiss, made up mostly of high-conductivity quartz. n is the number of data, m the median, μ the mean, and σ the standard deviation for both data sets. All samples were measured with a half-space line-source apparatus at room temperature and atmospheric pressure, in nearly fully water-saturated condition, i.e. 70-90 % [31]. Please note that cross-hatchure results from superposition of different domains.

(a) The effect of anisotropy and of the dominant mineral phase on thermal conductivity. Components parallel and perpendicular to foliation are determined from knowledge of dip and azimuth of foliation.

(b). Variation of thermal conductivity with direction of heat flow relative to foliation for a dry (broken line) and an almost fully water-saturated (70-90 %) sample (full line). The gneiss sample (squares) is from a depth of 1908.7 m, the amphibolite sample (circles) from 3839.5 m.

perpendicular and towards higher values for measurements parallel to foliation.

This directional dependence is further illustrated for two particular rock samples of amphibolite and gneiss in Figure 6b. It is quite apparent that thermal conductivity for the same rock sample may vary from 100 % (parallel) to about 60 % (perpendicular), depending on the azimuth of the measurement relative to the foliation. In contrast to this and in spite of an existing slight anisotropy, the variation of thermal conductivity in the amphibolite sample is less than about ± 5 %. It is interesting to note that the amount of anisotropy is identical irrespective of the state of saturation of the sample. In contrast to seismic velocity this indicates that anisotropy of thermal conductivity does not seem to be influenced by the pore-space or fracture geometry and the saturation of this rock. This is valid as long as the fluid's thermal conductivity is less than the rock's.

Robertson (1988) discusses an empirical approach which permits to account for the combined effects of porosity, saturating fluid and dominant mineral phase. Plotting measured thermal conductivities of various rocks versus the square of solidity γ (where γ is 1-porosity), he finds linear relationships whose slopes vary with the per cent content in a specific mineral (e.g. quartz, olivine, etc). He proposes an interpolation formula that accounts for the effects of both water- or air-filled porosity and variable mineral content:

$$\lambda = \lambda_f + \gamma^2 \cdot [(\lambda_s + p \cdot S) - \lambda_f], \quad (4)$$

where λ_f is the pore fluid's thermal conductivity, λ_s the solid rock intercept at $\gamma^2 = 1$ for zero per cent specific mineral content, p the actual percentage of the specific mineral, and S a slope constant equal to the change of λ with specific mineral content, determined from intercept values obtained from experimental data at $\gamma^2 = 1$. Table 2 lists some of the data reported by Robertson (1988) which may be inserted into equation (4) to obtain estimates of thermal conductivity as function of porosity, pore-fluid, and mineral content for mafic and felsic igneous rocks, and for sandstones.

4. THERMAL CONDUCTIVITY OF MINERALS

Thermal conductivity of minerals is much better constrained than that of rocks, as there is a well defined

TABLE 2a. Constants λ_f, λ_s, and S from equation (4) for mafic igneous rocks.[b]

solidity γ (-)	pore fluid	olivine content p (%)	λ (W m^{-1} K^{-1})	S (W m^{-1} K^{-1} %$^{-1}$)
0	air	0	λ_f = 0.188	
1	air	0	λ_s = 1.51	
1	air	30	λ_s = 1.96	0.015
0	water	0	λ_f = 0.75	
1	water	0	λ_s = 1.84	
1	water	30	λ_s = 2.60	0.025

[b]after [41]; determined on tholeitic basalt samples with 0 - 40 % olivine content [40]

TABLE 2b. Constants λ_f, λ_s, and S from equation (4) for felsic igneous rocks.[c]

solidity γ (-)	pore fluid	quartz content p (%)	λ (W m^{-1} K^{-1})	S (W m^{-1} K^{-1} %$^{-1}$)
0	air	0	λ_f = 0.026	
1	air	0	λ_s = 1.47	
1	air	100	λ_s = 5.23	0.038

[c]after [41]; determined on samples with 0 - 45 % quartz content [5, 8, 9]

TABLE 2c. Constants λ_f, λ_s, and S from equation (4) for sandstone.[d]

solidity γ (-)	pore fluid	quartz content p (%)	λ (W m^{-1} K^{-1})	S (W m^{-1} K^{-1} %$^{-1}$)
0	air	0	λ_f = 0.026	
1	air	0	λ_s = 1.47	
1	air	100	λ_s = 5.23	0.038
0	water	0	λ_f = 0.62	
1	water	0	λ_s = 1.52	
1	water	100	λ_s = 8.10	0.038

[d]after [41]; determined on samples with 0 - 100 % quartz content [1, 2, 8, 9, 11, 12, 15, 32, 35, 48, 49, 50, 54, 56]

specific crystal structure and chemical formula for each mineral. However there are two specific principal difficulties associated with the measurement of thermal conductivity on mineral samples: purity and sample size. Lattice imperfections in crystals significantly decrease the thermal conductivity of many minerals. Correction of alien mineral phases in samples is possible (Horai, 1971), but requires further microscopic and X-ray examination of the samples.

If measurements on single crystals or monomineralic, polycrystalline aggregates are performed with a divided-bar (or comparable) method, a minimum sample size is required. Large single crystals that can be machined to the desired size, however, are relatively rare. When monomineralic aggregates are used instead, uncertainty is introduced by porosity. Alternatively, Horai & Simmons (1969) and Horai (1971) use a needle-probe technique to measure the conductivity of finely ground samples of minerals saturated with water. This way sample size poses no problem, but all information on anisotropy is lost. Moreover, the interpretation of measurements of thermal conductivity on fragments is not without ambiguity, as pointed out by Sass et al. (1971): their comparison between Horai & Simmons' (1969) transient needle-probe method and their steady-state divided-bar "cell" method on splits from Horai & Simmons's (1969) original mineral samples indicates that the results obtained from measurements on fragments depend on both the measurement technique and the model used for inferring the thermal conductivity of the solid constituents of the mixture.

Table 3 presents both kinds of data, measured both on single crystals as well as on natural monomineralic, polycrystalline aggregates, and on artificial monomineralic aggregates produced from a mixture of powdered mineral specimens and distilled water. Data from three sources are presented: (1) Diment & Pratt (1988) who report their own measurements as well as those performed or reported previously by Birch (1942, 1954), Birch & Clark (1940a,b), Clark (1966), Coster (1947), Ratcliffe (1959), Robertson (1988), and Sass (1965), (2) Dreyer (1974), a compilation of data measured by a variety of researchers, and finally (3) Horai (1971), including Horai & Simmons (1969). Additionally, recommended values for rocksalt as function of temperature reported by Yang (1981) are included in the first group, as well as an aggregate value for graphite from Grigull & Sandner (1990) and data on artificial periclase measured by Kanamori et al. (1968) in the second one. The data from Diment & Pratt (1988) represent measurements on individual samples; averages and standard deviations are computed, when several values are available for the same mineral and for comparable P,T-conditions. Data reported in Dreyer (1974) are averages over an unspecified number of individual measurements. The data in Horai (1971) consist of individual needle-probe measurements on water-saturated mineral powder. Ambient conditions are specified as "ordinary temperature and pressure" by Horai (1971) and as "room temperature" by Dreyer (1974). Diment & Pratt (1988) quote specific temperature and pressure conditions during measurement for most of the data they report.

Comparing the data in the first two columns, there is a good general agreement. However there are exceptions, when lattice imperfections lead to a significant decrease in thermal conductivity, as can be seen, for instance, in artifical vs. natural periclase, halite and rock salt, as well as in chlorite, magnetite, corundum, pyrite and fluorite.

Aggregate data from Diment & Pratt (1988) and Dreyer (1974) are in generally good agreement with those from Horai (1971). There are exceptions, though, that can be related to the technical details of the sample preparation and the measurement technique. Horai's (1971) value for talc, for instance, is twice as high as the two other aggregate data, but does not quite reach the parallel conductivity value. This is probably due to an oriented sedimentation of the powdered talc particles in the saturated sample compartment. Thus a needle probe measurement, which produces radial heat flow, will preferentially sample the component of thermal conductivity which is parallel to the sheet-like crystal structure of the talc particles. A similar effect, however not quite as pronounced, can be observed with serpentine.

As with rocks, data on the temperature dependence of thermal conductivity for minerals not very abundant. Yang's (1981) temperature dependent data for rock salt represent "recommended values" based on a great number of individual determinations and cover the temperature range 0.4-1000 K. Table 4 lists thermal conductivity and thermal diffusivity function of temperature for some rock-forming minerals as reported by Kanamori et al. (1968). Table 5, finally, provides values for the constants D and E from equation (3b), which may be used for inferring the temperature dependence of λ^{-1}, the thermal resitivity, for some monomineralic aggregates (Clark, 1969). Diffusivity and conductivity are related by

$$\kappa = \frac{\lambda}{\rho \cdot c_p} \quad , \tag{5}$$

where ρ is density and c_p specific heat capacity at constant pressure. Therefore the information on diffusivity is included here as well, although diffusivity is not further discussed in this review. On the basis of equation (5)

TABLE 3. Thermal conductivity λ (W m^{-1} K^{-1}) of different rock-forming minerals.[c]

mineral	T, state, λ, (n) [24]	state, λ [25]	state, λ, (n) [28]
	MISCELLANEOUS		
graphite, C		λ_{11}: **355.0**, λ_{33}:**89.4**, a: **155.0** [27]	
diamond, iso		λ_{11}: **545.3**	
pyrex 774 glass (T in °C)	T/ λ, amorphous: 0/**1.21**, 50/**1.26**, 100/**1.32**, 150/**1.38**, 200/**1.44**, 250/**1.49**, 300/**1.55**, 350/**1.61**, 400/**1.66**, 450/**1.72**, 500/**1.83** [8]		
ice (0°C), H_2O		λ_{11}: **1.9**, λ_{33}: **2.3**, a: **2.0** (-125 °C: **4.0**)	
	ORTHO- AND RINGSILICATES		
olivine group			
forsterite, $Mg_2[SiO_4]$	30 °C, a: **4.65 ± 0.33** (3) [8] (dunite, 97 % $Fo_{92}Fa_8$)		a: **5.03 ± 0.18** (5) ($Fo_{98}Fa_2$-$Fo_{91}Fa_9$)
fayalite, $Fe_2[SiO_4]$	30 °C, a: **3.85 ± 0.07** (4) (dunite, mostly Fa)		a: **3.16** (Fo_4Fa_{96})
garnet group	$(Mg,Fe,Mn,Ca)_3(Al,Fe)_2[SiO_4]_3$		
almandine, iso	? °C, a: **3.56**	λ_{11}: **3.6**	a: **3.31**
grossularite, iso	? °C, a: **5.32**		a: **5.48 ± 0.21** (3)
zircon group			
zircon, $ZrSiO_4$		λ_{11}: **3.9**, λ_{33}: **4.8**	a: **5.54**
titanite group (sphene)			
titanite $CaTi[SiO_4][OH]$			a: **2.34**
Al_2SiO_5 group			
kyanite	35 °C, a: **7.15 ± 0.14** (4) 35 °C, a: **12.45 ± 0.58** (3) (< 5 % quartz impurity)		a: **14.16**
andalusite	35 °C, a: **6.56 ± 0.42** (8) (<5 % quartz impurity)		a: **7.58**
sillimanite	35 °C, a: **10.73 ± 0.52** (3)		a: **9.10**

TABLE 3. (continued)

mineral	T, state, λ, (n) [24]	state, λ [25]	state, λ, (n) [28]
epidote group			
epidote, $Ca_2(Al,Fe)_3Si_3O_{12}[OH]$	31 °C, ⊥: **3.10** 32 °C, ∥: **2.93** 31 °C, a: **2.50 ± 0.02** (2)		a: **2.83 ± 0.21** (2)
	CHAIN SILICATES		
pyroxene group	$(Na,Ca)(Mg,Fe,Al)(Al,Si)_2O_6$		
enstatite			a: **4.47 ± 0.30** (4)
diopside, augite	35 °C, a: **4.23 ± 0.05** (4)		a: **4.66 ± 0.31** (4)
jadeite	34 °C, a: **5.59 ± 0.86** (2)		a: **5.64 ± 1.02** (2)
amphibole group	$NaCa_2(Mg,Fe,Al)(Al,Si)_8O_{22}(OH)_2$		
hornblende	20 °C, a: **2.91 ± 0.09** (2) [16]	**2.81 ± 0.41** (2)	a: **2.81 ± 0.27** (2)
	SHEET SILICATES		
mica group			
muscovite, $KAl_2[AlSi_3O_{10}][OH]_2$	30 °C, ∥: **3.89** (2) 32-45 °C, ⊥: **0.62 ± 0.11** (4)		a: **2.28 ± 0.07** (3)
biotite, $K(Mg,Fe,..)_3Al_2[AlSi_3O_{10}](OH,F)_2$	33 °C, ∥: **3.14** 32 °C, ⊥: **0.52 ± 0.01** (2)		a: **2.02 ± 0.32** (2)
talc, $Mg_3[Si_4O_{10}][OH]_2$	29-34 °C, ∥: **10.69 ± 1.35** (5) 30 °C, ⊥: **1.76 ± 0.00** (2) 30 °C, a: **2.97** [7]	a: **3.0 ± 0.1** (2)	a: **6.10 ± 0.90** (2)
chlorite	30 °C, a: **3.06 ± 1.18**	a: **5.25 ± 0.15** (2)	a: **5.15 ± 0.77** (3)
serpentine, $Mg_6[Si_4O_{10}][OH]_8$	32 °C, ⊥: **2.41 ± 0.10** (2) ? °C, ∥: **2.76 ± 0.03** (4) 30-34 °C, a: **2.61 ± 0.38** (10)	a: **2.33 ± 0.21 (3)**	a: **3.53 ± 1.28** (3)
	FRAMEWORK SILICATES		
feldspar group			
orthoclase, $K[AlSi_3O_8]$	30 °C, (100): **2.34 ± 0.08** (2) [43] 30 °C, (010): **2.68** [43] 30 °C, (001): **2.30 ± 0.21** (2) [43]		a: **2.31**
microcline, $K[AlSi_3O_8]$	? °C, (001): **2.04** [43]		a: **2.49 ± 0.08** (3)
albite, $Na[AlSi_3O_8]$	25 °C, a: **2.34** [43]	a: **2.0 ± 0.1**	a: **2.14 ± 0.19** (4)
anorthite, $Ca[AlSi_3O_8]$	25 °C, a: **2.72** [43]	a: **2.1**	

TABLE 3. (continued)

mineral	T, state, λ, (n) [24]	state, λ [25]	state, λ, (n) [28]
silica group, SiO_2			
α quartz	30 °C, ⊥: **6.15** [38], ∥: **10.17** [8]	λ_{11}: **6.5**, λ_{33}: **11.3**	a: **7.69**
α quartz ⊥ (T in °C)	T/λ, x: 0/**6.82**, 50/**5.65**, 100/**4.94**, 150/**4.44**, 200/**4.06**, 250/**3.73**, 300/**3.52**, 350/**3.31** [8]		
α quartz ∥ (T in °C)	T/λ, x: 0/**11.43**, 50/**9.38**, 100/**7.95**, 150/**7.03**, 200/**6.32**, 250/**5.69**, 300/**5.15**, 350/**4.73** [8]		
silica glass	30 °C, amorphous: **1.38** [38]		a: **1.36**
silica glass (T in °C)	T/λ, amorphous: 0/**1.36**, 50/**1.44**, 100/**1.48**, 150/**1.53**, 200/**1.58**, 250/**1.64**, 300/**1.70**, 350/**1.78**, 400/**1.85**, 450/**1.94**, 500/**2.07** [8]		
	NON-SILICATES		
oxides			
magnetite, Fe_3O_4, iso	22-33 °C, a: **4.61 ± 0.42** (8)	λ_{11}: **9.7**	a: **5.10**
hematite, Fe_2O_3	30 °C, a: **12.42 ± 1.74** (3) [7,16]	λ_{11}: **14.7**, λ_{33}: **12.1**	a: **11.28**
ilmenite, $FeTiO_3$	35 °C, a: **1.49 ± 0.02** (3)		a: **2.38 ± 0.18** (2)
chromite, $(Fe,Mg)Cr_2O_4$, iso	35 °C, a: **2.19 ± 0.15** (3)		a: **2.52**
spinel, $MgAl_2O_4$, iso	35-70 °C, a: **12.14 ± 1.23** (3) [16]	λ_{11}: **13.8**	a: **9.48**
rutile, TiO_2	44-67 °C, ⊥: **7.95 ± 0.84** (2) 36-67 °C, ∥: **13.19 ± 0.63** (2) [16] ? °C, a: **4.90 ± 0.17** (3) [16]	λ_{11}: **9.3** λ_{33}: **12.9**	 a: **5.12**
corundum, Al_2O_3	23-77 °C, ⊥: **17.70 ± 3.11** (4) 26-70 °C, ∥: **18.37 ± 3.46** (5)	λ_{11}: **31.2** λ_{33}: **38.9**	
periclase, MgO, iso artificial periclase		λ_{11}: **33.5** 400 K, λ_{11}: **41.05** [33]	
sulfides			
pyrite, FeS_2, iso	35 °C, a: **23.15 ± 2.00** (3)	λ_{11}: **37.9**	a: **19.21**
pyrrhotite, FeS	35 °C, a: **3.53 ± 0.05** (3)		a: **4.60**
galena, PbS	35 °C, a: **2.76 ± 0.18** (3)		a: **2.28**

TABLE 3. (continued)

mineral	T, state, λ, (n) [24]	state, λ [25]	state, λ, (n) [28]
sulfates			
baryte, $BaSO_4$	25-100 °C, ⊥: **2.07 ± 0.02** (2) 25-100 °C, ∥: **2.92 ± 0.07** (4) 25-35 °C, a: **1.72 ± 0.04** (4)		a: **1.31**
anhydrite, $CaSO_4$	25-35 °C, a: **5.36 ± 0.27** (6)		a: **4.76**
gypsum, $CaSO_4 \cdot 2H_2O$	? °C, :, **1.30** [20]	⊥: **3.16**, ∥: **3.63** λ_{11}: **2.6**, λ_{22}: **1.6**, λ_{33}: **3.7**	
carbonates			
calcite, $CaCO_3$	30 °C, ⊥: **3.16**, ∥: **3.63** [8]	λ_{11}: **4.2**, λ_{33}: **5.0**	a: **3.59**
calcite ⊥ (T in °C)	T/λ, x: 0/**3.48**, 50/**3.00**, 100/**2.72**, 150/**2.52**, 200/**2.37**, 250/**2.25**, 300/**2.16**, 350/**2.09**, 400/**2.06** [8]		
calcite ∥ (T in °C)	T/λ, x: 0/**4.00**, 50/**3.40**, 100/**2.99**, 150/**2.73**, 200/**2.55**, 250/**2.41**, 300/**2.29**, 350/**2.20**, 400/**2.13** [8]		
aragonite, $CaCO_3$	25-100 °C, a: **2.37 ± 0.22** (11)		a: **2.24**
magnesite, $MgCO_3$	25-100 °C, ⊥: **7.32 ± 0.57** (4) 25-100 °C, ∥: **7.86 ± 0.17** (4) 34-35 °C, a: **8.18 ± 1.20** (5)		a: **5.84**
siderite, $FeCO_3$	35 °C, a: **2.99 ± 0.12** (3)		a: **3.01**
dolomite, $CaMg[CO_3]_2$	25-35 °C, a: **4.78 ± 0.54** (70)	a: **4.9**	a: **5.51**
phosphates			
apatite, $Ca_5[PO_4]_3(F,OH)$	35 °C, a: **1.27 ± 0.02** (3)		a: **1.38 ± 0.01** (2)
halides			
halite, NaCl, iso	0-35 °C, x: **5.55 ± 1,02** (8) [16]	a: **6.5**	
halite, NaCl, iso (T in °C)	T/λ, x: 0/**6.11**, 50/**5.02**, 70/**5.44**, 100/**4.21**, 150/**3.59**, 200/**3.12**, 250/**2.76**, 300/**2.49**, 350/**2.30**, 400/**2.09** [8]		
rocksalt, NaCl, iso	27 °C, a: **5.94 ± 0.83** (6)		

TABLE 3. (continued)

mineral	T, state, λ, (n) [24]	state, λ [25]	state, λ, (n) [28]
rocksalt, NaCl, iso (T in K)	T/λ: 0.4/**0.95**, 0.5/**1.78**, 0.6/**3.13**, 0.7/**4.97**, 0.8/**7.40**, 0.9/**10.0**, 1/**14.0**, 2/**99.3**, 3/**270**, 4/**443**, 5/**595**, 6/**735**, 7/**829**, 8/**880**, 9/**870**, 10/**836**, 15/**502**, 20/**306**, 25/**191**, 30/**130**, 40/**75.0**, 50/**54.0**, 75/**34.9**, 100/**24.3**, 150/**15.0**, 200/**10.9**, 250/**8.24**, 293/**6.65**, 300/**6.57**, 400/**4.80**, 500/**3.67**, 600/**2.98**, 700/**2.47**, 800/**2.08**, 900/**1.85**, 1000/**1.67** [55]		
sylvite, KCl, iso	0-12 °C, x: **6.95** ± **0.21** (2) [16]	λ_{11}: **6.4**	
fluorite, CaF_2, iso	0-36 °C, x: **8.63** ± **0.58** (6)	λ_{11}: **10.1**	a: **9.51**

[c]minerals marked "iso" are isotropic. T is ambient temperature, and (n) is number of data for mean and standard deviation. "x" denotes measurements of unknown orientation on single crystals, "a" on monomineralic aggregates. Directions of anisotropy are specified in one of three ways: (1) by the mineral's optical a-, b-, or c-axes (100, 010, 001), (2) by the diagonal elements of the thermal conductivity tensor (λ_{11}, λ_{22}, λ_{33}), where λ_{33} is parallel to the crystal's optical c-axis, and the optical a-axis lies within the plane defined by λ_{11} and λ_{22}, (3) by the thermal conductivity components normal or parallel to the direction of maximum thermal conductivity ($\perp$, $\parallel$).

TABLE 4. Thermal conductivity λ (W m^{-1} K^{-1}, lower, boldface number) and thermal diffusivity κ (10^{-6} m^2 s^{-1}, upper lightface number) at different temperatures for quartz, fused silica, olivine, and synthetic periclase.[f]

mineral	300 K	400 K	500 K	600 K	700 K	800 K	900 K	1000 K	1100 K
quartz (001)	7.14	3.57	2.38	1.69	1.37	1.14	1.41	1.54	1.64
	13.93	**8.20**	**6.24**	**4.81**	**3.91**	**3.56**	**3.87**	**4.56**	**5.15**
quartz (010)	3.33	2.00	1.45	1.15	0.96	0.89	1.00	1.14	1.28
	6.49	**4.60**	**3.83**	**3.29**	**2.90**	**2.79**	**2.75**	**3.39**	**4.03**
fused silica	0.725	0.715	0.705	0.700	0.715	0.741	0.800	0.885	-
	1.147	**1.348**	**1.499**	**1.612**	**1.725**	**1.854**	**2.060**	**2.323**	-
olivine (001)	1.85	1.49	1.22	1.08	1.03	1.04	1.09	1.2	1.35
($Fo_{82}Fa_{18}$)	**5.07**	**4.73**	**4.23**	**3.89**	**3.86**	**3.98**	**4.23**	**4.77**	**5.44**
periclase, MgO	-	12.5	8.70	6.67	5.56	4.65	4.00	3.57	3.23
(001)	-	**46.05**	**34.12**	**27.21**	**23.19**	**19.63**	**17.12**	**15.61**	**14.32**
jadeite, a	1.54	1.28	1.11	0.97	0.88	0.84	0.83	0.89	0.96
	-	-	-	-	-	-	-	-	-
garnet, x	1.10	1.00	0.91	0.85	0.81	0.79	0.80	0.81	0.83
(mean of 2)	-	-	-	-	-	-	-	-	-

TABLE 4. (continued)

mineral	300 K	400 K	500 K	600 K	700 K	800 K	900 K	1000 K	1100 K
spinel, x	-	-	3.45	3.13	2.86	2.56	2.44	2.25	2.13
	-	-	-	-	-	-	-	-	-
corundum, x	-	6.06	4.55	3.45	2.86	2.50	2.13	1.85	1.64
	-	-	-	-	-	-	-	-	-
alkali feldspar, x	7.09	6.67	6.49	6.71	6.99	7.30	7.81	8.33	8.93
(moonstone)	-	-	-	-	-	-	-	-	-

[f]after [33]; "x" denotes measurements of unknown orientation on single crystals, "a" on monomineralic aggregates. Directions of anisotropy are specified by the mineral's optical a-, b-, or c-axes (100, 010, 001). Temperature conversion: T(°C) = T(K) - 273.15

Robertson (1988) converts the feldspar diffusivity data of Kanamori et al. (1968) into conductivity, using a constant density of $\rho = 2.6$ g cm^{-3} and a temperature dependent specific heat capacity. However, a comparison of this data set with results from temperature dependent measurements of feldspar conductivity performed by other authors shows somewhat ambiguous results: Some measurements contradict the increase in conductivity with temperature displayed by Kanamori at al.'s (1968) converted data while those performed by Birch & Clark (1940a,b), seem to confirm it, at least in the temperature range 25-300 °C.

5. CONCLUSION

This review provides information on thermal conductivity of crustal rocks in general. For modest temperatures and pressures there is a great variation of thermal conductivity which decreases significantly for temperatures and pressures above 300 °C and 20 MPa, respectively. As thermal conductivity for any specific rock type varies according to its mineral content, porosity, pore fluid, and anisotropy, a table of thermal conductivity purely according to rock type

TABLE 5. Constants D and E from equation (3b) for monomineralic aggregates.[g]

mineral	T (°C)	D (10^{-3} m K W^{-1})	E (10^{-3} m W^{-1})
NaCl	0-400	-52.55	0.788
MgO	100-800	-21.50	0.127
Al_2O_3	100-800	-28.66	0.155
SiO_2 (*)	100-400	62.10	0.387
$MgAl_2O_4$	100-1000	19.11	0.122
$ZrSiO_4$	100-800	131.37	0.093
Mg_2ZrSiO_4	100-600	85.98	0.282
$(Mg,Fe)SiO_3$	100-300	200.63	0.222

[g]after [17]; *: single SiO_2 crystal, $\perp$ to optical axis

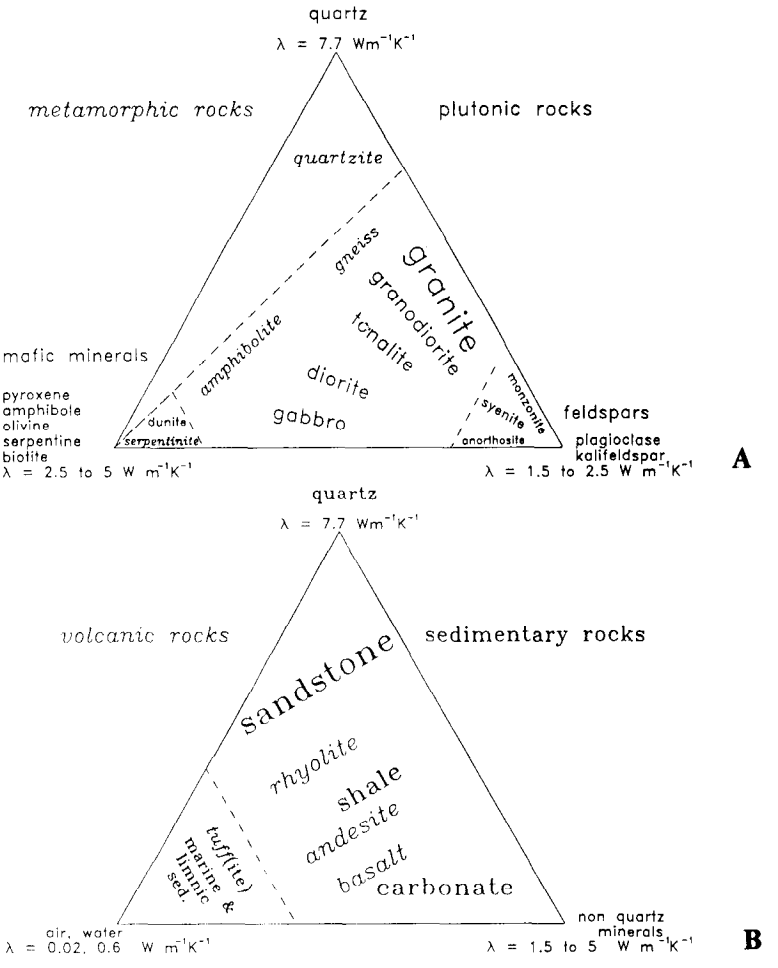

Fig. 7. Thermal conductivity of basic rock-forming minerals and compositional relationship with rocks. (a) metamorphic and plutonic rocks, (b) volcanic and sedimentary rocks. Metamorphic and volcanic rocks are in italics, plutonic and sedimentary rocks are not italicized. For volcanic and sedimentary rocks the third "mineral" phase is air or water, due to the great importance of porosity for the thermal conductivity of these rocks.

cannot provide site-specific information. Here site-specific measurements are required.

For these reasons no table of thermal conductivity versus rock type is given. However, in order to illustrate the various factors that influence thermal conductivity at least in a semi-quantitative way, we summarize the results of our review in two ternary diagrams. These relate different types of rocks with those factors that have the most pronounced effect on their thermal conductivity. Two diagrams are provided, one for metamorphic and plutonic rocks (Figure 7a), and one for volcanic and sedimentary rocks (Figure 7b). The different rocks are representative for various classes of rocks within each group, thus representing the total spectrum of thermal conductivity in each group. Feldspars are not further classified according to the IUGS (International Union of Geological Sciences) system because of their low variability in thermal conductivity. The position of a rock's name in the compositional triangle indicates in a qualitative way its thermal conductivity. In principle, these two diagrams thus reflect the information contained in Figures 1a-1d, presenting it in a somewhat different way: metamorphic and plutonic rocks are made up of quartz, feldspars, and mafic minerals, and the content of minerals from these three groups basically determines a rock's thermal conductivity. In volcanic and sedimentary rocks the third mineral component is replaced by air or water, as the high variability of porosity in these rocks is a major factor controlling their thermal conductivity.

Acknowledgements. This work benefitted a great deal from the interdisciplinary approach and enthusiasm for cross-disciplinary discussions of members of the KTB team of scientists. Ulli Harms was a knowledgable partner in many discussions on the thermal consequences of petrological peculiarities and provided guidance through the system of petrological classifications. Alan Beck (Univ. of Western Ontario, London, Ont.) shared with us his command of literature on the subject and made available original data sets compiled by himself for his contribution to Roy et al. (1981). Ulfert Seipold (Geoforschungszentrum Potsdam) and Meinrad Reibelt (Tech. Univ. Berlin) contributed their published and unpublished data, Heiner Villinger (Univ. of Bremen) helped with marine data, and Lazi Rybach (ETH Zürich) provided valuable leads to recent literature. We are grateful to a number of kind and knowledgeable reviewers who helped to improve this manuscript: Thomas Ahrens, Alan Beck, Vladimir Čermák, Al Duba, Ralph Hänel, Daniel Pribnow, Lazi Rybach, John Sass, and Heiner Villinger.

REFERENCES

1. Anand, J., Somerton, W. H., and E. Gomaa, Predicting thermal conductivities of formations from other known properties, *Soc. Petrol. Eng. Journal, 13,* 267-273, 1973.
2. Asaad, Y., *A study on the thermal conductivity of fluid-bearing rocks,* 71 pp., Dissertation, Univ. of California, Berkeley, 1955.
3. Beck, A. E., Techniques of measuring heat flow on land, in *Terrestrial Heat Flow,* edited by W. H. K. Lee, pp. 24-57, Amer. Geophys. Union, Washington, 1965.
4. Beck, A. E., Methods for determining thermal conductivity and thermal diffusivity, in *Handbook of Terrestrial Heat Flow Density Determination,* edited by R. Hänel, L. Rybach and L. Stegena, pp. 87-124, Kluwer, Dordrecht, 1988.
5. Beck, A. E., and J. M. Beck, On the measurement of thermal conductivities of rocks by observations on a divided bar apparatus, *Trans. Amer. Geophys. Union, 39,* 1111-1123, 1958.
6. Birch, F., Thermal conductivity and diffusivity, in *Handbook of Physical Constants,* edited by F. Birch, J. F. Schairer, and H. C. Spicer, pp. 243-266, Geological Society of America, Special Paper 36, New York, 1942.
7. Birch, F., Thermal conductivity, climatic variation, and heat flow near Calumet, Michigan, *Am. J. Sci., 252(1),* 1-25, 1954.
8. Birch, F., and H. Clark, The thermal conductivity of rocks and its dependence upon temperature and composition, Part I, *Am. J. Sci., 238(8),* 529-558, 1940a.
9. Birch, F., and H. Clark, The thermal conductivity of rocks and its dependence upon temperature and composition, Part II, *Am. J. Sci., 238(9),* 613-635, 1940b.
10. Blackwell, D. D., Thermal conductivity of sedimentary rocks: measurement and significance, in *Thermal History of Sedimentary Basins,* edited by N. D. Naser and T. H. McCulloh, pp. 13-36, Springer, Berlin-Heidelberg, 1989.
11. Bullard, E. C., Heat flow in South Africa, *Proc. Roy. Soc. London, Series A, 173,* 474-502, 1939.
12. Bullard, E. C., and E. R. Niblett, Terrestrial heat flow in England, *Monthly Notices Roy. Astr. Soc. London, Geophys. Suppl., 6,* 222-238, 1951.
13. Buntebarth, G., Thermal properties of KTB-Oberpfalz VB core samples at elevated temperature and pressure, *Scientific Drilling, 2,* 73-80, 1991.
14. Čermák, V., and L. Rybach, Thermal conductivity and specific heat of minerals and rocks, in *Landolt-Börnstein: Numerical Data and Functional Relationships in Science and Technology, New Series, Group V (Geophysics and Space Research), Volume 1a (Physical Properties of Rocks),* edited by G. Angenheister, pp. 305-343, Springer, Berlin-Heidelberg, 1982.
15. Clark, H., The effects of simple compression and wetting on the thermal conductivity of rocks, *Trans. Amer. Geophys. Union, 22(II),* 543-544, 1941.
16. Clark, S. P. Jr., Thermal Conductivity, in *Handbook of Physical Constants,* edited by S. P. Clark Jr., pp. 459-482, Geol. Soc. of America, Memoir 97, New York, 1966.
17. Clark, S. P. Jr., Heat conductivity in the mantle, in *The Earth's Crust and Upper Mantle,* edited by P. J. Hart, pp. 622-626, Amer. Geophys. Union, Geophysical Monograph 13, Washington, 1969.
18. Clauser, C., Opacity - the concept of radiative thermal conductivity, in *Handbook of Terrestrial Heat Flow Density Determination,* edited by R. Hänel, L. Rybach and L. Stegena, pp. 143-165, Kluwer, Dordrecht, 1988.
19. Clauser, C., Permeability of crystalline rocks, *EOS Trans. Amer. Geophys. Union, 73(21),* 233,237, 1992.
20. Coster, H. P., Terrestrial heat flow in Persia, *Monthly Notices Roy. Astr. Soc., Geophys. Suppl., 5(5),* 131-145, 1947.
21. Davis, E. E., Oceanic heat flow density, in *Handbook of Terrestrial Heat Flow Density Determination,* edited by R. Hänel, L. Rybach and L. Stegena, pp. 223-260, Kluwer, Dordrecht, 1988.
22. Demongodin, L., B. Pinoteau, G. Vasseur, and R. Gable, Thermal conductivity and well logs: a case study in the Paris basin, *Geophys. J. Int., 105,* 675-691, 1991.
23. Desai, P. D., R. A. Navarro, S. E. Hasan, C. Y. Ho, D. P. DeWitt, and T. R. West, *Thermophysical Properties of Selected Rocks,* 256 pp., CINDAS Report 23, Center for Information and Numerical Data Analysis and Synthesis (CINDAS), Purdue Univ., West Lafayette, Indiana (USA), 1974.
24. Diment, W. H., and H. R. Pratt, Thermal conductivity of some rock-forming minerals: a Tabulation, *U.S.G.S. Open file report 88-690,* 15 pp., U. S. Geol. Survey, Denver Co., 1988.

25. Dreyer, W., *Properties of Anisotropic Solid-State Materials: Thermal and Electric Properties (Materialverhalten anisotroper Festkörper: Thermische und elektrische Eigenschaften)*, 295 pp., Springer, Wien, 1974 *(in German)*.
26. Etheridge, M. A., V. J. Wall, and R. H. Vernon, The role of the fluid phase during regional metamorphism and deformation, *J. Metamorph. Geol., 1*, 205-226, 1983.
27. Grigull, U., and H. Sandner, *Heat Conduction (Wärmeleitung)*, 2nd. edition, 163 pp., Springer, Berlin-Heidelberg, 1990 *(in German)*.
28. Horai, K., Thermal conductivity of rock-forming minerals, *J. Geophys. Res., 76(5)*, 1278-1308, 1971.
29. Horai, K., Thermal conductivity of Hawaiian basalt: a new interpretation of Robertson and Peck's data, *J. Geophys. Res., 96(B3)*, 4125-4132, 1991.
30. Horai, K., and G. Simmons, Thermal conductivity of rock-forming minerals, *Earth and Planet. Sci. Lett., 6*, 359-368, 1969.
31. Huenges, E., H. Burkhardt, and K. Erbaş, Thermal conductivity profile of the KTB pilot corehole, *Scientific Drilling, 1*, 224-230, 1990.
32. Hutt, J. R., and J. Berg Jr., Thermal and electrical conductivities of sandstone rocks and ocean sediment, *Geophysics, 33*, 489-500, 1968.
33. Kanamori, H., N. Fujii, and H. Mizutani, Thermal diffusivity measurement of rock-forming minerals from 300 ° to 1100 °K, *J. Geophys. Res., 73(2)*, 595-605, 1968.
34. Kappelmeyer, O., and R. Hänel, *Geothermics with Special Reference to Application*, 238 pp., Gebrüder Borntträger, Berlin-Stuttgart, 1974.
35. Kunii, D., and J. M. Smith, Thermal conductivities of porous rocks filled with stagnant fluid, *Soc. Petrol. Eng. Journal, 1(1)*, 37-42, 1961.
36. Messmer, J. H., The thermal conductivity of porous media. IV. Sandstones. The effect of temperature and saturation, in *Proceedings of the Fifth Conference on Thermal Conductivity, Vol. 1*, pp. 1-29, Univ. of Denver, Denver, Co., 1965.
37. Pribnow, D., C. F. Williams, and H. Burkhardt, Well log-derived estimates of thermal conductivity in crystalline rocks penetrated by the 4-km deep KTB Vorbohrung, *Geophys. Res. Lett., 20(12)*, 1155-1158, 1993.
38. Ratcliffe, E. H., Thermal conductivity of fused and crystalline quartz, *Brit. J. Appl. Phys., 10*, 22-25, 1959.
39. Reibelt, M., *Study of the Influence of Surface Structure and Fluid-Saturation of Rocks on the Determination of Thermal Conductivity using a Half-Space Line Source (Untersuchung des Einflusses der Oberflächenbeschaffenheit und der Fluidsättigung von Gesteinen auf die Messung der Wärmeleitfähigkeit mit einer Halbraumlinienquelle)*, 111 pp., Diploma Thesis (unpublished), Inst. f. Angew. Geophysik, Tech. Univ. Berlin, Berlin, 1991 *(in German)*.
40. Robertson, E. C., and D. L. Peck, Thermal conductivity of vesicular basalt from Hawaii, *J. Geophys. Res., 79(32)*, 4875-4888, 1974.
41. Robertson, E. C., Thermal properties of rocks, *U.S.G.S. Open file report 88-441*, 106 pp., U. S. Geol. Survey, Reston, Va., 1988.
42. Roy, R. F., A. E. Beck, and Y. S. Touloukian, Thermophysical properties of rocks, in *Physical Properties of Rocks and Minerals*, edited by Y. S. Touloukian, W. R. Judd, and R. F. Roy, pp. 409-502, McGraw-Hill/CINDAS Data Series on Material properties, Volume II-2, McGraw-Hill, New York 1981.
43. Sass, J. H., The thermal conductivity of fifteen feldspar specimens, *J. Geophys. Res., 70(16)*, 4064-4065, 1965.
44. Sass, J. H., A. H. Lachenbruch, and R. J. Monroe, Thermal conductivity of rocks from measurements on fragments and its application to heat-flow determinations, *J. Geophys. Res., 76(14)*, 3391-3401, 1971.
45. Sass, J. H., A. H. Lachenbruch, and T. H. Moses Jr., Heat flow from a scientific research well at Cajon Pass, California, *J. Geophys. Res., 97(B4)*, 5017-5030, 1992.
46. Seipold, U., Pressure and temperature dependence of thermal transport properties of granites, *High Temperatures - High Pressures, 22*, 541-548, 1990.
47. Somerton, W. H., *Thermal Properties and Temperature-Related Behaviour of Rock/Fluid Systems*, 257 pp., Elsevier, Amsterdam, 1992.
48. Sugarawa, A., and Y. Yoshizawa, An investigation on the thermal conductivity of porous materials and its application to porous rock, *Austral. J. Phys., 14(4)*, 469-480, 1961.
49. Sugarawa, A., and Y. Yoshizawa, An experimental investigation on the thermal conductivity of porous materials, *J. Appl. Phys., 33*, 3135-3138, 1962.
50. Sukharev, G. M., and Z. V. Sterlenko, Thermal properties of sandstone saturated with water and oil (Teplovye svotsva peshankov, nasyshennych presnoj vody i nefti), *Doklady Akademija Nauk, SSSR, 194*, 683-685, 1970 *(in Russian)*.
51. Torgersen, T., Crustal-scale fluid transport: magnitude and mechanisms, *EOS Trans. Amer. Geophys. Union, 71(1)*, pp. 1,4,13, 1990.
52. Tye, R. P. (Ed.), *Thermal Conductivity, vols. 1 and 2*, 422 and 353 pp., Academic Press, London, 1969.
53. Williams, C. F., and R. A. Anderson, Thermophysical properties of the earth's crust: in situ measurements from continental and oceanic drilling, *J. Geophys. Res., 95(B6)*, 9209-9236, 1990.
54. Woodside, W., and J. H. Messmer, Thermal conductivity of porous media, I: Unconsolidated sands, II. Consolidated rocks, *J. Appl. Phys., 32*, 1688-1706, 1961.
55. Yang, J. M., Thermophysical properties, in *Physical Properties Data for Rock Salt*, edited by L. H. Gevantman, pp. 205-221, Monograph 167, National Bureau of Standards, Washington, 1981.
56. Zierfuss, H., and G. van der Vliet, Measurement of heat conductivity of sedimentary rocks, *Bull. Am. Assoc. Petrol. Geol., 40*, 2475-2488, 1956.
57. Zoth, G., and Hänel, R., Appendix, in *Handbook of Terrestrial Heat Flow Density Determination*, edited by R. Hänel, L. Rybach and L. Stegena, pp. 449-466, Kluwer, Dordrecht, 1988.

Rock Failure

David A. Lockner

1. INTRODUCTION

1.1. Background

Analysis of a wide range of problems in the geosciences requires knowledge of the failure process in rock. This includes tunnel design and other engineering applications as well as geophysical problems such as earthquake prediction. The empirical Coulomb failure criterion

$$|\tau| = C + \mu_i{}'\sigma_n, \tag{1}$$

where C is cohesion, τ is shear strength and σ_n is normal stress, was proposed in the late 18^{th} century and continues to be of great practical use. In the 1920's, Griffith [48] demonstrated the importance of flaws, which act as stress concentrators, in controlling the strength of brittle materials. Using this approach, fracture mechanics (*e.g.* [5, 17]) has been highly successful in relating defect structures to fracture strength and related properties. Through the 1960's, many of the advances in the theory of fracture and friction in rock have had their origins in metallurgy; a fact that has mixed blessings since plastic yielding, commonly involved in the deformation of metals, may be completely absent in room-temperature brittle deformation of common silicates such as quartz [154]. Thus, in contrast to plastic yielding which has little or no pressure sensitivity, a material obeying the Coulomb equation (1) shows significant strengthening with pressure. Although a Coulombic material may deform in a manner described as plastic flow, the microscopic mechanisms of grain rolling or crushing and associated dilatancy, are quite different than those responsible for plasticity in metals. The same processes are likely to occur during shearing across a fault surface.

Before proceeding, a point of nomenclature must be clarified. Internal friction, as presented in (1) and commonly used in rock mechanics texts (*e.g.* [66]), refers to the local slope of a failure criterion in shear/normal stress space: $\mu_i{}' = \partial|\tau|/\partial\sigma_n$. The prime symbol is used to denote this local derivative. I will also make use of an alternate quantity, referred to as coefficient of friction defined as the simple ratio of shear to normal stress: $\mu_f = |\tau|/\sigma_n$. This parameter, written without the prime symbol, is commonly used in the analysis of stresses on preexisting faults and can also be applied to internal friction of intact rocks (referred to as μ_i). Due both to cohesion and to non-linearity in the failure envelopes of true rocks, it is common to find $\mu_i{}' < \mu_i$.

A number of comprehensive studies and reviews of the general field of rock failure and rheology currently exist [12, 38, 50, 66, 70, 71, 78, 120, 138]. By contrast, the present chapter will be more limited in scope and will be restricted to a discussion of brittle failure mechanics. It is intended to fulfill three main objectives: 1) an overview of recent progress in the study of rock failure - an evaluation which, by necessity, will be brief. 2) An extensive reference section is included to provide interested readers with an entry point into the relevant literature. 3) The chapter concludes with a number of summary plots and tables to provide a quick reference to the range of mechanical

D. A. Lockner, United States Geological Survey, 345 Middlefield Road, Menlo Park, CA 94025

Rock Physics and Phase Relations
A Handbook of Physical Constants
AGU Reference Shelf 3

properties that are observed for geologic materials.

Since I consider only brittle fracture, I will be concerned primarily with processes occurring in the mid to upper crust. For many silicate rocks under these conditions, temperature is low enough for brittle crack growth to compete and generally dominate thermally activated dislocation flow mechanisms. Even so, over geologic time scales, pressure solution and other fluid assisted deformation mechanisms may prevent, or at least subdue, brittle fracture. In general, brittle failure is enhanced by increasing strain rate and decreasing temperature, although these effects are relatively small compared to the influence of mean stress and pore pressure. In the following sections I discuss some of the important factors that influence fracture strength, although additional factors not addressed in detail include: alteration and weathering; porosity [35, 43, 125], fabric, minerology, and anisotropy [45, 62, 157, 158]; and intermediate stress [2, 151].

1.2. Conceptual Model of Brittle Fracture Process

The following descriptions are provided as a framework for the discussion of brittle fracture. When a sample is loaded in tension, preexisting flaws act as stress concentrators, intensifying the stress field at their tips. Since the tensile stress intensity K_I increases as the square root of crack length [79], the largest favorably oriented flaw generally experiences the greatest crack-tip stress. If the remote stress is increased until stress intensity on the critical flaw exceeds the fracture toughness K_{IC}, the flaw will grow in the plane perpendicular to the maximum tensile stress direction. For constant sample boundary conditions, each increment of crack growth results in a further increase in stress intensity. As a result, once crack growth is initiated, propagation continues unstably until the sample is fractured.

A more complicated process is involved in compressive brittle shear fracture. Open pores, contrasts in elastic properties of adjacent minerals and weak grain boundaries can all act as stress concentrators in compression [121, 152] and shearing along surfaces oblique to σ_1 is likely to play an important role in the development of large local stresses [4, 60, 96, 121, 134]. The local stresses induced near the crack tips contain a component of tension which leads to local tensile failure before the fracture toughness for failure in shear is achieved [79]. As a result, tensile 'wing' cracks grow which align themselves sub-parallel to the σ_1 direction. Unlike the case of remotely applied tensile stress, two important stabilizing processes take place during the loading of cracks in compression. First, as wing cracks extend, stress intensity decreases, so that additional deviatoric stress must be applied to cause further crack growth [28, 30, 60]. Second, diagonal flaws which are favorably oriented to act as nucleation points for shear failure, propagate out-of-plane (parallel to σ_1) and cannot maintain the necessary shear geometry [79, 94]. These stabilizing effects account for the factor of ten or more difference in compressive vs. tensile strength commonly observed in rocks. Eventually, crack densities become sufficiently large for significant crack interaction to occur, leading to a cooperative failure mechanism involving *en echelon* arrays of cracks [4, 30, 34, 60, 69, 96, 121, 126, 134]. Finally, quasi-static fault growth experiments [92, 93, 106] have demonstrated that following nucleation, shear fractures propagate in-plane due to their own stress field. This observation is important for laboratory scales since in past studies it was often argued that the eventual fracture plane began forming, as a region of high microcrack damage, well before peak strength occurred. While this interpretation may hold for samples containing large preexisting flaws, it appears that in homogeneous, isotropic rocks, there is generally little warning regarding the location and orientation of the eventual fracture plane. Similar results were reported in recent field studies [80] where nucleation zones for moderate-sized earthquakes were inferred to be less than 0.1% of the coseismic rupture surface area.

2. ROCK FAILURE ANALYSIS

2.1. Failure Criteria

One of the basic goals of rock mechanics has been to provide useful methods for predicting failure strength and associated parameters such as strain to failure and the effects of porosity and elastic moduli. The large number of competing effects that influence the fracture process has precluded the development of a universal law which can be used in any practical way to predict fracture strength for an arbitrary rock. As a result, a variety of classification systems have been developed to be used as predictive tools in estimating the load bearing capacity of various rock types. A number of these classification systems, using rock quality parameters such as Deere's RQD [31], the CSIR geomechanics classification [10], and the NGI quality index Q [7], are described in [58]. These classification systems attempt to take into account such factors as rock type, joint spacing, joint orientation and strength of joint-filling material. Many attempts at developing failure crite-

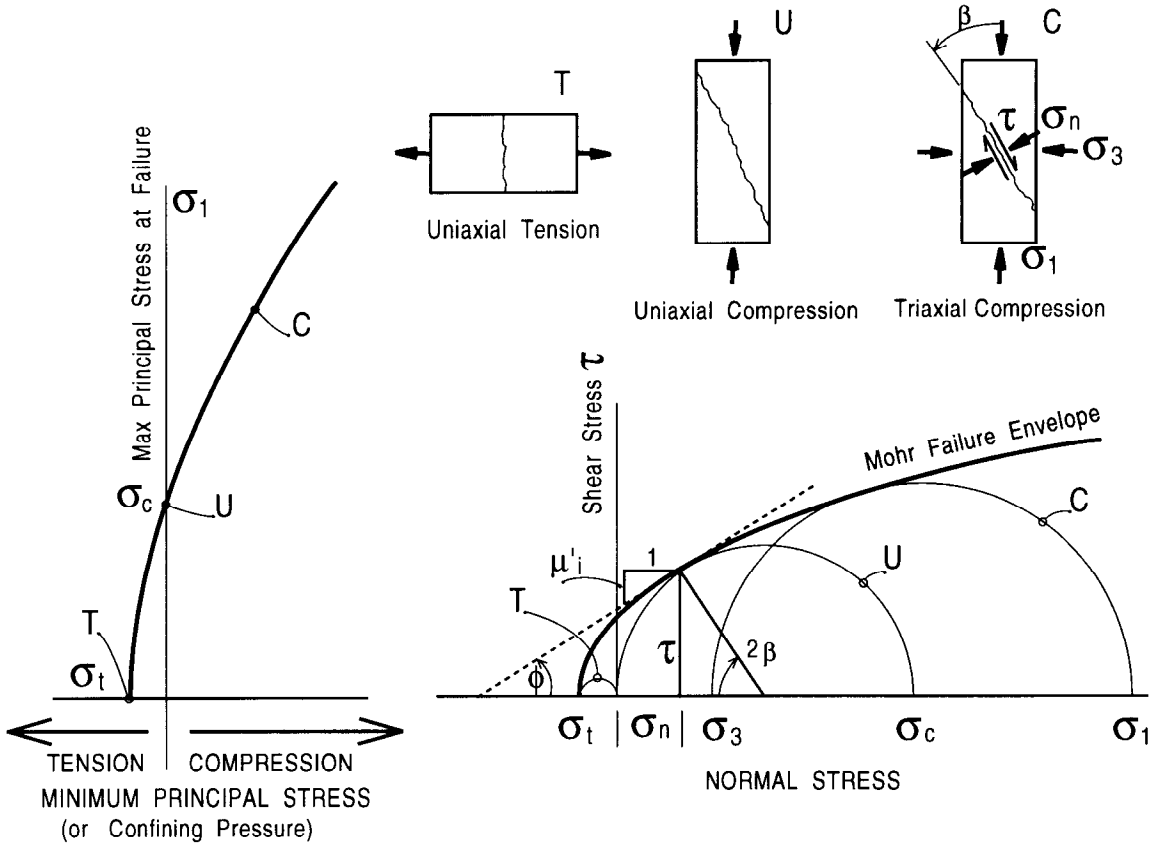

Fig. 1. Left: Relationship between principal stresses at failure. Right: Mohr failure envelope showing relationship between stresses and failure parameters. β is angle between failure surface and direction of maximum principal stress σ_1. Stresses are related by $\tau = 1/2(\sigma_1 - \sigma_3)\sin 2\beta$ and $\sigma_n = 1/2(\sigma_1 + \sigma_3) - 1/2(\sigma_1 - \sigma_3)\cos 2\beta$.

ria have relied on empirical fits to data sets of fracture strength, although increasingly sophisticated theoretical formulations, especially focusing on micromechanical deformation mechanisms, are also appearing. The linear Coulomb criterion (1) remains a simple and useful empirical relation. The additional assumption that failure occurs when (1) is first met on the most favorably oriented plane, leads to the well known Mohr-Navier-Coulomb relations

$$\phi = \tan^{-1}\mu_i' = \pi/2 - 2\beta, \tag{2a}$$

$$\sigma_1 = \sigma_c + [(\mu_i'^2 + 1)^{1/2} + \mu_i']^2\sigma_3 \tag{2b}$$

where ϕ is the angle of internal friction, β is the angle between the failure plane and the maximum principal stress direction, and σ_c is uniaxial compressive strength [66]. However, it is well known that failure envelopes for rocks are, in general, concave towards the σ_3 or σ_n axis. At high pressures, strength eventually becomes insensitive to pressure [4], a response generally referred to as plastic or ductile, even though the microscopic mechanisms may still remain brittle for some silicates. Geometric relations between various stress parameters are shown in Figure 1. Because of the curvature inherent in failure envelopes of real rocks, various investigators have proposed non-linear failure criteria, most of which are empirical in nature. Representative criteria include the following:

$$\sigma_1 = \sigma_3 + a(\sigma_1 + \sigma_3)^b \quad [41] \tag{3}$$

$$\sigma_1 = \sigma_3 + (a\sigma_c\sigma_3 + b\sigma_c^2)^{1/2} \quad [58] \tag{4}$$

$$\sigma_1/\sigma_3 = 1 + a(\sigma_c/\sigma_3)^b \qquad [166], [143] \qquad (5)$$

$$\sigma_1 = \sigma_c(1 - \sigma_3/\sigma_t)^b \qquad [140] \qquad (6)$$

where σ_t (negative in tension) is uniaxial tensile strength. In these relations, the various a's and b's are constants that represent material properties of the rock and generally vary between rock types. Equations (3) – (5) are designed to model confined strength data and have varying degrees of difficulty with unconfined or tensile conditions. For example, the unconfined condition is described by ($\sigma_3 = 0; \sigma_1 = \sigma_c$). In this case, (3) reduces to $\sigma_c = a\sigma_c^b$. Similarly, (4) requires $b = 1$, which is overly restrictive. equation (5) lacks real solutions for tensile conditions. Equation (6) seems to provide a satisfactory compromise between reasonable strength predictions near zero confinement and observed non-linearity at higher confinement. The interested reader is referred to the relevant articles cited for additional details regarding these formulas. Other empirical relations have been proposed to relate failure strength to material properties; for example

$$\sigma_c = a(E/\nu)^b \qquad [155] \qquad (7a)$$

$$\sigma_c = a\eta^b \qquad [35, 43] \qquad (7b)$$

where E is Young's modulus, ν is Poisson's ratio and η is porosity. Failure strength has also been related empirically to geophysical logging parameters:

$$\sigma_c = ae^{-bt} \qquad [101] \qquad (8a)$$

$$\sigma_c = a + b(\text{SNPU}) \qquad (8b)$$

where t is sonic interval travel time and SNPU is neutron log response.

2.2. Continuum Models

The transition from uniformly distributed deformation to shear localization has been analyzed theoretically from a continuum point of view. One example involves an instability, or bifurcation, that develops in the strain field as the result of strain weakening. Then, when a small region yields, in response to the applied boundary conditions, it becomes weaker than its surroundings and tends to continue deforming. This process tends to localize strain into a shear band [37, 39, 67, 77, 119, 130, 131, 150, 156]. In principal, the localization process does not require strain-weakening. This is an area of active research both theoretically and experimentally [118, 161]. Bifurcation theory deserves a much more thorough treatment than is allowed by space constraints in this section.

2.3. Damage Models

A different approach to brittle failure analysis, referred to as *damage mechanics*, has led to the development of a distinct class of models. In this case, failure is assumed to occur when a critical amount of damage has accumulated in the rock. Then an internal state variable D is developed that represents the degree of damage. The problem then becomes one of relating the microcrack damage in the rock to external variables such as stress and strain [4, 28–30, 68, 98, 148]. The most promising approach has been to use fracture mechanics to relate local crack tip stress intensities to remotely applied stresses [4, 30]. A similar approach [83], based on the Ashby and Sammis formulation, has been used to interpret time-dependent creep. Ashby and Sammis [4] have attempted to simplify the analysis to provide a universal form, based on a physical model of crack growth, which allows the damage parameter to be expressed in terms of macroscopic material properties and measurable microscopic quantities. As an example, they derive an expression (for loading at constant σ_3) for the normalized axial stress S_1 in terms of normalized confining pressure S_3 and damage D:

$$S_1 = c_2\left[D_r^{1/3} - c_5\right]^{3/2} \qquad (9a)$$

$$+S_3\left\{c_1\left[1 + \left[\frac{c_3 D_O^{2/3}}{1 - D^{2/3}}\right]\left(D_r^{1/3} - 1\right)^2\right] + c_4\left(D_r^{1/3} - 1\right)^2\right\}$$

$$\overline{\qquad 1 + c_3 \frac{D_O^{2/3}}{\left[1 - D^{2/3}\right]}\left[D_r^{1/3} - 1\right]^2 \qquad}$$

where $D_r = D/D_0$, D_0 is initial damage, and c_1 through c_5 are constants. D is defined by

$$D = 4/3\ \pi\ (l + \alpha c)^3 N_V \quad . \qquad (9b)$$

Here c is the half-length of the characteristic flaw population responsible for microcrack growth. l represents the length of the 'wing' cracks that grow from the initial flaws in response to the applied load. N_V is the number of flaws per unit volume and α is a geometric constant. D_0 is defined by (9b) with $l = 0$. Equation (9a) gives, to first approximation,

$$\sigma_1 = \sigma_c + a\sigma_3 \quad . \qquad (10)$$

The model provides a physical interpretation to a and σ_c, relating them to D_0, μ_f and the crack size.

Because the model is linearized, it cannot predict the curvature inherent in true failure envelopes. However, it is successful at predicting σ_c and the low-pressure slope of the failure envelope for a wide range of rock types. It is interesting to note that a multiple crack numerical model [94], when restricted to a crack growth criterion based strictly on K_{IC}, also results in a linear failure envelope (the Ashby and Sammis model also considers only tensile crack growth). When the numerical model is expanded to allow for a shear failure mechanism ($K_{IIC} = 15\ K_{IC}$), the transition to a shear growth mechanism at high confining pressure produced curvature of the failure envelope.

2.4. Acoustic Emission Applied to Fault Formation

The monitoring of acoustic emission (AE) has proven to be one of the more powerful tools available in analyzing brittle fracture (see [82] for a recent review). This non-destructive technique records the acoustic waves (generally in the 200 to 2000 kHz range) that are spontaneously radiated during impulsive microcrack growth or slip. The simplest procedure is to count the number of AE pulses during deformation. There is generally a good correlation between AE rate and inelastic strain rate so that the AE rate can be used to quantify damage accumulation occurring in the sample [30, 59, 84, 142]. Other studies have analyzed full waveforms of AE signals and, in particular, first motions in an attempt to infer source characteristics and focal mechanisms [13, 75, 115, 135, 146, 147]. Numerous studies have also confirmed that AE event amplitudes obey the power law frequency-magnitude relation observed for earthquakes [27, 91, 99, 137, 162, 167].

The other important aspect of AE studies is the determination of the spatial and temporal variations in microcracking during sample deformation. In this case, an array of acoustic transducers, attached to the sample, serves as a miniature seismic array. Then, from the arrival times of acoustic signals, event hypocenters can be determined. In some cases, AE locations have been used to follow the development of hydraulic fractures [86] and faults [25, 75, 85, 86, 100] during pore fluid injection. However, most AE event location studies have been devoted to the search for clustering patterns which would indicate the onset of fault nucleation. Many studies have shown microcrack clustering early in the loading history of rock samples [56, 91, 93, 115, 135, 146, 153, 165]. However, much of this early clustering appeared uncorrelated with the eventual fault plane and disappeared or migrated at higher stress levels. The early clustering is generally interpreted as representing preexisting strength heterogeneities in the samples. Yanagidani *et al.* [165] suggested that migration of events to the sample surface during unconfined experiments may be a stress corrosion effect in which atmospheric water vapor attacks the sample surface. A general consensus appears to be forming that for uniform loading in the absence of preexisting strength heterogeneity, microcrack localization occurs late in the loading cycle, *e.g.*, near or after peak stress in a constant strain rate experiment and coincident with tertiary (accelerating) creep in a constant stress experiment [56, 87, 115]. The abruptness of microcrack localization is demonstrated in Figure 2 in which AE activity is plotted throughout the progressive stages from early loading, through peak stress and fault nucleation, and finally fault propagation. In this case, the propagation phase was slowed down by controlling differential stress to maintain constant acoustic emission rate [92, 93].

2.5. Related Studies

To close this section I will mention a few related areas of study. Ongoing investigations are being conducted of a variety of physical properties related to rock fracture and pore structure. In many cases, these measurements are made to determine changes in pore geometry during rock deformation. Some of the more common measurements include acoustic velocity and attenuation [18, 49, 84, 97, 145, 149], permeability [8, 14, 40, 109-111, 113, 114] and electrical resistivity [88, 89, 107, 108].

3. FRICTION AND ROCK FAILURE

A discussion of rock failure must also consider rock friction since these processes are so intimately connected. For geologic materials, fracture and friction are macroscopic manifestations of the same processes: *e.g.*, grain crushing, crack growth and healing, plastic yielding, and chemical reactions such as dissolution, precipitation and alteration. While faults often contain hydrated alteration products of the host rock, many of the differences between intact strength and frictional strength are related more to geometry (interlocking, welded grains *versus* cohesionless gouge) and possibly scale effects (highly comminuted gouge can contain grains that are reduced to colloidal size). When viewed in this way, it is not surprising that the difference between intact and residual (or frictional) strength should vanish with increasing confining pressure [20, 65]. The open pore structure representative of disaggregated gouge will be

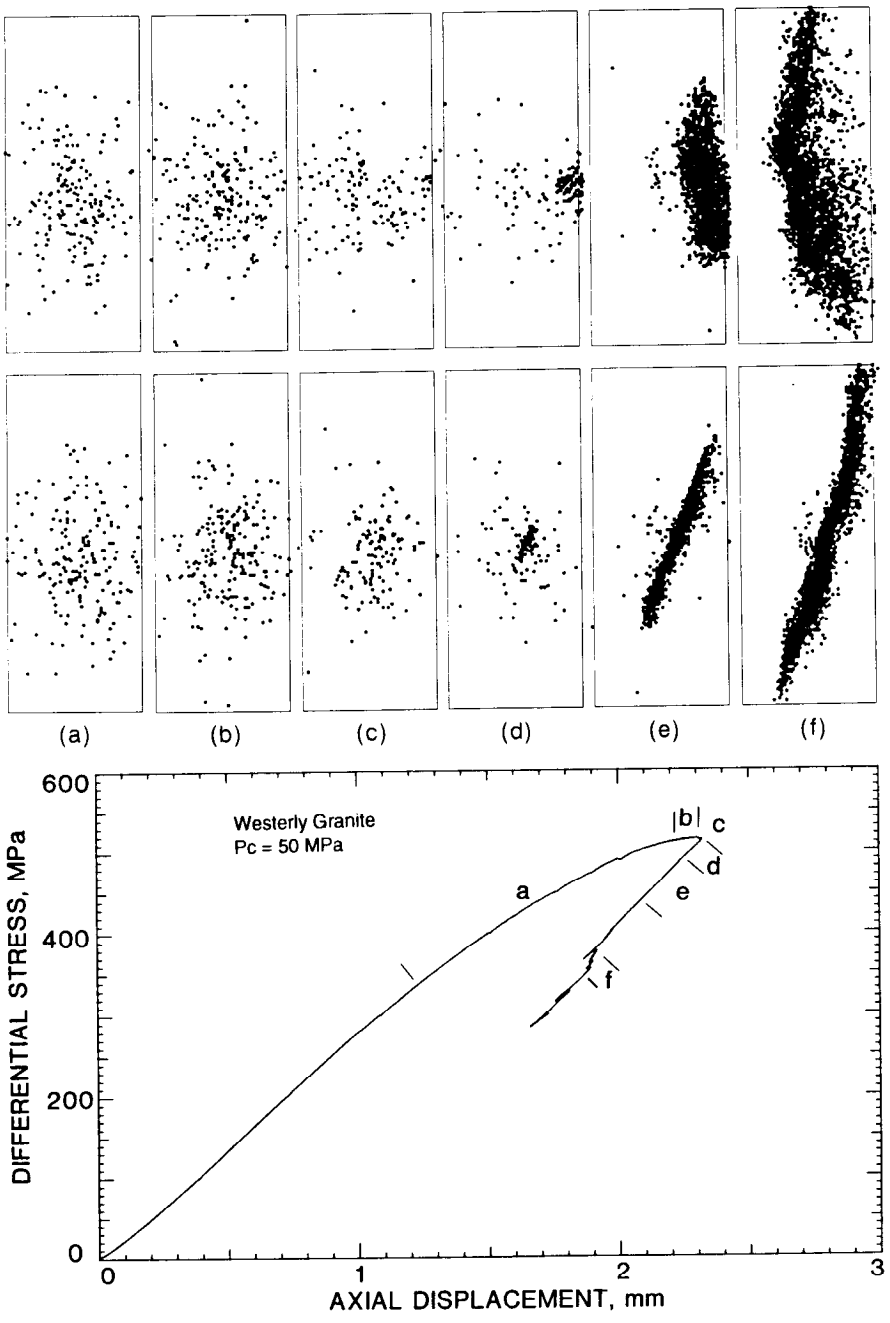

Fig. 2. Acoustic emission hypocentral locations during fault formation of initially intact Westerly granite. Time progresses from left to right. Bottom figures view sample along strike of eventual fault plane (which appears as diagonal feature in (e) and (f). Upper views show same AE events viewed perpendicular to strike. Accompanying stress-displacement curve indicates segments of the experiment from which acoustic emission plots are made. Fault nucleation occurs in (d).

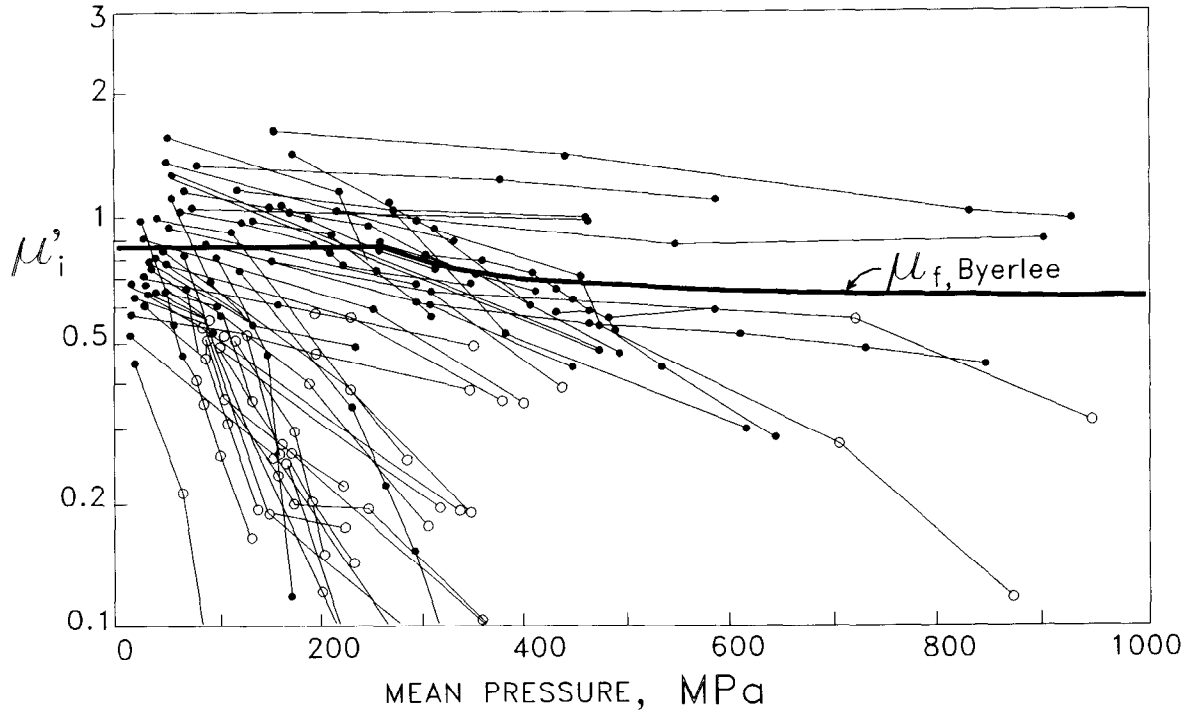

Fig. 3. Internal friction, μ_i', plotted as a function of mean pressure (after [103]) for a representative range of rock types. Mogi classified deformation mechanisms as brittle (closed circles) and ductile (open circles). The general decrease in μ_i' with increasing pressure reflects the curvature of the corresponding failure envelopes. Since ductile deformation generally has low pressure sensitivity, these values appear in the lower portion of the plot.

forced into a dense, interlocked structure by high confining pressure so that intact and fractured rock behave more and more alike. Fault frictional strength μ_f is really a lower bound for internal friction μ_i since a fault is a physically identifiable plane of weakness whereas internal friction refers to an imaginary plane within the bulk matrix. (Recall the distinction made in this chapter between the simple stress ratio $\mu_i = |\tau|/\sigma_n$ and the more conventional local derivative $\mu_i' = \partial|\tau|/\partial\sigma_n$.) Byerlee and Savage [23, 26] have recently provided an interesting link between μ_i and μ_f. In their analysis, they show that fault gouge, comprised of a Coulomb material that satisfies (1), will first deform along Coulomb shears that are not coplanar with the fault surfaces. As the material strain hardens, it approaches a stress state in which the plane of maximum shear stress is parallel to the fault surfaces. Even though the average strain must continue to be parallel to the fault to satisfy the simple shear geometry, the microscopic deformation must satisfy the Coulomb failure criterion which requires slip on surfaces oblique to the maximum shear stress direction. This basic incompatibility in strain orientations requires cooperative slip on conjugate microscopic slip planes. As a result, while the material locally satisfies (2a), on a macroscopic scale, the fault obeys $\mu_{\text{apparent}} = \sin\,\phi$. For the sake of argument, let us identify μ_i for the gouge with the value determined for intact rock of the same composition. Then, for typical confined intact rock values of $0.6 \leq \mu_i \leq 1.8$ (see Figures 3 and 4), we obtain $0.5 \leq \mu_{\text{apparent}} \leq 0.9$ [90]. It is intriguing that the apparent friction should fall so close to the observed range of values for natural materials (Figure 4). We expect some differences between intact and crushed rock due to packing (porosity) and the magnitude of the associated stress concentrators. Thus, a porosity correction similar to equation (7b) would be required for a general expression relating friction parameters between intact and crushed rock. Since the same processes of grain crushing and crack growth must be occurring in both cases, the close correspondence between μ_f and μ_{apparent} suggests that the boundary conditions imposed by rigid fault surfaces are largely responsible for the difference between μ_i and μ_f [90].

This section is ended with a brief technical comment

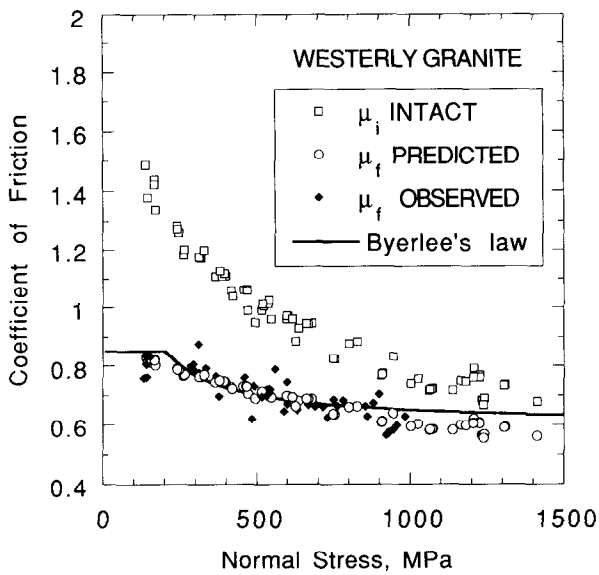

Fig. 4. Internal friction and sliding friction for Westerly granite. Internal and sliding friction can be related by $\mu_f = \sin(\tan^{-1}(\mu_i))$ (predicted values shown as open circles; see text for details). Byerlee's law is shown for comparison (data from [20]). Convergence of internal and sliding friction at high normal stress is commonly observed.

regarding the coefficient of friction. If we consider uniaxial fracture strength, then the mapping of μ_i' into μ_i, according to our nomenclature, can be accomplished by a simple construction on a Mohr diagram. The definition of μ_i leads to

$$\mu_i = \frac{|\tau|}{\sigma_n} = \sin \frac{2\beta}{(1-\cos\ 2\beta)} \ . \qquad \text{(uniaxial stress)} \qquad (11)$$

Similarly, μ_i' is the tangent of the failure envelope:

$$\mu_i' = \tan\ \phi = \tan\ (\tfrac{\pi}{2} - 2\beta) \qquad \text{(uniaxial stress)} \qquad (12a)$$

or

$$2\beta = \pi/2 - \tan^{-1}(\mu_i') \ . \qquad (12b)$$

Equations (11) and (12b) provide an explicit expression for μ_i in terms of μ_i' under uniaxial loading conditions. The typical range of $0.5 \leq \mu_i' \leq 1.5$ for unconfined compressive tests (Figure 3) corresponds to the range $1.6 \leq \mu_i \leq 3.3$. The differences between the uniaxial values of μ_i' and μ_i are due to cohesion and to curvature of the failure envelope. With increasing confining pressure, μ_i' and μ_i tend to decrease and μ_i also approaches μ_f (Figures 3 and 4).

3.1. Friction as a Lower Limit for Rock Strength

For brittle fracture in compression, experimentally determined values of internal friction typically fall in the range $0.5 < \mu_i' < 1.6$. The corresponding angle of internal friction $\phi = \tan^{-1}\mu_i'$ ranges from 26° to 58°. As I have already discussed, frictional strength often serves as a useful lower limit for rock strength; especially for large rock masses that contain joints and fractures. Analysis of room-temperature frictional strength data [22] revealed that a broad range of common rock types could be adequately represented by a simple empirical relation known as Byerlee's law. A non-linear normal stress dependence of friction was observed which could be adequately fit by two linear segments of the form of equation (1):

$$\tau = 0.85\ \sigma_n \qquad \sigma_n < 200 \text{ MPa} \qquad (13a)$$

$$\tau = 50 \text{ MPa} + 0.6\ \sigma_n \qquad 200 < \sigma_n < 1700 \text{ MPa} \ . \qquad (13b)$$

If we assume that the rock matrix is sufficiently fractured so that the most favorably oriented faults are present, this result can be expressed in terms of principal stresses as

$$\sigma_1 = 4.7\ \sigma_3 \qquad \sigma_3 < 114 \text{ MPa} \qquad (13c)$$

$$\sigma_1 = 177 \text{ MPa} + 3.1\ \sigma_3 \qquad 114 < \sigma_3 < 1094 \text{ MPa} \ . \qquad (13d)$$

Alternatively, a power law of the form

$$|\tau| = {\sigma_n}^{0.94} \text{ (MPa)} \qquad \sigma_n < 1700 \text{ MPa} \qquad (14)$$

provides a good fit to the experimental data. Figure 4 shows the effect of normal stress on μ_f and μ_i for Westerly granite. Equation (13) will be used as a reference curve for the summary plots at the end of this chapter. Notable exceptions to equations (13) and (14) are a number of clays and other sheet silicates, especially minerals containing interlayer water. For example, under low confining pressure, montmorillonite obeys $\mu_f \sim 0.2$ [112]. It is also important to note that fluid pressure has a first order effect in equations (13) and (14) by directly reducing normal stress (see section on pore pressure). It should also be emphasized that rock friction appears to be independent of scaling from fractions of a millimeter to field scales on the order of kilometers. This scale independence is not true for fracture strength as I discuss in the next section. The scale-independence of frictional strength as well as the overall insensitivity of friction to rock type greatly simplify the task of relating laboratory measurements to deformation in the crust.

I have mentioned that some regions of the Earth's crust appear to be fractured on all scales. Under

this condition, the crust would act as a cohesionless Coulomb material. Then, assuming an angle of internal friction $\phi = 30°$ ($\mu_i' = \mu_f = 0.58$), a hydrostatic fluid pressure due to a water column of density 1 Mg/m^3, and an average rock density of 2.7 Mg/m^3, the maximum and minimum effective stresses are constrained by ${\sigma_3}^{\text{eff}} \geq {\sigma_1}^{\text{eff}}/3$. Under these conditions, the stress state

$$3\ {\sigma_3}^{\text{eff}} = {\sigma_1}^{\text{eff}} \tag{15}$$

represents a condition for incipient failure. In a normal faulting regime, where vertical stress, $S_v = \sigma_1$, these same conditions give the minimum horizontal stress, $S_h = 0.58 S_v$. This principal stress ratio is often observed in normal faulting regimes. It has been explained by assuming uniaxial strain ($\varepsilon_x = \varepsilon_y = 0$) and a Poisson ratio $\nu \sim 0.25$. The alternative explanation described above depends on quite reasonable assumptions of friction and hydrostatic fluid pressure gradient. The same analysis applied to a thrust-faulting regime where $S_v = \sigma_3$, predicts incipient failure at a maximum horizontal stress $S_H = 2.26 S_v$. These relations, assuming full fluid connectivity, are shown as approximate lower bounds for crustal strength in Figure 5. Direct observations from deep bore holes indicate that fluid pressure seals can form in the Earth's crust and, combined with porosity loss, heating or dewatering, can result in fluid pressures that approach lithostatic. Under these conditions, shear strength of the crust could approach zero. At the other end of the spectrum, we use intact strength of Westerly granite to represent unfractured, crystalline rock. Incipient failure is plotted in Figure 5 for two cases. The strongest condition assumes dry rock with zero pore pressure, and the intermediate case represents wet, fully saturated rock with hydrostatic pore pressure and a loss of 50 MPa strength due to stress corrosion. This last effect represents static fatigue after approximately 100 years (see section on strain rate effect).

3.2. Recent Developments in Friction

We may well be in the early stages of a revolution in our understanding of fault systems and associated crustal stresses. A long-standing debate has occurred regarding the apparent weakness of mature faults such as the San Andreas in California (reviewed in [53]). The lack of a localized heat flow anomaly associated with the San Andreas was interpreted as indicating a low shear strength (<20 MPa averaged over the upper 14 km of the fault) [76]. This implies $\mu_f <$ 0.2. Recent stress orientation measurements along the San Andreas [139] suggest that it is also weak relative to surrounding subsidiary faults. At the same time, laboratory friction measurements [112] indicate that even the weakest clays (which are unlikely to be chemically stable at seismogenic depths) cannot satisfy this constraint. Elevated pore fluid pressure remains a viable explanation. However, mechanical arguments have suggested that the necessary fluid pressures could not be sustained. A recent breakthrough occurred in which it was recognized that a fluid pressure gradient from the center of the fault zone to the walls of the fault would allow high fluid pressure and vanishing shear strength in the interior, and at the same time not result in hydrofracture of the surrounding country rock [19, 24, 128]. Since this type of model requires a stable gradient in fluid pressure, it suggests that mature faults with thick gouge zones are likely to be weaker than immature, narrow faults. This model may also explain the apparent weakness of low-angle thrust faults. Furthermore, reports of high fluid pressure chambers in deep petroleum reservoirs [123] have led to the suggestion that mature fault zones may be similarly compartmentalized into chambers with varying degrees of fluid overpressure [24].

Much attention has been devoted recently to a class of slip rate- and history-dependent friction laws [33, 127, 132]. These laws characterize the fault as having an intrinsic friction comparable to Byerlee's law, but with second order variations, caused by velocity V, that decay with displacement. Part of the appeal of these constitutive relations is that their nonlinear nature results in a complex and wide range of behaviors, allowing them to replicate many of the phenomena attributed to earthquakes. A general form of the friction law can be expressed as

$$\tau = \sigma_n[\mu_o + a \ln (V/V^*) + \Sigma(b_i \psi_i)] \tag{16a}$$

$$d\psi_i/dt = -(V/L_i)[\psi_i + \ln (V/V^*)] \tag{16b}$$

where a and b_i's are constants, V^* is an arbitrary reference velocity, and L_i's are characteristic displacements over which memory is lost. State variables ψ_i are assumed to evolve according to (16b). Stability analysis [129] indicates that for $a < b$ (resulting in weakening with increasing velocity), slip can become unstable, leading to a stick-slip event in the laboratory or to an earthquake. Increasing $a - b$ tends to make the system more stable. Laboratory measurements of artificial gouge and bare rock surfaces indicate that variations in friction are typically ±1% or less per decade change in velocity. Bare surfaces tend to give more negative values of $a - b$ while clays seem to give consistently pos-

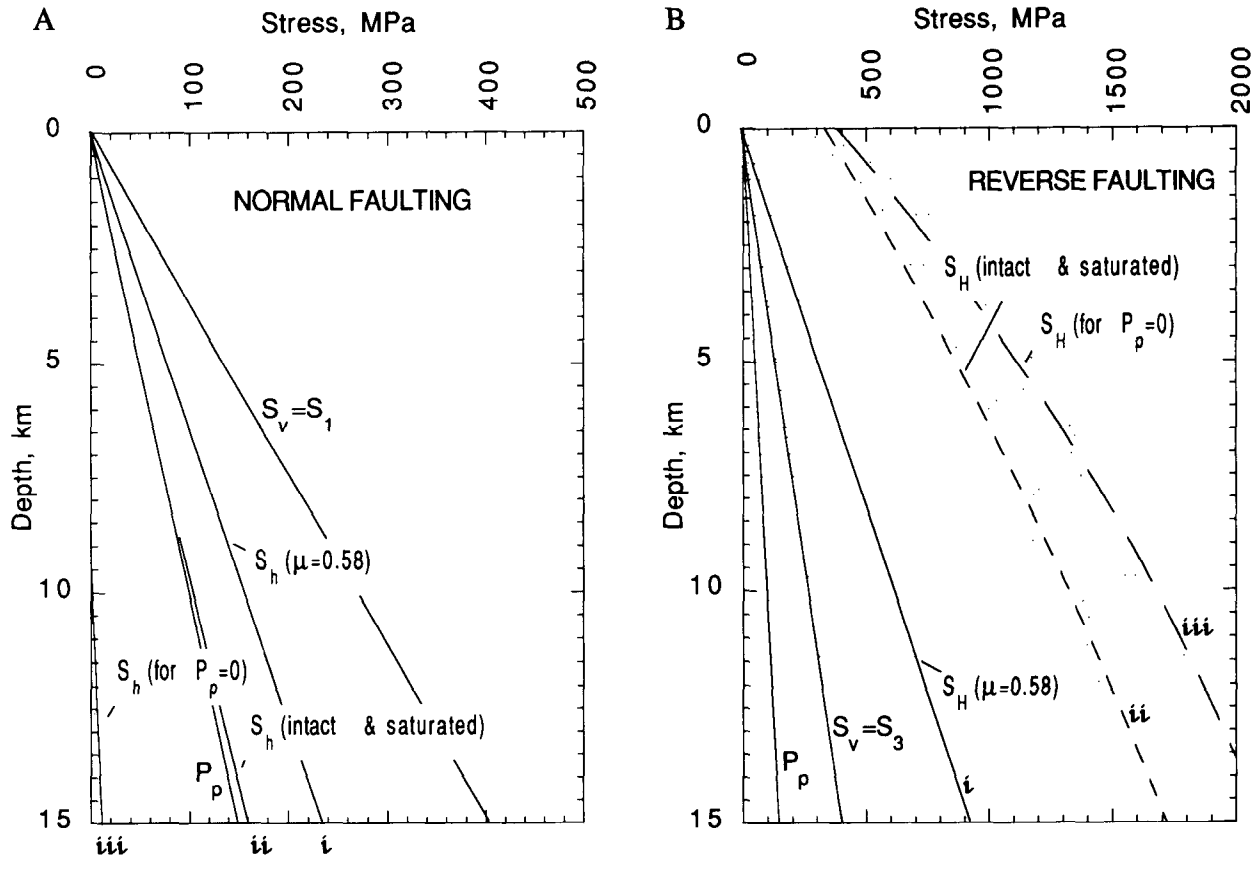

Fig. 5. Theoretical bounds on crustal stress state using Westerly granite to represent crystalline rock (data from [20, 160]). a) Normal faulting regime ($S_v = \sigma_1$): i) Incipient failure will occur on existing, favorably-oriented faults (assuming hydrostatic fluid pressure and $\mu_f = 0.58$). ii) Intact granite with hydrostatic pore pressure fails at S_h slightly above P_p. Due to uniaxial strength, rock will not fail in shear above approximately 8 km. At shallower depths, S_h is limited to approximately P_p by tensile failure of the rock. iii) Shear failure is limited to depths below 10 km for dry rock ($P_p = 0$). b) Reverse faulting regime ($S_v = \sigma_3$): The rock can theoretically support significantly higher deviatoric stresses in this case. The potential strength of intact rock, whether saturated or dry, is more than twice the frictional strength for all depths shown. Under these conditions, an increase in fluid pressure above hydrostatic will tend to drive the system towards failure along low-angle thrust faults. The three cases correspond to conditions described in a).

itive values. At temperatures between 100 and 300°C and high pore water pressure [11], laboratory samples of granite tend to exhibit greater instability than at higher temperatures where $a - b$ becomes strongly positive. This is an interesting observation since the 300° isotherm corresponds approximately with the base of the seismogenic zone on the San Andreas fault. I note in passing that all intact rocks exhibit a strong velocity-strengthening effect (see section on rate dependence). Just as I described a link between internal friction and sliding strength in the beginning of this chapter, so too can a link be made between the rate dependence of intact strength and frictional strength. A recent, concise review of friction studies in rock has been presented by Evans and Dresen [38].

4. FACTORS AFFECTING ROCK STRENGTH

In this section, we examine some of the variables that affect rock strength. Their relative importance can be summarized in the following way. If we consider a 'typical' granitic rock saturated with water at room temperature and confining pressure of 100 MPa, the following changes should each result in a reduction in strength of approximately 10%: a decrease in confining pressure of 24 MPa or an increase in pore pressure of 24 MPa, a decrease in strain rate of 3 ± 0.5 orders of

magnitude, an increase in temperature of 190 ± 40 °C, or an increase in sample dimension of 50–110%. Each of these effects is next considered separately.

4.1. Confining Pressure Effect

Confining pressure affects brittle fracture strength by suppressing the growth of dilatant microcracks. Microcracks tend to grow parallel to σ_1 when a sample is loaded in compression by locally overcoming the ambient compressive stress field near crack tips and developing a localized region of tensile stress. This process requires some specialized mechanism such as slip along grain boundaries or bending of a rigid grain that is adjacent to an open pore or more compliant grain [121, 126, 134, 152]. Such mechanisms are generally enhanced by deviatoric stress and suppressed by mean stress. In addition, slip along grain boundaries will not occur until frictional contact strength, which increases with mean stress, is overcome. The overall strengthening effect can be represented in a Mohr diagram such as Figure 6 for Westerly granite. A generalized version of this diagram, shown in Figure 1, demonstrates the well known relationships between $\tau, \sigma_n, \sigma_1, \sigma_3$, and friction angle $\phi = \tan^{-1} \mu_i'$. In general, the failure envelope is concave towards the normal stress axis and the difference between intact shear strength and frictional shear strength vanishes at high pressure [65].

The majority of strength measurements have been conducted under uniaxial or 'triaxial' stress conditions in which $\sigma_2 = \sigma_3$. A limited number of true triaxial measurements have been performed to explore the effect of intermediate principal stress on failure mode. While the most commonly used failure criteria (*e.g.*, Mohr-Coulomb) assume that failure is independent of intermediate stress,experimental evidence demonstrates that this assumption is not strictly true [3, 104, 105].

4.2. Pore Fluid

Effective pressure law. Pore fluids can affect fracture strength through a direct pressure effect as well as through chemical interactions with the rock matrix. Mechanically, pore pressure reduces the normal stress throughout the rock mass according to the effective pressure law [61]:

$$\sigma_n{}^{\text{eff}} = \sigma_n - \alpha P_p \tag{17}$$

where α is a constant related to pore geometry. While variations in α have been measured for the effect of pore pressure on transport properties [159], $\alpha = 1$ is appropriate for fracture strength of rock with well-connected

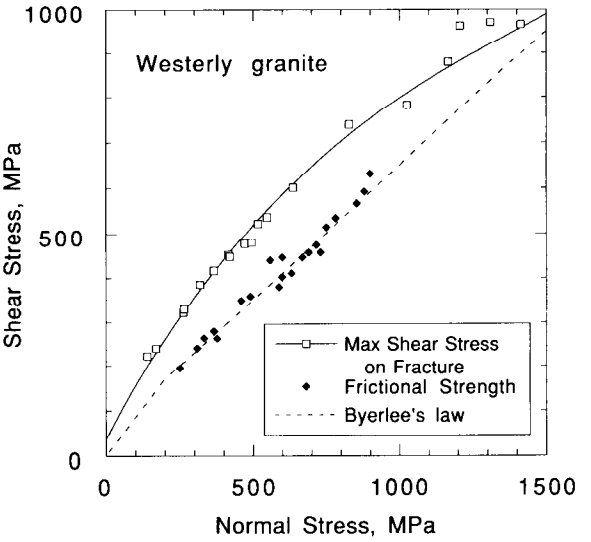

Fig. 6. Shear-normal stress plot for Westerly granite. Mohr-Coulomb failure envelope (solid line is concave towards normal stress axis.

porosity. If fluid pressures in the crust were low, the increase in mean stress with depth, due to overburden pressure, should result in large shear strength and the gradual change from brittle to ductile deformation in the mid to lower crust (as suggested by the convergence of frictional and intact strength in Figure 6). The normal hydraulic head for well-connected porous material will offset the overburden pressure by over one-third. However, for isolated porosity at depth, normal consolidation and dewatering processes can compress pore fluids to well above hydrostatic pressures and under proper circumstances may lead to repeated episodes in which the rock is hydraulically fractured. There is currently considerable interest in fluid overpressure phenomena and their relation to oil reservoir partitions [63, 123] as well as to larger-scale crustal processes such as earthquake cycles and the reduction of strength of mature faults [19, 23, 24, 116, 128].

Chemical interactions. Since water reacts with silicates to disrupt the *Si-O* bond, pore fluids can have a profound chemical effect on the physical properties of crustal silicate rocks. CO_2 concentration plays a similar role in the diagenesis and metamorphism of carbonates. Crack healing, cementation and densification all act to strengthen rock with time [55]. By contrast, chemically assisted crack growth is the primary mechanism for stress corrosion and static fatigue at temperatures in the 0 to 200°C range [73, 74, 83, 133], by providing a mechanism for crack growth below the critical stress intensity needed to split lattice bonds ($K_I < K_{IC}$) [6,

30]. Subcritical crack growth rate ν is generally related to K_I through a power law

$$\nu = A_1 K_I{}^n \tag{18}$$

or exponential form

$$\nu = A_2 \exp(b_2 K_I) \ . \tag{19}$$

An alternative view relates velocity to energy release rate $G_I (\propto K_I{}^2)$ [83]:

$$\nu = A_3 \exp(b_3 G_I) \ . \tag{20}$$

Experimental data are insufficient to identify which form is correct. However, there are theoretical arguments, based on reaction rate theory, to prefer (19) or (20) [28, 83]. Nominal values for n at room temperature and in wet rock [5] (Table 11.6) are 15 - 40 for quartz and quartz rocks; 10 – 30 for calcite rocks; 30 – 70 for granitic rocks; and 25 – 50 for gabbro and basalt. A typical value for b_2 for room temperature granite is 0.04 $(\text{MPa}\cdot\text{m}^{1/2})^{-1}$. The corrosive effect of the pore fluid can be altered significantly by varying the activity of dissolved species as well as altering the electrochemical potential [6, 36, 38, 54, 64]. This is a rich and promising area for future research.

4.3. Strain Rate

In the brittle deformation field, rocks typically exhibit a pseudo-viscous effect which is reflected in a strength increase with increasing strain rate. This effect is best known in the mining industry as static fatigue in which a pillar or other load-bearing structure will fail after some period of time under constant load. Subcritical tensile crack growth has been identified as the principal mechanism responsible for static fatigue in rock [73, 74, 83] and has been studied in recent years [6]. A practical lower limit for laboratory strain rates is 10^{-10} s^{-1} which is still much faster than geologic rates in even tectonically active regions. It does represent, however, a useful limit for many engineering applications. Experimental results covering a broad range of strain rates are shown in Figure 7. Average strain rates have been obtained from static fatigue tests on Barre granite [73] by dividing time-to-failure data by total inelastic strain. Various studies [28, 83, 95] have been successful in relating this macroscopic relation between stress and strain rate to subcritical microcrack growth rate and its sensitivity to stress intensity at crack tips. They determined an apparent activation volume of 0.43 ± 0.04 kJ·MPa/mole (4.3×10^{-4} m^3/mole) for crack growth in granite creep

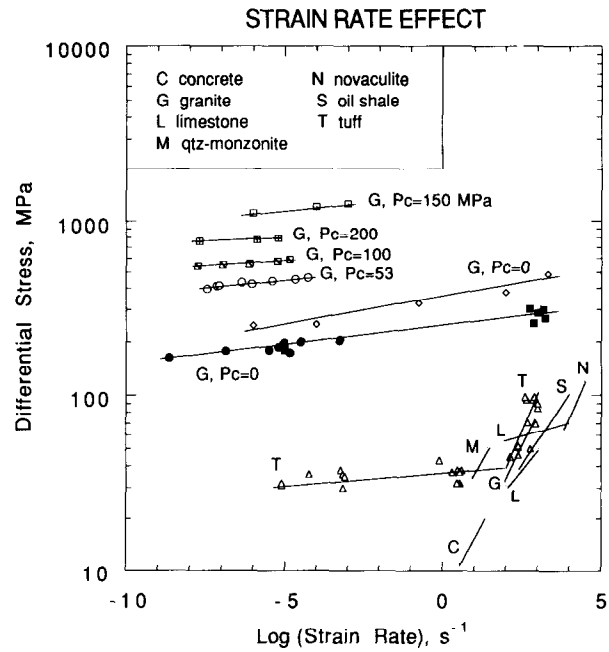

Fig. 7. Effect of strain rate on brittle fracture strength. Data taken from [15, 44, 46, 73, 117]. For strain rates below approximately 10/s, rate sensitivity is typically 5–10% strength increase per decade increase in strain rate. This effect is primarily due to the stress dependence of subcritical microcrack growth. Trend lines in lower-right quadrant (from [46]) are from dynamic tensile fracture experiments.

experiments. This approach provides a link between energetics of microcrack extension and bulk pseudoviscous response of rocks in creep. It may also prove useful as a way to incorporate time-dependent effects in damage mechanics applications [30]. This rate sensitivity is often expressed as a power law dependence of the form

$$\sigma_{\max} = a \, \dot{\varepsilon}^n \ . \tag{21}$$

Typical rate sensitivities in this regime are $0.02 \leq n \leq 0.04$.

By using shock and other impulsive loading techniques, strain rates in excess of 10^4 s^{-1} have been achieved for samples failing in tension [46]. While some question remains as to the importance of machine and boundary condition effects, numerous experiments show a transitional strain rate of approximately 10/s above which significantly larger rate dependence is observed. High-rate tensile experiments, taken from Grady and Lipkin [46], are summarized in the lower-right quadrant of Figure 7 as trend lines without accompanying data values. An upper limit of $n \leq 1/3$ has been indicated by both theory and experiment [15, 46, 47, 81, 117] for rate sen-

sitivity under these conditions.

4.4. Temperature

Mechanisms of crystal plasticity involving dislocation motion and twinning are thermally activated and will dominate brittle cracking as temperature increases [38, 70]. Some minerals, such as halite and calcite, will deform ductilely at room temperature if sufficient confining pressure is present to suppress brittle crack growth [42]. However, dry quartz appears to deform brittlely at room temperature even at confining pressures in excess of 1 GPa [154]. As previously mentioned, water has a significant effect on pressure-assisted grain-boundary deformation mechanisms such as pressure solution [11, 54]. These fluid-assisted mechanisms will often dominate at intermediate temperatures and, over geologic time scales, may play an important role in determining rock strength at room temperature [133]. Thus, even in the brittle regime, increasing temperature tends to reduce fracture strength [16, 136, 163]. The effect of temperature on fracture strength of Westerly granite is shown in Figure 8.

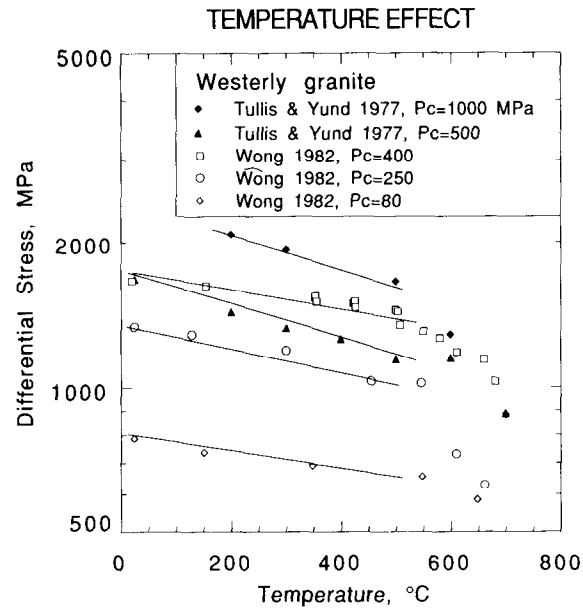

Fig. 8. Effect of temperature on brittle fracture strength of nominally dry Westerly granite. Above approximately 300°C in laboratory experiments (strain rates $> 10^{-8}$ s^{-1}), high pore fluid pressures can significantly reduce strength through a variety of thermally-activated dissolution/precipitation processes. At temperatures below 300°, fluid-assisted reactions become more and more sluggish. Even so, subcritical crack growth can still play an important role in reducing strength (see static fatigue and fluid effects).

4.5. Sample Size and Scaling

The ability in laboratory studies to provide precise control of pressure, temperature and other environmental conditions has resulted in a large volume of rock strength data obtained from laboratory measurements. However, there exists a significant question concerning the scaling rules appropriate for relating laboratory measurements to field applications [122]. The lack of adequate testing of these scaling rules may represent a significant weakness in our ability to apply laboratory measurements to large-scale engineering and field research problems. For example, the largest laboratory fault models (approximately 1-m^2 surface) are many orders of magnitude less than the fault area involved in a moderate earthquake. A general result of fracture mechanics analysis is that stress intensity at the tip of a flaw scales as the square root of the flaw size. Consequently, larger samples, which can contain larger flaws, are more likely to be weak. This argument assumes, of course, that small samples with visible flaws (and certainly flaws that completely bisect the sample) will be rejected and not included in the strength statistics. However, the degree of weakening has not been well determined and should vary from rock to rock depending on the flaw-size distribution. Scaling procedures have been proposed [1, 94, 98] that address this problem. In addition, both laboratory and field studies have been conducted [9, 32, 51, 52, 57, 72, 102, 124, 144] that show a general weakening with increased sample size (Figure 9). This effect can be large: as much as a 70% strength loss per decade sample size for the weathered diorite studied by Pratt *et al.* [124]. Available data are insufficient to allow a clear understanding of this effect. It is intriguing that the weak rock types show the greatest size effect. Pratt *et al.* noted a decrease in size sensitivity for samples greater than 1m length for both diorite and coal and suggested that this may represent an upper limit to the weakening region. Due to the small amount of existing data, it is not yet clear to what extent these tendencies can be generalized. If flaw size is the correct explanation for the weakening effect, then sample strength will depend as much on crack-size distribution as on minerology. Furthermore, the studies cited here are all unconfined. As already mentioned, we may expect large rock masses, especially in tectonically active regions, to support stresses that are comparable to their frictional strength rather than

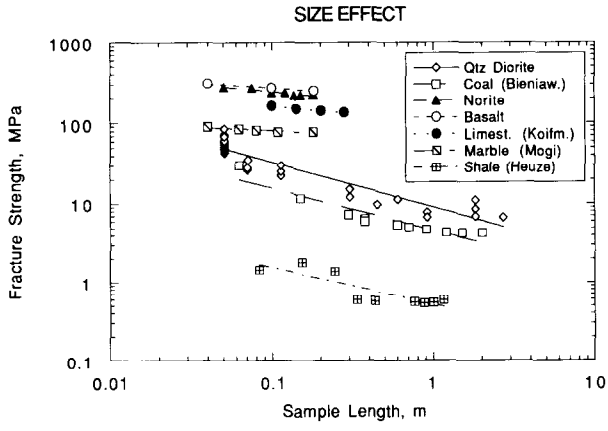

Fig. 9. Effect of sample size on fracture strength. Observed weakening is as much as 70% per decade increase in sample length.

laboratory-measured intact strength.

5. COMPILED STRENGTH DATA

The plots in this section are intended mainly as a quick reference to the range of typical rock strengths. The data presented are by no means exhaustive and undoubtedly suffer to some degree from sampling bias within the literature. For example, a preponderance of 'weak' tuffs may have been studied and reported by investigators for a period of time, giving a false impression that all tuffs are weak. Unconfined compressive strength and tensile strength ranges are plotted in Figures 10a and 10b. These are summaries of the data presented in [78] (Appendix II). Next come a series of plots (Figures 11a–e) showing the dependence of fracture strength on confining pressure. Data for these plots have been compiled from [20, 50, 65, 103, 141, 142, 160]. Again, this is not meant to be an exhaustive compilation of existing data, although approximately 1900 data pairs are represented in Figures 10 and 11. Individual data values have been shown in Figures 11a–e to provide a sense of the variability within different rock types. Other researchers have attempted to draw a single curve to represent 'characteristic' rock strength for different rock types. However, one of the long-standing problems in analyzing rock strength data is the fact that strength is quite variable; even within a given class of rocks. I have also included a representative trend line in the strength plots, although in some cases, there is such variability in fracture strength that this trend line has little significance. Granites and other low-porosity crystalline silicates appear to be among the most well-behaved classes. In this case, a characteristic strength curve may be followed to within approximately 25%. High-porosity silicates are weaker and their range of strengths show much more variability. In fact, it is not surprising that a strong inverse correlation exists between fracture strength and porosity. However, this is not a perfect correlation since such factors as grain size, grain shape, and cementation also affect strength.

For basalts and granites, the Byerlee friction law provides a consistent lower bound for rock strength. This result is in agreement with the earlier analysis in this chapter and suggests that some samples plotted in Figures 11a–b contained significant pre-existing flaws which, especially at higher confining pressures, result in lowered strength. Many of the sandstones and tuffs show fracture strengths significantly below Byerlee's law. This effect, which is closely correlated with porosity [125], is of potential importance in engineering applications. One explanation is that the failure

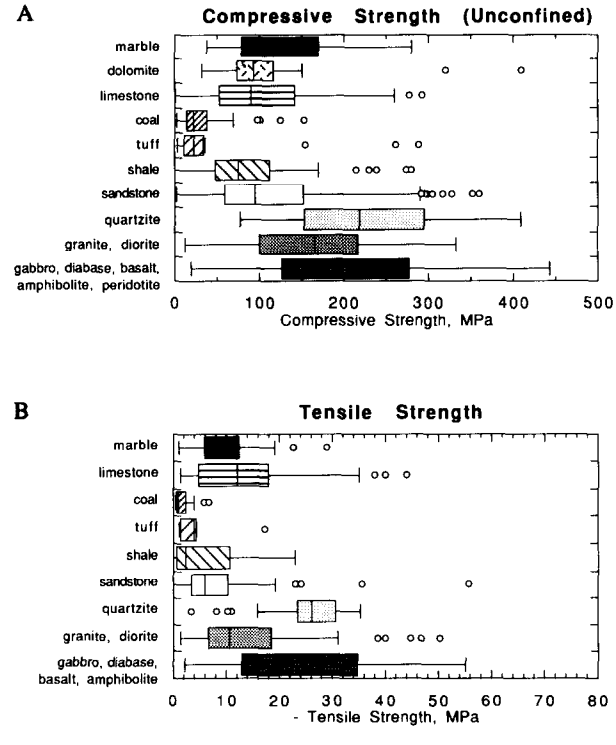

Fig. 10. a) Unconfined compressive strength at room temperature for a variety of rock types (data from [78] appendix II). Each box represents ±25% of the data about the median value (show as vertical line). Error bars represent the full range of the data with the exception of outliers which are plotted as individual circles. b) Tensile strength at room temperature for a variety of rock types (data from [78] appendix II). Explanation of symbols is the same as for (a).

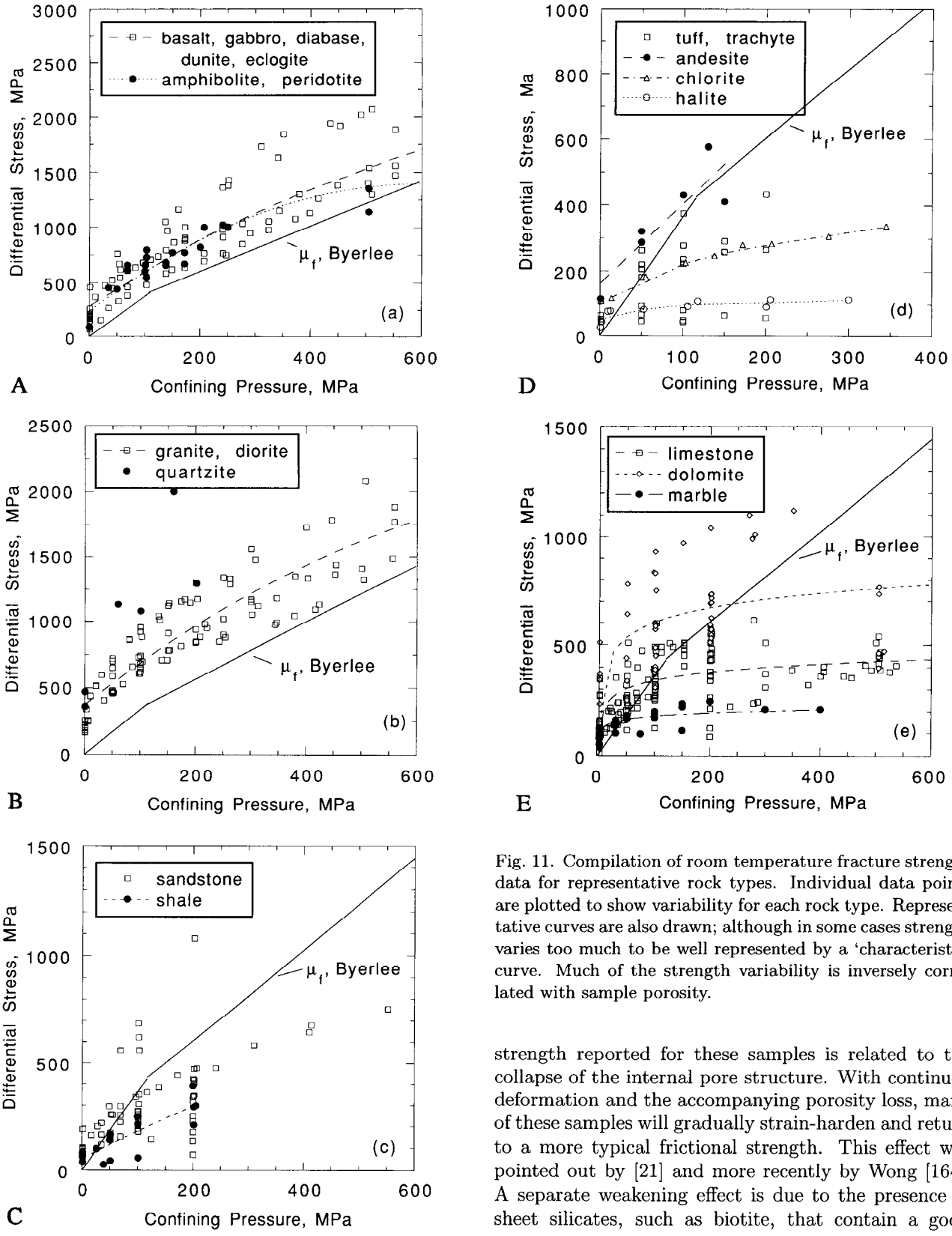

Fig. 11. Compilation of room temperature fracture strength data for representative rock types. Individual data points are plotted to show variability for each rock type. Representative curves are also drawn; although in some cases strength varies too much to be well represented by a 'characteristic' curve. Much of the strength variability is inversely correlated with sample porosity.

strength reported for these samples is related to the collapse of the internal pore structure. With continued deformation and the accompanying porosity loss, many of these samples will gradually strain-harden and return to a more typical frictional strength. This effect was pointed out by [21] and more recently by Wong [164]. A separate weakening effect is due to the presence of sheet silicates, such as biotite, that contain a good

cleavage plane. Many clays, especially expansive clays such as montmorillonite that include interlayer water, are unusually weak at room temperature and will deform at very low shear stresses [112]. Graphite also exhibits this effect at room temperature. Finally, some minerals are able to activate dislocation mechanisms at room temperature (especially with increasing mean stress) and exhibit a brittle-ductile transition in the classical sense. That is, at low confining pressure they deform by pressure-sensitive microcrack growth, then pass through a transition with increasing confining pressure to a ductile flow regime in which strength has little pressure sensitivity; deformation at high confining pressure involves, for example, dislocation glide and twinning. Carbonates and halite show this effect.

Acknowledgments. I thank R. Summers for his assistance in conducting the literature search for this chapter. J. Byerlee has been a great help in identifying the more important and useful concepts in this broad field of subject matter. I also thank A. McGarr, W. Olsson and an anonymous reviewer for their thoughtful suggestions.

REFERENCES

1. Allégre, C., J. LeMouel, and A. Provost, Scaling rules in rock fracture and possible implications for earthquake prediction, *Nature, 297*, 47-49, 1982.
2. Amadei, B., and M. J. Robison, Strength of rock in multiaxial loading conditions, in *Proc. 27th U.S. Symp. on Rock Mech.*, edited by H. L. Hartman, pp. 47-55, Soc. Mining Eng., Inc., Littleton, Co., 1986.
3. Amadei, B., M. J. Robison, and Y. Y. Yassin, Rock strength and the design of underground excavations, in *Large Rock Caverns*, edited by K. H. O. Saari, pp. 1135-1146, Pergamon Press, New York, 1987.
4. Ashby, M. F., and C. G. Sammis, The damage mechanics of brittle solids in compression, *Pure & Appl. Geophys., 133*, 489-521, 1990.
5. Atkinson, B. K. (Ed.), *Fracture Mechanics of Rock*, 534 pp., Academic Press, New York, 1987.
6. Atkinson, B. K., and P. G. Meredith, Experimental fracture mechanics data for rocks and minerals, in *Fracture Mechanics of Rock*, edited by B. K. Atkinson, pp. 477-525, Academic Press, New York, 1987.
7. Barton, N., R. Lien, and J. Lunde, Engineering classification of rock masses for the design of tunnel support, *Rock Mechanics, 6*, 189-236, 1974.
8. Bernabe, Y., The effective pressure law for permeability in Chelmsford granite and Barre granite, *Int. J. Rock Mech. Min. Sci. & Geomech. Abstr., 23*, 267-275, 1986.
9. Bieniawski, Z. T., The effect of specimen size on compressive strength of coal, *Int. J. Rock Mech. Min. Sci. & Geomech. Abstr., 5*, 325-335, 1968.
10. Bieniawski, Z. T., Rock mass classification in rock engineering, in *Proc. Symp. on Exploration for Rock Engineering*, edited by Z. T. Bieniawski, pp. 97–106, Johannesburg, 1976.
11. Blanpied, M. L., D. A. Lockner, and J. D. Byerlee, Fault stability inferred from granite sliding experiments at hydrothermal conditions, *Geophys. Res. Lett., 18*, 609-612, 1991.
12. Bock, H. (Ed.), An Introduction to Rock Mechanics, 342 pp., James Cook University of North Queensland, Townsville, Australia, 1978.
13. Bohler, F. M., and H. Spetzler, Radiated seismic energy and strain energy release in laboratory dynamic tensile fracture, *Pure Appl. Geophys., 124*, 759–772, 1986.
14. Brace, W. F., Permeability of crystalline and argillaceous rocks, *Int. J. Rock Mech. Min. Sci. & Geomech. Abstr., 17*, 241–251, 1980.
15. Brace, W. F., and A. H. Jones, Comparison of uniaxial deformation in shock and static loading of three rocks, *J. Geophys. Res., 76*, 4913-4921, 1971.
16. Bragg, R. A., and O. B. Andersland, Strain rate, temperature, and sample size effects on compression and tensile properties of frozen sand, *Eng. Geol., 18*, 35-46, 1981.
17. Broek, D., *Elementary Engineering Fracture Mechanics*, 469 pp., Martinus Nijhoff, The Hague, 1982.
18. Budiansky, B., and R. J. O'Connel, Seismic velocities in dry and saturated cracked solids, *J. Geophys. Res., 79*, 5412-5426, 1974.
19. Byerlee, J. D., Friction, overpressure and fault normal compression, *Geophys. Res. Lett., 17*, 2109-2112, 1990.
20. Byerlee, J. D., Frictional characteristics of granite under high confining pressure, *J. Geophys. Res., 72*, 3639-3648, 1967.
21. Byerlee, J. D., Brittle-ductile transition in rocks, *J. Geophys. Res., 73*, 4741-4750, 1968.
22. Byerlee, J. D., Friction of rocks, *Pure Appl. Geophys., 116*, 615-626, 1978.
23. Byerlee, J. D., The change in orientation of subsidiary shears near faults containing pore fluid under high pressure, *Tectonophysics, 211*, 295-303, 1992.
24. Byerlee, J. D., Model for episodic flow of high pressure water in fault zones before earthquakes, *Geology, 21*, 303-306, 1993.
25. Byerlee, J. D., and D. A. Lockner, Acoustic emission during fluid injection in rock, in *Proceedings, First Conference on Acous-*

tic Emission/Microseismic Activity in Geological Structures and Materials, edited by H. R. Hardy and F. W. Leighton, pp. 87-98, Trans. Tech. Publications, Clausthal-Zellerfeld, Germany, 1977.

26. Byerlee, J. D., and J. C. Savage, Coulomb plasticity within the fault zone, *Geophys. Res. Lett., 19*, 2341-2344, 1992.
27. Cai, D., Y. Fang, W. Sui, L. Zhang, J. Li, and N. Geng, The b-value of acoustic emission during the complete process of rock fracture, *Acta Seismologica Sinica, 2*, 129-134, 1988.
28. Costin, L. S., A microcrack model for the deformation and failure of brittle rock, *J. Geophys. Res., 88*, 9485-9492, 1983.
29. Costin, L. S., Damage mechanics in the post-failure regime,*Mechanics of Materials, 4*, 149-160, 1985.
30. Costin, L. S., Deformation and failure, in *Fracture Mechanics of Rock*, edited by B. K. Atkinson, pp. 167-215, Academic Press, New York, 1987.
31. Deere, D. U., Technical description of rock cores for engineering purposes, *Rock Mechanics and Eng. Geol., 1*, 17-22, 1964.
32. Dey, T., and P. Halleck, Some aspects of size-effect in rock failure, *Geophys. Res. Lett., 8*, 691-694, 1981.
33. Dieterich, J. H., Constitutive properties of faults with simulated gouge, in *Mechanical Behavior of Crustal Rocks*, pp. 103-120, Amer. Geophys. Union Monograph, Washington, 1981.
34. Du, Y., and A. Aydin, Interaction of multiple cracks and formation of echelon crack arrays, *Int. J. Numerical and Analytical Methods in Geomech., 15*, 205-218, 1991.
35. Dunn, D. E., L. LaFountain, and R. Jackson, Porosity dependence and mechanism of brittle fracture in sandstones, *J. Geophys. Res., 78*, 2403-2417, 1973.
36. Dunning, J. D., W. L. Lewis, and D. E. Dunn, Chemomechanical weakening in the presence of surfactants, *J. Geophys. Res., 85*, 5344-5354, 1980.
37. Estrin, Y., and L. P. Kubin, Plastic instabilities: phenomenology and theory, *Materials Sci. and Eng., A137*, 125-134, 1991.
38. Evans, B., and G. Dresen, Deformation of earth materials: six easy pieces, Reviews of Geophys., *IUGG Report*, 823-843, 1991.
39. Evans, B., and T.-f. Wong, Shear localization in rocks induced by tectonic deformation, in *Mechanics of Geomaterials*, edited by Z. Bazant, pp. 189-210, John Wiley, New York, 1985.
40. Fischer, G. J., and M. S. Paterson, Measurement of permeability and storage capacity in rocks during deformation at high temperature and pressure, in *Fault Mechanics and Transport Properties of Rocks*, edited by B. Evans and T.-F. Wong, pp. 213-252, Academic Press, London, 1992.
41. Franklin, J. A., Triaxial strength of rock materials, *Rock Mech., 3*, 86-98, 1971.
42. Fredrich, J., B. Evans, and T.-f. Wong, Micromechanics of the brittle to plastic transition in Carrara marble, *J. Geophys. Res., 94*, 4129-4145, 1989.
43. Friedman, M., Porosity, permeability, and rock mechanics - a review, in *17th U.S. Symp. on Rock Mechanics*, edited by W. S. Brown, S. Green and W. Hustrulid, pp. 2A1.1-2A1.17, Univ. of Utah, Salt Lake City, 1976.
44. Goldsmith, W., J. Sackman, and C. Ewert, Static and dynamic fracture strength of Barre granite, *Int. J. Rock Mech. Min. Sci. & Geomech. Abs., 13*, 303-309, 1976.
45. Gottschalk, R. R., A. K. Kronenberg, J. E. Russell, and J. Handin, Mechanical anisotropy of gneiss: failure criterion and textural sources of directional behavior, *J. Geophys. Res., 95*, 21613-21634, 1990.
46. Grady, D. E., and J. Lipkin, Criteria for impulsive rock fracture, *Geophys. Res. Lett., 7*, 255-258, 1980.
47. Green, S. J., J. Leasia, R. Perkins, and A. Jones, Triaxial stress behavior of Solenhofen limestone and Westerly granite at high strain rates, *J. Geophys. Res., 77*, 1972.
48. Griffith, A. A., The phenomena of rupture and flow in solids, *Philos. Trans. R. Soc. London Ser. A, 221*, 163-198, 1920.
49. Hadley, K., Comparison of calculated and observed crack densities and seismic velocities in Westerly granite, *J. Geophys. Res., 81*, 3484-3494, 1976.
50. Handin, J., Strength and ductility, in *Handbook of Physical Constants*, edited by S. P. Clark, pp. 223-289, *The Geological Soc. of Amer., Inc.*, New York, 1966.
51. Herget, G., and K. Unrug, In situ rock strength from triaxial testing, *Int. J. Rock Mech. Min. Sci. & Geomech. Abstr., 13*, 299-302, 1976.
52. Heuze, F. E., Scale effects in the determination of rock mass strength and deformability, *Rock Mech., 12*, 167-192, 1980.
53. Hickman, S. H., Stress in the lithosphere and the strength of active faults, *Reviews of Geophys., IUGG Report*, 759-775, 1991.
54. Hickman, S. H., and B. Evans, Experimental pressure solution in halite: the effect of grain/interphase boundary structure, *J. Geol. Soc., 148*, 549-560, 1991.
55. Hickman, S. H., and B. Evans, Growth of grain contacts in halite by solution-transfer: implications for diagenesis, lithification, and strength recovery, in *Fault Mechanics and Transport Properties of Rocks*, edited by B. Evans and T.-f. Wong, pp. 253-280, Academic Press, London, 1992.
56. Hirata, T., T. Satoh, and K. Ito, Fractal structure of spatial distribution of microfracturing in rock, *Geophys. J. R. Astr. Soc., 90*, 369-374, 1987.
57. Hodgson, K., and N. G. W. Cook, The effects of size and stress gradient on the strength of rock, in *Proc. 2nd Congress Inter. Soc. Rock Mech.*, pp. 31-34, Belgrad, Yugoslavia, 1970.

58. Hoek, E., and E. T. Brown, *Underground Excavations in Rock*, 527 pp., The Inst. of Mining and Metallurgy, London, 1980.
59. Holcomb, D. J., and L. S. Costin, Detecting damage surfaces in brittle materials using acoustic emissions, *J. Appl. Mech., 108*, 536-544, 1986.
60. Horii, H., and S. Nemat-Nasser, Brittle failure in compression:splitting, faulting and brittle-ductile transition, *Philos. Trans. R. Soc. London, ser. A*, 319, 337-374, 1986.
61. Hubbert, M. K., and W. W. Rubey, Role of fluid pressure in mechanics of overthrust faulting, *Bul. Geol. Soc. Amer., 70*, 115-166, 1959.
62. Hugman, R. H. H., III, and M. Friedman, Effects of texture and composition on mechanical behavior of experimentally deformed carbonate rocks, *Bul. Amer. Assoc. Pet. Geol., 63*, 1478-1489, 1979.
63. Hunt, J. M., Generation and migration of petroleum from abnormally pressured fluid compartments, *Am. Assoc. Petrol. Geol. Bull., 74*, 1-12, 1990.
64. Ishido, T., and H. Mizutani, Relationship between fracture strength of rocks and zeta-potential, *Tectonophysics, 67*, 13-23, 1980.
65. Ismail, I. A. H., and S. A. F. Murrell, The effect of confining pressure on stress-drop in compressive rock fracture, *Tectonophysics, 175*, 237-248, 1990.
66. Jaeger, J. C., and N. G. W. Cook, *Fundamentals of Rock Mechanics*, 593 pp., Chapman and Hall, New York, 1984.
67. Ju, J. W., On energy-based coupled elastoplastic damage theories: constitutive modeling and computational aspects, *Int. J. Solids Structures, 25*, 803-833, 1989.
68. Ju, J. W., On two-dimensional self-consistent micromechanical damage models for brittle solids, *Int. J. Solid Structures, 27*, 227-258, 1991.
69. Kemeny, J. M., and N. G. W. Cook, Crack models for the failure of rocks in compression, in *Constitutive Laws for Engineering Materials: Theory and Applications*, edited by C. S. Desai, pp. 878-887, Elsevier Science Pub. Co., Inc., 1987.
70. Kirby, S. H., and A. K. Kronenberg, Rheology of the lithoshpere: selected topics, *Rev. of Geophys., 25*, 1219-1244, 1987.
71. Kirby, S. H., and J. W. McCormick, Inelastic properties of rocks and minerals: strength and rheology, in *CRC Handbook of Physical Properties of Rocks*, edited by R. S. Carmichael, pp. 139-280, CRC Press, Inc., Boca Raton, Florida, 1984.
72. Koifman, M. I., The size factor in rock-pressure investigations, in *Mechanical Properties of Rocks*, edited pp. 109-117, Akademiya Nauk SSSR (English translation), Moscow, 1963.
73. Kranz, R. L., The effects of confining pressure and stress difference on static fatigue of granite, *J. Geophys. Res., 85*, 1854-1866, 1980.
74. Kranz, R. L., W. J. Harris, and N. L. Carter, Static fatigue of granite at 200°C, *Geophys. Res. Lett., 9*, 1-4, 1982.
75. Kranz, R. L., T. Satoh, O. Nishizawa, K. Kusunose, M. Takahashi, K. Masuda, and A. Hirata, Laboratory study of fluid pressure diffusion in rock using acoustic emissions, *J. Geophys. Res., 95*, 21593-21607, 1990.
76. Lachenbruch, A. H., and J. H. Sass, Heat flow and energetics of the San Andreas fault zone, *J. Geophys. Res., 85*, 6185-6222, 1980.
77. Lade, P., R. B. Nelson, and Y. M. Ito, Instability of granular materials with nonassociated flow, *J. Eng. Mechanics, 114*, 2173-2191, 1988.
78. Lama, R. D., and V. S. Vutukuri, *Handbook on Mechanical Properties of Rocks*, 481 pp., Trans Tech Publications, Clausthal, Germany, 1978.
79. Lawn, B. R., and T. R. Wilshaw, *Fracture of brittle solids*, 204 pp., Cambridge Univ. Press, 1975.
80. Linde, A. T., and M. J. S. Johnston, Source parameters of the October 1, 1987 Whittier Narrows earthquake from crustal deformation data, *J. Geophys. Res., 94*, 9633-9643, 1989.
81. Lipkin, J., and A. K. Jones, Dynamic fracture strength of oil shale under torsional loading, in *Proc. 20th U. S. Symposium on Rock Mechanics*, pp. 601-606, Austin, Texas, 1979.
82. Lockner, D. A., The role of acoustic emission in the study of rock fracture, *Int. J. Rock Mech. Min. Sci. & Geomech. Abstr., 30*, 883-899, 1993.
83. Lockner, D. A., Room temperature creep in saturated granite, *J. Geophys. Res., 98*, 475-487, 1993.
84. Lockner, D. A., and J. D. Byerlee, Acoustic emission and creep in rock at high confining pressure and differential stress, *Bull. of the Seismological Society of Amer., 67*, 247-258, 1977.
85. Lockner, D. A., and J. D. Byerlee, Acoustic emission and fault formation in rocks, in *Proceedings, First Conference on Acoustic Emission/ Microseismic Activity in Geological Structures and Materials*, edited by H. R. Hardy and W. F. Leighton, pp. 99-107, Trans Tech Publications, Clausthal-Zellerfeld, Germany, 1977.
86. Lockner, D. A., and J. D. Byerlee, Hydrofracture in Weber sandstone at high confining pressure and differential stress, *J. Geophys. Res., 82*, 2018-2026, 1977.
87. Lockner, D. A., and J. D. Byerlee, Development of fracture planes during creep in granite, in *Proceedings, Second Conference on Acoustic Emission/Microseismic Activity in Geological Structures and Materials*, edited by H. R. Hardy and W. F. Leighton, pp. 11-25, Trans-Tech Publications, Clausthal-Zellerfeld, Germany, 1980.
88. Lockner, D. A., and J. D. Byerlee, Complex resistivity measurements of confined rocks, *J. Geophys. Res., 90*, 7837-7847, 1985.

89. Lockner, D. A., and J. D. Byerlee, Changes in complex resistivity during creep in granite, *Pure Appl. Geophys., 124*, 659-676, 1986.
90. Lockner, D. A., and J. D. Byerlee, How geometric constraints contribute to the weakness of mature faults, *Nature, 363*, 250-252, 1993.
91. Lockner, D. A., and J. D. Byerlee, Precursory AE patterns leading to rock fracture, in *Proceedings, Fifth Conference on Acoustic Emission/Microseismic Activity in Geological Structures and Materials*, edited by H. R. Hardy, pp. 14 (in press), Trans-Tech Publications, Clausthal-Zellerfeld, Germany, 1994.
92. Lockner, D. A., J. D. Byerlee, V. Kuksenko, A. Ponomarev, and A. Sidorin, Quasi-static fault growth and shear fracture energy in granite, *Nature, 350*, 39-42, 1991.
93. Lockner, D. A., J. D. Byerlee, V. Kuksenko, A. Ponomarev, and A. Sidorin, Observations of quasistatic fault growth from acoustic emissions, in *Fault Mechanics and Transport Properties of Rocks*, edited by B. Evans and T.-F. Wong, pp. 3-31, Academic Press, London, 1992.
94. Lockner, D. A., and T. R. Madden, A multiple crack model of brittle fracture - 1. non-time-dependent simulations, J. Geophys. Res., 96, 19623-19642, 1991.
95. Lockner, D. A., and T. R. Madden, A multiple crack model of brittle fracture - 2. time-dependent simulations, *J. Geophys. Res., 96*, 19643-19654, 1991.
96. Lockner, D. A., D. E. Moore, and Z. Reches, Microcrack interaction leading to shear fracture, in *33rd U.S. Rock Mechanics Symposium*, edited by J. R. Tillerson and W. R. Wawersik, pp. 807-816, Balkema, A. A., Rotterdam, 1992.
97. Lockner, D. A., J. B. Walsh, and J. D. Byerlee, Changes in seismic velocity and attenuation during deformation of granite, *J. Geophys. Res., 82*, 5374-5378, 1977.
98. Madden, T. R., Microcrack connectivity in rocks: a renormalization group approach to the critical phenomena of conduction and failure in crystalline rocks, *J. Geophys. Res., 88*, 585-592, 1983.
99. Main, I. G., and P. G. Meredith, Classification of earthquake precursors from a fracture mechanics model, *Tectonophysics, 167*, 273-283, 1989.
100. Masuda, K., O. Nishizawa, K. Kusunose, T. Satoh, M. Takahashi, and R. Kranz, Positive feedback fracture process induced by nonuniform high-pressure water flow in dilatant granite, *J. Geophys. Res., 95*, 21583-21592, 1990.
101. McNally, G. H., Estimation of coal measures rock strength using sonic and neutron logs, *Geoexploration, 24*, 381-395, 1987.
102. Mogi, K., The influence of the dimensions of specimens on the fracture strength of rocks, *Bul. Earthquake Res. Inst., 40*, 175-185, 1962.
103. Mogi, K., Pressure dependence of rock strength and transition from brittle fracture to ductile flow, *Bull. Earthquake Research Inst., 44*, 215-232, 1966.
104. Mogi, K., Effect of the intermediate principal stress on rock failure, *J. Geophys. Res., 72*, 5117-5131, 1967.
105. Mogi, K., Effect of the triaxial stress system on rock failure, in *Rock Mechanics in Japan*, edited by S. Okamoto, pp. 53-55, Japan Society of Civil Engineers, Tokyo, 1970.
106. Moore, D. E., and D. A. Lockner, The role of microcracking in shear-fracture propagation in granite, *J. Struct. Geol.*, in press, 1994.
107. Morgan, F. D., E. R. Williams, and T. R. Madden, Streaming potential properties of Westerly granite with applications, *J. Geophys. Res., 94*, 12449-12461, 1989.
108. Morrow, C., and W. F. Brace, Electrical resistivity changes in tuffs due to stress, *J. Geophys. Res., 86*, 2929-2934, 1981.
109. Morrow, C., and J. Byerlee, Permeability of core samples from Cajon Pass Scientific Drillhole: results from 2100 to 3500 m depth, *J. Geophys. Res., 97*, 5145-5151, 1992.
110. Morrow, C., D. A. Lockner, S. Hickman, M. Rusanov, and T. Röckel, Effects of lithology and depth on the permeability of core samples from the Kola and KTB drill holes, *J. Geophys. Res., 99*, 7263-7274, 1994.
111. Morrow, C., D. Moore, and J. Byerlee, Permeability and pore-fluid chemistry of the Bullfrog tuff in a temperature gradient, in *Proc. 24th U. S. Symp. on Rock Mech.*, pp. 819-828, 1983.
112. Morrow, C., B. Radney, and J. Byerlee, Frictional strength and the effective pressure law of montmorillonite and illite clays, in *Fault Mechanics and Transport Properties of Rocks*, edited by B. Evans and T.-f. Wong, pp. 69-88, Academic Press, London, 1992.
113. Morrow, C. A., Z. Bo-Chong, and J. D. Byerlee, Effective pressure law for permeability of Westerly granite under cyclic loading, *J. Geophys. Res., 91*, 3870-3876, 1986.
114. Morrow, C. A., L. Q. Shi, and J. D. Byerlee, Permeability of fault gouge under confining pressure and shear stress, *J. Geophys. Res., 89*, 3193-, 1984.
115. Nishizawa, O., K. Onai, and K. Kusunose, Hypocenter distribution and focal mechanism of AE events during two stress stage creep in Yugawara andesite, *Pure Appl. Geophys., 122*, 36-52, 1984.
116. Nur, A., and J. Walder, Time-dependent hydraulics of the Earth's crust, in *The Role of Fluids in Crustal Processes*, pp. 113-127, National Academy Press, 1990.
117. Olsson, W. A., The compressive strength of tuff as a function of strain rate from 10-6 to 103/sec, *Int. J. Rock Mech. Min. Sci. & Geomech. Abs., 28*, 115-118, 1991.
118. Ord, A., I. Vardoulakis, and R. Kajewski, Shear band formation in Gosford sandstone, *Int. J. Rock Mechanics Min. Sci. & Geomech.*

Abstr., 28, 397-409, 1991.
119. Palmer, A. C., and J. R. Rice, The growth of slip surfaces in the progressive failure of over-consolidated clay, *Proc. Roy. Soc. Lond. A., 332*, 527-548, 1973.
120. Paterson, M., *Experimental Rock Deformation*, 254 pp., Springer, New York, 1978.
121. Peng, S., and A. M. Johnson, Crack growth and faulting in cylindrical specimens of Chelmsford granite, *Int. J. Rock Mech. Min. Sci. & Geomech. Abs., 9*, 37-86, 1972.
122. Pinto da Cunha, A. (Ed.), *Scale Effects in Rock Masses*, 339 pp., A. A. Balkema, Rotterdam, 1990.
123. Powley, D. E., Pressures and hydrogeology in petroleum basins, *Earth-Sci. Revs., 29*, 215-226, 1990.
124. Pratt, H. R., A. D. Black, W. S. Brown, and W. F. Brace, The effect of specimen size on the mechanical properties of unjointed diorite, *Int. J. Rock Mech. Min. Sci. & Geomech. Abstr., 9*, 513-529, 1972.
125. Price, R. H., and S. J. Bauer, Analysis of the elastic and strength properties of Yucca Mountain tuff, Nevada, in *26th U.S. Symp. of Rock Mechantcs*, pp. 89-96, A. A. Balkema, Rotterdam, 1985.
126. Reches, Z., and D. A. Lockner, Nucleation and growth of faults in brittle rocks, *J. Geophys. Res.*, in press, 1994.
127. Rice, J. R., Constitutive relations for fault slip and earthquake instabilities, *Pure Appl. Geophys., 121*, 443-475, 1983.
128. Rice, J. R., Fault stress states, pore pressure distributions, and the weakness of the San Andreas fault, in *Fault Mechanics and Transport Properties of Rocks*, edited by B. Evans and T.-f. Wong, pp. 475-503, Academic Press, London, 1992.
129. Rice, J. R., and A. L. Ruina, Stability of steady frictional slipping, *J. Appl. Mech., 50*, 343-349, 1983.
130. Rudnicki, J. W., Effects of dilatant hardening on the development of concentrated shear deformation in fissured rock masses, *J. Geophys. Res., 89*, 9259-9270, 1984.
131. Rudnicki, J. W., and J. R. Rice, Conditions for the localization of deformation in pressure-sensitive, dilatant materials, *J. Mech. Phys. Solids, 23*, 371-394, 1975.
132. Ruina, A. L., Slip instability and state variable friction laws, *J. Geophys. Res., 88*, 10359-10370, 1983.
133. Rutter, E. H., and D. H. Mainprice, The effects of water on stress relaxation of faulted and unfaulted sandstone, *Pure Appl. Geophys., 116*, 634-654, 1978.
134. Sammis, C. G., and M. F. Ashby, The failure of brittle porous solids under compressive stress states, *Acta metall., 34*, 511-526, 1986.
135. Satoh, T., O. Nishizawa, and K. Kusunose, Fault development in Oshima granite under triaxial compression inferred from hypocenter distribution and focal mechanism of acoustic emission, *Tohoku Geophys. J., 33*, 241-250, 1990.
136. Sayles, F. H., and D. L. Carbee, Strength of frozen silt as a function of ice content and dry unit weight, *Eng. Geol., 18*, 55-66, 1981.
137. Scholz, C. H., The frequency-magnitude relation of microfracturing in rock and its relation to earthquakes, *Bul. Seismological Soc. Amer., 58*, 399-415, 1968.
138. Scholz, C. H., *The mechanics of earthquakes and faulting*, 439 pp., Cambridge Univ. Press, New York, 1990.
139. Shamir, G., and M. D. Zoback, The stress orientation profile in the Cajon Pass, California, scientific drillhole, based on detailed analysis of stress induced borehole breakouts, in *Rock at Great Depth*, edited by V. Maury and D. Fourmaintraux, pp. 1041-1048, A. A. Balkema, Rotterdam, 1989.
140. Sheorey, P. R., A. K. Biswas, and V. D. Choubey, An empirical failure criterion for rocks and jointed rock masses, *Engineering Geol., 26*, 141-159, 1989.
141. Shimada, M., The method of compression test under high pressures in a cubic press and the strength of granite, *Tectonophysics, 72*, 343-357, 1981.
142. Shimada, M., A. Cho, and H. Yukutake, Fracture strength of dry silicate rocks at high confining pressures and activity of acoustic emission, *Tectonophysics, 96*, 159-172, 1983.
143. Singh, J., T. Ramamurthy, and G. Rao, Strength of rocks at depth, in *Rock at Great Depth*, edited by Maury and Fourmaintraux, pp. 37-44, Balkema, Rotterdam, 1989.
144. Singh, M. M., and P. J. Huck, Large scale triaxial tests on rock, in *Proc. 14th Symp. on Rock Mech.*, pp. 35-60, Amer. Soc. of Civil Engineers, New York, 1972.
145. Soga, N., H. Mizutani, H. Spetzler, and R. J. Martin, The effect of dilatancy on velocity anisotropy in Westerly granite, *J. Geophys. Res., 83*, 4451-4458, 1978.
146. Sondergeld, C. H., and L. H. Estey, Acoustic emission study of microfracturing during the cyclic loading of Westerly granite, *J. Geophys. Res., 86*, 2915-2924, 1981.
147. Sondergeld, C. H., and L. H. Estey, Source mechanisms and microfracturing during uniaxial cycling of rock, *Pure Appl. Geophys., 120*, 151-166, 1982.
148. Spetzler, H., H. Mitzutani, and F. Rummel, Fracture and flow, in *Anelasticity in the Earth*, edited by W. Schreyer, pp. 85-93, E. Schweizerbartische Verlagsbuchhandlung, Stuttgart, 1982.
149. Spetzler, H., G. Sobolev, C. Sondergeld, B. Salov, I. Getting, and A. Koltsov, Surface deformation, crack formation, and acoustic velocity changes in pyrophyllite under polyaxial loading, *J. Geophys. Res., 86*, 1070-1080, 1981.
150. Sulem, J., and I. Vardoulakis, Simplified bifurcation analysis of deep boreholes in rocks with microstructure, in *Rock at Great Depth*, edited by Maury and Fourmaintraux, pp. 845-852, Balkema, Rotterdam, 1989.
151. Takahashi, M., and H. Koide, Effect of the intermediate principal stress on strength and deformation behavior of sedimentary rocks at

the depth shallower than 2000 m, in *Rock at Great Depth*, edited by V. Maury and D. Fourmaintraux, pp. 19-26, A. A. Balkema, Rotterdam, 1989.

152. Tapponnier, P., and W. F. Brace, Development of stress-induced microcracks in Westerly granite, *Int. J. Rock Mech. Min. Sci. & Geomech. Abstr., 13*, 103-112, 1976.
153. Terada, M., T. Yanagidani, and S. Ehara, A. E. rate controlled compression test of rocks, in *3rd Conf. on Acoustic Emission/Microseismic Activity in Geol. Structures and Materials*,edited by H. R. Hardy and F. W. Leighton, pp. 159-171,Trans-Tech Publications,Clausthal-Zellerfeld, Germany, 1984.
154. Tullis, J., and R. A. Yund, Experimental deformation of dry Westerly granite, *J. Geophys. Res., 82*, 5705-5718, 1977.
155. Türk, N., and W. R. Dearman, A practical classification of rocks for engineering purposes, *Bul. Int. Assoc. Eng. Geology, 28*, 161-167, 1983.
156. Vardoulakis, I., M. Goldscheider, and G.Gudehus, Formation of shear bands in sand bodies as a bifurcation problem, *Inter. J. for Numerical and Analytical Methods in Geomech., 2*, 99-128, 1978.
157. Vernik, L., D. A. Lockner, and M. D. Zoback, Anisotropic strength of some typical metamorphic rocks from the KTB pilot hole, Germany, *Scientific Drilling, 3*, 153-160, 1992.
158. Vernik, L., and M. D. Zoback, Strength anisotropy in crystalline rock: implications for assessment of in situ stresses from wellbore breakouts, in *Proc., 31st U. S. Rock Mechanics Symposium*, edited by W. A. Hustrulid and G. A. Johnson, pp. 841-848, A. A. Balkema, Rotterdam, 1990.
159. Walsh, J. B., Effect of pore pressure and confining pressure on fracture permeability, *Int. J. Rock Mech. Min. Sci. & Geomech. Abstr., 18*, 429-435, 1981.
160. Wawersik, W. R., and W. F. Brace, Post-failure behavior of a granite and a diabase, *Rock Mech., 3*, 61-85, 1971.
161. Wawersik, W. R., J. W. Rudnicki, W. A. Olsson, D. J. Holcomb, and K. T. Chau, Localization of deformation in brittle rock: theoretical and laboratory investigations, in *Micromechanics of Failure of Quasi-brittle Materials*, edited by S. P. Shah, S. E. Swartz and M. L. Wang, pp. 115-124, Elsevier Science Pub., London, 1990.
162. Weeks, J. D., D. A. Lockner, and J. D. Byerlee, Changes in b-value during movement on cut surfaces in granite, *Bull. of the Seismological Society of Amer., 68*, 333-341, 1978.
163. Wong, T.-f., Effects of temperature and pressure on failure and post-failure behavior of Westerly granite, *Mechanics of Materials, 1*, 3-17, 1982.
164. Wong, T.-f., Mechanical compaction and the brittle-ductile transition in porous sandstones, in *Deformation Mechanisms, Rheology and Tectonics*, edited by R. J. Knipe and E. H. Rutter, pp. 111-122, Geological Soc. Special Publication No. 54, 1990.
165. Yanagidani, T., S. Ehara, O. Nishzawa, K. Kusunose, and M. Terada, Localization of dilatancy in Ohshima granite under constant uniaxial stress, *J. Geophys. Res., 90*, 6840-6858, 1985.
166. Yudhbir, W. Lemanza, and F. Prinzl, An empirical failure criterion for rock masses, in *Proc. 5th Int. Congress on Rock Mech.*, pp. B1-B8, Int. Soc. for Rock Mechanics, Balkema, Melbourne, 1983.
167. Zhaoyong, X., G. Naiguang, and M. Shirong, Acoustic emission m-values of rock failure and mechanic properties of the rock, *J. Seismological Res., 13*, 291-297, 1990.

Rheology of Rocks

Brian Evans and David L. Kohlstedt

1. LABORATORY MEASUREMENTS

1.1. Strategy and Techniques

For a rock of given mineralogy and microstructure, the variables important in determining strength are pressure, temperature, strain, strain history, strain rate, pore fluid pressure, grain size, fugacities of water and other volatiles, and chemical activities of the mineral components. Although earth scientists may now duplicate pressures and temperatures appropriate to the mantle and core in modern high pressure apparatus, they still cannot study mechanical properties under truly natural conditions. Time scales in the Earth are too long, and length scales too large.

Since exact deformation conditions cannot be duplicated in the laboratory, the experimenter's strategy must involve determining the kinetic parameters of the appropriate processes at laboratory conditions and extrapolating to much lower strain rates [58]. Two convenient techniques are available to aid laboratory studies. Temperature and, hence, kinetic rates may be increased, or processes may be studied at smaller length scales [60].

Testing at high temperatures also imposes constraints. For example, maintaining chemical and phase stability and producing accelerated deformation kinetics may be mutually exclusive goals. This conflict can be mitigated by testing single phase rocks or by fabricating synthetic rocks with specially designed phase compositions. The chemical fugacities of the mineral components and any volatiles, particularly water, must also be controlled. Unless the experimenter aims to investigate the properties of partial melts, eutectic melting needs to be avoided.

Deformation at low strain rates can also be studied by reducing a length scale. For mechanisms primarily limited by diffusion, the most important length scale is the grain size. Natural rocks with grain sizes of a few microns may be found, and synthetic aggregates of olivine, calcite, feldspars, and quartz have been produced in a range of very small grain sizes. Such synthetic rocks can be used to understand the effect of variations of grain size, second phase abundance, or dissolved hydroxyl content on the physical properties of rocks.

1.2. Apparatus

Modern apparatus use a variety of loading schemes, including rotary shear, double block shear, conventional triaxial, full triaxial, diamond anvil, and large volume, opposed multi anvil devices [60, 90]. The most common loading geometry is the conventional triaxial configuration (Figure 1). Such machines have cylindrical loading symmetry with coaxial stress and strain. If the axial compressive stress, σ_a, is larger than the confining pressure, P_c, then loading is triaxial compression; if $\sigma_a<P_c$ then the sample extends. When pore fluids are present, the effective stresses must be considered: the effective axial stress σ_a' is σ_a-P_f, the effective pressure is $P_c'=P_c-P_f$. By using forcing blocks with an inclined cut, non-coaxial experiments can be carried out in plane strain or pure shear. Displacements in this geometry are limited by jacket

B. Evans, Massachusetts Institute of Technology, Department of Earth, Atmospheric and Planetary Sciences, Cambridge, MA 02139-4307

D. L. Kohlstedt, University of Minnesota, Minneapolis, Department of Geology and Geophysics, Minneapolis, MN 55455

Rock Physics and Phase Relations
A Handbook of Physical Constants
AGU Reference Shelf 3

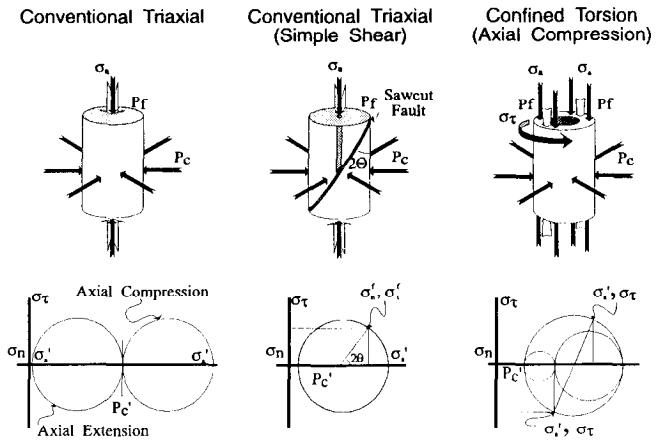

Fig. 1. Schematics of several different loading configurations in conventional triaxial machines; below these are Mohr's circles for each configuration. The experimenter independently controls the axial load, σ_a, the pressure of the confining medium, P_c, and the pore fluid pressure, P_f. Primed quantities are effective stresses, for example, $\sigma_a'=\sigma_a-P_f$. In the conventional triaxial configuration, when σ_a' is greater than P_c' the sample shortens along its axis; when σ_a' is less than P_c', the sample extends. The simple shear configuration allows plane strain experiments to be done, but slip distances are limited. During confined torsion an additional shear stress is applied; the principal stresses are no longer parallel to the sample axis. This configuration allows very large shear strains, but, thus far, only room temperature experiments have been done [90].

flexibility, and are typically a few millimeters. New rotary shear devices overcome this limitation, enabling tests to large strains.

The confining medium may be either a weak solid or a true fluid [60, 90]. Solid medium machines are capable of higher pressures and longer time spans, but, owing to the strength of the solid medium, uncertainties in stress and pressure exist; but those decrease as the strength of the pressure medium decreases. Media used are AlSiMag ceramic, pyrophyllite, magnesium oxide, calcite, and salt (listed in order of decreasing strength). The recent introduction of liquid salt cells significantly improved stress resolution [22]. Gas medium devices also have low uncertainty in stress; additionally, they provide independent control of pore fluid pressure. Whether porosity is drained or undrained is an important consideration for tectonic processes in the crust and lithosphere.

Heating is provided by a cylindrical furnace, made with graphite, tungsten, molybdenum, or platinum elements, placed either inside or outside the pressure vessel. In the solid medium assembly, samples are about 10 mm long, while those in the gas apparatus are about 25-50 mm. At higher temperatures, the chemical fugacities of volatiles are significant in determining the mechanical properties of the matrix minerals and must be controlled by a buffer system.

2. DEFORMATION MECHANISMS

In general, inelastic deformation occurs by defect motion. Brittle failure results from crack growth or frictional slip [48]; plastic flow results from motion of point defects, dislocations, and twins, or from grain boundary sliding [64]. To predict mechanical behavior the production, motion, and annihilation of strain-carrying defects must be related to parameters such as stress, temperature, fugacity, and pressure [63]. Plastic constitutive laws can be categorized by identifying the rate-controlling steps of the dominant mechanism [18]: Nabarro-Herring and Coble creep are point defect processes. Glide, climb, cross slip, and Harper-Dorn creep occur by dislocation motion. Twinning and grain boundary sliding involve planar defects. In pressure solution, ions are transported through a fluid.

3. DIFFUSION FLOW

Parts of the crust and mantle may deform by diffusion creep [5]. Rocks thought to be deformed in this regime are composed of small, equant grains lacking dislocation structures and lattice preferred orientation. Such microstructures are found in sheared olivine xenoliths, quartz mylonites, and calcite-dominated thrusts. Since minerals are composed of several ions, diffusion of the slowest ion along its fastest path (either grain matrix or grain boundary) will determine creep rate. Theory and experiments have identified three diffusion creep mechanisms. In the first, diffusion through matrix grains controls creep rate; in the second, grain boundary diffusion dominates; and in the third, reactions at the grain interface are governing.

Flow laws describing diffusion creep indicate strain rate is directly related to stress and inversely related to grain size [18]. If matrix diffusion dominates (Nabarro-Herring creep), the steady state creep rate is

$$\dot{\varepsilon} = 14\left(\frac{\sigma V}{RT}\right)\frac{D^L}{d^2} \qquad (1)$$

where σ is the differential stress, V is the molar volume, D^L is an effective matrix diffusion coefficient, d is the average grain size, R is the gas constant, and T is absolute temperature. If grain boundary diffusion is rate-controlling (Coble creep), the creep rate is

$$\dot{\varepsilon} = 44\left(\frac{\sigma V}{RT}\right)\frac{\delta D^{GB}}{d^3} \tag{2}$$

where δ is the grain boundary width, and D^{GB} is the boundary diffusion coefficient. For grains to remain in contact, grain boundary sliding must also occur. Analysis of diffusion creep accompanied by boundary sliding yields constitutive equations that differ from (2) only in the numerical prefactor.

3.1. Point Defect Chemistry

The magnitudes of lattice and grain boundary diffusion constants in (1) and (2) are affected by the number and mobility of the defects involving the slowest ion. Both constants follow Arrhenius laws characteristic of thermally activated processes [64, 18]. The diffusivity of a given ion depends on the concentration of other defects as well. Point defects in minerals are usually charged; consequently, the concentration of each point defect is coupled to that of others by the condition that the crystal be electrically neutral [76].

In addition to intrinsic defects involving stoichiometric components, extrinsic point defects (i.e. impurities) may also exist. Because of charge coupling, extrinsic defects can influence the number and mobility of intrinsic defects and, hence, the creep rate. Chief among the extrinsic lattice defects are those involving dissolved hydrogen, hydroxyl, or water. One extremely important conclusion of recent research is that diffusion flow is strongly affected by point defect chemistry [31].

In ternary or quaternary minerals, many point defects are possible, and special notations have been developed to describe them. The most common, called the Kröger-Vink notation, indicates the charge (superscript), site (subscript), and nature of the defect. For example, V''_{Me} denotes a vacancy on the cation (metal) sublattice with double negative charge, relative to a normal occupied site. The concentrations of the point defects will depend on the fugacities of other chemical species through point defect reactions. In actual crystals, the concentrations of one pair of oppositely charged defects, the majority point defects, greatly exceed those of all others over a wide range of thermodynamic conditions, so that the point defect chemistry can be described by only a few point defect reactions.

Despite the importance of defect chemistry for strength, details of the point defect chemistry have been explored only for Mg-Fe olivine [53]. The majority defects for that mineral are metal vacancies, V''_{Me} and electron holes, $h^{\cdot}$, localized near the octahedral metal cations, $Me^{\cdot}_{Me}$. Charge neutrality requires that the mole fraction of holes, $N_{h^{\cdot}}$, be twice that of the metal vacancies, $N_{V''_{Me}}$: $N_{h^{\cdot}} = 2N_{V''_{Me}}$. Metal vacancies, oxygen interstitials and silicon interstitials are formed in the following reactions:

$$\frac{1}{2}O_2(g) + MeSiO_3(g) + 3Me^x_{Me} = 2Me^{\bullet}_{Me} + V''_{Me} + Me_2SiO_4(g) \tag{3}$$

$$\frac{1}{2}O_2(g) + 2Me^X_{Me} = O''_I + 2Me^{\bullet}_{Me} \tag{4}$$

$$V''_{Me} + MeSiO_3(g) = Me^X_{Me} + Si^{\bullet\bullet\bullet\bullet}_I + 3O''_I \tag{5}$$

The Gibbs phase rule requires that point defect concentrations in a four-component compound depend on three activities, P, and T. For fixed Mg-to-Fe ratio, P and T, then point defect concentrations will be determined by the oxygen and orthopyroxene activities. Using the law of mass action, combined with the charge neutrality condition, the concentrations of Me vacancies, O interstitials and Si interstitials are given by

$$N_{V''_{Me}} = K_{Me} a_{O_2}{}^{1/6} a_{opx}^{1/3} \tag{6}$$

$$N_{O''_I} = K_O a_{O_2}{}^{1/6} a_{opx}^{-2/3} \tag{7}$$

$$N_{Si_i^{\bullet\bullet\bullet\bullet}} = K_{Si} a_{O_2}^{-1/3} a_{opx}^{10/3} \tag{8}$$

where the K_i's are functions of T and P only.

Now, the diffusivity of a component ion, D, is related to the concentration, N_i, and diffusivity, D_i, of its associated point defects by

$$D = N_i D_i \tag{9}$$

Thus, D is a function of the component activities, e.g., (6-8). Defect concentrations are small, $N_i < 10^{-3}$, and, therefore, the ion diffusivity will be much smaller than that of the point defects. Thus, point defect concentrations can adjust rapidly to changes in thermodynamic conditions, while bulk composition changes much more slowly [51].

TABLE 1. Diffusion Flow in Rocks

Sample	A'	n	m	Q ($kJmol^{-1}$)	Remarks	Source
Solnhofen Limestone	*4.2-4.9* $(Bar^{-n})(\mu m)^m$	1.7	2 or 3	214	Grain size <10 μm; boundary sliding ; equiaxed grains; but some flattening; Stresses below 100 MPa; Grain growth during experiment.	*77*
Synthetic Calcite	$10^{4.9}$ $(MPa^{-n})(\mu m)^m$	1.7	1.9	190	Synthetic hot pressed samples Grain size sensitive creep below 25 MPa; Grain sizes 2-40 μm; Some grain growth.	*92*
Synthetic Dunite (Dry)	$7x10^{-3}$ $(MPa^{-n})(\mu m)^m$	1.1	3.0	380	Synthetic hot pressed samples; Grain sizes from 3-13 μm;	*10*
Synthetic Dunite (wet)	$1.5x10^{-3}$ $(MPa^{-n})(mm)^m$	1.4	3.4	250[b]	Porosity from 5-15% 0.3 ml water added; Some grain growth; Very small amount of melt;	*38*
Synthetic Dunite (dry)	$7.7x10^{-2}$ $(MPa^{-n})(mm)^m$	1.4	1.7	290[c]	Some grain growth; trace melt;	*38*
Synthetic Albite					Diffusional flow identified by creep microstructure	*Tullis and Yund, pers. comm., 1993*

[a]mol =mole of the mineral (quartz, calcite, olivine, etc.)
[b]Activation energy assumed to be 2/3 of that for volume diffusion of O/Si
[c]Activation energy assumed to be same as Mg-Fe lattice diffusion

3.2. Diffusion Creep Experiments

The equations for Nabarro-Herring and Coble creep, (1) and (2), may be generalized to the form

$$\dot{\varepsilon} = A'\sigma^n \frac{D'}{d^m} \tag{10}$$

where D' is the diffusion coefficient for the slowest ion along its fastest path given by (9); m is either 2 or 3 depending on whether diffusion is faster through the matrix or along the boundary; and n should equal 1. By measuring creep rate as a function of grain size, stress, and temperature, the parameters m, n, and the activation energy of D' may be determined. Comparison of the experimental values with those expected theoretically may be used to identify diffusion flow. Substantial deviations of n from unity probably indicate that other processes, e.g. dislocation flow, are contributing to bulk deformation. Microstructural evidence for diffusion creep includes the maintenance of fine, equi-axed grains, lack of dislocations, and extensive grain boundary sliding.

Limited data exist for diffusion creep in limestone, olivine, and feldspar (Table 1). At stresses below 100 MPa, creep in Solnhofen limestone and fine-grained, synthetic marbles is sensitive to grain size. Grain boundary sliding contributes as much as two-thirds of the total strain [77, 92]. In Solnhofen, dislocations were present, and grains were somewhat flattened after deformation. A quantitative comparison of diffusion coefficients is not possible, because boundary diffusivities are not available for limestone.

In fine-grained synthetic dunite, Coble creep dominates when water is added, (m=3.4); but Nabarro-Herring creep may prevail when the sample is dry (m = 1.7) [38]. In both cases, values for n are greater than unity and may reflect some contribution by dislocation flow. The effective diffusivity for dry creep agrees with the value reported for interdiffusion of Mg and Fe in olivine, but is much larger than values for self-diffusion of oxygen or silicon [35, 36,

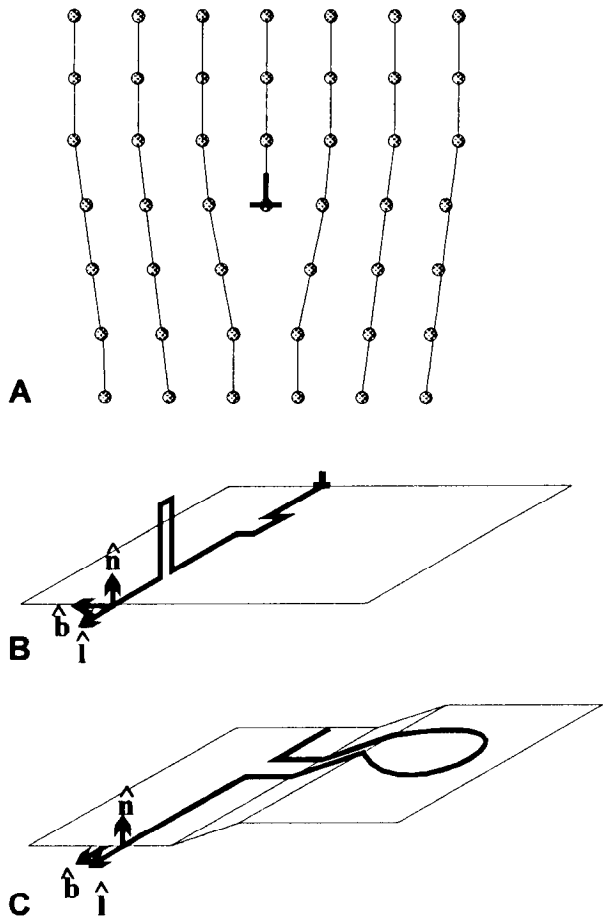

Fig. 2*a*. Schematic drawing of an edge dislocation in a simple cubic material. The edge of the extra half plane of atoms in the center of the crystal is the dislocation core.
Fig. 2*b*. In this schematic of an edge dislocation, the core region is drawn as a line. The normal to the glide plane is **n**, the Burgers vector is shown as **b**, and the line direction is **l**. Kinks are abrupt changes in the line direction which lie in the glide plane. Jogs are abrupt changes in direction which take the dislocation out of the glide plane. The size of the jog is greatly exaggerated here. Motion along the glide plane is conservative, requires no atomic diffusion, and proceeds by the migration of kinks in the plane. Dislocation climb occurs as jogs migrate and atoms diffuse into or out of the extra half plane. Diffusion transport can be along the dislocation core or through the lattice. The mobilities and numbers of jogs and kinks can be affected by the concentration and mobility of point defects in the crystal.
Fig. 2*c*. Screw dislocations can slip along any plane cozonal with **l**. Since **b** is parallel to **l** for all screw dislocations, and because **b** lies in any plane that is cozonal with **l**, slip in any of those planes is conservative.

74]. This result suggests that flux of oxygen and silicon are greater along boundaries than through the matrix, while the opposite is true for octahedral cations.

4. DISLOCATION FLOW

Dislocations are linear defects characterized by two vectors and a plane: the line direction, **l**, which is the tangent to the defect at any point; the Burgers vector, **b**, which is the closure failure of a circuit made around the dislocation; and the glide plane, which is represented by its normal vector, **n**. The glide plane contains both **l** and **b** (Figure 2). The Burgers vector, usually a low index direction of the crystal structure, gives the displacement induced by the passage of the dislocation. Dislocations with common **n** and **b** comprise a slip system. For plastic flow to occur homogeneously by dislocation glide alone, five independent slip systems must operate (the Von Mises criterion); but if strain is heterogeneous, this restriction is relaxed [57].

As rocks creep, dislocations are generated, migrate, and are annihilated, the applied stresses doing work during all three steps. In silicates, only small portions of the dislocation, called jogs and kinks, are mobile at a given instant. Dislocation motion in the glide plane occurs by kink migration; while climb out of the plane occurs by jog motion. The crystal structure offers intrinsic resistance to the motion of both; for kink migration, the resistance is called lattice friction. Each dislocation segment also interacts with the local stress field. When the force of that interaction, combined with thermal activation, is large enough, the segment migrates to cause strain.

The net local stress is the superposition of all externally applied stresses and any internal stresses arising from other dislocations, point defects, precipitates, or interfaces. The internal stress, which typically resists migration, may increase with strain (hardening) or decrease with time (recovery), depending on changes in the internal microstructure. The change of the internal stress field, $\Delta\sigma_i$ may be written as

$$\Delta\sigma_i = h' d\varepsilon - r' dt \tag{11}$$

where h' and r' are the strain-hardening coefficient and the recovery rate, respectively. When softening owing to recovery balances hardening, the steady state creep rate is

$$\dot{\varepsilon} = \frac{r'}{h'}. \tag{12}$$

Alternatively and equivalently, the creep rate may be written

$$\dot{\varepsilon} \propto \rho v b \tag{13}$$

where ρ is the density of the mobile defects, b is the length of the Burgers vector, and v is the velocity of the mobile defect [18].

4.1. Dislocation Flow Laws

To formulate a constitutive law one must identify the rate-limiting step in the sequence of generation, motion, and recovery of the pertinent defects. For example, dislocations may be generated at boundaries, intersections with other dislocations, or precipitates. Motion may occur by climb, glide, or cross-slip. Recovery may occur by cross-slip or climb allowing reactions with dislocations of opposite Burgers vector (recovery), or by interaction of a dislocation with a static or moving boundary (recrystallization).

Chemical activities can profoundly affect creep rate. In minerals, kinks and jogs may be charged. As with point defects, line defects may be surrounded by charge-compensating point defects which are dragged along during dislocation motion. Thus, the mobility and number of jogs and kinks probably depends on concentration and mobility of certain point defects [31]. Similarly, if recovery occurs by climb, which requires diffusion, the recovery rate will respond to diffusivity changes caused by variations in chemical activity.

The rate-limiting step for creep will, in general, be thermally activated, but may change with variations of stress, σ, temperature, T, elements of the microstructure, S, or chemical activities, a_i of all but one of the p components [3, 31]. In completely general form, the creep rate is

$$\dot{\varepsilon} = f\left(\sigma, S, T, P, a_1, \ldots, a_i, \ldots, a_{p-1}\right) \cdot exp\left(-\frac{\Delta G}{RT}\right) \tag{14}$$

where ΔG, the free energy of activation (often called Q), may be a function of stress or pressure.

Among the possible rate-limiting steps for creep are glide migration, climb migration, recovery by climb, recovery by cross slip, or dislocation generation. The deformation rate of the aggregate will be determined by the rate-limiting step of the fastest mechanism. If appropriate assumptions can be made as to which multiplication, migration, or recovery process controls strain and which step in that process controls strain rate, then theoretical constitutive laws may be developed. Some typical constitutive models are given in Table 2; the list is far from exhaustive.

Given accurate constitutive equations and appropriate materials properties, deformation maps may be constructed which indicate the area of dominance of each mechanism [18]. The independent variables of the map may be chosen as any two of the pertinent variables in (14), provided that the remaining parameters are fixed. The boundaries plotted on the map represent the conditions where the strain rates of two mechanisms are equal.

The mechanisms fall into several classes: (1) plasticity, controlled by glide, occurring at high stress or low temperature; (2) creep, controlled by climb or cross slip, occurring at high temperatures; or (3) Harper-Dorn creep, occurring at very low stresses, or high temperatures. Changes in the flow law are also accompanied by microstructural changes. For example, metals creeping at high temperature may be divided into two classes [85], called pure metal type, where n≅5, and alloy type, where n≅3. Microstructural observations indicate that dislocations organize to form subgrains in the first type, but are scattered homogeneously throughout the crystal even after large strains in the second. In metal types, creep is presumably controlled by the dislocation multiplication rate; while for alloy types, creep may be controlled by viscous migration. In metals, simple halides and oxides, it is often found that the activation energy for high-temperature creep is the same as the activation energy for self-diffusion of the slowest species.

4.2. Dislocation Creep Experiments

A common feature of many of the high-temperature constitutive laws is that creep rate is related to differential stress, σ, by a power law of the form,

$$\dot{\varepsilon} = A_{dis}^{exp}\left[\prod_{i=1}^{p-1} a_i^{q_i}\right]\sigma^n \cdot exp\left(-\frac{Q_{dis}^{exp}}{RT}\right), \tag{15}$$

where a_i is the activity of the ith component, q_i, n, and Q_{dis}^{exp} are constants, and A_{dis}^{exp} is a weak function of T. Often experimentalists simply adopt (15) and determine n experimentally (Table 3) [8, 15, 41]. At lower temperatures and higher stresses, creep is controlled by glide (glide or barrier models), leading to an exponential dependence of creep rate on stress. Scant data are available, but for olivine, this transition may occur at 200-600 MPa.

With more detailed examination, creep experiments in rocks show great complexity, belying naive trust in (15). Substantial differences may exist from one rock to another, even when they are dominantly monomineralic (Figures 3

TABLE 2. Constitutive Laws for Dislocation Creep

Mechanism	Constitutive Law	Remarks	Reference
Harper-Dorn	$\dot{\varepsilon} = A_{H\text{-}D}\frac{\Omega\rho_m}{\lambda}\frac{D\mu b}{kT}\left(\frac{\sigma}{\mu}\right)$	Low stress, low dislocation densities	*67*
Viscous Glide	$\dot{\varepsilon} = \frac{1}{8c_o\varepsilon_a^2}\left(\frac{kT}{\mu b^3}\right)\frac{D_{sol}}{b^2}\left(\frac{\sigma}{\mu}\right)^3$	Glide controlled; Dislocations dragging solute atmosphere. High temperature, Intermediate stress	*85*
High and Low Temperature	$\dot{\varepsilon} = A_{creep}D_{eff}\frac{\mu b}{kT}\left(\frac{\sigma}{\mu}\right)^{n'}$ $where\ D_{eff} = D_v + 10\frac{a_c}{b^2}\left(\frac{\sigma}{\mu}\right)^2 D_c$	Effective diffusion dominated by lattice diffusion (high temp.) or pipe diffusion (low temp.)	*18*
Recovery-controlled	$\dot{\varepsilon} = \frac{A_{rec}}{b^{3.5}}\frac{D}{M^{0.5}}\left(\frac{\sigma}{\mu}\right)^{4.5}\frac{\mu\Omega}{kT}$	Creep rate controlled by escape rate of pile ups High temperature, Intermediate stress	*94*
Cross slip Controlled	$\dot{\varepsilon} = \dot{\varepsilon}_{o\ cross\ slip}\left(\frac{\sigma}{\mu}\right)^2 exp-\left[\frac{Q_{xs}(\sigma)}{RT}\right]$ $Q_{xs}(\sigma) = A_{xs}\frac{\mu b^2}{4\pi}d_o\left[\left(1-\frac{b_o}{d_o}\right)^2 - \alpha_{xs}\frac{\sigma b}{\gamma_f}\right]$	Localized obstacles require cross slip; high temperature, intermediate stress	*63*
Glide controlled	$\dot{\varepsilon} = 12\upsilon a M^{-0.5}\left(\frac{\sigma}{\mu}\right)^{2.5} exp-\frac{\Delta G_{glide}}{kT}\left[1-\frac{\pi\sigma}{2\tau}\right]$	Stress-activated; Low temperature; high stress	*95*
Barrier controlled	$\dot{\varepsilon} = A_{barrier}exp\left[-\frac{\Delta G_{barrier}}{kT}\left(1-\frac{\sigma}{\tau}\right)^{p'}\right]^{q'}$	Obstacle dominated; stress-activated; Low temperature; high stress	*18*

and 4). For example, for Yule marble [28] and Carrara marble [78], the empirically determined flow law constants are, respectively, n=7.7 and 7.6 and Q_{dis}^{exp}=255 and 420 kJ/mole (for deformation at strain rates of 10^{-3} to 10^{-6} s^{-1} and temperatures of 500 to 1000°C). Thus, although there is general agreement concerning the stress exponent, activation energies for the two rocks differ significantly. Further, cross slip might be important [12], which would lead to an entirely different flow law (Table 2).

The largest data set currently available is for olivine-rich rocks (Figure 5). Coarse-grained olivine undergoes power law creep at stresses below 100 MPa with values of n in the range 3.3-4.5 and Q_{dis}^{exp} in the range 440-540 kJ/mol. In both polycrystals and single crystals, strain rate depends on intrinsic variables including temperature, oxygen fugacity and pyroxene activity, and on extrinsic dopants including water (or hydrogen) fugacity [3, 38] and, possibly, carbon activity [21]. Both single crystal and polycrystalline olivine are weakened at high temperature by a factor of 2.5 when water is added. The diffusion rate for hydrogen is fast -- 10^{-9} to 10^{-12} m^2s^{-1} at 800-1000°C, suggesting an extremely mobile defect, e.g., interstitial protons, charge-compensated by electron holes [38, 50].

In olivine single crystals, no one dislocation climb model

Symbols Used in Table 2	
a	Distance between Peierls hills
a_c	Cross sectional area of dislocation core
A_{creep}, A_{glide1}, A_{glide2}	Pre exponential factors, may be a function of temperature, etc.
b	Length of Burgers vector
b_o	Width of unsplit dislocation
c_o	Concentration of solute in crystal matrix
D	Constant for self-diffusion through lattice
D_c	Constant for core diffusion
D_{sol}	Diffusion coefficient of solute in crystal matrix
d_o	Width of split dislocation
$\Delta G_{glide1}, \Delta G_{glide2}$	Activation energy of pertinent process
ε_a	Elastic misfit of solute ion
ε_0	Preexponential constant, possibly a function of temperature
γ_f	Stacking fault energy
k	Boltzman's constant
λ	Adjustable parameter
M	Density of dislocation sources
μ	Shear modulus
n'	Exponent - often equal to 2
ν	Freq. of vibration of dislocation segments
p, q	Constants which depend on barrier geometry and strength
ρ_m	Dislocation density, stress independent
σ	Differential stress
T	Absolute temperature
τ	Peierls stress (i.e. Lattice friction stress at absolute zero)
Ω	Molecular volume

can account for the creep behavior over a wide set of conditions, nor is there a simple correspondence between any of the self-diffusion coefficients and that of creep rate. Both single crystals and polycrystals typically have activation energies for creep that are larger than those for self-diffusion. Thus, the data suggest that self-diffusion is not the rate-limiting step [3] or that the jog concentration is undersaturated [32].

Unlike olivine, quartz has very low concentrations of intrinsic point defects at relevant temperatures. Thus, its plastic flow strength is influenced greatly by extrinsic defects [59]. The strength of natural quartzite rocks deformed with water present is intermediate between that of natural single crystals and synthetic single crystals [42] (Figure 4). At high temperatures, the stress and temperature sensitivity of strain rate are the same for both "wet" and "dry" experiments.

The kinetics of equilibration of extrinsic point defects are apparently quite slow, and the defect concentrations are quite low [59]. Differences in chemical environment and purity probably account for much of the scatter in strength measurements. In nature and in experiments, water-related defects may be introduced through cracking, a process which may be important for strain localization in shear zones [44].

Water may affect dislocation creep through changes in multiplication rates [40, 52] changes in subgrain boundary migration rates, or changes in climb recovery rates [59, 87]. Multiplication effects might explain the upper and lower yield points often observed in synthetic single crystals and natural polycrystals [40, 42, 52]. Prismatic dislocations are apparently generated during the relaxation of pressure in the tiny water clusters which are found in weak crystals. Two mechanisms for climb enhancement have been proposed; both assume changes in the dislocation core region and the general impurity level [59]. Water accelerates self-diffusion of oxygen in quartz [17], but its effect on silicon transport is unknown. If hydrolytic weakening involves local changes of the dislocation core, leading to accelerated kink migration, for example, then pipe diffusion rates may also be important [59].

5. PRESSURE SOLUTION

Field observations and microscopic examinations suggest that rocks at temperatures and pressures up to greenschist facies are deformed by solution transport [83]. An essential element of the process is that deformation occurs at grain or interphase boundaries, not in the grain interior. Such pressure-solution surfaces may be distributed throughout the rock on the scale of millimeters or meters. The former distribution, called intergranular pressure solution, results in a fitted grain fabric, while the latter results in widely spaced features of localized strain, called stylolites or solution seams.

5.1. Constitutive Equations

Although *Gibbs* [19] considered a solid in contact with fluid reservoirs of differing pressures, uncertainties remain in the complete thermodynamic description of a porous, fluid-filled solid, loaded nonhydrostatically. Two classes of

TABLE 3a. Power Law Creep Constants: Calcite Rocks

Rock Name	*log A* *($MPa^{-n}s^{-1}$)*	*n*	*Q* *($kJmol^{-1}$)*	Remarks	Source
Yule (T cyl.)	*-3.6*	*7.7*	*256*		*28,71*
Yule (l cyl.)	*-3.9*	*8.3*	*260*		"
Carrara	*3.1*	*7.6*	*418*	Creep Regime "2"; Dry	*78*
Carrara	*8.0*	*4.2*	*427*	Creep Regime "3"; Dry	*78*
Solnhofen	*3.4*	*4.7*	*298*	Flow regime "2"; Dry	*77*
Synthetic	*2.00**	*3.3*	*190*	Grain size dependent: Flow law includes a factor $d^{-1.3}$	*92*

TABLE 3b. Power Law Creep Constants: Quartz Rocks (Dry)

Rock Name	*log A* *$(MPa)^{-n}s^{-1}$*	*n*	Q *($kJmol^{-1}$)*	Remarks	Source
Simpson		11.0	377		*27*
"	-11.17	6.5	266		*56*
"	-10.10	5.7	243		*26*
Heavitree	-2.90	2.0	168	α–quartz;	*79*
	-4.5	1.9	123	α–quartz	*24*
			195	α–quartz; transient strains to 0.8%	*69*
			51	β-quartz; transient strains to 0.8%	69
Heavitree	-5.0	2.4	163	α–quartz; NaCl medium	*37*
"	-3.507	2.3	171	calcite medium	*37*
"	-5.463	2.8	184	NaCl medium; vacuum dried	*37*
Heavitree	-5.30	2.9	170		*43*
"	-5.398	4.0	300	vacuum dried	*43*
Simpson	-5.936	2.7	134	α -quartz; P_c=1.0-1.25	*42*

TABLE 3c. Power Law Creep Constants: Quartz Rocks (Wet)

Rock Name	*log A* *$(MPa)^{-n}s^{-1}$*	*n*	*Q* *($kJmol^{-1}$)*	Remarks	Source
Canyon Creek	-1.35	2.6	230		*56*
Simpson	-1.7	1.8	167	α-quartz; 0.4% water added	*24*
Heavitree	-5.66	2.7	120	α-quartz; 0.4% water added	*43*
Heavitree	-2.28	1.4	146	α-quartz; 0.28% water added	*37*
"	-2.54	1.8	151	0.39% water added	*37*
Simpson	-5.94	2.7	134	α-quartz; water from medium; P_c=1.0-1.25	*42*
Synthetic		2.3	148	hot-pressed from gel; β-quartz	*49*
"		4.0	152	" from silicic acid; β-quartz	*49*
Average	-7.18	3.1	135	Best est. based on gel precursor	*49*
Average	-9.40	4.0	135	Est. for silicic acid precursor; P_{H2O}=300 MPa	*49*

TABLE 3d. Power Law Creep Constants. Olivine Rocks

Rock Name	*log A* ($MPa^{-n}s^{-1}$)	*n*	Q ($kJmol^{-1}$)	Remarks	Source
Mt. Burnett (Dry)	*3.1*	*3.3*	*465*		*7*
Mt Burnett (Wet)	*-1.0*	*2.1*	*226*		*7*
Mt. Burnett (Dry)		*3.0*	*419*		*39*
Mt Burnett (Wet)	*2.5*	*5.1*	*392*		*65*
Collected Data (Dry)	*4.8*	*3.0*	*502*	Analysis of single and polycrystalline creep data	*20*
Anita Bay (Dry)	*4.5*	*3.6*	*535*		*9*
Anita Bay (Wet)	*4.0*	*3.4*	*444*		*9*
Aheim (Wet)	*2.6*	*4.5*	*498*		*9*
Synthetic (Dry)	*5.4*	*3.5*	*540*	Dry; Q from *9*	*38*
Synthetic (Wet)	*3.3*	*3*	*420*	Wet; Q from *9*	*38*

mechanisms have been suggested: enhanced solution-transport along a high-diffusivity boundary phase (Table 4), and undercutting of the contact [4]. For the enhanced transport mechanisms, two possible rate-limiting steps are dissolution [66] and diffusion [14, 72, 96]. Most workers assume quasistatic equilibrium, but *Lehner and Bataille* [46, 47] have used non-equilibrium thermodynamics.

The properties of the fluid-laden contact zone are critical for kinetics. Estimates of boundary diffusivity vary by five orders of magnitude, depending on whether the fluid is supposed to be a continuous film or an impurity on a semicoherent boundary [6]. Some theories require an adsorbed water layer capable of supporting normal stresses [14, 72, 96]. If such a layer exists, it may have thermodynamic properties different from bulk water. Supporting this supposition are measurements of nonzero wetting angles in quartz, olivine, [33, 45, 93] and calcite [25, 34]. *Raj* [66] postulates a hybrid, island/channel structure allowing rapid transport in the channels, but still providing mechanical support at the contact. All the transport models have two aspects in common. First, they are linear in driving force (either effective stress, σ_e, effective pressure, P_e, or the difference between effective pressure and the ratio of the interfacial energy, γ, divided by the radius of curvature of the interface, r). Secondly, strain rate is proportional to 1/d when deformation is limited by interface transport, or to $1/d^3$ when it is limited by boundary diffusion.

Less work has been done on undercutting mechanisms, but some experiments have examined undercutting involving brittle or plastic processes [62, 84].

5.2. Pressure Solution Experiments

Of the many experiments designed to explore pressure solution in the laboratory, the great majority have measured densification of powdered aggregates or porous, natural rocks, although some have measured dissolution rates of stressed single crystals or the shear strength of a nearly dense polycrystalline aggregate. The densification configuration is identical to liquid phase sintering and hot pressing [81].

Microstructural evidence for solution transfer is often very convincing [11, 91], but identifying the rate-controlling step can be problematic. Experiments on KCl [62] and NaCl [82] suggest that failure of contacts between grains may occur via dislocation flow. Other experiments with brine-saturated, NaCl aggregates at 35-45°C, indicate that densification rate is inversely proportional to grain size, suggesting interface control [66]. *Pharr and Ashby's* [62] undercutting model, derived from experiments on KCl and sucrose, differs from the transport models in several important respects, but also assumes a low wetting angle. The nature of the interface is clearly quite important: deformation occurs more quickly when dissimilar materials are pressed together than when grains of the same material are pressed[29].

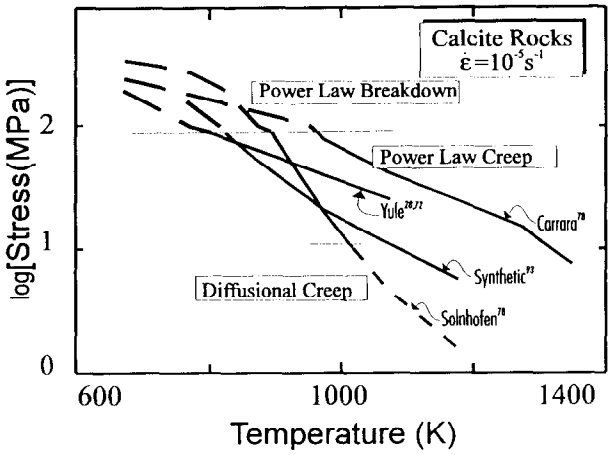

Fig. 3. Differential stress necessary to cause creep at a rate of 10^{-5} s^{-1} in several calcite rocks at various temperatures (see Table 3a for sources). The transition between power law creep and stress-activated, glide-controlled creep is the upper horizontal line (see Table 2). The transition to diffusional creep (lower horizontal line) has been observed for Solnhofen limestone.

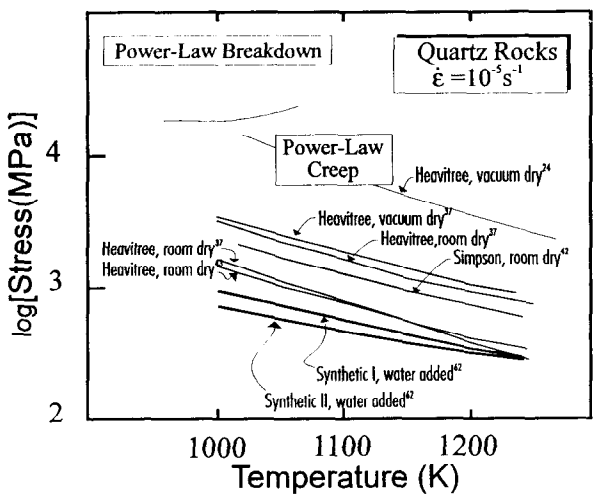

Fig. 4. Creep strengths for quartz rocks as a function of temperature at a strain rate of 10^{-5} s^{-1}. Rocks dried in vacuum prior to testing tend to be stronger than rocks tested under room "dry" conditions. Thicker lines show creep strengths for quartz rocks with added water. Equilibration is apparently very slow, leading to strengths which vary considerably, depending on the actual water concentration in the sample. No studies have definitively demonstrated diffusional flow in quartz-rich rocks.

6. BRITTLE-DUCTILE AND BRITTLE-PLASTIC TRANSITIONS

At the Earth's surface, most rocks fail by cataclastic mechanisms [48]. At greater depth, flow proceeds exclusively by plastic processes. The transition from brittle to plastic deformation occurs in two stages [16, 23]. The first, called the brittle-ductile transition, is a change in failure mode from localized to distributed failure. The second, brittle-plastic transition is a change from brittle cracking to plastic flow alone (Table 5) [73]. When brittle and plastic mechanisms occur simultaneously, deformation is called semibrittle.

The relative contribution of each mechanism is determined by mineral properties, phase chemistry, pore geometry, stress conditions, temperature, lithostatic pressure, fluid pressure, and chemical fugacities. Failure mode is determined by the above, the mechanical characteristics of the loading system, and the geometry of the load-bearing member. Localized failure is possible with plastic flow or brittle cracking, acting alone or in combination.

For conventional triaxial loading of rocks in the gas medium apparatus, the pressure of the brittle-ductile transition is predicted empirically by the intersection of the Mohr-Coulomb criterion with Byerlee's friction law [48]

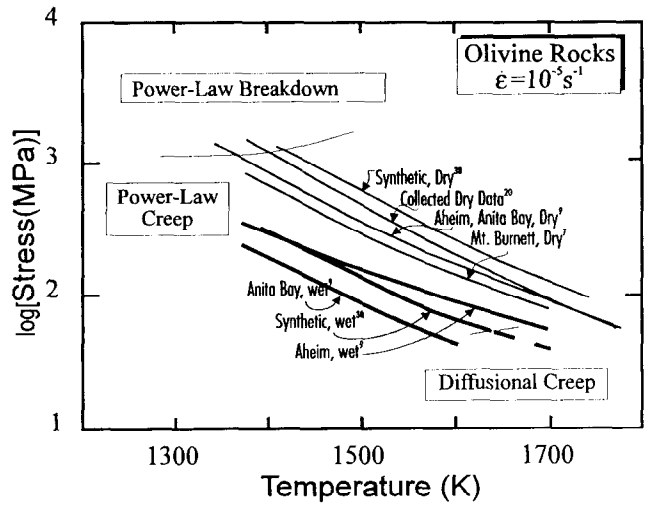

Fig. 5. Differential stresses necessary to cause creep at 10^{-5} s^{-1} in olivine rocks in the interval 1350-1750°C; f_{O_2} is buffered by the iron jackets at Fe-FeO. The presence of water causes a reduction in flow strength by a factor of about 2-5. Breakdown of the power-law relation occurs at about 500-1000 MPa.

TABLE 4. Interface Transport Models for Pressure Solution

Rate-Limiting Mechanism	Deviatoric Volumetric	Constitutive Law	Remarks	Ref.
Grain Boundary Diffusion	Deviatoric	$\dot{\varepsilon} = \frac{32\Omega\, C_o D_b \delta}{RT\rho_s}\frac{\sigma}{d^3}$	Grain boundary (gb) diffusion rate-limiting. Diffusion in pore space rapid. Pore fluid.	*14, 72*
Grain Boundary Diffusion	Deviatoric	$\dot{\varepsilon}_e = 2.3\frac{\Omega C_o \alpha}{(1-x)\eta}\frac{\sigma_e}{d^3}$	Cubic Packing Constant Volume No increase in internal energy	*66*
Interface Reaction	Deviatoric	$\dot{\varepsilon}_e = \frac{\Omega k_1' C_o}{(1-x)kT}\frac{\sigma_e}{d}$	Cubic packing Constant Volume Dissolution and precipitation rate-controlling and equal	*66*
Grain Boundary Diffusion	Volumetric	$\dot{\beta}_e = 6.9\frac{C_o \alpha}{\eta}\frac{\left(\frac{P_e}{(1-x)} - \frac{\gamma}{r}\Omega\right)}{d^3}$	Density of aggregate$\propto 1/r^2$ Diss. and precip. fast; gb diff. rate-controlling	*66*
Interface	Volumetric	$\dot{\beta}_e = \frac{3\, k_1' C_o}{kT}\frac{\left(\frac{P_e}{(1-x)} - \frac{\gamma}{r}\Omega\right)}{d}$	Cubic packing Solution nearly inviscid	*66*
Fluid Phase Boundary Diffusion	Volumetric	$\dot{\beta}_e = \frac{Z\Omega\, C_{gbf}(1-C_{gbf}) D_b \delta \rho_f}{kT\, V_{sf}\rho_s}\frac{(1-\beta_e)}{(\beta_\varepsilon)^n}\frac{P_e}{d^3}$	Fluid phase along boundary; n =2 for spherical grains, 4 for cubic grains	*80*
Grain Boundary Diffusion Island Model	Both	$\left[\rho_{agg}\left(w_n - v_n\right)\right] = -\frac{8\rho_f M_1 C_o D_{gb}}{RT\rho_s}\frac{\left(\overline{\sigma}_n + P_f\right)}{a^2}$	Rate of diss. along circular contact, radius a. Assumes that diss. rate is constant along the contact	*46*
Fluid Diffusion	Deviatoric	$\dot{\varepsilon}_1 = \frac{\Omega C_o D_f \Phi^{m_d}}{RT}\frac{\left\{(\sigma_3 - P_f) + 3(\sigma_1 - \sigma_3)\right\}}{d^2}$	Diff. in pore fluid rate-limiting. Effective bulk diff. in porous solid derived using Archie's law	*61*
Source/Sink Reaction	Deviatoric	$\dot{\varepsilon}_1 = \frac{\Omega^2 k'}{RT}\frac{\delta}{d_i}\frac{\left\{(\sigma_3 - P_f) + 3(\sigma_1 - \sigma_3)\right\}}{d}$	Reaction at solid-liquid interface rate-limiting. Island/channel boundary model assumed.	*61*
Source/Sink Diffusion	Deviatoric	$\dot{\varepsilon}_1 = \frac{\Omega}{RT}\frac{\delta D_{gb}}{d_i^2}\frac{\left\{(\sigma_3 - P_f) + 3(\sigma_1 - \sigma_3)\right\}}{d}$	Diffusion along grain contact rate-limiting. Island/channel model assumed.	*61*

Symbols used in Table 4	
a	Typical dimension of the grain-grain contact.
α	Product of area fraction of solid islands in contact and step height, divided by a lattice dimension: numerically.of order 1.
β_e, $\dot{\beta}_\varepsilon$	Equivalent volumetric strain and strain rate.
C_{gbf}	Solute concentration in boundary fluid of loaded interface.
C_o	Concentration of solute in contact with unstressed planar surface.
d	Grain size
δ	Width of the grain boundary.
d_i	Width of the island in the island-channel model
D_f	Diffusion coefficient of the solute in the fluid
D_b	Grain boundary diffusion coefficient.
$\dot{\varepsilon}_e$	Deviatoric strain rate.
$\dot{\varepsilon}_1$	Rate of change of greatest principal strain
γ	Specific surface energy of solid/liquid boundary
η	Viscosity of fluid.
$k_l' C_o$	Lineal growth rate of crystal in a solution with concentration C_o.
k'	Solution or precipitation rate constant in mol m^{-2} s^{-1}
m_{al}	Archie's law exponent relating porosity and electrical resistivity.
P_e	Applied lithostatic pressure, P_l, minus pore fluid pressure, P_f
ρ_s, ρ_f, ρ_{agg}	Density of the solid, fluid, and aggregate, respectively.
r	Curvature of the solid-liquid interface.
R, k	Gas constant and Boltzmann's constant.
σ	Applied differential stress, $\sigma_1 - \sigma_3$.
σ_e,	Equivalent stress, $\sigma_e = \{\frac{1}{2}[(\sigma_1-\sigma_2)^2+(\sigma_2-\sigma_3)^2+(\sigma_3-\sigma_1)^2]\}^{1/2}$
$\bar{\sigma}_n$	Effective normal stress on the grain boundary region
T	Absolute temperature.
v_n	Component of barycentric velocity normal to interface
V_s	Volume fraction of the island-channel region occupied by solid .
w_n	Speed of the interface along its normal.
x	Area fraction of the boundary actually bearing the load.
Z	Numerical constant = $216\sqrt{2}/\pi$
Ω	Molar volume of the solid.

(Figure 6). Abnormally high fluid pressure gradients or the presence of partial melts can induce semibrittle or completely brittle behavior, even at high temperatures or low strain rates.

The brittle-plastic transition is bounded in differential stress-pressure space by the criterion

$$\sigma_1 - \sigma_3 = P, \tag{16}$$

suggested by *C. Goetze* on the basis of *Edmond and Paterson's* data [13]. At pressures greater than the strength, deformation proceeds without cracking. Under those conditions, the relaxed von Mises criterion is satisfied. Semibrittle behavior occurs at lower pressures (for fixed temperature and strain rate), or at lower temperature (for fixed pressure and strain rate). Using (16), even with the current limited data, failure mode maps

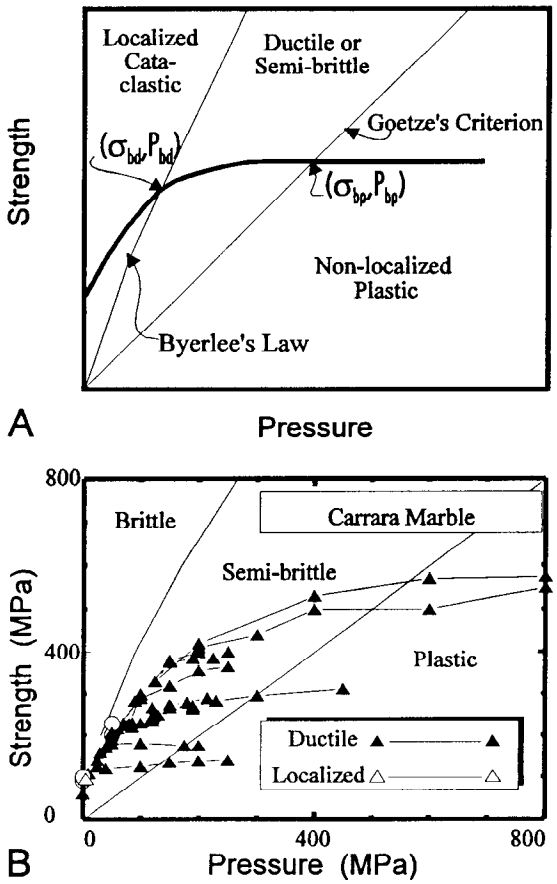

Fig. 6*a*. Schematic trend of strength versus pressure for a rock undergoing the brittle-plastic transition. Nonlocalized plastic flow occurs when the differential stress is less than the pressure. Nonlocalized brittle fracture occurs when the strength is greater than the pressure, but less than the strength to cause frictional sliding.

Fig. 6*b*. Similar curves based on data for Carrara marble deformed at a variety of strain rates and temperatures.

TABLE 5. Phenomenology of Brittle-Ductile Transition in Intact Rocks [16]

Failure Mode	<----------Localized----------> <----------Ductile---------->
Mechanism Class	<----------Brittle----------><-------- SemiBrittle-------- >< ---------- Plastic ---------- >
Strain to Failure	<----------<3%----------><---------- >3%---------- >< ---------- >5% ---------- >
Work Softening	<---------- ---------->
Stress Drops	<---------- ---------->
Loss in Cohesion	<---------- ---------->
Microcracking	<---------- ---------- ---------- ---------->
Dilatancy	<---------- ---------- ---------- ---------->
Acoustic Emission	<---------- ---------- ---------- ---------->
Press. Dep. Strength	<---------- ---------- ---------- ---------->
Temp. Dep. Strength	<---------- low ---------- ----------><---------- high ---------- ---------->
Deformation Mech.	Distributed and Localized Microcracking / Distributed Microcracking Local Plasticity / Fully Plastic
Macroscopic Appearance	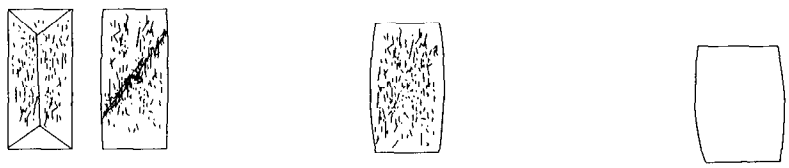

can be constructed in differential stress - pressure space or in pressure-temperature space.

In calcite and halite at elevated pressure, fully plastic flow is possible even at room temperature [16]. In contrast, feldspathic rocks deform by localized brittle fracture or distributed cataclasis at all pressures, for temperatures below 750°C [30, 86, 88]. High temperatures are also necessary for plastic flow in quartzites [89] and peridotites, but those rocks do not show a distributed cataclastic flow regime as do feldspar rocks.

6.1. Mechanics of Brittle-Ductile Transition

From a continuum mechanics point of view, localization in a pressure sensitive, dilatant material under axisymmetric loading is determined by three parameters [70]: an internal friction coefficient μ, a dilatancy factor β, and a hardening coefficient h. The normalized critical hardening modulus, h_{cr}, for the inception of strain localization is

$$\frac{h_{cr}}{g} = \frac{1+\nu}{9(1-\nu)}(\beta-\mu)^2 - \frac{1+\nu}{2}\left(N+\frac{\beta+\mu}{3}\right)^2, \qquad (17)$$

where g is the shear modulus, ν is Poisson's ratio, and N is $1/\sqrt{3}$ for axisymmetric compression. For most stress states, the model predicts negative h_{cr} for shear band formation, both for a yield vertex model and for isotropic hardening. With increasing confining pressure and decreasing dilatancy factor, h_{cr} is predicted to increase. Experiments on a variety of rocks agree with the mechanical analyses, except that the hardening modulus critical for incipient localization is predicted to be overly negative as compared with the experimental values.

During cataclastic failure of rocks in compression, dilatant microcracks nucleate, grow, and coalesce [48]. For dilatant wing cracks growing from an inclined preexisting flaw, fracture mechanics models [55, 75] indicate that strain hardening occurs until the dilatant cracks interact elastically; at which point strain softening and localization occur. Although rigorous tests of the fracture mechanics models do not exist, the theories do provide rational explanations for several observations, including, for example, dependence of fracture strength on the inverse of the square root of grain size. The models do not explain the empirical observation that the friction law bounds the brittle-ductile transition, unless fracture toughness and plastic flow strength scale with each other.

6.2. Mechanics of Semibrittle Deformation

Plastic flow mechanisms and brittle cracking can interact in a variety of ways. Cracks may be nucleated at dislocation pileups [97], intersecting twins, rigid second phases, or incoherent boundaries. Cavities may form during creep at sliding grain boundaries. Cracks may grow

or blunt by creep processes [54, 68]. Based on tensile failure experiments several broad classes of fracture mechanisms can be defined [2] depending on the partitioning of strain into rate independent plasticity, creep, and fracture processes: cleavage, intergranular brittle fracture, plastic void growth, and plastic rupture are low-temperature processes; intergranular creep fracture, creep void growth; and creep rupture are high-temperature processes.

As with brittle fracture, semibrittle deformation may be treated by prescribing a nucleation criterion and predicting growth to failure according to a separate failure criterion, often involving a critical damage state. Then, contours of time or strain to failure may be plotted in differential stress-temperature space. Most work has concentrated on tensile loading, but some attention has been paid to compressive, multiaxial loading [1, 55, 75]. In much the same way that confining pressure stabilizes the propagation of brittle wing cracks, an analysis of the Stroh crack mechanism [97] shows that cracks nucleated by dislocation pileups propagate to a length which scales with the number of dislocations in the pileup, and with the difference between the resolved applied stress and the Peierls stress.

Despite progress in understanding semibrittle failure, a satisfactory constitutive law does not exist. Because of the potential complexity of mixed deformation mechanisms, it is naive to expect one theory to represent semibrittle deformation over a range of conditions. In the same way that deformation maps are necessary to represent plastic flow, multimechanism maps will surely be needed to describe semibrittle deformation.

Acknowledgments: Funding for this work was provided by NSF Geosciences Division by grants EAR9118969 (BE), EAR901823 (DLK), and OCE920041 (DLK). We thank the editor and the reviewer for comments and forbearance, and apologize to the authors of many excellent papers which could not be cited, owing to space restrictions.

REFERENCES

1. Ashby, M. F., J. D. Embury, S. H. Cooksley, and D. Teirlinck, Fracture maps with pressure as a variable, *Scripta Metall. 19*, 385-390, 1985.
2. Ashby, M. F., C. Ghandi, and D. M. R. Taplin, Fracture mechanism maps and their construction for fcc metals and alloys, *Acta Metal. 27*, 699, 1979.
3. Bai, Q., S. J. Mackwell, and D. L. Kohlstedt, High-temperature creep of olivine single crystals: 1: Mechanical results for buffered samples, *J. Geophys. Res., 96*, 2441-2464, 1991.
4. Bathurst, R. G. C., Diagenetic fabrics in some British Dinantian limestones, *Liverpool Manchester Geol. J., 2*, 11-36, 1958.
5. Boullier, A.M. and Gueguen, Y., Origin of some mylonites by super plastic flow, *Contrib. Mineral. Petrol. 50*, 93-104 1975.
6. Brady, J. B., Intragranular diffusion in metamorphic rocks, *Amer. J. Sci., 283-A*, 540-88, 1983.
7. Carter, N. L., and H. G. AveLallemant, High temperature flow of dunite and peridotite, *Geol. Soc Am. Bull., 81*, 2181-2202, 1970.
8. Carter, N. L., and M. C. Tsenn, Flow properties of continental lithosphere, *Tectonophysics, 136*, 27-63, 1987.
9. Chopra, and M. S. Paterson, The experimental deformation of dunite, *Tectonophysics, 78*, 453-473, 1981.
10. Cooper, R. F., and D. L. Kohlstedt, Rheology and structure of olivine-basalt partial melts, *J. Geophys. Res., 91*, 9315-9323, 1986.
11. DeBoer, R. B., P. J. C. Nategaal, and E. M., Duyvis, Pressure solution experiments on quartz sand, *Geochimica Cosmochim. Acta, 41*, 257-64, 1977.
12. DeBresser, J. H. P., and C. J. Spiers, High-temperature deformation of calcite single crystals by r^+ and f^+ slip, in, *Deformation Mechanisms, Rheology and Tectonics, Geol. So. Spec. Publ. No. 54*, edited by R. J. Knipe, and E. H. Rutter, pp. 285-298, Geol. Soc. London, UK., 1990.
13. Edmond, J. M., and M. S. Paterson, Volume changes during the deformation of rocks at high pressures, *Int. J. Rock Mech. Min. Sci. Geomech. Abstr., 9*, 161-182, 1972.
14. Elliot, D., Diffusion flow law in metamorphic rocks, *Geol. Soc. Amer. Bull., 84*, 2645-2664, 1973.
15. Evans, B., and G. Dresen, Deformation of earth materials: Six easy pieces, *Reviews of Geophysics, Supplement*, 823-843, 1991.
16. Evans, B., Fredrich, J. T., and Wong, T.-f., The brittle to ductile transition in rocks: Recent experimental and theoretical progress, in *The Brittle-Ductile Transition - The Heard Volume, Geophys. Monogr. Ser.* vol 56, edited by A. G. Duba, W. B. Durham, J. W. Handin, H. F. Wang, pp. 1-20, AGU, Washington, D. C., 1990.
17. Farver, J. R., and R. A. Yund, Measurement of oxygen grain boundary diffusion in natural fine-grained quartz aggregates, *Geochim. Cosmochim. Acta, 55*, 1597-1607, 1991.
18. Frost, H. J., and M. F. Ashby, *Deformation-mechanism Maps*, Pergamon Press, Oxford, Great Britain, 166 pp., 1982.
19. Gibbs, J. W., On the equilibrium of heterogeneous systems, *Trans. Conn. Acad.*, Vol. III, 108-248, 1876.
20. Goetze, C., The mechanisms of creep in olivine, *Phil. Trans. R. Soc. London, A288*, 59-119,1978.
21. Green, H. W., II, Rheological implications of the dissolution of

volatiles in mantle olivine, *Phys. Earth Planet. Inter., 51*, 123-124, 1988.
22. Green, H. W., II, and R. S. Borch, A new molten salt cell for precise stress measurement at high pressure, *Eur. J. Mineral., 1*, 213-219, 1989.
23. Griggs, D. and J. Handin, Observations on fracture and a hypothesis of earthquakes, in *Rock Deformation, Mem. 79*, edited by D. Griggs and J. Handin, pp. 347-364, Geo. Soc. Am., N.Y. 1960.
24. Hansen, F. D. and N. L., Carter, Creep of selected crustal rocks at 1000 MPa, *EOS, Trans. Am. Geophys. Soc., 63*, 437, 1982.
25. Hay, R. S., and B. Evans, Intergranular distribution of pore fluid and the nature of high-angle grain boundaries in limestone and marble, *J. Geophys. Res., 93*, 8959-8974, 1988.
26. Heard, H. C., Comparisons of the flow properties of rocks at crustal conditions, *Philos. Trans. R. Soc. Lond, Ser. A*, 283, 173-186, 1976.
27. Heard, H. C. and N. L. Carter, Experimentally induced "natural" intergranular flow in quartz and quartzite, *Am. J. Sci., 266*, 1-42, 1968.
28. Heard, H. C. and, C. B. Raleigh, Steady-state flow in marble at 500-800°C, *Geol. Soc. Am. Bull. 83*, 935-956, 1972.
29. Hickman, S. H., and B. Evans, Experimental Pressure Solution in Halite, 1: The effect of grain/interphase boundary structure, *J. Geological Soc. London, 148*, 549-560, 1991.
30. Hirth, G., and J. Tullis, The effects of pressure and porosity on the micromechanics of the brittle-ductile transition in quartzite, *J. Geophys. Res., 94*, 17825-17838, 1989.
31. Hobbs, B. E., The influence of metamorphic environment upon the deformation of minerals, *Tectonophysics, 78*, 335-383, 1981.
32. Hobbs, B. E., Constraints on the mechanism of deformation of olivine imposed by defect chemistry, *Tectonophysics, 92*, 35-69, 1983.
33. Holness, M. B., Equilibrium dihedral angles in the system quartz-CO_2-H_2O-NaCl at 800°C and 1-15 kbar: the effects of pressure and fluid composition on the permeability of quartzite, *Earth Planet. Sci. Let., 114*, 171-184, 1992.
34. Holness, M. B., and C. M. Graham, Equilibrium dihedral angles in the system CO_2-H_2O-NaCl-calcite, and implications for fluid flow during metamorphism, *Contrib. Mineral. Petrol., 108*, 368-383, 1991.
35. Houlier, B., M. Cheraghmakani, and O. Jaoul, Silicon diffusion in San Carlos olivine, *Phys. Earth Planet. Inter., 62*, 329-340, 1991.
36. Houlier, B., O. Jaoul, F. Abel, and R. C. Liebermann, Oxygen and silicon self-diffusion in natural olivine at T= 1300°C., *Phys. Earth Planet. Inter., 50*, 240-250, 1988.
37. Jaoul, O., J. Tullis, and A. Kronenberg, The effect of varying water contents on the creep behavior of Heavitree quartzite, *J. Geophys. Res., 89*, 4297-4312, 1984.
38. Karato, S.-I., M. S. Paterson, and J. D. FitzGerald, Rheology of synthetic olivine aggregates: Influence of grain size and water, *J. Geophys. Res., 91*, 8151-8176, 1986.
39. Kirby, S. H., and C. B. Raleigh, Mechanisms of high-temperature, solid-state flow in minerals and ceramics and their bearing on the creep behavior of the mantle, *Tectonophysics, 19*, 165-194, 1973.
40. Kirby, S. H., and J. W. McCormick, Creep of hydrolytically weakened synthetic quartz crystals oriented to promote {2110} <001> slip: A brief summary of work to date, *Bull. Mineral., 102*, 124-137, 1979.
41. Kirby, S. H., and A. K. Kronenberg, Rheology of the lithosphere: Selected topics, *Rev. Geophys., 25*, 1219-1244, 1987.
42. Koch, P. S., J. M. Christie, A. Ord, and R. P. George Jr., Effect of water on the rheology of experimentally deformed quartzite, *J. Geophys. Res., 94*, 13975-13,996, 1989.
43. Kronenberg, A., and J. Tullis, Flow strengths of quartz aggregates: Grain size and pressure effects due to hydrolytic weakening, *J. Geophys. Res., 89*, 4281-4297, 1984.
44. Kronenberg, A. K., S. H. Kirby, R. D. Aines, and G. R. Rossman, Solubility and diffusional uptake of hydrogen in quartz at high water pressures: Implications for hydrolytic weakening, *J. Geophys. Res., 91*, 12,723-12,744, 1986.
45. Lee, V. W., S. J. Mackwell, and S. L. Brantley, The effect of fluid chemistry on wetting textures in Novaculite, *J. Geophys. Res., 96*, 10,023-10,037, 1991.
46. Lehner, F. K., Thermodynamics of rock deformation by pressure solution, in *Deformation Process in Minerals, Ceramics and Rocks*, edited by D. J. Barber and P. G. Meredith, pp. 296-333, Unwin-Hyman, Boston, 1990.
47. Lehner, F. K., and J. Bataille, Non equilibrium thermodynamics of pressure solution, *Pure Appl. Geophys., 122*, 53-85, 1985.
48. Lockner, D. A., Rock failure, in this volume, 1994.
49. Luan F.-c. and M. S. Paterson, Preparation and deformation of synthetic aggregates of quartz, *J. Geophys. Res., 97*, 301-344, 1992.
50. Mackwell, S. J., and D. L. Kohlstedt, Diffusion of hydrogen in olivine: Implications for water in the mantle, *J. Geophys. Res., 95*, 5079-5088, 1990.
51. Mackwell, S. J., D. Dimos, and D. L. Kohlstedt, Transient creep of olivine: Point-defect relaxation times, *Philos. Mag., 57*, 779-789, 1988.
52. McLaren, A. C., J. D. Fitz Gerald, and J. Gerretsen, Dislocation nucleation and multiplication in synthetic quartz: Relevance to water weakening, *Phys. Chem. Minerals, 16*, 465-482, 1989.
53. Nakamura, A., and H. Schmalzried, On the nonstoichiometry and point defects of olivine, *Phys. Chem. Miner., 10*, 27-37, 1983.
54. Needleman, A. and J. R. Rice, Plastic creep flow effects in the diffusive cavitation of grain boundaries, *Acta Metall., 28*, 1315-1332, 1980.
55. Nemat-Nasser, S., and H. Horii, Compression-induced non planar crack extension with application to

splitting, exfoliation, and rock burst, *J. Geophys. Res., 87*, 6805-6822, 1982.
56. Parrish, D. K., A. L. Krivz, and N. L. Carter, Finite element folds of similar geometry, *Tectonophysics, 32*, 183-207, 1976.
57. Paterson, M. S., The ductility of rocks, in *Physics of Strength and Plasticity*, edited by A. S. Argon, pp. 199-208, MIT Press, Cambridge, MA, 1969.
58. Paterson, M. S., Problems in the extrapolation of laboratory rheological data, *Tectonophysics, 133*, 33-43, 1987.
59. Paterson, M. S., Interaction of water with quartz and its influence in dislocation flow: An overview, in *Rheology of Solids and of the Earth*, edited by S.-i. Karato, and M. Toriumi, pp. 107-142, Oxford University Press, 1989.
60. Paterson, M. S., Rock deformation experimentation, in *The Brittle-Ductile Transition in Rocks, The Heard Volume, Geophys. Monogr. Ser.*, vol. 56, edited by A. G. Duba et al., pp. 187-194, AGU, Washington, 1990.
61. Paterson, M. S., A theory for granular flow accommodated by material transfer via an intergranular fluid, *Tectonophysics,* in press, 1994.
62. Pharr, G. M., and M. F. Ashby, On creep enhanced by a liquid phase, *Acta. metall., 31*, 129-138, 1983.
63. Poirier, J.-P., *Creep of crystals: High-temperature deformation processes in metal, ceramics and minerals,* Cambridge University Press, Cambridge, 260 pp. 1985.
64. Poirier, J.-P., Plastic rheology of crystals, companion volume 2, 1994.
65. Post, R. L. Jr., High-temperature creep of Mt. Burnet dunite, *Tectonophysics, 42*, 75-110, 1977.
66. Raj, R., Creep in polycrystalline aggregates by matter transport through a liquid phase, *J. Geophys. Res., 87*, 4731-4739, 1982.
67. Ranalli, G., *Rheology of the Earth*, Allen & Unwin, Boston, MA, pp. 235-317, 1986.
68. Rice, James R., Creep cavitation of grain interfaces, in *Three-dimensional constitutive relations and ductile fracture*, edited by S. Nemat-Nasser, pp. 173-184, North-Holland Publishing, 1981.
69. Ross, J. V., S. J. Bauer, and N. L. Carter, Effect of the α-β quartz transition on the creep properties of quartzite and granite, *Geophys. Res. Letters, 10,* 1129-1132, 1983.
70. Rudnicki, J. W., and J. R. Rice, Conditions for the localization of deformation in pressure-sensitive dilatant materials, *J. Mech. Phys. Solids, 23*, 371-394, 1975.
71. Rutter, E. H., The influence of temperature, strain-rate and interstitial water in the experimental deformation of calcite rocks, *Tectonophysics, 31*, T21-T28, 1974.
72. Rutter, E. H., The kinetics of rock deformation by pressure solution, *Phil. Trans. R. Soc. Lond.*, A, *283*, 203-219, 1976.
73. Rutter, E. H., On the nomenclature of mode of failure transitions in rocks, *Tectonophysics, 122*, 381-387, 1986.
74. Ryerson, F. J., W. B. Durham, D. J. Cherniak, and W. A. Lanford, Oxygen diffusion in olivine: Effect of oxygen fugacity and implications for creep, *J. Geophys. Res., 94*, 4105-4118, 1989.
75. Sammis, C. G., and M. F. Ashby, The failure of brittle porous solids under compressive stress states, *Acta Metall., 34*, 511-526, 1986.
76. Schmalzried, H., *Solid State Reactions, Mongr. Modern Chem. Ser.*, vol. 12, 254 pp., Academic Press, NY, 1981.
77. Schmid, S., J. N. Boland, and M. S. Paterson, Superplastic flow in finegrained limestone, *Tectonophysics, 43*, 257-291, 1977.
78. Schmid, S. M., M. S. Paterson and J. N. Boland, High-temperature flow and dynamic recrystallization in Carrara marble, *Tectonophysics, 65*, 245-280, 1980.
79. Shelton, G. L., Experimental deformation of single phase and polyphase crustal rocks at high pressures and temperatures, Ph.D. Diss., Brown Univ. Providence, R. I., 146 pp., 1981.
80. Spiers, C. J., and P. M. T. M. Schutjens, Densification of crystalline aggregates by fluid-phase diffusional creep, in *Deformation Processes in Minerals, Ceramics and Rocks*, edited by D. J. Barber and P. G. Meredith, pp. 334-353, Unwin-Hyman, Boston, 1990.
81. Swinkels, F. B., and M. F. Ashby, A second report on sintering diagrams, *Acta. metall., 29*, 259-281, 1981.
82. Tada, R., and R. Siever, Experimental knife-edge pressure solution of halite, *Geochim. Cosmochim. Acta, 50*, 29-36, 1986.
83. Tada, R., and R. Siever, Pressure solution during diagenesis: A review, *Ann. Rev. Earth Planet. Sci., 17*, 89-118, 1989.
84. Tada, R., R. Maliva, and R. Siever, A new mechanism for pressure solution in porous quartzose sandstone, *Geochim. Cosmochim. Acta, 51*, 2295-2301, 1987.
85. Takeuchi, S. and A. S. Argon, Review: Steady state creep of single-phase crystalline matter of high-temperatures., *J. Mater. Sci., 11*, 1542-1566, 1976.
86. Tullis, J., Experimental studies of deformation mechanisms and microstructures in quartzo-feldspathic rocks, in *Deformation Processes in Minerals, Ceramics, and Rocks*, edited by D. Barber and P. Meredith, pp. 190-227, Unwin and Hyman, Cambridge, 1990.
87. Tullis, J., and R. A. Yund, Hydrolytic weakening of experimentally deformed Westerly granite and Hale albite rock, *J. Struc. Geol., 2*, 439-451, 1980.
88. Tullis, J., and R. A. Yund, Transition from cataclastic flow to dislocation creep of feldspar: Mechanisms and microstructures, *Geology, 15*, 606-609, 1987.
89. Tullis, J., and R. A. Yund, The Brittle-ductile transition in feldspar aggregates: An experimental study, in *Fault Mechanics and Transport Properties of Rocks: A Festchrift for W. F. Brace*, edited by B. Evans and T.-f. Wong, pp. 89-118, Academic Press, London, U.K., 1992.
90. Tullis, T. E., and J. Tullis, Experimental rock deformation

techniques, in *Mineral and Rock Deformation: Laboratory Studies, The Paterson Volume, Geophys. Monogr. Ser.*, vol. 36., edited by B. E. Hobbs and H. C. Heard, pp. 297-324, AGU, Washington, D. C., 1986.

91. Urai, J. L., C. J. Spiers, H. J. Zwart, and G. S. Lister, Weakening of rock salt by water during long-term creep, *Nature*, 324, 554-557, 1986.
92. Walker, A. N., E. H. Rutter, and K. H. Brodie, Experimental study of grain-size sensitive flow of synthetic, hot-pressed calcite rocks, in *Deformation Mechanisms, Rheology and Tectonics, Geo. Soc. Spec, Pub. 54*, pp. 259-284, 1990.
93. Watson, E. B., and J. M. Brenan, Fluids in the lithosphere, part 1: Experimentally-determined wetting characteristics of CO_2-H_2O fluids and their implications for fluid transport, host-rock physical properties, and fluid inclusion formation, submitted to *Earth and Planetary Sci. Lett.*, *85*, 497-515, 1987.
94. Weertman, J., Steady-state creep of crystals, *J. Appl. Phys.*, *28*, 1185-1189, 1957.
95. Weertman, J., Dislocation climb theory of steady-state creep, *Trans. Am. Soc. Metal.*, *61*, 681-694, 1968.
96. Weyl, P. K., Pressure solution and the force of crystallization - a phenomenological theory, *J. Geophys. Res.*, *64*, 2001-2025, 1959.
97. Wong, T.-f., A note on the propagation behavior of a crack nucleated by a dislocation pile-up, *J Geophys. Res.*, *95*, 8639-8646, 1990.

Phase Equilibria of Common Rocks in the Crust and Mantle

Claude Herzberg

1. INTRODUCTION

Phase diagrams have played a fundamental role in understanding the origins of the common rocks that make up the Earth, and much of this progress has been made since the previous handbook was published in 1966 [12]. The purpose of this chapter is to acquaint the reader with some of the phase equilibria that have been published over the last 20 to 30 years, and some of the more important geological conclusions that have been drawn.

The large number of phase diagrams that have been published during this time interval arise from the chemical complexity of the Earth. But a complete description of this massive data base is beyond the scope of this chapter, and readers interested in a comprehensive bibliography are referred to the many excellent summaries in text and reference books [e.g., 7, 61]. As a means of condensing this information, preferential consideration is given to those phase equilibria that bear most directly on origin of common rocks in the crust and mantle. Readers interested in the melting and solid solution properties of individual crystalline phases that make up rocks are referred to Presnall (this volume).

Peridotite is an important component of the mantle, but a phase equilibrium control to its geochemistry remains controversial. Tholeiitic basalt is the major rock type that makes up the oceanic crust, and its origin by the partial melting of mantle peridotite is now well established. Basalt is also abundant at convergent lithospheric plate boundaries, and occurs together with other rocks of the calc-alkaline suite, typically high alumina basalt, andesite, and dacite; a role for H_2O is therefore indicated, and its effect on the phase relations is summarized. Another important volatile species in the Earth is CO_2, and its contribution to the generation of silica-deficient igneous rocks is also briefly reviewed. Granites are a major constituent of the continental crust, and a partial melting origin of preexisting crustal rocks is now generally accepted.

C. Herzberg, Rutgers University, Department of Geological Sciences, New Brunswick, NJ 08903

Rock Physics and Phase Relations
A Handbook of Physical Constants
AGU Reference Shelf 3

2. PERIDOTITE

Olivine, orthopyroxene, and clinopyroxene usually make up 94 to 99 % of the mineralogy of a peridotite, but they exhibit a chemical variability that ranges from samples that are fertile to samples that are depleted in basaltic components (Figure 1). The remaining 1 to 6 % of an anhydrous mineralogy consists of plagioclase, spinel, or garnet, depending on the temperature and pressure of equilibration. The boundaries amongst the plagioclase-, spinel-, and garnet-peridotite stability fields are given in Figure 2 for the analogue system CaO-MgO-Al_2O_3-SiO_2 [23, 34, 93]. The considerable amount of Al_2O_3 that can be dissolved into orthopyroxene (Figure 2) and clinopyroxene at high temperatures can give rise to spinel-free and garnet-free peridotite assemblages [ie., Ol + Opx + Cpx; Figure 3; Table 1; 27]. The effects of Na_2O and Cr_2O_3 are to expand to higher pressures the stability fields of plagioclase peridotite and spinel peridotite, respectively.

A great deal of experimental work has been done on a naturally-occurring peridotite sample KLB-1 [35, 84, 98], and the results are shown in Figure 3. It contains about 39 % MgO, 3 % CaO, and 3.5 % Al_2O_3, a composition intermediate between fertile and average mantle peridotite (Figure 1).

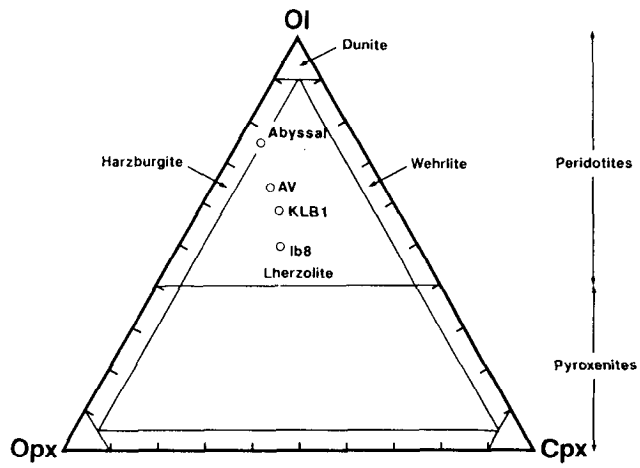

Fig. 1. Classification of ultramafic rocks [39] and compositions of various mantle peridotites. Data sources: fertile mantle peridotite Ib8 [82; similar to pyrolite]; KLB1 [84]; AV = average mantle peridotite [33; 668 samples]; Abyssal peridotite [15; 273 samples].

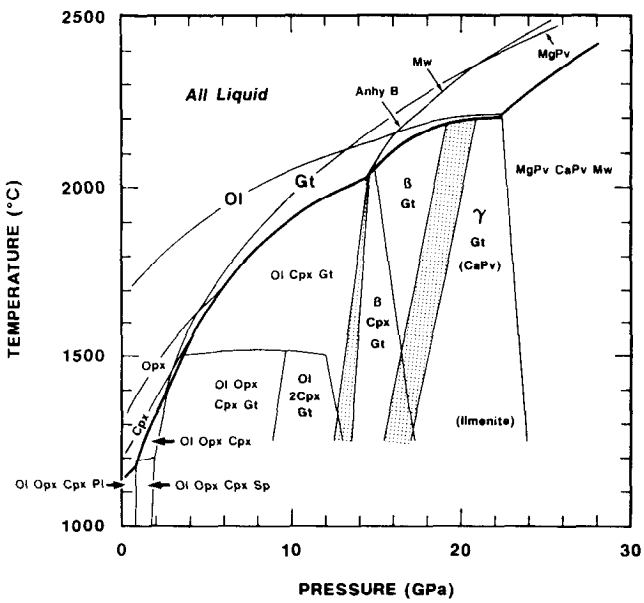

Fig. 3. Phase diagram for anhydrous mantle peridotite similar in composition to KLB1; compilation is from many sources [4, 24, 27, 35, 40, 41, 46, 84, 98]. Stability fields of phases in parentheses (CaPv) and (Ilmenite) are poorly known. Shaded regions contain coexisting (Ol + ß) and (ß + γ) estimated by Katsura and Ito [46], but are too wide at the solidus [98].

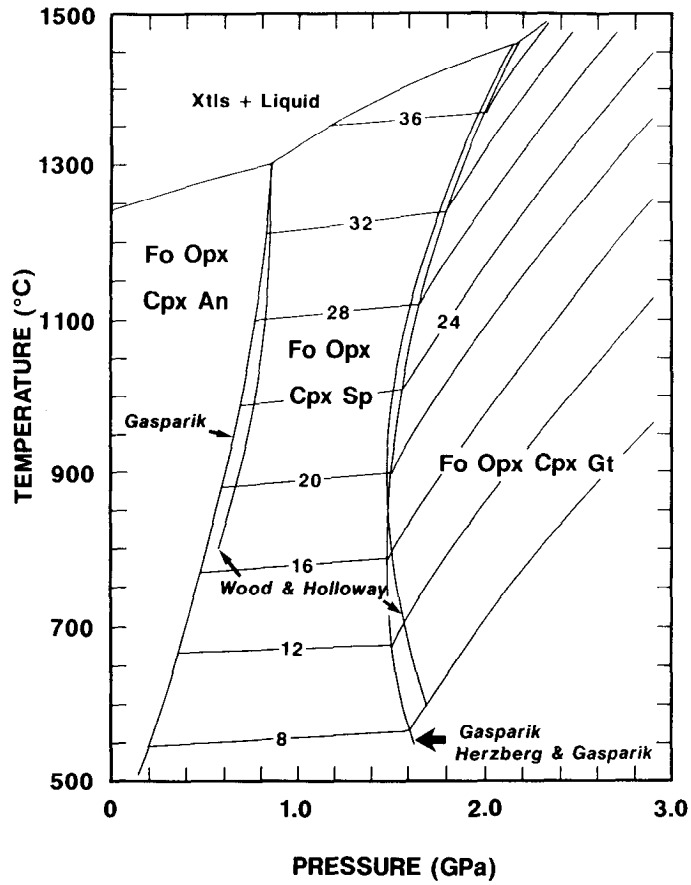

Fig. 2. Stability fields of plagioclase-, spinel-, and garnet-peridotite analogues in the system CaO-MgO-Al_2O_3-SiO_2. Numbered lines are alumina content of orthopyroxene [100Al/6 oxygens; 34]. Solidus to 2 GPa is from Presnall et al. [73].

At pressures where olivine and garnet are stable, the solidus for mantle peridotite can be described by the equation [35]:

$$T\ (°C) = (1263 + 123.7P - 5.36P^2 + 0.069P^3) - 100 \quad (1)$$

where P is in GPa.

High pressure liquidus phases for both mantle peridotite and chondritic compositions are majorite garnet, magnesiowüstite, and perovskite [1, 34, 35, 40, 68, 98]. They are important because fractionation of one or more of these phases from chondrite in a magma ocean is a possible way of forming mantle peridotite. But this phase equilibrium control on the formation of mantle peridotite remains conjectural [75], and is likely to be the subject of lively debate over the decades to come.

TABLE 1. Symbols for Phases in Figures and Text

Symbol	Phase
Fo	Forsterite
Ol	Olivine
An	Anorthite
Pl	Plagioclase
Ak	Alkali Feldspar
Qz	Quartz
St	Stishovite
Sp	Spinel ($MgAl_2O_4$)
Gt	Garnet
Opx	Orthopyroxene
En	Enstatite
OEn	Orthoenstatite
PEn	Protoenstatite
Pig	Pigeonite
Cpx	Clinopyroxene
Di	Diopside
AnhyB	Anhydrous B $(Mg,Fe)_{14}Si_5O_{24}$
ß	Modified Spinel $(Mg,Fe)_2SiO_4$
τ	Spinel $(Mg,Fe)_2SiO_4$
Mw	Magnesiowüstite
MgPv	Magnesium Perovskite
CaPv	Calcium Perovskite
Srp	Serpentine
Chl	Chlorite
Tr	Tremolite
Phl	Phlogopite
Br	Brucite
Sa	Sapphirine
Amp	Amphibole
Carb	Carbonate
Phase A	$Mg_7Si_2O_8(OH)_6$
Superphase B	$Mg_{10}Si_3O_{14}(OH)_4$

Addition of H_2O to peridotite stabilizes hydrous magnesium-rich silicates, and can give rise to a wide range of new mineral assemblages. Water is injected into the mantle by the recycling of sediment, altered basalt, and peridotite in subducted oceanic lithosphere [86]. It can be stored in serpentine, talc, chlorite, tremolite, and phlogopite at relatively low mantle pressures (Figure 4), but brucite has been observed in the 15 to 22 GPa range [26, 43, 45]. Water can also be stored in alphabet phases such as Phase A, Phase B, and Phase C at very high pressures [3, 25, 86], and it has been suggested that a substantial fraction of the total water content of the Earth may be stored in them [2]. However, they are unstable at relatively low temperatures [25, 86], and the water in them can be liberated by dehydration or by melting. Of the alphabet phases that have been synthesized, water will be subducted mostly in Phase A and Superphase B [25], and then only in very cold subduction zones (Figure 4). Free water can be liberated in hot subducted slabs by dehydration (Figure 4), and returned to the lithosphere where it may participate in arc volcanism [86]. At temperatures above the wet solidus, water is mostly stored in magmas. Hydrous phases can also stabilize stishovite (SiO_2) in peridotite compositions at transition zone pressures [24, 25].

3. BASALTIC ROCKS

The most common basalts on Earth are tholeiites [97], and the most simple way of understanding their phase relations is shown in Figure 5 as the subsystem An-Fo-Di-SiO_2 of the

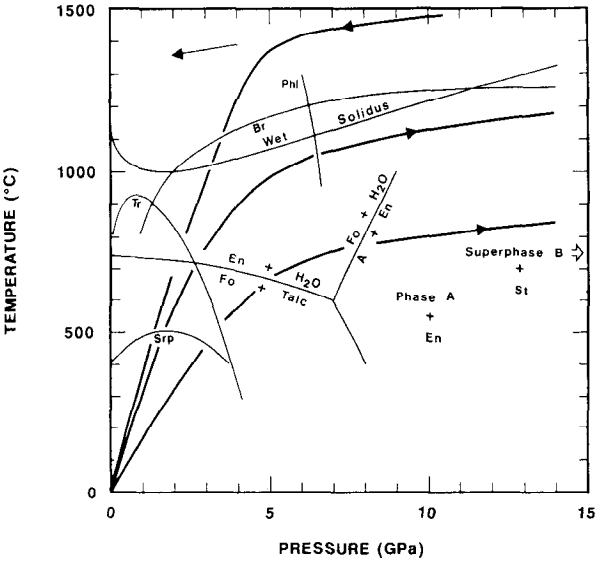

Fig. 4. Stability fields of hydrous magnesium silicates compared to the convective geotherm below oceanic ridges [58; left pointing arrow] and the geotherms in hot and cold subducted lithosphere [70; right pointing arrows]. Data sources: Phase A and Superphase B which is stable at P > 15 GPa [25, 96]; Brucite [26]; Phlogopite [83 as cited by 85]; Serpentine and Tremolite [14]. Hydrous phases are stable on the low T side sides of the boundaries, and dehydration/melting products are not shown. For brucite dT/dP > 0 to 22 GPa [26], and the curve shown has been interpreted as both melting [26] and dehydration [43]. Wet solidus is for peridotite with excess H_2O [86].

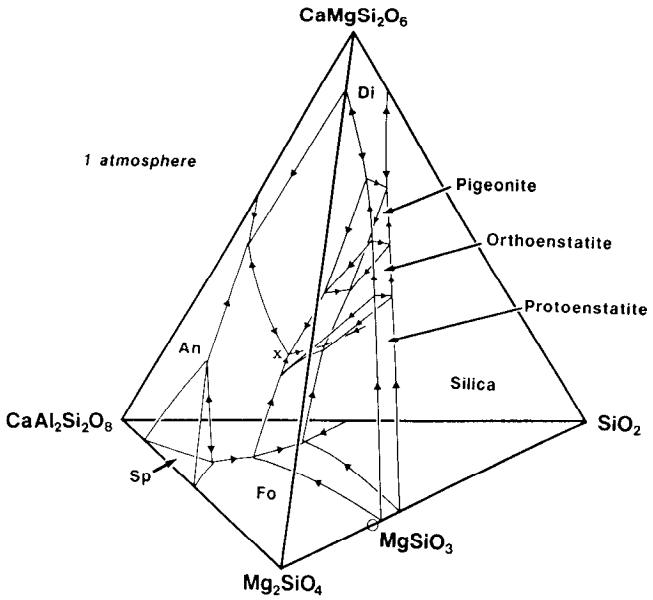

Fig. 5. Liquidus crystallization fields in the basalt portion of the system CaO-MgO-Al_2O_3-SiO_2 at 1 atmosphere from Presnall et al. [72] as modified by Longhi [54]. Arrows on cotectics point in the direction of falling temperature, but for preserving clarity, no distinction is made between odd and even crystallization reactions. X represents the composition of a liquid formed by melting a peridotite analogue L + Ol + An + En + Di.

system CaO-MgO-Al_2O_3-SiO_2 (CMAS). The tetrahedron was constructed from melting experiments done on compositions within it, and from compositions contained in the four bounding ternary planes: Fo-Di-SiO_2 An-Fo-SiO_2, An-Di-SiO_2, An-Fo-Di. The original experimental data base is too exhaustive to cite here, but many excellent reviews exist [38, 54, 61, 72].

The three dimensional character of Figure 5 can be simplified by projecting the phase relations of interest on a plane. Since plagioclase and augite are the most common minerals in basalts, the liquidus phase relations involving anorthite and diopside are chosen, and these are shown in Figure 6. Although these phase equilibria have many applications to basalt genesis, the following are generally accepted as the most important.

1. Equilibrium melting of a mantle peridotite analogue in CMAS at 1 atmosphere (L + Fo + OEn + Di + An) will yield a tholeiitic liquid (ie., X in Figure 6) that plots to the silica-rich side of the tholeiite plane An-Di-En. Although not shown, melting is peritectic and is described by L + Fo = An + Di + OEn.

2. Olivine basalts, contained to the Fo-rich side of the plane An-Di-En, can fractionate to form hypersthene basalts and quartz tholeiites, but the reverse cannot occur.

3. A thermal maximum involving L + Fo + An + Di is slightly more silica-rich than the plane Fo-An-Di [54], and prohibits the derivation of silica-poor alkali basalts from the

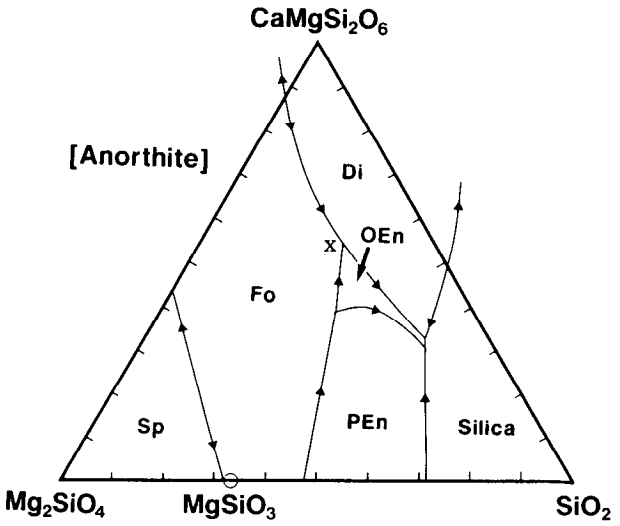

Fig. 6a. A projection from Anorthite of anorthite-saturated compositions in Fig. 5 onto the join Fo-Di-Qz, adapted from Longhi [54; oxygen units; CaO-MgO-Al_2O_3-SiO_2].

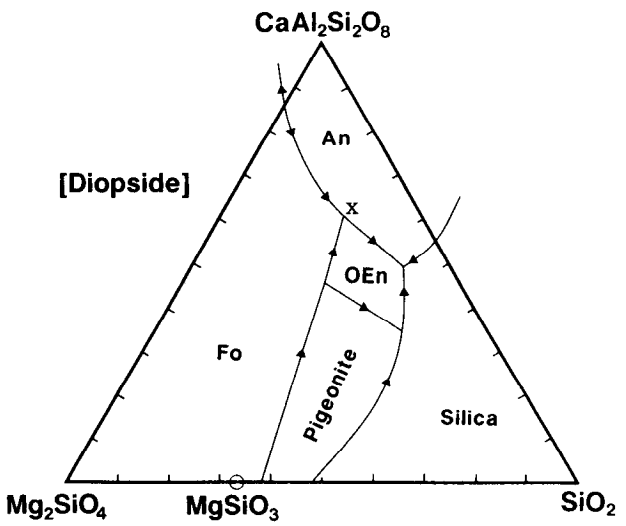

Fig. 6b. A projection from Diopside of diopside-saturated compositions in Fig. 5 onto the join Fo-Di-Qz, adapted from Longhi [54; oxygen units; CaO-MgO-Al_2O_3-SiO_2].

more silica-rich tholeiites by fractional crystallization or by partial melting at 1 atmosphere.

These conclusions do not change when other components are added to the system CMAS to make naturally-occurring basalts. Of the wide range of basaltic rocks on Earth, the mid-ocean ridge basalts (ie., MORB) are the most abundant. A total of 962 basalt glass analyses from the Atlantic, Pacific, and Indian ridges [59] are projected in Figure 7. It can be seen that they are similar in composition to experimentally-produced liquids that are multiply saturated in olivine + diopside + plagioclase at 1 atmosphere pressure [66, 89]. This important observation demonstrates that the major element geochemistry of MORB is phase equilibrium-controlled at shallow depths [66, 89], possibly reflecting crystallization within magma chambers that solidify to gabbros in the oceanic crust.

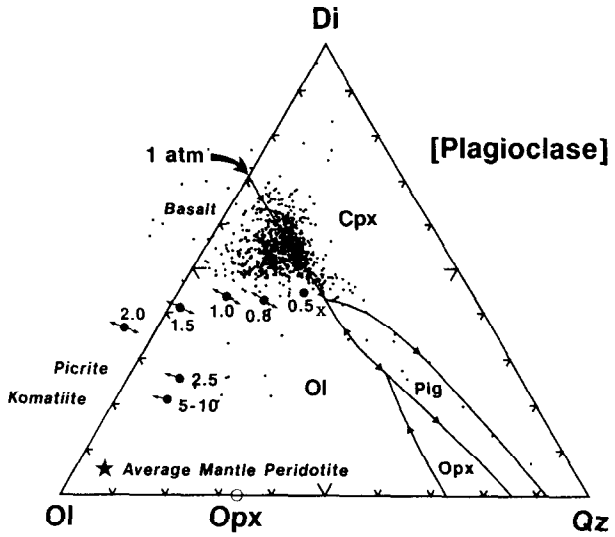

Fig. 7a. A projection from Plagioclase of plagioclase-saturated liquidus crystallization fields for naturally-occurring basaltic and andesitic compositions modified slightly from Grove and Baker [31; oxygen units]. One atmosphere boundaries are from data listed in Walker et al. [89], Grove and Baker [31], and Sack et al., [76]. Solid circles are compositions of liquids formed by 10 % equilibrium melting of mantle peridotite on the solidus at 0.5 to 2.0 GPa [47,48] and 2.5 to 10 GPa [33; CaO-MgO-FeO-Al_2O_3-SiO_2]. Solidus assemblage is L + Ol + Opx + Cpx + Al-rich phase (plagioclase, spinel, or garnet). Arrows projecting away and to silica show the effect of adding and subtracting Na_2O [47,48], respectively; CO_2 will have a similar effect [17]. Advanced melting above the solidus (ie., L + Ol + Opx) will increase SiO_2 [21,63]. Dots are 962 mid-ocean ridge basalt (MORB) glass analyses from Melson et al. [59], and average mantle peridotite is from Herzberg [33].

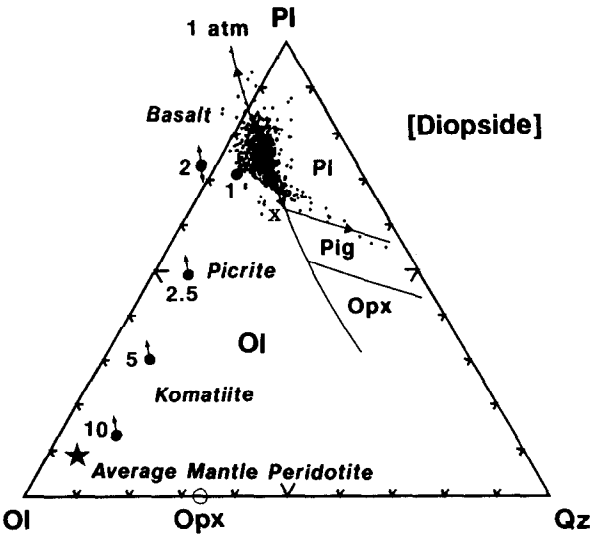

Fig. 7b. A projection from Diopside of diopside-saturated liquidus crystallization fields for naturally-occurring basaltic and andesitic compositions modified slightly from Grove and Baker [31; oxygen units].

The pseudoinvariant point L + Ol = Pl + Pig + Aug [31] occurs at point X in Figure 7, and it is special because it identifies the composition of a basaltic liquid formed by the initial melting of mantle peridotite at 1 atmosphere. It is similar to X in the system CMAS in that it plots to the silica-rich side of the plane Plag-Di-Opx, and is tholeiitic. The effects of Na_2O, K_2O, TiO_2, and FeO in MORB-like basalts can be readily seen by comparing Figure 6 with Figure 7. The plane Ol-Plag-Di remains a thermal divide, although addition of these extra components offers opportunities for crossing it [67].

The 1 atmosphere phase relations demonstrate that it is possible for the MORB basalt glass population to loose its identity by fractionating down temperature along the cotectic until pigeonite begins to crystallize. Any further crystallization will yield silica-rich ferrobasalts along the cotectic defined by L + Pl + Aug + Pig. Although glasses having these characteristics can be seen in Figure 7, they are comparatively rare. Of the spectrum of compositional possibilities, ranging from parental liquids that are enriched in an olivine component to high silica ferrobasalts, the compositions shown in Figure 7 are the most eruptable because they have the lowest densities [79, 81]. The more MgO- and FeO-rich types are denser and

may have been filtered out, and are likely to be more important in the gabbroic layer of the oceanic crust.

Of major interest is the composition of the primary magma from which ocean floor basalts were formed. A primary magma forms when the liquid in a partially melted parcel of mantle collects into pools, and retains the geochemical memory of the mineralogy, temperature, pressure, and volatile fugacity of the source region. It is now generally recognized that the composition of the primary magma is not the same as the average of the basalt glasses shown in Figure 7, but estimates have varied widely. Some workers believe that the rare glass compositions that project to the olivine-rich side of the MORB population may be primary magmas generated at 0.7 to 1.0 GPa [22, 28, 73 and references cited therein]. It has also been suggested that none of the glass compositions seen in Figure 7 are primary, that the primary magmas had considerably more olivine dissolved in them, and that they were formed at pressures in the 1.5 to 3.0 GPa range [19, 21, 66, 67, 80 and references cited therein]. It is now becoming apparent that primary magmas are generated at all levels of the melt column [49, 58], extending from near the surface to pressures where garnet is stable [77], in excess of 2.5 GPa. The compositions of erupted basalts are therefore likely to be an average of primary magmas formed over a range of pressures [49,58], modified by variable amounts of olivine fractionation.

Basaltic magmas which crystallize at depth can develop mineral assemblages that differ from basalts and gabbros near the Earth's surface. In particular, olivine and plagioclase are restricted to relatively low pressures (Figure 2), and garnet becomes stable at high pressures [23, 29, 42, 52, 92, 93, 97; Figure 8]. Gabbros transform to garnet granulites, and the pressure at which this occurs is somewhat elevated for more silica-rich compositions (Figure 9). Plagioclase transforms to pyroxene and quartz over a broad range of pressures, and its eventual disappearance gives rise to eclogite. Garnet granulite and eclogite are confined to the lower reaches of normal or thicken continental crust, and to high pressures characteristic of subduction zones and the mantle (Figure 8). The introduction of H_2O can give rise to a plethora of chlorite- and amphibole-bearing phase assemblages for wet olivine- and quartz-normative basaltic compositions; these can be retrieved from Figure 9 [65].

4. PICRITES AND KOMATIITES

Pressure increases the melting temperatures of most crystalline phases, but dT/dP is greater for some minerals than for others [Presnall, this volume]. This will strongly influence the compositions of liquids where the crystallization fields meet, which are surfaces, lines, and points of multiple phase saturation. Pressure, therefore, causes liquidus crystallization fields to expand or contract (Figure 10). O'Hara [67] demonstrated that the liquidus crystallization field of olivine contracts with increasing pressure, and initial liquids formed on the solidus become enriched in an olivine component (Figure 10). Liquids generated at 2.5 to 10 GPa are picritic to komatiitic in composition [33], high in MgO (Figure 7). Partial melting at these high pressures is likely to be characteristic of volcanism in plumes rather than ridges [33]. Komatiites and picrites may occur together with basalt in vast eruptions of magma which can form gigantic oceanic plateaus [33].

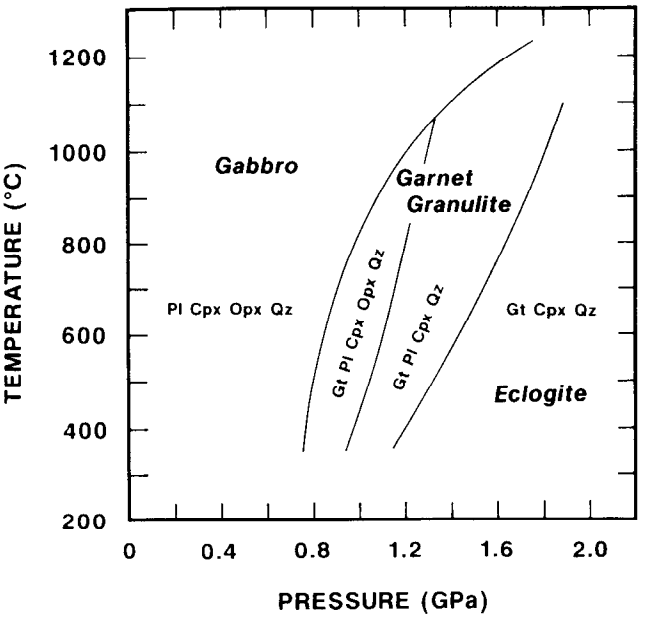

Fig. 8. The gabbro to eclogite transformation for a quartz tholeiite composition [92].

5. ANDESITES AND RELATED ARC ROCKS

Although liquids formed by the melting of mantle peridotite at 1.0 +/- 0.1 GPa are similar in composition to many primitive MORB glasses (Figure 7), they are also similar to some high alumina basalts from arc environments [6]. This indicates that some high alumina basalts (17 - 18 % Al_2O_3) may be parental to many basaltic andesites and andesites [6, 10, 32, 44].

Mid-ocean ridge basalts are largely devoid of H_2O, but can contain 0.2 % CO_2 [13]. Important amounts of water can be dissolved in subduction-related magmas [60], and the ability of silicate liquids to dissolve H_2O causes pronounced

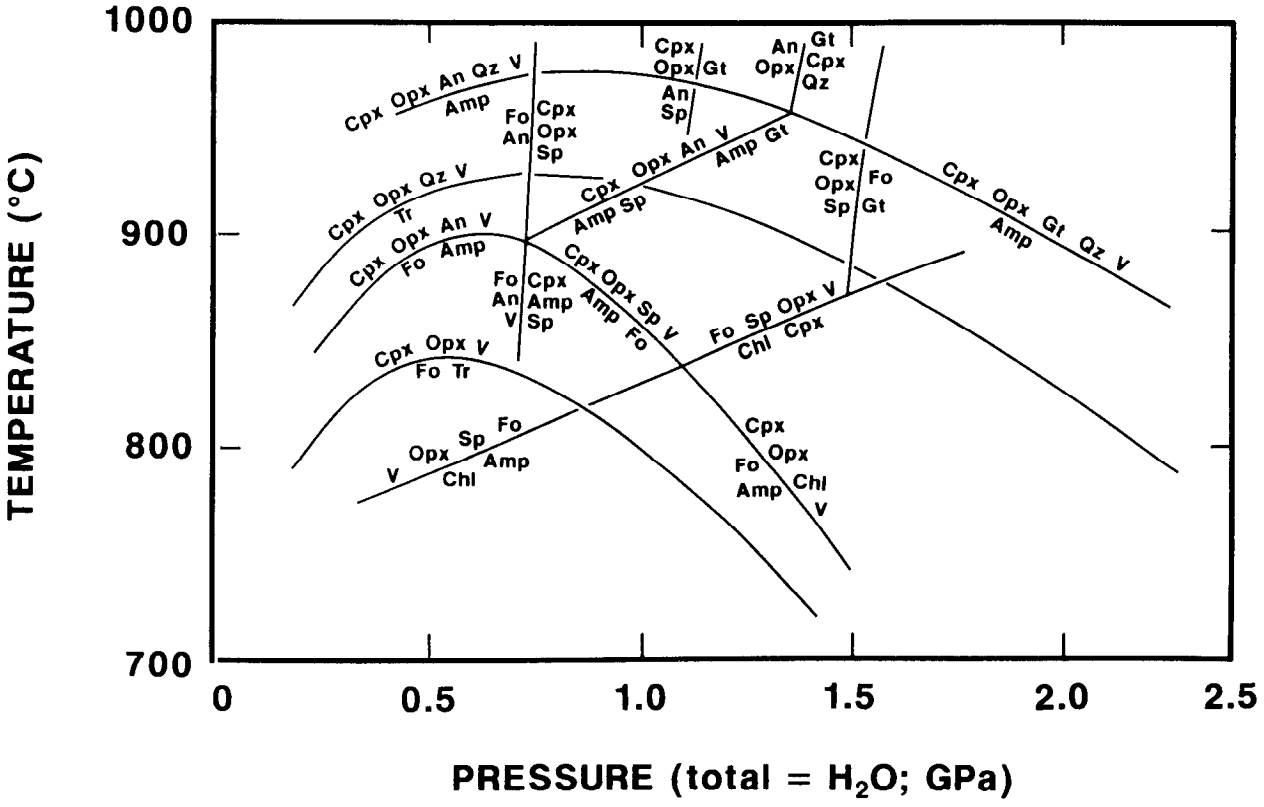

Fig. 9. Univariant curves and invariant points for basalt and peridotite analogue compositions in the system CaO-MgO-Al_2O_3-SiO_2-H_2O after Obata and Thompson [65]. The wide spectrum of chlorite-, tremolite-, and aluminous amphibole-assemblages can be retrieved by positioning the bulk composition into the T-P space of interest [65].

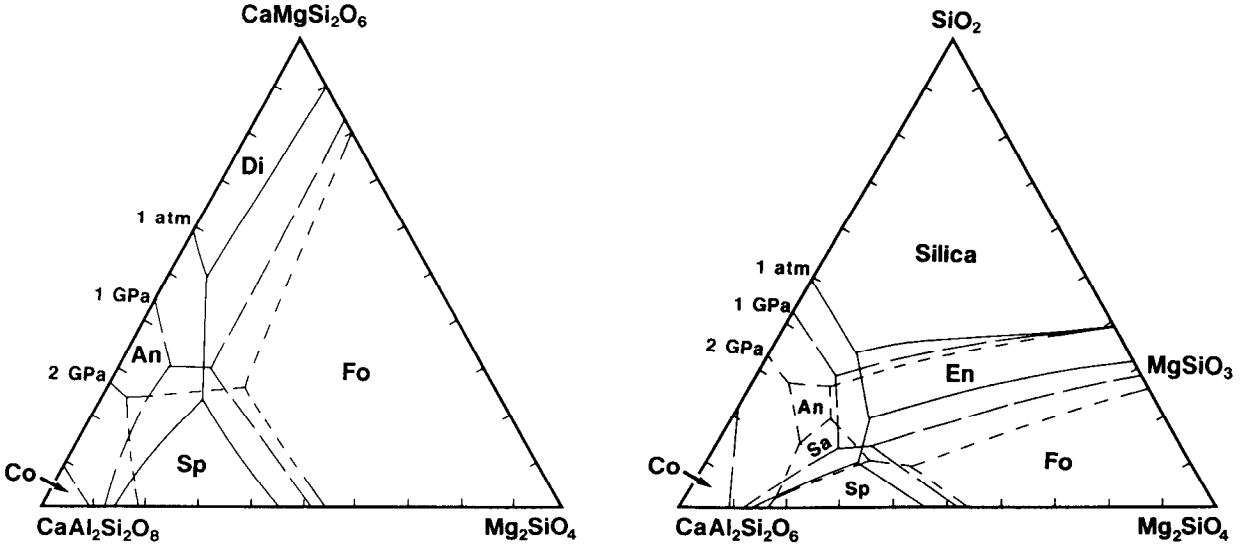

Fig. 10. The effect of pressure on the liquidus crystallization fields for two ternary systems [53, 72, 78], in weight %.

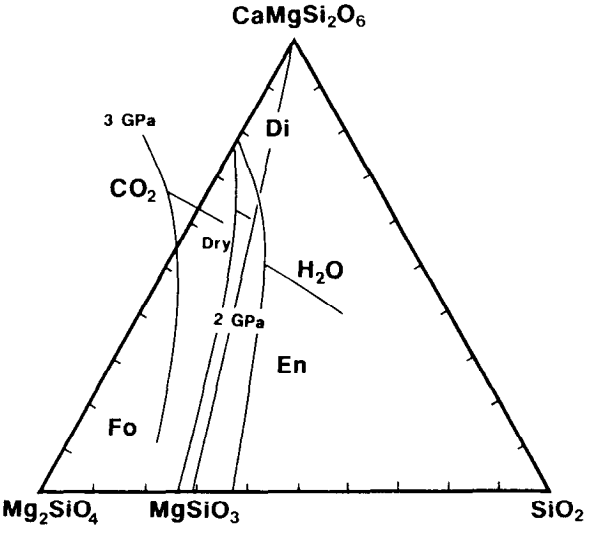

Fig. 11. Liquidus crystallization fields of forsterite, enstatite and diopside at 2 GPa dry and H_2O saturated [51], and at 3 GPa CO_2 saturated [17].

depressions to occur in melting temperatures. This also causes important changes to occur in the compositions of liquids at multiple phase saturation surfaces, lines, and points and, in particular, the compositions of magmas that are generated on the solidus.

Addition of water tends to expand the crystallization field of olivine at the expense of the crystallization field of low calcium pyroxene [51], and this is shown in Figure 11. Liquids in equilibrium with wet mantle peridotite are therefore enriched in silica compared to anhydrous systems, and are potentially important in arc volcanism [51, 62]. However, some high alumina basalts are parental to andesites [eg., 6], and since these can be formed under anhydrous conditions at 1 GPa (Figure 7) the amount of H_2O involved can be variable. Water also causes an expansion of the crystallization field of pyroxene at the expense of both quartz [51] and plagioclase [5, 60] and this will contribute SiO_2 and Al_2O_3 to both fractionated arc magmas and to magmas formed by the wet melting of basalt [30]. Indeed, trondhjemites and tonalites, which are major rock types of the Archean continental crust, could have formed by the wet melting of amphibolite and eclogite [74] in ancient subduction zones. Finally, water also stabilizes amphibole, and its fractionation from basaltic magmas may also contribute to the formation of andesites [11, 30, 36].

6. SILICA-DEFICIENT IGNEOUS ROCKS

The existence of volatile-laden kimberlites and carbonatites on land points to the importance of H_2O and CO_2 in the subcontinental mantle. Addition of CO_2 tends to expand the liquidus crystallization field of low Ca pyroxene at the expense of olivine [17], and this is also shown in Figure 11. Liquids in equilibrium with mantle peridotite will therefore have lower contents of SiO_2 compared to anhydrous systems, and can range from nepheline normative to carbonatitic in composition [17, 90, 95]. A wide variety of magma compositions can potentially be produced by the melting of mantle peridotite with mixed H_2O and CO_2, and these include andesites, tholeiites, nephelinites, melilitites, carbonatites (references cited above), in addition to kimberlites [9, 18]. Some of these magma types are positioned in Figure 12, which shows the solidus temperatures and subsolidus assemblages for mantle peridotite in the presence of a small amount of H_2O and CO_2 [69].

7. GRANITE

Phase equilibrium data reported by Tuttle and Bowen [87] for the system $NaAlSi_3O_8$ - $KAlSi_3O_8$ - SiO_2 - H_2O at 0.05 to 0.3 GPa remain the basic framework for understanding the origin of granites. Their results are summarized in Figure 13 together with data at higher pressures [55, 56], and the amount of water contained in this system is sufficiently high to form separate vapor phase, so the system is water saturated. In the pressure range of 1 atmosphere to 0.35 GPa the system contains a thermal minimum on the cotectic curve L + Ak + Qz + V [87]. At pressures greater than 0.35 GPa the thermal minimum transforms to a ternary eutectic L + Ak + Pl + Qz + V

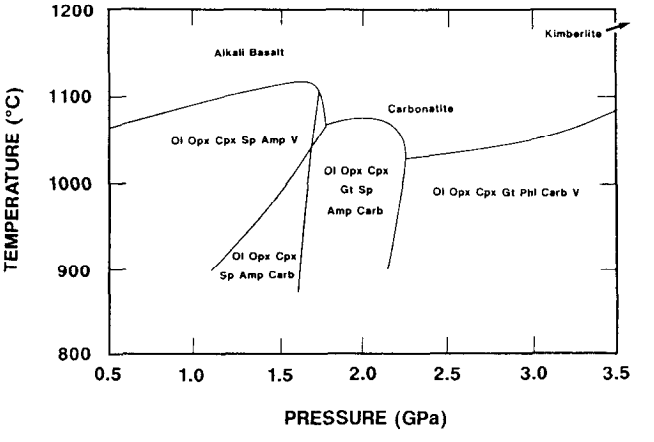

Fig. 12. Phase relations of a peridotite composition with about 0.3 weight % H_2O and 0.7 weight % CO_2 (molar $CO_2/(CO_2 + H_2O) = 0.5$), and compositions of liquids produced near the solidus, from Olafsson and Eggler [69].

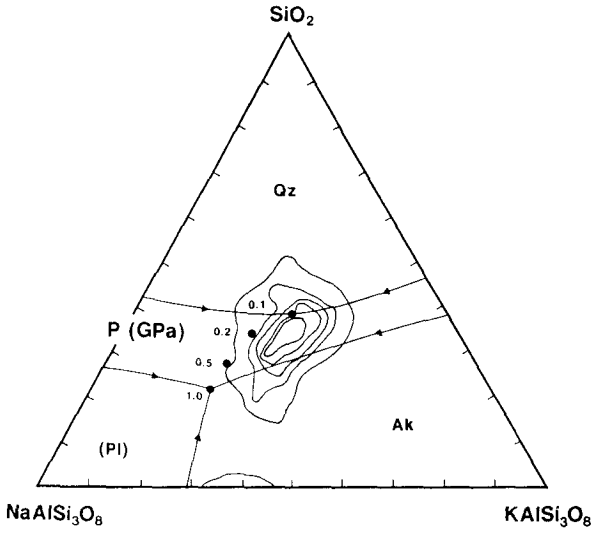

Fig. 13. Liquidus crystallization fields of quartz, alkali feldspar, and albite plagioclase in the system $NaAlSi_3O_8$ - $KAlSi_3O_8$ - SiO_2 - H_2O at the water pressures indicated. At pressures less than about 0.35 GPa the alkali feldspar liquidus crystallization field extends across the join $NaAlSi_3O_8$ - $KAlSi_3O_8$, and the closed circles position the compositions of thermal minima. At higher pressures there is a separate liquidus crystallization field of albite plagioclase, and the closed circles position the compositions of eutectics. Data from Tuttle and Bowen [87], Luth et al. [56] and Luth [55]. Contours are compositions of 571 plutonic granites from Tuttle and Bowen [87].

[55, 56]. The similarity in composition between these thermal minima and the geochemistry of granite was used as evidence for a magmatic origin [87]. But despite this apparent success, a careful examination of Figure 13 shows clearly that most granites are enriched in $KAlSi_3O_8$ compared to these thermal minima and eutectics.

There are several ways of explaining these differences. Addition of anorthite ($CaAl_2Si_2O_8$) has the effect of greatly expanding the crystallization field of plagioclase, and liquids formed by initial melting on the cotectic L + Pl + Ak + Qz + V will be enriched in $KAlSi_3O_8$ [64, 71, 91]. But granites are unlikely to have formed under water saturated conditions, and variable water contents can profoundly affect the phase equilibria, either by a reduced activity of water ($aH_2O < 1.0$) or by fluid absent melting [57, 91, 94]. Ebadi and Johannes [16] have suggested that thermal minima and eutectics in the system SiO_2-$NaAlSi_3O_8$-$KAlSi_3O_8$-H_2O-CO_2 shift to higher $KAlSi_3O_8$ when the activity of water is less than 1.0, but this is is conflict with a thermodynamic analysis of these equilibria [64]. A reduced water activity can either have no effect on the size of the quartz crystallization field [16], or it can expand it [64, 91].

Granites are extremely rare on the Earth's moon [8]. On Earth, granites become abundant only during the last 2,500 Ma; the oldest granite-like continental crust of Archean age actually consists of arc-like tonalite, trondhjemite, and granodiorite, all of which contain considerably less alkali feldspar than those shown in Figure 13 [20, 50]. These observations demonstrate that granites *sensu stricto* were not formed by fractional crystallization of basalt or andesite, but rather by partial melting of preexisting crustal rocks such as metapelites, in agreement with other phase equilibrium studies [71, 88].

Acknowledgements. Mike Carr is thanked for providing plots of mid-ocean ridge basalt glasses and their related projections, and Dean Presnall is thanked for comments. This work was partially supported by NSF grant EAR 91-17184 to C. Herzberg. This is Mineral Physics Institute publication # 56 at the Department of Earth and Space Sciences, SUNY Stony Brook.

REFERENCES

1. Agee, C., A new look at differentiation of the Earth from melting experiments on the Allende meteorite, *Nature, 346*, 834-837, 1990.
2. Ahrens, T.J., Water storage in the mantle, *Nature, 342*, 122-123, 1989.
3. Akaogi, M., and S.-I. Akimoto, High-pressure stability of a dense hydrous magnesian silicate $Mg_{23}Si_8O_{42}H_6$ and some geophysical implications, *J. Geophys. Res., 85*, 6944-6948, 1980.
4. Akaogi, M., E. Ito, and A. Navrotsky, Olivine-modified spinel-spinel transformations in the system Mg_2SiO_4-Fe_2SiO_4: calorimetric measurements, thermochemical calculation, and geophysical application, *J. Geophys. Res., 94*, 15,671-15,685, 1989.
5. Baker, D.R. and D.H. Eggler, Compositions of anhydrous and hydrous melts coexisting with plagioclase, augite, and olivine or low-Ca pyroxene from 1 atm to 8 kbar: Application to the Aleutian volcanic center of Atka, *Am. Mineral., 72*, 12-28, 1987.
6. Bartels, K.S., R.J. Kinzler, and T.L. Grove, High pressure phase relations of primitive high-alumina basalts from Medicine Lake volcano, northern California, *Contrib. Mineral. Petrol., 108*, 253-270, 1991.
7. Basaltic Volcanism Study Project, Basaltic Volcanism on the Terrestrial Planets, Pergamon Press, Inc., New York, 1286 pp., 1981.
8. Campbell, I.H., and S.R. Taylor, No water, no granites - no oceans, no continents, *Geophys. Res. Lett., 10*,

1061-1064, 1983.
9. Canil, D., and C.M. Scarfe, Phase relations in peridotite + CO_2 systems to 12 GPa: implications for the origin of kimberlite and carbonate stability in the Earth's upper mantle, *J. Geophys. Res., 95*, 15,805-15,816, 1990.
10. Carr, M.J., Symmetrical and segmented variation of physical and geochemical characteristics of the Central American volcanic front, *J. Volcan. Geotherm. Res., 20*, 231-252, 1984.
11. Cawthorn, R.G., and M.J. O'Hara, Amphibole fractionation in calc-alkaline magma genesis, *Am. J. Sci., 276*, 309-329, 1976.
12. Clark, S.P.Jr., Handbook of Physical Constants, 587 pp., *Geol. Soc. Am. Mem., 97*, 1966.
13. Delaney, J.R., D.W. Muenow, and D.G. Graham, Abundance and distribution of water, carbon and sulfur in the glassy rims of submarine pillow basalts, *Geochim. Cosmochim. Acta, 42*, 581-594, 1978.
14. Delany, J.M., and H.C. Helgeson, Calculation of the thermodynamic consequences of dehydration in subducting oceanic crust to 100 kb and > 800°C, *Am. J. Sci., 278*, 638-686, 1978.
15. Dick, H.J.B., R.L. Fisher, and W.B. Bryan, Mineralogic variability of the uppermost mantle along mid-ocean ridges, *Earth Planet. Sci. Lett., 69*, 88-106, 1984.
16. Ebadi, A., and W. Johannes, Beginning of melting and composition of first melts in the system Qz-Ab-Or-H_2O-CO_2, *Contrib. Mineral. Petrol., 106*, 286-295, 1991.
17. Eggler, D.H., Volatiles in ultrabasic and derivative rock systems, *Carnegie Inst. Wash. Yb., 73*, 215-224, 1974.
18. Eggler, D.H. and R.F. Wendlandt, Experimental studies on the relationship between kimberlite magmas and partial melting of peridotite, In *Kimberlites, Diatremes and Diamonds: Their Geology, Petrology, and Geochemistry*, edited by F.R. Boyd and H.O.A. Meyer, pp. 330-338, AGU, Washington, D.C., 1979.
19. Elthon, D., and C.M. Scarfe, High-pressure phase equilibria of a high-magnesia basalt and the genesis of primary oceanic basalts, *Am. Mineral., 69*, 1-15, 1984.
20. Engel, A.E.J., S.P. Itson, C.G. Engel, D.M. Stickney, and E.J. Cray, Jr., Crustal evolution and global tectonics: a petrogenic view, *Geol. Soc. Amer. Bull., 85*, 843-858, 1974.
21. Falloon, T.J., D.H. Green, C.J. Hatton, and K.L. Harris, Anhydrous partial melting of a fertile and depleted peridotite from 2 to 30 kb and application to basalt petrogenesis, *J. Petrol., 29*, 1257-1282, 1988.
22. Fujii, T., and C.M. Scarfe, Composition of liquids coexisting with spinel lherzolite at 10 kbar and the genesis of MORBs, *Contrib. Mineral. Petrol., 90*, 18-28, 1985.
23. Gasparik, T., Two-pyroxene thermobarometry with new experimental data in the system CaO-MgO-Al_2O_3-SiO_2, *Contrib. Mineral. Petrol., 87*, 87-97, 1984.
24. Gasparik, T., Phase relations in the transition zone, *J. Geophys. Res., 95*, 15,751-15,769, 1990.
25. Gasparik, T., The role of volatiles in the transition zone, *J. Geophys. Res.*, in press, 1993.
26. Gasparik, T., and J. Zhang, Stability of hydrous phases at pressures corresponding to the Earth's transition zone, *Eos Trans. AGU*, Western Pacific Meeting suppl., *73*, 53, 1992.
27. Green, D.H., and A.E. Ringwood, The stability fields of aluminous pyroxene peridotite and garnet peridotite and their relevance in upper mantle structure, *Earth Planet. Sci. Lett., 3*, 151-160, 1967a.
28. Green, D.H., and A.E. Ringwood, The genesis of basaltic magmas, *Contrib. Mineral. Petrol., 15*, 103-190, 1967b.
29. Green, D.H., and A.E. Ringwood, An experimental investigation of the gabbro to eclogite transformation and its petrological applications, *Geochim. Cosmochim. Acta, 31*, 767-833, 1967c.
30. Green, T.H., Anatexis of mafic crust and high pressure crystallization of andesite, *In Andesites*, edited by R.S. Thorpe, pp. 465-488, John Wiley & Sons, New York, 1982.
31. Grove, T.L., and M.B. Baker, Phase equilibrium controls on the tholeiitic versus calc-alkaline differentiation trends, *J. Geophys. Res., 89*, 3253-3274, 1984.
32. Gust, D.A., and M.R. Perfit, Phase relations of a high-Mg basalt from the Aleutian Island arc: implications for primary island arc basalts and high-Al basalts, *Contrib. Mineral. Petrol., 97*, 7-18, 1987.
33. Herzberg, C., Depth and degree of melting of komatiites, *J. Geophys. Res., 97*, 4521-4540, 1992.
34. Herzberg, C., and T. Gasparik, Garnet and pyroxenes in the mantle: a test of the majorite fractionation hypothesis, *J. Geophys. Res., 96*, 16,263-16,274, 1991.
35. Herzberg, C., T. Gasparik, and H. Sawamoto, Origin of mantle peridotite: constraints from melting experiments to 16.5 GPa, *J. Geophys. Res., 95*, 15,779-15,803, 1990.
36. Holloway, J.R., and C.W. Burnham, Melting relations of basalt with equilibrium water pressure less than total pressure, *J. Petrol.*, 13, 1-29, 1972.
37. Irifune, T., An experimental investigation of the pyroxene-garnet transformation in a pyrolite composition and its bearing on the constitution of the mantle, *Phys. Earth Planet. Inter., 45*, 324-336, 1987.
38. Irvine, T.N., Olivine-pyroxene-plagioclase relations in the system Mg_2SiO_6-$CaAl_2Si_2O_8$-$KAlSi_3O_8$-SiO_2 and their bearing on the differentiation of stratiform intrusions, *Carnegie Inst. Wash. Yb., 74*, 492-500, 1975.
39. IUGS (International Union of Geological Sciences) Subcommission on the Systematics of Igneous Rocks, Plutonic rocks, classification and nomenclature, *Geotimes, 18*, 26-30, 1973.
40. Ito, E., and E. Takahashi, Melting of peridotite at uppermost lower-mantle conditions, *Nature, 328*, 514-517, 1987.
41. Ito, E., and E. Takahashi, Postspinel transformations in the system Mg_2SiO_4-Fe_2SiO_4 and some geophysical implications, *J. Geophys. Res., 94*, 10,637-10,646, 1989.
42. Ito, K., and G.C. Kennedy, The fine structure of the basalt-eclogite

tranformation, *Mineral. Soc. Amer. Spec. Paper, 3*, 77-83, 1970.

43. Johnson, M.C., and D. Walker, Thermal compaction assists interpretation of poorly quenchable reactions: $Mg(OH)_2 = MgO + H_2O$, *Eos Trans. AGU, 73*, 619, 1992.
44. Johnston, A.D., Anhydrous P-T phase relations of near-primary high-alumina basalt from the South Sandwich Islands, *Contrib. Mineral. Petrol., 92*, 368-382, 1986.
45. Kanzaki, M., Dehydration of brucite ($Mg(OH)_2$) at high pressures detected by differential thermal analysis, *Geophys. Res. Lett., 18*, 2189-2192, 1991.
46. Katsura, T., and E. Ito, The system Mg_2SiO_4 - Fe_2SiO_4 at high pressures and temperatures: precise determination of stabilities of olivine, modified spinel, and spinel, *J. Geophys. Res., 94*, 15,663-15,670, 1989.
47. Kinzler, R.J., and T.L. Grove, Primary magmas of mid-ocean ridge basalts 1. Experiments and Methods, *J. Geophys. Res., 97*, 6885-6906, 1992a.
48. Kinzler, R.J., and T.L. Grove, Primary magmas of mid-ocean ridge basalts 2. Applications, *J. Geophys. Res., 97*, 6907-6926, 1992b.
49. Klein, E.M., and C.H. Langmuir, Global correlations of ocean ridge basalt chemistry with axial depth and crustal thickness, *J. Geophys. Res., 92*, 8089-8115, 1987.
50. Kroner, A., Evolution of the Archean continental crust, *Ann. Rev. Earth Planet. Sci., 13*, 49-74, 1985.
51. Kushiro, I., The system forsterite-diopside-silica with and without water at high pressures, *Am. J. Sci., 267-A*, 269-294, 1969.
52. Kushiro, I., and H.S. Yoder, Anorthite-forsterite and anorthite-enstatite reactions and their bearing on the basalt-eclogite transformation, *J. Petrol., 7*, 337-362, 1966.
53. Liu, T.-C., and D.C. Presnall, Liquidus phase relationships on the join anorthite-forsterite-quartz at 20 kbar with applications to basalt petrogenesis and igneous sapphirine, *Contrib. Mineral. Petrol., 104*, 735-742, 1990.
54. Longhi, J., Liquidus equilibria and solid solution in the system $CaAl_2Si_2O_8$-Mg_2SiO_4-SiO_2 at low pressure, *Am. J. Sci., 287*, 265-331, 1987.
55. Luth, W.C., Granitic Rocks, *In The Evolution of the Crystalline Rocks*, edited by D.K. Bailey and R. MacDonald, pp. 335-417, Academic Press, London, 1976.
56. Luth, W.C., R. Jahns, and F. Tuttle, The granite system at pressures of 4 to 10 kilobars, *J. Geophys. Res., 69*, 759-773, 1964.
57. Maaloe, S., and P.J. Wyllie, Water content of a granite magma deduced from the sequence of crystallization determined experimentally with water-undersaturated conditions, *Contrib. Mineral. Petrol., 52*, 175-191, 1975.
58. McKenzie, D., and M.J. Bickle, The volume and composition of melt generated by extension of the lithosphere, *J. Petrol., 29*, 625-679, 1988.
59. Melson, W.G., G.R. Byerly, J.A. Nesen, T.L. Wright, and T. Vallier, A catalog of the major element chemistry of abyssal volcanic glasses, *Smithson. Contrib. Earth Sci., 19*, 31-60, 1977.
60. Merzbacher, C., and D.H. Eggler, A magmatic geohygrometer: Application to Mount St. Helens and other dacitic magmas, *Geology, 12*, 587-590, 1984.
61. Morse, S.A., Basalts and Phase Diagrams, Springer-Verlag, New York, pp. 493, 1980.
62. Mysen, B.Y., and A.L. Boettcher, Melting of a hydrous mantle: II. Geochemistry of crystals and liquids formed by anatexis of mantle peridotite at high pressures and high temperatures as a function of controlled activities of water, hydrogen, and carbon dioxide, *J. Petrol., 16*, 549-593, 1975.
63. Mysen, B.O., and I Kushiro, Compositional relations of coexisting phases with degree of melting of peridotite in the upper mantle, *Am. Mineral., 62*, 843-865, 1977.
64. Nekvasil, H., Calculated effect of anorthite component on the crystallization paths of H_2O-undersaturated hapogranitic melts, *Am. Mineral., 73*, 966-981, 1988.
65. Obata, M., and A.B. Thompson, Amphibole and chlorite in mafic and ultramafic rocks in the lower crust and upper mantle: a theoretic approach, *Contrib. Mineral. Petrol., 77*, 74-81, 1981.
66. O'Hara, M.J., Are ocean floor basalts primary magmas? *Nature, 220*, 683-686, 1968a.
67. O'Hara, M.J., The bearing of phase equilibria studies in synthetic and natural systems on the origin and evolution of basic and ultrabasic rocks, *Earth Sci. Rev., 4*, 69-133, 1968b.
68. Ohtani, E., and H. Sawamoto, Melting experiment on a model chondritic mantle composition at 25 GPa, *Geophys. Res. Lett., 14*, 733-736, 1987.
69. Olafsson, M., and D.H. Eggler, Phase relations of amphibole, amphibole-carbonate, and phlogopite-carbonate peridotite: petrologic constraints on the asthenosphere, *Earth Planet. Sci. Lett., 64*, 305-315, 1983.
70. Peacock, S.M. Fluid Processes in subduction zones, *Science, 248*, 329-337, 1990.
71. Presnall, D.C., and P.C. Bateman, Fusion relations in the system $NaAlSi_3O_8$ - $CaAl_2Si_2O_8$ - $KAlSi_3O_8$ - SiO_2 - H_2O and generation of granitic magmas in the Sierra Nevada batholith, *Geol. Soc. Amer. Bull., 84*, 3181-3202, 1973.
72. Presnall, D.C., S.A. Dixon, J.R. Dixon, T.H. O'Donnell, N.L. Brenner, R.L. Schrock, and D.W. Dycus, Liquidus phase relations on the join diopside-forsterite-anorthite from 1 atm to 20 kbar: Their bearing on the generation and crystallization of basaltic magma, *Contrib. Mineral. Petrol., 66*, 203-220, 1978.
73. Presnall, D.C., J.R. Dixon, T.H. O'Donnell, and S.A. Dixon, Generation of mid-ocean ridge tholeiites, *J. Petrol., 20*, 3-35, 1979.
74. Rapp, R.P., E.B. Watson, and C.F. Miller, Partial melting of amphibolite/eclogite and the origin of Archean trondhjemites and tonalites, *Precambrian Res., 51*, 1-25, 1991.
75. Ringwood, A.E., Phase transformations and their bearing on the constitution and dynamics of the mantle, *Geochim. Cosmochim. Acta, 55*, 2083-2110, 1991.

76. Sack, R.O, D. Walker, and I.S.E. Carmichael, Experimental petrology of alkalic lavas: constraints on cotectics of multiple saturation in natural basic liquids, *Contrib. Mineral. Petrol., 96*, 1-23, 1987.
77. Salters, V.J.M., and S.R. Hart, The hafnium paradox and the role of garnet in the source of mid-ocean-ridge basalts, *Nature, 342*, 420-422, 1989.
78. Sen, G., and D.C. Presnall, Liquidus phase relationships on the join anorthite-forsterite-quartz at 10 kbar with applications to basalt petrogenesis, *Contrib. Mineral. Petrol., 85*, 404-408, 1984.
79. Sparks, R.S.J., P. Meyer, and H. Sigurdson, Density variation amongst mid-ocean ridge basalts: implications for magma mixing and the scarcity of primitive magmas, *Earth Planet. Sci. Lett., 46*, 419-430, 1980.
80. Stolper, E., A phase diagram for mid-ocean ridge basalts: preliminary results and implications for petrogenesis, *Contrib. Mineral. Petrol., 74*, 13-27, 1980.
81. Stolper, E., and D. Walker, Melt density and the average composition of basalt, *Contrib. Mineral. Petrol., 74*, 7-12, 1980.
82. Stosch, H.-G., and H.A. Seck, Geochemistry and mineralogy of two spinel peridotite suites from Dreiser Weiher, West Germany, *Geochim. Cosmochim. Acta, 44*, 457-470, 1980.
83. Sudo, A., Stability of phlogopite in the upper mantle: implication for subduction zone magmatism, M.Sc. thesis Kyoto Univ., Kyoto, Japan, 1988.
84. Takahashi, E., Melting of a dry peridotite KLB-1 up to 14 GPa: implications on the origin of peridotitic upper mantle, *J. Geophys. Res., 91*, 9367-9382, 1986.
85. Tatsumi, Y., Migration of fluid phases and genesis of basalt magmas in subduction zones, *J. Geophys. Res., 94*, 4697-4707, 1989.
86. Thomspon, A.B., Water in the Earth's upper mantle, *Nature, 358*, 295-302, 1992.
87. Tuttle, O.F., and N.L. Bowen, Origin of granite in the light of experimental studites in the system $NaAlSi_3O_8$ - $KAlSi_3O_8$ - SiO_2 - H_2O, *Geol. Soc. Amer. Mem., 74*, 1-154, 1958.
88. Vielzeuf, D., and J.R. Holloway, Experimental determination of the fluid-absent melting relations in the pelitic system: consequences for crustal differentiation, *Contrib. Mineral. Petrol., 98*, 257-276, 1988.
89. Walker, D., T. Shibata, and S.E. DeLong, Abyssal tholeiites from the oceanographer fracture zone, II. Phase equilibria and mixing, *Contrib. Mineral. Petrol., 70*, 111-125, 1979.
90. Wallace, M.E., and D.H. Green, An experimental determination of primary carbonatite magma composition, *Nature, 335*, 343-346, 1988.
91. Whitney, J.A., The effects of pressure, temperature, and X H_2O on phase assemblage in four synthetic rock compositions, *J. Geol., 83*, 1-31, 1975.
92. Wood, B.J., Thermodynamics of multicomponent systems containing several solid solutions, In: Thermodynamic modeling of geological materials: minerals, fluids and melts, edited by I.S.E. Carmichael and H.P. Eugster, Mineralogical Society of America, *Reviews in Mineralogy, 17*, 71-95, 1987.
93. Wood, B.J., and J.R. Holloway, A thermodynamic model for subsolidus equilibria in the system CaO-MgO-Al_2O_3-SiO_2, *Geochim. Cosmochim. Acta, 48*, 159-176, 1984.
94. Wyllie, P.J., The Dynamic Earth, John Wiley & Sons, New York, pp. 416, 1971.
95. Wyllie, P.J., Magmas and volatile components, *Am. Mineral., 64*, 469-500, 1979.
96. Yamamoto, K., and S.-I.Akimoto, The system MgO-SiO_2-H_2O at high pressures and temperatures - stability field for hydroxyl-chondrodite, hydroxyl-clinohumite and 10 A-Phase, *Am. J. Sci. 277*, 288-312, 1977.
97. Yoder, H.S., and C.E. Tilley, Origin of basalt magmas: an experimental study of natural and synthetic rock systems, *J. Petrol., 3*, 342-532, 1962.
98. Zhang, J., and C. Herzberg, Melting experiments on peridotite KLB-1 to 22 GPa, *Eos Trans. AGU, 74*, in press, 1993.

Reflectance Spectra

Roger N. Clark

1. INTRODUCTION

Reflectance spectroscopy is the study of light as a function of wavelength that has been reflected or scattered from a solid, liquid, or gas. In this chapter I will discuss the reflectance spectroscopy of minerals, but the principles apply to any material.

As photons enter a mineral, some are reflected from grain surfaces, some pass through the grain, and some are absorbed. Those photons that are reflected from grain surfaces or refracted through a particle are said to be scattered. Scattered photons may encounter another grain or be scattered away from the surface so they may be detected and measured.

Photons are absorbed in minerals by several processes. The variety of absorption processes and their wavelength dependence allows us to derive information about the chemistry of a mineral from its reflected light. The human eye is a crude reflectance spectrometer: we can look at a surface and see color. Our eyes and brain are processing the wavelength-dependent scattering of visible-light photons to reveal something about what we are observing, like the red color of hematite or the green color of olivine. A modern spectrometer, however, can measure finer details over a broader wavelength range and with greater precision. Thus, a spectrometer can measure absorptions due to more processes than can be seen with the eye.

R. N. Clark, United States Geological Survey, MS 964, Box 25046; Denver Federal Center, Denver, CO 80225-0046

Rock Physics and Phase Relations
A Handbook of Physical Constants
AGU Reference Shelf 3

2. THE ABSORPTION PROCESS

When photons enter an absorbing medium, they are absorbed according to Beers Law:

$$I = I_0 e^{-kx}, \quad (1)$$

where I is the observed intensity, I_0 is the original light intensity, k is an absorption coefficient and x is the distance traveled through the medium. The absorption coefficient is traditionally expressed in units of cm^{-1} and x in cm. Equation 1 holds for a single wavelength. At other wavelengths, the absorption coefficient is different, and the observed intensity varies. The absorption coefficient as a function of wavelength is a fundamental parameter describing the interaction of photons with a material.

3. CAUSES OF ASORPTION

3.1 Electronic Processes

Isolated atoms and ions have discrete energy states. Absorption of photons of a specific wavelength causes a change from one energy state to a higher one. Emission of a photon occurs as a result of a change in an energy state to a lower one. When a photon is absorbed it is usually not emitted at the same wavelength. For example, it can cause heating of the material, resulting in grey-body emission at longer wavelengths.

In a solid, electrons may be shared between individual atoms. The energy level of shared electrons may become smeared over a range of values called "energy bands." However, bound electrons will still have quantized energy states.

The most common electronic process revealed in the spectra of minerals is due to unfilled electron shells of

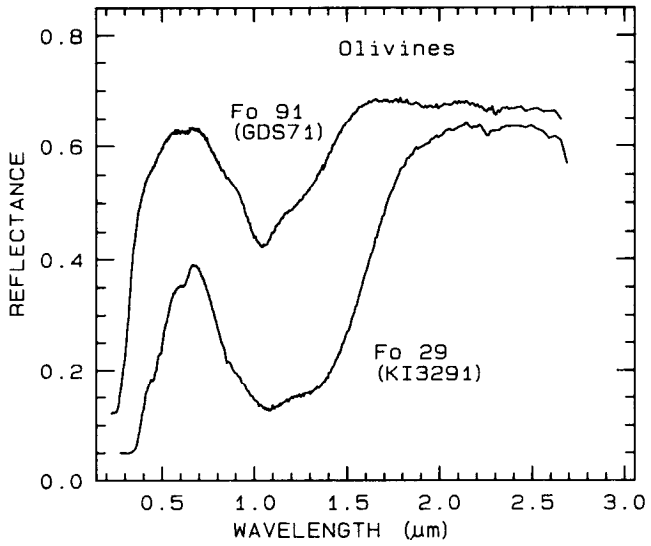

Fig. 1a. Reflectance spectra of two olivines showing the change in band position and shape with composition. The 1-μm absorption band is due to a crystal field absorption of Fe^{2+}. The Fo 29 sample (KI3291 from King and Ridley, 1987) has an FeO content of 53.65%, while the Fo 91 sample (GDS 71; labeled Twin Sisters Peak in King and Ridley, 1987) has an FeO content of 7.93%. The mean grain size is 30 and 25 μm respectively. The 1-μm band position varies from about 1.08 μm at Fo 10 to 1.05 μm at Fo 90 (King and Ridley, 1987).

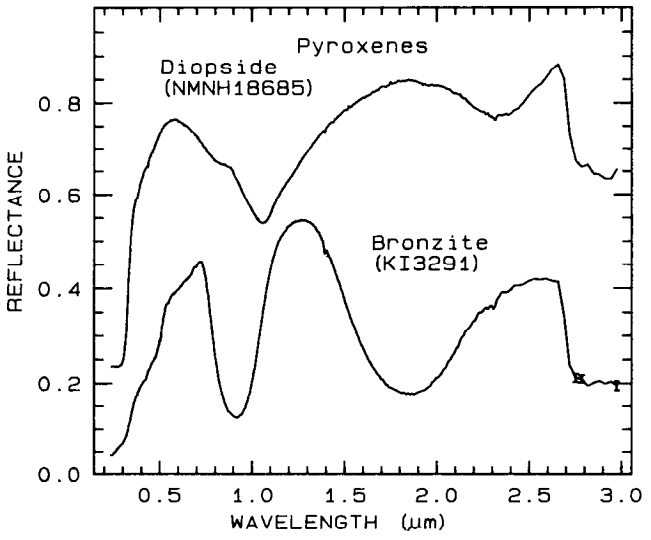

Fig. 1b. Reflectance spectra of two pyroxenes showing the change in band position and shape with composition (from Clark *et al.*, 1993b). The 1- and 2-μm bands are due to a crystal field absorption of Fe^{2+}. The 1-μm versus the 2-μm band position of a pyroxene describes the pyroxene composition (e.g. Adams 1974)

transition elements and iron is the most common transition element in minerals. For all transition elements, unfilled d orbitals have identical energies in an isolated ion, but the energy levels split when the atom is located in a crystal field. This splitting of the orbital energy states enables an electron to be moved from a lower level into a higher one by absorption of a photon having an energy matching the energy difference between the states. The energy levels are determined by the valence state of the atom (e.g. Fe^{2+}, Fe^{3+}), its coordination number, and the symmetry of the site it occupies. The levels are also influenced by the type of ligands formed, the extent of distortion of the site, and the value of the metal-ligand interatomic distance [e.g. 3]. The crystal field varies with crystal structure from mineral to mineral, thus the amount of splitting varies and the same ion (like Fe^{2+}) produces obviously different absorptions, making specific mineral identification possible from spectroscopy (Figure 1).

The unfilled shells of rare earth ions involve deep-lying electrons which are well shielded from crystal fields so the energy levels remain largely unchanged. Thus, absorption bands due to rare earth elements are not diagnostic of mineralogy but to the presence of the ions in the mineral (Figure 2).

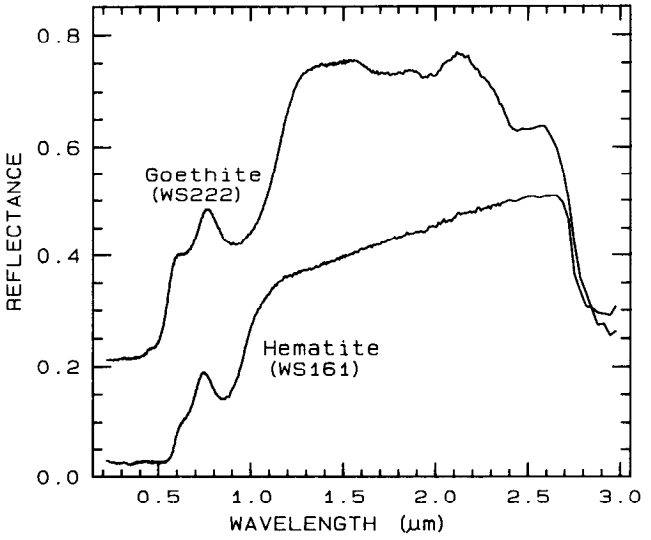

Fig. 1c. Reflectance spectra of the iron oxides hematite and goethite. The intense charge-transfer band in the UV is "saturated" in reflectance (< 0.4 μm), so only first surface reflection is seen in these spectra. The 0.9-μm and 0.86-μm bands are due Laporte-forbidden transitions (e.g. Morris *et al,* 1985; Sherman, 1990 and references therein). Spectra from Clark *et al.* (1993b).

Absorption bands can also be caused by charge transfer, or inter-element transition where the absorption of a photon causes an electron to move between ions or between ions and ligands. The transition can also occur between the same metal in different valence states, such as between Fe^{2+} and Fe^{3+}. In general, absorption bands caused by charge transfer are diagnostic of mineralogy. Their strengths are typically hundreds to thousands of times stronger than crystal field transitions. The band centers usually occur in the ultraviolet with the wings of the absorption extending into the visible, which are the main cause of the red color of iron oxides (Figure 1c).

In some minerals, there are two energy levels in which electrons may reside: a higher level called the "conduction band," where electrons move freely throughout the lattice, and a lower energy region called the "valence band," where electrons are attached to individual atoms. The difference between the energy levels is called the band gap. The band gap is typically small or non-existent in metals, and very large in dielectrics. In semiconductors, the band gap corresponds to the energy of visible or near-infrared photons and the spectrum in these cases is approximately a step function. The yellow color of sulfur is caused by such a band gap. The minerals cinnabar (HgS) and rutile (TiO_2) have spectra showing the band gap in the visible (Figure 3).

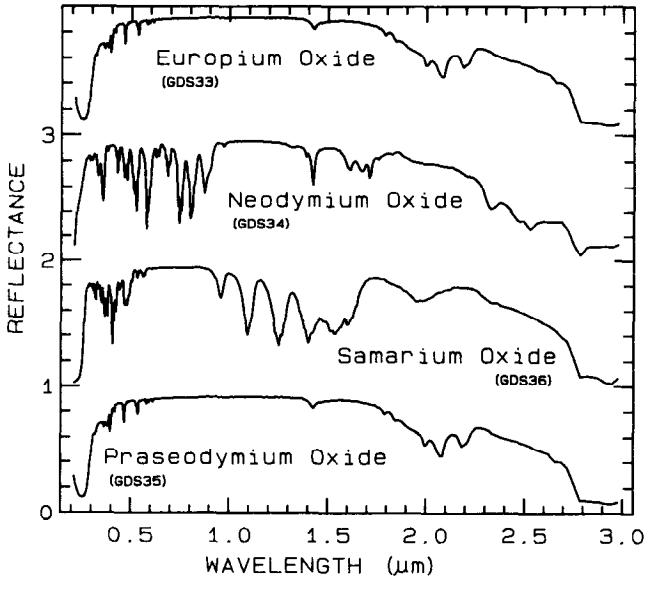

Fig. 2. Reflectance spectra of rare-earth oxides. These absorptions are due to crystal-field transitions involving deep-lying electrons of the rare-earth element. These absorptions due not shift when the rare-earth ion is in another mineral, thus the bands are indicative of the element, regardless of the mineral. Spectra from Clark *et al.* (1993b).

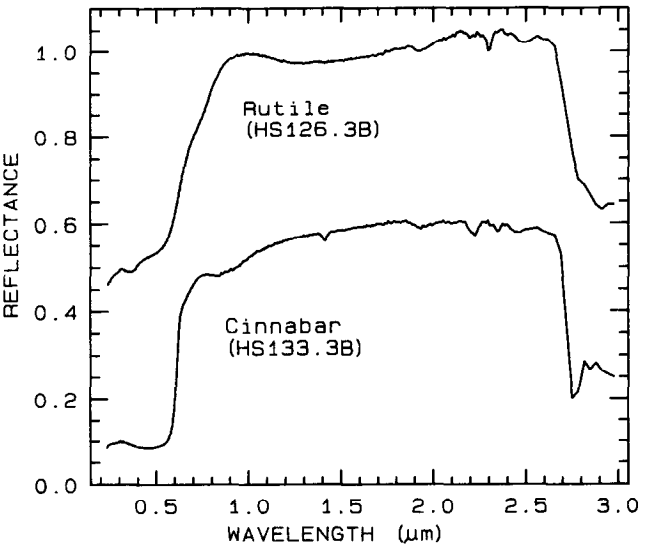

Fig. 3. Reflectance spectra of rutile (top) and cinnabar (bottom) showing conduction bands in the visible (from Clark *et al.*, 1993b).

A few minerals show color by "color centers." A color center is caused by irradiation (e.g. by solar UV radiation) of an imperfect crystal. Energy levels are produced because of the defects and electrons can become bound to them. The movement of an electron into the defect requires photon energy. The yellow, purple and blue colors of fluorite are caused by color centers.

More detailed discussions of electronic processes can be found in the review paper by Hunt [19] and the book by Burns [3].

3.2 Vibrational Processes

The bonds in a molecule or crystal lattice are like springs with attached weights: the whole system can vibrate. The frequency of vibration depends on the strength of each spring and their masses. For a molecule with N atoms, there are 3N-6 normal modes of vibrations called fundamentals. Each vibration can also occur at roughly multiples of the original fundamental frequency. The additional vibrations are called overtones when involving multiples of a single fundamental, and combinations when involving different types of vibrations. A vibrational absorption will be seen in the infrared spectrum only if the molecule responsible shows a dipole moment (it is said to be infrared active). A symmetric molecule, like N_2 is not normally infrared active unless it is distorted (for example under high pressure). Vibrations from two or more modes can occur at the same frequency, and because they can't be distinguished, are said to be degenerate. An isolated

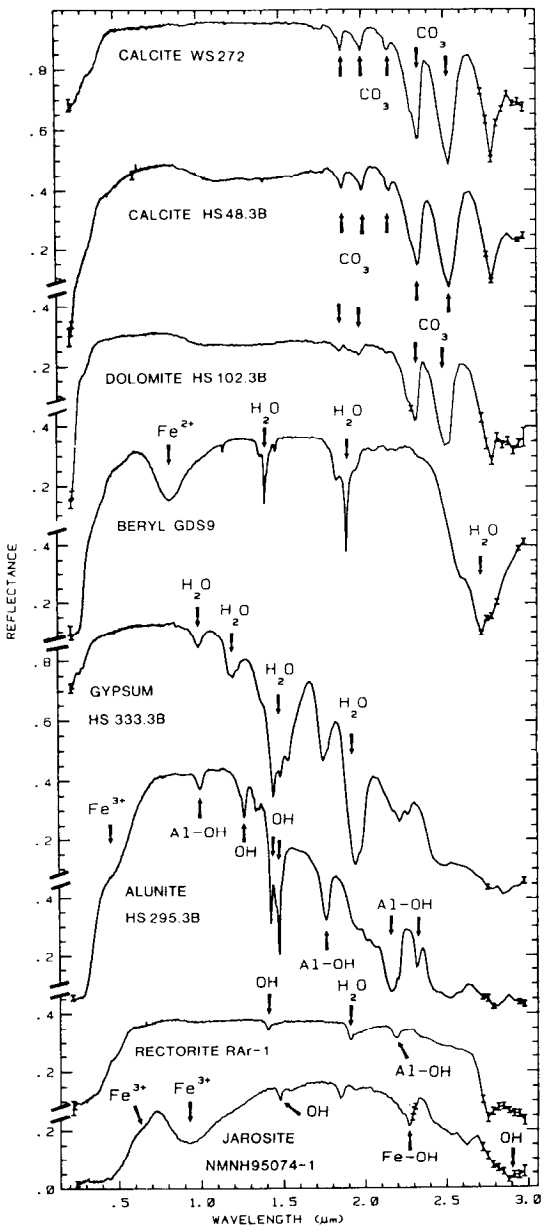

Fig. 4a. Reflectance spectra of calcite, dolomite, beryl, gypsum, alunite, rectorite, and jarosite showing vibrational bands due to OH, CO_3 and H_2O (from Clark *et al.*, 1990).

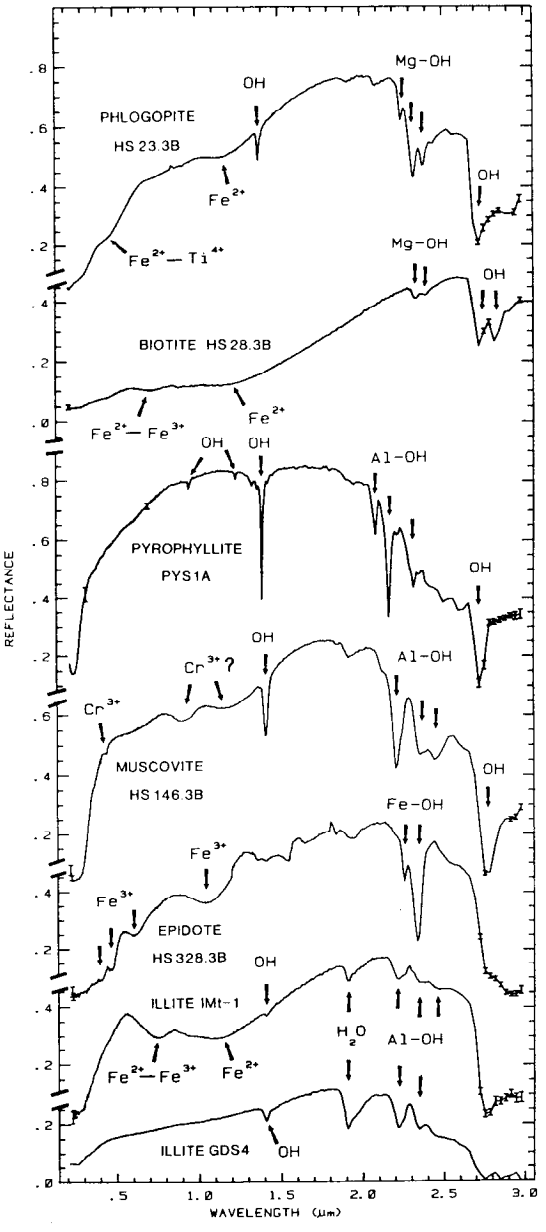

Fig. 4b. Reflectance spectra of phlogopite, biotite, pyrophyllite, muscovite, epidote, and illite showing vibrational bands due to OH and H_2O (from Clark *et al.*, 1990).

molecule with degenerate modes may show the modes at slightly different frequencies in a crystal because of the non-symmetric influences of the crystal field.

Traditionally, the frequencies of fundamental vibrations are labeled with the letter v and a subscript. If a molecule has vibrations v_1, v_2, v_3, then it can have overtones and combinations at approximately $2v_1$, $3v_1$, $2v_2$, v_1+v_2, and so on. Each higher overtone or combination is typically 30 to 100 times weaker than the last. Consequently, the spectrum of a mineral can be quite complex. In reflectance spectroscopy, these weak absorptions can be measured easily and diagnostic information routinely gained from 2nd and 3rd overtones and combinations.

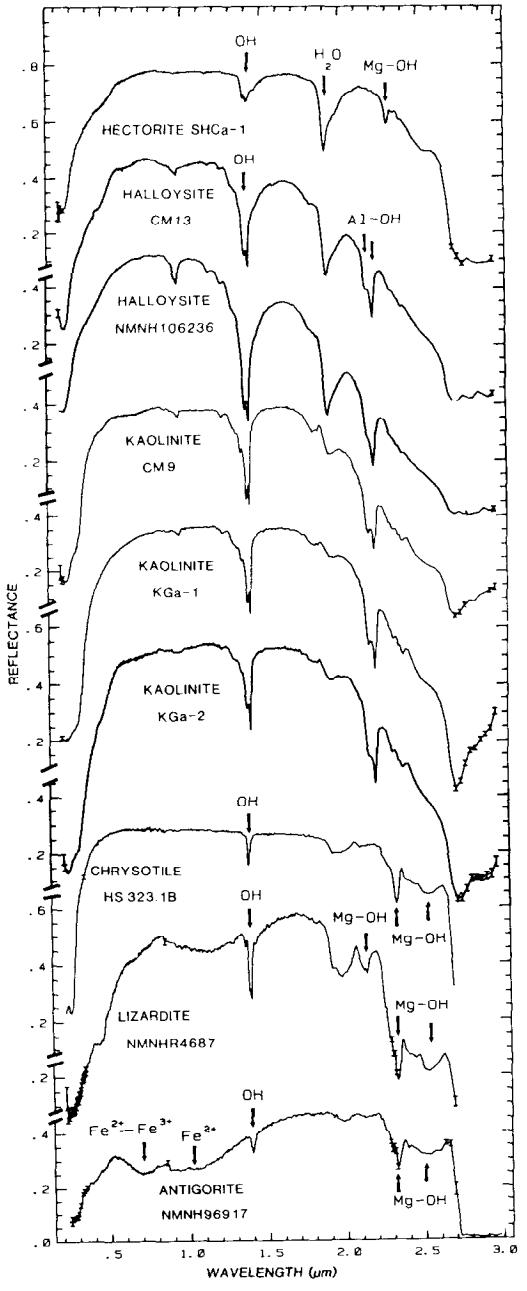

Fig. 4c. Reflectance spectra of hectorite, halloysite, kaolinite, chrysotile, lizardite, and antigorite showing vibrational bands due to OH (from Clark *et al.*, 1990). Note the subtle changes in the kaolinite doublet at 2.2-μm. Kaolinite CM9 is well crystallized while KGa-2 is poorly crystallized. The shorter wavelength band becomes less well defined as the crystallinity decreases. The chrysotile, lizardite and antigorite are isochemical members of the serpentine group, yet show subtle differences in the OH bands (King and Clark, 1989). The subtleties are more evident in higher resolution spectra shown in Figure 6.

Water and OH (hydroxyl) produce particularly diagnostic absorptions in minerals. The water molecule (H_2O) has N=3, so there are 3N-6=3 fundamental vibrations. In the isolated molecule (vapor phase) they occur at 2.738 μm (υ_1, symmetric OH stretch), 6.270 μm (υ_2, H-O-H bend), and 2.663 μm (υ_3, asymmetric OH stretch). In liquid water the frequencies shift due to hydrogen bonding: υ_1=3.106 μm, υ_2=6.079 μm, and υ_3=2.903 μm.

The overtones of water are seen in reflectance spectra of H_2O-bearing minerals. The first overtones of the OH stretches occur at about 1.4 μm and the combinations of the H-O-H bend with the OH stretches are found near 1.9 μm. Thus, a mineral whose spectrum has a 1.9-μm absorption band contains water, but a spectrum that has a 1.4-μm band but no 1.9-μm band indicates that only hydroxyl is present.

The hydroxyl ion has only one stretching mode and its wavelength position is dependent on the ion to which it is attached. In spectra of OH-bearing minerals, the absorption is typically near 2.7 to 2.8 μm, but can occur anywhere in the range from about 2.67 μm to 3.45 μm. The OH commonly occurs in multiple crystallographic sites of a specific mineral and is typically attached to metal ions. Thus there may be more than one OH feature. The metal-OH bend occurs near 10 μm (usually superimposed on the stronger Si-O fundamental in silicates). The combination metal-OH bend plus OH stretch occurs near 2.2 to 2.3 μm and is very diagnostic of mineralogy.

Carbonates also show diagnostic vibrational absorption bands. The observed absorptions are due to the planar CO_3^{-2} ion. There are four vibrational modes in the free CO_3^{-2} ion: the symmetric stretch, υ_1: 1063 cm^{-1} (9.407 μm); the out-of-plane bend, υ_2: 879 cm^{-1} (11.4 μm); the asymmetric stretch, υ_3: 1415 cm^{-1} (7.067 μm); and the in-plane bend, υ_4: 680 cm^{-1} (14.7 μm). The υ_1 band is not infrared active in minerals. There are actually six modes in the CO_3^{-2} ion, but 2 are degenerate with the υ_3 and υ_4 modes. In carbonate minerals, the υ_3 and υ_4 bands often appear as a doublet. The doubling has been explained in terms of the lifting of the degeneracy (e.g. see White, 1974) due to mineral structure and anion site.

Phosphates, borates, arsenates, and vanadates also have diagnostic vibrational spectra.

Typical spectra of minerals with vibrational bands are shown in Figure 4. See Hunt and Salisbury [21], Hunt *et al.* [22, 23, 24, 25, 26], Hunt [19, 20], Gaffey [14, 15], Clark *et al*, [7], King and Clark [27] and Farmer [13] for more details. A summary of absorption band positions is shown in Figure 5.

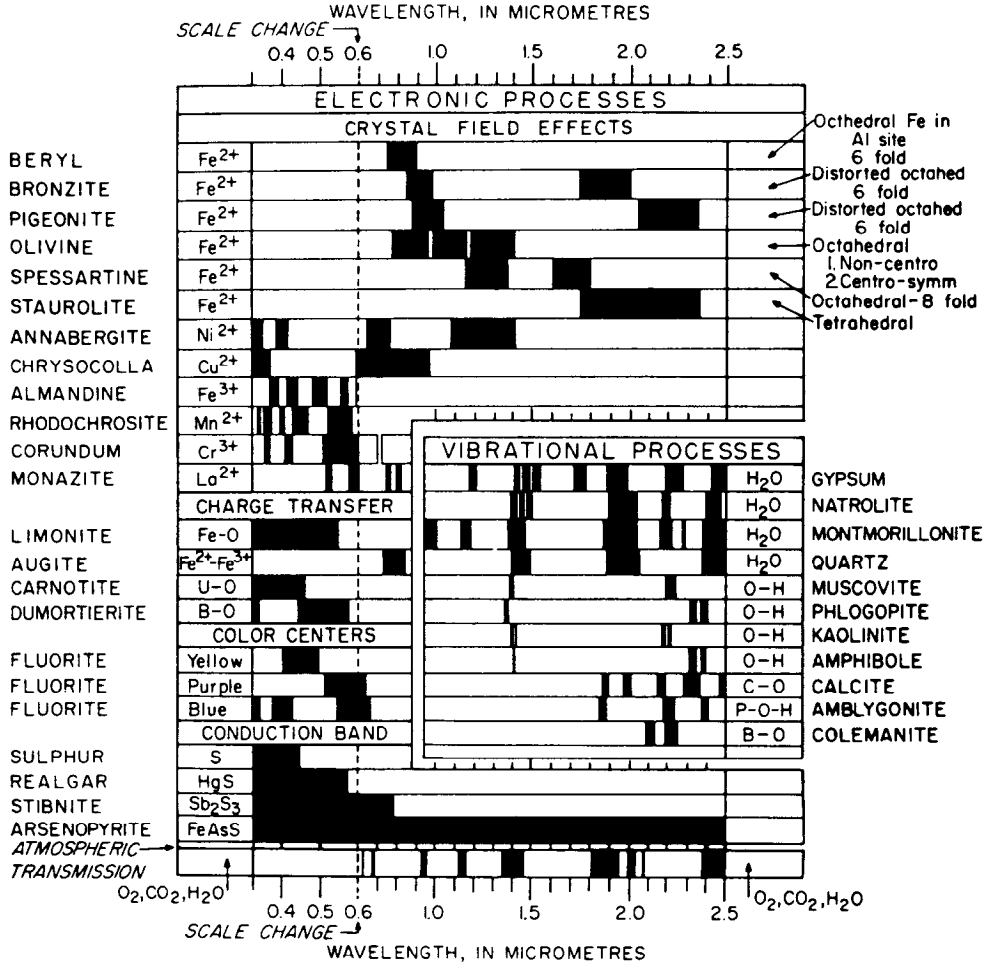

Fig. 5. Spectral signature diagram (from Hunt, 1977). The widths of the black bars indicate the relative widths of absorption bands.

4. THE SENSITIVITY OF ABSORPTION BANDS TO CRYSTAL STRUCTURE AND CHEMISTRY

Reflectance spectroscopy shows a wealth of information about mineralogy. Why, then, is spectroscopy not a more widely used technique? In many cases spectroscopy is overly sensitive to subtle changes in crystal structure or chemistry. This has resulted in confusion in the past. More recently, this sensitivity has been recognized as a powerful means of studying the structure and composition of minerals. Additional problems occur with reflectance spectra due to scattering and will be discussed below.

Because spectroscopy is sensitive to so many processes, the spectra can be very complex and there is still much to learn. However, it is because of this sensitivity that spectroscopy has great potential as a diagnostic tool. Here, a few examples of the possibilities will be shown. As shown in Figure 1b, the iron bands near 1 and 2 μm shift with pyroxene composition. This series has been calibrated by Adams [2], Cloutis *et al.* [11], and Cloutis and Gaffey [10]. The olivine 1-μm band also shifts with composition (Figure 1a), although more subtly than with pyroxenes, and the shift has been calibrated by King and Ridley [28].

The sharper OH-related absorption bands allow ever smaller band shifts to be measured. These bands can be so sensitive that it is possible to distinguish between the isochemical end-members of the Mg-rich serpentine group (chrysotile, antigorite, and lizardite; [27], and Figure 6). The Fe:Fe+Mg ratio can be estimated from reflectance spectra of minerals with brucite-like structure ([7], and

Figure 6). The structure of the 2.2-μm Al-OH band has been shown to be diagnostic of disorder of kaolinite-dickite mixtures [12] and the degree of kaolinite crystallinity [7] and is illustrated in Figure 4c.

The strong and sharp OH features have proven particularly diagnostic of clay mineralogy, perhaps better than with X-ray diffraction (XRD) analysis (like any method, spectroscopy has advantages in some areas and XRD in others). For example, it appears easy to distinguish kaolinite from halloysite with spectroscopy [e.g. 7], as shown in Figure 4c. Montmorillonite is easily distinguished from illite [e.g. 7] whereas XRD analysis combines them into the general term smectites.

Reflectance spectroscopy can be used without sample preparation, and it is non-destructive. This makes mapping of minerals from aircraft possible, including detailed clay mineralogy [e.g. 8]. Spectroscopy, on the other hand, is insensitive to some mineralogy in the visible and near-infrared wavelength region. For example, quartz has no diagnostic spectral features in the visible and near-infrared; in fact it is used as optical components in many telescopes and prisms. Quartz must be detected at its fundamental Si-O stretching region near 10 μm.

5. THE SCATTERING PROCESS

Scattering is the process that makes reflectance spectroscopy possible: photons enter a surface, are scattered one or more times, and while some are absorbed, others are scattered from the surface so we may see and detect them. Scattering can also be thought of as scrambling information. The information is made more complex, and because scattering is a non-linear process, recovery of quantitative information is difficult.

Consider the simple Beers Law in equation 1. In transmission, light passes through a slab of material. There is little or no scattering (none in the ideal case; but there are always internal reflections from the surfaces of the medium). Analysis is relatively simple. In reflectance, however, the optical path of photons is a random walk. At each grain the photons encounter, a certain percentage are absorbed. If the grain is bright, like a quartz grain at visible wavelengths, most photons are scattered and the random walk process can go on for hundreds of encounters. If the grains are dark, like magnetite, the majority of photons will be absorbed at each encounter and essentially all photons will be absorbed in only a few encounters. The random walk process, scattering and the mean depth of photon penetration are discussed in Clark and Roush [6]. This process also enhances weak features not normally seen

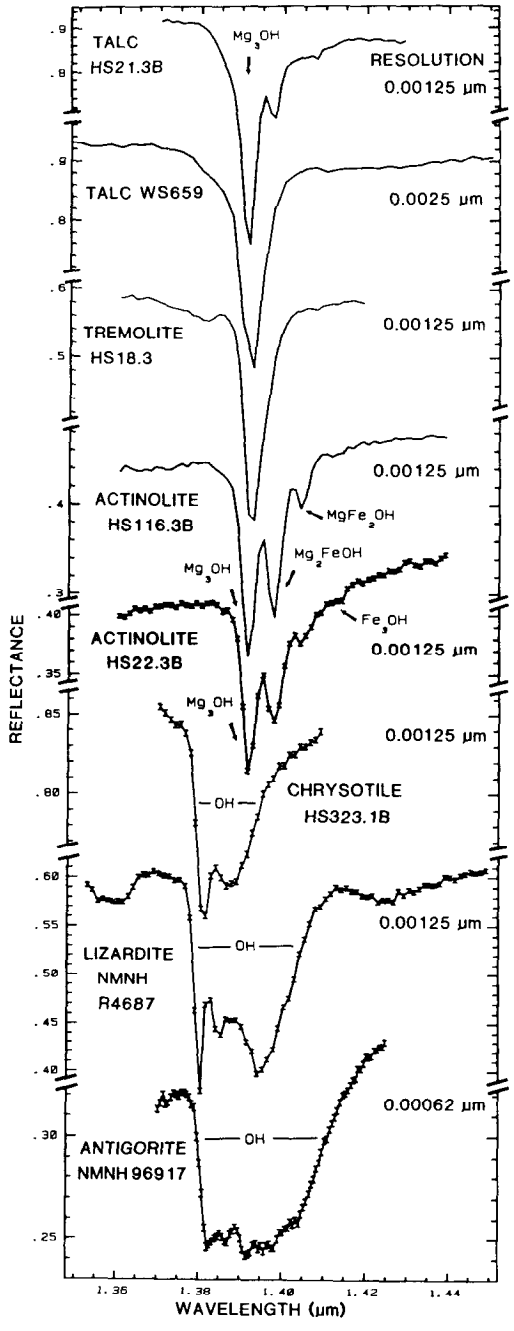

Fig. 6. High spectral resolution reflectance spectra of the first overtone of OH in talc, tremolite, actinolite, crysotile, lizardite, and antigorite. The three sharp absorption bands in talc, tremolite and actinolite are caused by Mg and Fe ions associated with the hydroxyls, causing small band shifts. The Fe:Fe+Mg ratio can be estimated. In chrysotile, lizardite and antigorite, the absorptions change with small structural differences even though the composition is constant (from Clark *et al.*, 1990).

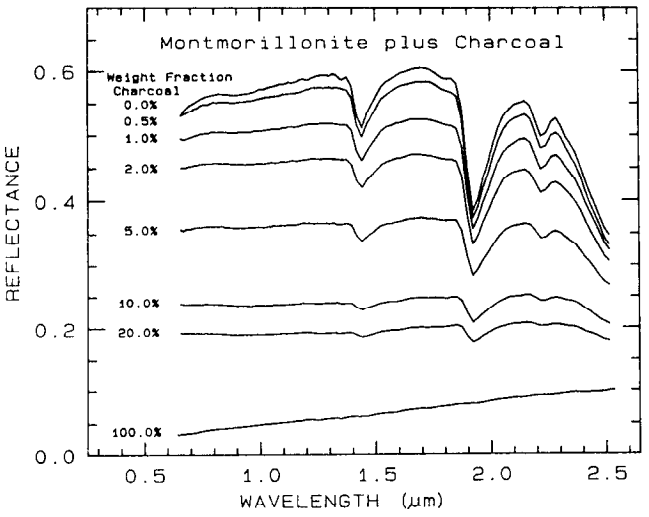

Fig. 7. Reflectance spectra of intimate mixtures of montmorillonite and charcoal illustrates the non-linear aspect of reflectance spectra of mixtures. The darkest substance dominates at a given wavelength. From Clark (1983).

in transmittance, further increasing reflectance spectroscopy as a diagnostic tool.

In a mixture of light and dark grains (e.g. quartz and magnetite) the photons have such a high probably of encountering a dark grain that a few percent of dark grains can drastically reduce the reflectance, much more than their weight fraction. A general rule with mixtures is that at any given wavelength, the darker component will tend to dominate the reflectance. The effect is illustrated in Figure 7 with spectra of samples having various proportions of charcoal grains mixed with montmorillonite.

The amount of light scattered and absorbed by a grain is dependent on grain size. A larger grain has a larger internal path where photons may be absorbed according to Beers Law. It is the reflection from the surfaces and internal imperfections that control scattering. In a smaller grain there are proportionally more surface reflections compared to internal photon path length, or in other words, the surface-to-volume ratio is a function of grain size. As the grain size increases, the reflectance decreases, as shown in the spectra for pyroxene in Figure 8.

Absorptions in a spectrum have two components: continuum and individual features. The continuum is the "background absorption" onto which other absorption features are superimposed. It may be due to the wing of a larger absorption feature. For example, in the pyroxene spectra in Figure 8, the weak feature at 2.3 μm is due to a trace amount of tremolite in the sample and the absorption is superimposed on the larger 2-μm pyroxene band. The broader pyroxene absorption is the continuum to the narrow 2.3-μm feature. The pyroxene 1.0-μm band is superimposed on the wing of a stronger absorption centered in the ultraviolet.

The depth of an absorption band, D, is usually defined relative to the continuum, R_c:

$$D = 1 - R_b / R_c \quad (2)$$

where R_b is the reflectance at the band bottom, and R_c is the reflectance of the continuum at the same wavelength as R_b.

The depth of an absorption is related to the abundance of the absorber and the grain size of the mineral. Consider a particulate surface with two minerals, one whose spectrum has an absorption band. As the abundance of the second mineral is increased, the band depth, D, of the absorption will decrease. Next consider the reflectance spectrum of a pure powdered mineral. As the grain size is increased from a small value, the absorption band depth, D, will first increase, reach a maximum, and then decrease. This can be seen with the pyroxene spectra in Figure 8. If the particle size were made larger and larger, the reflectance spectrum would eventually consist only of first surface reflection. The reflectance can never go to zero because of this reflection, unless the index of refraction of the material is 1.0.

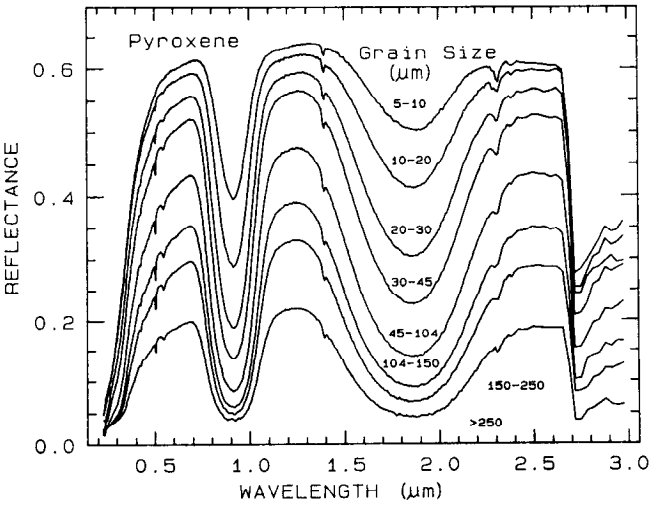

Fig. 8. Reflectance Spectra of pyroxene as a function of grain size. As the grain size becomes larger, more light is absorbed and the reflectance drops (from Clark *et al.*, 1993b).

6. QUANTITATIVE UNDERSTANDING: RADIATIVE TRANSFER TEORY

There have been many attempts over the years to quantify the scattering process. Kubelka-Munk theory was one of the first and still finds uses today. A growing popular method in some industries is log (1/R), where R is reflectance, but this is a less robust attempt at quantifying the scattering process than the decades-old Kubelka-Munk theory. This latter method is usually combined with computing the derivatives of the log (1/R) spectra and doing a correlation analysis to find particular trends. This has popularly become known as Near-Infrared Reflectance Analysis (NIRA). Either method has its uses in controlled situations, but there is a modern, more effective alternative. The limitations of these older methods are due to a poor representation of the scattering process and are discussed in Clark and Roush [6].

Fortunately, in the early 1980's three independent groups provided reasonable solutions to the complex radiative transfer problem as applied to particulate surfaces. These theories provide for non-isotropic scattering of light from particles, shadowing between particles, and first surface reflection from grain surfaces, important processes not considered in earlier theories. One theory, that of Hapke [17, 18] also provides for mixtures, and because of its relative simplicity compared to the other two, has become the dominant theory used in the planetary and to some degree the terrestrial remote sensing communities.

From the optical constants of a mineral, the reflectance can be computed from Hapke's equation 36:

$$r'(\bar{w},\lambda,\mu,g) = \frac{\bar{w}}{4}\,\frac{\mu}{\mu+\mu_o}\,\{[1+B(g)]P(g)+ H(\mu)H(\mu_o)-1\} \qquad (3)$$

where r' is the reflectance at wavelength λ, μ_o is the cosine of the angle of incident light, μ is the cosine of the angle of emitted light, g is the phase angle, $\bar{w}$ is the average single scattering albedo, B(g) is a backscatter function, P(g) is the average single particle phase function, and H is the Chandrasekhar [4] H-function for isotropic scatterers. When r' > 0.9 Hapke's approximation of the H-function shows considerable error and equation 3 deviates from measurements [17]. Because of this deviation, a table interpolation subroutine using "exact" values from Chandrasekhar [4] can be used. The table interpolation is faster computationally than the Hapke approximation, as well as being more accurate.

The single scattering albedo is the probability that a photon survives an interaction with a single particle, which includes Fresnel reflection, absorption, scattering, and diffraction due to the presence of an individual grain. Hapke [17] developed the theory further by deriving a relation between the single scattering albedo, the complex index of refraction, the grain size, and a scattering parameter to describe scattering centers within non-perfect grains. The single scattering albedo of a grain can be found from his equation 24:

$$w = S_E + \frac{(1-S_E)(1+S_E)\{r_1 + \exp[-2(k(k+s))^{1/2}\, d/3]\}}{1 - r_1 S_I + (r_1 - S_I)\exp[-2(k(k+s))^{1/2}\, d/3]} \qquad (4)$$

where S_E and S_I are the external and internal scattering coefficients, respectively, which can be computed from the complex index of refraction [17, eqn (21)], s is a scattering coefficient, d is the particle diameter, k is the absorption coefficient (note Hapke uses α instead of k here), and

$$r_1 = \frac{1 - [k/(k+s)]^{1/2}}{1 + [k/(k+s)]^{1/2}}, \qquad (5a)$$

$$= \frac{1 - [kd/(kd+sd)]^{1/2}}{1 + [kd/(kd+sd)]^{1/2}} \quad .$$

In a monomineralic surface, $w = \bar{w}$, the case studied here. For a multimineralic surface, $\bar{w}$ can be computed from equation 17 of Hapke [17]:

$$\bar{w} = \{\sum_i M_i\, w_i / (\rho_i\, d_i)\} \,/\, \{\sum_i (M_i / (\rho_i\, d_i)\}, \qquad (11)$$

where i refers to the ith component, M_i is the mass fraction, ρ_i is the density of the material, d_i the mean grain diameter, and w_i the single scattering albedo of the ith component.

With the Hapke reflectance theory, and the optical constants of minerals, reflectance spectra of pure minerals at a single grain size, spectra of a pure mineral with a grain size distribution, and mineral mixtures with varying grain size components can all be computed. Clark and Roush [6] also showed that a reflectance spectrum can be inverted to determine quantitative information on the abundances and grain sizes of each component.

5. CONCLUSIONS AND DISCUSSION

Reflectance spectroscopy is a rapidly growing science that can be used to derive significant information about mineralogy and with little or no sample preparation. It may be used in applications when other methods would be too time consuming. For example, imaging spectrometers are already acquiring millions of spatially gridded spectra over an area from which mineralogical maps are being made. It

is possible to set up real-time monitoring of processes using spectroscopy, such as monitoring the mineralogy of drill cores at the drilling site. Research is still needed to better understand the subtle changes in absorption features before reflectance spectroscopy will reach its full potential. Good spectral databases documenting all the absorption features are also needed before reflectance spectroscopy can be as widely used a tool as XRD. Spectral databases are now becoming available [e.g. 9], and research continues on the spectral properties of minerals, but it will take about a decade before general software tools are available to allow reflectance spectroscopy to challenge other analytical methods. For certain classes of minerals, however, spectroscopy is already an excellent tool. Among these classes are clay mineralogy, OH-bearing minerals, olivines and pyroxenes.

Space limits the contents of any review article covering such a broad topic. Other review articles are Adams [1], Hunt [19], Gaffey *et al.*, [16] and Salisbury [30].

Acknowledgements. This work was supported by NASA interagency agreement W15805.

REFERENCES

1. Adams, J.B., Interpretation of visible and near-infrared diffuse reflectance spectra of pyroxenes and other rock-forming minerals, in *Infrared and Raman Spectroscopy of Lunar and Terrestrial Minerals,* Academic Press, New York, 94-116, 1975.
2. Adams, J.B., Visible and Near-Infrared Diffuse Reflectance Spectra of Pyroxenes as Applied to Remote Sensing of Solid Objects in the Solar System, *J. Geophys Res.* **79,** 4829-4836, 1974.
3. Burns, R., *Mineralogical Applications of Crystal Field Theory*, Cambridge University Press, Cambridge, 551p. 1993.
4. Chandrasekhar, S., *Radiative Transfer,* Dover Publ. Inc., New York, NY, 393p, 1960.
5. Clark, R.N., Spectral Properties of Mixtures of Montmorillonite and Dark Carbon Grains: Implications for Remote Sensing Minerals Containing Chemically and Physically Adsorbed Water, *J. Geophys. Res.* **88,** 10635-10644, 1983.
6. Clark, R.N., and Roush, T.L., Reflectance spectroscopy: Quantitative analysis techniques for remote sensing applications, *J. Geophys. Res.*, **89,** 6329- 6340, 1984.
7. Clark, R.N., T.V.V. King, M. Klejwa, G. Swayze, and N. Vergo, High Spectral Resolution Reflectance Spectroscopy of Minerals, *J. Geophys Res.* **95,** 12653-12680, 1990.
8. Clark, R.N., G.A. Swayze, and A. Gallagher, Mapping Minerals with Imaging Spectroscopy, *U.S. Geological Survey, Office of Mineral Resources Bulletin 2039,* pp. 141-150, 1993a.
9. Clark, R.N., G.A. Swayze, A. Gallagher, T.V.V. King, and W.M. Calvin, The U. S. Geological Survey, Digital Spectral Library: Version 1: 0.2 to 3.0 μm, *U.S. Geological Survey, Open File Report 93-592,* 1326 pages, 1993b.
10. Cloutis, E.A., M.J. Gaffey, Pyroxene Spectroscopy revisited: Spectral-Compositional Correlations and relationships to geotherometry, *J. Geophys Res.*, **96**, 22809-22826, 1991.
11. Cloutis, E.A., M.J. Gaffey, T.L. Jackowski, and K.L. Reed, Calibrations of Phase Abundance, Composition, and Particle Size Distribution of Olivine-Orthopyroxene mixtures from Reflectance *Spectra, J. Geophys Res.*, **91**, 11641-11653, 1986.
12. Crowley, J.K. and Vergo, N., Near-infrared reflectance spectra of mixtures of kaolin group minerals: use in clay studies, *Clays and Clay Min.,* **36,** 310-316, 1988.
13. Farmer, V.C., The layer silicates, in *The Infra-Red Spectra of Minerals,* (V.C. Farmer, ed.) Mineralogical Society, London, 331-364, 1974.
14. Gaffey, S.J., Spectral reflectance of carbonate minerals in the visible and near infrared (0.35-2.55 μm): Calcite, aragonite and dolomite, *Am. Mineral.* **71,** 151-162, 1986.
15. Gaffey, S.J., Spectral reflectance of carbonate minerals in the visible and near infrared (0.35-2.55 μm): Anhydrous carbonate minerals, *J. Geophys. Res.* **92,** 1429-1440, 1987.
16. Gaffey, S.J., L.A. McFadden, D. Nash, and C.M. Pieters, Ultraviolet, Visible, and Near-infrared Reflectance Spectroscopy: Laboratory spectra of Geologic Materials, in *Remote Geochemical Analysis: Elemental and Mineralogical Composition* (C. M. Pieters, and P.A.J. Englert, eds.), Cambridge University Press, Cambridge, 43-78, 1993.
17. Hapke, B., Bidirectional reflectance spectroscopy 1. Theory, *J. Geophys. Res.* **86,** 3039-3054, 1981.
18. Hapke, B., *Introduction to the Theory of reflectance and Emittance Spectroscopy*, Cambridge University Press, New York, 1993.
19. Hunt, G.R., Spectral signatures of particulate minerals, in the visible and near-infrared, *Geophysics* **42,** 501-513, 1977.
20. Hunt, G.R., Near-infrared (1.3-2.4 μm) spectra of alteration minerals-Potential for use in remote sensing, *Geophysics* **44,** 1974-1986, 1979.
21. Hunt, G.R., and Salisbury, J.W., Visible and near infrared spectra of minerals and rocks. I. Silicate minerals, *Mod. Geology* **1,** 283-300, 1970.
22. Hunt, G.R., and Salisbury, J.W., Visible and near infrared spectra of minerals and rocks. II. Carbonates, *Mod. Geology* **2,** 23-30, 1971.
23. Hunt, G.R., Salisbury, J.W. and

Lenhoff, C.J., Visible and near infrared spectra of minerals and rocks. III. Oxides and hydroxides, *Mod. Geology* **2,** 195-205, 1971a.

24. Hunt, G.R., Salisbury, J.W. and Lenhoff, C.J., Visible and near infrared spectra of minerals and rocks. IV. Sulphides and sulphates, *Mod. Geology* **3,** 1-14, 1971b.
25. Hunt, G.R., Salisbury, J.W. and Lenhoff, C.J., Visible and near infrared spectra of minerals and rocks. V. Halides, arsenates, vanadates, and borates, *Mod. Geology* **3,** 121-132, 1972.
26. Hunt, G.R., Salisbury, J.W. and Lenhoff, C.J., Visible and near infrared spectra of minerals and rocks. VI. Additional silicates, *Mod. Geology* **4,** 85-106, 1973.
27. King, T.V.V. and Clark, R.N., Spectral characteristics of serpentines and chlorites using high resolution reflectance spectroscopy, *J. Geophys. Res.* **94,** 13997-14008, 1989.
28. King, T.V.V. and W.I. Ridley, Relation of the Spectroscopic Reflectance of Olivine to Mineral Chemistry and Some Remote Sensing Implications, *J. Geophys. Res.* **92,** 11457-11469, 1987.
29. Morris, R.V., Lauer, H.V., Lawson, C.A., Gibson, E.K. Jr., Nace, G.A., and Stewart, C. Spectral and other physiochemical properties of submicron powders of hematite (α-Fe2O3), maghemite (γ-Fe2O3), maghemite (Fe3O4), goethite (α-FeOOH), and lepidochrosite (γ-FeOOH), *J. Geophys. Res.* **90,** 3126-3144, 1985.
30. Salisbury, J.W., Mid-infrared spectroscopy: Laboratory data, in *Remote Geochemical Analysis: Elemental and Mineralogical Composition* (C. M. Pieters, and P.A.J. Englert, eds.), Cambridge University Press, Cambridge, 79-98, 1993.
31. Sherman, D.M. Crystal Chemistry, electronic structures and spectra of Fe sites in clay minerals, in *Spectroscopic Characterization of Minerals and their Surfaces* L.M. Coyne, S.W.S. McKeever, and D.F. Drake, eds.) pp. 284-309. American Chemical Society, Washington DC, 1990.

Magnetic Properties of Rocks and Minerals

Christopher P. Hunt, Bruce M. Moskowitz, Subir K. Banerjee

1. INTRODUCTION

This is an updated collation of magnetic parameters of rocks and minerals for geologists, geochemists, and geophysicists. Since the publication of the previous edition of Handbook of Physical Constants [74], two other collations have appeared [16, 18]. In addition, selected magnetic parameters have also been assembled [19, 22, 38, 41, 88]. Rather than produce a fully comprehensive collection, we have aimed for high-precision data obtained from well-characterized samples.

Both tables and figures have been used for presenting the data, and best-fit equations have been provided for some of the displayed data so that interpolations can be made easily. In an attempt to discourage the use of the outdated cgs system, all values are in the SI system (see Moskowitz, this volume). References have been cited for the sources used here. However, a more comprehensive bibliography has also been provided from which information can be extracted for samples which have not been included.

The single-crystal constants and their variation with temperature and composition are for use by rock magnetists. Paleomagnetists and magnetic anomaly modelers have been provided with the magnetic properties of rocks and polycrystalline mineral samples. Lastly, we have made an effort to address the needs of environmental magnetists, a new group of researchers who require the values of size- and composition-dependent magnetic parameters of a variety of iron-bearing minerals.

C. P. Hunt, B. M. Moskowitz, and S. K. Banerjee, University of Minnesota, Institute for Rock Magnetism and Department of Geology and Geophysics, 310 Pillsbury Drive SE, Minneapolis, MN 55455

Rock Physics and Phase Relations
A Handbook of Physical Constants
AGU Reference Shelf 3

2. MAGNETIC SUSCEPTIBILITY

Magnetic susceptibility is a measure of the magnetic response of a material to an external magnetic field. The volume susceptibility k, measured in dimensionless units, is defined as the ratio of the material magnetization J (per unit volume) to the weak external magnetic field H:

$$J = kH. \tag{1}$$

Alternatively, the specific or mass susceptibility χ, measured in units of m^3kg^{-1}, is defined as the ratio of the material magnetization J (per unit mass) to the weak external magnetic field H:

$$J = \chi H. \tag{2}$$

All materials have magnetic susceptibility, which can be either positive (paramagnetic) or negative (diamagnetic). In materials which display hysteresis, the initial slope of the hysteresis loop is taken to be the initial or low-field susceptibility χ_0. Magnetic susceptibility values are useful in geophysical exploration, and in models of both crustal magnetization and magnetic anomalies. Table 1 lists the (initial) susceptibility for common rocks and minerals.

In ferro-, ferri-, or canted antiferromagnetic materials, hysteresis and the presence of magnetic domains cause the initial susceptibility to become grain-size dependent. This dependence for magnetite is plotted in Figure 1.

Initial magnetic susceptibility is temperature dependent. The susceptibility of paramagnetic materials is inversely proportional to absolute temperature, but the susceptibility

TABLE 1. Magnetic Susceptibilities of Selected Rocks and Minerals

Rock/Mineral	Chemical Formula	Density (10^3 kg m^{-3})	Volume k (10^{-6} SI)	Mass χ (10^{-8} m^{3}kg^{-1})	References
Igneous Rocks					
andesite		2.61	170,000	6,500	114
basalt		2.99	250–180,000	8.4–6,100	95, 107, 114, 115
diabase		2.91	1,000–160,000	35–5,600	114
diorite		2.85	630–130,000	22–4,400	114, 115
gabbro		3.03	1,000–90,000	26–3,000	95, 107, 114, 115
granite		2.64	0–50,000	0–1,900	95, 107, 114, 115
peridotite		3.15	96,000–200,000	3,000–6,200	114
porphyry		2.74	250–210,000	9.2–7,700	114
pyroxenite		3.17	130,000	4,200	114
rhyolite		2.52	250–38,000	10–1,500	114
igneous rocks		2.69	2,700–270,000	100–10,000	22
average acidic igneous rocks		2.61	38–82,000	1.4–3,100	114
average basic igneous rocks		2.79	550–120,000	20–4,400	114
Sedimentary Rocks					
clay		1.70	170–250	10–15	114
coal		1.35	25	1.9	114
dolomite		2.30	-10–940	-1–41	95, 114
limestone		2.11	2–25,000	0.1–1,200	22, 107, 114, 115
red sediments		2.24	10–100	0.5–5	22
sandstone		2.24	0–20,900	0–931	107, 114, 115
shale		2.10	63–18,600	3–886	114
average sedimentary rocks		2.19	0–50,000	0–2,000	114
Metamorphic Rocks					
amphibolite		2.96	750	25	114, 115
gneiss		2.80	0–25,000	0–900	107, 114, 115
granulite		2.63	3,000–30,000	100–1,000	126
phyllite		2.74	1,600	60	114
quartzite		2.60	4,400	170	114
schist		2.64	26–3,000	1–110	114, 115
serpentine		2.78	3,100–18,000	110–630	114
slate		2.79	0–38,000	0–1,400	107, 114, 115
average metamorphic rocks		2.76	0–73,000	0–2,600	114
Non-Iron-Bearing Minerals					
graphite	C	2.16	-80–-200	-3.7–-9.3	16, 95, 107, 114
calcite	$CaCO_3$	2.83	-7.5–-39	-0.3–-1.4	16, 18, 22, 114
anhydrite	$CaSO_4$	2.98	-14–-60	-0.5–-2.0	16, 18, 95
gypsum	$CaSO_4 \cdot 2H_2O$	2.34	-13–-29	-0.5–-1.3	16, 107, 114
ice	H_2O	0.92	-9	-1	107
orthoclase	$KAlSi_3O_8$	2.57	-13–-17	-0.49–-0.67	16
magnesite	$MgCO_3$	3.21	-15	-0.48	22
forsterite	Mg_2SiO_4	3.20	-12	-0.39	16
serpentinite	$Mg_3Si_2O_5(OH)_4$	2.55	3,100–75,000	120–2,900	107
halite	NaCl	2.17	-10–-16	-0.48–-0.75	16, 18, 107, 114
galena	PbS	7.50	-33	-0.44	16
quartz	SiO_2	2.65	-13–-17	-0.5–-0.6	16, 18, 22, 73, 95
cassiterite	SnO_2	6.99	1,100	16	114
celestite	$SrSO_4$	3.96	-16–-18	-0.40–-0.450	16
sphalerite	ZnS	4.00	-31–750	-0.77–19	16, 114

TABLE 1. (continued)

Iron-Bearing Minerals					
garnets	$A_3B_2(SiO_4)_3$	3.90	2,700	69	16
illite	clay w/1.4% FeO, 4.7% Fe_2O_3	2.75	410	15	18, 22
montmorillonite	clay w/ 2.8% FeO, 3.0% Fe_2O_3	2.50	330–350	13–14	18, 22
biotites	$K(Mg,Fe)_3(AlSi_3O_{10})(OH)_2$	3.00	1,500–2,900	52–98	16, 18, 22
siderite	$FeCO_3$	3.96	1,300–11,000	32–270	16, 18, 47, 73, 114
chromite	$FeCr_2O_4$	4.80	3,000–120,000	63–2,500	114
orthoferrosilite	$FeSiO_3$	4.00	3,700	92	18
orthopyroxenes	$(Fe,Mg)SiO_3$	3.59	1,500–1,800	43–50	16, 18, 22
fayalite	Fe_2SiO_4	4.39	5,500	130	18
olivines	$(Fe,Mg)_2SiO_4$	4.32	1,600	36	16
jacobsite	$MnFe_2O_4$	4.99	25,000	500	18
franklinites	$(Zn,Fe,Mn)(Fe,Mn)_2O_4$	5.21	450,000	8,700	114
Iron Sulfides					
chalcopyrite	$CuFeS_2$	4.20	23–400	0.55–10	16, 114
arsenopyrite	FeAsS	6.05	3,000	50	114
troilite	FeS	4.83	610–1,700	13–36	16, 47, 73
pyrrhotites	$Fe_{1-x}S$	4.62	460–1,400,000	10–30,000	18, 20, 22, 29, 95, 114, 115, 127
pyrrhotite	$Fe_{11}S_{12}$	4.62	1,200	25	16
pyrrhotite	$Fe_{10}S_{11}$	4.62	1,700	38	16
pyrrhotite	Fe_9S_{10}	4.62	170,000	3,800	16
pyrrhotite	Fe_7S_8	4.62	3,200,000	69,000	16
pyrite	FeS_2	5.02	35–5,000	1–100	16, 47, 95, 114
Iron-Titanium Oxides					
hematite	α-Fe_2O_3	5.26	500–40,000	10–760	16, 18, 22, 47, 70, 73, 114, 115
maghemite	γ-Fe_2O_3	4.90	2,000,000–2,500,000	40,000–50,000	1, 115
ilmenite	$FeTiO_3$	4.72	2,200–3,800,000	46–80,000	16, 18, 22, 47, 106, 114, 115
magnetite	Fe_3O_4	5.18	1,000,000–5,700,000	20,000–110,000	16, 18, 22, 55, 61, 62, 75, 114, 115
titanomagnetite	$Fe_{3-x}Ti_xO_4$, x=0.60	4.98	130,000–620,000	2,500–12,000	18, 44, 62
titanomaghemite	$Fe_{(3-x)R}Ti_{xR}\square_{3(1-R)}O_4$, R=8/[8+z(1+x)]	4.99	2,800,000	57,000	22
ulvöspinel	Fe_2TiO_4	4.78	4,800	100	22
Other Iron-Bearing Minerals					
iron	Fe	7.87	3,900,000	50,000	22
goethite	α-FeOOH	4.27	1,100–12,000	26–280	16, 32, 47, 115
lepidocrocite	γ-FeOOH	4.18	1,700–2,900	40–70	16, 47, 115
limonite	$FeOOH{\cdot}nH_2O$	4.20	2,800–3,100	66–74	16, 115

Notes: All susceptibilities were measured in weak fields at room temperature and at one atmosphere pressure. Literature values for susceptibilities were converted to SI units when necessary, and from volume to mass normalization using accepted values for material densities [22, 73, 114]. Susceptibility values have been rounded to the number of significant figures given in the original. Most values come from other tabulations, to which the reader should refer for more information. Values for the more important magnetic minerals (magnetite, titanomagnetite, hematite, pyrrhotite, and goethite) were collated from recent original sources.

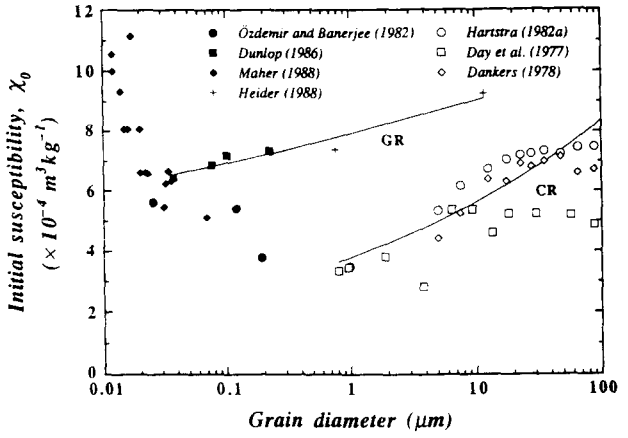

Fig. 1. The grain-size dependence of initial magnetic susceptibility (χ_0) in magnetite. Experimental data from crushed grains (open symbols) and grown crystals (closed symbols and cross). Solid lines are power-law fits for grown (GR) and crushed (CR) samples.

of diamagnetic materials has no temperature dependence. In magnetic materials, there is often a "Hopkinson peak" [e.g., 88] where susceptibility increases just below the Curie temperature before dropping to relatively small values. Examples are shown in Figure 2. The peak occurs at high temperatures because both number and mobility of domain walls in MD grains increase, and thermal activation of SD moments increases, all leading to an increase in response to an external field.

Hydrostatic pressure does not affect the magnitude of magnetic susceptibility in experiments of up to 2 kbar [e.g., 76]. However, uniaxial stress will change the susceptibility both in amount and direction, dependent on the orientation of the applied stress relative to the magnetic field. When the applied stress is parallel to the magnetic field the susceptibility decreases; when the stress and field are perpendicular, there is an increase in magnetic susceptibility [e.g., 82]. The amount of change is reversible, and is dependent both on composition and on magnetic grain size. Changes in susceptibility can be ±40% at 2 kbar of differential stress [76, 82]. However, uniaxial stresses greater than 1–2 kbar are unlikely to be sustained in materials residing at elevated temperatures in the lower crust.

Initial susceptibility is dependent upon the frequency at which it is measured. This is because susceptibility depends on the magnetic domain state of a sample, which in turn depends on the length of time over which the sample is measured or observed. The parameter known as the "frequency dependence of susceptibility" χ_{fd} is usually defined by

$$\chi_{fd} = \frac{\chi_{470Hz} - \chi_{4700Hz}}{\chi_{470Hz}} \times 100\%, \quad (3)$$

where χ_{470Hz} and χ_{4700Hz} are the susceptibility of a sample measured at 470 Hz and that measured at 4700 Hz, respectively. In magnetic materials, there is a small window of grain sizes (near 20 nm in magnetite) which will be magnetically unstable (superparamagnetic) at 470 Hz, but stable (single-domain) at 4700 Hz. Over relatively long "observation times" at 470 Hz, such a grain will appear to be magnetically unstable, and will contribute significantly to the total susceptibility of the sample. But over shorter times at 4700 Hz, the same grain will appear to be stable, and will contribute little to the total susceptibility. A sample containing a significant fraction of such grains will thus have a high value (up to about 12%) of χ_{fd}. This parameter can be used only qualitatively to detect the presence of ultrafine grains of magnetic material such as magnetite or maghemite, which are often found in soils [e.g., 115].

The susceptibility of a sample can also vary with direction, depending on the fabric of the constituent minerals. Anisotropy of magnetic susceptibility (AMS) can be used to determine sedimentary flow directions, or metamorphic deformation parameters [e.g., 57].

3. GRAIN-SIZE DEPENDENCE

Various magnetic properties show a strong grain-size dependence [e.g., 41, 111]. This dependence occurs not because of any intrinsic control of grain size on magnetization, but because these parameters are influenced by the magnetic domain state of the samples, which in turn is a

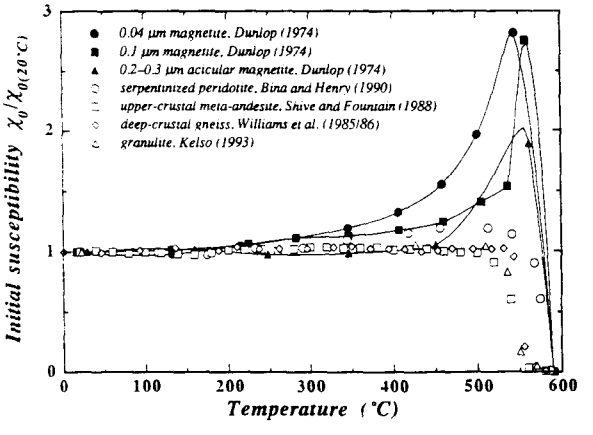

Fig. 2. Temperature dependence of initial magnetic susceptibility (χ_0) for crustal rocks and synthetic fine-grained magnetite. Note the presence of only a very weak Hopkinson peak in the rock data.

function of grain size. Domain states change from superparamagnetic (SPM), to single domain (SD), and finally to multidomain (MD) with increasing grain size. Domain-transition grain sizes depend on composition, temperature, and microstructure. Magnetic granulometry is any magnetic method for determining either the physical or the magnetic grain size of a magnetic material. Magnetic grain size refers to the magnetic domain state and behavior in a magnetic particle, regardless of the physical dimensions of the particle. Here, we are interested in magnetic granulometry of natural magnetic grains, such as magnetite (Fe_3O_4), hematite (α-Fe_2O_3), maghemite (γ-Fe_2O_3), and the various titanium-substituted compositions of these three minerals (titanomagnetite, titanohematite, and titanomaghemite). The composition of the various Fe-Ti oxides and their solid-solution series are shown in Figure 3. These minerals are found in soils, in ocean and lake sediments, and in sedimentary, igneous, and metamorphic rocks.

Both hysteresis and remanence are strongly dependent on grain size. Magnetic hysteresis results when a magnetic mineral is cycled between large positive and negative magnetic field values at room temperature. Remanence properties are measured in a field-free space after a magnetic field has been applied to a sample.

A second category of magnetic granulometry is based on measuring magnetic parameters as a function of temperature, or equivalently, as a function of thermal activation energy/stability. Examples include the frequency dependence of susceptibility discussed above, and low-temperature thermal demagnetization of remanence. In the latter case, remanence acquired at low temperature is lost upon warming, because of the thermal unblocking of magnetic grains, which is dependent on grain size.

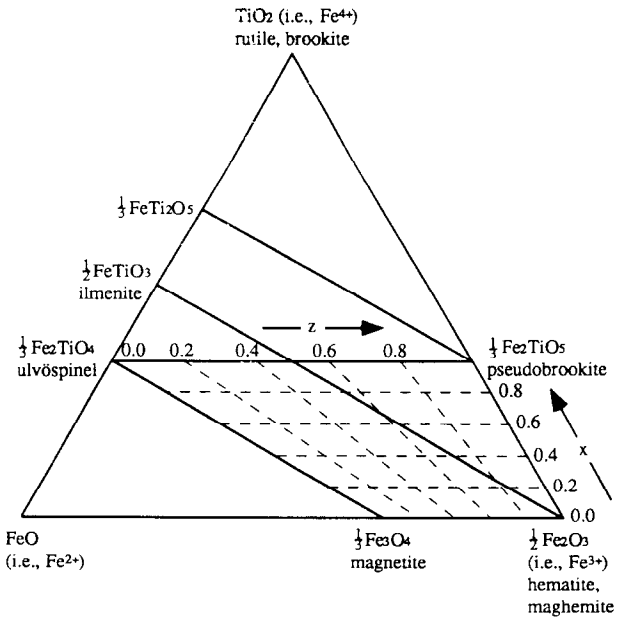

Fig. 3. Ternary diagram of the iron-titanium oxides and their solid-solution series; x is the composition parameter (Ti content) in the titanomagnetite series, and z is the oxidation parameter for titanomaghemites. Figure redrawn from [41].

TABLE 2. Reference Guide for Grain-Size Dependence of Magnetic Parameters

Mineral	References
hematite	25, 30
titanomagnetite	28, 87, 100
titanohematite	125
pyrrhotite	20, 29, 31, 35, 77, 127
goethite	32, 33, 34
maghemite	25

Magnetite has been one of the most extensively studied magnetic minerals, and the important grain-size-dependent hysteresis parameters for this mineral are presented here [e.g., 40]. References for grain-size dependent properties in other minerals systems are listed in Table 2. The grain-size dependence of coercive force (H_c), remanence coercivity (H_{cr}), and reduced saturation remanence (J_{rs}/J_s) for magnetite from various studies are plotted in Figures 4–6. The data, compiled from the literature, are from magnetites that have been synthesized by several different methods: (1) grown crystals (GR) produced either by hydrothermal recrystallization at high temperatures, or by aqueous precipitation at low temperatures [e.g., 3, 40, 55, 75]; (2) crushed grains (CR) produced by crushing and sieving large crystals [e.g., 25, 28, 50]; and (3) glass-ceramic samples (GL) produced by quenching iron-rich glasses from high temperature and then annealing at temperatures below 1000°C [128]. As shown in Figures 4–6, variations in a particular magnetic parameter, such as H_c, for the same nominal grain size are sensitive to the method of sample preparation [e.g., 40], and hence show the importance of microstructure and crystal defects on magnetic behavior. The unique stress-strain histories that different samples have experienced result in different crystal defect populations. For example, hydrothermally recrystallized samples are thought to have low residual strains and a low defect density [55]. In contrast, crushed grains that have been milled have probably undergone extensive brittle/plastic deformation at low temperatures, resulting both in a rapid increase in the number of defects and in a high defect density. The grain-size dependence and magnitude of coercivity, remanence, and susceptibility are important, and are used extensively by environmental magnetists [e.g., 115].

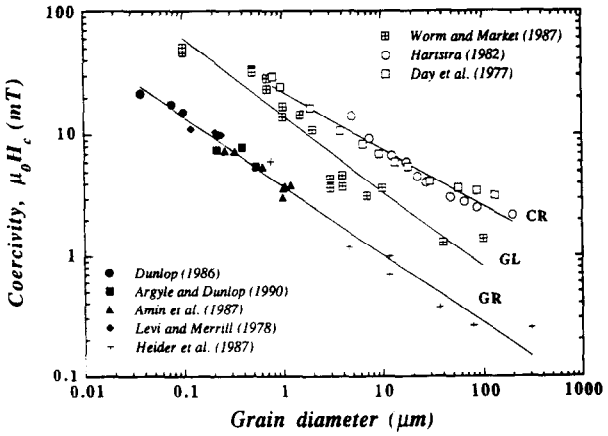

Fig. 4. Grain-size dependence of coercivity (H_c) in magnetite. Experimental data from crushed grains (open symbols), grown crystals (closed symbols and cross), and glass ceramics (hatched symbol). Solid lines are power-law fits for grown (GR), crushed (CR), and glass ceramic (GL) samples.

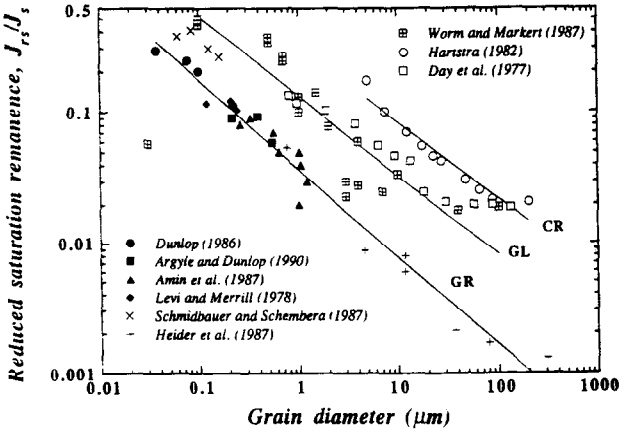

Fig. 6. Grain-size dependence of reduced saturation magnetization (J_{rs}/J_s) in magnetite. Experimental data from crushed grains (open symbols), grown crystals (closed symbols and cross), and glass ceramics (hatched symbol). Solid lines are power-law fits for grown, (GR), crushed (CR), and glass ceramic (GL) samples.

4. INTRINSIC PARAMETERS

4.1. Saturation Magnetization and Curie Temperature

Curie temperatures (T_C) and saturation magnetization (J_s) are intrinsic properties which depend on chemical composition and crystal structure. Saturation magnetization is a function of temperature and disappears at the Curie temperature. Rapid thermomagnetic measurement of T_C aids in determining the composition of magnetic mineral phases.

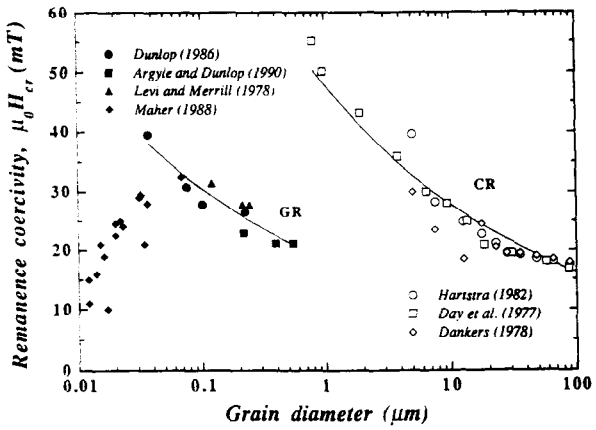

Fig. 5. Grain-size dependence of remanence coercivity (H_{cr}) in magnetite. Experimental data from crushed grains (open symbols) and grown crystals (closed symbols and cross). Solid lines are power-law fits for grown (GR) and crushed (CR) samples.

The composition dependence both of J_s (measured at room temperature) and of T_C for titanomagnetites, titanomaghemites, and titanohematites is shown in Figures 7–9; Table 3 lists T_C and J_s data for other minerals. The thermal dependence of J_s for magnetite and for hematite is given in Table 4 and in Figure 10, respectively.

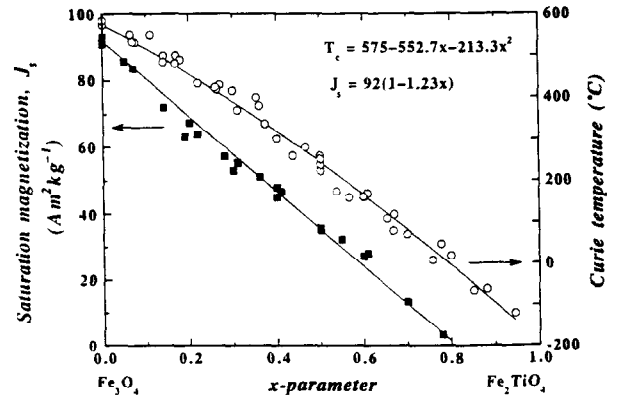

Fig. 7. Variation of room-temperature saturation magnetization (J_s) and Curie temperature (T_C) with composition (x-parameter) in the titanomagnetite ($Fe_{3-x}Ti_xO_4$) solid-solution series. End members are magnetite ($x=0$) and ulvöspinel ($x=1$). Curie temperature data denoted by open circles, and J_s data by solid squares. Solid lines are (1) linear fit to the J_s data [2, 59, 85, 100, 124]; (2) best fit second-order polynomial to T_C data [2, 85, 94, 100, 103, 120]. Best-fit equations are given in the Figure.

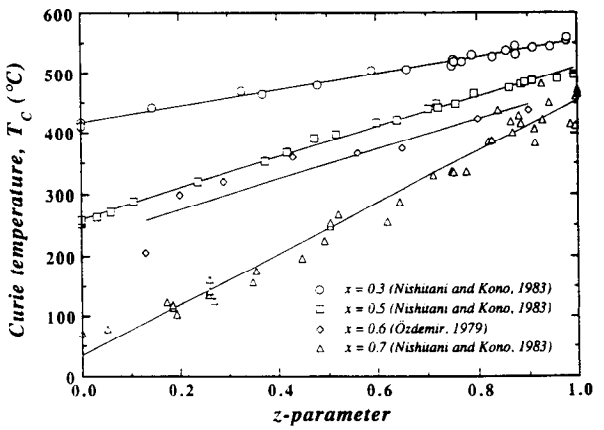

Fig. 8. Variation of Curie temperature (T_C) with degree of oxidation (z-parameter) for the titanomaghemite series ($Fe_{(3-x)R}Ti_{xR}\square_{3(1-R)}O_4$, R = 8/[8+z(1+x)], where □ denotes a lattice vacancy). Solid lines are linear best-fits for each series.

Long-range magnetic ordering below the Curie temperature is achieved by the mechanism of exchange or superexchange interactions, and is usually described by an exchange constant, A [e.g., 24], which is an important parameter in micromagnetic domain theory. From an analysis of a synthesis of published data on inelastic neutron scattering in magnetite [54], the best-fit fourth-order polynomial for the temperature dependence of $A(T)$, useful for reproducing the experimental results, is given by

$$A(T) = (-1.344 + 2.339\times10^{-2}T - 0.706\times10^{-4}T^2 + 8.578\times10^{-8}T^3 - 3.868\times10^{-11}T)\times10^{-11}\ \mathrm{Jm^{-1}}, \quad (4)$$

where T is the absolute temperature.

4.2. Magnetocrystalline Anisotropy

Magnetocrystalline anisotropy and magnetostriction arise from spin-orbit coupling of ionic magnetic moments, resulting in crystallographically controlled easy and hard directions of magnetization [e.g., 11, 24]. The magnetocrystalline anisotropy energy (E_K) for a cubic crystal is given by

$$E_K = K_1(\alpha_1^2\alpha_2^2 + \alpha_2^2\alpha_3^2 + \alpha_3^2\alpha_1^2) + K_2(\alpha_1^2\alpha_2^2\alpha_3^2), \quad (5)$$

where K_1 and K_2 are empirical anisotropy constants, and α's are the direction cosines of magnetization with respect to the principal cubic axes.

For a hexagonal crystal, anisotropy can be expressed in terms of a uniaxial constant that determines the anisotropy between the c-axis and the (0001) plane, and a triaxial constant that determines the in-plane anisotropy perpendicular to the c-axis.

The anisotropy constants depend on mineral composition, crystal structure, temperature, and pressure, but are independent of grain size. Room-temperature values of anisotropy constants for titanomagnetites, maghemite, hematite, and pyrrhotite are listed in Table 5. The values of the anisotropy constants listed in Table 5 were determined for single crystals either by high-field torque measurements [e.g., 45, 46, 113], or by analysis of magnetization curves [e.g., 5, 58]. The temperature dependence both of the basal plane anisotropy constant for hematite, as well as of K_1 for magnetite, are illustrated in Figures 10 and 11, respectively.

4.3. Low-Temperature Magnetic Transitions

Certain magnetic properties may change greatly as a function of temperature below 300 K. Such low-temperature transitions may be diagnostic of mineral composition (see Table 5). In magnetite, there is a crystallographic Verwey phase transition near 118 K [e.g., 11]. Also associated with this transition is a magnetic isotropic point (T_v)—the temperature where K_1 becomes zero as it changes sign, and the characteristic easy directions of magnetization change their orientation (see Figure 11). A remanence given either

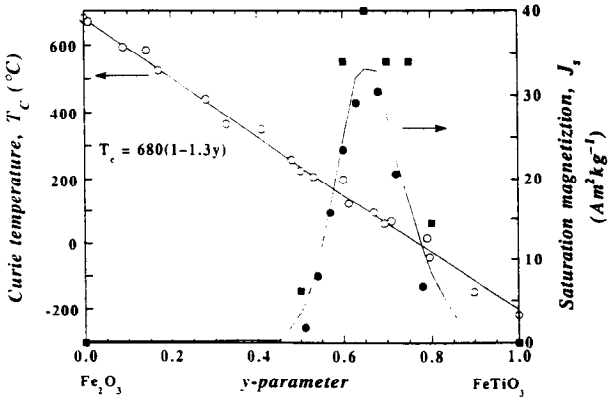

Fig. 9. Variation of room-temperature saturation magnetization (J_s) and Curie temperature (T_C) with composition (y-parameter) in the titanohematite ($Fe_{2-y}Ti_yO_3$) solid-solution series. End members are hematite (y = 0) and ilmenite (y = 1). Curie temperature data is denoted by open symbols, and J_s data by solid symbols. Solid straight line is a linear fit to the T_C data [56, 108, 120]. Best-fit equation is given in the Figure. J_s data from [125, 69]. The complex variation of J_s with composition is due to a change in magnetic ordering from canted antiferromagnetism to ferrimagnetism at $y \cong 0.45$.

TABLE 3. Magnetic Properties of Selected Minerals

Mineral	Composition	Magnetic Order	T_C[a] (°C)	J_s[b] (Am^2kg^{-1})
Oxides				
cobalt ferrite	$CoFe_2O_4$	ferrimagnetic	520	80
copper ferrite	$CuFe_2O_4$	ferrimagnetic	455	25
hematite	α-Fe_2O_3	canted antiferromagnetic	675	0.4
maghemite	γ-Fe_2O_3	ferrimagnetic	~600	70–80
ilmenite	$FeTiO_3$	antiferromagnetic	-233	
magnetite	Fe_3O_4	ferrimagnetic	575–585	90–92
ulvöspinel	Fe_2TiO_4	antiferromagnetic	-153	
magnesioferrite	$MgFe_2O_4$	ferrimagnetic	440	21
jacobsite	$MnFe_2O_4$	ferrimagnetic	~300	77
trevorite	$NiFe_2O_4$	ferrimagnetic	585	51
Sulfides				
troilite	FeS	antiferromagnetic	305	
pyrrhotite	Fe_7S_8	ferrimagnetic	320	20
greigite	Fe_3S_4	ferrimagnetic	~333	~25
Oxyhydroxides				
goethite	α-FeOOH	antiferromagnetic/weak ferromagnetic	~120	<1
feroxyhyte	δ-FeOOH	ferrimagnetic	~180	<10
lepidocrocite	γ-FeOOH	antiferromagnetic(?)	-196	
Metals and Alloys				
cobalt	Co	ferromagnetic	1131	161
wairauite	CoFe	ferromagnetic	986	235
iron	Fe	ferromagnetic	770	218
nickel	Ni	ferromagnetic	358	55
awaruite	Ni_3Fe	ferromagnetic	620	120

[a] T_C = Curie temperature (ferromagnetic materials) or Néel temperature (ferrimagnetic and antiferromagnetic materials).
[b] J_s = Saturation magnetization at room temperature.
References: [24, 78, 115].

above or below this transition will be reduced upon passing through T_v. In hematite, the transition is called the Morin transition and occurs near 263 K in bulk samples, but is suppressed in fine grains less than 20 nm because of internal dilatational strain [84]. A newly discovered transition in pyrrhotite occurs near 34 K [35, 101], but its microscopic cause is unknown. All these transition temperatures are known to be sensitive to impurities, grain size, and non-stoichiometry; in some cases, the transition can be totally suppressed [e.g., 6, 11, 111]. Thus, low-temperature remanence transitions for mineral identification should be used with caution. Depending on the type of experiment, a distinction is made in Table 5 between isotropic points (T_v), where K_1 becomes zero, and remanence transitions (T_R), where a change in remanence or susceptibility occurs.

4.4. Magnetostriction

Magnetostriction is the change in crystal dimensions that accompanies the process of magnetization, and can be defined as the strain dependence of magnetocrystalline anisotropy. The linear saturation magnetostriction constant λ is the fractional change in length $\Delta\ell/\ell$ of a material when it is magnetized from a demagnetized state to saturation. It can be positive (elongation) or negative (contraction), and it is usually anisotropic in single crystals. The microscopic origin of magnetostriction is the same spin-orbit coupling that produces magnetocrystalline anisotropy [e.g., 24].

In cubic crystals, the linear magnetostriction λ is described by the two-constant expression [e.g., 24],

$$\lambda = \tfrac{3}{2}\lambda_{100}(\alpha_1^2\beta_1^2 + \alpha_2^2\beta_2^2 + \alpha_3^2\beta_3^2 - \tfrac{1}{3}) + 3\lambda_{111}(\alpha_1\alpha_2\beta_1\beta_2 + \alpha_2\alpha_3\beta_2\beta_3 + \alpha_1\alpha_3\beta_1\beta_3), \quad (6)$$

where λ is the strain measured in the direction defined by direction cosines β_i, and α_i are the direction cosines of the magnetization. Both β_i and α_i (i = 1, 2, 3) are measured relative to the principal cubic axes. The magnetostriction

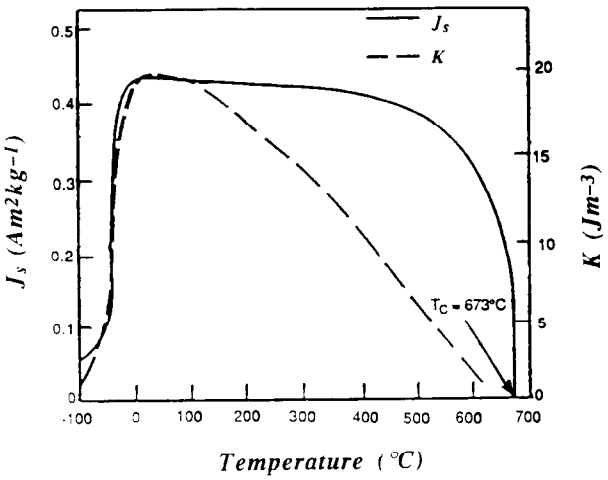

Fig. 10. Variation of saturation magnetization (J_s) and basal plane anisotropy constant (K) with temperature for a natural crystal of hematite from Ascension. Note the effect of the Morin transition below –10°C. Figure modified after [11, 45].

constants along the <100> and <111> crystal directions are λ_{100} and λ_{111}, respectively. A related parameter is the polycrystalline magnetostriction constant λ_s, given by

$$\lambda_s = \frac{3}{5}\lambda_{100} + \frac{2}{5}\lambda_{111}. \quad (7)$$

Like the magnetocrystalline anisotropy constants, magnetostriction constants vary as a function of composition, crystal structure, temperature, and pressure. Room-temperature values of single-crystal and polycrystal magnetostriction constants for titanomagnetites, maghemite, hematite, and pyrrhotite are listed in Table 5. The temperature dependence of the magnetostriction constants for magnetite is shown in Figure 12.

4.5. Pressure Dependence

Only a weak hydrostatic pressure dependence of magnetocrystalline anisotropy, magnetostriction, and Curie temperature has been detected in magnetite. The results of one study [83] were that K_1 and K_2 decrease with pressure at the rate of –0.05%/MPa (–5%/kbar), whereas λ_{100} and λ_{111} increase at the rate of +0.15%/MPa (15%/kbar). The results of another [105] were that the Curie temperature for magnetite and for various titanomagnetites increases with pressure at approximately 0.02 K/MPa (2 K/kbar).

5. REMANENCES

Remanent magnetization is the permanent magnetization of a sample in the absence of an external magnetic field, and thus occurs only in materials which exhibit hysteresis. A remanence can be a volume magnetization (magnetic moment per volume, measured in units of Am^{-1}), or a mass magnetization (magnetic moment per mass, measured in units of Am^2kg^{-1}).

Thermal remanent magnetization (TRM) is the remanence acquired by a sample when it cools to room temperature starting at or above its Curie/Néel point in the presence of an external magnetic field (usually 50–100 μT). TRM is often used as a laboratory model for the acquisition of

TABLE 4. Temperature Dependence of Saturation Magnetization in Magnetite

Absolute Temperature T (K)	Saturation Magnetization J_s^a (Am^2kg^{-1})
20.4	98.80
77.1	98.37
284.6	92.14
325.2	90.36
372.7	87.49
415.9	84.82
452.3	82.15
498.9	78.40
539.5	74.84
586.1	69.99
631.0	64.85
678.4	58.82
728.4	51.51
761.5	45.18
790.3	37.86
830.1	22.54

[a] J_{s0} = 98.86 Am^2kg^{-1} at absolute zero. Reference: [96].

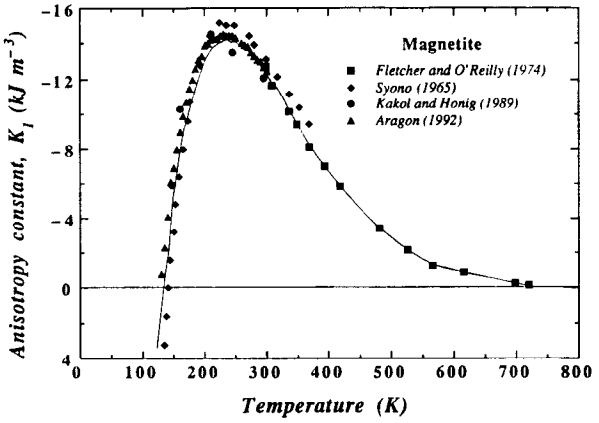

Fig. 11. Variation of first-order magnetocrystalline anisotropy constant (K_1) of magnetite with absolute temperature.

TABLE 5. Room-Temperature Values of Magnetocrystalline and Magnetostriction Constants

Mineral	K_1 ($\times 10^4$ Jm^{-3})	K_2 ($\times 10^4$ Jm^{-3})	λ_{111} ($\times 10^{-6}$)	λ_{100} ($\times 10^{-6}$)	λ_s ($\times 10^{-6}$)	T_v[a] (K)	T_R[a] (K)	References
Titanomagnetites								
Fe_3O_4 [TM0]	−1.23[b]	0.44	78	−20	39	120–130	118	5, 6, 47, 60, 113
TM04	−1.94[c]	−0.18[c]	87	−6	50	112		113
TM05	−1.5	0.2				95*		60
TM10	−2.50	0.48	96	4	59.2	92		113
TM18	−1.92		109	47	84.2			113
TM19	−2.04	1.0				<50		60
TM28	−1.92	−0.3				<50		60
TM31	−1.81		104	67	89.2			113
TM36	−1.6	0.3				68*		60
TM40			148.2	146.5	147.5			68
TM40 (PC)[d]					122.7			80
TM41	−1.4	0.3				125		60
TM52							133	117
TM55	≈0	1.4						60
TM56	−0.70					228		113
TM59							211	117
TM60			79.3	137.9	102.7			68
TM60 (PC)[d]					111.3			80
TM60							243	117
TM65							262	117
TM68	0.18					≈300		113
TM70			9.3	65.4	31.7			68
Other Minerals								
γ-Fe_3O_4	−0.46 (SCF)[d]				−(5–10) (PC)[d]	None	None	12
α-Fe_2O_3	7–188$\times 10^{-5}$[e]				≈8	263		45, 79
Fe_7S_8	11.8[f]	32.2[f]			<10[g]		35	14, 31, 110

Notes: An asterisk indicates an extrapolated value.
[a]T_v is temperature where $K_1 = 0$, T_R is temperature where a change in remanence or susceptibility occurs.
[b]Average value from listed references.
[c]Data from [60], which have the following error limits: K_1 ±5%, K_2 ±20%.
[d]PC = polycrystalline sample, SCF = single crystal thin film.
[e]In-plane anisotropy constant.
[f]K_3 and K_4 anisotropy constants.
[g]Based on domain observations [110].

remanence by magnetic minerals in newly-formed igneous rocks which cool through their Curie temperatures in the Earth's field. Experimental studies have been made on TRM as a function of grain size for magnetite (see Figure 13), and as a function of composition in titanomagnetites [e.g., 26, 87, 93, 100, 119], in titanomaghemites [e.g., 86, 89], and in titanohematites [e.g., 69, 120]. Reverse TRM has been found for certain compositions of titanohematite (see Figure 14).

Anhysteretic remanent magnetization (ARM) is a laboratory remanence acquired by a sample at room temperature during treatment in an decaying, alternating magnetic field (peak field about 100 mT) with a superimposed steady field (usually 50–100 μT). ARM has been used as an analog for TRM, but avoids the possibility of altering the magnetic minerals at high temperature. It is also commonly used in environmental magnetism for magnetic granulometry [e.g., 115]. The results of several studies of the grain-size dependence of ARM in magnetite are plotted in Figure 15.

Isothermal remanent magnetization (IRM) is a laboratory remanence acquired by a sample at after exposure to a steady external magnetic field at a given temperature. If the external field is strong enough to saturate the magnetic minerals in the sample (typically 1 T), then the remanence is

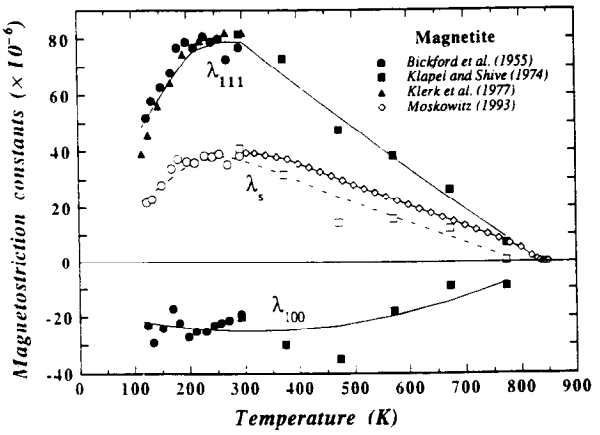

Fig. 12. Variation of magnetostriction constants (λ_{111}, λ_{100}, and λ_s) for magnetite with absolute temperature. Single crystal data from [13,67,68]; polycrystalline data from [80]. λ_s calculated from single crystal data or measured directly by [80].

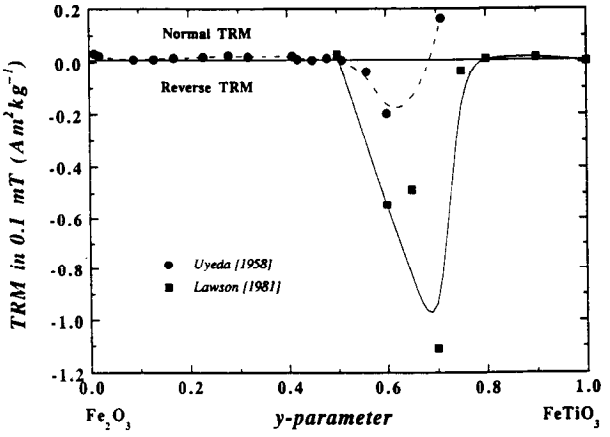

Fig. 14. Variation of weak-field TRM intensity with composition (y-parameter) for titanohematites ($Fe_{2-y}Ti_yO_3$). Note the reverse TRM acquired when titanium content is in the range 0.55 to 0.75. TRM data have been normalized to an induction field of to 0.1 mT (80 Am^{-1}, or 1 Oe).

called a saturation isothermal remanent magnetization (SIRM). SIRM is essentially the same as J_{rs} from a hysteresis loop. Variations in IRM and SIRM are related to the coercivity spectrum of a sample, and can thus be used for magnetic mineralogy determinations in environmental magnetism studies [e.g., 65].

Natural remanent magnetization (NRM) is the remanence in a rock before any demagnetization treatment in the laboratory. It is usually acquired parallel to the Earth's magnetic field at the time of formation or alteration. NRM is the most variable of magnetic parameters because it depends not only on mineralogy and grainsize, but also on the mode of remanence acquisition, and on thermal and magnetic history. Nevertheless, NRM is a critical parameter in crustal magnetization studies that try to model the sources of marine and continental magnetic anomalies. A summary of several models of oceanic crust magnetization is shown in Figure 16 [116].

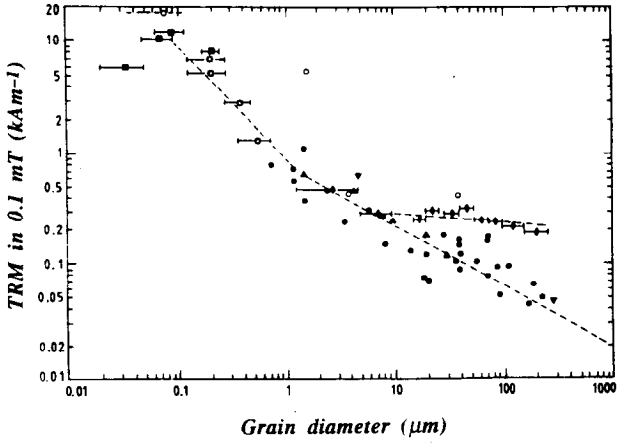

Fig. 13. Grain-size dependence of weak-field thermal remanent magnetization (TRM) intensity for magnetite. Data from crushed grains (> 1 μm), grown crystals (< 1 μm), and magnetite of other origins compiled by [41]. See original paper for references. Figure modified after [41].

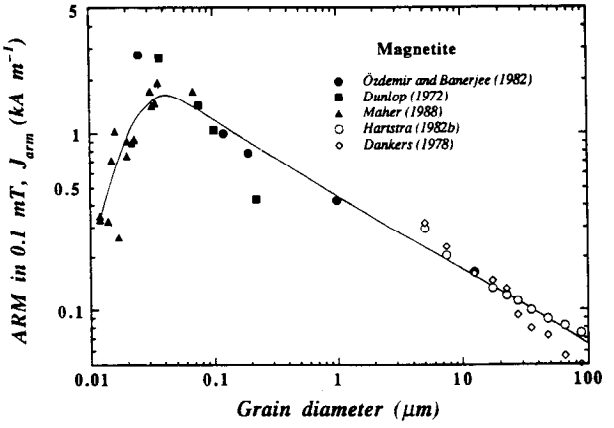

Fig. 15. Grain-size dependence of weak-field anhysteretic remanent magnetization (ARM) intensity for magnetite. Experimental data from crushed grains (open symbols) and grown crystals (closed symbols). ARM data have been normalized to an induction field of 0.1 mT (80 Am^{-1}, or 1 Oe).

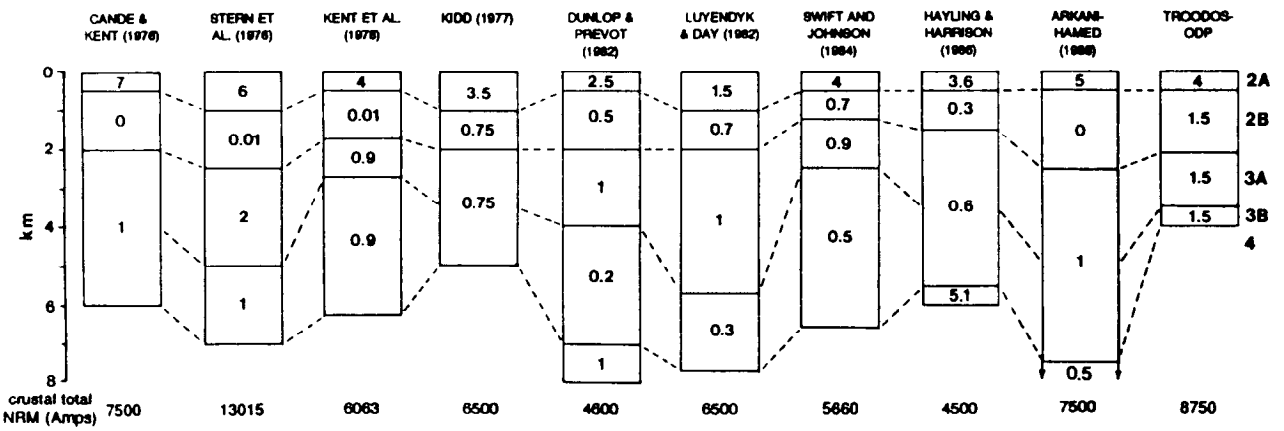

Fig. 16. Models of natural remanent magnetization (NRM) in the oceanic crust. Seismic layers are identified at right. NRM values within layers are in Am^{-1}. Values at the bottom of columns are the crustal total NRM in amperes, neglecting values from below the Moho. See original paper for references. Figure from [116].

TABLE 6. Koenigsberger Ratios for Selected Rocks

Rocks	Koenigsberger Ratio, Q_n	References
Sedimentary Rocks		
marine sediments	5	18
red sediments	1.6–6	18
siltstone	0.02–2	18
silty shale	5	18
avg sedimentary rocks	0.02–10	18, 107
Igneous Rocks		
granite	0.1–28	18, 107
granodiorite	0.1–0.2	18, 107
dolerite	2–3.5	18, 107
diabase	0.2–4	18, 107
gabbro	1–9.5	18, 107
oceanic gabbro	0.1–58.4	66
intrusions	0.1–20	18, 107
volcanics	30–50	18
subaerial basalt	1–116	18, 98
oceanic basalt	1–160	18, 107
seamounts	8–57	107
avg igneous rocks	1–40	18
Metamorphic Rocks		
granulites	0.003–50	63, 116, 122
Others		
magnetite ore	1–94	18, 107
manganese ore	1–5	107
lunar rocks	0.001–1	18

TABLE 7. Reference Guide for Other Remanences

Remanence	References
Chemical (CRM)	17, 48, 64, 91, 92, 97, 112
Depositional (DRM)	4, 7, 8, 71
Viscous (VRM)	10, 39, 43, 49

The relative importance of NRM compared with induced magnetization is characterized by the Koenigsberger ratio Q_n, a dimensionless quantity given by

$$Q_n = \mathrm{NRM} / kH_e, \tag{8}$$

where NRM is the magnitude of the natural remanent magnetization (per unit volume), k is the volume susceptibility, and H_e is the magnitude of the Earth's magnetic field at the site under consideration (H_e = 24–48 Am^{-1}, $B_e = \mu_0 H_e$ = 30–60 μT). Values of Q_n for several rock types are collected in Table 6.

Other types of remanence—including chemical (CRM), depositional (DRM), viscous (VRM)—have also been the subject of extensive study, but are not included here. The interested reader can refer to the papers cited in Table 7 for further discussion.

Acknowledgements. Thanks are due to Paul Kelso for helpful input. This is contribution number 9301 of the Institute for Rock Magnetism (IRM). The IRM is funded by the W. M. Keck Foundation, the National Science Foundation, and the University of Minnesota.

REFERENCES

1. Adnan, J., A. de Sa, and W. O'Reilly, Simultaneous measurement of the variations in the magnetic susceptibility and remanence of materials in the temperature range 10–700°C and at elevated pressure (16–160 MPa), *Meas. Sci. Technol.*, *3*, 289-295, 1992.
2. Akimoto, S., Magnetic properties of FeO–Fe_2O_3–TiO_2 system as a basis of rock magnetism, *J. Phys. Soc. Jpn.*, *17, suppl. B1*, 706-710, 1962.
3. Amin, N., S. Arajs, and E. Matijevic, Magnetic properties of uniform spherical magnetic particles prepared form ferrous hydroxide gels, *Phys. Stat. Sol. A*, *101*, 233-238, 1987.
4. Anson, G. L., and K. P. Kodama, Compaction-induced inclination shallowing of the post-depositional remanent magnetization in a synthetic sediment, *Geophys. J. R. Astr. Soc.*, *88*, 673-692, 1987.
5. Aragón, R., Cubic magnetic anisotropy of nonstoichiometric magnetite, *Phys. Rev. B*, *46*, 5334-5338, 1992.
6. Aragón, R., D. J. Buttrey, J. P. Shepherd, and J. M. Honig, Influence of nonstoichiometry on the Verwey transition, *Phys. Rev. B*, *31*, 430-436, 1985.
7. Arason, P., and S. Levi, Compaction and inclination shallowing in deep-sea sediments from the Pacific Ocean, *J. Geophys. Res.*, *95B*, 4501-4510, 1990*a*.
8. Arason, P., and S. Levi, Models of inclination shallowing during sediment compaction, *J. Geophys. Res.*, *95B*, 4481-4500, 1990*b*.
9. Argyle, K. S., and D. J. Dunlop, Low-temperature and high-temperature hysteresis of small multidomain magnetites (215–540 nm), *J. Geophys. Res.*, *95B*, 7069-7083, 1990.
10. Arkani-Hamed, J., Thermoviscous remanent magnetization of oceanic lithosphere inferred from its thermal evolution, *J. Geophys. Res.*, *94B*, 17,421-17,436, 1989.
11. Banerjee, S. K., Magnetic properties of Fe-Ti oxides, in *Oxide Minerals: Petrologic and Magnetic Significance*, vol. 25, edited by D. H. Lindsley, pp. 107-128, Mineralogical Society of America, Reviews in Mineralogy, Washington, 1991.
12. Bate, G., Recording materials, in *Ferromagnetic Materials*, *2*, edited by E. P. Wohlfarth, pp. 381-507, Elsevier North-Holland, New York, 1980.
13. Bickford, L. R., Jr., J. Pappis, and J. Stull, Magnetostriction and permeability of magnetite and cobalt-substituted magnetite, *Phys. Rev.*, *99*, 1210-1214, 1955.
14. Bin, M., and R. Pauthenet, Magnetic anisotropy in pyrrhotite, *J. Appl. Phys.*, *34*, 1161-1162, 1963.
15. Bina, M. M., and B. Henry, Magnetic properties, opaque mineralogy, and magnetic anisotropies of serpentinized peridotites from ODP Hole 670A near the mid-Atlantic ridge, *Phys. Earth Planet. Inter.*, *65*, 88-103, 1990.
16. Bleil, U., and N. Petersen, Magnetic properties, in *Landolt-Börnstein Numerical Data and Functional Relationships in Science and Technology; Group V: Geophysics and Space Research; vol. 1b, Physical Properties of Rocks*, edited by G. Angenheister, pp. 308-432, Springer-Verlag, New York, 1982.
17. Brown, K., and W. O'Reilly, The effect of low temperature oxidation on the remanence of TRM-carrying titanomagnetite $Fe_{2.4}Ti_{0.6}O_4$, Phys. Earth Planet. Inter., 52, 108-116, 1988.
18. Carmichael, R. S. (Ed.), *Practical Handbook of Physical Properties of Rocks and Minerals*, 741 pp., CRC Press, Boca Raton, FL, 1989.
19. Clark, D. A., Comments on magnetic petrophysics, *Bull. Aust. Soc. Explor. Geophys.*, *14*, 49-62, 1983.
20. Clark, D. A., Hysteresis properties of sized dispersed monoclinic pyrrhotite grains, *Geophys. Res. Lett.*, *11*, 173-176, 1984.
21. Coey, J. M. D., Magnetic properties of iron in soil iron oxides and clay minerals, in *Iron in Soils and Clay Minerals*, edited by J. W. Stucki, B. A. Goodman, and U. Schwertmann, pp. 397-466, Reidel Publishing, Dordrecht, 1988.
22. Collinson, D. W., *Methods in Rock Magnetism and Palaeomagnetism: Techniques and Instrumentation*, vol. 11, 503 pp., Chapman and Hall, New York, 1983.
23. Craik, D. J., *Structure and Properties of Magnetic Materials*, 244 pp., Pion, Ltd., London, 1971.
24. Cullity, B. D., *Introduction to Magnetic Materials*, 666 pp., Addison-Wesley, Reading, MA, 1972.
25. Dankers, P. H. M., Magnetic properties of dispersed natural iron-oxides of known grain-size, Ph. D. Dissertation, University of Utrecht, 1978.
26. Day, R., The effect of grain size on the magnetic properties of the magnetite–ulvöspinel solid solution series, Ph. D. Dissertation, University of Pittsburgh, 1973.
27. Day, R., TRM and its variation with grain size: a review, *J. Geomagn. Geoelectr.*, *29*, 233-265, 1977.
28. Day, R., M. Fuller, and V. A. Schmidt, Hysteresis properties of titanomagnetites: grain-size and compositional dependence, *Phys. Earth Planet. Inter.*, *13*, 260-266, 1977.
29. Dekkers, M. J., Magnetic properties of natural pyrrhotite Part I: Behaviour of initial susceptibility and saturation-magnetization-related rock-magnetic parameters in a grain-size dependent framework, *Phys. Earth Planet. Inter.*, *52*, 376-393, 1988.
30. Dekkers, M. J., Rock magnetic properties of fine-grained natural low-temperature haematite with reference to remanence acquisition mechanisms in red beds, *Geophys. J. Int.*, *99*, 1-18, 1989*a*.
31. Dekkers, M. J., Magnetic properties of natural pyrrhotite. II. High- and low-temperature behavior of J_{rs} and TRM as a function of grain size, *Phys. Earth Planet. Inter.*, *57*, 266-283, 1989*b*.
32. Dekkers, M. J., Magnetic properties of natural goethite—I. Grain-size dependence of some low- and high-field related rock magnetic parameters measured at room temperature, *Geophys. J.*, *97*, 323-340, 1989*c*.
33. Dekkers, M. J., Magnetic properties of natural goethite—II. TRM behaviour during thermal and alternating field demagnetization and low-temperature treatment, *Geophys. J.*, *97*, 341-355, 1989*d*.
34. Dekkers, M. J., Magnetic properties of natural goethite—III. Magnetic behaviour and properties of minerals originating from goethite dehydration

during thermal demagnetization, *Geophys. J. Int.*, *103*, 233-250, 1990.

35. Dekkers, M. J., J.-L. Mattéi, G. Eillon, and P. Rochette, Grain-size dependence of the magnetic behavior of pyrrhotite during its low-temperature transition at 34K, *Geophys. Res. Lett.*, *16*, 855-858, 1989.
36. Dunlop, D. J., Grain-size dependence of anhysteresis in iron oxide micropowders, *IEEE Trans. Magn., MAG-8*, 211-213, 1972.
37. Dunlop, D. J., Thermal enhancement of magnetic susceptibility, *J. Geophys.*, *40*, 4339-4351, 1974.
38. Dunlop, D. J., The rock magnetism of fine particles, *Phys. Earth Planet. Inter.*, *26*, 1-26, 1981.
39. Dunlop, D. J., Viscous magnetization of 0.04–100 μm magnetites, *J. Geophys.*, *74*, 667-687, 1983.
40. Dunlop, D. J., Hysteresis properties of magnetite and their dependence on particle size: a test of pseudo-single-domain remanence models, *J. Geophys. Res.*, *91B*, 9569-9584, 1986.
41. Dunlop, D. J., Developments in rock magnetism, *Rep. Prog. Phys.*, *53*, 707-792, 1990.
42. Dunlop, D. J., and K. S. Argyle, Thermoremanence and anhysteretic remanence of small multidomain magnetites, *J. Geophys. Res.*, *95B*, 4561-4577, 1990.
43. Dunlop, D. J., and Ö. Özdemir, Alternating field stability of high-temperature viscous remanent magnetization, *Phys. Earth Planet. Inter.*, *65*, 188-196, 1990.
44. Dunlop, D. J., Ö. Özdemir, and R. J. Enkin, Multidomain and single-domain relations between susceptibility and coercive force, *Phys. Earth Planet. Inter.*, *49*, 181-191, 1987.
45. Flanders, P. J., and W. J. Scheuele, Temperature-dependent magnetic properties of hematite single crystals, Proceedings of the International Conference on Magnetism, Nottingham, U. K., 1964.
46. Fletcher, E. J., and W. O'Reilly, Contribution of Fe^{2+} ions to the magnetocrystalline anisotropy constant K_1 of $Fe_{3-x}Ti_xO_4$ ($0 < x < 0.1$), *J. Phys. C*, *7*, 171-178, 1974.
47. Foëx, G., C.-J. Gorter, and L.-J. Smits, *Constantes Sélectionées: Diamagnétisme et Paramagnétisme; Relaxation Paramagnétique*, vol. 7, 317 pp., Union Internationale de Chimie, Masson & Cie., Paris, 1957.
48. Gapeev, A. K., S. K. Gribov, D. J. Dunlop, Ö. Özdemir, and V. P. Shcherbakov, A direct comparison of the properties of CRM and VRM in the low-temperature oxidation of magnetites, *Geophys. J. Int.*, *105*, 407-418, 1991.
49. Halgedahl, S. L., Experiments to investigate the origin of anomalously elevated unblocking temperatures, *J. Geophys. Res.*, *in press*, 1993.
50. Hartstra, R. L., Grain-size dependence of initial susceptibility and saturation magnetization-related parameters of four natural magnetites in the PSD-MD range, *Geophys. J. R. Astr. Soc.*, *71*, 477-495, 1982*a*.
51. Hartstra, R. L., A comparative study of the ARM and I_{rs} of some natural magnetites of MD and PSD grain size, Geophys. *J. R. Astr. Soc.*, *71*, 497-518, 1982*b*.
52. Hartstra, R. L., TRM, ARM, and I_{rs} of two natural magnetites of MD and PSD grain size, *Geophys. J. R. Astr. Soc.*, *73*, 719-737, 1983.
53. Heider, F., Magnetic properties of hydrothermally grown Fe_3O_4 crystals, Ph. D. Dissertation, University of Toronto, 1988.
54. Heider, F., and W. Williams, Note on temperature dependence of exchange constant in magnetite, *Geophys. Res. Lett.*, *15*, 184-187, 1988.
55. Heider, F., D. J. Dunlop, and N. Sugiura, Magnetic properties of hydrothermally recrystallized magnetite crystals, *Science*, *236*, 1287-1290, 1987.
56. Ishikawa, Y., and S. Akimoto, Magnetic properties of the $FeTiO_3$–Fe_2O_3 solid solution series, *J. Phys. Soc. Jpn.*, *12*, 1083-1098, 1957.
57. Jackson, M. J., and L. Tauxe, Anisotropy of magnetic susceptibility and remanence: developments in the characterization of tectonic, sedimentary, and igneous fabric, *Rev. Geophys.*, *29, suppl. (IUGG Report–Contributions in Geomagnetism and Paleomagnetism)*, 371-376, 1991.
58. Kakol, Z., and J. M. Honig, Influence of deviations from ideal stoichiometry on the anisotropy parameters of magnetite $Fe_{3(1-\delta)}O_4$, *Phys. Rev. B*, *40*, 9090-9097, 1989.
59. Kakol, Z., J. Sabol, and J. M. Honig, Cation distribution and magnetic properties of titanomagnetites $Fe_{3-x}Ti_xO_4$ ($0 \quad x < 1$), *Phys. Rev. B*, *43*, 649-654, 1991*a*.
60. Kakol, Z., J. Sabol, and J. M. Honig, Magnetic anisotropy of titanomagnetites $Fe_{3-x}Ti_xO_4$, $0 \quad x \quad 0.55$, *Phys. Rev. B*, *44*, 2198-2204, 1991*b*.
61. Kapicka, A., Magnetic susceptibility under hydrostatic pressure of synthetic magnetite samples, *Phys. Earth Planet. Inter.*, *70*, 248-252, 1992.
62. Kean, W. F., R. Day, M. Fuller, and V. A. Schmidt, The effect of uniaxial compression on the initial susceptibility of rocks as a function of grain size and composition of their constituent titanomagnetites, *J. Geophys. Res.*, *81*, 861-872, 1976.
63. Kelso, P. R., S. K. Banerjee, and C. Teyssier, The rock magnetic properties of the Arunta Block, central Australia and their implication for the interpretation of long wavelength magnetic anomalies, *J. Geophys. Res., in press*, 1993.
64. Kelso, P. R., S. K. Banerjee, and H.-U. Worm, The effect of low-temperature hydrothermal alteration on the remanent magnetization of synthetic titanomagnetites: a case for the acquisition of chemical remanent magnetization, *J. Geophys. Res.*, *96B*, 19,545-19,553, 1991.
65. King, J. W., and J. E. T. Channell, Sedimentary magnetism, environmental magnetism, and magnetostratigraphy, *Rev. Geophys., 29, suppl. (IUGG Report–Contributions in Geomagnetism and Paleomagnetism)*, 358-370, 1991.
66. Kikawa, E., and J. Pariso, Magnetic properties of gabbros from hole 735B at the Southwest Indian Ridge, *Proc. ODP Sci. Res.*, *118*, 285-307, 1991.
67. Klapel, G. D., and P. N. Shive, High-temperature magnetostriction of magnetite, *J. Geophys. Res.*, *79*, 2629-2633, 1974.
68. Klerk, J., V. A. M. Brabers, and A. J. M. Kuipers, Magnetostriction of the mixed series $Fe_{3-x}Ti_xO_4$, *J. Phys.*, *38 C1*, 87-189, 1977.

University, 1981.

70. Lefever, R. A., Fe oxides and Fe-Me-O compounds, in *Landolt-Börnstein Numerical Data and Functional Relationships in Science and Technology; Group III: Crystal and Solid State Physics; vol. 12b, Magnetic and Other Properties of Oxides and Related Compounds*, edited by K.-H. Hellwege and A. M. Hellwege, pp. 1-53, Springer-Verlag, New York, 1980.
71. Levi, S., and S. K. Banerjee, On the origin of inclination shallowing in redeposited sediments, *J. Geophys. Res., 95B*, 4383-4390, 1990.
72. Levi, S., and R. T. Merrill, Properties of single domain, pseudo-single domain, and multidomain magnetite, *J. Geophys. Res., 83B*, 309-323, 1978.
73. Lide, D. R. (Ed.), *CRC Handbook of Chemistry and Physics*, 73rd ed., CRC Press, Boca Raton, FL, 1992.
74. Lindsley, D. H., G. E. Andreasen, and J. R. Balsley, Magnetic properties of rocks and minerals, in *Handbook of Physical Constants, Memoir 97*, edited by S. P. Clark, pp. 543-552, Geological Society of America, New York, 1966.
75. Maher, B. A., Magnetic properties of some synthetic submicron magnetites, *Geophys. J., 94*, 83-96, 1988.
76. Martin, R. J., III, Is piezomagnetism influenced by microcracks during cyclic loading?, *J. Geomagn. Geoelectr., 32*, 741-755, 1980.
77. Menyeh, A., and W. O'Reilly, The magnetization process in monoclinic pyrrhotite (Fe_7S_8) particles containing few domains, *Geophys. J. Int., 104*, 387-399, 1991.
78. Merrill, R. T., and M. W. McElhinny, *The Earth's Magnetic Field: Its History, Origin, and Planetary Perspective*, vol. 32, 401 pp., Academic Press, Orlando, 1983.
79. Mizushima, K. T., and K. Iida, Effective in-plane anisotropy field in α-Fe_2O_3, *J. Phys. Soc. Jpn., 26*, 1521-1526, 1969.
80. Moskowitz, B. M., High-temperature magnetostriction of magnetite and titanomagnetites, *J. Geophys. Res., 98B*, 359-371, 1993.
81. Nagata, T., *Rock Magnetism*, 2nd ed., 350 pp., Maruzen, Tokyo, 1961.
82. Nagata, T., Basic magnetic properties
69. Lawson, C. A., Magnetic and microstructural properties of minerals of the ilmenite-hematite solid solution series with special reference to the phenomenon of reverse thermoremanent magnetism, Ph. D. Dissertation, Princeton of rocks under the effect of mechanical stresses, *Tectonophys., 9*, 167-195, 1970.
83. Nagata, T., and H. Kinoshita, Effect of hydrostatic pressure on magnetostriction and magnetocrystalline anisotropy of magnetite, *Phys. Earth Planet. Inter., 1*, 44-48, 1967.
84. Nininger, R. C., Jr., and D. Schroeer, Mössbauer studies of the Morin transition in bulk and microcrystalline α-Fe_2O_3, *J. Phys. Chem. Solids, 39*, 137-144, 1978.
85. Nishitani, T., and M. Kono, Curie temperature and lattice constant of oxidized titanomagnetite, *Geophys. J. R. Astr. Soc., 74*, 585-600, 1983.
86. Nishitani, T., and M. Kono, Effect of low-temperature oxidation on the remanence properties of titanomagnetites, *J. Geomag. Geoelectr., 41*, 19-38, 1989.
87. O'Donovan, J. B., D. Facey, and W. O'Reilly, The magnetization process in titanomagnetite ($Fe_{2.4}Ti_{0.6}O_4$) in the 1–30 μm particle size range, *Geophys. J. R. Astr. Soc., 87*, 897-916, 1986.
88. O'Reilly, W., *Rock and Mineral Magnetism*, 230 pp., Blackie, Glasgow, 1984.
89. Özdemir, Ö., An experimental study of thermoremanent magnetization acquired by synthetic monodomain titanomagnetites and titnomaghemites, Ph. D. Dissertation, University of Newcastle upon Tyne, 1979.
90. Özdemir, Ö., and S. K. Banerjee, A preliminary magnetic study of soil samples from west-central Minnesota, *Earth Planet. Sci. Lett., 59*, 393-403, 1982.
91. Özdemir, Ö., and D. J. Dunlop, Crystallization remanent magnetization during the transformation of maghemite to hematite, *J. Geophys. Res., 93B*, 6530-6544, 1988.
92. Özdemir, Ö., and D. J. Dunlop, Chemico-viscous remanent magnetization in the Fe_3O_4–γFe_2O_3 system, *Science, 243*, 1043-1047, 1989.
93. Özdemir, Ö., and W. O'Reilly, An experimental study of thermoremanent magnetization acquired by synthetic monodomain titanomaghemites, *J. Geomag. Geoelectr., 34*, 467-478, 1983.
94. Ozima, M., and E. E. Larson, Low- and high-temperature oxidation of titanomagnetite in relation to irreversible changes in the magnetic properties of submarine basalts, *J. Geophys. Res., 75*, 1003-1018, 1970.
95. Parasnis, D. S., *Principles of Applied Geophysics*, 3rd ed., 275 pp., Chapman and Hall, London, 1979.
96. Pauthenet, R., Variation thermique de l'aimantation spontaneé des ferrites de nickel, cobalt, fer et manganèse, *C. R. Acad. Sci. (Paris), Sér. B, 230*, 1842-1844, 1950.
97. Pick, T., and L. Tauxe, Chemical remanent magnetization in synthetic Fe_3O_4, *J. Geophys. Res., 96B*, 9925-9936, 1991.
98. Radhakrishnamurty, C., and E. R. Deutsch, Magnetic techniques for ascertaining the nature of iron oxide grains in basalts, *J. Geophys., 40*, 453-465, 1974.
99. Radhakrishnamurty, C., S. D. Likhite, E. R. Deutsch, and G. S. Murthy, A comparison of the magnetic properties of synthetic titanomagnetites and basalts, *Phys. Earth Planet. Inter., 26*, 37-46, 1981.
100. Robins, B. W., Remanent magnetization in spinel iron-oxides, Ph. D. Dissertation, University of New South Wales, 1972.
101. Rochette, P., et al., Magnetic transition at 30-34 Kelvin in pyrrhotite: insight into a widespread occurrence of this mineral in rocks, *Earth Planet. Sci. Lett., 98*, 319-328, 1990.
102. Roquet, J., Sur les rémanences magnétiques des oxydes de fer et leur intérêt en géomagnétisme, *Ann. Géophys., 10*, 226-247 and 282-325, 1954.
103. Schmidbauer, E., and P. W. Readman, Low temperature magnetic properties of Ti-rich Fe-Ti spinels, *J. Magn. Magn. Mater., 27*, 114-118, 1982.
104. Schmidbauer, E., and N. Schembera, Magnetic hysteresis properties and anhysteretic remanent magnetization of spherical Fe_3O_4 particles in the grain size range 60–160 nm, *Phys. Earth Planet. Inter., 46*, 77-83, 1987.
105. Schult, A., Effect of pressure of the

Curie temperature of titanomagnetites $[(1-x)\cdot Fe_3O_4 - x\cdot TiFe_2O_4]$, *Earth Planet. Sci. Lett.*, *10*, 81-86, 1970.

106. Senftle, F. E., A. N. Thorpe, C. Briggs, C. Alexander, J. Minkin, and D. L. Griscom, The Néel transition and magnetic properties of terrestrial, synthetic, and lunar ilmenites, *Earth Planet. Sci. Lett.*, *26*, 377-386, 1975.
107. Sharma, P. V., *Geophysical Methods in Geology*, 2nd ed., 442 pp., Elsevier, New York, 1986.
108. Shirane, G., D. E. Cox, W. J. Takei, and S. L. Ruby, A study of the magnetic properties of the $FeTiO_3$–αFe_2TiO_3 system by neutron diffraction and the Mössbauer effect, *J. Phys. Soc. Jpn.*, *17*, 1598-1611, 1962.
109. Shive, P. N., and D. M. Fountain, Magnetic mineralogy in an Archean crustal section: implications for crustal magnetization, *J. Geophys. Res.*, *93B*, 12,177-12,186, 1988.
110. Soffel, H. C., Pseudo-single domain effects and the single domain-multidomain transition in natural pyrrhotite deduced from domain structure observations, *J. Geophys.*, *42*, 351-359, 1977.
111. Stacey, F. D., and S. K. Banerjee, *The Physical Principles of Rock Magnetism*, 195 pp., Elsevier, Amsterdam, 1974.
112. Stokking, L. B., and L. Tauxe, Acquisition of chemical remanent magnetization by synthetic iron oxide, *Nature*, *327*, 610-612, 1987.
113. Syono, Y., Magnetocrystalline anisotropy and magnetostriction of Fe_3O_4–Fe_2TiO_4 series, with special application to rock magnetism, *Jpn. J. Geophys.*, *4*, 71-143, 1965.
114. Telford, W. M., L. P. Geldart, and R. E. Sheriff, *Applied Geophysics*, 2nd ed., 770 pp., Cambridge University Press, New York, 1990.
115. Thompson, R., and F. Oldfield (Eds.), *Environmental Magnetism*, 227 pp., Allen and Unwin, London, 1986.
116. Toft, P. B., and J. Arkani-Hamed, Magnetization of the Pacific Ocean lithosphere deduced from MAGSAT data, *J. Geophys. Res.*, *97B*, 4387-4406, 1992.
117. Tucker, P., Low-temperature magnetic hysteresis properties of multidomain single-crystal titanomagnetite, *Earth Planet. Sci. Lett.*, *54*, 167-172, 1981.
118. Tucker, P., and W. O'Reilly, A magnetic study of single crystal titanomagnetite ($Fe_{2.4}Ti_{0.6}O_4$), *Phys. Earth Planet. Inter.*, *16*, 183-189, 1978.
119. Tucker, P., and W. O'Reilly, The acquisition of thermoremanent magnetization by multidomain single crystal titanomagnetite, *Geophys. J. R. Astr. Soc.*, *60*, 21-36, 1980.
120. Uyeda, S., Thermo-remanent magnetism as a medium of palaeomagnetism, with special reference to reverse thermo-remanent magnetism, *Jpn. J. Geophys.*, *2*, 1-123, 1958.
121. von Philipsborn, H., and L. Treitinger, Spinels, in *Landolt-Börnstein Numerical Data and Functional Relationships in Science and Technology; Group III: Crystal and Solid State Physics; vol. 12b, Magnetic and Other Properties of Oxides and Related Compounds*, edited by K.-H. Hellwege and A. M. Hellwege, pp. 54-284, Springer-Verlag, New York, 1980.
122. Wasilewski, P. J., and M. A. Mayhew, Crustal xenolith magnetic properties and long wavelength anomaly source requirements, *Geophys. Res. Lett.*, *9*, 329-332, 1982.
123. Wasilewski, P. J., and M. A. Mayhew, The Moho as a magnetic boundary revisited, *Geophys. Res. Lett.*, *19*, 2259-2262, 1992.
124. Wechsler, B., D. H. Lindsley, and C. T. Prewitt, Crystal structure and cation distribution in titanomagnetites ($Fe_{3-x}Ti_xO_4$), *Am. Mineral.*, *69*, 754-770, 1984.
125. Westcott-Lewis, M. F., and L. G. Parry, Magnetism in rhombohedral iron-titanium oxides, *Aust. J. Phys.*, *24*, 719-734, 1971.
126. Williams, M. C., P. N. Shive, D. M. Fountain, and R. B. Frost., Magnetic properties of exposed deep crustal rocks from the Superior Province of Manitoba, *Earth Planet. Sci. Lett.*, *76*, 176-184, 1985/86.
127. Worm, H.-U., Multidomain susceptibility and anomalously strong low field dependence of induced magnetization in pyrrhotite, *Phys. Earth Planet. Inter.*, *69*, 112-118, 1991.
128. Worm, H.-U., and H. Markert, Magnetic hysteresis properties of fine particle titanomagnetites precipitated in a silicate matrix, *Phys. Earth Planet. Inter.*, *46*, 84-93, 1987.

Mixture Theories for Rock Properties

James G. Berryman

1. INTRODUCTION

Two general references for the theory of mixtures are the textbooks of Beran [5] and Christensen [29]. Review articles by Batchelor [3], Hale [41], Hashin [42], Torquato [95], and Willis [110] are also recommended.

1.1. Rocks Are Inhomogeneous Materials

A rock is a naturally occurring mixture of minerals. Rocks are normally inhomogeneous both due to their mixed mineral content and due to the presence of cracks and voids. A specimen of a single pure mineral without any cracks or voids is usually called a single crystal, unless the specimen is a jumble of anisotropic and randomly oriented single crystals in which case it is called a polycrystal. When single crystals of different anisotropic minerals are jumbled together randomly, the rock is called a polycrystalline aggregate.

1.2. General Assumptions and Caveats

The theory of mixtures as presented here is a macroscopic theory, and assumes that the constituents of the mixture are immiscible (*i.e.*, one component does not dissolve in the presence of another). The theory also assumes at the outset that we know what minerals are contained in a composite (say, using spectroscopic analysis), what the pertinent physical constants of single crystals of these minerals are (preferably from direct measurements or possibly from independent measurements tabulated in reference books like this one), and usually what the relative volume fractions of these constituents are. In addition, it is sometimes supposed that further information about short-range or long-range order, geometrical arrangements of constituents and pores, or some other pertinent information may be available. Thomsen [93] discusses some of the potential pitfalls involved in using mixture theories to analyze rock data.

We concentrate on three-dimensional results, but wish to point out that two-dimensional results are usually also available and often are somewhat stronger (for example, bounds might be tighter or actually become equalities) than the results quoted here.

When used with real data, all the formulas presented should be analyzed for sensitivity to error propagation from measurement statistics.

The body of knowledge called the theory of mixtures (or the theory of composites) has grown so much in the last 30 years that it is clearly impossible to review all the results pertinent to rocks in a short space. It is the intention of the author to summarize the best established and most generally useful results and then to provide pointers to the literature for more recent and more specialized contributions. Clearly much significant work must be omitted in a review of this size.

1.3. Types of Results

The results to be presented are organized into three general categories: exact results, bounds, and estimates. An exact result is a formula relating the desired physical property to other (usually) more easily mea-

J. G. Berryman, Lawrence Livermore Laboratory, Earth Science, POB 808, L-202, Livermore, CA 94551-9900

Rock Physics and Phase Relations
A Handbook of Physical Constants
AGU Reference Shelf 3

sured physical properties. Rigorous bounds are generally based on thermodynamic stability criteria, or on variational principles. For example, the Voigt [98] and Reuss [80] estimates were shown to be rigorous bounds by Hill [46] using variational principles. An estimate is any formula that is neither exact nor a rigorous bound; a truncated series expansion is an example of such an estimate. Derivations of the results are omitted, but may be found in the references.

The significance of these results for rocks differs somewhat from their significance for other types of composite materials used in mechanical design. For example, if one wishes to design a strong but very light weight material (say, for use in structures), bounding methods are clearly superior to estimates: properties of typical elastic composites can be very well approximated when closely spaced bounds are known. However, since rocks virtually always have some porosity, one of the bounds will be practically useless (being either essentially zero or infinity) and, therefore, estimates can play a very significant role in evaluating rock properties.

1.4. Choice of Physical Properties

Results are known for anisotropic composites composed of isotropic constituents and for either isotropic or anisotropic composites of anisotropic constituents. However, to keep this article within bounds, we will say very little about anisotropy. Likewise, frequency dependent results and estimates (or bounds) for complex constants will be largely ignored.

1.5. Format for Presentation of Results

To simplify presentation of results and to emphasize similarities among various estimates and bounds, it will prove convenient to introduce some special notation. Let $x_1, \ldots, x_N$ be the volume fractions of the N constituents of the composite. We assume that $x_1 + \ldots + x_N = 1$, so that all the components of the composite are counted. If cracks or voids are present, then the corresponding constituent constants are either zero or infinity (*e.g.*, electrical resistance $\rho = \infty$ implies a perfect insulator). A volume average of any quantity $Q(\mathbf{r})$ is given by

$$\langle Q(\mathbf{r}) \rangle = \sum_{i=1}^{N} x_i Q_i, \tag{1}$$

where Q_i is the value of $Q(\mathbf{r})$ in the i-th component. Reference will be made to the minimum and maximum values Q takes among all N constituents, given by $Q_{min} = \min_i Q_i$ and $Q_{max} = \max_i Q_i$.

To fix notation, we define σ_{eff} as the true effective conductivity, $\sigma^{\pm}$ are the upper(+) and lower (−) bounds on conductivity satisfying $\sigma^- \leq \sigma_{eff} \leq \sigma^+$, and σ^* is an estimate such that $\sigma_{eff} \simeq \sigma^*$. The precise meaning of the expresion $\sigma_{eff} \simeq \sigma^*$ will usually not be specified, but we generally consider only those estimates that are known to satisfy $\sigma^- \leq \sigma^* \leq \sigma^+$. The same subscript and superscript notation will be used for all physical properties.

We also introduce certain functions of the constituents' constants [8,11,66,99]. For the conductivity $\sigma(\mathbf{r})$, we introduce

$$\begin{aligned} \Sigma(s) &\equiv \left\langle \frac{1}{\sigma(\mathbf{r}) + 2s} \right\rangle^{-1} - 2s \\ &= \left(\sum_{i=1}^{N} \frac{x_i}{\sigma_i + 2s} \right)^{-1} - 2s. \end{aligned} \tag{2}$$

For the bulk modulus $K(\mathbf{r})$, we use

$$\begin{aligned} \Lambda(u) &\equiv \left\langle \frac{1}{K(\mathbf{r}) + \frac{4}{3}u} \right\rangle^{-1} - \frac{4}{3}u \\ &= \left(\sum_{i=1}^{N} \frac{x_i}{K_i + \frac{4}{3}u} \right)^{-1} - \frac{4}{3}u. \end{aligned} \tag{3}$$

For the shear modulus $\mu(\mathbf{r})$, we have

$$\begin{aligned} \Gamma(z) &\equiv \left\langle \frac{1}{\mu(\mathbf{r}) + z} \right\rangle^{-1} - z \\ &= \left(\sum_{i=1}^{N} \frac{x_i}{\mu_i + z} \right)^{-1} - z. \end{aligned} \tag{4}$$

Each of these three functions increases monotonically as its argument increases. Furthermore, when the argument of each function vanishes, the result is the *harmonic mean* of the corresponding physical property:

$$\Sigma(0) = \left\langle \frac{1}{\sigma(\mathbf{r})} \right\rangle^{-1}, \quad \Lambda(0) = \left\langle \frac{1}{K(\mathbf{r})} \right\rangle^{-1}, \quad \text{and} \quad \Gamma(0) = \left\langle \frac{1}{\mu(\mathbf{r})} \right\rangle^{-1}. \tag{5}$$

Similarly, an analysis of the series expansion for each function at large arguments shows that, in the limit when the arguments go to infinity, the functions approach the *mean* of the corresponding physical property:

$$\Sigma(\infty) = \langle \sigma(\mathbf{r}) \rangle, \quad \Lambda(\infty) = \langle K(\mathbf{r}) \rangle, \quad \text{and} \quad \Gamma(\infty) = \langle \mu(\mathbf{r}) \rangle. \tag{6}$$

Thus, these functions contain both the Reuss [80] and Voigt [98] bounds as limits for positive arguments. Hashin-Shtrikman lower (upper) bounds [44, 45] are obtained by using the minimum (maximum) value of the appropriate constituent property, that is, $\sigma_{HS}^- = \Sigma(\sigma_{min})$, $\sigma_{HS}^+ = \Sigma(\sigma_{max})$, $K_{HS}^- = \Lambda(\mu_{min})$, $K_{HS}^+ = \Lambda(\mu_{max})$, etc. Most of the still tighter bounds that are known may be expressed in analogous fashion, but we do not have space to present such results in this review.

Examples, together with comparisons to experiment, are presented to conclude each topic.

2. ELECTRICAL CONDUCTIVITY, DIELECTRIC PERMITTIVITY, MAGNETIC PERMEABILITY, THERMAL CONDUCTIVITY, ETC.

The problem of determining the effective electrical conductivity σ of a multiphase conductor is mathematically equivalent to many problems in inhomogeneous materials. Ohm's law relates the current density $\mathbf{J}$ and the electric field $\mathbf{E}$ by

$$\mathbf{J} = \sigma\mathbf{E}. \tag{7}$$

In the absence of current sources or sinks, the current density is conserved and therefore satisfies the continuity equation $\nabla\cdot\mathbf{J} = 0$. The electric field is the gradient of a potential Φ, so $\mathbf{E} = -\nabla\Phi$, and is therefore also curl free, so $\nabla\times\mathbf{E} = 0$.

For dielectric media, if $\mathbf{D}$ and $\mathbf{E}$ are the displacement and electric fields, then the dielectric permittivity ϵ satisfies

$$\mathbf{D} = \epsilon\mathbf{E}, \tag{8}$$

where $\nabla\cdot\mathbf{D} = 0$ in the absence of a charge distribution and $\nabla\times\mathbf{E} = 0$.

For magnetic media, if $\mathbf{B}$ and $\mathbf{H}$ are the magnetic induction and field intensity, then the magnetic permeability μ satisfies

$$\mathbf{B} = \mu\mathbf{H}, \tag{9}$$

where $\nabla\cdot\mathbf{B} = 0$ and in the absence of currents $\nabla\times\mathbf{H} = 0$ [52].

For thermal conduction, if $\mathbf{Q}$ is the heat flux and θ is the scalar temperature, then the thermal conductivity k satisfies

$$\mathbf{Q} = -k\nabla\theta, \tag{10}$$

where heat is conserved according to $\nabla\cdot\mathbf{Q} = 0$.

Thus, all of these rather diverse physical problems have the same underlying mathematical structure. We will treat the electrical conductivity as the prototypical problem, although occasionally we use terminology that arose originally in the study of dielectric media.

Historical and technical reviews of the theory of electrical conductivity in inhomogeneous materials are given by Hale [41] and Landauer [59]. Batchelor [3] compares analysis of various transport properties.

2.1. Bounds

Hashin-Shtrikman bounds [44,66] for electrical conductivity may be written using (2)

$$\sigma_{HS}^- \equiv \Sigma(\sigma_{min}) \le \sigma_{eff} \le \Sigma(\sigma_{max}) \equiv \sigma_{HS}^+, \tag{11}$$

where we may suppose that the constituents' conductivities have been arranged so that $\sigma_{min} = \sigma_1 \le \sigma_2 \le \cdots \le \sigma_N = \sigma_{max}$.

Rigorous bounds on the conductivity of polycrystals have been derived by Molyneux [67] and Schulgasser [86].

2.2. Estimates

We may use the rigorous bounds to help select useful approximations. Any approximation that violates the bounds may be discarded, since it is not as accurate an estimate as the bounds themselves. We therefore prefer estimates that satisfy (or at worst coincide with) the bounds.

2.2.1 Spherical inclusions. One of the earliest estimates of the effective dielectric constant is associated with various names, such as Clausius-Mossotti, Maxwell-Garnett, and Lorentz-Lorenz (see Bergman [6]). The formula for a two-component ($N = 2$) composite with type-2 host containing type-1 spherical inclusions is

$$\frac{\epsilon_{CM}^* - \epsilon_2}{\epsilon_{CM}^* + 2\epsilon_2} = x_1\frac{\epsilon_1 - \epsilon_2}{\epsilon_1 + 2\epsilon_2}$$

or

$$\frac{1}{\epsilon_{CM}^* + 2\epsilon_2} = \left\langle \frac{1}{\epsilon(\mathbf{r}) + 2\epsilon_2} \right\rangle. \tag{12}$$

Using definition (2), the equivalent result for conductivity is given by

$$\sigma_{CM}^* = \Sigma(\sigma_2). \tag{13}$$

Interchanging the roles of the host and inclusion phases gives a second result $\sigma_{CM}^* = \Sigma(\sigma_1)$. Thus, we see that these *estimates* are actually the same as the Hashin-Shtrikman *bounds*.

The self-consistent (SC) effective medium theory for dielectric or conducting composites was derived by Bruggeman [22] and Landauer [58], respectively. Using conductivity as our example, the formula can be written either as

$$\sum_{i=1}^{N} x_i \frac{\sigma_i - \sigma_{SC}^*}{\sigma_i + 2\sigma_{SC}^*} = 0, \tag{14}$$

or equivalently as

$$\frac{1}{\sigma_{SC}^* + 2\sigma_{SC}^*} = \left\langle \frac{1}{\sigma(\mathbf{x}) + 2\sigma_{SC}^*} \right\rangle. \tag{15}$$

Using definition (2), we see that σ_{SC}^* is the fixed point of the function $\Sigma(\sigma)$ given by

$$\sigma_{SC}^* = \Sigma(\sigma_{SC}^*). \tag{16}$$

This equation makes it clear that the solution is found through iteration, and that is one reason the method is called "self-consistent."

The differential (D) effective medium approach was first proposed by Bruggeman [22]. If there are only two constituents whose volume fractions are $x = v_1$ and $y = v_2 = 1 - x$ with type-1 material being the host and type-2 being inclusion, then suppose the value of the effective conductivity $\sigma_D^*(y)$ is known for the value y. Treating $\sigma_D^*(y)$ as the host conductivity and $\sigma_D^*(y+dy)$ as that of the infinitesimally altered composite, we find

$$(1-y)\frac{d}{dy}\left[\sigma_D^*(y)\right] = \frac{\sigma_2 - \sigma_D^*(y)}{\sigma_2 + 2\sigma_D^*(y)}\left[3\sigma_D^*(y)\right]. \tag{17}$$

This equation can be integrated analytically. Starting with $\sigma_D^*(0) = \sigma_1$, we find

$$\left(\frac{\sigma_2 - \sigma_D^*(y)}{\sigma_2 - \sigma_1}\right)\left(\frac{\sigma_1}{\sigma_D^*(y)}\right)^{\frac{1}{3}} = 1 - y. \tag{18}$$

Milton [65] has shown that the self-consistent effective medium method produces results that are realizable and therefore always satisfy the rigorous bounds. Norris *et al.* [71] have shown the corresponding result for the differential effective medium theory.

2.2.2. Nonspherical inclusions. When considering nonspherical inclusions (generally assumed to be ellipsoidal), it is convenient to introduce the factors R defined by

$$R^{mi} = \frac{1}{9}\sum_{p=a,b,c} \frac{1}{L_p\sigma_i + (1 - L_p)\sigma_m} \tag{19}$$

(examples are displayed in Table 1). The superscripts m and i refer to matrix (host) and inclusion phases, while the L_ps are the depolarization factors along each of the principle directions (a, b, c) of an ellipsoidal inclusion. A generalization of the Clausius-Mossotti formula for nonspherical inclusions in an isotropic composite is (see Cohen *et al.* [32] and Galeener [39])

$$\frac{\sigma_{CM}^* - \sigma_m}{\sigma_{CM}^* + 2\sigma_m} = \sum_{i=1}^{N} x_i(\sigma_i - \sigma_m)R^{mi}. \tag{20}$$

A generalization of the self-consistent formula for nonspherical inclusions in an isotropic composite is

$$\sum_{i=1}^{N} x_i(\sigma_i - \sigma_{SC}^*)R^{*i} = 0. \tag{21}$$

The asterisk superscript for R simply means that the host material has the conductivity σ_{SC}^*. Thus, (20) is explicit, while (21) is implicit.

Tabulations of the depolarizing factors L_p for general ellipsoids are given by Osborn [72] and Stoner [91].

For aligned ellipsoids (*i.e.*, for certain anisotropic conductors), if the depolarization factor of the axis aligned with the applied field is L, then Sen *et al.* [88] show that the differential effective medium estimate can again be integrated analytically and produces the result

$$\left(\frac{\sigma_2 - \sigma_D^*(y)}{\sigma_2 - \sigma_1}\right)\left(\frac{\sigma_1}{\sigma_D^*(y)}\right)^{L} = 1 - y. \tag{22}$$

TABLE 1. Three examples of coefficients R for spherical and nonspherical inclusions in isotropic composites. The superscripts m and i refer to matrix (host) and inclusion phases, respectively.

Inclusion shape	Depolarizing factors L_a, L_b, L_c	R^{mi}
Spheres	$\frac{1}{3}, \frac{1}{3}, \frac{1}{3}$	$\frac{1}{\sigma_i + 2\sigma_m}$
Needles	$0, \frac{1}{2}, \frac{1}{2}$	$\frac{1}{9}\left(\frac{1}{\sigma_m} + \frac{4}{\sigma_i + \sigma_m}\right)$
Disks	$1, 0, 0$	$\frac{1}{9}\left(\frac{1}{\sigma_i} + \frac{2}{\sigma_m}\right)$

The result (18) is seen to be a special case of this more general result with $L = \frac{1}{3}$.

A paper by Stroud [92] introduced a self-consistent effective medium theory for conductivity of polycrystals.

2.2.3. Series expansion methods. Brown [21] has shown how to obtain estimates of conductivity using series expansion methods.

2.3. Example

2.3.1. Formation factor of glass-bead packings. The formation factor F for a porous medium is defined as

$$F = \sigma/\sigma^*, \tag{23}$$

where σ is the electrical conductivity of the pore fluid and σ^* is the overall conductivity of the saturated porous medium -- assuming that the material composing the porous frame is nonconducting. A related quantity called the electrical tortuosity τ is determined by the formula

$$\tau = \phi F. \tag{24}$$

Johnson *et al.* [54] have measured the electrical conductivity of a series of glass-bead packings with conducting fluid saturating the porosity ϕ. The corresponding values of F are shown in Figure 1 and Table

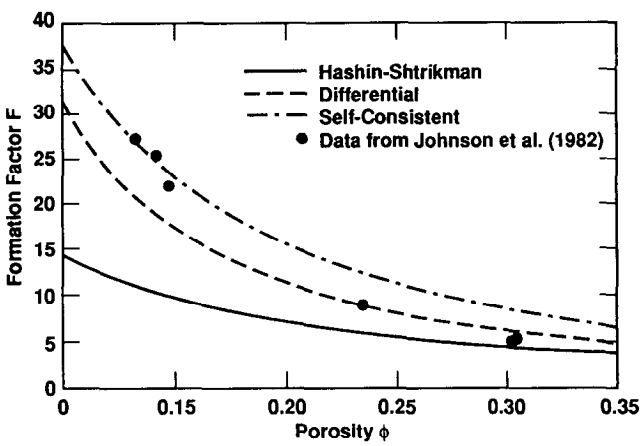

Fig. 1. Measurements of formation factor F compared to Hashin-Shtrikman bounds and estimates based on the differential (D) scheme for spherical insulating particles in a conducting fluid and the self-consistent (SC) method for spherical insulators and needle-shaped conductors. Data from Johnson *et al.* [54].

TABLE 2. Comparison of measured and calculated formation factor F for packings of glass beads. Data from Johnson *et al.* [54].

Porosity	*Experimental*	*Spheres*	*Spheres-Needles*
ϕ	F	F_D	F_{SC}
0.133	27.2	20.6	26.6
0.142	25.4	18.7	24.5
0.148	22.0	17.6	23.2
0.235	8.8	8.8	12.3
0.303	5.0	6.0	8.2
0.305	5.2	5.9	8.1

2. All the values lie above the Hashin-Shtrikman lower bound on F, given by

$$F_{HS}^{-} = 1 + \frac{3}{2}\frac{1-\phi}{\phi}, \tag{25}$$

as expected.

The paper by Sen *et al.* [88] shows that the differential (D) method predicts the formation factor should be given by

$$F_D = \phi^{-\frac{3}{2}}, \tag{26}$$

assuming that the glass beads are treated as nonconducting spheres imbedded in a host medium corresponding to the conducting fluid. This approach guarantees that the conducting fluid contains connected (and therefore conducting) pathways at all values of the porosity.

The self-consistent (SC) method can also be used by assuming the glass beads are spheres in the conducting fluid in the very high porosity limit and that the porosity is in the form of needle-shaped voids in the glass in the low porosity limit. The resulting formula is given by

$$F_{SC} = \frac{1}{2}\left(X - 1 + \left[(X+1)^2 + 32\right]\right)^{\frac{1}{2}}, \tag{27}$$

where

$$X = -3 + \frac{9}{2}\frac{1-\phi}{\phi}. \tag{28}$$

(If the sphere-sphere version of the SC approximation had been used instead, we would have found that the SC method predicts there are no conducting paths through the sample for porosities $\phi \leq \frac{1}{3}$. However, this result just shows that a spherical geometry for the

TABLE 3. Conversion formulas for the various elastic constants.

Bulk modulus	*Shear modulus*	*Young's modulus*	*Poisson's ratio*
K	μ	E	ν
$K = \frac{E}{3(1-2\nu)}$	$\mu = \frac{E}{2(1+\nu)}$	$\frac{1}{E} = \frac{1}{9K} + \frac{1}{3\mu}$	$\nu = \frac{3K-2\mu}{2(3K+\mu)}$

pores is an inadequate representation of the true microstructure at low porosities. That is why we choose needles instead to approximate the pore microstructure.)

These two theoretical estimates are also listed and shown for comparison in Table 2 and Figure 1. We find that the differential method agrees best with the data at the higher porosities ($\simeq$ 25-30 %), while the self-consistent effective medium theory agrees best at the lower porosities ($\simeq$ 15 %). These results seem to show that needle-shaped pores give a reasonable approximation to the actual pore shapes at low porosity, while such an approximation is inadequate at the higher porosities.

3. ELASTIC CONSTANTS

For isotropic elastic media, the bulk modulus K is related to the Lamé parameters λ, μ of elasticity [see Eq. (54)] by

$$K = \lambda + \tfrac{2}{3}\mu, \tag{29}$$

where μ is the shear modulus. Bounds and estimates are normally presented in terms of the bulk and shear moduli. However, results of mechanical measurements are often expressed (particularly in the engineering literature) in terms of Young's modulus E and Poisson's ratio ν. Useful relations among these constants are displayed for ease of reference in Table 3.

A very useful review article on the theory of elastic constants for inhomogeneous media and applications to rocks is that of Watt *et al.* [108]. The textbook by Christensen [29] may also be highly recommended. Elastic anisotropy due to fine layering has been treated by Backus [2].

3.1. Exact

When all the constituents of an elastic composite have the same shear modulus μ, Hill [47] has shown that the effective bulk modulus K_{eff} is given by the exact formula

$$\frac{1}{K_{eff} + \frac{4}{3}\mu} = \left\langle \frac{1}{K(\mathbf{x}) + \frac{4}{3}\mu} \right\rangle, \tag{30}$$

or equivalently

$$K_{eff} = \Lambda(\mu), \tag{31}$$

using the function defined in (3). Clearly, $\mu_{eff} = \mu$ if the shear modulus is constant.

If all constituents are fluids, then the shear modulus is constant and equal to zero. Thus, Hill's result (30) shows that the bulk modulus of a fluid mixture is just the Reuss average or harmonic mean of the constituents' moduli. This fact is the basis of Wood's formula [see (48)] for wave speeds in fluid/fluid mixtures and fluid/solid suspensions.

3.2. Bounds

Hashin-Shtrikman [43] bounds for the bulk modulus are

$$K_{HS}^{-} \equiv \Lambda(\mu_{min}) \le K_{eff} \le \Lambda(\mu_{max}) \equiv K_{HS}^{+}. \tag{32}$$

For the shear modulus, we first define the function

$$\zeta(K,\mu) = \frac{\mu}{6}\left(\frac{9K+8\mu}{K+2\mu}\right). \tag{33}$$

Note that $\zeta(K,\mu)$ is a monotonically increasing function of its arguments whenever they are both positive. When the constituents' elastic moduli are well-ordered so that $K_{min} = K_1 \le \ldots \le K_N = K_{max}$ and $\mu_{min} = \mu_1 \le \ldots \le \mu_N = \mu_{max}$, then the Hashin-Shtrikman bounds for the shear modulus are

$$\begin{aligned} \mu_{HS}^{-} &\equiv \Gamma(\zeta(K_{min},\mu_{min})) \le \mu_{eff} \\ &\le \Gamma(\zeta(K_{max},\mu_{max})) \equiv \mu_{HS}^{+}, \end{aligned} \tag{34}$$

using (33). When the constituents' properties are not

well-ordered, we may still number the components so that $K_{min} = K_1 \leq \ldots \leq K_N = K_{max}$, but now $\mu_{min} \equiv \min_{i=1,N} \mu_i$ and $\mu_{max} \equiv \max_{i=1,N} \mu_i$. Then, the bounds in (34) are still valid (with the different definitions of μ_{min} and μ_{max}), but they are usually called either the Walpole bounds [99] or the Hashin-Shtrikman-Walpole bounds.

Since experimental data are very often presented in terms of E and ν — Young's modulus and Poisson's ratio, respectively — we should consider the transformation from the (K, μ)-plane to the (E, ν)-plane (see Figure 2) and its impact on the corresponding bounds. The Hashin-Shtrikman bounds define a rectangle in (K, μ) with the corners given by the points (K^-, μ^-), (K^+, μ^-), (K^+, μ^+), and (K^-, μ^+). Each of these corners corresponds to a distinct limiting value of either E or ν. For example, since Young's modulus is determined from the expression

$$\frac{1}{E} = \frac{1}{9K} + \frac{1}{3\mu}, \tag{35}$$

we see that E is a monotonically increasing function of both K and μ. Thus, the diagonal corners (K^-, μ^-) and (K^+, μ^+) of the Hashin-Shtrikman rectangle determine the lower and upper HS bounds (E^-_{HS} and E^+_{HS}) on Young's modulus. Similarly, since

$$\mu = \frac{3(1-2\nu)}{2(1+\nu)} K, \tag{36}$$

and since the coefficient of K in (36) is a monotonically decreasing function of ν for all physical values in the range $(-1, 1/2)$, we find easily that minimum and maximum values of Poisson's ratio ν^-_{HS} and ν^+_{HS} occur respectively at the corners (K^-, μ^+) and (K^+, μ^-). Although these bounds are rigorous, better bounds in the (E, ν)-plane are given by the solid outlines of the quadrilateral region shown in Figure 2; the full range of possible pairs (E, ν), as determined by the Hashin-Shtrikman bounds [116], lies within this quadrilateral. The displayed equations for the four dotted lines shown in Figure 2 follow easily from the relations in Table 3.

If the composite contains porosity, then the lower Hashin-Shtrikman bounds on the bulk and shear moduli become trivial (zero), so the Hashin-Shtrikman rectangle is bounded by the K and μ axes. Similarly, when transformed into the (E, ν)-plane, we find that the only nontrivial universal bound remaining is E^+_{HS}, since the overall bounds on Poisson's ratio are the same as the physical limits $\nu^-_{HS} = -1$ and $\nu^+_{HS} = 1/2$. The full range of possible pairs (E, ν) is now determined by the triangular region shown in Figure 3. In some of our tables, the value $\nu(K^+_{HS}, \mu^+_{HS})$ is listed — not because it is a bound (it is not) — but because it is the value of ν corresponding to the point of highest possible $E = E^+_{HS}$.

Finally, note that data are also sometimes presented in terms of (E, μ) pairs. The preceding results

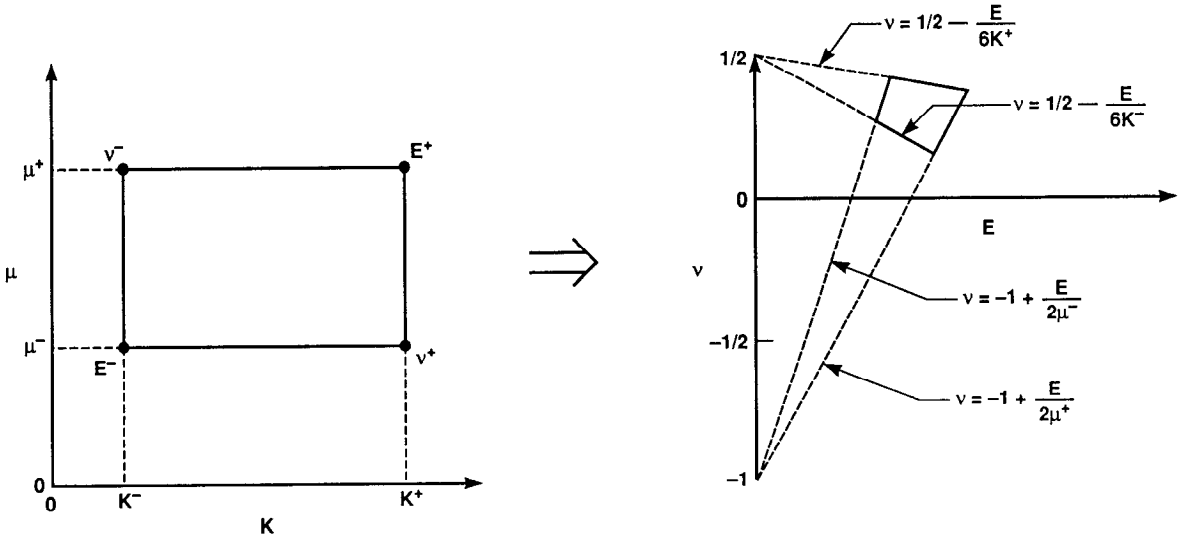

Fig. 2. Schematic illustration of the transformation of a Hashin-Shtrikman rectangle for (K, μ)-bounds to a quadrilateral for (E, ν)-bounds. Corners of the (K, μ) rectangle correspond to the bounding values in (E, ν).

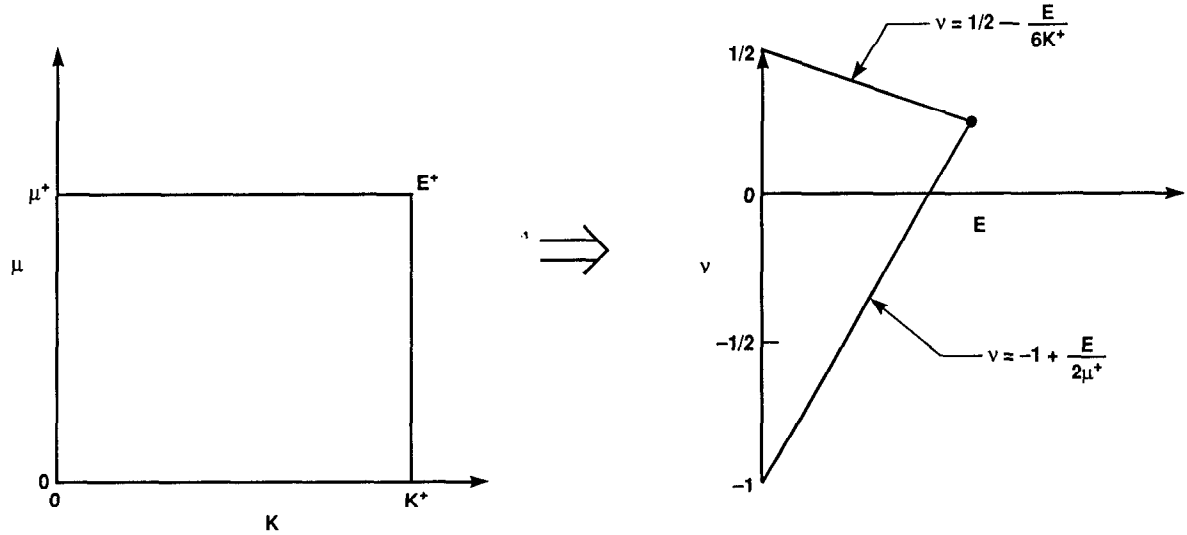

Fig. 3. Schematic as in Fig. 2, but for porous materials where $K^-_{HS} = 0 = \mu^-_{HS}$. Hashin-Shtrikman rectangles in (K, μ) become triangles in (E, ν).

show that the HS rectangle in the (K, μ)-plane then transforms to another rectangle in the (E, μ)-plane.

Hashin and Shtrikman [45] also derived variational bounds for the effective moduli of polycrystals of materials with cubic symmetry. Peselnick and Meister [76] derived bounds like those of Hashin and Shtrikman for the effective moduli of polycrystals composed of materials with hexagonal and trigonal symmetries. Walpole [100] provides an elegant derivation of these bounds for polycrystals. Simmons and Wang [89] tabulate single crystal data and also the bounds for polycrystals of many cubic minerals. Watt [107] has reviewed the literature on applications of Hashin-Shtrikman bounds to polycrystals and found very good agreement betweeen the bounds and data when experimental errors in the data are taken into account.

3.3. Estimates

Since rigorous bounds are known, it is preferable to consider estimates that always satisfy (or are at least no worse than) the bounds.

3.3.1. Voigt-Reuss-Hill. Hill [46] has shown that the Voigt and Reuss averages are upper and lower bounds on the moduli. A common approximation (see Chung [30], Peselnick [75], Peselnick and Meister [76], and Thomsen [93]) based on these bounds is the Voigt-Reuss-Hill estimate obtained by taking the arithmetic mean of the bounds. Brace [18] made extensive use of this estimate and found that for low porosity rocks at high pressure the agreement with experiment was excellent.

3.3.2. Spherical inclusions. A review of the derivation of various single-scattering approximations in elasticity is contained in Berryman [9].

Kuster and Toksöz [55] derive estimates of bulk and shear moduli of composites within a single-scattering approximation assuming that one of the constituents (say type-1) serves as the host medium. For spherical scatterers,

$$K^*_{KT} = \Lambda(\mu_1) \quad \text{and} \quad \mu^*_{KT} = \Gamma(\zeta(K_1, \mu_1)), \quad (37)$$

where $\zeta(K, \mu)$ was defined in (33). These formulas have the advantage of being explicit (*i.e.*, requiring neither iteration nor integration). There are also as many estimates as constituents, since any constituent desired may be chosen as the host. If the host medium is either the stiffest or the most compliant, then these formulas produce the same values as the corresponding Hashin-Shtrikman bounds.

For inclusions that are spherical in shape, the self-consistent effective medium estimates [7,23,48,101] for the bulk and shear moduli are

$$K^*_{SC} = \Lambda(\mu^*_{SC}) \text{ and } \mu^*_{SC} = \Gamma(\zeta(K^*_{SC}, \mu^*_{SC})), \quad (38)$$

where $\zeta(K, \mu)$ was defined in (33). These values are found by iterating to the fixed point which is known to be stable and unique for positive values of the moduli. This estimate is completely symmetric in all the constituents, so no single component plays the role of host for the others.

TABLE 4. Four examples of coefficients P and Q for spherical and nonspherical scatterers. The superscripts m and i refer to matrix (host) and inclusion phases, respectively. Special characters are defined by $\beta = \mu[(3K + \mu)/(3K + 4\mu)]$, $\gamma = \mu[(3K + \mu)/(3K + 7\mu)]$, and $\zeta = (\mu/6)[(9K + 8\mu)/(K + 2\mu)]$. The expression for spheres, needles, and disks were derived by Wu [112] and Walpole [101]. The expressions for penny-shaped cracks were derived by Walsh [102] and assume $K_i/K_m << 1$ and $\mu_i/\mu_m << 1$. The aspect ratio of the cracks is α.

Inclusion shape	P^{mi}	Q^{mi}
Spheres	$\frac{K_m+\frac{4}{3}\mu_m}{K_i+\frac{4}{3}\mu_m}$	$\frac{\mu_m+\zeta_m}{\mu_i+\zeta_m}$
Needles	$\frac{K_m+\mu_m+\frac{1}{3}\mu_i}{K_i+\mu_m+\frac{1}{3}\mu_i}$	$\frac{1}{5}\left(\frac{4\mu_m}{\mu_m+\mu_i}+2\frac{\mu_m+\gamma_m}{\mu_i+\gamma_m}+\frac{K_i+\frac{4}{3}\mu_m}{K_i+\mu_m+\frac{1}{3}\mu_i}\right)$
Disks	$\frac{K_m+\frac{4}{3}\mu_i}{K_i+\frac{4}{3}\mu_i}$	$\frac{\mu_m+\zeta_i}{\mu_i+\zeta_i}$
Penny cracks	$\frac{K_m+\frac{4}{3}\mu_i}{K_i+\frac{4}{3}\mu_i+\pi\alpha\beta_m}$	$\frac{1}{5}\left(1+\frac{8\mu_m}{4\mu_i+\pi\alpha(\mu_m+2\beta_m)}+2\frac{K_i+\frac{2}{3}(\mu_i+\mu_m)}{K_i+\frac{4}{3}\mu_i+\pi\alpha\beta_m}\right)$

The differential effective medium approach [31] applies an idea of Bruggeman [22] to the elastic constant problem. If there are only two constituents whose volumes fractions are $x = v_1$ and $y = v_2 = 1 - x$ with the type-1 material being host and type-2 being inclusion, then suppose the value of the effective bulk modulus $K_D^*(y)$ is known for the value y. Treating the $K_D^*(y)$ as the bulk modulus of the host medium and $K_D^*(y+dy)$ as the modulus of the composite, we find

$$(1-y)\frac{d}{dy}[K_D^*(y)] = \frac{K_2 - K_D^*(y)}{K_2 + \frac{4}{3}\mu_D^*(y)} \times \left[K_D^*(y) + \frac{4}{3}\mu_D^*(y)\right] \quad (39)$$

and similarly

$$(1-y)\frac{d}{dy}[\mu_D^*(y)] = \frac{\mu_2 - \mu_D^*(y)}{\mu_2 + \zeta(K_D^*(y), \mu_D^*(y))} \times [\mu_D^*(y) + \zeta(K_D^*(y), \mu_D^*(y))], \quad (40)$$

where ζ was defined in (33). Note that (39) and (40) are coupled and therefore must be integrated simultaneously. Unlike the self-consistent effective medium results quoted in the preceding paragraph, the differential effective medium approach is not symmetric in the components and therefore produces two different estimates depending on which constituent plays the role of host and which the inclusion phase.

3.3.3. Nonspherical inclusions. In the presence of nonspherical inclusions, the Kuster-Toksöz and self-consistent effective medium methods can both be easily generalized [7, 55].

Using the symbols P and Q defined in Table 4, the formulas for the general Kuster-Toksöz approach are

$$(K_{KT}^* - K_m)\frac{K_m + \frac{4}{3}\mu_m}{K_{KT}^* + \frac{4}{3}\mu_m} = \sum_{i=1}^{N} x_i(K_i - K_m)P^{mi} \quad (41)$$

for the bulk modulus, and

$$(\mu_{KT}^* - \mu_m)\frac{\mu_m + \zeta_m}{\mu_{KT}^* + +\zeta_m} = \sum_{i=1}^{N} x_i(\mu_i - \mu_m)Q^{mi} \quad (42)$$

for the shear modulus. Formulas (41) and (42) are clearly uncoupled and can be rearranged to show they are also explicit, *i.e.*, requiring neither iteration nor integration for their solution.

Similarly, the formulas for the self-consistent effective medium approximations are

$$\sum_{i=1}^{N} x_i(K_i - K_{SC}^*)P^{*i} = 0 \quad (43)$$

for the bulk modulus, and

$$\sum_{i=1}^{N} x_i(\mu_i - \mu_{SC}^*)Q^{*i} = 0 \quad (44)$$

for the shear modulus. The asterisk superscript for P and Q simply means that the host material has the

TABLE 5. Values of isothermal bulk moduli of porous P-311 glass measured at room temperature compared to theoretical estimates. Bulk and shear moduli of the pure glass were measured to be $K = 46.3$ and $\mu = 30.5$ GPa, respectively. All data from Walsh *et al.* [104].

Porosity	*Experimental*	*Hashin-Shtrikman*	*Spherical Voids*	*Needles-Spheres*
ϕ	K (GPa)	K_{HS}^{+} (GPa)	K_D (GPa)	K_{SC} (GPa)
0.00	46.1	46.3	46.3	46.3
0.00	45.9	46.3	46.3	46.3
0.05	41.3	41.6	41.5	41.4
0.11	36.2	36.6	36.1	35.6
0.13	37.0	35.1	34.4	33.7
0.25	23.8	27.0	25.2	22.8
0.33	21.0	22.5	19.9	16.4
0.36	18.6	21.0	18.1	14.2
0.39	17.9	19.6	16.4	12.3
0.44	15.2	17.3	13.7	9.4
0.46	13.5	15.5	12.7	8.5
0.50	12.0	14.8	10.9	6.7
0.70	6.7	7.7	3.8	2.1

moduli K_{SC}^{*} and μ_{SC}^{*}. The solutions to (43) and (44) are found by simultaneous iteration.

Based on earlier work by Eshelby [35] for ellipsoidal inclusions, Wu [112], Kuster and Toksöz [55], and Berryman [7] give general expressions for P^{mi} and Q^{mi} for spheroidal inclusions.

3.3.4. Series expansion methods. Beran [5] and Molyneux and Beran [68] have used series expansion methods to obtain estimates of the elastic constants.

3.4. Examples

3.4.1. Porous glass. Walsh *et al.* [104] made measurements on the compressiblity $(1/K)$ of a porous glass over a wide range of porosities. The samples they used were fabricated from P-311 glass powder. The powder and binder were die-pressed and then sintered. Depending on the thermal history of the samples, they obtained a porous glass foam with porosities ranging from 0.70 to near zero. Porosity measurements were stated to be accurate ± 0.01. Linear compressibility of the samples was measured. Their results agreed well with the theoretical predictions of Mackensie [63]. It turns out that Mackensie's result for the bulk modulus of a porous solid is also identical to the upper Hashin-Shtrikman bound for this problem. Thus, Walsh *et al.* [104] actually showed that their porous glass satisfies the HS bounds for a wide range of porosities and, furthermore, that the values they found closely track the upper bound.

Results of the theoretical calculations are shown in Table 5 and Figure 4. To be consistent with the microgeometry of these porous glasses for the SC approximation, we have treated the glass as if it were shaped like needles randomly dispersed in the void at the highest porosities; the voids are treated as spherical inclusions in the glass at the lowest porosities. (If instead we had chosen to treat the glass as spheres, the SC approximation would have vanished at porosities of 50 % and greater. However, spheres of glass serve as a very unrealistic representation of the true microstructure of the porous medium at high porosities.) Since the differential approximation treats the glass as host medium at all values of porosity, we need assume only that the voids are spherical for this estimate. We see that both theories (SC and D) do well at predicting

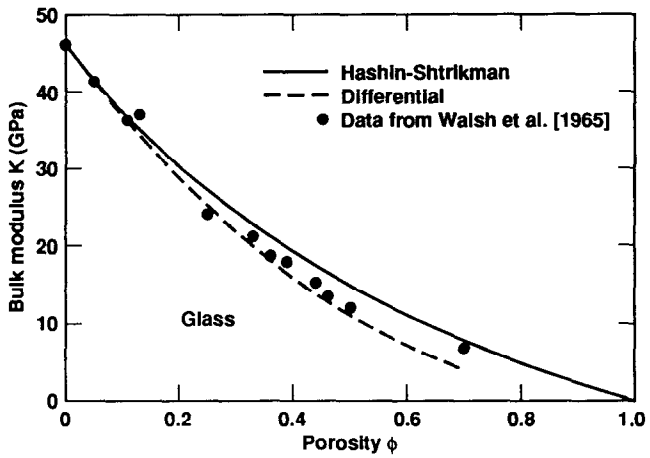

Fig. 4. Isothermal bulk modulus K of porous P-311 glass measured at room temperature compared to the Hashin-Shtrikman upper bound (solid line) and differential (D) scheme (dashed line) assuming spherical voids. Data from Walsh *et al.* [104].

the measured values out to about 25% porosity. For higher porosities, both theories overestimate the influence of the voids while the Hashin-Shtrikman bound (equivalent to the KT theory for this problem) does somewhat better at estimating the measured values over the whole range of porosities. Also see Zimmerman [115].

3.4.2. Porous silicon nitride. Fate [36] has performed a series of experiments measuring elastic constants of polycrystalline silicon nitride (Si_3N_4). The elastic constant data are believed to be accurate to ±3%, but errors may be somewhat larger for the lowest density samples. The data are shown in Table 6 and Figure 5. Fate showed approximate agreement with Budiansky's theory [23] in the original paper, but, for this problem, Budiansky's theory is just the same as our SC approximation for spherical inclusions. For comparison, the SC estimates for spherical particles and needle-shaped pores are also listed in the Table. The overall agreement with the data is improved somewhat using this estimate. The differential estimate for spherical inclusions was also computed (but is not shown here) and again found to overestimate the importance of the voids in the overall properties of the composite for porosities greater than 15 %.

There is one anomaly in this data set at $\phi = 0.025$. The measured value of E is larger than the value for the sample at $\phi = 0.0$, suggesting either that the true value of Young's modulus for the nonporous sample has been underestimated, or that the actual value of the porosity for that sample was overestimated. See the data of Fisher *et al.* [37] and Fisher *et al.* [38].

4. ACOUSTIC AND SEISMIC VELOCITIES

In isotropic elastic solids, the compressional wave speed V_c is related to the elastic constants and density ρ by

$$V_c = \left(\frac{K + \frac{4}{3}\mu}{\rho} \right)^{\frac{1}{2}} \tag{45}$$

and the shear wave speed V_s is given by

$$V_s = \left(\frac{\mu}{\rho} \right)^{\frac{1}{2}}. \tag{46}$$

In a pure fluid, the shear modulus is negligible so no shear wave appears and the acoustic velocity V_f is

$$V_f = \left(\frac{K_f}{\rho_f} \right)^{\frac{1}{2}}. \tag{47}$$

Reviews of mixture theory for wave propagation are given in Hudson [51] and Willis [110], and also in the reprint volume edited by Wang and Nur [106].

4.1. Exact

In a fluid mixture or a fluid suspension (solid inclusions completely surrounded by fluid), Wood's formula [111] for sound velocity is determined by using the bulk modulus of a suspension (the harmonic mean) and the average density, so

$$V_{Wood} = \left(\frac{K_{eff}}{\rho_{eff}} \right)^{\frac{1}{2}}, \tag{48}$$

where

$$\frac{1}{K_{eff}} = \frac{x_f}{K_f} + \sum_{i=1}^{N-1} \frac{x_i}{K_i} \tag{49}$$

and

$$\rho_{eff} = x_f \rho_f + \sum_{i=1}^{N-1} x_i \rho_i. \tag{50}$$

This result is essentially exact for low frequencies (*i.e.*, when the wavelength is long compared to the size of the inclusions), since (49) [also see (31)] is the exact effective bulk modulus for quasistatic deformations. How-

TABLE 6. Values of adiabatic elastic moduli of porous polycrystalline silicon nitride measured at room temperature compared to theoretical estimates. Young's modulus and the shear modulus of the pure Si_3N_4 were measured to be $E = 289.0$ and $\mu = 118.2$ GPa, respectively. All data from Fate [36].

Porosity	*Experimental*	*Hashin-Shtrikman*	*Sphere-Sphere*	*Sphere-Needle*
ϕ	E (GPa)	E^+_{HS} (GPa)	E_{SC} (GPa)	E_{SC} (GPa)
0.000	289.0	289.0	289.0	289.0
0.025	292.1	274.9	274.4	272.2
0.028	259.3	273.1	272.7	270.2
0.041	244.4	266.2	265.3	261.5
0.151	172.3	213.1	201.6	189.3
0.214	142.9	187.0	165.1	149.3
0.226	131.8	182.4	158.2	141.7
0.255	128.2	171.3	141.5	123.6
ϕ	μ (GPa)	μ^+_{HS} (GPa)	μ_{SC} (GPa)	μ_{SC} (GPa)
0.000	118.2	118.2	118.2	118.2
0.025	117.6	112.5	112.3	111.4
0.028	111.0	111.8	111.6	110.6
0.041	100.7	109.0	108.6	107.1
0.151	72.4	87.4	82.8	77.8
0.214	61.1	76.8	67.9	61.5
0.226	53.4	74.9	65.1	58.4
0.255	54.8	70.4	58.3	51.0

ever, care should be taken to use the adiabatic (as opposed to the isothermal) moduli in (49). Although the difference between adiabatic and isothermal moduli is generally small for solids, it may be significant for fluids.

4.2. Bounds

Bounds on wave speed may be obtained using Fermat's principle of least traveltime. Since Fermat's principle states that traveltime T_{AB} along a ray path from point A to point B is given by

$$T_{AB} = \min_{\{paths\}} \int \frac{1}{V(\mathbf{x})} dl, \tag{51}$$

where dl is the infinitesimal increment along the ray path. Then, if the straight-line distance between A and B is L_{AB}, the effective wave speed is related to constituent wave speeds by

$$\frac{1}{V_{eff}} \equiv \frac{T_{AB}}{L_{AB}} \leq \frac{x_f}{V_f} + \sum_{i=1}^{N-1} \frac{x_i}{V_i} \equiv \frac{1}{V^-_{Wyllie}}, \tag{52}$$

where V_f is the wave speed of the primary fluid and the V_is are the compressional wave speeds of the other constituents, while x_f and x_i are the corresponding volume fractions. The inequality in (52) is based on the assumption that any macroscopic straight line of length L_{AB} in a random medium will have lengths $\sum x_i L_{AB}$ passing through solid and $x_f L_{AB}$ passing through fluid. An actual ray path will not be straight however (due to refraction), so the true traveltime will be less than that predicted by the average slowness

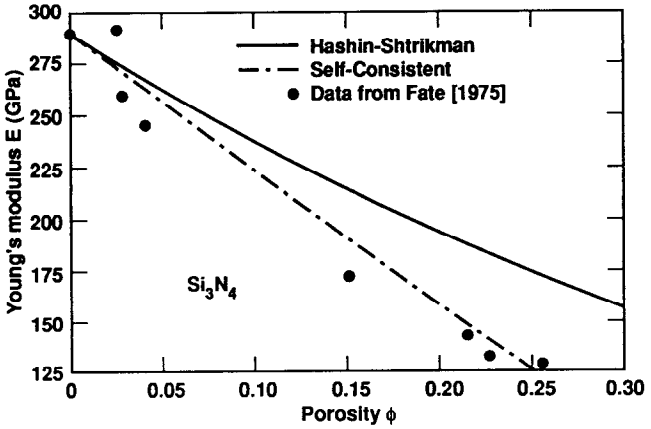

Fig. 5a. Young's modulus E of porous silicon nitride (Si_3N_4). Hashin-Shtrikman upper bound is the solid line. The self-consistent (SC) estimate assuming spherical particles and needle-shaped pores is the dot-dash line. Data from Fate [36].

on the right of (52) known as Wyllie's time average formula [113,114]. Since Wyllie *et al.*'s estimate of the sound speed in a mixture is based in part on Fermat's principle, it should be viewed as a lower bound not as an estimate.

4.3. Estimates

Estimates of the wave velocities are usually based on the corresponding estimates of the bulk and shear moduli, such as those discussed in Section 3.3.

4.4. Examples

Constituent properties required for the three examples are listed in Table 7.

4.4.1. Liquid/gas mixture. Wood's formula is known to apply to a liquid/gas mixture. Considering air in water, we have $K_{air} = 1.2 \times 10^{-4}$ GPa, $\rho_{air} = 0.0012$ g/cc, $K_{water} = 2.25$ GPa, $\rho_{water} = 1.00$ g/cc. Figure 6 shows the result of the calculation.

Wyllie's formula should not be applied to mixtures containing gas.

4.4.2. Liquid/liquid mixture. Wang and Nur [105] obtained ultrasonic velocity data for pure hydrocarbons and mixtures. Although the hydrocarbons are miscible and, therefore, violate the usual immiscibility assumption of mixture theories, we still expect that these data may be properly analyzed using Wood's formula and Wyllie's time average equation. The measured velocities and densities for the pure alkenes used in the mixture are presented in Table 7 along with the computed adiabatic bulk moduli. This information is used in Table 8 and Figure 7 to show that the two formulas agree with the data to within 1%. Also note the general relationship between V_{Wood} and V_{Wyllie} illustrated here that

$$\left[\sum x_i\rho_i \sum \frac{x_i}{K_i}\right]^{-\frac{1}{2}} = V_{Wood} \leq V_{Wyllie} = \left[\sum x_i \left(\frac{\rho_i}{K_i}\right)^{\frac{1}{2}}\right]^{-1}, \quad (53)$$

which is valid for all fluid/fluid mixtures. (Wood's formula is only correct for fluid mixtures and suspensions, whereas Wyllie's formula applies to arbitrary liquid/liquid and solid/liquid mixtures. Thus, the inequality (53) is of interest for liquid/liquid mixtures). Inequality (53) follows from Cauchy's inequality for sums: $(\sum a_i b_i)^2 \leq \sum a_i^2 \sum b_i^2$.

4.4.3. Liquid/solid suspensions. Kuster and Toksöz [56] performed ultrasonic experiments on suspensions of solid particles in liquids. The results of one of these series of experiments is shown in Figure 8. The host liquid was acetylene tetrabromide (ATB) and the solid particles in suspension were glass. Physical properties of the constituents are listed in Table 7. The solid curve in the Figure is the prediction of Wood's formula for these values. The agreement is again quite good.

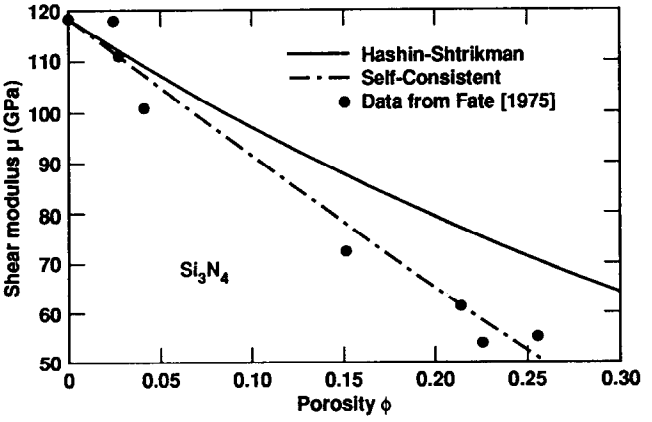

Fig. 5b. Shear modulus μ of porous silicon nitride. Significance of the lines is the same as in FIG. 5A. Data from Fate [36].

TABLE 7. Material constants for constituents of some fluid mixtures and suspensions. Data from Kuster and Toksöz [56],Rossini *et al.* [83], and Wang and Nur [105].

Constituent	*Velocity* V (km/sec)	*Density* ρ (g/cc)	*Bulk Modulus* K (GPa)
Water	1.500	1.000	2.25
Air	0.316	0.0012	1.2×10^{-4}
1-Decene ($C_{10}H_{20}$)	1.247	0.7408	1.152
1-Octadecene ($C_{18}H_{36}$)	1.369	0.7888	1.478
ATB	1.025	2.365	2.485
Glass	6.790	2.405	76.71

5. THERMOELASTIC CONSTANTS

The equations of linear and isotropic thermoelasticity [13] are

$$\rho\frac{\partial^2\mathbf{u}}{\partial t^2} = (\lambda+\mu)\nabla\nabla\cdot\mathbf{u} + \mu\nabla^2\mathbf{u} - 3\alpha(\lambda+\frac{2}{3}\mu)\nabla\theta \tag{54}$$

and

$$\frac{1}{D}\frac{\partial\theta}{\partial t} + \beta\frac{\partial\nabla\cdot\mathbf{u}}{\partial t} = \nabla^2\theta, \tag{55}$$

where $\mathbf{u}$ is the vector of displacement, θ is the increment of temperature, λ and μ are the Lamé parameters, α is the (linear) thermal expansion coefficient, $D = k/C_v$ is the thermal diffusivity, and $\beta = 3\alpha K\theta_0/k$, with C_v heat capacity at constant volume, θ_0 absolute temperature, and k thermal conductivity. The Lamé constants λ and μ have the same significance as in linear elasticity and the bulk modulus is again $K = \lambda + \frac{2}{3}\mu$.

Detailed derivations of most of the results quoted here may be found in the textbook of Christensen [29]. The review articles by Hale [41] and Hashin [42] also discuss thermal expansion. Applications of thermoelasticity to rocks are discussed by McTigue [64] and Palciauskas and Domenico [73]. Ledbetter and Austin [61] have given an example of applications of the theory to data on a SiC-reinforced aluminum composite.

5.1. Exact

Levin's formula [62, 87] for the effective thermal expansion coefficient α_{eff} for a two-component composite is given by

$$\frac{\alpha_{eff}-\alpha_2}{\alpha_1-\alpha_2} = \frac{1/K_{eff}-1/K_2}{1/K_1-1/K_2}, \tag{56}$$

where K_{eff} is the effective bulk modulus of the composite and α_1, α_2 and K_1, K_2 are, respectively, the thermal expansion coefficients and bulk moduli of the constituents. Equation (56) also implies that

$$\frac{\alpha_{eff}-\langle\alpha(\mathbf{r})\rangle}{\alpha_1-\alpha_2} = \frac{1/K_{eff}-\langle 1/K(\mathbf{r})\rangle}{1/K_1-1/K_2}. \tag{57}$$

The corresponding exact results for specific heats [82] are

$$(C_p)_{eff} = \langle C_p(\mathbf{r})\rangle + 9\theta_0\left(\frac{\alpha_1-\alpha_2}{1/K_1-1/K_2}\right)^2 \times \left(\frac{1}{K_{eff}} - \left\langle\frac{1}{K(\mathbf{r})}\right\rangle\right) \tag{58}$$

and

$$(C_v)_{eff} = (C_p)_{eff} - 9K_{eff}\alpha_{eff}^2\theta_0, \tag{59}$$

where C_p and C_v are the specific heats at constant pressure and constant volume, respectively, while θ_0 is the absolute temperature. In contrast, Kopp's law states that the specific heat of a solid element is the same whether it is free or part of a solid compound. Thus, Kopp's law implies that $(C_p)_{eff} = \langle C_p(\mathbf{r})\rangle$, whereas the exact result for two components shows in-

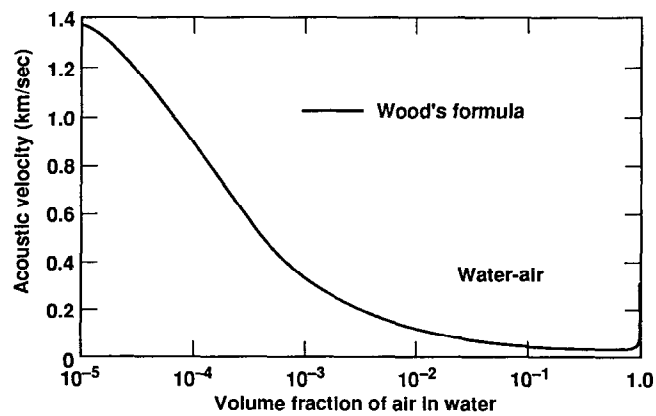

Fig. 6. Predicted acoustic velocities of water/air mixtures using Wood's formula (48).

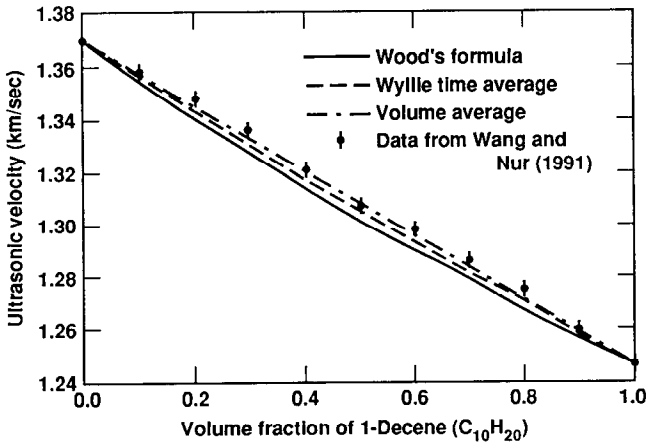

Fig. 7. Ultrasonic velocities of liquid hydrocarbon mixtures of 1-decene in 1-octadecene at room temperature. Data from Wang and Nur [105].

stead that there is a temperature dependent (but small for low temperatures) correction to this empirical law. Note that this correction (proportional to θ_0) is always negative, since the harmonic mean $< 1/K >^{-1}$ is a lower bound on K_{eff}.

5.2. Bounds

Levin [62] also used the Hashin-Shtrikman bounds on bulk modulus together with (56) to obtain bounds on α_{eff}. When $\alpha_1 > \alpha_2$, $K_1 > K_2$, and $\mu_1 > \mu_2$, the resulting bounds are

$$\frac{x_1 K_1(3K_2+4\mu_2)}{3K_1K_2+4\mu_2(x_1K_1+x_2K_2)} \le \frac{\alpha_{eff}-\alpha_2}{\alpha_1-\alpha_2} \le \frac{x_1K_1(3K_2+4\mu_1)}{3K_1K_2+4\mu_1(x_1K_1+x_2K_2)}, \quad (60)$$

or equivalently, using the function Λ defined in (3) with $N = 2$,

$$\frac{1/\Lambda(\mu_2)-1/\Lambda(0)}{1/K_1-1/K_2} \le \frac{\alpha_{eff}-\langle\alpha(\mathbf{r})\rangle}{\alpha_1-\alpha_2} \le \frac{1/\Lambda(\mu_1)-1/\Lambda(0)}{1/K_1-1/K_2}. \quad (61)$$

Rosen and Hashin [82] and Schapery [85] have obtained other (more complex) bounds on the effective thermal expansion coefficient.

Bounds on specific heat are shown by Christensen [29] and Rosen and Hashin [82] to be

$$9\theta_0\frac{\langle K(\mathbf{r})\alpha(\mathbf{r})\rangle^2}{\langle K(\mathbf{r})\rangle} \le (C_p)_{eff}-\langle C_v(\mathbf{r})\rangle \le 9\theta_0\langle K(\mathbf{r})\alpha(\mathbf{r})^2\rangle. \quad (62)$$

5.3. Estimates

Two simple estimates of the thermal expansion coefficient may be derived from (57) by applying the Reuss and Voigt bounds to K_{eff}. When K_{eff} is replaced by $\langle 1/K(\mathbf{r})\rangle$ in (57), we obtain

$$\alpha^* = \langle\alpha(\mathbf{r})\rangle. \quad (63)$$

When K_{eff} is replaced by $\langle K(\mathbf{r})\rangle$ in (57), we obtain

$$\alpha^* = \frac{\langle K(\mathbf{r})\alpha(\mathbf{r})\rangle}{\langle K(\mathbf{r})\rangle}. \quad (64)$$

In the two component case, these estimates are actually rigorous bounds - although which is the upper bound and which the lower one depends on the sign of the ratio $(\alpha_1-\alpha_2)/(K_1-K_2)$. When $N > 2$, we can use these formulas as general nonrigorous estimates. The second estimate (64) was first introduced by Turner [97].

Budiansky [24] and Laws [60] show that the self-consistent effective medium theory predicts the thermal expansion coefficient estimate is

$$\frac{K^*_{SC}\alpha^*_{SC}}{K^*_{SC}+\frac{4}{3}\mu^*_{SC}} = \left\langle\frac{K(\mathbf{r})\alpha(\mathbf{r})}{K(\mathbf{r})+\frac{4}{3}\mu^*_{SC}}\right\rangle \quad (65)$$

and the heat capacity estimate is

$$(C_v)^*_{SC} = \langle C_v(\mathbf{r})\rangle + \theta_0\left\langle\frac{[K(\mathbf{r})\alpha(\mathbf{r})-K^*_{SC}\alpha^*_{SC}]^2}{K(\mathbf{r})+\frac{4}{3}\mu^*_{SC}}\right\rangle, \quad (66)$$

where K^*_{SC} and μ^*_{SC} are given by (38). The correction term proportional to θ_0 is clearly always positive. Budiansky [24] and Duvall and Taylor [34] also give estimates of the effective Gruneisen constant ($\gamma = K\alpha/C_v$) for a composite.

6. POROELASTIC CONSTANTS (BIOT-GASSMANN THEORY)

Elastic response of solid/fluid mixtures is described by the equations of linear poroelasticity (also known

as Biot's equations [14–16]):

$$\rho\frac{\partial^2\mathbf{u}}{\partial t^2}+\rho_f\frac{\partial^2\mathbf{w}}{\partial t^2}=(H-\mu)\nabla\nabla\cdot\mathbf{u}+\mu\nabla^2\mathbf{u}-C\nabla\zeta \tag{67}$$

and

$$(\frac{\rho_f\eta}{\kappa})\frac{\partial\mathbf{w}}{\partial t}+\rho_f\frac{\partial^2\mathbf{u}}{\partial t^2}=-\nabla p_f, \tag{68}$$

where $\mathbf{u}$ is the solid displacement, $\mathbf{w}=\phi(\mathbf{u}-\mathbf{u}_f)$ is the average relative fluid-solid displacement, the solid dilatation is $e=\nabla\cdot\mathbf{u}$, the increment of fluid content is $\zeta=-\nabla\cdot\mathbf{w}$, the fluid pressure is given by

$$p_f=M\zeta-Ce, \tag{69}$$

and the average density is

$$\rho=\phi\rho_f+(1-\phi)\rho_{grain}. \tag{70}$$

When the porous solid is microhomogeneous (composed of only one type of solid grain), Gassmann [40] has shown that the principal elastic constant is given by

$$H=K_{undrained}+\frac{4}{3}\mu, \tag{71}$$

with the precise meaning of the remaining constants $K_{undrained}$, M and C to be given below. The shear modulus of the porous solid frame is μ. The density of the granular material composing the frame is ρ_{grain}. The bulk modulus and density of the saturating fluid are K_f and ρ_f. Kinematic viscosity of the fluid is η; permeability of the porous frame is κ. We have used a low frequency simplification to obtain (68), since our main interest here is in quasistatic effects. Burridge and Keller [27] have shown that this macroscopic form of the equations follows from the coupling of the equations of linear elasticity and the Navier-Stokes equations at the microscopic level for a mixture of fluids and solids.

Results for poroelastic constants of porous composites (*i.e.*, for solid frames composed of multiple types of solid constituents) can be obtained by exploiting a rigorous analogy between poroelasticity and thermoelasticity [12, 70]; however, spatial constraints do not permit a discussion of this analogy here. Instead, we will first examine the mixture properties of the coefficients in the microhomogeneous case (containing only one mineral), since even in this rather simple problem we still have a mixture of fluid and solid; then we consider the general properties of the coefficients for inhomogeneous rocks (containing two or more minerals).

TABLE 8. Ultrasonic velocities measured by Wang and Nur [105] for a sequence of binary hydrocarbon mixtures at 20° C compared to velocities computed using Wood's formula and Wyllie's time average equation. Table 7 contains the data required for computing Wood's formula. The formula for the 1-decene/1-octadecene hydrocarbon mixture is $(C_{10}H_{20})_x(C_{18}H_{36})_{(1-x)}$, where x is the volume fraction of 1-decene. Units of all velocities are km/s.

x	V_{meas}	V_{Wood}	V_{Wyllie}
0.00	1.369	1.369	1.369
0.10	1.358	1.354	1.356
0.20	1.348	1.340	1.343
0.294	1.336	1.328	1.331
0.40	1.321	1.314	1.317
0.50	1.307	1.301	1.305
0.60	1.298	1.290	1.293
0.70	1.286	1.279	1.281
0.80	1.275	1.267	1.270
0.90	1.260	1.257	1.258
1.00	1.247	1.247	1.247

The book on this subject by Bourbié *et al.* [17] is recommended.

6.1. Exact

6.1.1. Microhomogeneous frame (one mineral). Gassmann's formula for a microhomogeneous porous medium saturated with fluid wherein the fluid is confined to the pores during the deformation is

$$K_{undrained}=K_{drained}+(1-K_{drained}/K_{grain})^2M, \tag{72}$$

$$\frac{1}{M}=\frac{\phi}{K_f}+\frac{1-\phi-K_{drained}/K_{grain}}{K_{grain}}, \tag{73}$$

and

$$C=(1-K_{drained}/K_{grain})M. \tag{74}$$

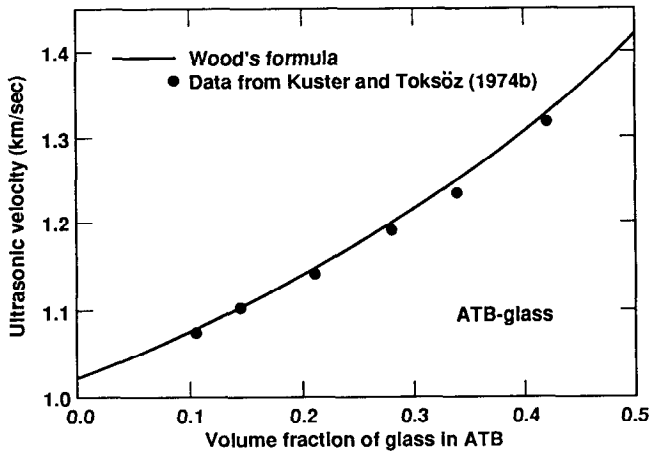

Fig. 8. Ultrasonic velocities in acetylene tetrabromide (ATB) with suspended particles of glass. Data from Kuster and Toksöz [56].

K_{grain} is the bulk modulus of the granular material of which the porous frame is constituted, while $K_{drained}$ is the bulk modulus of the porous solid frame defined by

$$\frac{1}{K_{drained}} = -\frac{1}{V}\left(\frac{\partial V}{\partial p_d}\right)_{p_f}. \tag{75}$$

V is the total volume of the sample. The differential pressure $p_d = p_c - p_f$ is the difference between the external (confining) pressure p_c and the fluid pressure p_f. The constant $K_{drained}$ is sometimes known (see Stoll [90]) as the "jacketed bulk modulus." The constant $K_{undrained}$ is also sometimes known as the "confined" modulus or as the "saturated" modulus.

6.1.2. Inhomogeneous frame (two or more minerals). When the porous solid composing the frame is not microhomogeneous, Gassmann's equation is no longer strictly applicable, although it is commonly applied by introducing an averaged bulk modulus for K_{grain} in the formulas. This procedure is not quite correct however. Rigorous generalizations of Gassmann's equation have been discussed by Brown and Korringa [20] and Rice and Cleary [81].

The result for $K_{undrained}$ is again of the form

$$K_{undrained} = K_{drained} + (1 - K_{drained}/K_s)^2 M, \tag{76}$$

where now

$$\frac{1}{M} = \phi\left(\frac{1}{K_f} - \frac{1}{K_\phi}\right) + \frac{(1 - K_{drained}/K_s)}{K_s} \tag{77}$$

and

$$C = (1 - K_{drained}/K_s)M. \tag{78}$$

The frame constant $K_{drained}$ is defined as before in (75) and K_s and K_ϕ are defined by

$$\frac{1}{K_s} = -\frac{1}{V}\left(\frac{\partial V}{\partial p_f}\right)_{p_d}, \tag{79}$$

and

$$\frac{1}{K_\phi} = -\frac{1}{V_\phi}\left(\frac{\partial V_\phi}{\partial p_f}\right)_{p_d}, \tag{80}$$

where $V_\phi = \phi V$ is the pore volume. The modulus K_s is sometimes called (see Stoll [90]) the "unjacketed bulk modulus." The modulus K_ϕ is the effective bulk modulus of the pore volume.

6.2. Bounds

6.2.1. Microhomogeneous frame. Since the Voigt and Reuss bounds show that $0 \le K_{drained} \le (1-\phi)K_{grain}$ and since the right hand side of (72) is a monotonically increasing function of $K_{drained}$, it is straightforward to show that

$$\left(\frac{\phi}{K_f} + \frac{1-\phi}{K_{grain}}\right)^{-1} \le K_{undrained} \le \phi K_f + (1-\phi)K_{grain}. \tag{81}$$

Thus, $K_{undrained}$ is bounded above and below by appropriate Voigt and Reuss bounds.

As a function of K_{grain}, $K_{undrained}$ is also a monotonically increasing function of K_{grain}. Using the fact that $K_{drained}/(1-\phi) \le K_{grain} \le \infty$, we find

$$\phi K_f \le K_{undrained} - K_{drained} \le K_f/\phi. \tag{82}$$

6.2.2. Inhomogeneous frame. Since $K_{undrained}$ is a monotonically increasing function of $K_{drained}$, we obtain bounds on $K_{undrained}$ by considering the inequalities $0 \le K_{drained} \le (1-\phi)K_s$, where the lower bound is rigorous and the upper bound is empirical. We find that

$$\left[\frac{1}{K_s} + \phi\left(\frac{1}{K_f} - \frac{1}{K_\phi}\right)\right]^{-1} \le K_{undrained} \le (1-\phi)K_s + \phi\left[\frac{1}{K_f} + \left(\frac{1}{K_s} - \frac{1}{K_\phi}\right)\right]^{-1} \tag{83}$$

which reduces to (81) if $K_s = K_\phi = K_{grain}$.

TABLE 9. Material constants for constituents of some solid/fluid mixtures. Data from Plona [77] and Murphy [69].

Constituent	*Velocity* V_+ (km/sec)	*Velocity* V_s (km/sec)	*Density* ρ (g/cc)	*Bulk Modulus* K (GPa)	*Shear Modulus* μ (GPa)
Water	1.49	—	0.997	2.2	—
Air	0.32	—	0.0012	1.2×10^{-4}	—
Glass	5.69	3.46	2.48	40.7	29.7
Sand grains	5.08	3.07	2.65	35.0	25.0

Since $K_{undrained}$ is also a monotonically increasing function of K_s if $M \leq K_s$ (which is generally true), we can obtain bounds on $K_{undrained}$ by considering $K_{drained}/(1-\phi) \leq K_s \leq \infty$, where the lower bound is empirical and the upper bound is rigorous. We find that

$$\phi^2 \left[\phi\left(\frac{1}{K_f} - \frac{1}{K_\phi}\right) + \frac{(1-\phi)}{K_{drained}}\right]^{-1} \leq K_{undrained} - K_{drained} \leq \left[\phi\left(\frac{1}{K_f} - \frac{1}{K_\phi}\right)\right]^{-1}. \quad (84)$$

If K_ϕ is positive, thermodynamic stability [12] requires that $\phi K_s/(1 - K_{drained}/K_s) \leq K_\phi \leq \infty$. The generalized Gassmann formula for $K_{undrained}$ is also a monotonically decreasing function of K_ϕ, so we find

$$\left(\frac{\phi}{K_f} + \frac{(1 - K_{drained}/K_s)}{K_s}\right)^{-1} \leq \frac{K_{undrained} - K_{drained}}{(1 - K_{drained}/K_s)^2} \leq K_f/\phi. \quad (85)$$

6.3. Estimates

Various approximations for the coefficients in the equations of poroelasticity have been discussed by Budiansky and O'Connell [25, 26], Thomsen [94], and Berryman [9].

6.4. Examples

We consider two examples of applications of Biot's theory to real porous materials. Since both cases involve ultrasonic experiments, equation (68) must be generalized to take account of some higher frequency effects. To do this, we introduce the Fourier transform (assuming time dependence of the form $\exp -i\omega t$) of both (67) and (68), and then replace the coefficient of the first term in (68) so we have

$$-\omega^2 [q(\omega)\mathbf{w} + \rho_f \mathbf{u}] = -\nabla p_f, \quad (86)$$

where the coefficient

$$q(\omega) = \frac{\tau \rho_f}{\phi} + iQ(\xi)\frac{\rho_f \eta}{\kappa\omega}. \quad (87)$$

The electric tortuosity is τ. The definition of the complex function $Q(\xi)$ may be found in Biot [15]. The argument $\xi = (\omega h^2/\eta)^{\frac{1}{2}}$ depends on a length parameter h playing the role of hydraulic radius.

Some of the constituent data required for these examples is displayed in Table 9.

6.4.1. Fluid-saturated porous glass. Plona [77] observed two distinct compressional waves in a water-saturated, porous structure made from sintered glass beads (see Table 10). The speeds predicted by Biot's equations of poroelasticity are compared to the values observed by Plona shown in Figure 9.

The input parameters to the model are $K_s = 40.7$ GPa, $\mu_s = 29.7$ GPa, $\rho_s = 2.48$ g/cc, $K_f = 2.2$ GPa, $\rho_f = 1.00$ g/cc, $\nu = 1.00$ centistoke, and $\omega = 2\pi \times 500$ kHz. The frame moduli K and μ were calculated assuming spherically shaped glass particles and needle-shaped inclusions of voids. We use $\tau = \phi^{-\frac{1}{2}}$ for the tortuosity. The permeability variation with porosity was taken to obey the Kozeny-Carman relation

$$\kappa = const \times \phi^3/(1-\phi)^2, \quad (88)$$

which has been shown empirically to provide a reasonable estimate of the porosity variation of permeability. We choose $\kappa_0 = 9.1 \times 10^{-8}$ cm^2 ($\simeq 9.1$ D) at $\phi_0 = 0.283$ and then use (88) to compute the value of κ for all other porosities considered. No entirely satisfactory model for the characteristic length h has been

TABLE 10. Values of poroelastic wave speeds in porous glass at 2.25 MHz. All velocities have dimensions of km/sec. Data from Plona [77], Johnson and Plona [53], and Plona and Johnson [78].

Porosity	*Experiment*	*Theory*	*Experiment*	*Theory*	*Experiment*	*Theory*
ϕ	V_+	V_+	V_s	V_s	V_-	V_-
0.000	5.69	5.69	3.46	3.46	—	0.00
0.075	5.50	5.33	3.31	3.22	—	0.52
0.105	5.15	5.17	2.97	3.12	0.58	0.65
0.162	4.83	4.86	2.68	2.92	0.70	0.77
0.185	4.84	4.72	2.93	2.83	0.82	0.79
0.219	4.60	4.50	2.68	2.68	0.88	0.82
0.258	4.18	4.22	2.50	2.50	1.00	0.85
0.266	3.98	4.15	2.21	2.46	0.94	0.86
0.283	4.05	4.02	2.37	2.36	1.04	0.87
0.335	3.19	3.53	1.68	2.04	0.99	0.90
0.380	2.81	3.01	1.41	1.67	0.96	0.90

found. However, dimensional analysis suggests that h^2 must be comparable to κ, so we have taken

$$h^2/\kappa = h_0^2/\kappa_0 = const. \tag{89}$$

At $\phi_0 = 0.283$, we choose $h_0 = 0.02$ mm corresponding to an average pore radius $\frac{1}{5}$ to $\frac{1}{7}$ of the grain radius (the glass beads in Plona's samples were 0.21–0.29 mm in diameter before sintering).

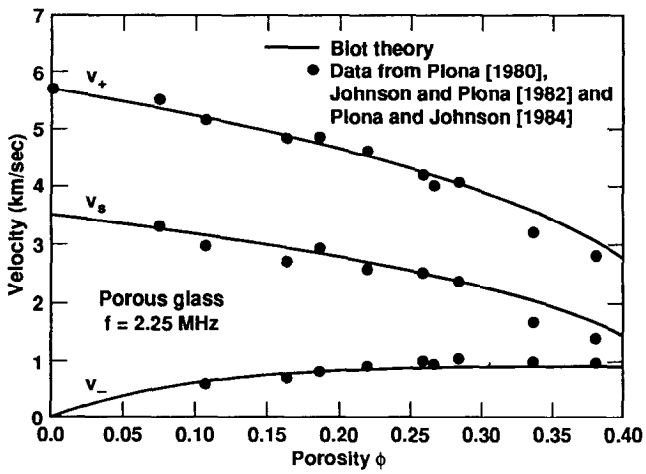

Fig. 9. Ultrasonic velocities (slow compressional – v_-, shear – v_s, fast compressional – v_+) in water-saturated porous glass. Theoretical curves from Biot's theory as described in the text. Data from Plona [77], Johnson and Plona [53], and Plona and Johnson [78].

The theoretical results for the fast compressional wave and the shear wave agree with Plona's measurements within the experimental error (±3% relative error in measured speeds and and an absolute error of ±0.005 in measured porosity).

6.4.2. Massilon sandstone. Murphy [69] has presented data on compressional and shear velocities in partially saturated Massilon sandstone. To calculate the expected behavior of the compressional and shear velocities as a function of water content, the pore fluid is taken to be a water/air mixture with bulk modulus given by the harmonic mean and density given by the volume average as in Wood's formula. The parameters used in the calculations are $K = 1.02$ GPa, $\mu = 1.44$ GPa, $K_s = 35.0$ GPa, $\mu_s = 25.0$ GPa, $\rho_s = 2.65$ g/cc, $K_l = 2.25$ GPa, $\rho_l = 0.997$ g/cc, $K_g = 1.45 \times 10^{-4}$ GPa, $\rho = 1.20 \times 10^{-3}$ g/cc, $\phi = 0.23$, $\kappa = 260$ mD, $h = 15\mu$m, and $\omega = 2\pi \times 560$ Hz. The electrical tortuosity has value $\tau = 2.76$. The values of K and μ for the frame were chosen to fit the experimental data at full water saturation. The remaining points of the theoretical curve (the solid lines) in Figure 10 follow without further adjustment of parameters. The agreement between theory and experiment is quite good for this example. The observed agreement is as much a confirmation of Wood's formula as it is of the equations of poroelasticity.

7. FLUID PERMEABILITY (DARCY'S CONSTANT)

A qualitative difference between fluid permeability (also known as hydraulic conductivity or Darcy's constant) and other transport properties such as electrical or thermal conductivity is that the pertinent macroscopic equation (Darcy's law) does not have the same form as the microscopic equation (Navier-Stokes equation).

A porous medium of total volume V filled with a fluid occupying the pore volume V_ϕ has an applied stress tensor Π_{ij} known on the exterior boundary. The applied stress takes the form

$$\Pi_{ij} = -p_f \delta_{ij} + \tau_{ij}, \tag{90}$$

where the viscosity tensor τ_{ij} is related to the fluid velocity field v_i by

$$\tau_{ij} = \rho_f \eta (v_{i,j} + v_{j,i}) \quad \text{for} \quad i,j = 1,2,3. \tag{91}$$

In this notation, i and j index the directions in a cartesian coordinate system ($x = x_1$, $y = x_2$, $z = x_3$) and the subscript appearing after a comma refers to a partial derivative: thus, $v_{2,3} = \partial v_2 / \partial z$. The fluid pressure is p_f and the fluid viscosity is $\rho_f \eta$. The energy dissipation in the fluid is given by [57]

$$\mathcal{D} = \frac{1}{2\rho_f \eta V} \int_{V_\phi} \tau_{i,j} \tau_{i,j} \, d^3x \geq 0, \tag{92}$$

where the summation convention is assumed for repeated indices in (92).

Neglecting body forces (*e.g.*, gravity) and supposing the macroscopic applied pressure gradient arises due to the pressure difference ΔP across a distance ΔZ in the direction $\hat{z}$, the relationship between the microscopic stresses and the macroscopic forces is given by

$$\mathcal{D} = \frac{\kappa}{\rho_f \eta} \left(\frac{\Delta P}{\Delta Z} \right)^2 \tag{93}$$

or equivalently

$$\mathcal{D} = -\mathbf{J} \cdot \hat{z} \frac{\Delta P}{\Delta Z}, \tag{94}$$

where $\mathbf{J}$ is the volumetric flow rate per unit area and

$$\mathbf{J} = -\hat{z} \frac{\kappa}{\rho_f \eta} \frac{\Delta P}{\Delta Z} = -\frac{\kappa}{\rho_f \eta} \nabla p_f. \tag{95}$$

Equation (95) is Darcy's law in the absence of body forces. The new constant appearing in (93) and (95) is the fluid permeability or Darcy's constant κ. Although the macroscopic equation (95) has the same form as that discussed in Section 2, the fact that the microscopic equation has a different form from that of the macroscopic equation makes it essential to perform a separate analysis for this problem. A key difference is the no-slip boundary condition for fluid flow through porous media.

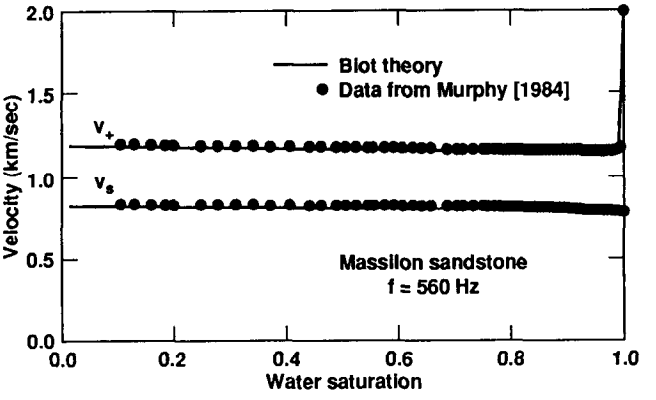

Fig. 10. Ultrasonic velocities (shear – v_s, fast compressional – v_+) in partially saturated Massilon sandstone. Theoretical curves from Biot's theory as described in the text. Data from Murphy [69].

General references on fluid flow through porous media are Bear [4], Dullien [33], and Adler [1].

7.1. Bounds

Most bounds on fluid permeability [10, 84] require knowledge of the geometrical arrangement of solid material and are therefore beyond the scope of the present review.

One exception to this rule is the variational bound of Weissberg and Prager [109] derived for a particularly simple model of a random composite called the "penetrable sphere model." The penetrable sphere model is a theoretical construct for which exact information is available about the statistics of the microgeometry [96]. The model is constructed by throwing points randomly in a box and then letting spheres grow around the points until the desired porosity is reached. The result of Weissberg and Prager [109] is

$$\kappa \leq -\frac{2}{9} \frac{\phi R^2}{\ln \phi}, \tag{96}$$

where R is the radius of the spheres and ϕ is the porosity.

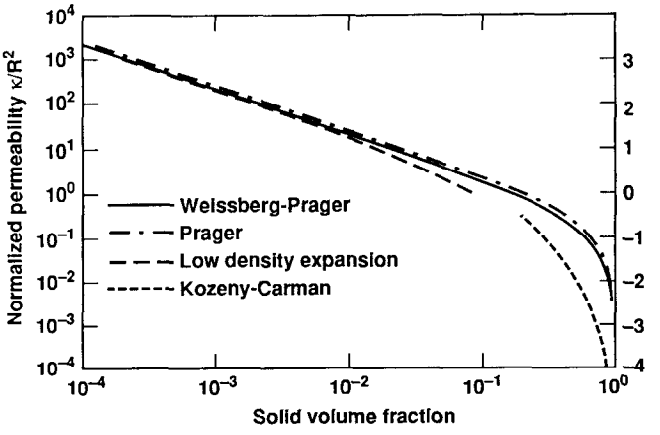

Fig. 11. Bounds and estimates on normalized permeability κ/R^2 for the penetrable sphere model. Various equations used are defined in the text.

7.2. Estimates

7.2.1. Kozeny-Carman model. Empirical formulas for fluid permeability associated with the names of Kozeny and Carman are common [74,103]. One typical example of such a formula is

$$\kappa = \frac{\phi^2}{2s^2F}, \tag{97}$$

where ϕ is the porosity, s is the specific surface area for an equivalent smooth-walled pore, and F is the electrical formation factor (ratio of the conductivity of a saturating pore fluid to the overall conductivity of the saturated sample).

7.2.2. Series expansion method. Among the well-known estimates of permeability are those due to Brinkman [19], Childress [28], Howells [50], and Hinch [49]. The low density expansion for the permeability of a random assemblage of hard spheres has the form

$$\kappa_{Stokes}/\kappa = 1 + \frac{3}{\sqrt{2}}(1-\phi)^{\frac{1}{2}} + \frac{135}{64}(1-\phi)\ln(1-\phi) + 16.5(1-\phi) + \ldots, \tag{98}$$

where the exact result for Stokes flow through a dilute assemblage of spheres of radius R is

$$\kappa_{Stokes} = \frac{2R^2}{9(1-\phi)}. \tag{99}$$

7.3. Examples

7.3.1. Penetrable sphere model. Results for the penetrable sphere model [96] are shown in Figure 11. The solid volume fraction is $1-\phi$ and κ/R^2 is the normalized permeability, where R is the radius of the spheres in the model. The Kozeny-Carman empirical relation used in the plot is

$$\kappa_{Stokes}/\kappa_{KC} = 10(1-\phi)/\phi^3, \tag{100}$$

where the Stokes permeability in a dilute assemblage of spheres of radius R is given by (99). The formula of Weissberg and Prager [109] appears in (96), while the results for the Prager [79] bound have been taken from numerical results found in Berryman and Milton [10]. The series expansion results are given by (98).

Acknowledgments. I thank P. A. Berge, G. M. Mavko, G. W. Milton, and R. W. Zimmerman for helpful conversations. This work was performed under the auspices of the U. S. Department of Energy by the Lawrence Livermore National Laboratory under contract No. W-7405-ENG-48 and supported specifically by the Geosciences Research Program of the DOE Office of Energy Research within the Office of Basic Energy Sciences, Division of Engineering and Geosciences.

REFERENCES

1. Adler, P. M., *Porous Media - Geometry and Transports*, 544 pp., Butterworth-Heinemann, Boston, MA, 1992.
2. Backus, G. E., Long-wave elastic anisotropy produced by horizontal layering, *J. Geophys. Res.*, *67*, 4427–4440, 1962.
3. Batchelor, G. K., Transport properties of two-phase materials with random structure, in *Annual Reviews of Fluid Mechanics*, Vol. 6, edited by M. Van Dyke, W. G. Vincenti, and J. V. Wehausen, pp. 227–255, Annual Reviews, Palo Alto, CA, 1974.
4. Bear, J., *Dynamics of Fluids in Porous Media*, 764 pp., Elsevier, New York, 1972.
5. Beran, M. J., *Statistical Continuum Theories*, 424 pp., Wiley, New York, 1968.
6. Bergman, D. J., The dielectric constant of a composite material - A problem in classical physics, *Physics Reports*, *43*, 377–407, 1978.
7. Berryman, J. G., Long-wavelength propagation in composite elastic media, *J. Acoust. Soc. Am.*, *68*, 1809–1831, 1980.
8. Berryman, J. G., Effective medium theory for elastic composites, in *Elas-*

tic Wave Scattering and Propagation, edited by V. K. Varadan and V. V. Varadan, pp. 111–129, Ann Arbor Science, Ann Arbor, Michigan, 1982.

9. Berryman, J. G., Single-scattering approximations for coefficients in Biot's equations of poroelasticity, *J. Acoust. Soc. Am.*, *91*, 551–571, 1992.

10. Berryman, J. G., and G. W. Milton, Normalization constraint for variational bounds on fluid permeability, *J. Chem. Phys.*, *83*, 754–760, 1985.

11. Berryman, J. G., and G. W. Milton, Microgeometry of random composites and porous media, *J. Phys. D: Appl. Phys.*, *21*, 87–94, 1988.

12. Berryman, J. G., and G. W. Milton, Exact results for generalized Gassmann's equations in composite porous media with two constituents, *Geophysics*, *56*, 1950–1960, 1991.

13. Biot, M. A., Thermoelasticity and irreversible thermodynamics, *J. Appl. Phys.*, *27*, 240–253, 1956a.

14. Biot, M. A., Theory of propagation of elastic waves in a fluid-saturated porous solid. I. Low-frequency range, *J. Acoust. Soc. Am.*, *28*, 168–178, 1956b.

15. Biot, M. A., Theory of propagation of elastic waves in a fluid-saturated porous solid. II. Higher frequency range, *J. Acoust. Soc. Am.*, *28*, 179–191, 1956c.

16. Biot, M. A., Mechanics of deformation and acoustic propagation in porous media, *J. Appl. Phys.*, *33*, 1482–1498, 1962.

17. Bourbié, T., O. Coussy, and B. Zinszner, *Acoustics of Porous Media*, 334 pp., Chapter 3, Gulf, Houston, 1987.

18. Brace, W. F., Some new measurements of linear compressibility of rocks, *J. Geophys. Res.*, *70*, 391–398, 1965.

19. Brinkman, H. C., A calculation of the viscous force exerted by a flowing fluid on a dense swarm of particles, *Appl. Sci. Res.*, *A1*, 27–34, 1947.

20. Brown, R. J. S., and J. Korringa, On dependence of the elastic properties of a porous rock on the compressibility of a pore fluid, *Geophysics*, *40*, 608–616, 1975.

21. Brown, W. F., Jr., Dielectric constants, permeabilities, and conductivities of random media, *Trans. Soc. Rheol.*, *9*, 357–380, 1965.

22. Bruggeman, D. A. G., Berechnung verschiedener physikalischer Konstanten von heterogenen Substanzen, *Ann. Physik. (Leipzig)*, *24*, 636–679, 1935.

23. Budiansky, B., On the elastic moduli of some heterogeneous materials, *J. Mech. Phys. Solids*, *13*, 223–227, 1965.

24. Budiansky, B., Thermal and thermoelastic properties of isotropic composites, *J. Comp. Mater.*, *4*, 286–295, 1970.

25. Budiansky, B., and R. J. O'Connell, Elastic moduli of dry and saturated cracked solids, *Int. J. Solids Struct.*, *12*, 81–97, 1976.

26. Budiansky, B., and R. J. O'Connell, Bulk dissipation in heterogeneous media, in *Solid Earth Geophysics and Geotechnology*, edited by S. Nemat-Nasser, pp. 1–10, ASME, New York, 1980.

27. Burridge, R., and J. B. Keller, Poroelasticity equations derived from microstructure, *J. Acoust. Soc. Am.*, *70*, 1140–1146, 1981.

28. Childress, S., Viscous flow past a random array of spheres, *J. Chem. Phys.*, *56*, 2527–2539, 1972.

29. Christensen, R. M., *Mechanics of Composite Materials*, 348 pp., Chapter IX, pp. 311–339, Wiley, New York, 1979.

30. Chung, D.-H., Elastic moduli of single crystal and polycrystalline MgO, *Phil. Mag.*, *8*, 833–841, 1963.

31. Cleary, M. P., I.-W. Chen, and S.-M. Lee, Self-consistent techniques for heterogeneous media, *ASCE J. Eng. Mech.*, *106*, 861–887, 1980.

32. Cohen, R. W., G. D. Cody, M. D. Coutts, and B. Abeles, Optical properties of granular silver and gold films, *Phys. Rev. B*, *8*, 3689–3701, 1973.

33. Dullien, F. A. L., *Porous Media: Fluid Transport and Pore Structure*, 574 pp., Chapter 3, Academic Press, San Diego, 1992.

34. Duvall, G. E., and S. M. Taylor, Jr., Shock parameters in a two component mixture, *J. Composite Mat.*, *5*, 130–139, 1971.

35. Eshelby, J. D., The determination of the elastic field of an ellipsoidal inclusion, and related problems, *Proc. Roy. Soc. London A*, *241*, 376–396, 1957.

36. Fate, W. A., High temperature elastic moduli of polycrystalline silicon nitride, *J. Appl. Phys.*, *46*, 2375–2377, 1975.

37. Fisher, E. S., M. H. Manghnani, and J. L. Routbort, A study of the elastic properties of Al_2O_3 and Si_3N_4 matrix composites with SiC whisker reinforcement, in *High Performance Composites for the 1990's*, edited by S. K. Das, C. P. Ballard, and F. Maarikar, pp. 365–370, The Minerals, Metals and Materials Society, Warrendale, Pennsylvania, 1991.

38. Fisher, E. S., M. H. Manghnani, and J.-F. Wang, Elastic properties of Al_2O_3 and Si_3N_4 matrix composites with SiC whisker reinforcement, *J. Am. Ceramics Soc.*, *75*, 908–914, 1992.

39. Galeener, F. L., Optical evidence for a network of cracklike voids in amorphous germanium, *Phys. Rev. Lett.*, *27*, 1716–1719, 1971.

40. Gassmann, F., Über die elastizität poröser medien, *Veirteljahrsschrift der Naturforschenden Gesellschaft in Zürich*, *96*, 1–23, 1951.

41. Hale, D. K., The physical properties of composite materials, *J. Mater. Sci.*, *11*, 2105–2141, 1976.

42. Hashin, Z., Analysis of composite materials – a survey, *ASME J. Appl. Mech.*, *50*, 481–505, 1983.

43. Hashin, Z., and S. Shtrikman, Note on a variational approach to the theory of composite elastic materials, *J. Franklin Inst.*, *271*, 336–341, 1961.

44. Hashin, Z., and S. Shtrikman, A variational approach to the theory of the effective magnetic permeability of

multiphase materials, *J. Appl. Phys.*, *33*, 3125–3131, 1962a.

45. Hashin, Z., and S. Shtrikman, A variational approach to the theory of elastic behaviour of polycrystals, *J. Mech. Phys. Solids*, *10*, 343–352, 1962b.

46. Hill, R., The elastic behaviour of crystalline aggregate, *Proc. Phys. Soc. London*, *A65*, 349–354, 1952.

47. Hill, R., Elastic properties of reinforced solids: Some theoretical principles, *J. Mech. Phys. Solids*, *11*, 357–372, 1963.

48. Hill, R., A self-consistent mechanics of composite materials, *J. Mech. Phys. Solids*, *13*, 213–222, 1965.

49. Hinch, E. J., An averaged-equation approach to particle interactions, *J. Fluid Mech.*, *83*, 695–720, 1977.

50. Howells, I. D., Drag due to the motion of a Newtonian fluid through a sparse random array of small fixed rigid objects, *J. Fluid Mech.*, *64*, 449–475, 1974.

51. Hudson, J. A., Overall properties of heterogeneous material, *Geophys. J. Int.*, *107*, 505–511, 1991.

52. Jackson, J. D., *Classical Electrodynamics*, pp. 118–119, Wiley, New York, 1962.

53. Johnson, D. L., and T. J. Plona, Acoustic slow waves and the consolidation transition, *J. Acoust. Soc. Am.*, *72*, 556–565, 1982.

54. Johnson, D. L., T. J. Plona, C. Scala, F. Pasierb, and H. Kojima, Tortuosity and acoustic slow waves, *Phys. Rev. Lett.*, *49*, 1840–1844, 1982.

55. Kuster, G. T., and M. N. Toksöz, Velocity and attenuation of seismic waves in two-phase media: Part I. Theoretical formulations, *Geophysics*, *39*, 587–606, 1974a.

56. Kuster, G. T., and M. N. Toksöz, Velocity and attenuation of seismic waves in two-phase media: Part II. Experimental results, *Geophysics*, *39*, 607–618, 1974b.

57. Landau, L. D., and E. M. Lifshitz, *Fluid Mechanics*, pp. 53–54, Pergamon, London, 1959.

58. Landauer, R., The electrical resistance of binary metallic mixtures, *J. Appl. Phys.*, *23*, 779–784, 1952.

59. Landauer, R., Electrical conductivity in inhomogeneous media, in *Electrical, Transport, and Optical Properties of Inhomogeneous Media*, edited by J. C. Garland and D. B. Tanner, pp. 2–43, Proceedings of the Conference at Ohio State University, September, 1977, American Institute of Physics, New York, 1978.

60. Laws, N., On the thermostatics of composite materials, *J. Mech. Phys. Solids*, *21*, 9–17, 1973.

61. Ledbetter, H., and M. Austin, Thermal expansion of an *SiC* particle-reinforced aluminum composite, *Int. J. Thermophys.*, *12*, 731–739, 1991.

62. Levin, V. M., Thermal expansion coefficients of heterogeneous materials, *Mech. Solids*, *2*, 58–61, 1967.

63. Mackensie, J. K., The elastic constants of a solid containing spherical holes, *Proc. Phys. Soc. London B*, *63*, 2–11, 1950.

64. McTigue, D. F., Thermoelastic response of fluid-saturated porous rock, *J. Geophys. Res.*, *91*, 9533–9542, 1986.

65. Milton, G. W., The coherent potential approximation is a realizable effective medium scheme, *Comm. Math. Phys.*, *99*, 463–500, 1985.

66. Milton, G. W., and R. V. Kohn, Variational bounds on the effective moduli of anisotropic composites, *J. Mech. Phys. Solids*, *36*, 597–629, 1988.

67. Molyneux, J. E., Effective permittivity of a polycrystalline dielectric, *J. Math. Phys.*, *11*, 1172–1184, 1970.

68. Molyneux, J. E., and M. J. Beran, Statistical properties of the stress and strain fields in a medium with small random variations in elastic coefficients, *J. Math. Mech.*, *14*, 337–351, 1965.

69. Murphy, W. F., III, Acoustic measures of partial gas saturation in tight sandstones, *J. Geophys. Res.*, *89*, 11549–11559, 1984.

70. Norris, A. N., On the correspondence betweeen poroelasticity and thermoelasticity, *J. Appl. Phys.*, *71*, 1138–1141, 1992.

71. Norris, A. N., P. Sheng, and A. J. Callegari, Effective-medium theories for two-phase dielectric media, *J. Appl. Phys.*, *57*, 1990–1996, 1985.

72. Osborn, J. A., Demagnetizing factors of the general ellipsoid, *Phys. Rev.*, *67*, 351–357, 1945.

73. Palciauskas, V. V., and P. A. Domenico, Characterization of drained and undrained response of thermally loaded repository rocks, *Water Resources Res.*, *18*, 281–290, 1982.

74. Paterson, M. S., The equivalent channel model for permeability and resistivity in fluid-saturated rocks – A reappraisal, *Mech. Mater.*, *2*, 345–352, 1983.

75. Peselnick, L., Elastic constants of Solenhofen limestone and their dependence upon density and saturation, *J. Geophys. Res.*, *67*, 4441–4448, 1962.

76. Peselnick, L., and R. Meister, Variational method of determining effective moduli of polycrystals: (A) Hexagonal symmetry and (B) trigonal symmetry, *J. Appl. Phys.*, *36*, 2879–2884, 1965.

77. Plona, T. J., Observation of a second bulk compressional wave in a porous medium at ultrasonic frequencies, *Appl. Phys. Lett.*, *36*, 259–261, 1980.

78. Plona, T. J., and D. L. Johnson, Acoustic properties of porous systems: I. Phenomenological description, in *Physics and Chemistry of Porous Media*, edited by D. L. Johnson and P. N. Sen, pp. 89–104, American Institute of Physics, New York, 1984.

79. Prager, S., Viscous flow through porous media, *Phys. Fluids*, *4*, 1477–1482, 1961.

80. Reuss, A., Berechung der Fliessgrenze von Mischkristallen, *Z. Angew. Math. Mech.*, *9*, 55, 1929.

81. Rice, J. R., and M. P. Cleary, Some basic stress diffusion solutions for fluid-saturated elastic porous media with compressible constituents, *Rev. Geo-*

phys. Space Phys., 14, 227-241, 1976.

82. Rosen, B. W., and Z. Hashin, Effective thermal expansion coefficients and specific heats of composite materials, *Int. J. Engng. Sci., 8*, 157–173, 1970.

83. Rossini, F. D., K. S. Pitzer, R. L. Arnet, R. M. Braun, and G. C. Pimentel, *Selected Values of Physical and Thermodynamic Properties of Hydrocarbons and Related Compounds*, p. 52, Carnegie Press, Pittsburgh, Pennsylvania, 1953.

84. Rubinstein, J., and S. Torquato, Flow in random porous media: mathematical formulation, variational principles, and rigorous bounds, *J. Fluid Mech., 206*, 25–46, 1989.

85. Schapery, R. A., Thermal expansion coefficients of composite materials based on energy principles, *J. Comp. Mater., 2*, 380–404, 1968.

86. Schulgasser, K., Bounds on the conductivity of statistically isotropic polycrystals, *J. Phys. C, 10*, 407–417, 1977.

87. Schulgasser, K., Thermal expansion of polycrystals, *J. Material Sci. Lett., 8*, 228–229, 1989.

88. Sen, P. N., C. Scala, and M. H. Cohen, A self-similar model for sedimentary rocks with application to the dielectric constant of fused glass beads, *Geophysics, 46*, 781–795, 1981.

89. Simmons, G., and H. Wang, *Single Crystal Elastic Constants and Calculated Aggregate Properties: A Handbook*, 300 pp. MIT Press, Cambridge, MA, 1971.

90. Stoll, R. D., Acoustic waves in saturated sediments, in *Physics of Sound in Marine Sediments*, edited by L. Hampton, pp. 19–39, Plenum, New York, 1974.

91. Stoner, E. C., The demagnetizing factors for ellipsoids, *Phil. Mag., 36*, 803 821, 1945.

92. Stroud, D., Generalized effective-medium approach to the conductiv-

Phys. Rev. B, 12, 3368–3373, 1975.

93. Thomsen, L., Elasticity of polycrystals and rocks, *J. Geophys. Res., 77*, 315–327, 1972.

94. Thomsen, L., Biot-consistent elastic moduli of porous rocks: Low-frequency limit, *Geophysics, 50*, 2797–2807, 1985.

95. Torquato, S., Random heterogeneous media: Microstructure and improved bounds on effective properties, *Appl. Mech. Rev., 44*, 37–76, 1991.

96. Torquato, S., and G. Stell, Microstructure of two-phase random media. III. The n-point matrix probability functions for fully penetrable spheres, *J. Chem. Phys., 79*, 1505–1510, 1983.

97. Turner, P. S., Thermal-expansion stresses in reinforced plastics, *J. Res. NBS, 37*, 239–250, 1946.

98. Voigt, W., *Lehrbuch der Kristallphysik*, p. 962, Teubner, Leipzig, 1928.

99. Walpole, L. J., On bounds for the overall elastic moduli of inhomogeneous systems – I., *J. Mech. Phys. Solids, 14*, 151–162, 1966a.

100. Walpole, L. J., On bounds for the overall elastic moduli of inhomogeneous systems – II., *J. Mech. Phys. Solids, 14*, 289–301, 1966b.

101. Walpole, L. J., On the overall elastic moduli of composite materials, *J. Mech. Phys. Solids, 17*, 235–251, 1969.

102. Walsh, J. B., New analysis of attenuation in partially melted rock, *J. Geophys. Res., 74*, 4333–4337, 1969.

103. Walsh, J. B., and W. F. Brace, The effect of pressure on porosity and the transport properties of rock, *J. Geophys. Res., 89*, 9425–9431, 1984.

104. Walsh, J. B., W. F. Brace, and A. W. England, Effect of porosity on compressibility of glass, *J. Am. Ceram. Soc., 48*, 605–608, 1965.

105. Wang, Z., and A. Nur, Ultrasonic velocities in pure hydrocarbons and mixtures, *J. Acoust. Soc. Am., 89*, 2725–2730, 1991.

106. Wang, Z., and A. Nur, *Seismic and Acoustic Velocities in Reservoir Rocks, Volume 2, Theoretical and Model Studies*, 457 pp., Society of Exploration Geophysicists, Tulsa, Oklahoma, 1992.

107. Watt, J. P., Elastic properties of polycrystalline minerals: Comparison of theory and experiment, *Phys. Chem. Minerals, 15*, 579–587, 1988.

108. Watt, J. P., G. F. Davies, and R. J. O'Connell, Elastic properties of composite materials, *Rev. Geophys. Space Phys., 14*, 541–563, 1976.

109. Weissberg, H. L., and S. Prager, Viscous flow through porous media. III. Upper bounds on the permeability for a simple random geometry, *Phys. Fluids, 13*, 2958–2965, 1970.

110. Willis, J. R., Variational and related methods for the overall properties of composites, in *Advances in Applied Mechanics*, Vol. 21, edited by C.-S. Yih, pp. 1–78, Academic Press, New York, 1981.

111. Wood, A. W., *A Textbook of Sound*, p. 360, Bell, London, 1955.

112. Wu, T. T., The effect of inclusion shape on the elastic moduli of a two-phase material, *Int. J. Solids Struct., 2*, 1–8, 1966.

113. Wyllie, M. R. J., A. R. Gregory, and L. W. Gardner, Elastic wave velocities in heterogeneous and porous media, *Geophysics, 21*, 41–70, 1956.

114. Wyllie, M. R. J., A. R. Gregory, and G. H. F. Gardner, An experimental investigation of factors affecting elastic wave velocities in porous media, *Geophysics, 23*, 459–493, 1958.

115. Zimmerman, R. W., Elastic moduli of a solid containing spherical inclusions, *Mech. Mater., 12*, 17–24, 1991.

116. Zimmerman, R. W., Hashin-Shtrikman bounds on the Poisson ratio of a composite material, *Mech. Res. Commun., 19*, 563–569, 1992.

Subject Index